University of Nottingham
UK | CHINA | MALAYSIA

Photophysics in Conventional and Supercritical Fluids:

Excited State Dynamics and Sensing Applications

Bethany Sarah Adams (MSci)

Thesis submitted to the University of Nottingham for the degree of Doctor of Philosophy

Date Submitted: May 2017

Declaration

I hereby declare that all the work contained in this Thesis has been undertaken by myself, unless acknowledged otherwise.

Bethany Adams

Date: 21/08/2017

Nottingham

Acknowledgements

First and foremost I would like to thank my supervisor Mike George for all his help and support throughout this process. I am grateful for his unwavering optimism and good sense of humour.

I owe an inordinate amount of thanks to Drs. Raphael Horvath and Ashley Love, who have taught me so much and answered all my questions with so much patience. Their help and advice has made this work possible. I would also like to thank Drs. Charlotte Clark, Han Xue, Zac Amara, Alisdair Wriglesworth and Darren Lee for all their help and support.

I thank Dr Xue-Zhong Sun for all his help with the ultrafast TRIR experiments in Nottingham. I am grateful to all the staff at the ULTRA facility at the Rutherford Appleton Laboratory for their help with ultrafast experiments. I am also grateful to Dr Stephen Davies for his help with the electrochemistry measurements. I thank the University of Nottingham's workshop including Clive Dixon, Peter Fields, Richard Wilson and Dave Litchfield, whose ability to design and create the equipment used within this Thesis has made the work possible, and their knack for fixing it with such patience after I inevitably broke it.

I thank my collaborators for their help throughout this thesis including Prof. Keith Gordon, Drs. Chris Larsen, James Crowley and Greg Huff, and Georgina Shillito at the University of Otago. Similar thanks goes to everyone involved in the SCFED project. I also thank my two 4th year Masters Project students, Katherine Reynolds and Elizabeth Hampson whose work has contributed to this thesis.

I thank all members of the George group both past and present for making these years so enjoyable including Ashley, Calum, Charlotte, Charlotte, Dave, Han Xue, Jack, Paul, Raph, Tom, Wu Xue, Zac and Katie, the latter of whom I credit for helping to keep my sanity. Their friendship and kindness has been invaluable over the years.

I also thank my family and friends for their continued love and support throughout my studies. I am especially thankful to my parents, whose love and encouragement has helped me be where I am today. Also to my grandparents for their love and support which has helped me immeasurably and to my brothers and Dónal for always lifting my spirits. Finally, I thank Alisdair for his love, patience and ability to always look on the bright side.

Abstract

Chapter 1

This Chapter gives a brief introduction to photophysics and the study of excited states. The technique of time-resolved infrared spectroscopy (TRIR), which is used throughout this Thesis to ascertain the nature of excited states, is also introduced. The utility of the techniques to examine the nature and kinetics of excited states is detailed. Subsequently, the effect of solvent medium in which the measurements take place is also discussed.

Chapter 2

The photophysical properties of rhenium dipyrido[3,2-*a*:2',3'-*c*]phenazine complexes appended with diphenylamine (NPh_2) groups have been investigated through the use of a range of techniques, including time-resolved infrared spectroscopy, cyclic voltammetry and DFT calculations.

The effect of the diphenylamine donor group has been assessed with comparisons drawn between [Re(dppz-NPh_2)$(CO)_3$Cl] and [Re(dppz)$(CO)_3$Cl]. The addition of the donor group results in the observation of three ligand centred excited states in the TRIR spectra, unlike the MLCT states observed for [Re(dppz)$(CO)_3$Cl]. These states exhibit a complex interplay, whereby States I and III are initially formed, and the former decays to State II on the picosecond timescale. States II and III are then observed to decay to the ground state on the microsecond and nanosecond timescales respectively. A detailed assignment of these states is given, with States I and II assigned to ^{1}IL$\pi\pi^*$ and ^{3}IL$\pi\pi^*$ states respectively. State III was assigned to a $NPh_2(\pi)$phz(π^*) charge transfer state. Good evidence of the presence of three distinct states has been obtained through TRIR measurements conducted in the fingerprint region, where a marker band for State II has been observed. The molecular orbital calculations performed on the complexes indicate charge transfer character, where the highest occupied molecular orbital is observed to

be based on the NPh_2 ligand, unlike for $[Re(dppz)(CO)_3Cl]$ complexes where the highest energy occupied molecular orbitals are normally metal based. The lifetime of the charge transfer state is shown to be relatively independent of the number of NPh_2 donors appended, where a similar lifetime is observed for $[Re(dppz\text{-}PhNPh_2)(CO)_3Cl]$ and $[Re(dppz\text{-}(PhNPh_2)_2)(CO)_3Cl]$.

The effect of the bridge type between the NPh_2 donor and phz acceptor has also been investigated. This work details the effects on all three excited states, with the charge transfer state of most interest. The effect of the bridge length has been assessed through study of phenyl-moiety bridges which possess varying lengths. It was observed that as the bridge length increased, the lifetime of the charge transfer state decreased, and this has been attributed to an increased level of insulator character. The nature of the bridge has been investigated, where phenyl, thiophene and triazole bridge moieties have been compared to an analogous complex without a bridge. The results indicated that insulator character of the bridges increases as follows, thiophene < phenyl < triazole, and this chantes the lifetimes of the charge transfer states of the resulting complexes by a factor of 100.

Chapter 3

The photophysical properties of rhenium dipyrido[3,2-*a*:2',3'-*c*]phenazine complexes modified on the phenazine like portions of the ligands have been investigated through the use of time resolved infrared spectroscopy and DFT calculations.

Firstly, substitution with a nitrogen heteroatom at the ortho (2) and meta (3) positions (the phenazine like part of the ligand), resulting in $[Re(dppp2)(CO)_3Cl]$, $[Re(dppp3)(CO)_3Cl]$ and $[Re(dppp2Br)(CO)_3Cl]$ respectively, has been investigated. The additional nitrogen atom is observed to lower the energy of the molecular orbital based on the phenazine portion of the ligand and resulting in the population of an MCLT(phz) state. A marker band for the MLCT(phz) state has been assigned in the fingerprint region, a spectral region which has proven important to ascertain the nature of these

excited states. The position of the nitrogen atom was also found to be significant, where substitution at the meta-position, [Re(dppp3)$(CO)_3$Cl], is observed to lower the phz energy to a greater extent than in the ortho-position, [Re(dppp2)$(CO)_3$Cl].

The effect of the solvent on the rate of the MLCT(phen)/MLCT(phz) states interconversion was found to be negligible, which is unlike observations made for [Re(dppz)$(CO)_3$Cl]. However the nature of the most stable excited state was observed to change significantly. For the most polar solvent (DMSO, ε_r = 46.7), the most stable excited states is best described as an equilibrium of MLCT(phz)/IL$\pi\pi^*$ states, and for the lowest polarity solvent (toluene, ε_r = 2.3) the lowest excited state is MLCT(phen). Additionally, the excited state lifetime is observed to increase with decreasing solvent polarity. This has been attributed to a greater MLCT(phen) contribution observed in lower polarity media.

The bromine substitution also has an effect on the excited state, where [Re(dppp2Br)$(CO)_3$Cl] exhibits a lower energy phz state than for [Re(dppp2)$(CO)_3$Cl]. This is further investigated with the previously unreported complex [Re(dppz-I)$(CO)_3$Cl] and compared to other [Re(dppz-X)$(CO)_3$Cl] complexes.

Finally, the effect of amine substituents has been investigated by studying the complex [Re(dpppn-$(NH_2)_2$)$(CO)_3$Cl] (amine substitution is at the 2nd and 4th positions of the phenazine like ligand) in a range of solvents, with dielectric constants ranging from 2.3 to 46.7 and again this was supplemented by DFT calculations. Comparisons have been made to the complexes detailed in Chapter 2, and to the [Re(dppp2)$(CO)_3$Cl] and [Re(dppp3)$(CO)_3$Cl] complexes. The TRIR spectral profile of the complex in the highest dielectric solvent is observed to be similar to the complexes in Chapter 2 and is assigned as a ^{1}IL$\pi\pi^*$ state decaying to a ^{3}IL$\pi\pi^*$ state. A marker band for the ^{3}IL$\pi\pi^*$ state is observed in the fingerprint region and is comparable to the State II ^{3}IL$\pi\pi^*$ marker band from Chapter 2 for the [Re(dppz-NPh_2)$(CO)_3$Cl] complexes. The nature of the excited states are observed to change with the solvent medium and these results are discussed.

Chapter 4

The photophysical properties of the nitro-appended rhenium dipyrido[3,2-*a*:2',3'-*c*]phenazine complexes [Re(dppz-12-NO_2)$(CO)_3$Cl] and [Re(dppz-13-NO_2)$(CO)_3$Cl], have been comprehensively investigated through time resolved infrared, cyclic voltammetry and DFT calculations.

The electron withdrawing nitro-group is observed to lower the energy of the MLCT(phz) state compared to the unsubstituted complex. Furthermore, significant NO_2 contribution in the excited state is observed, where the first reduction potential is considerably more positive than that observed for [Re(dppz)$(CO)_3$Cl]. Therefore the radical anion is located on the phz like portion of the molecule with a significant contribution from the NO_2 group. This is consistent with the molecular orbital calculations and the one electron reduced species absorption spectra in this Chapter.

Furthermore, the 12-substituted nitro-group is shown to have a stronger electron withdrawing effect than the corresponding 13-substituted nitro-group. This has been attributed to an increase in resonance effects associated with the 12-position and is correlated to the dihedral angle between the NO_2 group and the phz moiety.

Chapter 5

The photophysical properties of rhenium diimine dyes in apolar media have been investigated in Chapter 5. As a result of poor solubility, photophysical studies of [Re(dppz)$(CO)_3$L]$^+$ and [Re(bpy)$(CO)_3$L]$^+$ complexes have been limited to higher polarity media. The ability to investigate organometallic dyes in apolar media opens up a range of avenues, including CO_2 reduction without the need for a co-solvent. This Chapter explores these well reported complexes in the previously unstudied apolar media. The use of the large fluorinated anion of tetrakis[3,5-bis(perfluorohexyl)phenyl]borate has been implemented to yield the complexes [Re(dppz)$(CO)_3$(DMAP)][BAr^{f6}] and [Re(bpy)$(CO)_3$(DMAP)][BAr^{f6}]. Their photophysical properties have been investigated

in perfluoromethylcyclohexane (ε_r 1.8) through TRIR, absorption and emission spectroscopies, and DFT calculations.

$[Re(dppz)(CO)_3(DMAP)][BAr^{f6}]$ was shown to exhibit a long lived IL$\pi\pi^*$ state in perfluoromethyl cyclohexane. This state differs significantly from the IL$\pi\pi^*$/MLCT(phen) states observed for $[Re(dppz)(CO)_3(DMAP)]^+$ complexes in more conventional polar media.

Chapter 6

The drive for smaller technology is a foremost requirement in the fabrication of electrical devices which possess greater processing power. This Chapter discusses supercritical fluid electrodeposition as a fabrication method, along with its desirable properties which are also detailed. In order to guide the SCFED process, further understanding of fluid behaviour within the nanoporous templates employed is vital. The work within this Chapter focusses on the development and implementation of a method for high pressure luminescence spectroscopy to probe confined fluid behaviour.

Luminescence spectroscopy of high pressure fluids confined within nanoporous templates has not previously been investigated. Therefore, the first section of this Chapter focusses on the development of a methodology in order to conduct luminescence measurements of supercritical fluids confined within nanopores. This includes an investigation into an appropriate dye, and the design of the high pressure apparatus required for luminescence measurements within porous materials.

Anthracene and 5,10,15,20-tetrakis(pentafluorophenyl)porphyrin have been identified as suitable luminescence probes for the measurements required. Following this, the density of CO_2 under bulk conditions has been probed with both dyes. The former is observed to exhibit a solvatochromic shift in the emission, and the latter a change in the peak intensity with CO_2 density. This has allowed for the calibration of the probe dye behaviour with CO_2 density.

The density of CO_2 confined within nanoporous templates, possessing mean pore widths of 8.3, 4.5 and 3.2 nm are investigated. The results show that the density of CO_2 is considerably higher in the confined environment than in the bulk. The results are consistent between the two dyes indicating that luminescence spectroscopy is a valid method to probe fluid behaviour both in bulk and confined environments.

Finally, the use of luminescence measurements to elucidate fluid polarisability has been explored. An investigation towards quantifying fluid polarisability of CO_2 when confined within the porous templates have been discussed. This includes the implementation of an anthracene dye to probe the polarisability of bulk CO_2 conditions. These results are then compared to the literature. Subsequently, the method was used to elucidate the fluids polarisability. The polarisability of CO_2 within the confines of the porous materials was observed to increase with increasing bulk CO_2 pressure.

Chapter 7

This Chapter summarises the results obtained within this work and outlines the implications that these results may have. This is followed by a detailed future outlook, including suggested avenues of study that may arise from this Thesis.

Chapter 8

The apparatus and methodology developed to carry out this work is detailed, including the methodology for the high pressure luminescence spectroscopic measurements. The spectroscopic techniques used throughout this Thesis are detailed including descriptions of the equipment, procedures and materials used.

Contents

Acknowledgements iv

Abstract v

Abbreviations xv

Chapter 1 1

Introduction 1

1 Photophysics 1

2 Spectroscopic Techniques for Monitoring Excited States 2

2.1 Time resolved Spectroscopy 2

2.2 Luminescence Spectroscopy 4

2.3 Solvent Dependent Photophysics 5

Chapter 2 7

The Photophysical Properties of Donor-Appended Rhenium Dipyrido[3,2-*a*:2',3'-*c*]phenazine Complexes 7

1 Introduction 7

1.1 Excited States of M(dppz) Complexes 8

1.2 Tuning the Excited States of M(dppz) Complexes 12

1.3 Donor-Bridge-Acceptor Complexes 21

2 Aims 34

3 Results 35

3.1 Time Resolved Infrared Studies 36

3.2 Absorption Spectroscopy 54

3.3 Cyclic Voltammetry 55

3.4 Infrared Spectroelectrochemistry 56

3.5 EPR Spectroelectrochemistry 58

3.6 Molecular Orbital Calculations 60

3.7 Assignment of the Observed Excited States 63

3.8 The Photophysical Properties Observed for NPh_2 Appended Complexes 65

4 Conclusions 74

Chapter 3 77

The Photophysical Properties of Phenazine Modified Rhenium Dipyrido[3,2-*a*:2',3'-*c*]phenazine Complexes 77

1 Introduction 77

2 Aims 90

3 Results and Discussion 91

3.1 Time Resolved Infrared Spectroscopy 91

3.2 Absorption Spectra 107

3.3 Molecular Orbital Calculations 108

3.4 The Nature of the Excited States Observed 110

3.5 An Investigation into Photophysical Properties of 115

$[Re(dppz\text{-}I)(CO)_3Cl]$ 115

3.6 An Investigation into the Photophysical Properties of $[Re(dpppn\text{-}(NH_2)_2)(CO)_3Cl]$ 120

4 Conclusions 129

Chapter 4 131

The Photophysical Properties of Nitro-Appended Rhenium Dipyrido[3,2-*a*:2',3'-*c*]phenazine Complexes 131

1 Introduction 131

2 Aims 137

3 Results and Discussion 138

3.1 Absorption Spectroscopy 138

3.2 Cyclic Voltammetry 140

3.3 Infrared Spectroelectrochemistry 142

3.4 Absorption Spectroelectrochemistry 143

3.5 Time Resolved Infrared Studies 145

3.6 Molecular Orbital Calculations 155

3.7 Effect of NO_2 substitution 158

4.4 Conclusions 162

Chapter 5 163

The Photophysical Properties of Rhenium Diimine Complexes in Apolar Media 163

1 Introduction 163

2 Aims 173

3 Results and Discussion 174
3.1 Photophysical Properties of $[Re(bpy)(CO)_3(DMAP)]^+$ 177
3.2 Photophysical Properties of $[Re(dppz)(CO)_3(DMAP)]^+$ 181
3.3 Molecular Orbital calculations 187
4 Conclusions 190
Chapter 6 191
1 Introduction 191
1.1 Limitations in the Current Fabrication Methods of Nanoscale Electronics 192
1.2 Supercritical Fluid Electrodeposition 193
1.3 Supercritical Fluids 195
1.4 Probing Phase Behaviour within Porous Materials 196
1.5 Fluorescent Based Sensors in Supercritical Fluids 200
1.6 Fluorescent Sensors for Polarisability 209
1.7 Spectroscopic Cell Designs for High Pressure Measurements 213
2 Aims 218
3 Results and Discussion 219
3.1 Cell Design and Development 219
3.2 Porous Measurements Development of a Methodology in Order to Measure Emission Spectra from within the Pores 221
3.3 Towards Density Sensing of CO_2 Using Luminescence 226
3.4 Anthracene as a Density Sensor 229
6.3.5 Measuring the Density of CO_2 Confined in Porous Materials 232
3.5 Using 5,10,15,20–Tetrakis(pentafluorophenyl)porphyrin as a Potential Density Sensor 236
3.6 Towards a Density Sensor Using Luminescence in Difluoromethane 243
3.7 Probing Fluid Polarisability and Dielectric constant 245
4 Conclusions 252
Chapter 7 255
Conclusions and Future Outlook 255
1 Summary 255
2 Implications and Future Work 260

Chapter 8 263

Experimental 263

1 Materials 263

1.1 Commercially Available Compounds and Solvents 263

1.2 Non-Commercially Provided Samples 264

2 Synthetic Procedures 266

2.1 Synthesis Chapter 3 266

2.2 Synthesis Chapter 4 268

2.3 Synthesis Chapter 5 271

3 Experimental Techniques 276

3.1 Time Resolved Infra-Red Spectroscopy 276

3.2 Luminescence Spectroscopy 280

3.3 UV/Visible Absorption Spectroscopy 280

3.4 Fourier Transform Infra-Red Spectroscopy 281

3.5 Mass Spectrometry 281

3.6 Electrochemistry 281

3.7 Band fitting 282

3.8 DFT Calculations 282

4 Method Development of High Pressure Luminescence Spectroscopic Measurements of Fluids confined in Porous Templates 283

4.1 Anthracene and MCM-41 control experiment 283

4.2 High Pressure Bulk Luminescence Spectroscopic Measurements 284

References 288

Appendix A I

A.1 Chapter 2 I

A.2 Chapter 3 II

A.3 Chapter 4 XIII

A.4 Chapter 6 XIV

A.5 NMR spectra for complexes synthesised within this work XV

Appendix B XX

Abbreviations

Commonly used abbreviations within this Thesis are defined below. Any abbreviations that are not listed are used infrequently and defined within the body of the text.

ΔAbs	change in absorbance
ε_r	dielectric constant
λ_{ex}	excitation wavelength
τ	lifetime
A	acceptor
Abs	absorbance
B	bridge
bpy	2,2'-bipyridine
CH_2Cl_2	dichloromethane
CH_3CN	acetonitrile
CO	carbonyl
CT	charge transfer
CV	cyclic voltammetry
D	donor
DFT	density functional theory
DMAP	dimethylamino pyridine
DMSO	dimethyl sulfoxide
DNA	deoxyribonucleic acid
dppp2	pyrido[2',3':5,6]pyrazino[2,3-*f*][1,10]phenanthroline
dppp3	pyrido[2',4':5,6]pyrazino[2,3-*f*][1,10]phenanthroline
dppp2Br	11-bromopyrido[2',3':5,6]pyrazino[2,3-*f*][1,10]phenanthroline
dpppn	pterdino[6,7-*f*][1,10]phenanthroline-11,13-diamine
dppz	dipyrido[3,2-*a*:2',3'-*c*]phenazine
E_{ox}	oxidation potential
E_{red}	reduction potential
ET	electron transfer
EWG	electron withdrawing group
Fc	ferrocene
FP	fingerprint
FTIR	Fourier transform infrared
GS	ground state
HOMO	highest occupied molecular orbital

IC	internal conversion
IL	intraligand
IR	infrared
ISC	intersystem crossing
LUMO	lowest unoccupied molecular orbital
MLCT	metal to ligand charge transfer
MO	molecular orbital
(NN)	α-diimine ligand
ns	nanosecond
OER	One electron reduced
PFMCH	perfluoromethylcyclohexane
phen	1,10-phenanthroline
phz	phenazine
ps	picosecond
psi	pounds per square inch, 1 psi = 0.00689 MPa
py	pyridine
Re	rhenium
Ru	ruthenium
RS	reduced state
S_1	singlet excited state
SCFED	supercritical fluid electrodeposition
SCRF	self-consistent reaction field
tfpp	5,10,15,20-tetrakis(pentafluorophenyl)porphyrin
Th	Thiophene
THF	tetrahydrofuran
TRIR	time resolved infrared
TR^MPS	time resolved multiple probe spectroscopy
UV/vis	ultraviolet-visible

Chapter 1

Introduction

This Thesis examines the photophysics of dyes in order to investigate the nature of their excited states in conventional and supercritical fluids. This Chapter will give an overview of excited states and the techniques used within this Thesis. The remaining Chapters will investigate metal bound excited states and the use of these excited states to answer key questions regarding phase phenomena, in applications such as electrodeposition into nanoporous.

A review of the relevant literature and the aims of the work are provided at the start of each chapter.

1 Photophysics

The work within this Thesis focusses on the behaviour of molecules and dyes when exposed to light of varying wavelengths. The complexes studied within this work exhibit interesting photophysical properties and therefore, the investigation into their excited state behaviour allows for the nature of their excited states, solvent environment and decay pathways to be identified. This may allow insight for the implementation of these photosensitive dyes in practical applications.

Photophysics is commonly defined as the study of the physical properties of molecules in excited electronic states, where the chemical integrity of the molecule is unchanged *i.e.* no permanent chemical transformations are involved.[1] Therefore, the work within this Thesis will be based on the study of the physical properties of molecules following the absorption of light.

2 Spectroscopic Techniques for Monitoring Excited States

In order to probe the photophysical behaviour of complexes, both steady state and time resolved techniques have been employed within this Thesis. The detection of emitted photons from a complex can be observed using luminescence spectroscopy, which is primarily employed in Chapter 6. However to elucidate kinetic information and to detect excited states which are not emissive, time resolved infrared spectroscopy has been utilised.

For detection of these excited states and their kinetics, time resolved measurements with an '*ultrafast*' approach have been utilised. This is because the excited state behaviour of the complexes studied possess very short lifetimes, in the order of 10^{-6} – 10^{-12} s. Therefore, the elucidation of their short lived nature is not a trivial matter.

2.1 Time resolved Spectroscopy

The work within this Thesis will exploit time resolved spectroscopy to study reactive intermediates on timescales in the order of 10^{-12} s. Time resolved spectroscopy involves a pump-probe approach, Figure 1-1, whereby a chemical or physical change in the system is initiated by a pump, usually a short pulse of light which has a length which is less than the transient species lifetime. This change is then probed spectroscopically allowing for any intermediates to be identified. Furthermore, by monitoring the transient species as a function of time, reaction kinetics can then be calculated.

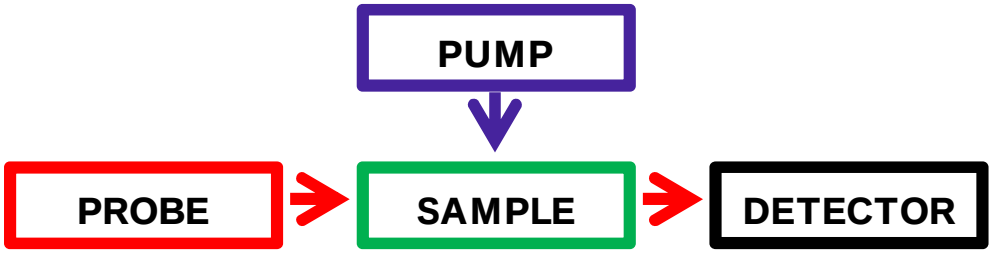

Figure 1-1: A simplified schematic of a pump-probe spectroscopic method.

The pump-probe technique was first developed by Norrish and Porter in the 1940s,[2, 3] where the process utilised a high power gas-discharge flash of light as the pump and a

lower power UV/Vis lamp as the probe for time resolved transient absorption experiments.

2.1.1 Time Resolved Infrared Spectroscopy

The work within this Thesis primarily utilises time resolved infrared (TRIR) spectroscopy. TRIR often exploits reporter groups such as CO in order to probe the nature of the excited states. These groups make it possible to track changes in the electron density of the complex through changes in the vibrational energy, manifesting as changes in absorption. TRIR uses an infrared probe and commonly a UV/vis pump source.

Early work often employed nanosecond step-scan TRIR apparatus with the ability to record a spectrum on the millisecond timescale.[4] Further ultrafast pump-probe experiments have demonstrated the possibility of picosecond and nanosecond measurements.[5] The picosecond and nanosecond work within this Thesis was carried out using the ultrafast TRIR spectroscopic apparatus in Nottingham and at the Rutherford Appleton Laboratory (RAL). Picosecond time resolution is obtained by a spatial delay of a probe pulse relative to the pump or excitation pulse. A schematic of this ultrafast system is shown in Figure 1-2.

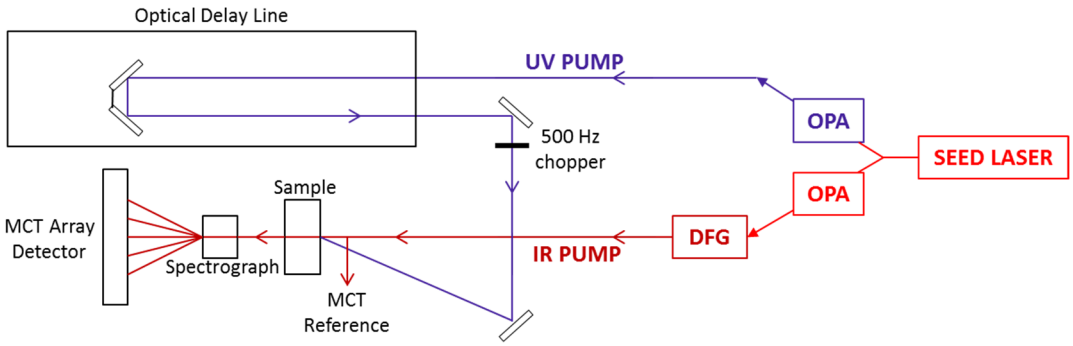

Figure 1-2: A schematic of the ultrafast TRIR setup used within this Thesis.

2.2 Luminescence Spectroscopy

Within this Thesis luminescence spectroscopy has also been employed to study the photophysics of a variety of molecules. Luminescence spectroscopy is a technique highly sensitive to viscosity and local solvent environment.[6, 7] This technique allows for the excitation and emission of a complex to be probed, where the latter is paramount for the work presented. For emission spectroscopy, light of a set wavelength is absorbed by the sample and any resultant emission is detected, a schematic for this process is shown in Figure 1-3.

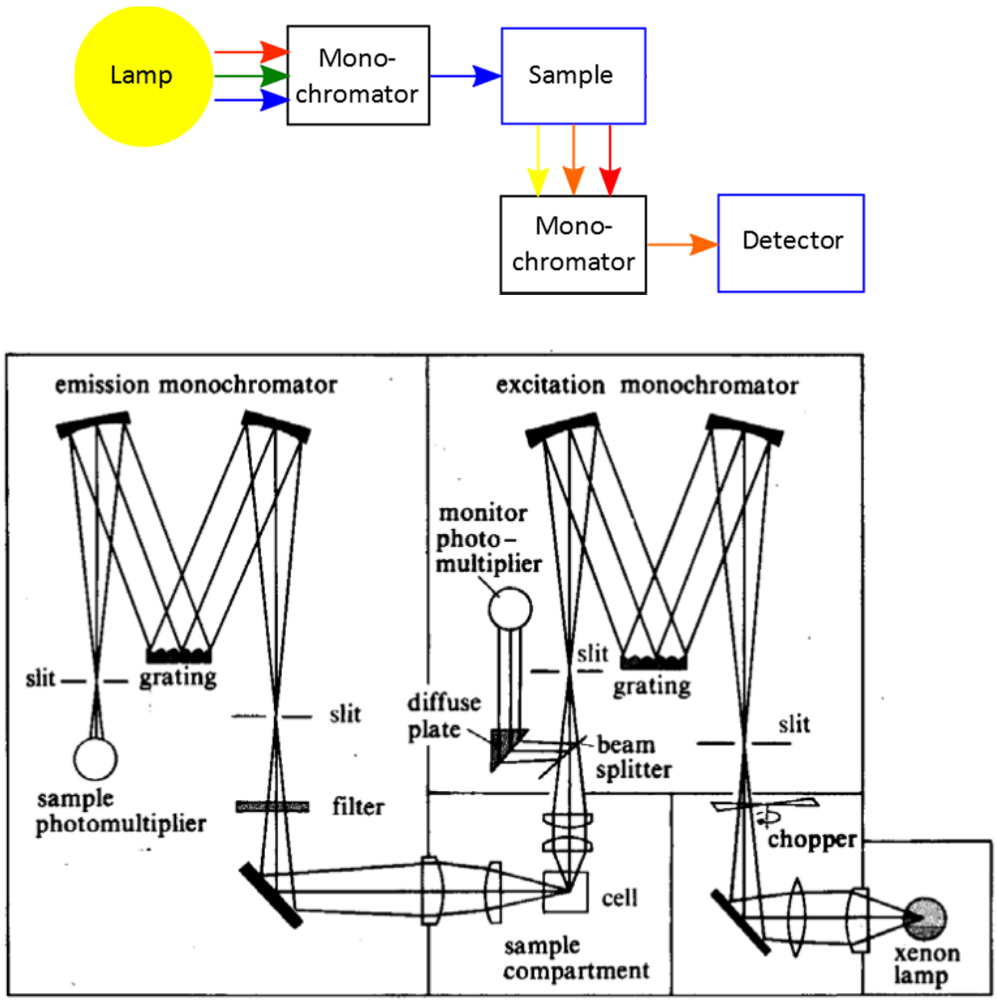

Figure 1-3: A schematic of the fluorescence spectrometer used for all luminescence measurements (top) and an optical layout of a commercial fluorimeter similar to the spectrometer used to conduct the work within this thesis (bottom), reproduced from Ref 8.

2.3 Solvent Dependent Photophysics

A key focus of the work within this Thesis is the effect of the surrounding solvent medium on the observed photophysical properties of dyes. Emission is often observed to change with solvent environment, where this effect is known as solvatochromism, and is key for Chapter 6. However, the stabilisation of excited states with solvent environment has been discussed throughout this Thesis, and a schematic for this process is detailed below.

The electron distribution in a molecule changes upon excitation and thus different bonding forces and dipole moments arise. Excitation of the molecule into the excited state yields an excited state dipole (μ_E) and the solvent dipoles reorientate around this excited state to stabilise it and therefore lower its energy,[8] Figure 1-4. Typically μ_E is larger than the dipole of the ground state (μ_G) and as a result, an increase in solvent polarity will stabilise the excited state. Therefore, as solvent polarity increases, the emission is seen at lower energies (*i.e.* redshifted) and thus, a larger Stokes shift is observed; this effect is known as positive solvatochromism, Figure 1-4.[8-11]

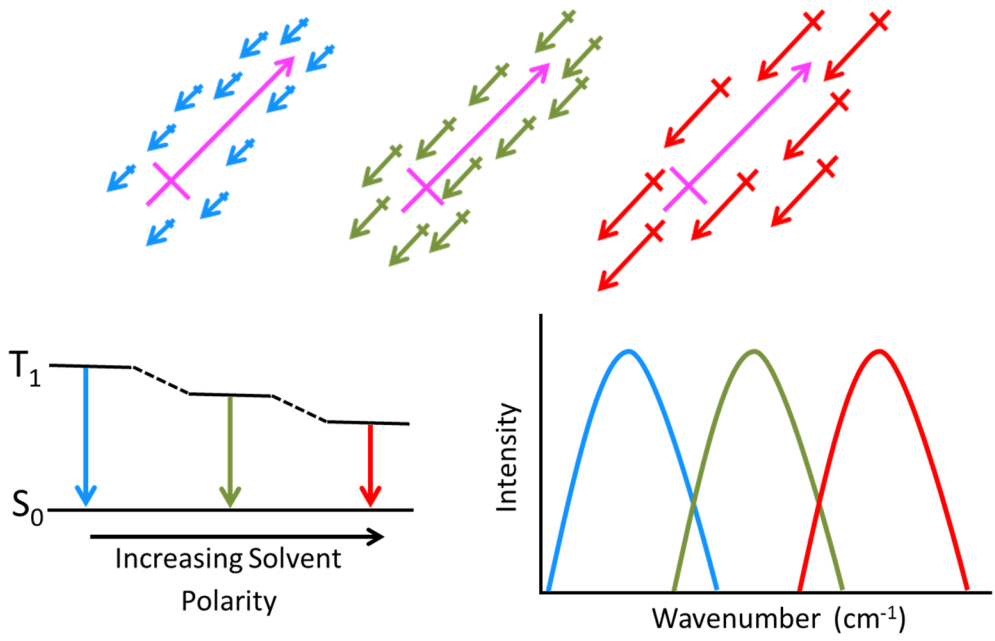

Figure 1-4: Positive solvatochromism which arises from the further stabilisation of the excited state (bottom, left) which results from solvent reorientation around the excited state (top). This is observed as a decrease in emission energy as solvent polarity increases (bottom, right).

Chapter 2

The Photophysical Properties of Donor-Appended Rhenium Dipyrido[3,2-*a*:2',3'-*c*]phenazine Complexes

1 Introduction

The photophysical properties of transition metal polypyridyl complexes have been utilised in a wide range of applications including as reporters for DNA,[12-15] solar cells,[16, 17] organic light emitting diodes to improve display technology,[18] sensors,[19-21] and energy conversion and storage.[22]

This Chapter focusses on metal α-diimine (NN) complexes such as $[M(NN)(CO)_3R]$ shown in Figure 2-1, where M is a metal, either ruthenium or rhenium, and NN is a derivative of dipyrido[3,2-*a*:2',3'-*c*]phenazine (dppz) or 2,2'-bipyridine (bpy).

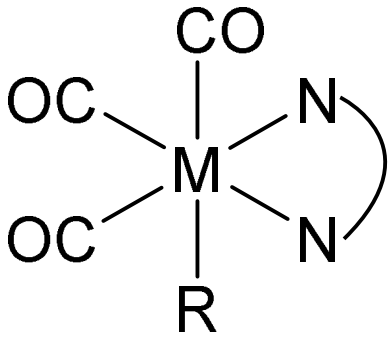

Figure 2-1: The structure of $[M(NN)(CO)_3R]$, where NN is 2,2'-bipyridine or dipyrido[3,2-*a*:2',3'-*c*]phenazine.

For M(dppz) complexes it is often possible to tune their electronic properties through substituents onto the complex. The ligand dppz may be thought of as containing the α-diimine chelating ligands, bpy and 1,10-phenanthroline (phen),[23] as well as a 1,4-diazine in the form of phenazine (phz) or quinoxaline (quin) as shown in Figure 2-2.[24, 25]

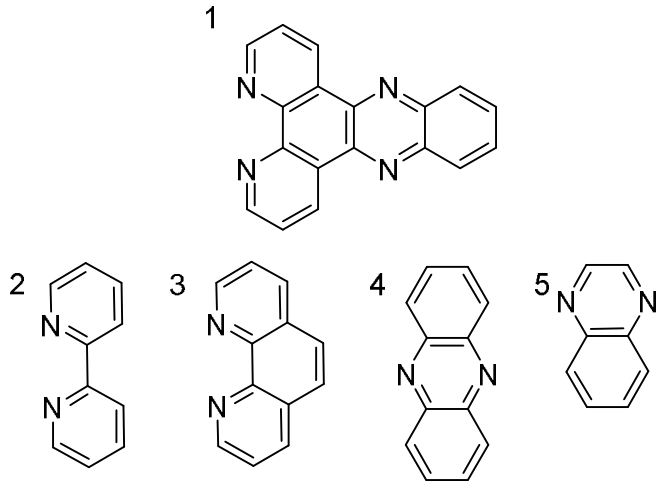

Figure 2-2: The structure of dipyrido[3,2-a:2'3'-c]phenazine ligand (1) which can be thought of as consisting of 2,2'-bipyridine (2), 1,10-phenanthroline (3), phenazine (4) and quinoxaline (5) moieties.

1.1 Excited States of M(dppz) Complexes

The assignment of molecular orbitals (MOs) responsible for the photophysics observed for transition M(dppz) complexes can prove complicated owing to the large manifold of excited states often exhibited. Discussions in the literature of the photophysics of dppz complexes usually centre on the idea of the ligand consisting of two distinct low lying unoccupied MOs, a phen and a phz. These two MOs give rise to the commonly observed transitions for Ru(dppz) of a metal to ligand charge transfer from the Ru(dπ) to the phen(π*) or phz(π*) yielding an MLCT(phen) or MLCT(phz) state respectively. The presence of these two distinct states, MLCT(phen) and MLCT(phz), is supported through electrochemical studies on the ground state molecule,[24, 25] and ultrafast transient absorption spectroscopy experiments.[13] Throughout this work unless otherwise stated, excited states denoted are of triplet character, *i.e.* MLCT(phen) will refer to ^{3}MLCT(phen).

Furthermore, the MLCT(phen) state may be thought of as emissive and the MLCT(phz) state as non-emissive, where this emissive and non-emissive behaviour has been exploited in the so called '*light switch effect*' observed for aqueous samples in the presence of DNA.[13, 22, 24, 26-28] Thus, Ru(dppz) complexes may act as luminescent probes for DNA as they are non-emissive in aqueous solution but are brightly luminescent when bound to DNA, owing to the decay pathway which results. This *light switch effect* has been shown to be solvent dependent and it was initially thought that state reversal between the phen and the phz states occurred such that in protic solvents, hydrogen bonding to the phz nitrogens would stabilise the dark MLCT(phz) state. Conversely, in aprotic solvents or when intercalated into DNA this hydrogen bonding does not occur and the phz state is less stable leaving the MLCT(phen) emissive state lower in energy, Figure 2-3.[12-15]

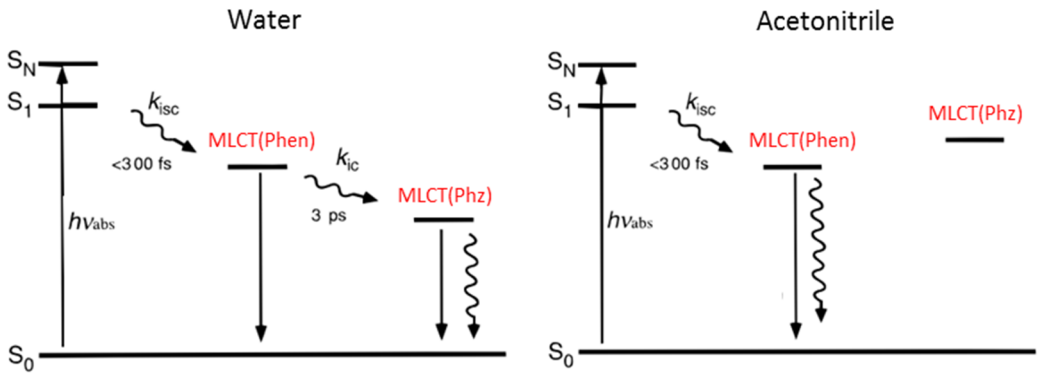

Figure 2-3: The Jabłoński diagram of the environment dependent photophysics of $[Ru(phen)_2(dppz)]^{2+}$. In protic solvents the phz (dark) state is shown to be lowest in energy and state reversal is observed (left) compared to non-protic solvents where the phen state is lowest in energy (right). Reproduced from reference 13.

Subsequent studies by Brennaman *et al*.[29, 30] reported temperature dependent lifetime measurements of $[Ru(bpy)_2(dppz)]^{2+}$ excited states in different solvents and suggested that it is unlikely the phen (bright state) and phz (dark state) change in energy only with solvent environment. Instead it was proposed that the dark phz state is enthalpically favoured, *i.e.* state reversal does not occur. At low temperatures the phz state is populated for $[Ru(bpy)_2(dppz)]^{2+}$ and as the temperature is increased the phen state begins to be populated. Further increases in the temperature results in a '*roll over effect*' being observed whereby the phen state decays *via* population of metal based dd states,

Figure 2-4.[31] Thus, the phz state is always lowest in energy regardless of solvent environment.

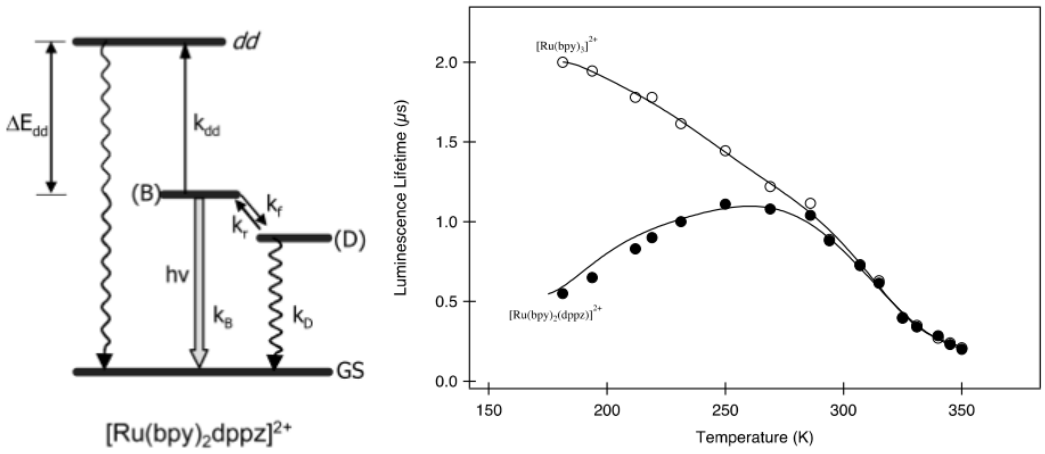

Figure 2-4:The Jabłoński diagram of $[Ru(bpy)_2dppz]^{2+}$ (left) where B and D refer to bright and dark MLCT states respectively associated with dppz. K_B is the total relaxation rate, k_D is non radiative decay. The schematic representation of luminescence lifetime with temperature for $[Ru(bpy)_3]^{2+}$ and $[Ru(bpy)_2(dppz)]^{2+}$ (right). Reproduced from references 29 and 30.

The photophysics of M(dppz) complexes is further complicated by the occurrence of transitions not involving the metal, as well as the previously discussed MLCT, these transitions are observed occurring between the π-π* of the dppz ligand and are therefore intraligand transitions (IL). The dppz ligand generally exhibits electronic absorption bands in the UV region (270-380 nm) where lower energy bands (*ca.* 340-380 nm) are nπ* in nature and bands which are higher in energy (*ca.* 270-290) are ππ* in nature.[24, 28] Complexation of the ligand to the metal results in a red shift and most commonly the lowest energy absorption band is MLCT in nature.

The work within this Chapter will focus on Re(dppz) complexes, which are important luminophores and sensitisers and possess several excited states, the relative energy of which can be controlled by varying the substituents and the environment.[4, 32-42] Previous work has shown that on very short timescales after photolysis (λ_{ex} *ca.* 400 nm) a singlet excited state is initially observed,[43] which undergoes rapid ISC, yielding a longer lived triplet state. Measurement of ISC timescales for similar Ru(NN) such as $[Ru(bpy)(CO_3)Cl]$ demonstrate this process occurring within *ca.* 100 fs.[43] The final

longer lived triplet state can be either IL$\pi\pi^*$, MLCT(phen) or MLCT(phz) in nature. Direct population of the phz state is unlikely because of the negligible overlap between Re($d\pi$) and phz(π^*) molecular orbitals, thus rapid transition to the phz moiety *via* interconversion following population of the phen MO is required to achieve an MLCT(phz) state.[24]

Previous research on the photophysics of M(dppz) complexes has utilised various techniques including emission, absorption, Raman, transient absorption, EPR, and Infrared spectroscopies.[4, 24, 25, 32-42, 44] Infrared spectroscopy, is a particularly valuable technique for studying metal-carbonyl complexes, due to the high oscillator strength of the infrared ν(CO) band which is clearly visible in the IR spectrum. Furthermore, the sensitivity of the energy and the bandwidth of this ν(CO) band to the complexes electronic and molecular structure are well studied and defined.[4] Thus metal-carbonyl bands in the excited state TRIR spectra may be used to elucidate the natures of excited states in $[Re(dppz)(CO)_3L]^+$ systems as well as obtaining kinetic data by analysing the changes in absorption of transient IR bands.[45-49] TRIR spectroscopy can be used to infer excited state structure which may not be possible with other time resolved spectroscopic methods such as transient absorption spectroscopy.

Formation of an MLCT excited state of a metal-carbonyl complex results in an effective oxidation of the metal and reduction of the ligand. Spectrally this results in an increase *i.e.* blue shift in the frequency observed for the CO bands. This is due the movement of electron density away from the metal resulting in a decrease in the amount of electron density present for back-bonding between the Re($d\pi$) and CO(π^*).[24] This causes an increase in the strength of the CO bond and a blue shift in $\Delta\nu$(CO). This shift is dictated by the magnitude of the change in electron density of the back bonding from the Re($d\pi$) to CO(π^*).[24] In contrast, for IL transitions the increase in electron density in the ligand(π^*) results in an increase in electron density in the Re($d\pi$) orbitals. As a result, more electron density is on the metal and so more back bonding occurs, thus the CO band is weakened and there is a red shift in $\Delta\nu$(CO). This shift is smaller in magnitude than the blue shift observed for MLCT excited states.

For Re(dppz) complexes it is possible to spectroscopically differentiate between population of the MLCT(phen) and of the MLCT(phz) states using the ν(CO) bands. It has shown that a $\Delta\nu$(CO) of *ca.* +40 cm^{-1} and of +60 cm^{-1} with respect to the parent is expected for MLCT(phen) and MLCT(phz) respectively.[32] This ν(CO) shift is indicative of the proximity of the dppz components to the metal, whereby for an MLCT(phz) the electron resides at a position further from the metal than for the MLCT(phen). Thus for an MLCT(phz) transition charge separation distance is higher than for an MLCT(phen) and the CO bond is stronger. Although the ν(CO) bands are very diagnostic, the fingerprint region (FP) of 1600-1300 cm^{-1} can also be used to determine the natures of the excited states of M(dppz) complexes, as clearer spectral differences exist in this region of the IR spectrum for M(dppz) complexes.[40] The assignments in this region can be more difficult than for the CO region due to the lower oscillator strength of the reporter groups, overlapping and solvent bands, the presence of spectator ligands and the shifts are less intuitive in their interpretation. As a result there are fewer examples of TRIR being exploited to elucidate the nature of M(diimine) complexes using the FP region, where most studies have focussed on Ru(diimine) complexes.[50, 51] Of particular relevance to the work presented in this Chapter is the recent report of a brief TRIR study examining the fingerprint region for [Re(dppz-$PhNPh_2$)$(CO)_3$(DMAP)].[40] The complexes studied within this Chapter exhibit only one diimine ligand, (dppz) and this simplifies assignment of the fingerprint bands, as the spectra are not complicated by the presence of the spectator ligands.

1.2 Tuning the Excited States of M(dppz) Complexes

The photophysics of transition M(dppz) complexes may be tuned by changing the ancillary ligand or the substituents on the phen and phz moiety of the dppz ligand (Figure 2-5). X and Y represent substitution points on the phz and phen part of the dppz ligand respectively and L is a monodentate ligand.

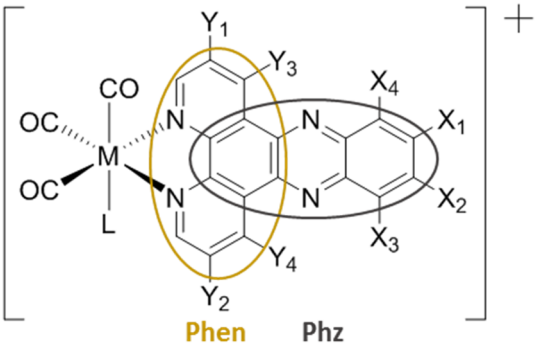

Figure 2-5: The structure of a transition metal dppz complex $[M(CO)_3(dppz)L]^+$ where L is the ancillary ligand, and x and y indicate substituents on the phenazine and phenanthroline constituents of the dppz ligand respectively.

Substituents may be broadly split into two groups: those which are electron withdrawing in nature *e.g.* Cl, F, CF_3 and Br and those which are electron donating in nature such as CH_3. Modification of the substituent at X and Y may change the energy of the phz and phen states respectively.[22, 24, 25]

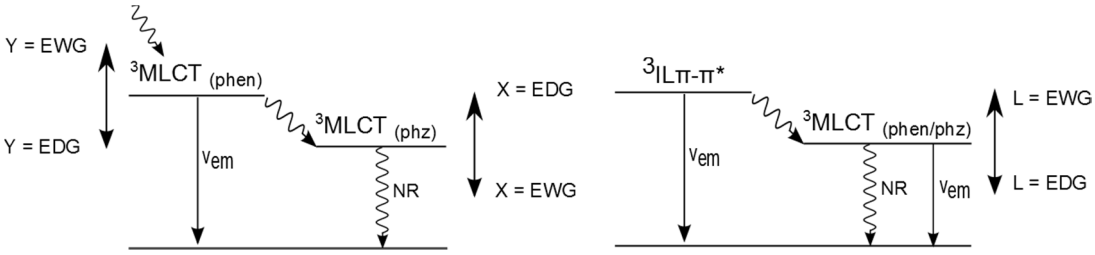

Figure 2-6: The modification of substituents on the phz (X) portion of the dppz ligand changes the occupancy of the lowest excited state and modification of substituents on the phen (Y) portion of the dppz ligand changes the MLCT(phen) energy (left). Varying the monodentate ligand, L, changes the electron density on the metal (right).

Previous studies of $[Ru(bpy)_2(dppz)]^{2+}$ have shown that dppz is more easily reduced than bpy due to the lower energy phz(π*) orbital, thus the π-accepting site of dppz is localised on the phz moiety and so the LUMO is predominantly phz in nature. Therefore, modifying X changes the occupancy of this lowest excited state.[22, 24, 25] In contrast, modifying Y leads to a change in the phen localised energy.[32] Varying L changes the electron density present on the metal, such that for electron donating groups Re(dπ) may become higher in energy compared to the π* of the dppz ligand (Figure 2-6).

Table 2-1: A summary of ps and ns-TRIR studies of complexes $[Re(dppz)(CO)_3(L)]^+$ carried out with λ_{ex} = 400 and 355 nm. Where two states are given an equilibrium exists, where all states observed have been assigned as triplet in character.

Complex	Solvent	TRIR	τ (ns)	Ref
$[Re(dppz)(CO)_3Cl]$	CH_2Cl_2	IL$\pi\pi^*$/MLCT(phen)	40 ± 10	32
$[Re(dppz)(CO)_3Cl]$	CH_3CN	IL$\pi\pi^*$/MLCT(phen)	0.01[a]	32
		MLCT(phz)	2.5 ± 0.8	
$[Re(dppz)(CO)_3Cl]$	C_3H_7CN	IL$\pi\pi^*$/MLCT(phen)	0.025[a]	32
		MLCT(phz)	3.5 ± 1	
$[Re(dppz\text{-}(CH_3)_2)(CO)_3Cl]$	CH_2Cl_2	IL$\pi\pi^*$/MLCT(phen)	420 ± 80	32
$[Re(dppz\text{-}(CH_3)_2)(CO)_3Cl]$	CH_3CN	IL$\pi\pi^*$/MLCT(phen)	4.7 ± 0.5	32
[Re(dppz-COOEt)$(CO)_3$Cl]	CH_3CN	MLCT(phz)	0.22 ± 0.06	33
[Re(dppz-Br)$(CO)_3$Cl]	CH_2Cl_2	MLCT(phen)	<0.02	34
		MLCT(phz)	1.2	
$[Re(dppz\text{-}Br_2)(CO)_3Cl]$	CH_2Cl_2	MLCT(phen)	<0.02	34
		MLCT(phz)	1.3	
$[Re(dppz\text{-}Br(CF_3))(CO)_3Cl]$	CH_2Cl_2	IL$\pi\pi^*$	0.530	34
$[Re(dppz\text{-}Cl_2)(CO)_3Cl]$	CH_3CN	MLCT(phen)	0.15 ± 0.02	35, 32
$[Re(dppz\text{-}Cl_2)(CO)_3Cl]$	CH_2Cl_2	MLCT(phz)	1.5 ± 0.2	32
$[Re(dppz\text{-}F_2)(CO)_3Cl]$	CH_2Cl_2	MLCT(phen)	0.006[a]	32
		MLCT(phz)	3.05 ± 0.04	
$[Re(dppz\text{-}F_2)(CO)_3Cl]$	CH_3CN	MLCT(phen)	0.004	32
		MLCT(phz)	0.24 ± 0.02	

[Re(dppz-F_2)$(CO)_3$Cl]	C_3H_7CN	MLCT(phen)	0.051	32
		MLCT(phz)	0.25	
[Re(dppz-F_2)$(CO)_3$Cl]	CH_3OH	MLCT(phen)	0.009[a]	32
		MLCT(phz)	0.09	
$[Re(CO)_3(dppz\text{-}Cl_2)(py)]^+$	CH_3CN	ILππ*	0.002	35
$[Re(CO)_3(dppz\text{-}F_2)(py)]^+$	D_2O	ILππ*	0.073[a]	36
		MLCT(phz)	0.732	
$[Re(CO)_3(dppz\text{-}F_2)(py)]^+$	D_2O	ILππ*	430 ± 40, 2300 ± 300	37
		MLCT	400 ± 40, 2500 ± 100	
$[Re(CO)_3(dppz\text{-}F_2)(py)]^+$	CH_3CN	ILππ*	0.018 ± 0.0002, >0.5	37
$[Re(CO)_3(dppz\text{-}F_2)(py)]^+$	CH_3CN	ILππ*	430 ± 40[a], 2300 ± 300	36
		MLCT(phz)	2500 ± 100	
$[Re(CO)_3(dppz)(py)]^+$	CH_3CN	ILππ*	500, 3500	38
		MLCT(phz)	3500	
$[Re(CO)_3(dppz\text{-}Me_2)(py)]^+$		ILππ*	870 ± 20, 5600 ± 600	36
		MLCT(phz)	6000 ± 400	
$[Re(CO)_3(dppz\text{-}CO_2Et)(py)]^+$	CH_3CN	ILππ*	1000	52
		MLCT(phz)	10000	
$[Re(CO)_3(dppz\text{-}CO_2Et)(DMAP)]^+$	CH_3CN	ILππ*/MLCT(phen)	0.07 ± 0.0002[a], 1.6 ± 0.4	52
$[Re(CO)_3(dppz\text{-}Cl_2)(DMAP)]^+$	CH_3CN	ILππ*/MLCT(phen)	0.002 – 2.5[a], 1 ± 0.2	35
[Re(dppz-$PhNPh_2$)$(CO)_3$(DMAP)]$^+$	CH_2Cl_2	State I	0.020 (0.22)	40
		ILCT	0.30	
		ILCT	2800	

[Re(dppz-12-NO_2)$(CO)_3$(DMAP)]$^+$	CH_3CN	ILππ*/MLCT(phen)	0.12 ± 0.02	53
[Re(dppz)$(CO)_3(PPh)_3]^+$	CH_3CN	ILππ*[b]	42000	4
[Re(dppz-$(CH_3)_2$)$(CO)_3$(4-Etpy)]$^+$	CH_3CHCl_2	ILππ*		41
[Re(dppz-$(CH_3)_2$)$(CO)_3$(py-PTZ)]$^+$	CH_3CHCl_2	ILCT	63	41
[Re(dppz)$(CO)_3$(py-PTZ)]$^+$	CH_3CHCl_2	ILCT	110	41
		ILππ*	>300	

[a]Equilibrium from a lower energy state
[b]Time resolved step scan FTIR

The effect on the photophysics of Re(dppz) related complexes has been investigated by varying substituents on the phz moiety, and probing the effect of symmetrical and asymmetrical substitutions at X_1 and X_2. Electron withdrawing groups (EWG) in positions X_1 and X_2 lower the MLCT(phz) energy resulting in a red shift in absorption. For Re(dppz) complexes where substituents X_1 and X_2 are electron withdrawing, the dppz ligand is more readily reduced compared to analogous unsubstituted Re(dppz) complexes.[28]

Electron donating substituents increase the population of the IL$\pi\pi^*$(dppz) state and conversely, electron withdrawing groups tend to increase conversion to the IL$\pi\pi^*$(dppz) state to an MLCT(phz) state and subsequent deactivation to the ground state. For example the IL$\pi\pi^*$(dppz) state is the most stable excited state observed when dimethyl (X_1, X_2 = CH_3) substituents are present, whilst for the difluorinated compound (X_1, X_2 = F) conversion of the IL$\pi\pi^*$(dppz) state to an MLCT(phz) state appears to be increased. This is further evidenced by the emission of the difluorinated compound in CH_3CN which may be quenched through the addition of water, consistent with the population of an MLCT(phz) state. Conversely for the dimethyl complex the emission intensifies with the addition of water in CH_3CN, consistent with the population of IL$\pi\pi^*$(dppz) state.[36]

Work by Olofsson *et al.* and Hartshorn *et al.* further explored methyl substituted dppz complexes of the form $[Ru(bpy)_2(dppz)]^{2+}$ by investigating the effect of the position of substitution on to the dppz ligand with emissive behaviour in water and polyol solvents.[54, 55] Both the monosubstituted (where X_3 = CH_3) and disubstituted (where X_1, X_2 = CH_3) complexes demonstrated an increased luminescence lifetime and higher quantum yield compared to the non-substituted parent complex. The results demonstrate that adding a methyl substituent decreases hydrogen bonding of solvent molecules in the excited state, indicating the methyl groups exhibit a steric hindrance to the formation of the 'solvent cage' located around the molecule. Furthermore, if the phen part of dppz is methyl substituted (Y_3, Y_4 = CH_3) again an increase in luminescence lifetime is observed compared to the parent.[56]

Kuimova *et al*. reported DFT calculations of the complexes [Re(dppz-X_2)$(CO)_3$Cl], where X is CH_3, H, Cl and F, which showed that the relative energy of the LUMO decreases dramatically with increasing electron withdrawing ability of the substituent at position X_1 and X_2 as shown in Figure 2-7.[32] The LUMO is localised on the phz moiety of the dppz ligand and is of π symmetry, while the HOMO is predominately Re(dπ) based and contains significant CO character. This decrease in the relative energy of the LUMO is reflected in the lifetime and nature of the excited state.

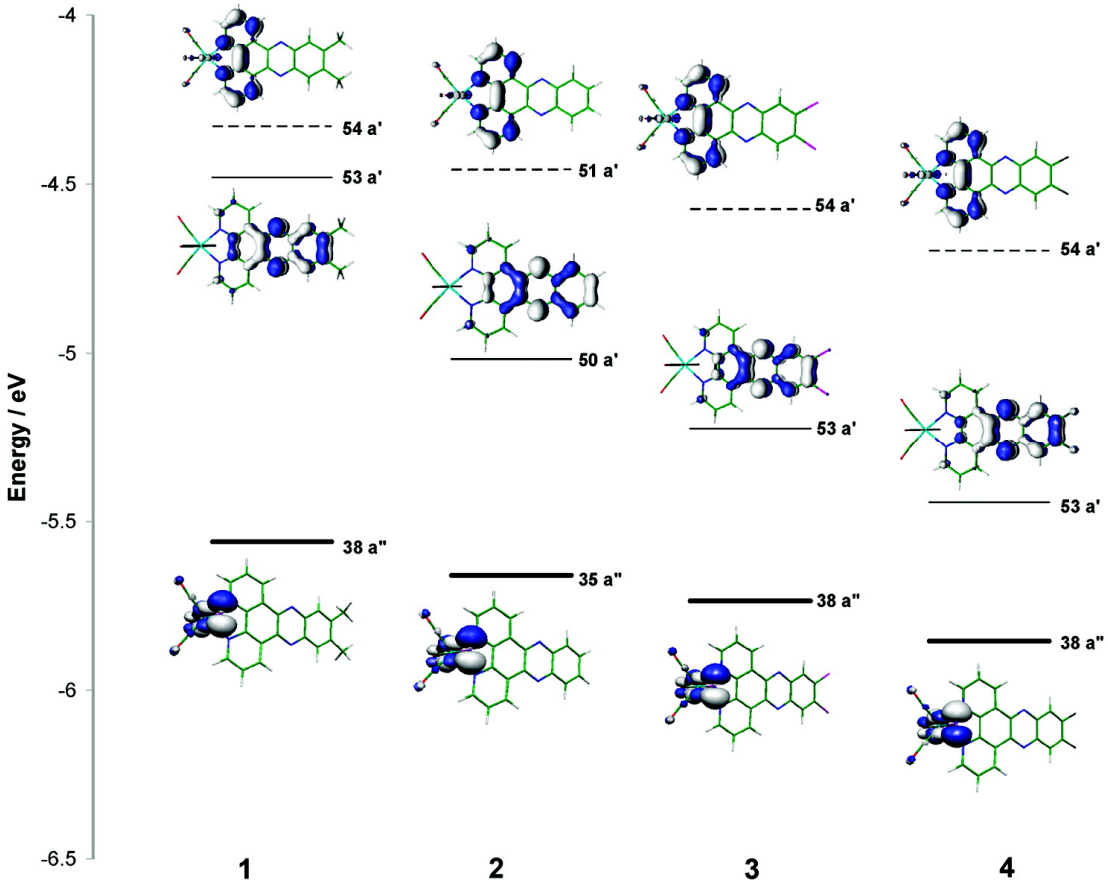

Figure 2-7: The partial energy level diagram for [Re(dppz-X_2)$(CO)_3$Cl], X = CH_3 (1), H (2), Cl (3) and F (4) calculated in its ground state in the gas phase and three-dimensional plots of the electron density for the HOMO (thick solid line), LUMO (thin solid line), and LUMO+1 (dashed line). Relative energy of the LUMO decreases with increasing electron donating ability of X. Reproduced from reference 32.

TRIR spectroscopic studies of the same complexes have shown that the excited state lifetime is observed to decrease with increasing electron withdrawing ability of the substituent from 420 (± 80) to 3.05 (± 0.04) ns for X_2 = CH_3 and F respectively, also observed was a decrease in the HOMO/LUMO gap calculated by DFT. The results

show that as the strength of the electron withdrawing substituent increases, more MLCT(phz) character is observed, shown as a more blue shifted transient band in relation to the parent, Figure 2-8. For X_2 = H and CH_3, an additional IL$\pi\pi^*$ is also observed as a transient band slightly red shifted to the parent.

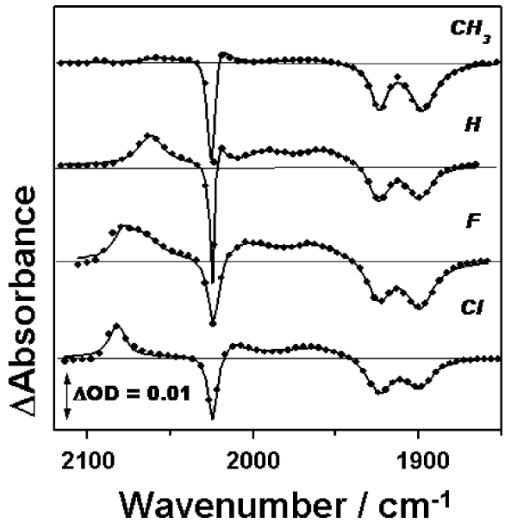

Figure 2-8: The TRIR spectra of [Re(dppz-X)(CO)$_3$Cl], where X = CH_3, H, Cl, F and CF_3, in CH_2Cl_2 following 400 nm photoexcitation. Reproduced from reference 32.

The effect of electron withdrawing ability of a substituent on the photophysical properties of $[Re(dppz)(CO)_3L]^+$ has been further examined by van der Salm *et al.*[34] Studies of the complexes [Re(dppz-Br_2)(CO)$_3$Cl], [Re(dppz-Br)(CO)$_3$Cl], [Re(dppz-Br(CF_3))(CO)$_3$Cl] have shown that the latter, dppz-Br(CF_3) complex, has the most positive reduction potentials and thus the LUMO, which is phz based, is most affected by the electron withdrawing substituents. Furthermore for all complexes, except [Re(dppz-Br_2)(CO)$_3$Cl], an MLCT(phen) state is observed. For [Re(dppz-Br_2)(CO)$_3$Cl] there appears an equilibrium of MLCT(phen)/MLCT(phz) states and the position of the equilibrium responds qualitatively with reduction potentials.[34]

Modification of L may change the energy and population of the MLCT state by affecting the electron density on the metal. Previous work on the complex $[Re(CO)_3(dppz)(py)]^+$ has assigned the lowest-lying excited state as being ligand centred $\pi\pi^*$ which is dppz in nature.[13, 38, 57] TRIR spectroscopy has been used to demonstrate the presence of an MLCT state and the formation of an IL$\pi\pi^*$ state at *ca.* 600 and 250 ns after photoexcitation respectively. This indicates that the MLCT state forms from the

IL$\pi\pi^*$(dppz) state. It is further indicated through similar rates of decay for both states, that the energetically close lying IL$\pi\pi^*$(dppz) and MLCT states are in equilibrium.[38] For $[Re(dppz)(CO)_3(DMAP)]^+$ where DMAP is dimethylaminopyridine a similar profile of excited states are observed, where an initially formed IL$\pi\pi^*$(dppz) state after photoexcitation subsequently decays to an equilibrium with an MLCT state.[46]

A comparison in the nature of the excited states for L = py and DMAP has made by Kuimova *et al.*[52] In CH_3CN the irradiation of $[Re(CO)_3(dppz\text{-}CO_2Et)(py)][PF_6]$ resulted in the formation of a IL$\pi\pi^*$ state within the first few picoseconds, centralised on the dppz ligand, which partially decays to yield an equilibrium between IL$\pi\pi^*$(dppz) and MLCT(phz) excited states.[52] In contrast irradiation of the corresponding DMAP complex, $[Re(CO)_3(dppz\text{-}CO_2Et)(DMAP)][PF_6]$ generates both MLCT(phen) and IL$\pi\pi^*$ excited states. Furthermore, in contrast to the py complex, the MLCT(phen) state partially decays on a picosecond timescale to yield an equilibrium between IL$\pi\pi^*$(dppz) and MLCT(phen) states which then rapidly decays to the ground state, Figure 2-9. Additionally, the absorption spectra of the py complex has clearly resolved vibrational structure indicative of IL$\pi\pi^*$(dppz) character whilst in contrast, the DMAP complex is broad and featureless indicating MLCT character. The red shift observed in absorption from py to DMAP is consistent with DMAP having higher electron donating ability.

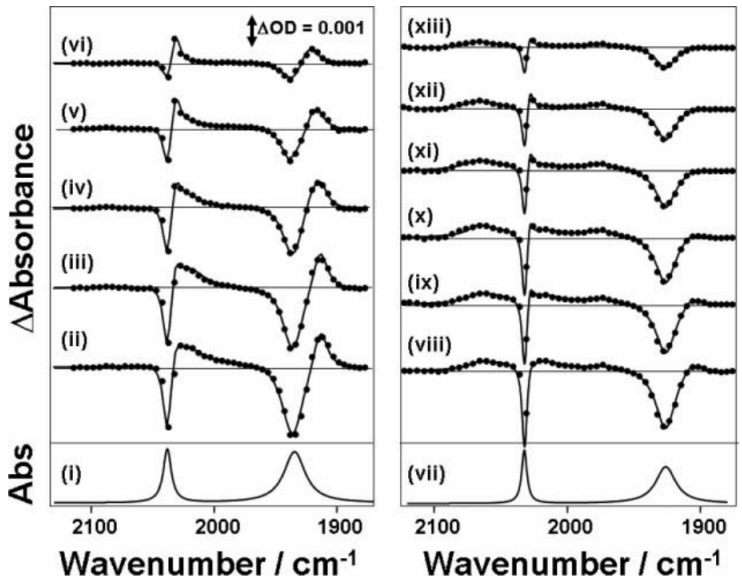

Figure 2-9: The FTIR (i) and TRIR spectra at time delays of (ii)2ps, (iii) 5ps, (iv) 15 ps, (v) 30 ps, (vi) 2500 ps of [($Re(CO)_3$(dppz-CO_2Et)(py)][PF_6] in CH_3CN following 400 nm photoexcitation (left) and the FTIR (vii) and TRIR at time delays of (viii) 2ps, (ix) 7 ps, (x) 20 ps, (xi) 50 ps, (xii) 200 ps, (xiii) 1000 ps of [($Re(CO)_3$(dppz-CO_2Et)(DMAP)][PF_6] (right) in CH_3CN following 400 nm photoexcitation (right). Reproduced from reference 52.

When the axial ligand (L) is a terthiophene derivative and X_1 is a oxadiazole derivative as shown in Figure 2-10, the electron withdrawing oxadiazole group results in a less negative reduction potential for the complex than for [$Re(dppz)(CO)_3Cl$] and thus the LUMO is lower in energy than for dppz.[18] Furthermore, the presence of the terthiophene moiety results in less positive potentials for oxidation than observed for [$Re(dppz)(CO)_3Cl$], indicating the HOMO is greater in relative energy for the complex than for [$Re(dppz)(CO)_3Cl$]. Thus, the complex has a greater propensity to lose an electron.[18]

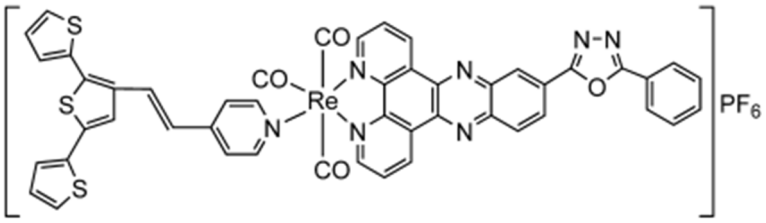

Figure 2-10: The [$Re(dppz\text{-}X_1)(CO)_3L$] derivative complex where X_1 is an oxadiazole derivative and L is a terthiophene derivative.

1.3 Donor-Bridge-Acceptor Complexes

The work presented within this Chapter pertains to charge transfer (CT) complexes which are defined as an electron-donor-electron-acceptor complex characterised by electronic transition(s) to an excited state in which there is partial or full transfer of electronic charge from the donor to the acceptor moiety,[58, 59] described as charge transfer and electron transfer respectively, between donor (D) and acceptor (A) moieties connected by a spacer group.[49, 50] CT complexes play a vital role in many photophysical and photochemical processes including photosynthesis and dye sensitised solar cells.[60, 61]

Energy transfer between D and A occurs either *via* a radiative process such as the emission of a real photon followed by subsequent reabsorption, or *via* a non-radiative process.[61] The transfer of excitation energy may occur between freely diffusing D and A molecules *i.e.* D* + A → D + A*, or between D and A subunits of a supramolecule *i.e.* D*BA → DBA*. The latter process often requires the presence of a bridge (B).[61]

The transition energy and oscillator strength are linked to coupling between D and A, where the weaker the coupling the smaller the excitation energy as shown in Figure 2-11.[62]

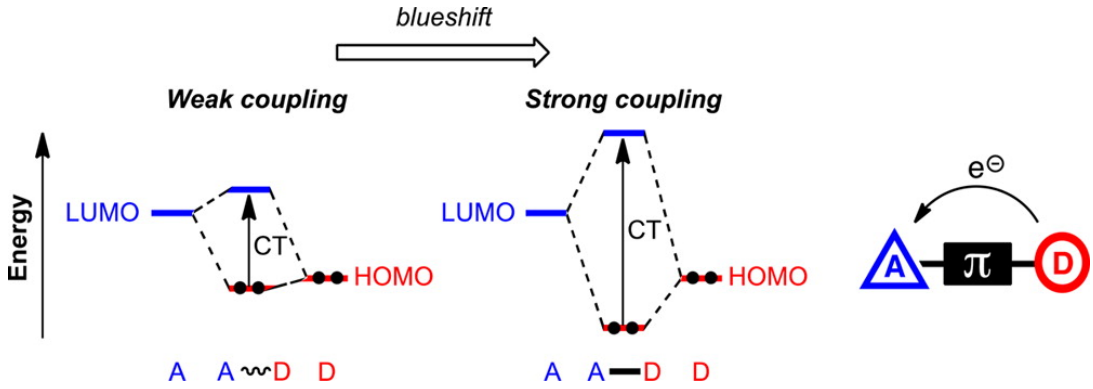

Figure 2-11: The relationship between coupling and excitation energy observed in D-A complexes. Reproduced from reference 62.

Weak coupling results in a lower oscillator strength, which may prevent direct excitation and the probability that direct excitation occurs is zero for non-coupling D-A complexes. This coupling between D and A is often dictated by the nature of the spacer. The population of CT states for coupled and non-coupled D-A complexes is shown in Figure 2-12. For coupled D-A complexes CT states result from a lower lying state *via* the absorption of photon. For a non-coupled or '*pure*' CT state the oscillator strength is zero and therefore the CT state will not be directly populated by light absorption. The process proceeds *via* an intermediate, higher energy state that subsequently couples to the CT state *via* an internal conversion process. For non-coupled CT states, the overall process is referred to as light induced electron transfer instead of direct CT excitation.[62]

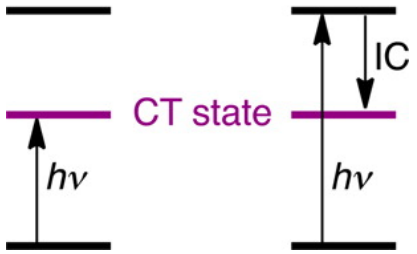

Figure 2-12: The direct excitation to CT state (left) and the excitation to a higher lying bright state followed by IC to CT state for light induced ET process (right). Reproduced from reference 62.

The charge-transfer complexes within the work in this Chapter are comprised of the structure donor-bridge-acceptor (DBA), where partial or full electron transfer occurs from D to A *via* B. Thus two overall transitions are observed: D*→D and A→A*. The term bridge can be interchangeable with wire in the literature and to be clear for this work when the charge is localised on the spacer between the D and A during transfer the spacer is nominally called a wire. Conversely when the charge is observed to tunnel through the spacer and thus never localised on it is referred to as a bridge.[61] As a result a spacer could effectively act as a wire or bridge depending on the D and A system implemented.

There have been various studies that have been carried out into the effect of the bridge on charge transfer, including bridges which are chains of covalently linked structural subunits and stacks of dissimilar aromatic molecules.[63] In this introduction a few choice examples are used to highlight points which are relevant to the work presented in this Chapter.

D-A compounds were originally studied for energy transfer as well as charge transfer. Early work by Keller and Dolby demonstrated energy transfer of triplet energy within two D-A systems using emission studies.[64] Firstly from a benzophenone-4-carboxylic acid donor moiety to a naphthalene acceptor moiety, and secondly from an alcohol donor moiety to a naphthalene donor moiety, as shown in Figure 2-13, where for both types of systems the bridge is a steroid. The lowest state energy of benzophenone-4-carboxylic acid is lower in energy than the lowest singlet state of naphthalene. Therefore it is possible to excite the benzophenone-4-carboxylic acid at a wavelength which is too low

in energy to excite naphthalene. The process demonstrated a faster rate constant for benzophenone (25 sec^{-1}) compared to the alcohol system (0.04 sec^{-1}), which mirrors the magnitude of difference in the triplet state lifetime for the two donor chromophores.

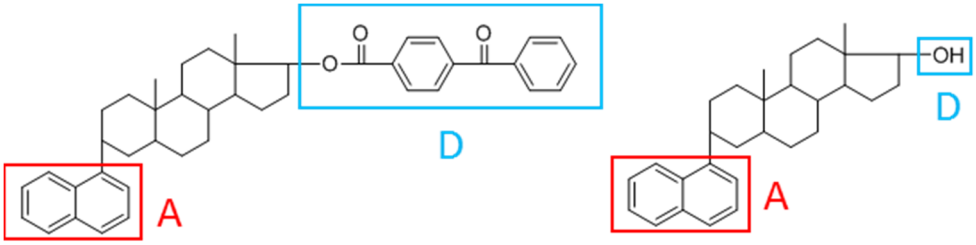

Figure 2-13: The structures of donor–acceptor complexes of benzophenone-4-carboxylic acid (D) and naphthalene (A) (left) and alcohol (D) and naphthalene (A) (right).

It has been consistently demonstrated in literature that for donor-acceptor complexes separated by a bridge, the rate of energy transfer decreases as bridge length increased, both experimentally,[65-69] and theoretically.[70-73] Conjugated organic systems are commonly used as a bridge between donor and acceptor moieties due to their rigidity which results in holding the donor and acceptor groups in specific positions. Early work calculated an expression for the electronic coupling between donor and acceptor groups separated by a bridge composed of identical sub-units.[71-73] Models predicted that the electronic coupling depends on the D-A energy gap and that this gap decreases near-exponentially with distance. However, this model is observed to break down for π-conjugated bridges, thus the dependence of CT on distance is often no longer exponential.[61]

For π-conjugated bridges, varying the bridge length may change the level of π-conjugation observed, such that when the length of a π-conjugated bridge is extended in D-B-A complexes, the HOMO-LUMO gap will decrease resulting in a red shift in the absorption wavelength. For example Numuangruk *et al.* observed that as the number of thiophene spacers increase in a D-D-B-A complex, where D-D represents the attachment of an additional donor, a red shift in absorption of *ca.* 6-9 nm per additional thiophene bridge occurs indicating a decrease in the HOMO-LUMO gap.[74]

Kroon *et al.* have investigated the effect of spacer length on D-A charge-transfer complexes, with naphthalene as a donor moiety and carbonyl as an acceptor moiety,

shown in Figure 2-14.[67] The fluorescence lifetime of naphthalene was observed to increase with bridge length and conversely the calculated rate of intramolecular charge transfer was shown to decrease with increasing bridge length. Both of these trends are observed regardless of solvent. Rate constant calculations as a function of solvent density by Brunschwig *et al.* have supported the conclusion that the rate constant of the charge transfer decreases with increasing bridge length.[70]

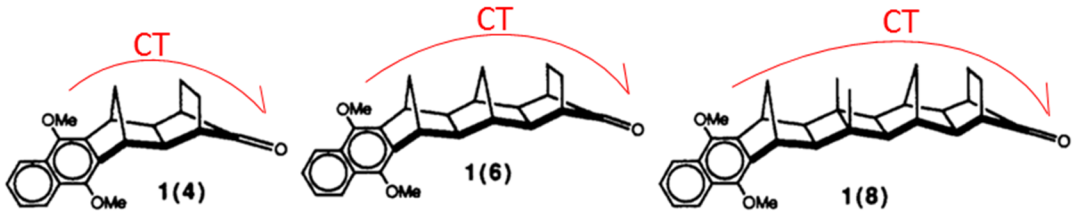

Figure 2-14: The structures of naphthalene (D) and carbonyl (A) complexes. Reproduced from reference 67.

Table 2-2: The naphthalene donor fluorescence lifetime (τ) and the calculated rate of intramolecular energy transfer (κ) with increasing bridge length, for the naphthalene donor to carbonyl acceptor moieties with increasing bridge length. Values taken from reference 67.

Solvent	1(4)		1(6)		1(8)	
	τ (ps)	κ (10^6 s^{-1})	τ (ps)	κ (10^6 s^{-1})	τ (ps)	κ (10^6 s^{-1})
n-hexane	85	11660	3400	193	7600	31
cyclohexane	80	12400	3100	218	7100	37
benzene	263	3630	3700	101	5400	16
di-n-butyl ether	100	9870	3400	163	6300	27
diethyl ether	125	7870	3900	123	6500	21
ethyl acetate	270	3550	4400	71	6000	10
tetrahydrofuran	265	3610	4100	80	5800	8
acetonitrile	1200	700	6500	21	7650	0

Other studies of D-B-A complexes using a rigid androstane derivative bridge to keep a constant and known distance between the naphthalene donor and the biphenyl acceptor.[65, 66, 68] have shown electronic coupling between naphthalene and biphenyl is approximately constant throughout the androstane series. The observed rate variation is attributed to the nuclear coordinates causing a variation in the Franck-Condon factors. The trend in rate constant is shown to be reasonably independent of concentration and solvent polarity in agreements with Kroon *et al.*[67]

Moore *et al.* demonstrated the formation of a long-lived charged-separated state for the compound shown in Figure 2-15, with a carotenoid (C) donor and a quinone (Q) acceptor.[69] The proposed scheme for achieving a charge separated state inferred from spectroscopic studies is shown in Figure 2-15. The longest lived charge-separated state, with a lifetime on the microsecond timescale, was observed when the bridge was a neutral porphyrin (P).

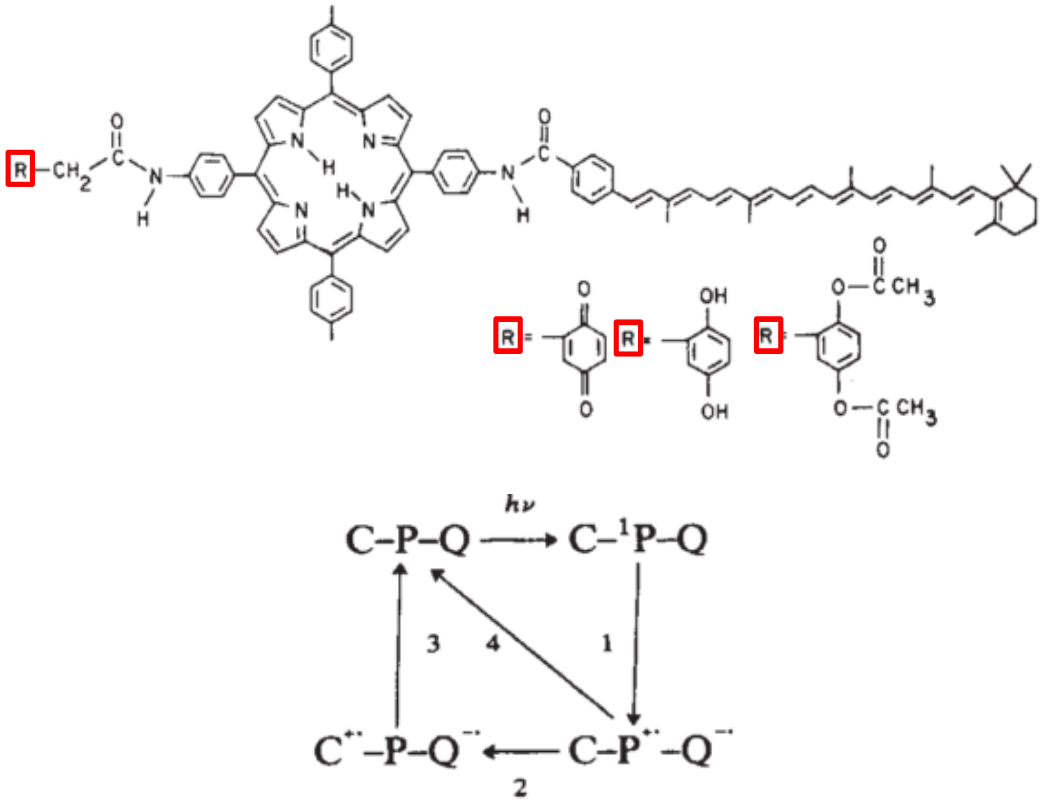

Figure 2-15: The complexes used by Moore et al (top) with R groups (middle). The scheme proposed for achieving a charge separated state (bottom). Reproduced from reference 69.

Further studies to understand when a charge transfer state may occur have focussed on whether a dimeric donor is required to stabilise charge separation from excited singlet states of porphyrin derivatives and to assess the influence of redox potential difference in controlling electron transfer kinetics.[75] Studies of complexes consisting of a quinone donor unit and a porphyrin acceptor unit, separated by a rigid bridge of phenyl units, demonstrate a decrease in electron transfer rate from quinone to the porphyrin with increasing spacer length.[60]

As discussed previously the transition energy and oscillator strength are linked to the coupling of the donor and acceptor and this coupling is dictated by the insulator or conductor nature of the bridge. Nielsen *et al.* used gas phase absorption spectroscopy studies, allowing understanding of the complexes behaviour in the absence of solvent environment, to investigate the functionalisation of the bridge on charge transfer excitation energy.[62] By investigating nitrophenolate anions which contain a phenolate oxygen donor and a nitro group acceptor and bridges of varying natures were investigated, Figure 2-16.

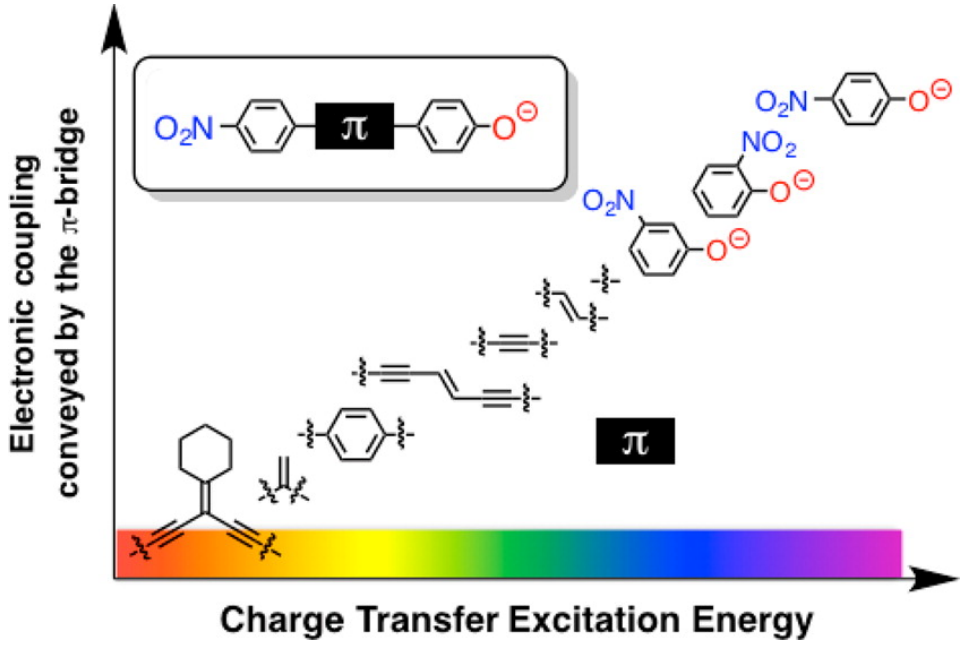

Figure 2-16: The complexes studied by Nielsen *et al. via* gas phase absorption under vacuum to investigate the relationship between charge transfer excitation energy and electronic coupling. Reproduced from reference 62.

The vacuum gas absorption results and coupled cluster theoretical model show that the CT excitation energy decreases with electronic decoupling between donor and acceptor moieties as a result of either cross conjugation or non-planarity. Therefore, a bridge such as an alkene has more charge transfer character than a phenyl bridge. Furthermore, the position of the donor and acceptor substituents can have an effect, whereby more charge transfer is observed from phenolate to the nitro group when the two groups are substituted in the para position compared to the meta position, Figure 2-17. This result is interesting, as the affect is not always observed with solvent present due to the interference from the solvent.[62]

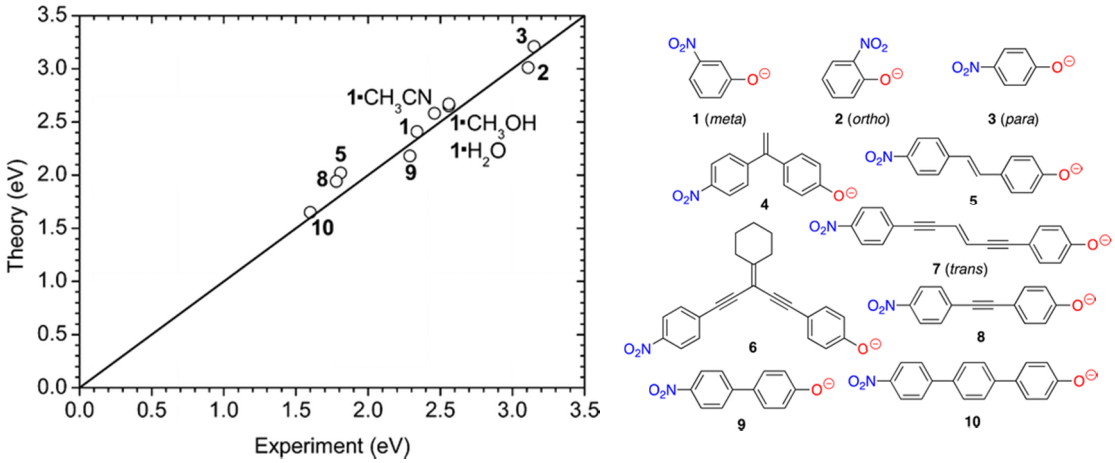

Figure 2-17: The gas absorption band maxima under vacuum (Experiment eV) and coupled cluster theoretical model (Theory eV) demonstrate that CT excitation energy decreases with electronic decoupling between D and A. Reproduced from Reference 62.

The highest CT excitation energy and thus the greatest magnitude of electronic coupling is exhibited by complex (3) the para isomer of the nitrophenolate, followed closely by (2) the ortho isomer. This is due to the linear conjugation observed most strongly for the para-isomer, and to a lesser extent the ortho-isomer, compared to the cross conjugation exhibited by the meta-isomer (Figure 2-18).

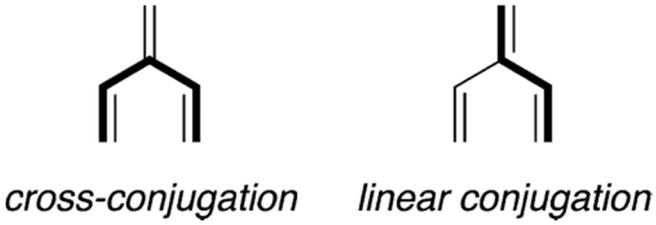

Figure 2-18: A representation of cross conjugation exhibited by (1) meta isomer and linear conjugation exhibited by (2) and (3) the ortho and para isomers of nitrophenolate respectively. Reproduced from reference 62.

Subsequently, the ethylene (5) and acetylene (8) derivative bridges are observed at lower energies to the nitrophenolate ions without a bridge. These two bridges demonstrate the negligible difference between an alkene and an alkyne spacer where the alkyne bridge demonstrates slightly more CT character and lower excitation energy than the alkene. The highest CT character is demonstrated by phenylene bridge compound (10) which is assigned as exhibiting the most conjugation.

Velusamy *et al.* observed that a bridge consisting of thiophene units red shifts a complexes absorption spectra more compared to a bridge consisting of phenyl units.[76] This red shift has been explained by theoretical calculations which show that a bridge consisting of thiophene units lowers the LUMO energy more than a bridge consisting of phenyl subunits. This results in an increase in effective conjugation length and thus red shifting the band observed in the absorption spectra.[77, 78]

The planarity of a π-conjugated bridge has an effect on the degree of conjugation observed. Increasing the planarity of spacers is likely to extend the effective π conjugation length and thus decrease the HOMO-LUMO gap. A common method for increasing planarity is to provide rigidity in the sub-units which form the bridge. For example, Kang demonstrated that including a planar and cyclic indeno[1,2-b]thiophene instead of a non-planar analogue such as phenyl-thiophene, results in a red shift in the absorption.[79] To this end a range of planar units have been used or incorporated into bridge design to increase overall bridge planarity including fluorene,[78, 80] cyclopentadithiophene,[81] dithieno-[3,2-b;2',3'-d]thienyl,[82] and indenofluorene.[83]

Tan *et al*. used DFT and TD-DFT to show that for diphenyl amine (DPA)-π-cyanoacrylic acid (CAA) complexes, Figure 2-19, the change from phenyl to thiophene bridge moiety for the π-conjugated bridge had a large effect on the planarity of the bridge.[84]

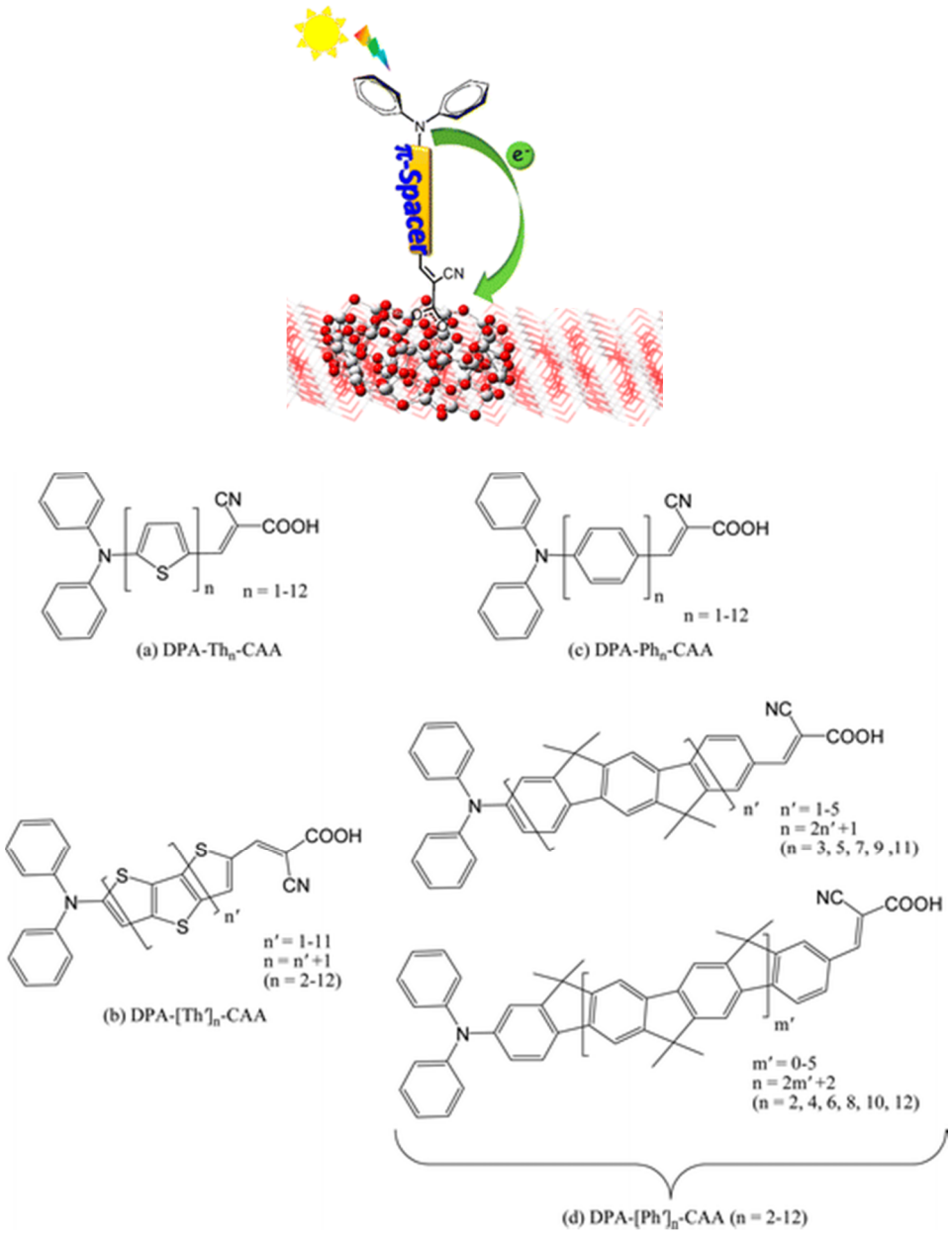

Figure 2-19: The structures of diphenylamine (DPA)-π-cyanoacrylic acid (CAA) complexes separated by various bridges: thiophene (a), phenyl (c) thiophene derivative (b) and phenyl derivative (d). Reproduced from reference 84.

For DPA-Ph_n-CAA and DPA-Th_n-CAA complexes, it was shown that as *n>1* for the phenyl compounds, non-planarity is observed between the neighbouring phenyl rings with a dihedral angle of *ca.* 30-35^{o}. This indicates the steric repulsion between the phenyl rings. A decrease in planarity causes a decrease in the effective π-conjugation length and thus an increase in the HOMO-LUMO gap, causing a blue shift in absorption. Conversely, for DPA-Th_n-CAA compounds where *n*>1, planarity or near-planarity is

observed between the thiophene units with a dihedral angle of *ca.* 0-11°. This planarity is due to the anti-configuration of the Th rings which has been shown to be more stable than the syn-configuration. This appears to show that the Th ring is a better π-conjugated bridge than a phenyl ring. However for DPA-[Ph']$_n$-CAA and DPA-[Th']$_n$-CAA the bridges are nearly planar for both sets of complexes where the value of *n* makes negligible difference.

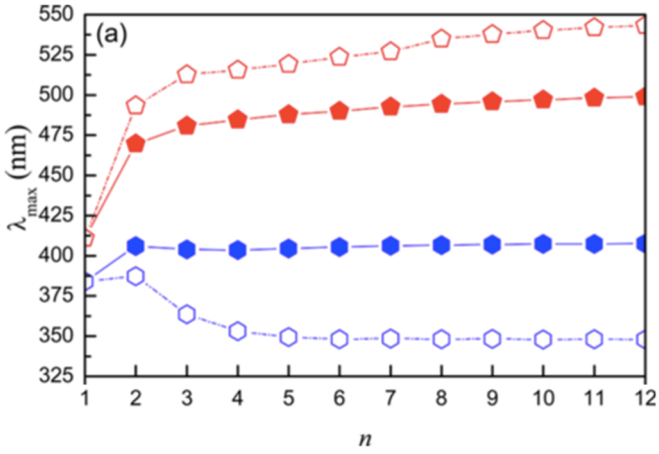

Figure 2-20: DFT calculated λ_{max} (a) and calculated oscillator strength (b) for the complexes DPA-Th$_n$-CAA, DPA-[Th']$_n$-CAA, DPA-Ph$_n$-CAA and DPA-[Ph']$_n$-CAA as a function of n values. Reproduced from reference 84.

Theoretical studies have been used to indicate the effect of the D-A dihedral angle on the CT observed, where a simple tight-binding model has been used to demonstrate that variation of D-A angles results in static changes in the magnitude of electronic coupling along the bridge length or dynamic fluctuations of this quantity on the certain characteristic time scale (τ_{rot}).[63] This leads to the functional breakdown of the Condon Approximation, by which electronic transition dipoles are independent of nuclear positions and as a result the modelling of charge transfer beyond the Condon approximation reveals two types of non-Condon effects.

To assign these two non-Condon effects, Berlin *et al.* carried out theoretical studies on the effects of D-A dihedral angle on charge transfer using systems with bridges which were short enough to allow an electron to be irreversibly transferred from D to A *via.* quantum mechanical tunnelling.[63] Three types of bridge were investigated in this study: (i) Flat rigid linkers with electronic coupling that does not vary with length, (ii) inflexible

bridges with disorder resulting from static variations of the D-A angle and (iii) dynamic bridges in which electronic coupling can fluctuate in time due to torsional motion of adjacent structural subunits relative to each other.

For bridge type (i) the charge transfer kinetics over a given distance are characterised by a time-independent rate coefficient. Therefore, in the tunnelling regime the rate coefficient decreases with bridge length following the exponential length dependence. Conversely for bridge type (ii) the rate of charge transfer is characterised by a time-dependent rate constant. Whereby the static torsional disorder results in time scale invariance of the charge transfer process. Furthermore, a time dependent rate of charge transfer is observed for bridge type (iii), where the torsional disorder of the bridge causes dynamic fluctuations of electronic coupling between two neighbouring molecular subunits, resulting in two non-Condon effects: (a) when torsional motion and charge transfer in the absence of disorder occur on comparable time scales and (b) when torsional motion occurs much faster than charge transfers. As a result of both non-Condon effects, the concept of constant rate coefficient to describe the tunnelling regime of charge transfer through bridge type (iii) is only applicable when torsional fluctuations are on much faster time scales than charge transfer between D and A in the absence of static or dynamic disorder.

Closs *et al.* studied the dihedral angle in D-A acceptor complexes where the biphenyl (Bi) donor and napthalene (Na) acceptor are separated by a bridge consisting of aromatic cyclohexane rings, shown in Figure 2-21.[66] The study concerned the angle between the aromatic ring plane and the C-H bond at the attachment position of the cyclohexane ring. Defined from MO caluclations for the aromatic substituent the equitorial (e) stereochemistry favours a dihedral angle close to 0^{o}, conversely for the axial (a) stereochemistry the preferred angle is 55^{o}. The rate constant for charge transfer is observed to increase when closer to the preferred dihedral angle, shown in Table 2-3.

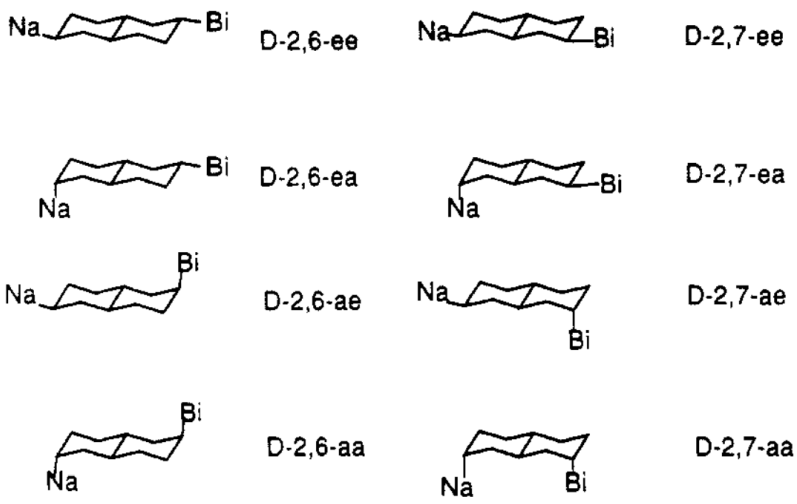

Figure 2-21: The structures of biphenyl-2-napthyl donor-acceptor complexes. Reprodced from reference 66.

Table 2-3: The angle and rate constants of compounds with 4-biphenyl-2-napthyl donor-acceptor. Values taken from reference 66.

Compound	$(R_{DA})_{center}$ / Å	$(R_{DA})_{edge}$ / Å	$k,^{b}$ / s^{-1}
D-2,61			
ee	14.0	6.7	5.0×10^{7}
ea	11.4	6.3	5.9×10^{7}
ae	11.0	6.3	2.3×10^{7}
aa	11.9	6.1	5.8×10^{7}
D-2,7			
ee	12.5	6.4	2.9×10^{8}
ea	11.4	6.0	3.0×10^{8}
ae	10.9	6.0	1.75×10^{8}
aa	6.2	5.3	25×10^{8}

2 Aims

The main aim of this work is to further understand the effect of electron donating (NPh_2) substituents on the photophysics of [Re(dppz)$(CO)_3$Cl] complexes. This aim has been split into three key objectives.

1. To ascertain the effect of an NPh_2 donor appended group on the nature and kinetics of the excited states observed, by investigated the photophysical properties for a series of [Re(dppz-NPh_2)$(CO)_3$Cl] derivative complexes through the use of time resolved infrared and absorption spectroscopy, cyclic voltammetry, spectroelectrochemistry and DFT calculations

2. To understand the effect of the bridge in [Re(dppz-(bridge)-NPh_2)$(CO)_3$Cl] complexes on the photophysical properties. This will include investigations into the effect of bridge length and bridge nature.

3. To elucidate the effect of the dihedral angle between the NPh_2 (donor) and the phz (acceptor) on the photophysical properties observed.

3 Results

The photophysics of the complexes [**Re(dppz-NPh_2)**$(CO)_3Cl$], [**Re(dppz-$(PhNPh_2)_2$)**$(CO)_3Cl$], [**Re(dppz-Ph_2NPh_2)**$(CO)_3Cl$], [**Re(dppz-Ph_3NPh_2)**$(CO)_3Cl$], [**Re(dppz-$(C_4H_3S)PhNPh_2$)**$(CO)_3Cl$], [**Re(dppz-$(Ph\text{-}(OCH_3)_2)NPh_2$)**$(CO)_3Cl$] and [**Re(dppz-$(N_3C_2H)PhNPh_2$)**$(CO)_3Cl$] (Figure 2-22) have been investigated using TRIR, absorption, emission and EPR studies. The abbreviations used for these complexes throughout this Chapter are notated above in bold.

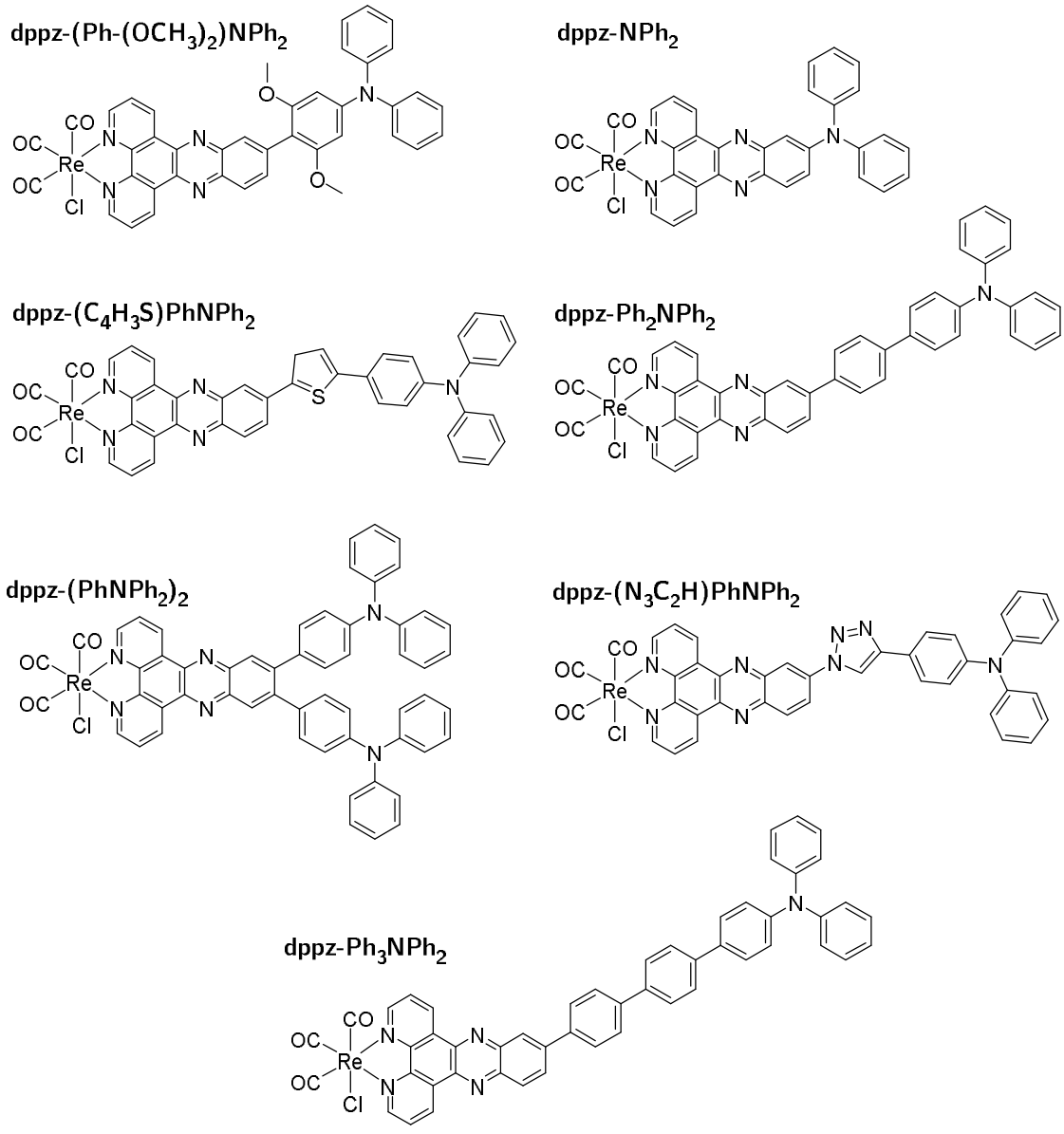

Figure 2-22: The NPh_2 donor-appended complexes $[Re(dppz\text{-}NPh_2)(CO)_3Cl]$ studied within this work.

3.1 Time Resolved Infrared Studies

3.1.1 TRIR Spectroscopy of Re(dppz-NPh$_2$)

The photophysical properties of Re(dppz-NPh$_2$) were probed on the picosecond and nanosecond timescales using TRIR spectroscopy, where Figure 2-23 shows the TRIR spectra of Re(dppz-NPh$_2$) obtained at several time delays after photoexcitation at 355 nm and the features observed are summarised in Table 2-4. The spectra obtained 1 ps after photoexcitation clearly shows that the parent bands at 2027, 1925, 1899 cm^{-1} are bleached and simultaneously transient peaks at 2016, 2006 and 1888 cm^{-1} are formed, which subsequently shift to slightly higher energies over the first 30 ps.

There is a prominent shoulder at *ca.* 2006 cm^{-1}, labelled as State I, which decays at the same time (τ = 37 ± 3 ps) as a band is formed (τ = 40 ± 3 ps) at 2019 cm^{-1} labelled as State II. The lower energy parent bleaches (1925 and 1899 cm^{-1}) appear to recover (τ = 40 ± 10 ps) and this is most likely due to overlap of the parent and new transient features as the amount of recovery varies across the parent bleach. More detailed analysis and band fitting suggests that a band decays at 1888 cm^{-1} (State I) to form a band at 1891 cm^{-1} (State II) with an additional decay and growth occurring around 1920 cm^{-1}. The assignments of these two states (State I and II) are further confirmed using global analysis (Figure 2-25).

The TRIR bands at 2019 and 1888 cm^{-1} exhibit a bi-exponential decay of τ = 2.2 ± 0.2 and 1800 ± 100 ns respectively, as shown Figure 2-24. This biexponential decay is consistent with the presence of two states, which are labelled State II and State III. The bands assigned to States II and III are in good agreement with the recovery of the parent bleaches of 2.3 ± 0.5 and 2200 ± 500 ns. The former shorter component of this parent bleach recovery lifetime is assigned as State III and the longer to State II, indicating that States II and III decay directly to the ground state.

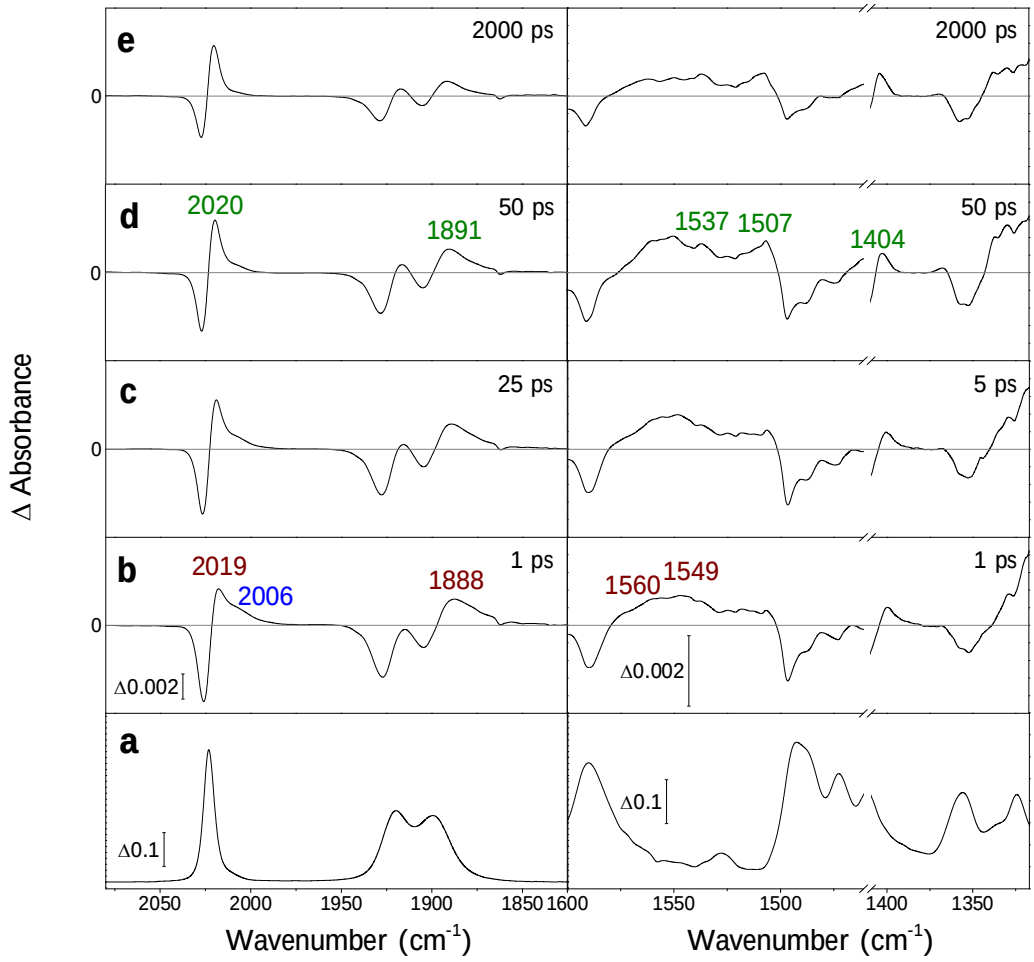

Figure 2-23: The FTIR (a) and TRIR (b-e) spectra of Re(dppz-NPh_2) in CH_2Cl_2 for both the CO (left) and the FP (right) IR regions following 355 nm photoexcitation. The FTIR was acquired in the solid state for the FP region due to poor solubility.

Table 2-4: A summary of the FTIR and TRIR spectral features observed for Re(dppz-NPh_2) in CH_2Cl_2 following 355 nm photoexcitation.

ν(CO) (cm^{-1})	ν(FP) (cm^{-1})	τ decay (ns)	τ growth (ns)	Assignment
2006	-	0.037 ± 0.002	-	State I
2019, 1888	1560, 1549	2.5 ± 0.3		State III
2020, 1891	1537, 1507, 1404	2300 ± 500	0.04 ± 0.002	State II
2027, 1925, 1905	1589, 1496, 1357, 1351	-	2.45 ± 0.05, 1900 ± 600	Parent
2024, 1920, 1899	1589, 1527, 1492, 1473, 1356, 1325	-	-	GS FTIR
2016, 1908, 1891	1586, 1526, 1340, 1320	-	-	$1e^-$ RS FTIR

From the ν(CO) TRIR kinetics alone it is difficult to unambiguously assign whether: (i) State I decays to States II + III; (ii) States I and III are formed simultaneously and State I decays to State II or (iii) State I decays to State II which subsequently decays to State III. The spectral shifts in the ν(CO) bands to lower energies exhibited by States I-III are indicative of an increase in electron density in the carbonyl antibonding orbitals which is consistent with the presence of both dppz-centred ππ* and charge transfer (CT) states.[4, 35, 38] Therefore the data in the fingerprint IR region has been investigated to further inform on both the nature of the excited states and their kinetics.

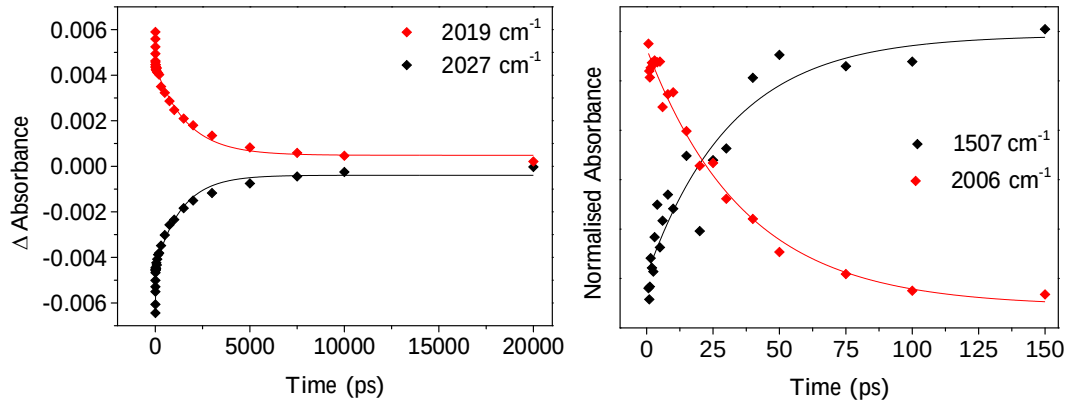

Figure 2-24: The kinetics of Re(dppz-NPh$_2$) in CH_2Cl_2 following 355 nm photoexcitation. The biexponential recovery of the band at 2027 cm^{-1} assigned to the parent and the biexponential decay of the transient band at 2019 cm^{-1} assigned to States III and II (left). The decay of the band at 2006 cm^{-1} assigned to State I against the growth of the transient band at 1527 cm^{-1} assigned to State II (right).

In the fingerprint IR region a number of bleaches corresponding to the ground state spectra are observed after photoexcitation at 355 nm (Figure 2-23), together with a number of excited state features, which are also summarised in Table 2-4. At early times there are many subtle changes but there are clear bands at 1537, 1507, and 1404 cm^{-1}, which are formed at similar times (40 ± 10 ps) as the shoulder at 2006 cm^{-1}, assigned as the decay of State I (37 ± 2 ps), with the kinetics for this process shown in Figure 2-24. Therefore the bands at 1537, 1507 and 1404 cm^{-1} are considered marker bands for the formation of a secondary photoproduct, State II, and the lack of parent recovery indicates that State I decays to State II. The bands at 1537, 1507, and 1404 cm^{-1} decay on the microsecond timescale as the parent bands fully reform (2.3 ± 0.5 μs), consistent with the assignment of these bands to State II. There is a clear band at

ca. 1549 cm^{-1} which decays on the nanosecond timescale (τ = 2.2 ± 0.2 ns) at the same rate as the parent bands partially reform and this is consistent with the decay of the ν(CO) bands discussed above. Therefore, this band has been attributed to State III. No new bands are observed to grow in on this timescale (τ = 2-3 ns) and this further indicates that State III decays to the ground state.

The global analyses of Re(dppz-NPh_2) show the presence of three states, (Figure 2-25), with lifetimes of 30 ps, 2.2 ns and 1400 ns which are consistent with the three states from the ν(CO) and ν(FP) IR data. Furthermore, the initial state possesses obvious peaks at 2009 and 1879 cm^{-1}, which are consistent with the observed features at 2006 and 1880 cm^{-1} at early times and are assigned above to State I. The global analysis predicts that the other two states formed possess very similar IR spectra in the ν(CO) region to those observed for the States II and III, with excited state bands at 2018, 1916 and 1892 cm^{-1}. Furthermore, it is evident from the global analysis that States II and III are indistinguishable by analysis of the ν(CO) region alone. From the global analyses of ν(FP) region shown in Figure 2-25, three states are also observed. The initial process is predicted to consist of decay of bands at 1575, 1488 and 1397 cm^{-1} (State I), with simultaneous growth at 1559, 1549, 1534, 1506, and 1404 cm^{-1} (State II). For State II the above mentioned band at 1560 cm^{-1} in addition to weaker bands at 1504 and 1403 cm^{-1} are present, while State III is most prominently characterised by bands at 1537 and 1507 cm^{-1}. In summary the above results indicate that two states are initially formed simultaneously, States I and III, where the former decays to State II. States II and III are observed to decay solely to the ground state.

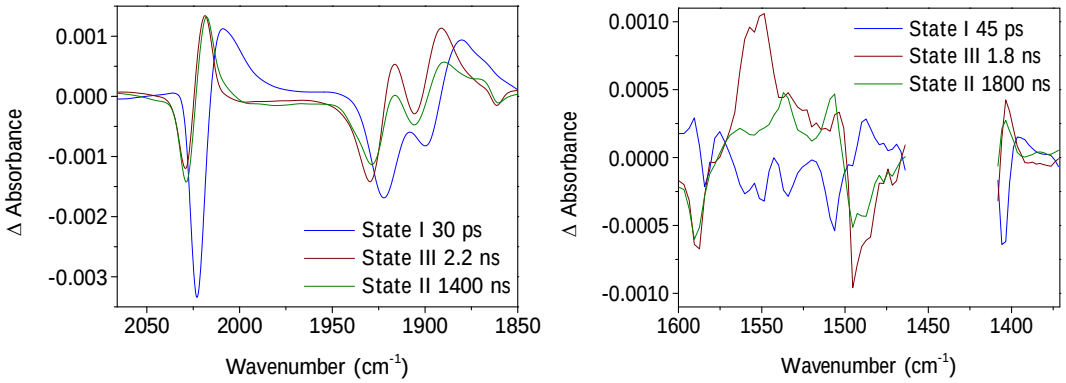

Figure 2-25: The global analysis of Re(dppz-NPh_2) in the CO (left) and FP (right) IR regions, in CH_2Cl_2 following 355 nm photoexcitation. Three clear states are elucidated.

3.1.2 TRIR Spectroscopy of Re(dppz-($PhNPh_2$)$_2$), Re(dppz-Ph_2NPh_2), Re(dppz-Ph_3NPh_2), Re(dppz-(C_4H_3S)NPh_2) and Re(dppz-(Ph-(OCH_3)$_2$)NPh_2)

The TRIR spectra of Re(dppz-($PhNPh_2$)$_2$), Re(dppz-Ph_2NPh_2), Re(dppz-Ph_3NPh_2), Re(dppz-(C_4H_3S)NPh_2) and Re(dppz-(Ph-(OCH_3)$_2$)NPh_2) have also been collected at several time delays following 355 nm photoexcitation in CH_2Cl_2. These complexes display a similar TRIR spectral profile to Re(dppz-NPh_2) with band positions and kinetics for the three observed processes for each complex are detailed below, Figures 2-26 to 2-35 and Tables 2-5 to 2-9.

All of the complexes show three distinct states, (I, II and III) and analogous assignments can be made to Re(dppzNPh_2). States I and III are observed at 1 ps following photoexcitation. State I is then observed to decay to State II and subsequently States II and III are observed to decay to the ground state. Marker bands for State II are observed in the fingerprint region.

TRIR Spectroscopy of Re(dppz-(Ph-(OCH_3)$_2$)NPh_2)

The TRIR spectra of Re(dppz-(Ph-(OCH_3)$_2$)NPh_2) have been collected in CH_2Cl_2 following 355 nm photoexcitation shown in Figure 2-26, and the kinetic traces for the

processes observed are shown in Figure 2-27. The band positions and kinetics are summarised in Table 2-5.

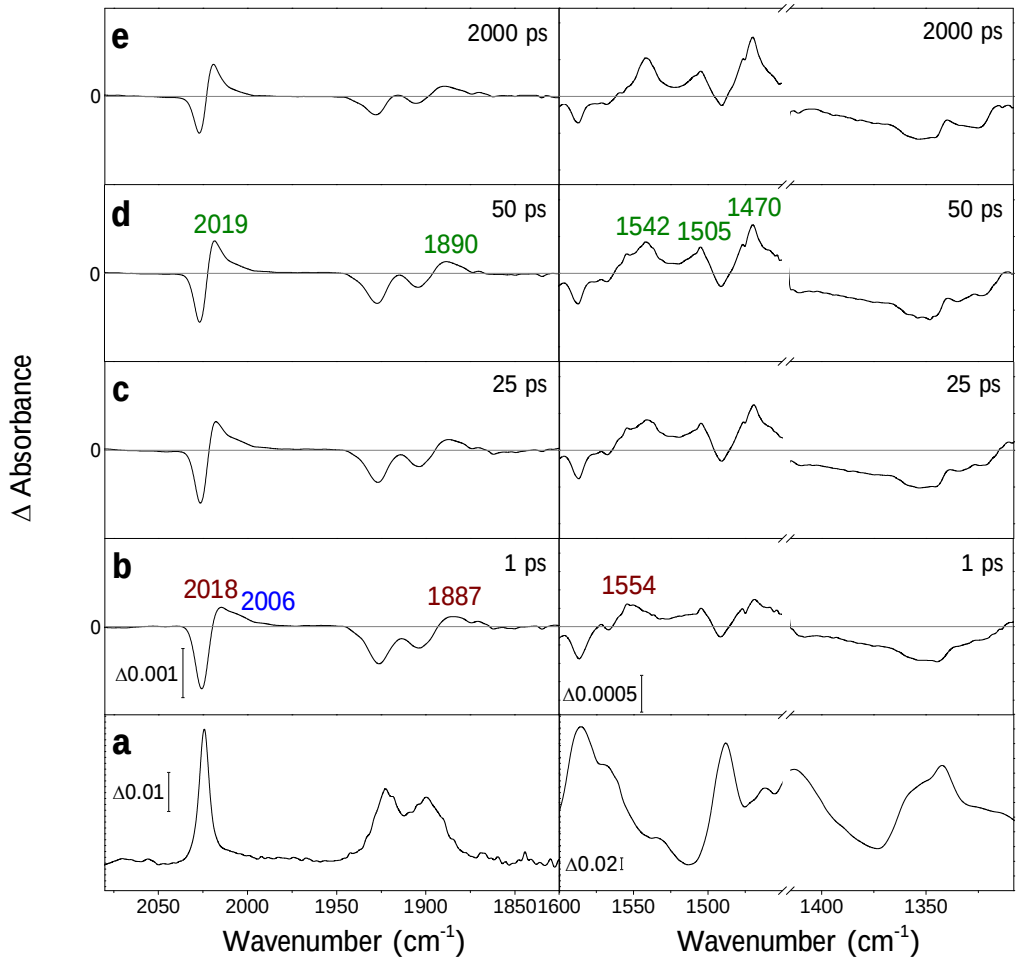

Figure 2-26: The FTIR (a) and TRIR (b-e) spectra of Re(dppz-(Ph-(OCH$_3$)$_2$)NPh$_2$) in CH$_2$Cl$_2$ for both the CO (left) and FP (right) IR regions following 355 nm photoexcitation. The FTIR was acquired in the solid state for the FP region due to poor solubility.

Table 2-5: A summary of the FTIR and TRIR spectral features observed for Re(dppz-(Ph-(OCH$_3$)$_2$)NPh$_2$) in CH$_2$Cl$_2$ following 355 nm photoexcitation.

ν(CO) (cm^{-1})	ν(FP) (cm^{-1})	τ decay (ns)	τ growth (ns)	Assignment
2006		0.043 ± 0.006	-	State I
2018, 1887	1554, 1311	2 ± 1		State III
2019, 1890	1542, 1505, 1470	2900 ± 500	0.027 ± 0.005	State II
2027, 1926, 1903	1590, 1493, 1354, 1326	-	2.3 ± 0.8 3200 ± 500	Parent
2024, 1922, 1899	1584, 1568, 1488, 1413, 1353, 1342	-	-	GS FTIR

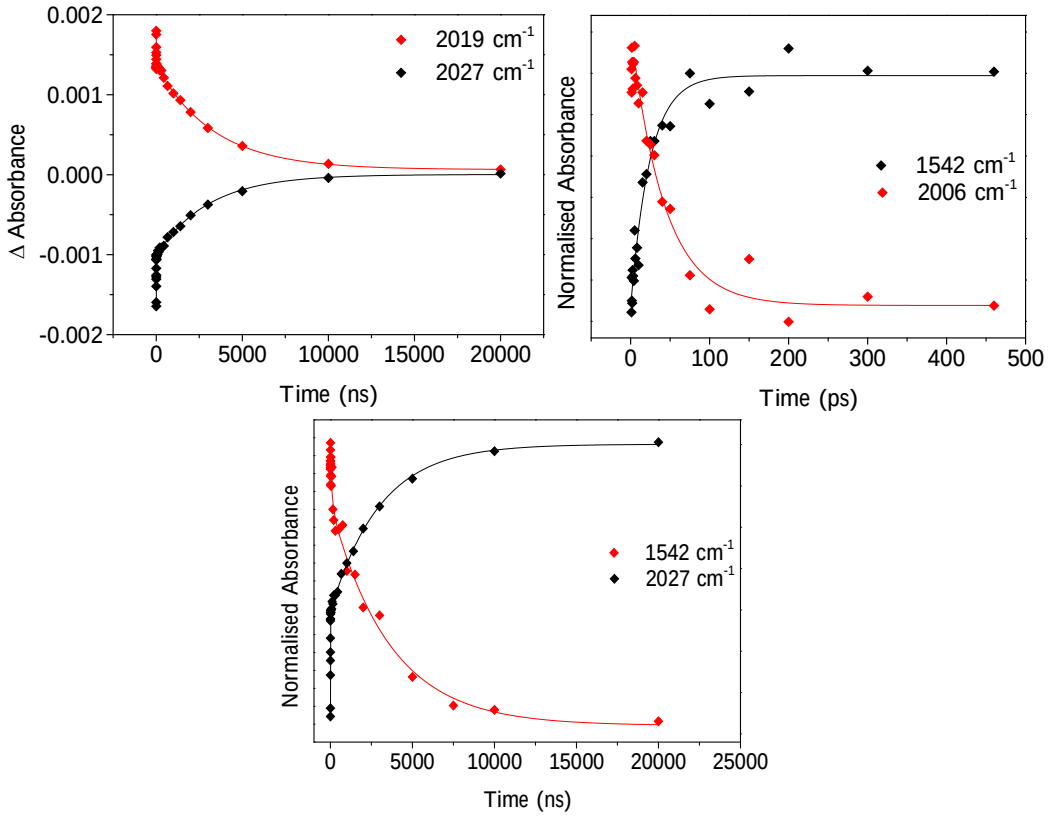

Figure 2-27: The kinetics of Re(dppz-(Ph-$(OCH_3)_2$)NPh_2) in CH_2Cl_2 following 355 nm photoexcitation. The biexponential recovery of the band at 2027 cm^{-1} assigned to the parent which is in good agreement with the biexponential decay of the transient band at 2019 cm^{-1} assigned to States III and II (top left). The decay of the band at 2006 cm^{-1} assigned to State I which is in good agreement with the growth of the transient band at 1542 cm^{-1} assigned to State II (top right). The long part of the biexponential recovery of the band at 2027 cm^{-1} assigned to the parent, which is in good agreement with the decay of band at 1542 cm^{-1} assigned to State II (bottom).

TRIR Spectroscopy of Re(dppz-(C_4H_3S)PhNPh$_2$)

The TRIR spectra of Re(dppz-(C_4H_3S)PhNPh$_2$) have been collected in CH_2Cl_2 following 355 nm photoexcitation shown in Figure 2-28, and the kinetic traces for the processes observed are shown in Figure 2-29. The band positions and kinetics are summarised in Table 2-6.

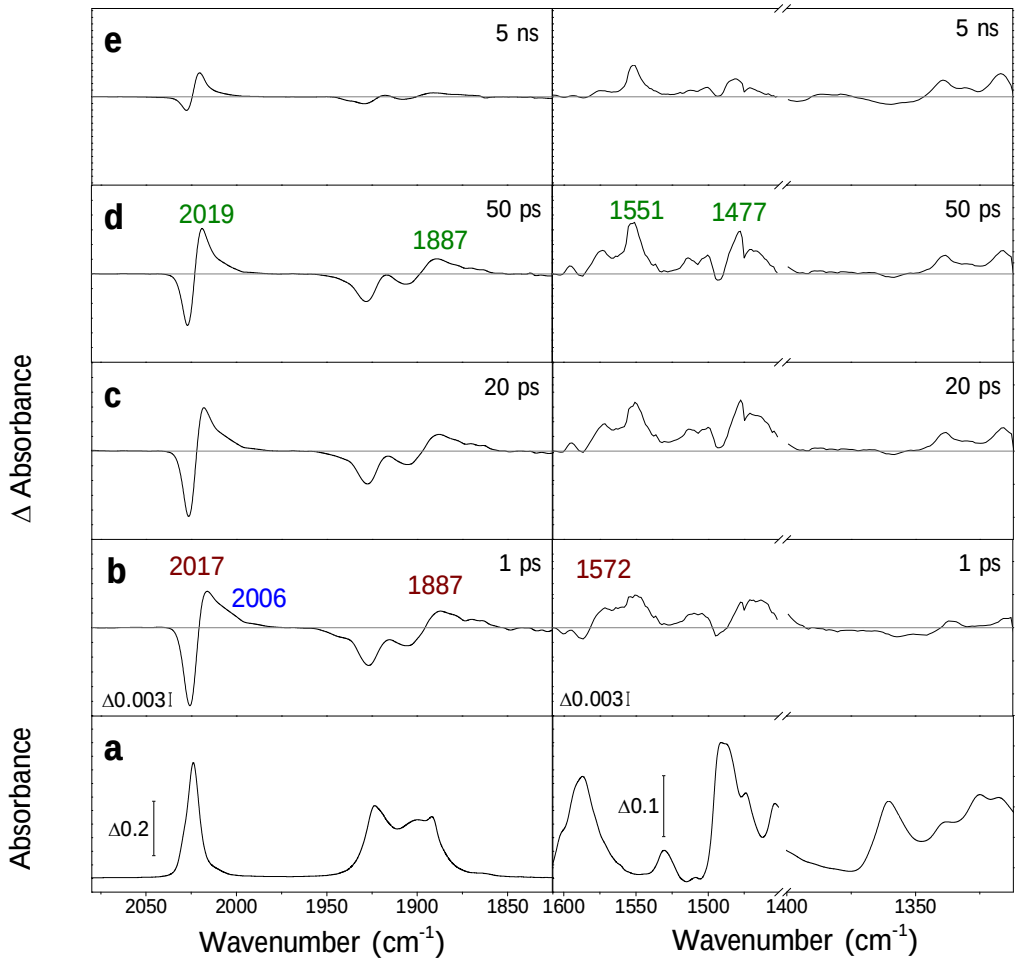

Figure 2-28: The FTIR (a) and TRIR (b-e) spectra of Re(dppz-(C_4H_3S)PhNPh$_2$) in CH_2Cl_2 for both the CO (left) and FP (right) IR regions following photoexcitation at 355 nm. The FTIR was acquired in the solid state for the FP region due to poor solubility.

Table 2-6: A summary of the FTIR (a) and TRIR (b-e) spectral features observed for Re(dppz-(C_4H_3S)PhNPh_2) in CH_2Cl_2 following 355 nm photoexcitation.

ν(CO) (cm^{-1})	ν(FP) (cm^{-1})	τ decay (ns)	τ growth (ns)	Assignment
2006	-	0.040 ± 0.002		State I
2017, 1887	1572	3 ± 1		State III
2019, 1887	1551	1280 ± 50	0.18 ± 0.02	State II
2027, 1926, 1905	1602, 1588, 1494, 1477, 1360, 1345		1.8 ± 0.6, 1300 ± 100	Parent
2024, 1922, 1900	1588, 1531, 1491, 1361, 1338, 1325, 1317	-	-	GS FTIR
2017, 1909, 1892	1589, 1372, 1360, 1343, 1335	-	-	$1e^-$ RS FTIR

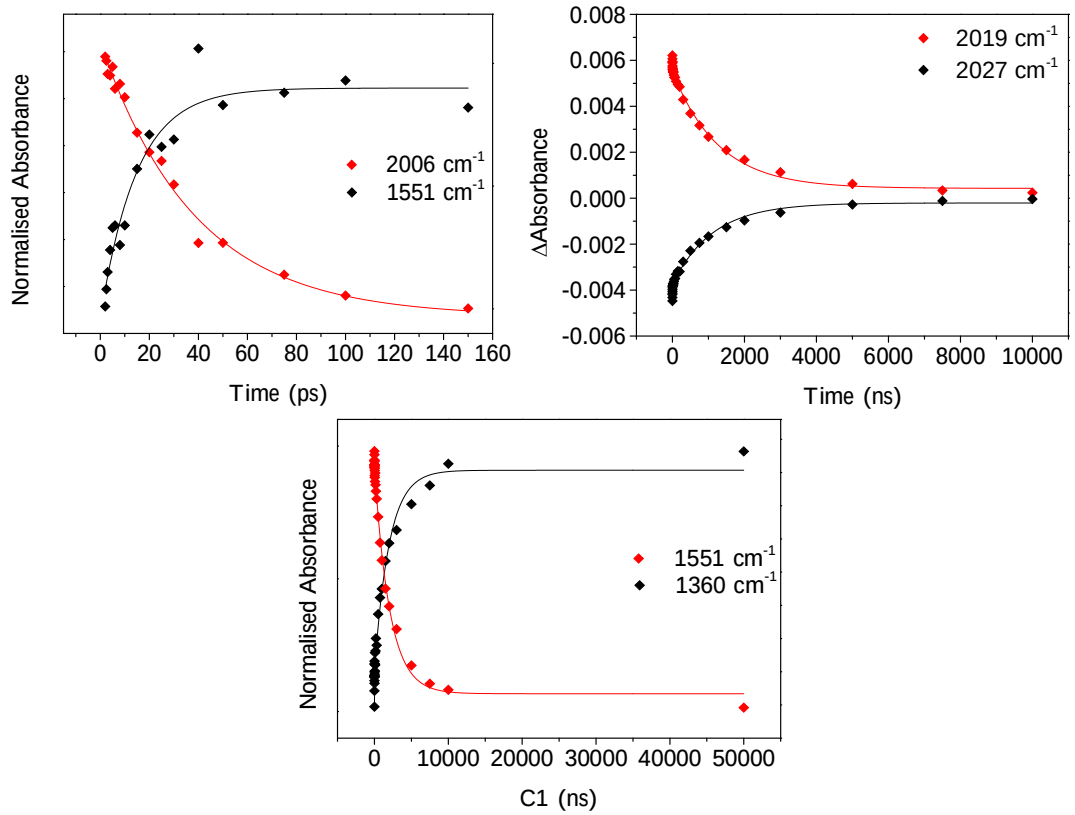

Figure 2-29: The kinetics of Re(dppz-(C_4H_3S)PhNPh_2) in CH_2Cl_2 following 355 nm photoexcitation. The decay of the band at 2006 cm^{-1} assigned to State I which is in good agreement with the growth of the band at 1551 cm^{-1} assigned to State II (top, left). The biexponential decay of the band at 2019 cm^{-1} assigned to States II and III, which is in good agreement with the biexponential of the band at 2027 cm^{-1} assigned to the parent (top, right). The biexponential decay of the band at 1551 cm^{-1} assigned to States III and II which is in good agreement with the biexponential growth of the band at 1360 cm^{-1} assigned to the parent (bottom).

TRIR Spectroscopy of Re(dppz-Ph_2NPh_2)

The TRIR spectra of Re(dppz-(Ph_2NPh_2) have been collected in CH_2Cl_2 following 355 nm photoexcitation shown in Figure 2-30, and the kinetic traces for the processes observed shown in Figure 2-31. The band positions and kinetics are summarised in Table 2-7.

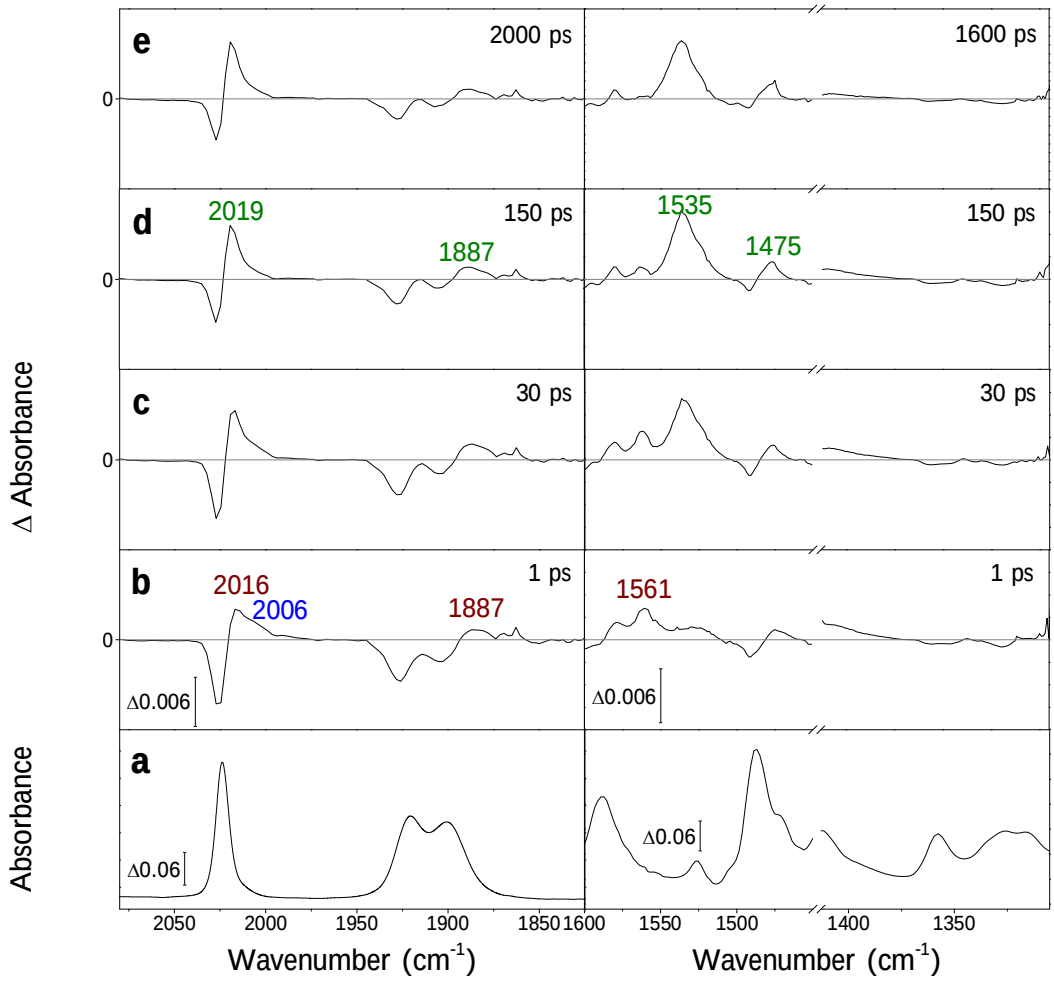

Figure 2-30: The FTIR (a) and TRIR (b-e) spectra of Re(dppz-Ph_2NPh_2) in CH_2Cl_2 for both the CO (left) and FP (right) IR regions following 355 nm photoexcitation. The FTIR was acquired in the solid state for the FP region due to poor solubility..

Table 2-7: A summary of the FTIR and TRIR spectral features observed for Re(dppz-Ph_2NPh_2) in CH_2Cl_2 following 355 nm photoexcitation.

ν(CO) (cm^{-1})	ν(FP) (cm^{-1})	τ decay (ns)	τ growth (ns)	Assignment
2006	-	0.044 ± 0.003	-	State I
2016, 1887	1561	0.14 ± 0.02		State III
2019, 1887	1535, 1475	1280 ± 30	0.020 ± 0.001	State II
2027,1926, 1905	1491, 1350, 1319	-	0.081 ± 0.005 1400 ± 200	Parent
2025, 1922, 1900	1588, 1487, 1473, 1412, 1357, 1325, 1316	-	-	GS FTIR
2017, 1910, 1894	1591, 1497, 1342, 1327, 1309	-	-	$1e^-$ RS FTIR

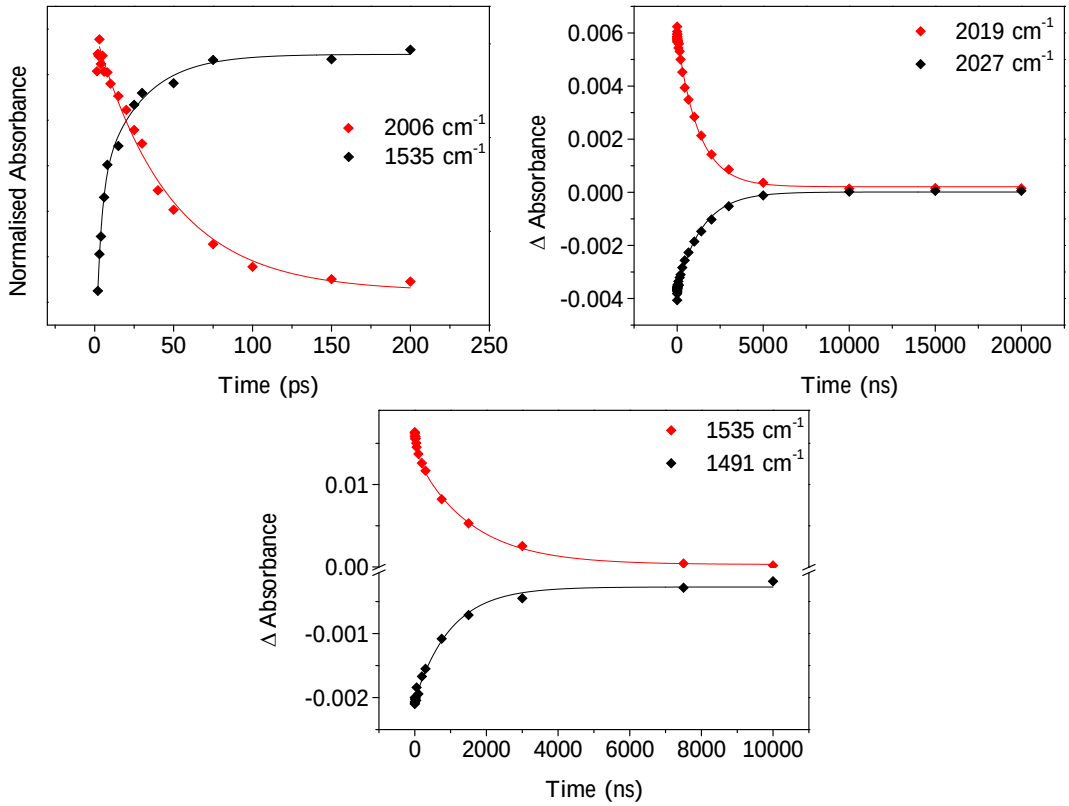

Figure 2-31: The kinetics of Re(dppz-Ph_2NPh_2) in CH_2Cl_2 following 355 nm photoexcitation. The decay of the band at 2006 cm^{-1} assigned to State I, which is in good agreement with the growth of the band at 1535 cm^{-1} assigned to State II (top left). The biexponential decay of the band at 2019 cm^{-1} assigned to States III and II which is in good agreement with biexponential recovery of the band at 2027 cm^{-1} assigned to the parent (top, right). The decay of the band at 1535 cm^{-1} assigned to State II in good agreement with the long part of the biexponential recovery of the band at 1491 cm^{-1} assigned to the parent (bottom).

TRIR Spectroscopy of Re(dppz-Ph_3NPh_2)

The TRIR spectra of Re(dppz-(Ph_3NPh_2) have been collected in CH_2Cl_2 following 355 nm photoexcitation and are shown in Figure 2-32. The kinetic traces for the processes observed are shown in Figure 2-33. The band positions and kinetics are summarised in Table 2-8.

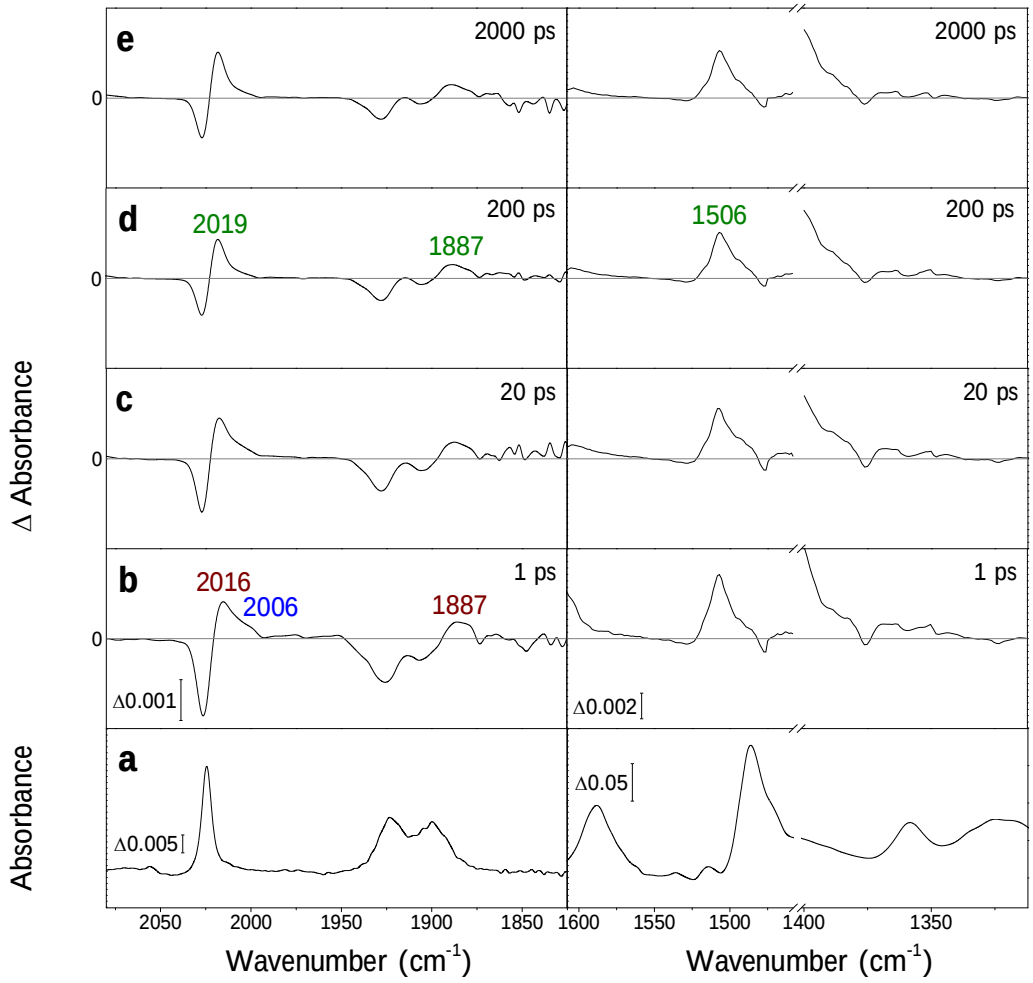

Figure 2-32: The FTIR (a) and TRIR (b-e) spectra of Re(dppz-Ph_3NPh_2) in CH_2Cl_2 following 355 nm photoexcitation for both the CO (left) and FP (right) IR regions. The FTIR was acquired in the solid state for the FP region due to poor solubility.

Table 2-8: A summary of the FTIR and TRIR spectral features observed for Re(dppz-Ph_3NPh_2) in CH_2Cl_2 following 355 nm photoexcitation.

ν(CO) (cm^{-1})	ν(FP) (cm^{-1})	τ decay (ns)	τ growth (ns)	Assignment
2006		0.03 ± 0.005	-	State I
2016, 1887		0.038 ± 0.006	-	State III
2019, 1887	1506	950 ± 90	0.06 ± 0.02	State II
2027, 1928, 1904	1375, 1475	-	0.030 ± 0.007 1000 ± 100	Parent
2025, 1924, 1900	1589, 1487, 1358, 1325	-	-	GS FTIR

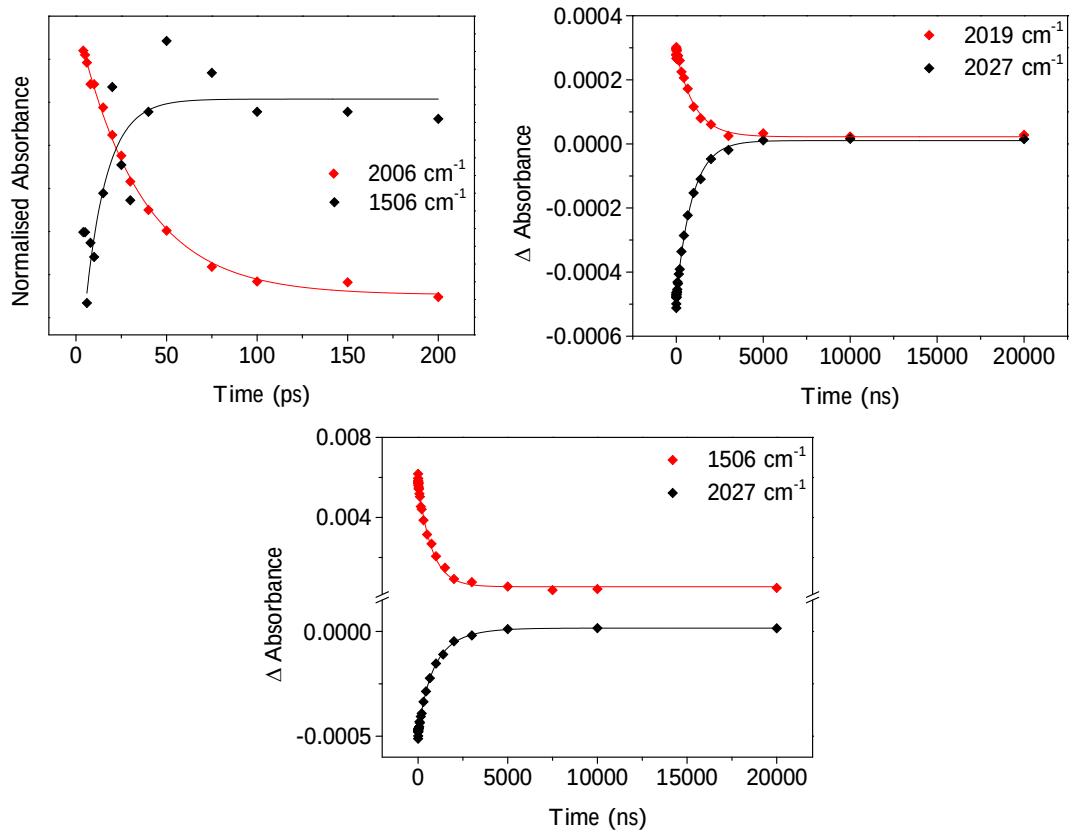

Figure 2-33: The kinetics of Re(dppz-Ph_3NPh_2) in CH_2Cl_2 following 355 nm photoexcitation. The decay of the band at 2006 cm^{-1} assigned to State I is in good agreement with the growth of the band at 1506 cm^{-1} assigned to State II (top left). The biexponential decay of the band at 2019 cm^{-1} assigned to States III and II, is in good agreement with the biexponential recovery of the band at 2027 cm^{-1} assigned to the parent (top, right). The decay of the band at 1506 cm^{-1} assigned to State II, is in good agreement with the long part of the biexponential decay of the band at 2027 cm^{-1} assigned to the parent (bottom).

TRIR Spectroscopy of Re(dppz-(PhNPh$_2$)$_2$)

The TRIR spectra of Re(dppz-(PhNPh$_2$)$_2$) have been collected in CH_2Cl_2 following 355 nm photoexcitation shown in Figure 2-34, and the kinetic traces for the processes observed shown in Figure 2-35. The band positions and kinetics are summarised in Table 2-9.

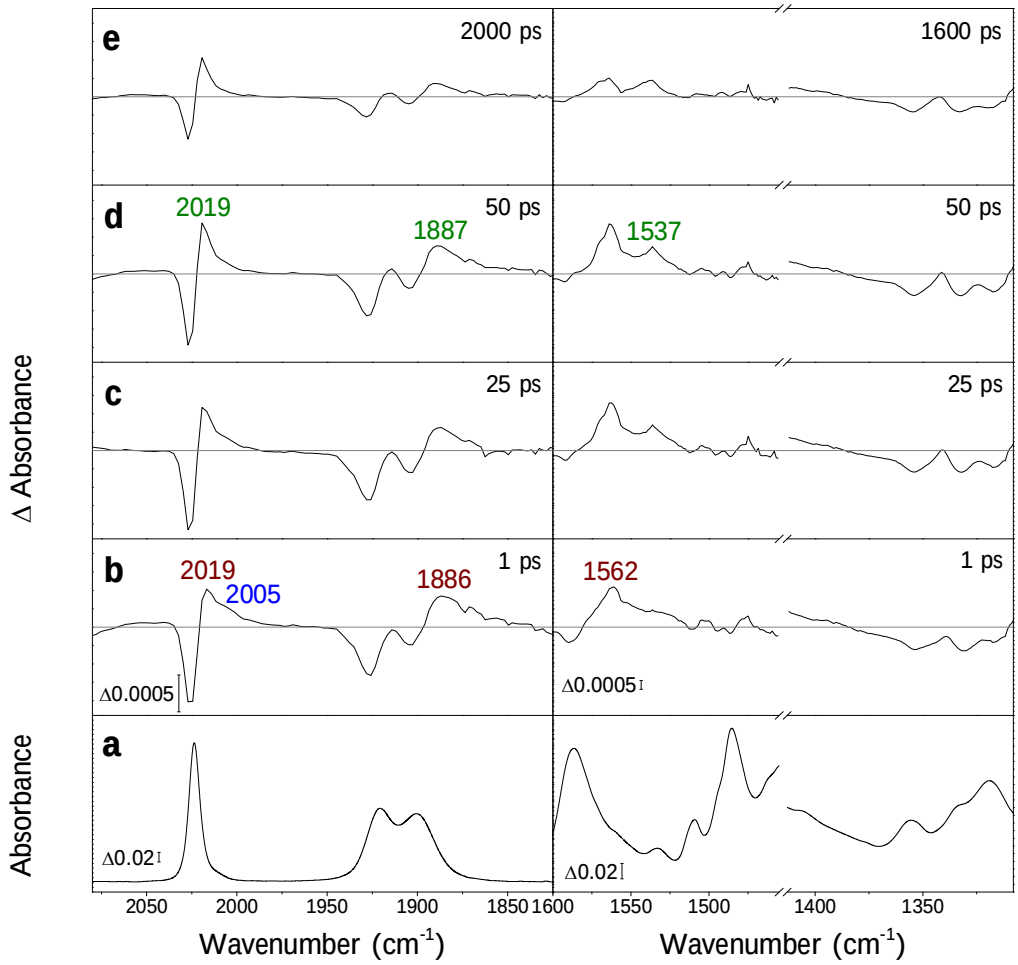

Figure 2-34: FTIR (a) and TRIR (b-e) spectra of Re(dppz-(PhNPh$_2$)$_2$) in CH_2Cl_2 for both CO region (left) and fingerprint region (right) following 355 nm photoexcitation. The FTIR was acquired in the solid state for the FP region due to poor solubility.

Table 2-9: A summary of the FTIR and TRIR spectral features observed for Re(dppz-(PhNPh$_2$)$_2$) in CH_2Cl_2 following 355 nm photoexcitation.

ν(CO) (cm^{-1})	ν(FP) (cm^{-1})	τ decay (ns)	τ growth (ns)	Assignment
2006		0.028 ± 0.004		State I
2019, 1886	1562,	1.5 ± 0.5		State III
2019, 1887	1537	2200 ± 600	0.03 ± 0.01	State II
2027, 1928, 1905	1603, 1591, 1354,		3 ± 1	Parent
	1332		1900 ± 400	
2024, 1921, 1900	1587, 1509, 1486,	-	-	GS FTIR
	1356, 1319			
2017, 1909, 1893	1589, 1508, 1360,	-	-	1e$^-$ RS FTIR
	1343, 1313			

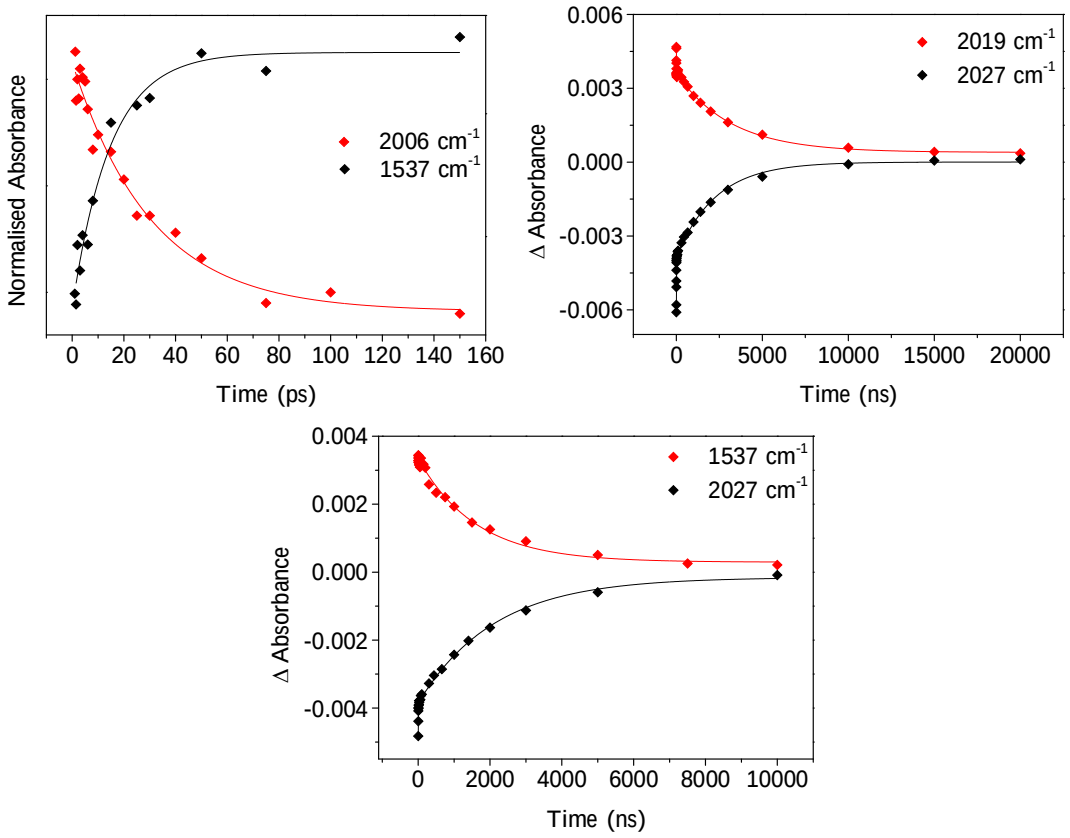

Figure 2-35: The kinetics of Re(dppz-(PhNPh$_2$)$_2$) in CH_2Cl_2 following 355 nm photoexcitation. The decay of the band at 2006 cm^{-1} assigned to State I, is in good agreement with the growth of the band at 1537 cm^{-1} assigned to State II (top, left). The biexponential decay of the band at 2019 cm^{-1} assigned to States III and II, is in good agreement with biexponential recovery of the band at 2027 cm^{-1} assigned to the parent (top, right). The decay of the band at 1537 cm^{-1} assigned to State II, is in good agreement with the long part of the biexponential recovery of the band at 2027 cm^{-1} assigned to the parent (bottom).

TRIR Spectroscopy of Re(dppz-(N_3C_2H)PhNPh$_2$)

The complex Re(dppz-(N_3C_2H)PhNPh$_2$) exhibits a different spectral profile to the previous complexes studied. The results collected from the TRIR in both the CO and FP IR regions are detailed in Table 2-10, with the spectra shown in Figures 2-36 and 2-37. From the TRIR results probing the CO region the following observations were made. Following photoexcitation on the picosecond timescale, parent bleaching and the formation of transient bands at *ca.* 2016 and 1887 assigned to State III and a shoulder at 2006 cm^{-1} assigned to State I were observed, consistent with the other complexes. However, a transient band at 2080 cm^{-1}, previously unseen in the other complexes, is also observed and this is assigned to an MLCT(phz) state. As with the other complexes, bands at 2019 and 1887 cm^{-1} (State II) are observed and grow in with a similar lifetimes to the decay of the band at 2006 cm^{-1} assigned to State I decay.

On the ps-timescale a shoulder at 2006 cm^{-1} is observed assigned to State I, which decays with lifetime of 32 ± 6 ps as shown in Figure 2-36. The band at 2080 cm^{-1} is assigned to an MLCT(phz) state owing to the $\Delta\nu = +53\ cm^{-1}$ with respect to the parent,[33] decays on the ps timescale as well with a lifetime of 60 ± 10 ps. Due to the low population of the MLCT state it is not possible to observe the transitions occurring from the kinetics; however, it is likely that the MLCT state decays to the ground state, although decay to an excited state cannot be ruled out. On the nanosecond timescale, bands at 2019 and 1887 cm^{-1} assigned to State II decay with lifetime 1400 ± 200 ns which is in good agreement with the recovery of the parent of 1420 ± 90 ns, Figure 2-37.

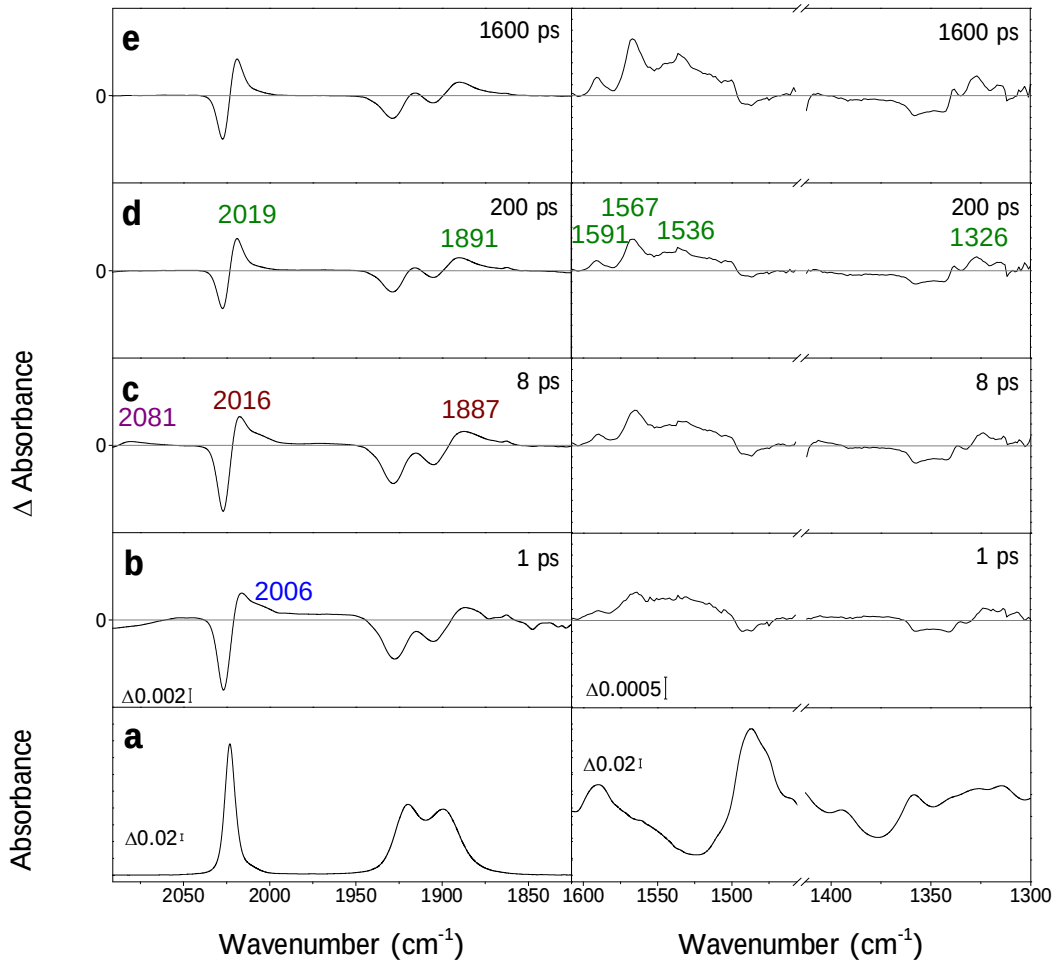

Figure 2-36: The FTIR (a) and TRIR (b-e) spectra of Re(dppz-(N_3C_2H)PhNPh_2) in both the CO (left) and FP (right) IR regions following photoexcitation at 355 nm in CH_2Cl_2. The FTIR was acquired in the solid state for the FP region due to poor solubility.

Table 2-10: A summary of the FTIR and TRIR spectral features and kinetics observed for Re(dppz-(N_3C_2H)PhNPh_2) in CH_2Cl_2 following photoexcitation at 355 nm.

ν(CO) (cm^{-1})	ν(FP) (cm^{-1})	τ decay (ns)	τ growth (ns)	Assignment
2081	-	0.055 ± 0.007	-	MLCT
2006	-	0.034 ± 0.001	-	State I
2016, 1887	-	0.04 ± 0.01	-	State III
2019, 1891	1567, 1591, 1545, 1536, 1335, 1326	800 ± 300	0.029 ± 0.005	State II
2027, 1931, 1907	1492, 1486, 1358, 1343	-	0.033 ± 0.006 1000 ± 300	parent
2024, 1925, 1901	1591, 1487, 1394, 1360	-	-	GS FTIR

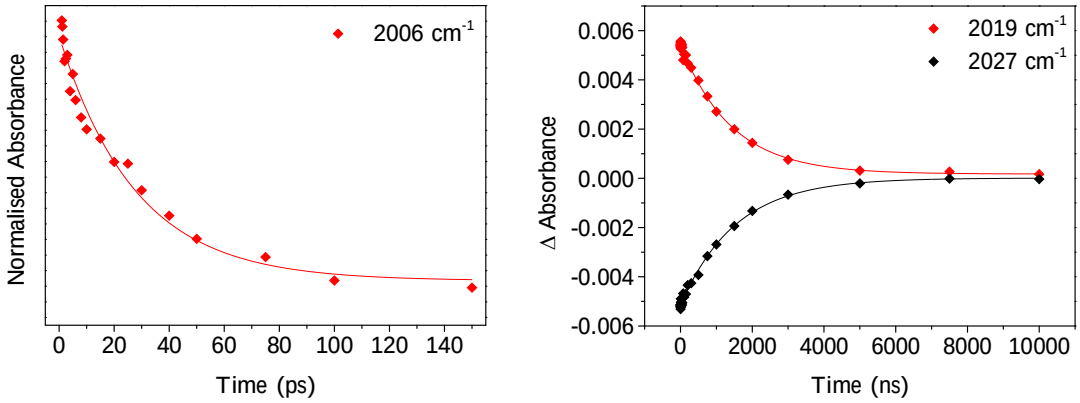

Figure 2-37: The kinetics of Re(dppz-(N_3C_2H)PhNPh$_2$) in CH_2Cl_2 following photoexcitation at 355 nm. The decay of the band at 2006 cm^{-1} assigned to State I (left). The biexponential decay of the band at 2019 cm^{-1} assigned to States III and II, is in good agreement with the biexponential recovery of the band at 2027 cm^{-1} assigned to the parent (right).

The fingerprint IR region has also been probed following photoexcitation and on the picosecond time scale parent bleaching and the formation of several transient bands is observed as shown in Figure 2-36. Although, no peaks decaying with a *ca.* 32 ps lifetime, to match state I decay from the CO region are observed, bands at 1591, 1561, and 1536 are observed to grow in. These bands are considered marker bands for State II, indicating that State I likely decays to State II. State II then decays with lifetime of 600 ± 200 ns as the parent recovers with lifetime 600 ± 200 ns.

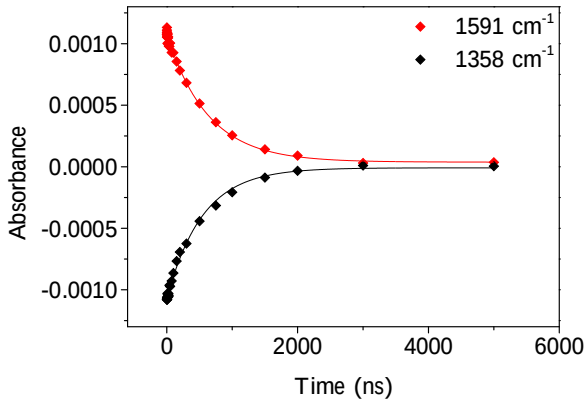

Figure 2-38: The kinetics of Re(dppz-(N_3C_2H)PhNPh$_2$) in CH_2Cl_2 following photoexcitation at 355 nm. The decay of the band at 1591 cm^{-1} assigned to State II, is in good agreement with the long part of the biexponential decay of the band at 1358 cm^{-1} assigned to the parent.

3.2 Absorption Spectroscopy

The absorption spectra of Re(dppz-NPh_2), Re(dppz-$(PhNPh_2)_2$), Re(dppz-(Ph-$(OCH_3)_2$)NPh_2), Re(dppz-Ph_2NPh_2), Re(dppz-Ph_3NPh_2), Re(dppz-$(N_3C_2H)PhNPh_2$) and Re(dppz-$(C_4H_3S)PhNPh_2$) have been acquired in CH_2Cl_2 and are shown in Figure 2-39 with band positions detailed in Table 2-11. The absorption spectra exhibit a large number of bands in the 250-380 nm region indicative of IL$\pi\pi^*$ transitions centred on the dppz ligand and NPh_2 core consistent with previous literature.[28, 53, 85-88]

The band at *ca.* 500 nm observed for Re(dppz-$(C_4H_3S)PhNPh_2$) and Re(dppz-$(PhNPh_2)_2$) and most clearly for Re(dppz-NPh_2), has been assigned as intramolecular charge transfer from the NPh_2 donor to the phz acceptor, consistent with previous literature of triphenylamine based donor-acceptor complexes.[87-90] Absorption bands at *ca.* 350 nm observed for Re(dppz-Ph_2NPh_2), Re(dppz-(Ph-$(OCH_3)_2NPh_2$), Re(dppz-Ph_2NPh_2), Re(dppz-Ph_3NPh_2) are consistent with IL$\pi\pi^*$ dppz centre transition and also a Re(dπ)→phen(π^*) transition observed for [Re(dppz)$(CO)_3Cl$].[28, 53, 85, 86]

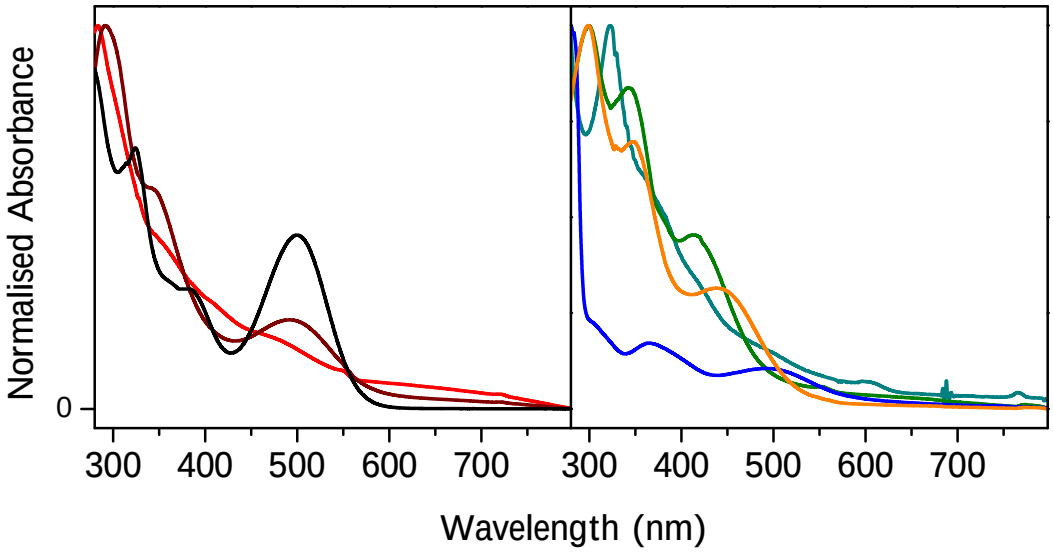

Figure 2-39: The absorption spectra of Re(dppz-NPh_2) (black), Re(dppz-$(PhNPh_2)_2$) (brown), Re(dppz-(Ph-$(OCH_3)_2$)NPh_2) (red), Re(dppz-Ph_2NPh_2) (orange), Re(dppz-Ph_3NPh_2) (green), Re(dppz-$(N_3C_2H)PhNPh_2$) (turquoise) and Re(dppz-$(C_4H_2S)PhNPh_2$) (blue) in CH_2Cl_2.

Table 2-11: The absorption wavelengths for complexes Re(dppz-NPh_2), Re(dppz-$(PhNPh_2)_2$), Re(dppz-(Ph-$(OCH_3)_2$)NPh_2), Re(dppz-Ph_2NPh_2), Re(dppz-Ph_3NPh_2), Re(dppz-(N_3C_2H)PhNPh2) and Re(dppz-$(C_4H_2S)PhNPh_2$) in CH_2Cl_2. Where a shoulder is abbreviated to sh.

Complex	λ_{abs} (nm)
Re(dppz-NPh_2)	325, 386, 501
Re(dppz-$(PhNPh_2)_2$)	293, 342, 493
Re(dppz-(Ph-$(OCH_3)_2$)NPh_2)	283, 353(sh), 411(sh), 476(sh)
Re(dppz-Ph_2NPh_2)	300, 348, 445
Re(dppz-Ph_3NPh_2)	300, 344, 414
Re(dppz-$(N_3C_2H)PhNPh_2$)	323, 379(sh), 417(sh), 489(sh), 601
Re(dppz-$(C_4H_3S)PhNPh_2$)	309(sh), 365, 502

3.3 Cyclic Voltammetry

The electrochemical potentials of Re(dppz-NPh_2), Re(dppz-$(PhNPh_2)_2$), Re(dppz-Ph_2NPh_2), Re(dppz-Ph_3NPh_2), Re(dppz-$(C_4H_3S)NPh_2$), Re(dppz-(Ph-$(OCH_3)_2$)NPh_2) and Re(dppz-$(N_3C_3H)PhNPh_2$), alongside literature values for [Re(dppz)$(CO)_3$Cl] and [Re(dppz-$PhNPh_2$)$(CO)_3$Cl] are shown in Table 2-12.

Table 2-12: The electrochemical data for Re(dppz-NPh_2), Re(dppz-$(PhNPh_2)_2$), Re(dppz-Ph_2NPh_2), Re(dppz-Ph_3NPh_2), Re(dppz-$(C_4H_3S)NPh_2$), Re(dppz-(Ph-$(OCH_3)_2$)NPh_2), Re(dppz-$(N_3C_3H)PhNPh_2$, [Re(dppz)$(CO)_3$Cl] and [Re(dppz-$PhNPh_2$)$(CO)_3$Cl] in CH_2Cl_2 containing 0.4 M $[Bu_4N][BF_4]$.

Complex	*vs.* Fc*/$(Fc^*)^+$		*vs.* SCE	
	E_{red} (V)	E_{ox} (V)	E_{red} (V)	E_{ox} (V)
[Re(dppz)$(CO)_3$Cl][a]	-1.42	0.96	-	-
Re(dppz-NPh_2)	-1.00	1.25	-1.06	1.19
[Re(dppz-$PhNPh_2$)$(CO)_3$Cl][b]	-	-	-0.97	1.05
Re(dppz-Ph_2NPh_2)	-0.92	1.05	-0.97	1.00
Re(dppz-Ph_3NPh_2)	-0.91	0.12	-0.97	0.97
Re(dppz-$(C_4H_3S)NPh_2$)	-0.88	1.00	-0.94	0.94
Re(dppz-(Ph-$(OCH_3)_2$)NPh_2)	-0.99	1.09	-1.04	1.03
Re(dppz-$(N_3C_2H)PhNPh_2$)	-0.80	1.06	-0.86	1.00

[a]Data for [Re(dppz)$(CO)_3$Cl] taken from Reference 32

[b]Data for [Re(dppz-$PhNPh_2$)$(CO)_3$Cl] taken from reference 40

All of the complexes studied within this work show a more positive E_{red} value compared to [Re(dppz)$(CO)_3$Cl] from -1.42 to -1.00 V for [Re(dppz)$(CO)_3$Cl] and Re(dppz-NPh_2) respectively, indicating all of the complexes are more easily reduced compared to the Re(dppz). Furthermore, Re(dppz-$(N_3C_3H)PhNPh_2$) is shown to be the most easily reduced complex followed by Re(dppz-$(C_4H_3S)NPh_2$), Re(dppz-Ph_3NPh_2), Re(dppz-Ph_2NPh_2) which exhibit similar E_{red} values. Re(dppz-$(Ph\text{-}(OCH_3)_2)NPh_2$) and Re(dppz-$NPh_2$) are observed to be the least easily reduced of the complexes with similar E_{red} values.

3.4 Infrared Spectroelectrochemistry

The FTIR spectra of the one electron reduced species ($1e^-$ RS) of complexes Re(dppz-NPh_2), Re(dppz-$(C_4H_4S)NPh_2$), Re(dppz-Ph_2NPh_2) and Re(dppz-$(PhNPh_2)_2$) have been acquired within this work and the band positions shown in Table 2-13. The spectra of Re(dppz-NPh_2) shown in Figure 2-40 and for the other complexes are shown in Appendix A.

For all of the complexes the $1e^-$ RS in the ν(CO) region show three bands, which are red shifted (*ca.* 10 cm^{-1}) in energy compared to the ground state and this is consistent with the electron residing in a π^* orbital of the dppz ligand. As a result the CO bond is weakened due to increased back bonding. The observed 10 cm^{-1} red shift for the $1e^-$ RS compared to the non-reduced state is smaller than that observed for [Re(bpy)$(CO)_3$Cl] and [Re(phen)$(CO)_3$Cl] which is *ca.* 30 cm^{-1}.[91] Therefore the spectroelectrochemistry FTIR results are consistent with the electron occupying the phz(π^*) orbital, as this smaller shift indicates that reduction results in the electron centralised at a further distance from the Re centre. The ν(FP) region is more convoluted and the spectra shows a slight red shift for the $1e^-$ RS compared to the non-reduced species.

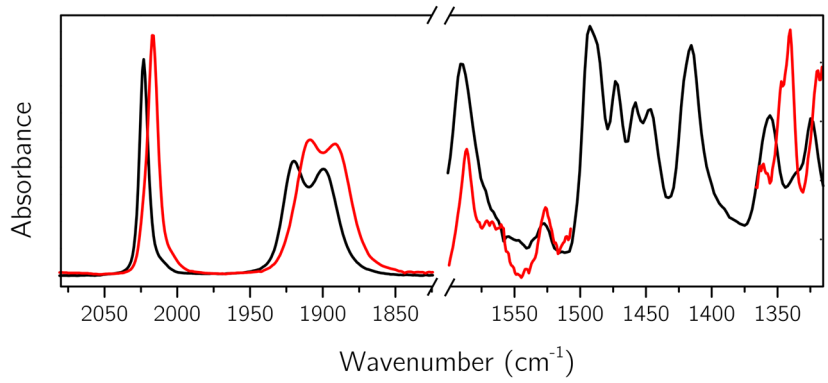

Figure 2-40: The ground state (black) and 1e$^-$ reduced state (red) FTIR spectra of Re(dppz-NPh$_2$) in CH$_2$Cl$_2$, 0.4 M [(Bu$_3$N)(BF$_4$)].

Table 2-13: The shift observed in the FTIR spectra of Re(dppz-NPh$_2$), Re(dppz-(C$_4$H$_4$S)NPh$_2$), Re(dppz-Ph$_2$NPh$_2$) and Re(dppz-(PhNPh$_2$)$_2$) upon 1e$^-$ reduction in CH$_2$Cl$_2$, 0.4 M [(Bu$_4$N)(BF$_4$)].

Complex	FTIR (cm^{-1})		
	Non-reduced	1e$^-$ RS	Δν(CO) upon 1e$^-$ reduction
Re(dppz-NPh$_2$)	2024, 1920, 1899	2016, 1908, 1891	8, 12, 8
[Re(dppz-(PhNPh$_2$)$_2$	2024, 1921, 1900	2017, 1909, 1886	7, 12, 7
Re(dppz-(C$_4$H$_4$S)NPh$_2$)	2024, 1922, 1900	2017, 1909, 1892	7, 13, 8
Re(dppz-Ph$_2$NPh$_2$)	2025, 1922, 1900	2017, 1910, 1894	8, 12, 6

3.5 EPR Spectroelectrochemistry

The one electron reduced species ($1e^-$ RS) of Re(dppz-NPh_2), Re(dppz-$(C_4H_4S)NPh_2$), Re(dppz-Ph_2NPh_2) and Re(dppz-$(PhNPh_2)_2$) were generated by electrolysis at a controlled potential and were subsequently studied by EPR spectroscopy, Figure 2-41. The EPR spectrum of the reduced species for all of the complexes had a g value *ca.* 2.004, which is very close to the g value for a free electron, g = 2.0023.[92] Therefore the complexes obtained were the $1e^-$ RS.

A small amount of hyperfine coupling from the dppz ligand was observed for some of the complexes. The EPR spectra of the four complexes consists of 5 lines, which result from the interaction between the unpaired electron with a pair of equivalent nitrogen atoms, a_{2N} = 5 G. Simulated EPR spectra obtained by the sum of Gaussian shape lines show the interaction between an unpaired electron and the spin active nuclei on the dppz ligand.

The electron residing on an equivalent pair of nitrogen atoms could be due to the unpaired electron interacting with either the phen nitrogens or the phz nitrogens. Based on the EPR spectra, the location of the unpaired electron is assigned as phz based. A broad structureless spectrum would be expected for a phen based electron due to interaction between the metal and the unpaired electron, which has been previously documented for $[Ru(phen)_3]^{2+}$ and $[Fe(phen_3)]^{2+}$,[93] and for $[Pt(bpy)L_2]$ complexes (L = Cl, CN, py).[94] Furthermore, if the unpaired electron interaction was phen based then a considerably smaller g value, *ca.* <2, for the radical would be expected due to the large spin-orbit coupling contribution resulting from the heavy metal.[94]

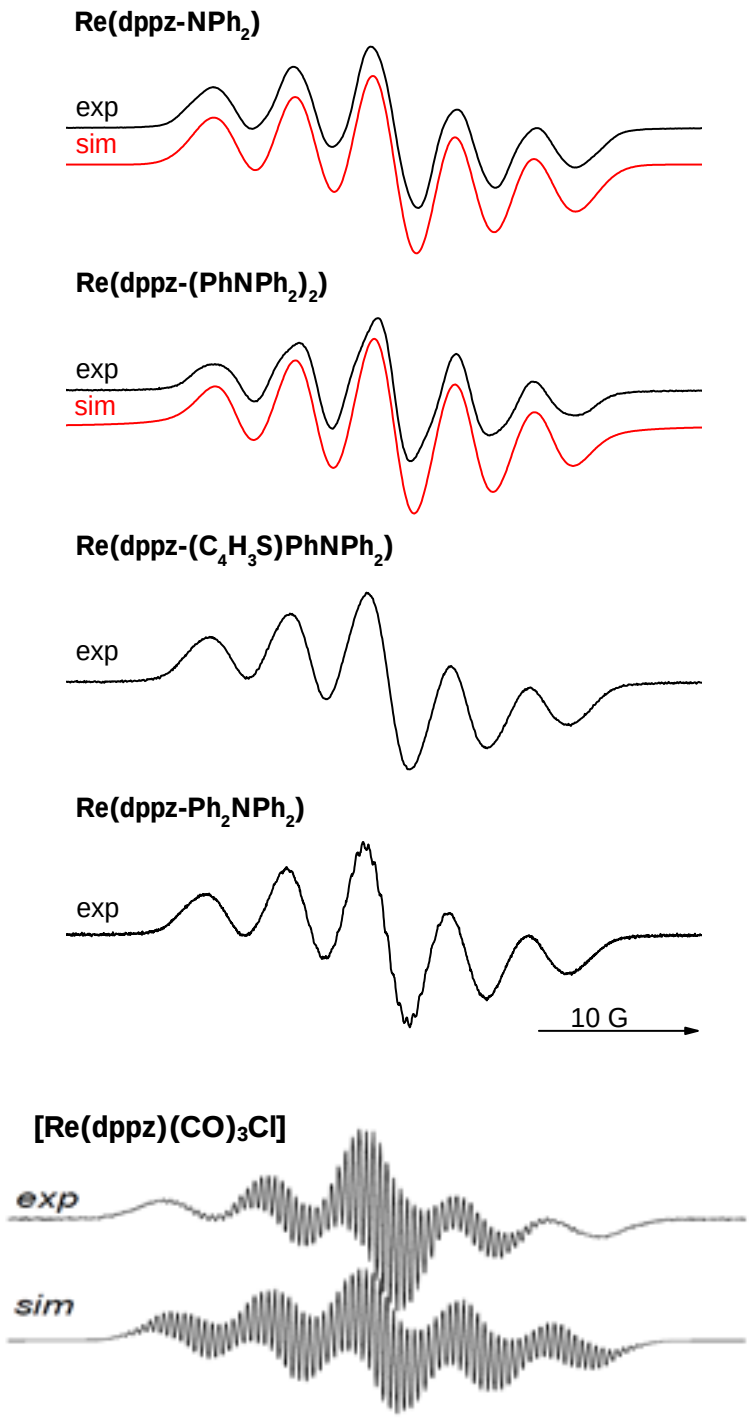

Figure 2-41: The 1e$^-$ RS EPR of Re(dppz-NPh$_2$), Re(dppz-(PhNPh)$_2$), Re(dppz-(C$_4$H$_3$S)PhNPh$_2$) and Re(dppz-Ph$_2$NPh$_2$) measured within this work. The 1e$^-$ RS EPR of [Re(dppz)(CO)3Cl] vs Fc*/(Fc*)$^+$ which has been reproduced from reference 92.

3.6 Molecular Orbital Calculations

The frontier molecular orbitals for the complexes Re(dppz-NPh_2), Re(dppz-(Ph-$(OCH_3)_2NPh_2$), Re(dppz-$PhNPh_2$) and Re(dppz-$(PhNPh_2)_2$) have been calculated using density functional theory. The partial energy diagram and representative MOs are shown in Figure 2-43, with all MOs shown in Appendix B. The calculations have provided a clear insight into the MO framework and are used to support the states identified from spectroscopic data.

The HOMO for the complexes is predominantly based on the NPh_2 ligand. Two metal based occupied molecular orbitals (HOMO-1 and HOMO-2) are calculated at lower energies. There is a significant energy gap observed, *ca.* 1 eV, between the NPh_2 ligand based (HOMO) and Re based (HOMO-1 and HOMO-2) orbitals while a near-negligible gap is observed between the two Re based MOs. For Re(dppz-$(PhNPh_2)_2$) the NPh_2 ligand based HOMO is split into two near-degenerate orbitals, reflecting the presence of two NPh_2 ligand moieties on the dppz ligand.

For all four complexes, the occupied Re(dπ) orbitals (HOMO-1 and HOMO-2) show negligible variation in energy. This indicates that the distance between the Re and the NPh_2 based ligand is sufficient to shield the Re from the influence of the phz substituents. However, the energy level of the HOMO is significantly affected by the NPh_2 derivative ligand. There is a change in energy of (+0.3 eV) from Re(dppz-NPh_2) to Re(dppz-(Ph-$(OCH_3)_2NPh_2$), Re(dppz-$PhNPh_2$) and Re(dppz-$(PhNPh_2)_2$). This indicates that the presence of a phenyl bridge directly affects the energy of the HOMO state. Furthermore, substitution of this phenyl ring or increasing the number of NPh_2 donors appears to have negligible effect on the energy level of the HOMO.

The four lowest unoccupied MOs for all four complexes are π based and are assigned as phz(LUMO), phen(LUMO+1), dppz(LUMO+2 and LUMO+3) in character. The LUMO is phz based for all the complexes and clearly depends on the NPh_2 derivative ligand. The LUMO is observed to decrease in energy by *ca.* 0.2 eV from [Re(dppz-$PhNPh_2$)$(CO)_3Cl$] to Re(dppz-$(PhNPh_2)_2$) indicating that the nature of the phenyl bridge separating the NPh_2 ligand from the dppz ligand has a distinct effect on the

LUMO energy. Overall the HOMO-LUMO energy gap is observed to decrease from 5.08 eV for Re(dppz-NPh_2) to 4.55 eV for Re(dppz-$(PhNPh_2)_2$).

The frontier molecular orbitals for the complex [Re(dppz)$(CO)_3$Cl] have also been calculated and the partial energy diagram shown in Figure 2-42, including representative MO, with all MOs for energies shown in Appendix B. The HOMO is Re(dπ) in nature with a ligand based MO phz(π) occupied orbital at considerably lower energy (*ca.* 2 eV below the HOMO). The LUMO is phz(π*) in nature with a phen(π*) and dppz(π*) calculated at higher energies.

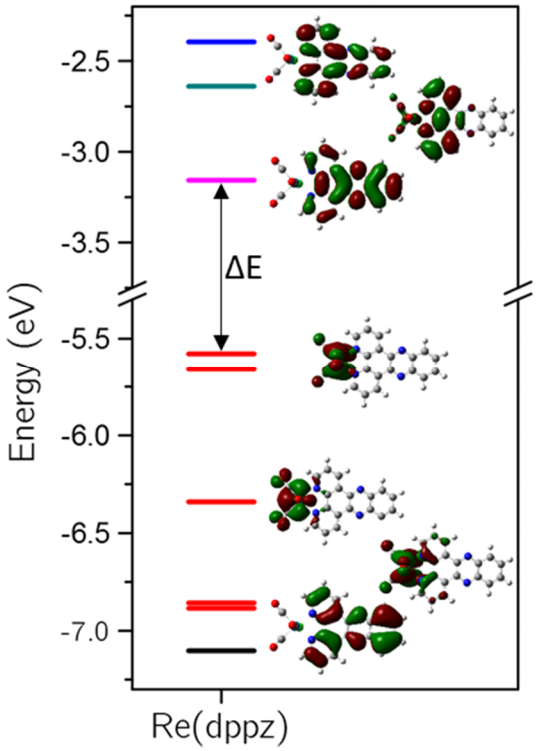

Figure 2-42: The partial energy diagram and representative calculated frontier molecular orbitals for [Re(dppz)$(CO)_3$Cl], labelled as Re(dppz). Metal based occupied MOs are shown in red and ligand centred occupied MOs in black. The unoccupied phen, phz and dppz MOs are shown in pink, turquoise and blue respectively.

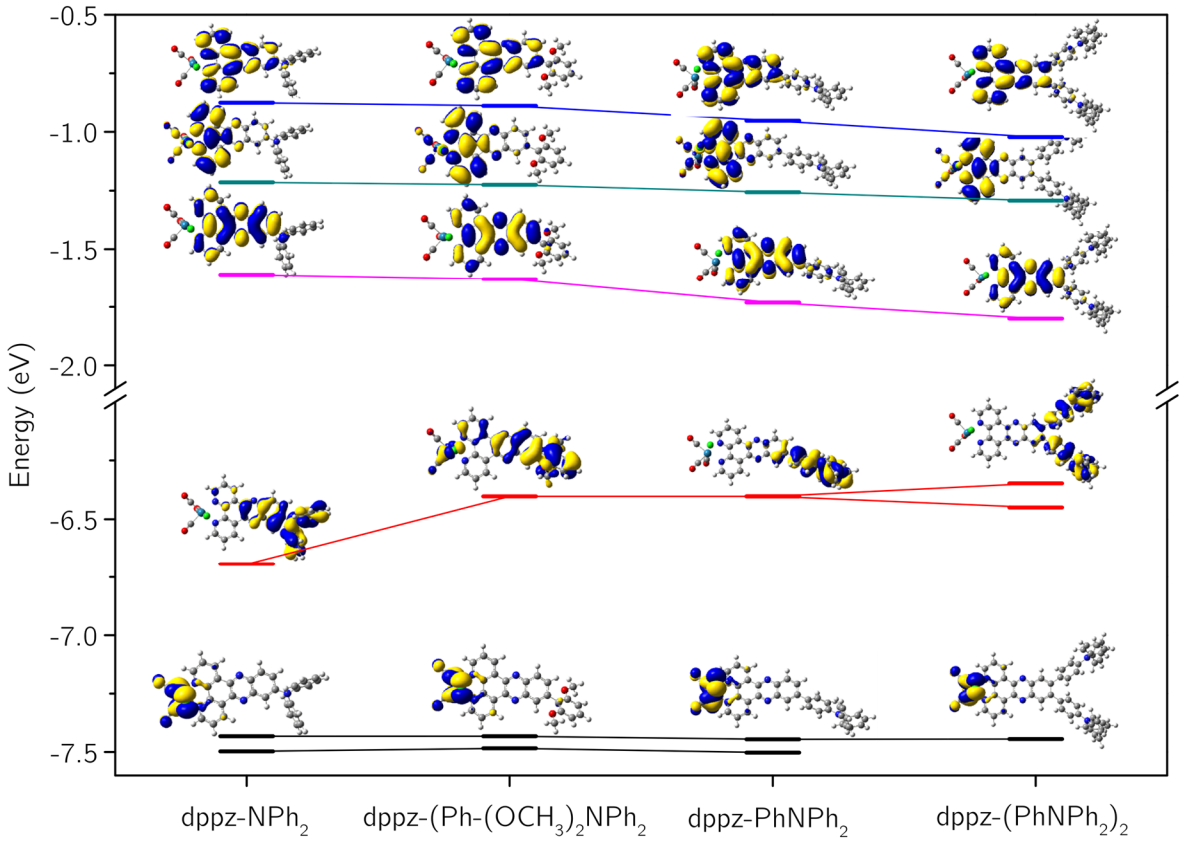

Figure 2-43: The energy levels (eV) and representative frontier molecular orbitals from DFT calculations for Re(dppz-NPh_2), Re(dppz-(Ph-$(OCH_3)_2NPh_2$), Re(dppz-$PhNPh_2$) and Re(dppz-$(PhNPh_2)_2$). Metal based occupied MOs are shown in black and ligand centred occupied MOs in red. The unoccupied phen, phz and dppz MOs are shown in pink, turquoise and blue respectively.

3.7 Assignment of the Observed Excited States

Three excited states are identified for the complexes Re(dppz-NPh_2), Re(dppz-$(PhNPh_2)_2$, Re(dppz-Ph_2NPh_2), Re(dppz-Ph_3NPh_3), Re(dppz-(Ph_3NPh_2), Re(dppz-$(C_4H_3S)NPh_2$), Re(dppz-$(Ph\text{-}(OCH_3)_3)NPh_2$) and Re(dppz-$(N_3C_2H)PhNPh_2$). The states have been labelled State I, II and III. State I shown spectrally as the presence of a small shoulder at *ca.* 2006 cm^{-1} which decays on the ps-time scale could be attributed to several processes such as transition between different IL excited states,[38] vibrational cooling,[40, 53] or conversion of the initially formed singlet state into a triplet,[95] although this conversion would normally be expected on a fs-timescale.[43]

Firstly, for each complex State I decays as transient bands at slightly higher energies are observed to grow in. This may indicate conversion between the following electronically distinct states: MLCT of Re(dπ)dppz(π*) in nature; $^1\pi\pi^*$(dppz) to $^3\pi\pi^*$(dppz) or $^3\pi\pi^*$(phen) to $^3\pi\pi^*$(phz) where each is discussed herein. A Re(dπ) to dppz(π*) transition has previously been reported in literature with distinctive absorptions in the ν(CO) infrared region which are not observed here, therefore the conversion from Re to dppz can effectively be ruled out.[13, 38, 96, 97] For a transition from $^3\pi\pi^*$(phen) to $^3\pi\pi^*$(phz) the shift to higher wavenumbers of the ν(CO) observed is consistent with conversion from phen to phz excited states.[35, 43]

The singlet to triplet conversion required for $^3\pi\pi^*$(phz) state is normally on a sub-picosecond timescale,[35, 43] and therefore a similar shoulder to that observed has been assigned as a vibrationally hot state for similar complexes.[40, 53] However, previous work has shown that longer timescales of ISC from S_1 to T_1 are possible,[98] where picosecond ISC has been observed for ReGV-$PhNMe_2$ shown in Figure 2-44.[95] The observation of slow ISC is explained by the symmetry constraints on the spin-orbit coupling, as the Re metal may be considered as isolated from the ligand moiety.

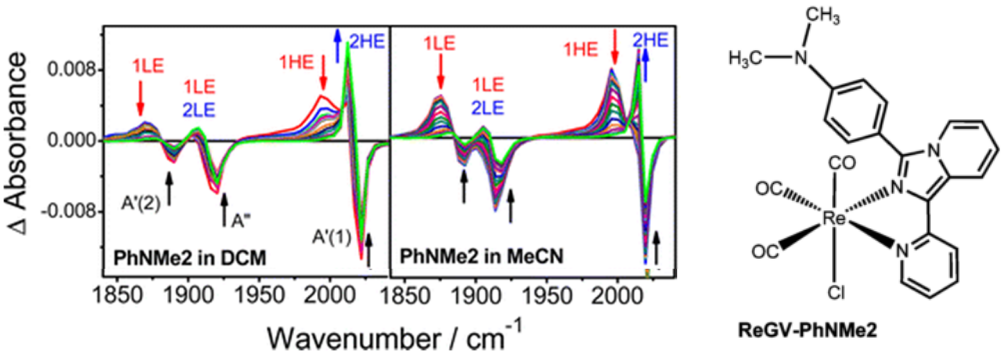

Figure 2-44: The ps TRIR spectra of ReGV-PhNMe$_2$ showing a shoulder labelled as 1HE, assigned to a ^{1}ILππ* state, which is observed to decay as the band labelled as 2HE assigned to a ^{3}ILππ* state. This spectra represents the picosecond ISC observed. Reproduced from reference 95.

Furthermore, other TRIR spectroscopy work on similar compounds has also indicated that an observed shoulder is due to the presence of a distinct excited state.[40] The DFT MO calculations, Figure 2-43, indicate a ^{1}ILππ* to ^{3}ILππ* state is possible, from the little contribution of the Re metal. Therefore State I has tentatively been assigned as a ^{1}ILππ* state. State I is shown to decay to State II, which is characterised by a long lifetime and a small shift to lower energy with respect to the parent. This is indicative of a ^{3}ILππ* state located on the dppz ligand, analogous to previous observations for [Re(CO)$_3$(dppz)(L)], where L = pyridine[36, 38] and triphenylphosphine.[4]

The TRIR spectrum of State III possesses a band in the fingerprint region at *ca.* 1560-1583 cm^{-1}, which has been tentatively assigned as oxidised TPA, based on previous literature.[99-101] This would indicate that State III is a charge transfer state, where TPA acts as a donor and dppz as an acceptor. The electrochemically generated 1e$^-$ reduced state for complexes Re(dppz-NPh$_2$), Re(dppz-(PhNPh$_2$)$_2$), Re(dppz-(C$_4$H$_3$S)PhNPh$_2$) and Re(dppz-Ph$_2$NPh$_2$) show IR bands at *ca.* 2016, 1909 and 1891 cm^{-1} and this supports the charge transfer state assignment of State III. A CT state has been observed for similar complexes [Re(dppz-PhNPh$_2$)(CO)$_3$(DMAP)]$^+$ and [Re(dppz-PhNPh$_2$)(CO)$_3$(py)]$^+$.[40] Therefore, State III has been tentatively assigned as a charge transfer from PhNPh$_2$(π) to phz(π*).

3.8 The Photophysical Properties Observed for NPh_2 Appended Complexes

Following the assignment of three distinct states observed in the TRIR, the effect of the NPh_2 derivative substituents on the photophysical properties observed has been assessed. Four key trends are identified: (i) the effect of donor substitution and number of donor groups; (ii) the distance between the donor and the acceptor moieties; (iii) the nature of the bridge between the donor and the acceptor moieties, and (iv) the dihedral angle between the donor and the acceptor moieties.

(i) The Effect of the Donor Substitution and the Number of Donor Moieties

The effect of substitution of an NPh_2 group on to the phz portion of the dppz ligand on the photophysical properties observed is discussed herein. Complexes $[Re(dppz)(CO)_3Cl]$, $Re(dppz\text{-}NPh_2)$, $Re(dppz\text{-}PhNPh_2)(CO)_3Cl]$ and $Re(dppz\text{-}(PhNPh_2)_2)$ are compared.

Table 2-14: The lifetimes of States I-III for $[Re(dppz)(CO)_3Cl]$, $Re(dppz\text{-}NPh_2)$, $[Re(dppz\text{-}PhNPh_2)(CO)_3Cl]$ and $Re(dppz\text{-}(PhNPh_2)_2)$. Values taken from the TRIR data.

Complex	State Lifetime (ns)			
	I	III	II	^{3}ILππ*/ MLCT(phen)
$[Re(dppz)(CO)_3Cl]$[a]	-	-	-	40 ± 10
$Re(dppz\text{-}NPh_2)$	0.037 ± 0.002	2.5 ± 0.3	2300 ± 500	-
$[Re(dppz\text{-}PhNPh_2)(CO)_3Cl]$[b]		1.6 ± 0.3	3300 ± 500	
$Re(dppz\text{-}(PhNPh_2)_2)$	0.028 ± 0.004	1.5 ± 0.5	2200 ± 600	-

[a]Data for $[Re(dppz)(CO)_3Cl]$ taken from reference 32.
[b]Data for $[Re(dppz\text{-}PhNPh_2)(CO)_3Cl]$ taken from reference 40.

The TRIR spectrum of $[Re(dppz)(CO)_3Cl]$ in CH_2Cl_2 has been previously reported in literature,[32] transient bands which are blue shifted relative to the parent are observed and assigned to an MLCT(phen) state in addition to bands slightly red shifted to parent which are assigned to an $IL\pi\pi^*$ state. Therefore the overall excited states are MLCT(phen)/$IL\pi\pi^*$ in nature and this equilibrium of states exhibits a lifetime of 40 ±

10 ns. However, upon substitution of the phz moiety with the NPh_2 group yielding the complexes Re(dppz-NPh_2), [Re(dppz-$PhNPh_2$)$(CO)_3$Cl] and Re(dppz-Ph_2NPh_2), three ligand centred excited states are observed labelled States I-III.

The NPh_2 group is electron donating in nature and as such will increase the electron density on the dppz ligand. This increased electron density is likely to increase the relative energy of the MLCT(phen/phz) states and thus the IL$\pi\pi^*$ state may become relatively lower in energy. Therefore the most stable and long lived state observed for Re(dppz-NPh_2), [Re(dppz-$PhNPh_2$)$(CO)_3$Cl] and Re(dppz-Ph_2NPh_2) is assigned as an IL$\pi\pi^*$ state, State II. The lifetime of State II is similar for Re(dppz-Ph_2NPh_2) and Re(dppz-NPh_2). This would suggest that the IL$\pi\pi^*$ state is reasonably independent of the number of NPh_2 donor moieties substituted onto the dppz ligand.

The addition of an NPh_2 group may cause the conversion of a singlet to triplet, required for a ^{3}IL$\pi\pi^*$, to occur on picosecond timescales. The presence of the NPh_2 moiety is likely to cause symmetry constraints on the spin orbit coupling, as a result the Re metal is considered isolated from the dppz, therefore ISC is tentatively assigned as occurring at a slow enough rate to observe spectroscopically (*ca.* 30 ps). Additionally the presence of the NPh_2 donor group causes the formation of a CT state, State III. The CT state lifetime is similar for Re(dppz-$PhNPh_2$) and for Re(dppz-$(PhNPh_2)_2$), indicating that two $PhNPh_2$ donor moieties seems to have negligible effect on the rate of back electron transfer, compared to one $PhNPh_2$ donor.

Closer inspection of the reduction potentials for each of the complexes shows that the addition of NPh_2 groups results in a less negative 1st reduction potential, from -1.42 to -1.00 V *vs.* Fc*/$(Fc^*)^+$ for [Re(dppz)$(CO)_3$Cl] and Re(dppz-NPh_2) respectively. This is consistent with the formation of a charge transfer state for Re(dppz-NPh_2) and derivative complexes which is not observed [Re(dppz)$(CO)_3$Cl]. Furthermore, the 1e$^-$ reduction potential is less negative with increasing NPh_2 groups from -1.06 to -0.97 eV vs. SCE for Re(dppz-NPh_2) and Re(dppz-$(PhNPh_2)_2$) respectively. The difference in reduction potential is not as stark as for [Re(dppz)$(CO)_3$Cl] and Re(dppz-NPh_2), indicating that the introduction of a NPh_2 donor moiety has a large effect, but the number of NPh_2 groups has a significantly lesser effect.

The MO calculations are consistent with the assignment of State III as CT. The energy gap observed for $NPh_2(\pi)$ to phz(π^*) is -5.08, -4.67 and -4.55 eV for Re(dppz-NPh_2), [Re(dppz-$PhNPh_2$)$(CO)_3Cl$] and Re(dppz-$(PhNPh_2)_2$). This energy gap change is reflected in State III lifetime which decreases from 2.5 ns to 1.6 ns for Re(dppz-NPh_2) and Re(dppz-$PhNPh_2$) respectively. Furthermore the negligible difference in State III lifetime between [Re(dppz-$PhNPh_2$)$(CO)_3Cl$] and Re(dppz-$(PhNPh_2)_2$) is reflected by the negligible energy gap difference observed from the calculated MOs.

(ii) The Distance Between the Donor and the Acceptor Moieties

The distance between the NPh_2 donor and the phz acceptor moieties separated by a bridge consisting of varying number of phenyl subunits has been investigated.

Table 2-15: The lifetimes of States I-III for Re(dppz-NPh_2), [Re(dppz-$PhNPh_2$)$(CO)_3Cl$], Re(dppz-Ph_2NPh_2) and Re(dppz-Ph_3NPh_2). The values are taken from the TRIR data.

Complex	State Lifetime (ns)		
	I	III	II
Re(dppz-NPh_2)	0.037 ± 0.002	2.5 ± 0.3	2300 ± 500
[Re(dppz-$PhNPh_2$)$(CO)_3Cl$][a]	-	1.6 ± 0.3	3300 ± 500
Re(dppz-Ph_2NPh_2)	0.044 ± 0.003	0.14 ± 0.02	1280 ± 30
Re(dppz-Ph_3NPh_2)	0.030 ± 0.005	0.038 ± 0.006	950 ± 90

[a]Data for complex [Re(dppz-$PhNPh_2$)$(CO)_3Cl$] taken from reference 40.

For State I, assigned previously as a $^1IL\pi\pi^*$ state, the lifetime appears to be independent of bridge length. The lifetime of State II decreases with increasing bridge length from 2300 ± 500 ns to 950 ± 90 ns for Re(dppz-NPh_2) and Re(dppz-Ph_3NPh_2) respectively. Previous research of M(dppz) complexes has shown that electron donating groups are shown to drastically increase the observed excited state lifetime from 1.3 ns to 420 ns for [Re(dppz-Br_2)$(CO)_3Cl$] and [Re(dppz-$(CH_3)_2$$(CO)_3Cl$] respectively.[32, 34] Therefore as the NPh_2 group is electron donating, it is tentatively assigned that the spacer length between the NPh_2 donor and the dppz ligand is increased, the electron density observed on the dppz ligand is decreased and therefore the $IL\pi\pi^*$ state lifetime decreases. In agreement with previous work which has shown as the electron donor to acceptor

distance increases, the amount of electron transfer onto the acceptor also decreases.[65-73]

The E_{red} results of the complexes *vs.* SCE show a decrease with the addition of phenyl rings from -1.06 V for Re(dppz-NPh_2) to -0.97 V for the other three complexes. This indicates that the addition of a phenyl ring makes the complex easier to reduce but the addition of more than one phenyl ring appears to have negligible effect.

The lifetime of State III increases dramatically with decreasing bridge length from 38 ± 6 ps to 2.5 ± 0.3 ns for Re(dppz-Ph_3NPh_2) and Re(dppz-NPh_2) respectively. From the MO calculations the energy gap from the NPh_2 based ligand (HOMO) to phz (LUMO) decreases for Re(dppz-$PhNPh_2$) (4.55 eV) compared to Re(dppz-NPh_2) (5.08 eV), Figure 2-43, tentatively reflected in the shorter lifetime observed for State III for the former compared to the latter. Furthermore, from the absorption spectra the band assigned as CT from the $NPh_2(\pi)$ to the phz(π^*) is clearly observed for Re(dppz-NPh_2) and not for Re(dppz-Ph_2NPh_2) and Re(dppz-Ph_3NPh_2), indicating CT character decreases with increasing NPh_2 to phz distance, consistent with previous literature.[65-73] This decrease in CT lifetime may be attributed to the decrease in planarity that occurs as the number of phenyl units increases.[62, 79, 84] Previous DFT studies of diphenylamine-phenyl bridge-cyanoacrylic acid have shown that for two and three Ph unit spacers there is non-planarity between the two neighbouring Ph rings with a dihedral angle of *ca.* 30-35°.[84] A decrease in planarity results in a decrease in the effective π-conjugation length of the Ph bridge which in turn yields a larger HOMO-LUMO gap and making a bridge which is less conductive in nature. Therefore less CT state character results and this may be reflected in the decrease in State III lifetime with increasing Ph subunits.

In addition to planarity, the difference in lifetime of State III between the complexes may be attributed to aromaticity. The bridge length increases the aromaticity and thus increasing the insulator character, resulting in a less effective bridge. Resulting from both hypotheses is that insulator character of the bridge increases with increasing number of phenyl subunits, indicating that as the bridge conductivity decreases alternate states are preferred and thus, the CT lifetime is decreased.

This increase in insulator character with increasing bridge length is consistent with the $1e^-$ reduced species EPR spectroscopy. For [Re(dppz)$(CO)_3$Cl] the $1e^-$ reduced species EPR shows 5 bands characteristic of the electron residing on the phz. In addition, there is significant hyperfine coupling attributed to contribution from the aromatic hydrogens of the dppz ligand. For Re(dppz-NPh_2) and Re(dppz-Ph_2NPh_2), 5 bands are also observed indicating the electron is residing on two nitrogens, unlike for Re(dppz-Ph_2NPh_2) where 5 bands with the presence of hyperfine coupling is observed. This indicates that $1e^-$ reduced species of Re(dppz-Ph_2NPh_2) behaves more like [Re(dppz)$(CO)_3$Cl] than Re(dppz-NPh_2), further indicating that the larger the distance between donor and acceptor the more insulating character the bridge possesses.

(iii) The Nature of the Bridge Between the Donor and the Acceptor Moieties

The complexes [Re(dppz-$PhNPh_2$)$(CO)_3$Cl], Re(dppz-Ph_2NPh2), Re(dppz-$(C_4H_3S)PhNPh_2$) and Re(dppz-$(N_3C_2H)PhNPh_2$) differ by the nature of the bridge between the $PhNPh_2$ donor and phz acceptor. The effect of the nature of the bridge on the photophysical properties observed is discussed herein.

Table 2-16: The lifetime of States I-III for Re(dppzNPh_2), [Re(dppz-$PhNPh_2$)$(CO)_3$Cl], Re(dppz-Ph_2NPh_2), Re(dppz-$(C_4H_3S)PhNPh_2$) and Re(dppz-$(N_3C_2H)PhNPh_2$), values taken from the TRIR data.

Complex	State Lifetime (ns)			
	I	III	II	MLCT
[Re(dppz-$PhNPh_2$)$(CO)_3$Cl][a]	-	1.6 ± 0.3	3300 ± 500	
Re(dppz-Ph_2NPh2)	0.044 ± 0.003	0.14 ± 0.02	1280 ± 30	
Re(dppz-$(C_4H_3S)PhNPh_2$)	0.030 ± 0.005	3 ± 1	1280 ± 50	
Re(dppz-$(N_3C_2H)PhNPh_2$)	0.034 ± 0.001	0.04 ± 0.01	800 ± 300	0.055 ± 0.007

[a]Data for [Re(dppz-$PhNPh_2$)$(CO)_3$Cl] taken from reference 40.

State I lifetime is indifferent to the nature of the bridge within the complexes studied, consistent with the assignment of a $^1IL\pi\pi^*$ state and with the indifference between bridge length discussed above.

State II lifetime decreases Re(dppz-$PhNPh_2$)>Re(dppz-Ph_2NPh_2)=Re(dppz-(C_4H_3S)$PhNPh_2$)>Re(dppz-(N_3C_2H)$PhNPh_2$) indicating that electron transfer onto the phz is highest for Re(dppz-$PhNPh_2$) and lowest for Re(dppz-(N_3C_2H)$PhNPh_2$). This is consistent with observations from the CV where the E_{red} values are observed to decrease from -0.97 to -0.86 V for [Re(dppz-$PhNPh_2$)$(CO)_3Cl$] and Re(dppz-(N_3C_2H)$PhNPh_2$) *vs.* SCE respectively, indicating that the less charge transfer from $PhNPh_2$ to the phz, *i.e.* the more insulator character of the bridge, the more easily reduced the complex is.

The lifetime of State III, assigned as a CT state, decreases dramatically with bridge nature from 1.6 ± 0.3 ns for [Re(dppz-$PhNPh_2$)$(CO)_3Cl$] to 40 ± 10 ps for Re(dppz-(N_3C_2H)$PhNPh_2$). The bridge plays a part in shielding the dppz ligand from the electron donating ability of the $PhNPh_2$ ligand. Therefore it is expected that as shielding ability of the bridge increases, less electron density will be observed on the phz portion of the dppz ligand and thus, subsequently on the Re. Therefore the decrease in State III lifetime indicates that C_4H_3S bridge exhibits the least insulator character followed by Ph and then N_3C_2H. Furthermore, Re(dppz-(C_4H_3S)$PhNPh_2$) exhibits a State III lifetime similar to Re(dppz-$PhNPh_2$), indicating that C_4H_3S has almost negligible insulator character.

The $1e^-$ reduced species EPR spectrum of Re(dppz-NPh_2), Re(dppz-(C_4H_3S)$PhNPh_2$) and [Re(dppz-$PhNPh_2$)$(CO)_3Cl$] shows 5 lines consistent with the electron residing on two phz nitrogens as discussed previously, Figure 2-41. From the $1e^-$ reduced EPR spectroscopy of Re(dppz-NPh_2), Re(dppz-(C_4H_3S)$PhNPh_2$) and [Re(dppz-$PhNPh_2$)$(CO)_3Cl$], the NPh_2 complex demonstrates negligible hyperfine coupling. This indicates that in the NPh_2 complex the electron resides only on the two phz nitrogens and is not residing on the rest of the aromatic dppz system. However, the C_4H_3S and the Ph bridge complexes exhibit a small contribution of hyperfine coupling, indicating more insulator behaviour of the bridges in the complexes Re(dppz-Ph_2NPh_2) and Re(dppz-(C_4H_3S)$PhNPh_2$) compared to Re(dppz-$PhNPh_2$).

Previous DFT calculations for diphenylamine (NPh_2) donor and cyanoacrylic acid (CAA) acceptor complexes have shown that C_4H_3S exhibits more planarity as a bridge than Ph.[84] Planarity increases the effective π conjugation length and so in turn decreasing the HOMO-LUMO gap.[62, 79, 84] Therefore C_4H_3S is tentatively considered to have more

conductor character than Ph bridge, consistent with the lifetimes observed here for State III where Re(dppz-(C_4H_5S)PhNPh_2) exhibits a CT state lifetime similar to [Re(dppz-PhNPh_2)$(CO)_3$Cl] and longer than Re(dppz-Ph_2NPh_2). Furthermore, from the CV measurements Re(dppz-(C_4H_3S)PhNPh_2) is more easily reduced than Re(dppz-Ph_2NPh_2). This is consistent with the absorption spectra where the band assigned as CT from NPh_2 to phz is clearly visible for Re(dppz-NPh_2) and to a lesser extent Re(dppz-(C_4H_2S)PhNPh_2) and not at all for Re(dppz-Ph_2NPh_2), indicating that C_4H_2S exhibits stronger conductor character than Ph. Additionally the absorption spectra is more red shifted for Re(dppz-(C_4H_3S)PhNPh_2) than for Re(dppz-Ph_2NPh_2) assigned to an increased effective conjugation length for the former compared to the latter, consistent with previous investigations and calculations of phenyl and thiophene bridge, D-B-A complexes.[76-78]

Furthermore, Re(dppz-(N_3C_2H)PhNPh_2) which exhibits the shortest CT state lifetime also exhibits an additional state in the TRIR spectra which is MLCT in nature. The presence of an MLCT(phz) state is consistent with the assignment of the Re(dppz-(N_3C_2H)PhNPh_2) acting as an insulator, as a result the electron density onto the dppz ligand is less compared to the other complexes. Therefore there is comparatively less electron density on the Re allowing for effective oxidation of the metal centre and an MLCT(phz) state to be observed.

(iv) The Dihedral Angle between the Donor and the Acceptor Moieties

The effect of NPh_2 donor substitution has been discussed above alongside the effect the nature of the bridge has on the photophysical properties observed. A further important consideration is the dihedral angle of substitution between the NPh_2 donor and the phz acceptor, where donor-acceptor angle has been shown previously to have a significant effect on the photophysical properties observed.[63, 66, 84]

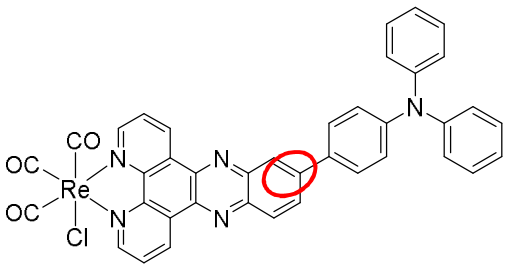

Figure 2-45: The structure of Re(dppz-PhNPh$_2$) with the D-A angle of interest shown in red.

Table 2-17: The lifetimes of States I-III for complexes [Re(dppz-NPh$_2$)(CO)$_3$Cl], [Re(dppz-(PhNPh$_2$)$_2$)(CO)$_3$Cl] and [Re(dppz-(Ph-(OCH$_3$)$_2$)NPh$_2$)(CO)$_3$Cl]. Values taken from the TRIR data.

Complex	Calculated D-A angle (°)	State Lifetime (ns)		
		I	III	II
[Re(dppz-PhNPh$_2$)(CO)$_3$Cl][a]	33.4		1.6 ± 0.3	3300 ± 500
Re(dppz-(PhNPh$_2$)$_2$)	47.3, 51.0	0.028 ± 0.004	1.5 ± 0.5	2200 ± 600
Re(dppz-(Ph-(OCH$_3$)$_2$)NPh$_2$)	52.2	0.043 ± 0.006	2 ± 1	2900 ± 500

[a]Data for [Re(dppz-PhNPh$_2$)(CO)$_3$Cl] taken from reference 40.

The following trend focusses on the donor-acceptor (D-A) angle; where D is the NPh$_2$ moiety and A is the phz portion of the dppz ligand. The angle of concern is between the plane of rings of the phz of dppz and the phenyl ring linking dppz and the NPh$_2$ ligand, highlighted in Figure 2-45 for [Re(dppz-PhNPh$_2$)(CO)$_3$Cl]. DFT calculations have shown that the D-A angle increases with increasing steric factors of the PhNPh$_2$ derivative. The D-A angle is largest for Re(dppz-(Ph-(OCH$_3$)$_2$)NPh$_2$) at 52.2° and smallest for [Re(dppz-PhNPh$_2$)(CO)$_3$Cl] at 33.4°.

As observed for the previous trends, State I appears independent of substituent group owing to its short lived nature. State II, as previously discussed, decreases with increasing electron donating substituted onto the dppz. The results for D-A angle demonstrate a weak correlation between lifetime and electron donating group, where the least electron transfer to the phz is observed for Re(dppz-(PhNPh$_2$)$_2$) and the most for Re(dppz-(Ph-PhNPh$_2$) as State II lifetime increases from 2200 ± 600 to 3300 ± 500 ns for each

complex respectively. This would suggest that although two donor groups are present for Re(dppz-$(PhNPh_2)_2$), the D-A angle is increased resulting in less electron transfer than observed for [Re(dppz-$PhNPh_2$)$(CO)_3$Cl]. Although Re(dppz-$(OCH_3)_2$-$PhNPh_2$) exhibits the largest D-A angle, and therefore would be expected to exhibit the shortest State II lifetime, the presence of the additional electron donating groups (OCH_3) increases the overall electron transfer to the phz. Therefore the State II lifetime observed for Re(dppz-$(OCH_3)PhNPh_2$) is longer than expected at 2900 ± 500 ns.

Previous work has shown that as non-planarity increases *i.e.* D-A angle increases, there is a decrease in effective π-conjugation length.[63, 79, 84] As a result there is an increase in the HOMO/LUMO gap causing less charge transfer character and a longer State III lifetime observed. From DFT calculations the HOMO/LUMO gap decreases following the trend: Re(dppz-(Ph-$(OCH_3)_2$)NPh_2) > Re(dppz-$PhNPh_2$) > Re(dppz-$(PhNPh_2)_2$), and as the HOMO is NPh_2 based and the LUMO is phz based the HOMO/LUMO gap could be considered indicative of this charge transfer. However, the decrease in HOMO/LUMO energy is small, decreasing from 4.77 to 4.55 eV and this may explain the lack of discernible trend between HOMO/LUMO energy and State III lifetime.

4 Conclusions

The photophysical properties of Re(dppz-NPh_2) donor-acceptor complexes have been explored in detail through time resolved infrared, absorption, cyclic voltammetry, spectroelectrochemistry and DFT calculations.

The presence of an NPh_2 donor moiety appended onto the phenazine has been shown to cause significant changes to the photophysical properties observed. From the TRIR spectra of [Re(dppz-NPh_2)$(CO)_3$Cl], [Re(dppz-$(PhNPh_2)_2$$(CO)_3$Cl], [Re(dppz-$Ph_2NPh_2$)], [Re(dppz-$Ph_3NPh_3$)$(CO)_3$Cl], Re(dppz-$(Ph_3NPh_2)$], Re(dppz-$(C_4H_3S)NPh_2$)$(CO)_3$Cl], [Re(dppz-$(Ph\text{-}(OCH_3)_3)NPh_2$)$(CO)_3$Cl] and [Re(dppz-$(N_3C_2H)PhNPh_2$)$(CO)_3$Cl] acquired in both the CO and FP IR regions, three distinct states are assigned. Firstly, States I and III are initially formed, where the former is observed to decay to a subsequent state, State II *ca.* 30 ps. States II and III are observed to decay to the ground state *ca.* τ = 2000 ns and 2 ns respectively. State I has been assigned as a ^{1}IL$\pi\pi^*$ state which decays on the ps timescale to a ^{3}IL$\pi\pi^*$ (State II), this slow intersystem crossing has previously been observed for Re(diimine) complexes and is attributed to symmetry constraints. State III has been assigned as an $NPh_2(\pi)$phz(π^*) state. An additional MLCT(phen) state is observed for the complex Re(dppz-$(N_3C_2H)PhNPh_2$) which is tentatively assigned as decaying to the ground state. For the non-donor appended [Re(dppz)$(CO)_3$Cl] complex, an equilibrium of excited states IL$\pi\pi^*$/MLCT(phen) in nature is observed. The electron donating NPh_2 ligand has been shown to make this MLCT state unfavourable.

Additionally DFT calculations have shown that the HOMO is NPh_2 ligand based and the LUMO is phz based, in comparison to the Re(dπ) HOMO observed for the non-donor appended [Re(dppz)$(CO)_3$Cl]. The number of NPh_2 substitutions has subsequently been investigated, the results show that there is little discernible difference between Re(dppz-$PhNPh_2$) and Re(dppz-$(PhNPh_2)_2$). This indicates that the introduction of an NPh_2 group has a large effect but the addition of subsequent NPh_2 groups has negligible effect.

The effect of distance between the donor and acceptor moieties has been investigated by comparing the complexes [Re(dppz-NPh_2)$(CO)_3$Cl], [Re(dppz-$(PhNPh_2)_2$$(CO)_3$Cl],

[Re(dppz-Ph_2NPh_2)] and [Re(dppz-Ph_3NPh_3)$(CO)_3Cl$]. The CT lifetime is observed to sharply decrease with increasing D-A distance, supported by the more positive reduction values with increasing bridge length and through EPR studies. This has been attributed to changes in planarity and aromaticity.

The effect of the bridge nature has subsequently been investigated and the conductive character of the bridge has been assigned to follow the trend: C_4H_2S>Ph>N_3C_2H, where N_3C_2H exhibits the most insulator character. Charge transfer is observed to decrease with increasing insulator character. Furthermore, N_3C_2H is a sufficient insulator for an MLCT(phen) state to be populated and observed spectroscopically. This state is unfavourable for the other complexes owing to the less insulating nature of the bridge groups present.

Finally the dihedral angle between the $PhNPh_2$ donor and the phz acceptor has been explored. The difference in charge transfer is observed to be negligible with changing dihedral angle, consistent with the negligible change in HOMO/LUMO gap observed. The additional electron donating OCH_3 groups are observed to have more of an effect on charge transfer than dihedral angle.

Chapter 3

The Photophysical Properties of Phenazine Modified Rhenium Dipyrido[3,2-*a*:2',3'-*c*]phenazine Complexes

1 Introduction

The effect of the NPh_2 electron donating group substituted onto the phz moiety of dppz has been investigated in detail in Chapter 2. Following on, this Chapter will focus on the modification of the phz moiety of dppz. This includes the effect of the substitution of a nitrogen atom into the phz moiety, as well as the addition of amine or halogen groups. Furthermore, the effect of substituent position within the phz moiety on the photophysical properties will also be assessed.

As stated in Chapter 2, Re and Ru diimine complexes exhibit many potential applications,[12-22] including potential catalysts for use in photochemical and electrochemical reduction of CO_2. The Re(I) complexes most commonly investigated for this are based on the $[Re(NN)(CO)_3(L)]^+$ motif, where NN is a diimine (most often bpy or a derivative thereof) and L is a halide,[102-112] nitrogen-donor[109, 113-115] or phosphine[109, 114, 115] ligand. For Ru(II), the most commonly studied complexes are based on the homoleptic $[Ru(NN)]^{2+}$ or heteroleptic $[Ru(NN)_2(NN')]^{2+}$, where NN and NN' are derivatives of bpy[110-112, 116-124] or phen.[125,126]

The reduction of CO_2 is of considerable interest and has grown rapidly in the last few decades as a response to the increasing amount of CO_2 in the atmosphere. The

photochemical and electrochemical reduction of CO_2 to useful products is often considered to be of interest due to the relatively energy intensive process of the direct addition of an electron to CO_2, with a reduction potential of -1.9 V (*vs.* normal hydrogen electrode NHE).[127-129] The overall process requires appropriate catalysts and energy input, where the source of this energy can include a photon or an electron.

Two routes have been suggest for the electrochemical reduction of CO_2 using $[Re(bpy)(CO)_3Cl]$ as a catalyst, a one and two electron process, shown in Figure 3-1. The first step for both pathways involves the generation of the one electron reduced species (OER) $[Re(bpy^{\bullet-})(CO)_3Cl]^{-1}$. The loss of the Cl ligand from this OER species is slow and yields the $17e^-$ metal centre radical, $[Re(bpy^{\bullet-})(CO)_3]^-$. This metal centre radical is quickly trapped by a solvent molecule, to form the ligand centre radical, $[Re(bpy^{\bullet-})(CO)_3(solv)]^+$.

In the $1e^-$ process the solvent is replaced by CO_2 and subsequent disproportionation with another CO_2 molecule forms CO and CO_3^{2-}. In contrast, for the $2e^-$ pathway the reduction of the solvent-coordinated radical results in the formation of a five coordinate $18e^-$ metal based anion, $[Re(bpy^{\bullet-})(CO)_3]^-$. Further coordination of CO_2 followed by reaction with additional CO_2 as an oxide receptor results in the formation of CO and CO_3^{2-}. Following CO formation both $1e^-$ and $2e^-$ pathways form a cationic solvent-coordinated species $[Re(bpy)(CO)_3(solv)]^+$, which upon reduction regenerates the solvent coordinated ligand and thus closing the catalytic cycle.

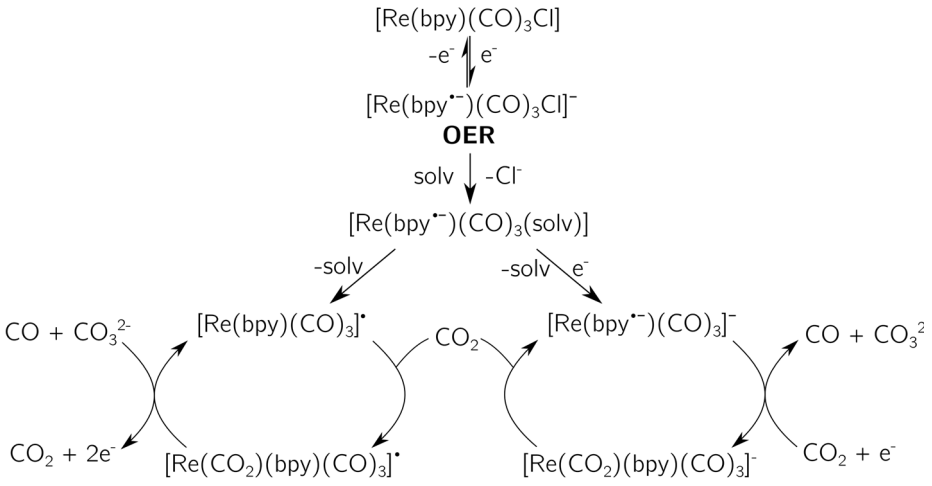

Figure 3-1: The $1e^-$ and $2e^-$ pathways for electrochemical CO_2 reduction. Adapted from references 91 and 128.

The photochemical reduction of CO_2 consists of a homogeneous CO_2 photoreduction system comprised of a molecular catalyst (cat), photosensitiser (P) and a sacrificial electron donor (D).[130] The photosensitiser absorbs radiation in the ultraviolet or visible region resulting in the generation of the excited state (P^*). The excited state is reductively quenched by the donor resulting in the formation of a singly reduced photosensitiser (P^-) and an oxidised donor (D^+), Figure 3-2.[130] The photosensitiser must be able to transfer electrons to the catalyst to generate the reduced catalyst (cat^-). The CO_2 then binds to the reduced photosensitiser (P^-) to result in a mechanism that produces the desired products.

$$P + h\nu \rightarrow P^* \quad (3a)$$

$$P^* + D \rightarrow P^- + D^{\cdot} \quad (3b)$$

$$P^- + cat \rightarrow P + cat^- \quad (3c)$$

$$cat^- + CO_2 \rightarrow cat + products \quad (3d)$$

Figure 3-2: The photochemical reduction of CO_2 system comprised of a photosensitiser (P) which absorbs radiation and generates the excited state (P*). P* is reductively quenched by donor (D) to form singly reduced photosensitiser (P^-) and an oxidised donor (D^+).

Re(diimine) complexes have been shown to be efficient catalysts for photoreduction of CO_2 such as $[Re(bpy)(CO)_3X]^+$ as the complexes are able to act as both a photosensitiser and a catalyst, shown in Figure 3-3. [130]

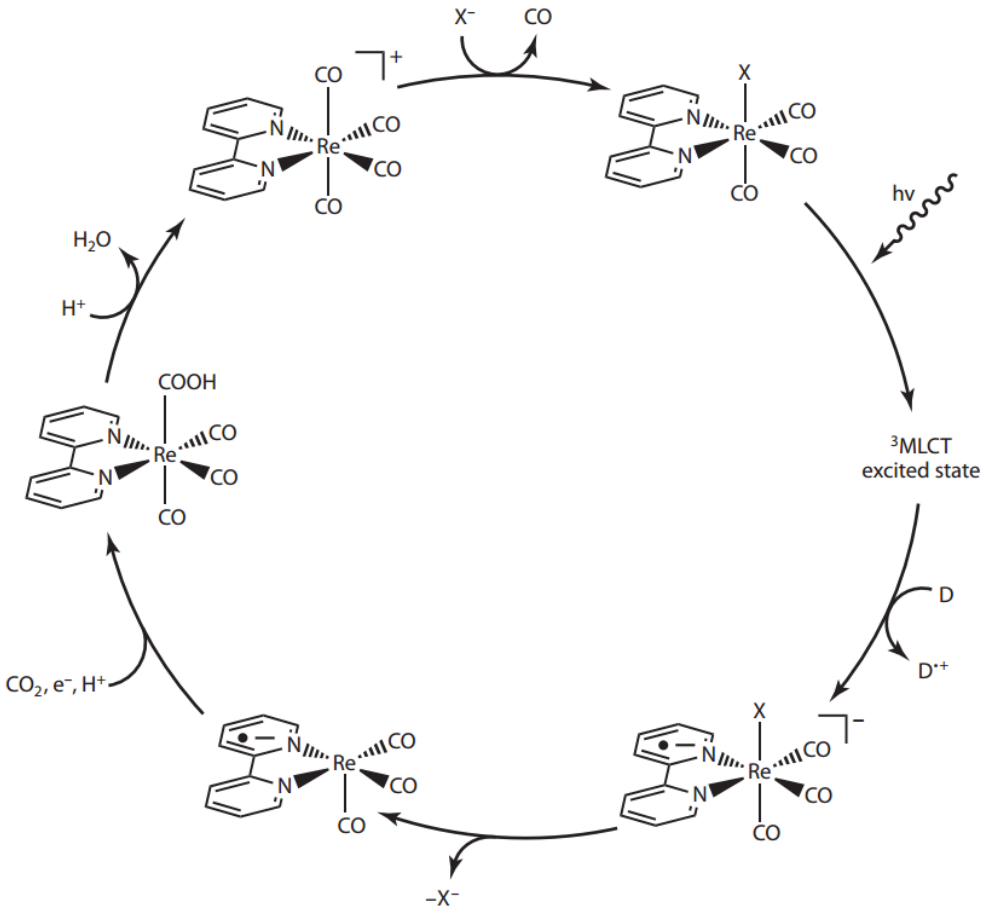

Figure 3-3: The proposed photocatalytic mechanism for CO production from a $[Re(bpy)(CO)_3X]^+$ catalyst. Reproduced from reference 130.

As shown above M(diimine) complexes have been shown to be effective photocatalysts for CO_2 reduction, where commonly CO is produced. In order to implement a Re(diimine) complex as a photocatalyst an in depth understanding of the photophysical properties of the complex is crucial.

Further work on photo and electrocatalysts for CO_2 reduction has shown that pyridine can catalyse the formation of the $6e^-$ reduced product methanol over the more common $2e^-$ reduced products such as CO and formate.[131-135] The catalytic process involving pyridine is proposed as occurring in a sequential manner starting with the reduction of the pyridium cation (pyH^+) to the neutral radical ($pyH^\bullet$), this is followed by the insertion of CO_2 into the NH bond resulting in a radical carbamate intermediate. Subsequent reactions yield the products where Figure 3-4 shows this process.

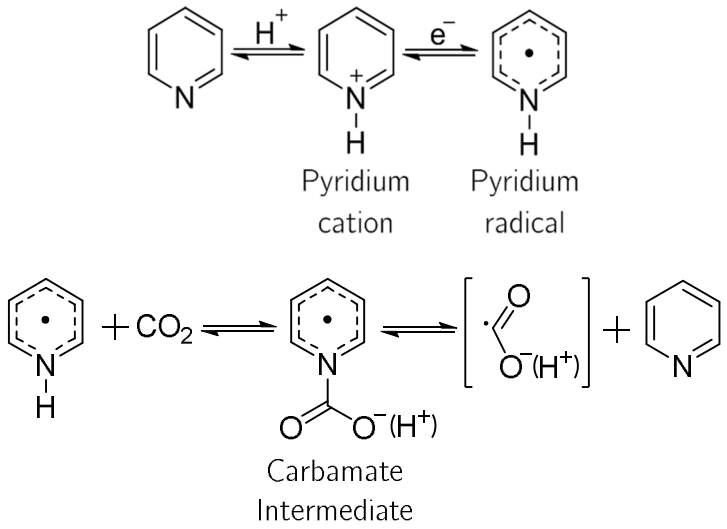

Figure 3-4: The insertion of CO_2 in the NH bond of the neutral pyridium radical ($pyH^{\bullet}$) (top) to produce a carbamate intermediate which undergoes subsequent reactions to yield the pyridine catalyst and methanol product (middle). The overall regeneration of the pyridine catalyst is also shown (bottom). Reproduced from references 132 and 134.

Subsequent work has investigated the electro and photocatalytic reduction of CO_2 with Re(diimine) complexes that contain a pyridine derivative. This has focussed on the incorporation of an additional nitrogen heteroatom into the phz portion of the dppz ligand and a comparison was drawn to Ru(dppz) complexes. To this end the complexes $[Ru(dppz)(phen)_2]^{2+}$, $[Ru(dppp2)(phen)_2]^{2+}$ and $[Ru(dppp3)(phen)_2]^{2+}$ shown in Figure 3-5, have been investigated as potential electro and photocatalysts for CO_2 reduction.[136]

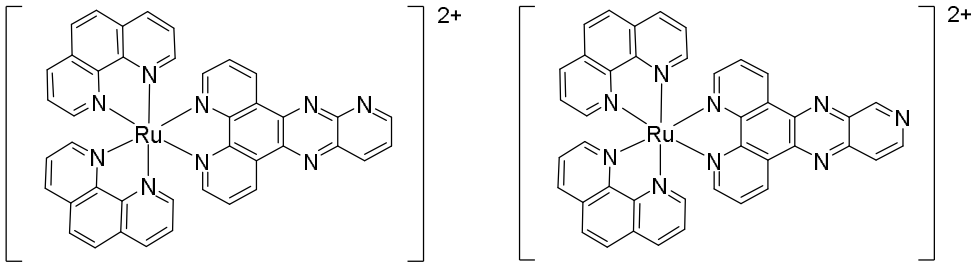

Figure 3-5: The structures of $[Ru(dppp2)(phen)_2]^{2+}$ and $[Ru(dppp3)(phen)_2]^{2+}$.

$[Ru(dppz)(phen)_2]^{2+}$ was shown to be electrochemically inactive in DMF:H_2O mixtures, while conversely electrocatalytic reduction of CO_2 by $[Ru(dppp2)(phen)_2]^{2+}$ and $[Ru(dppp3)(phen)_2]^{2+}$ was observed by simply bubbling CO_2 through the solution.[136] Large increases in the cathodic current are observed at -0.64 and -0.60 V for

$[Ru(dppp2)(phen)_2]^{2+}$ and $[Ru(dppp3)(phen)_2]^{2+}$ respectively which indicates the electrocatalytic reduction of CO_2, shown in Figure 3-6.

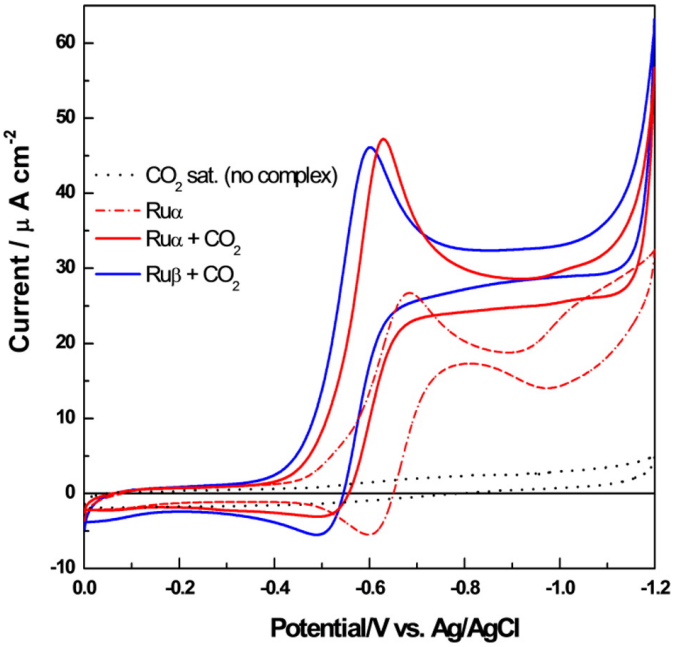

Figure 3-6: The CV for $[Ru(dppp2)(phen)_2]^{2+}$ (red solid line) and $[Ru(dppp3)(phen)_2]^{2+}$ (blue solid line) in DMF:H_2O (1 M) solution saturated with CO_2. The CV of $[Ru(dppp2)(phen)_2]^{2+}$ in DMF:H_2O (1 M) before saturation with CO_2 (red dash line). The CV of DMF:H_2O (1 M) solution saturated with CO_2 without the presence of a Ru complex which is included as a reference (black dot line). All voltammograms were run at 5mV/s with a glassy carbon working electrode. Reproduced from reference 136.

The electrochemical inactivity or $[Ru(dppz)(phen)_2]^{2+}$ would suggest that the additional nitrogen is important for the catalytic activity, where the pyridyl is required to form the initial CO_2 adduct, the carbamate intermediate shown in Figure 3-4. Further calculations of $[Ru(dppp3)(phen)_2]^{2+}$, $[Ru(phen)_3]^{2+}$ and $[Ru(bpy)_3]^{2+}$ have shown that the standard redox potentials are lower for $[Ru(dppp3)(phen)_2]^{2+}$ than for $[Ru(phen)_3]^{2+}$ and $[Ru(bpy)_3]^{2+}$.[137] This has been attributed to the accessible Brønsted base sites for the protons as a result of the pyridyl moiety and the significantly larger π* system that can accommodate electrons. Where previous work has shown that the increase in Brønsted acids increases the catalytic activity,[138]

The complexes $[Ru(dppp2)(phen)_2]^{2+}$ and $[Ru(dppp3)(phen)_2]^{2+}$ have also been shown to be able to acts as photocatalysts for CO_2 reduction in DMF:H_2O (1 M) with triethylamine (0.25 M) saturated with CO_2, through time dependent absorption

studies,[136] where the CO_2 is observed to react with the reduced catalytic complex.[44, 139, 140]

This is contradictory to the suggested electrochemical route which indicates that the CO_2 reacts with the radical product, however these data are assigned to a fast and reversible formation of a CO_2 radical adduct. Subsequent reactions have indicated that the photocatalytic reduction of CO_2 could be repeated with the Ru complexes studied.

Despite previous work demonstrating that Ru(dppp2) and Ru(dppp3) complexes may act as photocatalysts for CO_2 reduction, there is limited research into the effect of the introduction of an additional heteroatom into the phz part of the dppz ligand for M(dppz) complexes on the observed photophysical properties. Furthermore, this previous work has focussed on Ru based complexes, $[Ru(dppp2)_{3-n}(bpy)_n]^{2+}$ n=1-3, and $[Ru(dppp3)(bpy)_2]^{2+}$.

These complexes were first studied by Turro *et al.*[31] where the photophysics of $[Ru(dppp2)(bpy)_2]^{2+}$ was investigated through viscosity studies. The complex was shown to intercalate into DNA as is observed for its dppz counterpart, $[Ru(dppz)(bpy)_2]^{2+}$; however, unlike for dppz, the dppp2 complex demonstrates negligible light switch behaviour and minimal increase in the emission intensity in the presence of DNA. Electrochemical studies further demonstrate that the first reduction potential is far more positive for dppp2 complex than dppz, -0.5 and -1.02 V respectively,[31, 141] although the second reduction potential of an electron onto an auxiliary bpy ligand is shown to be similar for both complexes. The lack of light switch effect and the lower reduction potential indicates that there is far larger separation in energy of the lower excited states for dppp2 than for dppz, a conclusion further supported by DFT calculated MO orbitals shown in Figure 3-7. Therefore population of the phz(π^*) orbital is favoured more for $[Ru(dppp2)(bpy)_2]^{2+}$ compared to the $[Ru(dppz)(bpy)_2]^{2+}$ and thus weaker emission is observed for $[Ru(dppz)(bpy)_2]^{2+}$ than for $[Ru(dppp2)(bpy)_2]^{2+}$.

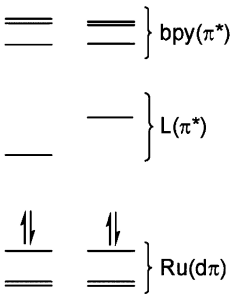

Figure 3-7: The molecular orbital diagrams comparing the relative energies of the metal centred MOs, Ru(dπ), with the contributions located on the phenazine based portion of the ligands, L(π*) and those localised on the phen/bpy portion of dppz ligands or the two ancillary bpy ligands, bpy(π*) for $[Ru(dppz)(bpy)_2]^{2+}$ (left) and $[Ru(dppp2)(bpy)_2]^{2+}$ (right). Reproduced from reference 31.

Further work has shown that the very weak emission observed for $[Ru(dppp2)(bpy)_2]^{2+}$ is highly solvent dependent (Figure 3-8).[139] A red shift in emission maxima from 653 to 752 nm was accompanied by a decrease in quantum yield from Φ_{em} = 0.038 to 0.002 for CH_2Cl_2 and CH_3CN respectively. This red shift is far smaller than that observed for $[Ru(dppz)(bpy)_2]^{2+}$ which is only 17 nm, from 614 nm to 631 nm for CH_2Cl_2 and CH_3CN. The observed solvatochromic effect indicates that the MLCT(phz) state is more populated for dppp2 compared to the MLCT(phen) state for dppz. The MLCT(phz) state is more sensitive to changes in polarity of the surrounding media as MLCT(phz) is a larger distance charge separated state than MLCT(phen). This energy difference between MLCT(phz) and MLCT(phen) varies as a function of solvent polarity and thus affects the rate of inter-conversion from MLCT(phen)→MLCT(phz) with the rate decreasing by a factor of 2.6 in CH_2Cl_2 compared to CH_3CN.[139]

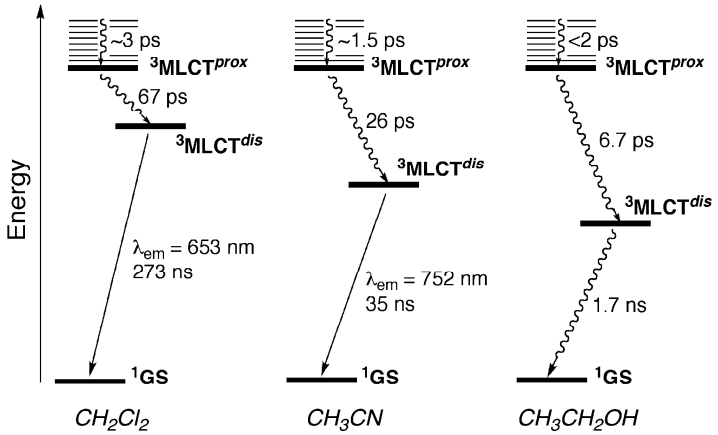

Figure 3-8: The Jabłoński diagram of $[Ru(dppp2)(bpy)_2]^{2+}$ in CH_2Cl_2 (left), CH_3CN (middle) and CH_3CH_2OH (right). Where $^3MLCT^{prox}$ and $^3MLCT^{dis}$ relate to MLCT(phen) and MLCT(phz) respectively. Reproduced from reference 139.

Subsequently, the effect of the number of dppp2 groups present has also been probed. The highly solvent dependent emission of $[Ru(bpy)_3]^{2+}$, $[Ru(dppp2)_2(bpy)]^{2+}$, $[Ru(dppp2)(bpy)_2]^{2+}$ and $[Ru(dppp2)_3]^{2+}$ have been explored in CH_3CN with varying fractions of CH_2Cl_2. For all complexes, the emission was observed to originate from the same excited state, shown in Figure 3-9.[139] With increasing fractions of CH_2Cl_2 the MLCT(phen)/MLCT(phz) energy gap is decreased, where MLCT(phen) and MLCT(phz) are labelled as $MLCT^{prox}$ and $MLCT^{dis}$ respectively.

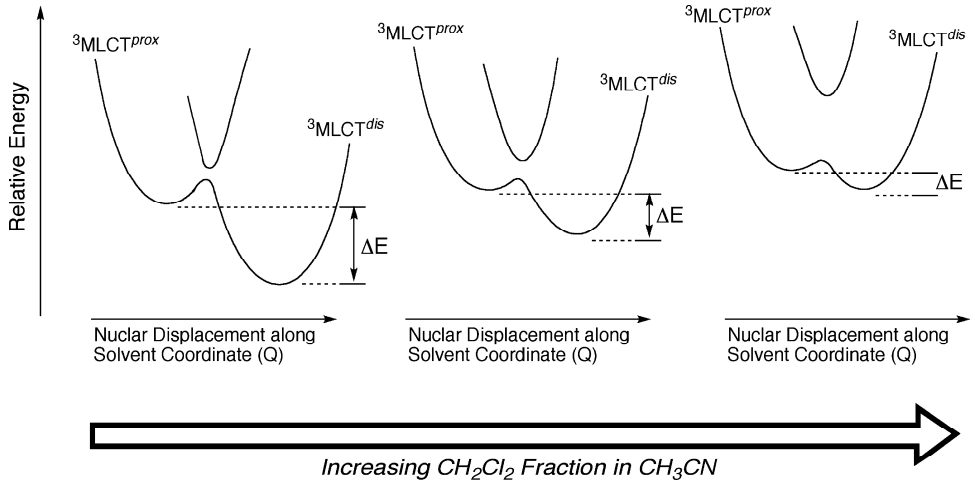

Figure 3-9: A schematic representation of the shift in potential energy surfaces of the low-lying excited states of $[Ru(dppp2)(bpy)_2]^{2+}$, $[Ru(dppp2)_2(bpy)]^{2+}$ and $[Ru(dppp2)_3]^{2+}$ with increasing fractions of CH_2Cl_2 in CH_3CN, where the MLCT(phen)/MLCT(phz) states energy gap is observed to decrease. The MLCT(phen) and MLCT(phz) states are labelled as $MLCT^{prox}$ and $MLCT^{dis}$ respectively. Reproduced from reference 139.

As shown above for the complex $[Ru(dppp2)(bpy)_2]^{2+}$, the excited state is clearly affected by the solvent environment. In addition to investigating the effect of an electron withdrawing group within the phz moiety, this Chapter will explore the effect of the solvent medium on the observed photophysics for Re(dppp) complexes. As discussed in Chapter 2, the MLCT(phz) state is lower in energy than the MLCT(phen) state for M(dppz) complexes.[29] The charge transfer states, MLCT(phen) and MLCT(phz), exhibit large dipoles which may be stabilised by the surrounding solvent media. As stated above, MLCT(phz) is a larger distance charge separated state than MLCT(phen) state. As a result, a polar solvent will stabilise the MLCT(phz) state more than the MLCT(phen) state causing a larger energy separation between the MLCT(phen) and

MLCT(phz) states. The more stabilised the charge transfer state the shorter the lifetime observed.[8-11]

This is similar for other Re complexes; for example, [Re(dppz)(CO)$_3$Cl] exhibits more MLCT(phen) character when in the less polar solvent CH_2Cl_2 compared to the more MLCT(phz) character in the more polar solvent C_3H_7CN, shown in Figure 3-10.

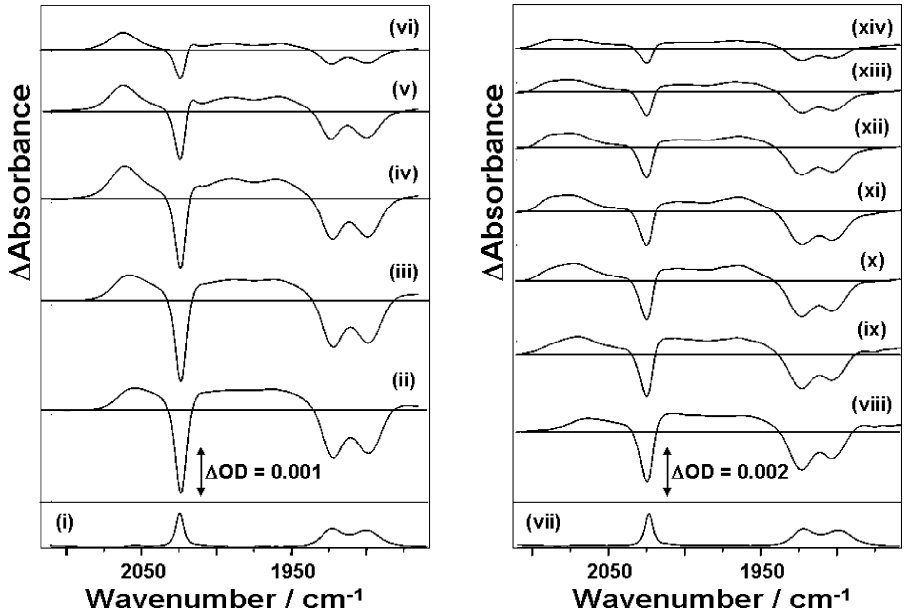

Figure 3-10. The spectra of [Re(dppz)(CO)$_3$Cl] in CH_2Cl_2 (left) at room temperature showing the FTIR spectra (i) and TRIR spectra in CH_2Cl_2 following 400 nm photoexcitation obtained at time delays of (ii) 2 ps; (iii) 4 ps; (iv) 20 ps; (v) 100 ps; and (vi) 2 ns (left). The spectra of [Re(dppz)(CO)$_3$Cl] in C_3H_7CN at room temperature showing the FTIR spectra (vii) and TRIR spectra following 400 nm photoexcitation at time delays of (viii) 2 ps; (ix) 10 ps; (x) 20 ps; (xi) 70 ps; (xii) 500 ps; (xiii) 1 ns; and (xiv) 2 ns (right). Reproduced form reference 32.

The excited state lifetime of [Re(dppz-X_2)(CO)$_3$Cl], X = CH_3, H, F, Cl and CF_3 decreases with increasing solvent polarity, shown in Table 3-1. Furthermore the rate of MLCT(phen) to MLCT(phz) increases with increasing dielectric constant where for [Re(dppz-F_2)(CO)$_3$Cl] in C_3H_7CN at time delays >10 ps, only MLCT(phz) is observed in the TRIR spectra. In contrast, in CH_2Cl_2 at Δt = 0.002 - 10 ns, an equilibrium of MLCT(phen) and MLCT(phz) states is observed, Figure 3-11.

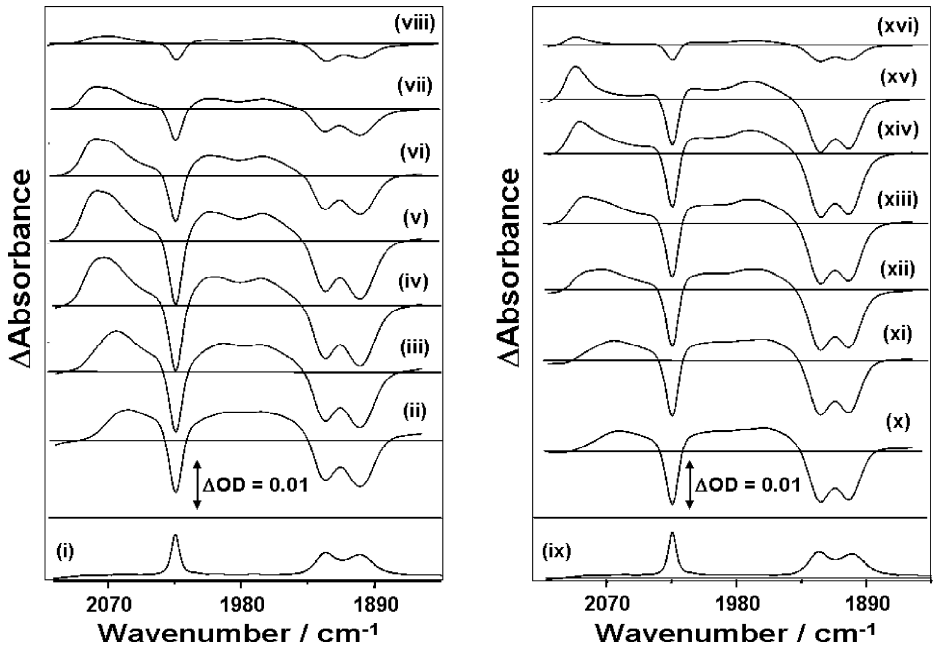

Figure 3-11. The spectra of [Re(dppz-F_2)$(CO)_3$Cl] in CH_2Cl_2 at room temperature showing the FTIR spectra (i) and TRIR spectra following 400 nm photoexcitation at time delays of (ii) 2 ps; (iii) 4 ps; (iv) 20 ps; (v) 500 ps; (vi) 1 ns; (vii) 2 ns; and (viii) 4 ns (left). The spectra of [Re(dppz-F_2)$(CO)_3$Cl] in C_3H_7CN at room temperature showing the FTIR spectra (ix) and TRIR spectra obtained at time delays of (x) 1.5 ps; (xi) 2 ps; (xii) 4 ps; (xiii) 6 ps; (xiv) 10 ps; (xv) 100 ps; and (xvi) 500 ps (right). Reproduced from reference 32.

Table 3-1: The excited state lifetimes and MLCT(phen)/MLCT(phz) states interconversion times obtained from ps-TRIR for [Re(dppz-F_2)$(CO)_3$Cl], in the solvents listed following photoexcitation at 400 nm. Values taken from reference 32.

Solvent	ε_r	τ MLCT(phen)→MLCT(phz) (ps)	τ MLCT(phz) (ps)
CH_2Cl_2	8	ca. 6	3050 ± 40
C_3H_7OH	20	51 ± 6	250 ± 40
C_3H_7CN	24	6.0 ± 0.2	330 ± 5
CH_3OH	35	9 ± 2	90 ± 12
CH_3CN	37	4.0 ± 0.5	240 ± 20

Further work has compared $[Ru(dppp2)_2(bpy)]^{2+}$ and $[Ru(dppp2)_2(phen)]^{2+}$ where for both complexes the DNA binding ability was observed to be lower than for the analogous dppz complex.[142, 143] In the presence of DNA a small red shift in the absorption energy (*ca.* 5 nm) for both complexes is observed. This is suggested to be the result of the π* orbital of the intercalative ligand (i.e. the dppz) coupling with the π orbitals of the base pairs resulting in a decrease in the ππ* transition energies. Additionally, for both

complexes hypochromism of the absorption bands occurs with the presence of DNA, indicating that the ligand has intercalated into the DNA. This hypochromism in ^{1}MLCT absorption in the presence of DNA is also observed for substituted dppp2 complexes, $[Ru(phen)_2(dppp2Br)]^{2+}$ and $[Ru(phen)_2(dppp2Ph)]^{2+}$, Figure 3-12.[144]

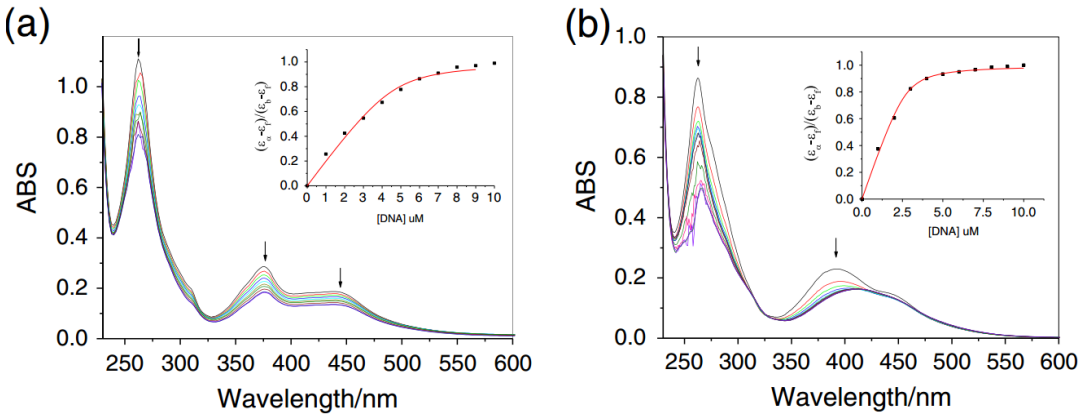

Figure 3-12: The hypochromism of the MLCT absorption band observed in the presence of DNA for $[Ru(phen)_2(dppp2Br)]^{2+}$ (left) and $[Ru(phen)_2(dppp2Ph)]^{2+}$ (right). Reproduced from reference 144.

Due to the weaker conjugation effect of the pyridine (for dppp2 and dppp3 complexes) compared to benzene (in dppz), hydrogen bonds between the nitrogen atoms of pyridine and hydrogen atoms of the DNA base pairs are formed, which hinder the insertion of the intercalation of the dppp complexes.

Substituted dppz complexes with two additional nitrogen heteroatoms in the phz moiety (dpppn) have been previously reported where the complexes $[Ru(dpppn\text{-}(NH_2)_2)(NN)_2)]^{2+}$, where NN is bpy,[145-147] phen,[145, 146] and imidazole-phenanthroline,[148] have been previously investigated in the literature with limited work into the photophysics or electrocatalytic ability of these complexes. The structure of the ligand (dpppn-$(NH_2)_2$)

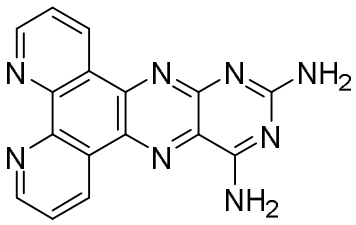

Figure 3-13: The structure of the dpppn-$(NH_2)_2$ ligand, where Ru(dpppn-$(NH_2)_2$) derivative complexes have been previous studied in literature.

The complexes are all shown to exhibit hypochromism of absorption band assigned to $Re(d\pi) \rightarrow dpppn(NH_2)_2(\pi^*)$ in nature ^{1}MLCT state, and a small red shift with increasing DNA concentration as observed for Ru(dppp2) and Ru(dppp3) complexes, indicating DNA intercalation. Calculations of the frontier molecular orbital energies of $[Ru(dpppn(NH_2)_2)(bpy)_2]^{2+}$ and $[Ru(dpppn(NH_2)_2)(phen)_2]^{2+}$ show that these complexes have similar energies to their dppz counterpart complex. Furthermore, both complexes exhibit the light switch effect unlike the analogous mono-nitrogen substituted dppp complexes.

2 Aims

The aim of this chapter is to investigate the photophysical properties of phz-modified Re(dppz) derivative complexes, focusing on the effect of the substitution of a nitrogen atom into the phz moiety and the effect of amide or halogen group addition. Including how the solvent environment can change the photophysical properties observed. This aim has been split into four objectives.

1. To establish the effect of a nitrogen atom substitution within the phz moiety, and the position of this substitution, on the photophysical properties observed, by comparing [Re(dppp2)$(CO)_3$Cl] and [Re(dppp3)$(CO)_3$Cl] complexes.

2. To establish the effect of halogen substitution on the photophysics of nitrogen substituted phz complexes by comparing [Re(dppp2)$(CO)_3$Cl] and [Re(dppp2Br)$(CO)_3$Cl].

3. To further investigate halogen addition onto the phz moiety by investigating the photophysical properties of the previously unreported [Re(dppz-I)$(CO)_3$Cl] complex to other [Re(dppz-X)$(CO)_3$Cl] complexes.

4. To compare the effect of the addition of an NH_2 group on to a nitrogen substituted phz moiety by exploring the photophysics of [Re(dpppn-$(NH_2)_2$)$(CO)_3$Cl], drawing parallels where possible to Chapter 2.

3 Results and Discussion

The photophysics of [Re(dppp2)(CO)$_3$Cl] (Re(dppp2)), [Re(dppp3)(CO)$_3$Cl] (Re(dppp3)) and [Re(dppp2Br)(CO)$_3$Cl] (Re(dppp2Br)), structures shown in Figure 3-14, have been studied in a range of solvents with varying dielectric constants (ε_r = 2.3 - 46.7) using TRIR spectroscopy. The nitrogen heteroatom is substituted into the phz portion of the ligand, therefore affording a phz-like moiety, which will be referred to as phz within this work.

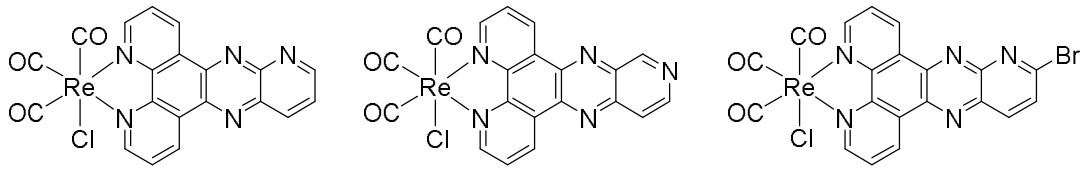

Figure 3-14: The structures of Re(dppp2) (left), Re(dppp3) (middle) and Re(dppp2Br) (right).

3.1 Time Resolved Infrared Spectroscopy

The photophysical properties of all three complexes were probed on the picosecond and nanosecond timescales using TRIR in the ν(CO) and, where possible, limited by solvent absorption, ν(FP) IR region, and are detailed below. The TRIR spectral profile of Re(dppp2), Re(dppp3) and Re(dppp2Br) are similar in solvents d-DMSO, CH_3CN, CH_2Cl_2 and THF, as a result the spectra is shown for Re(dppp2), Re(dppp3) and Re(dppp2Br) in d-DMSO as representative spectra within this Chapter, with the other spectra given in Appendix A.

3.1.1 TRIR Spectroscopy in d-DMSO

The TRIR of Re(dppp2), Re(dppp3) and Re(dppp2Br) in d-DMSO following 400 nm photoexcitation have been collected and are shown in Figure 3-15 and 3-16 for ν(CO) and ν(FP) IR regions respectively with features summarised in Table 3-2.

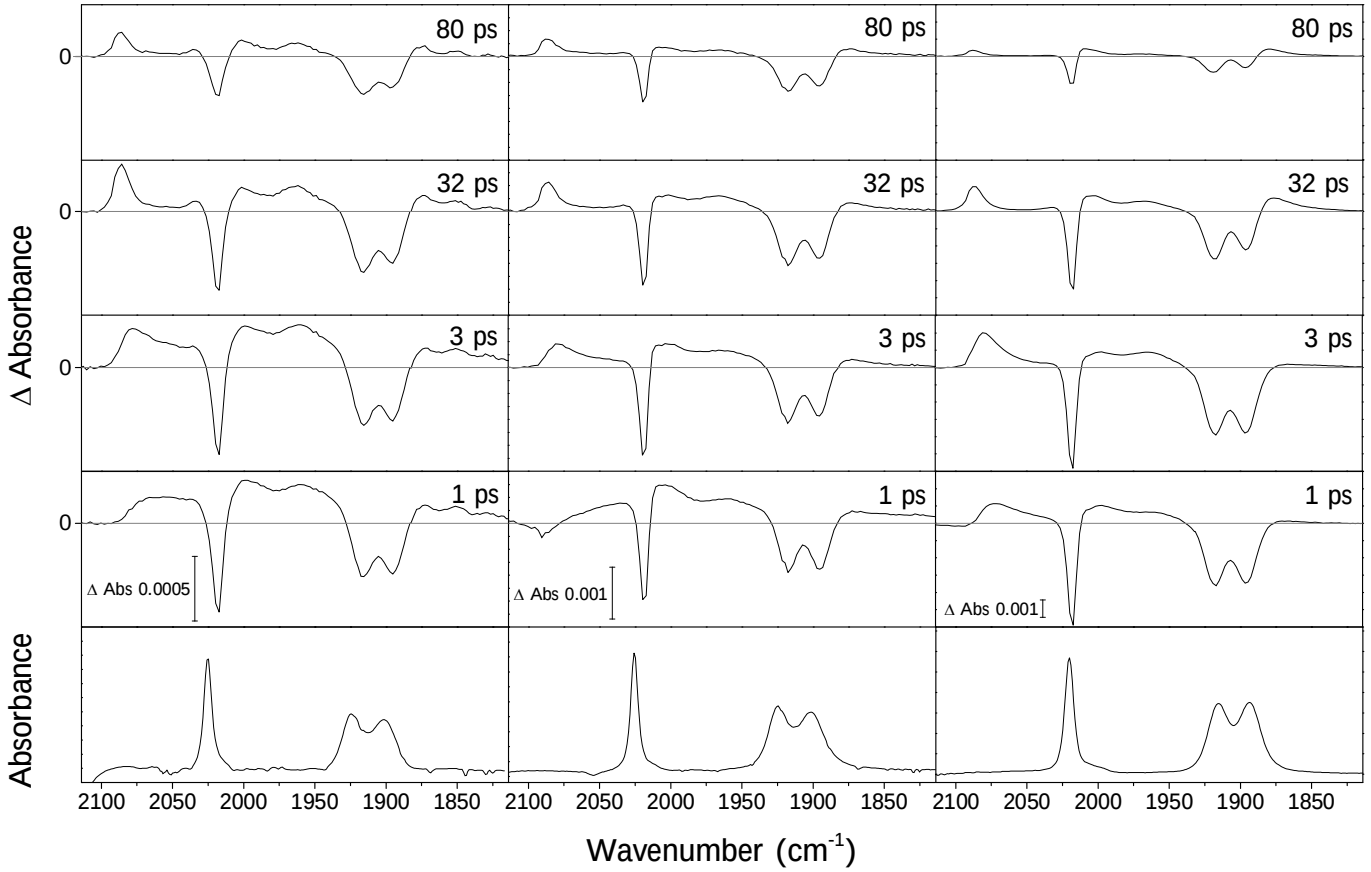

Figure 3-15: The FTIR (a) and TRIR (b-e) spectra in the CO IR region for Re(dppp2) (left), Re(dppp3) (middle) and Re(dpp2Br) (right) in d-DMSO following 400 nm photoexcitation. The FTIR shown was acquired in CH_2Cl_2 due to solubility.

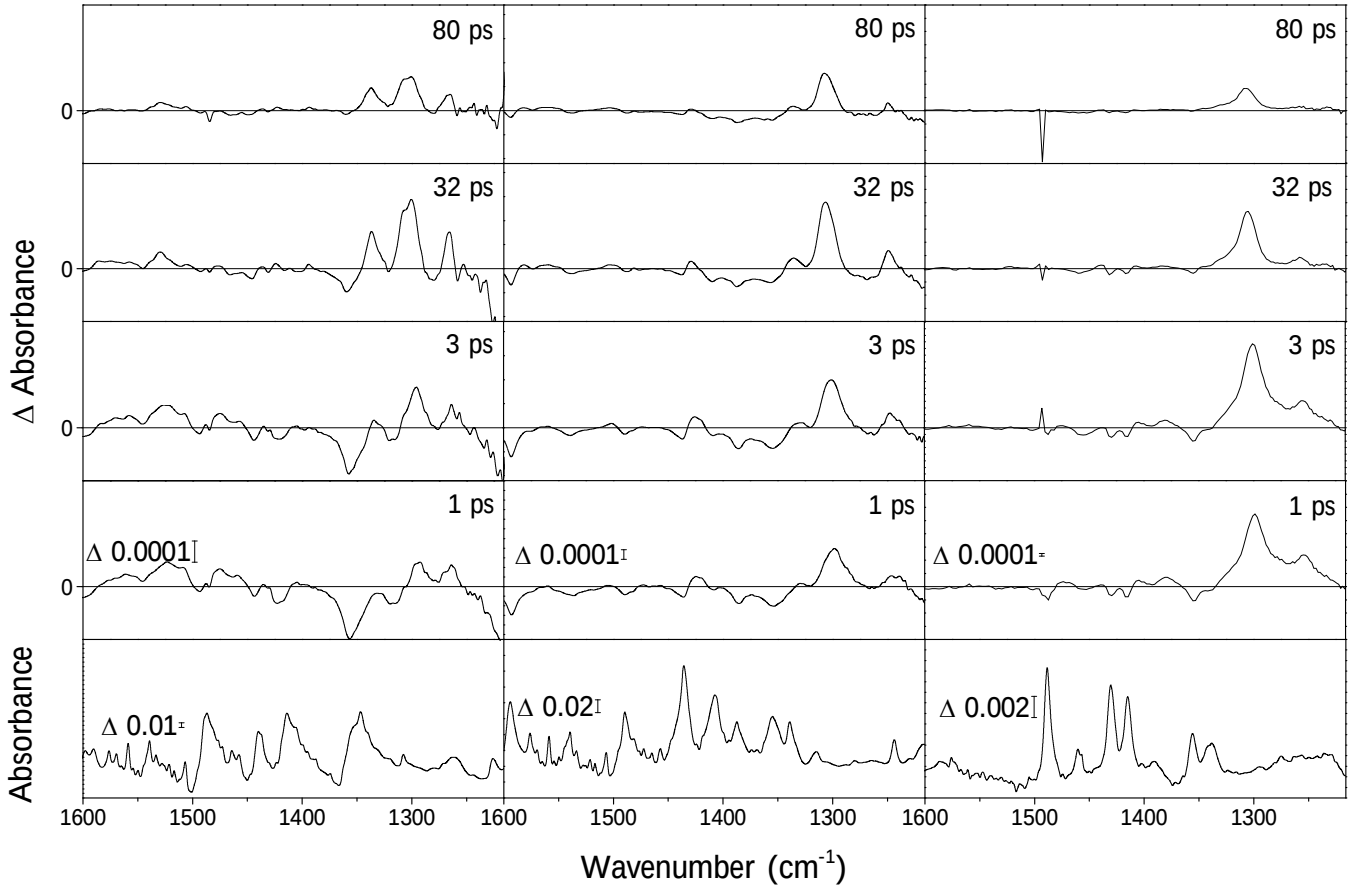

Figure 3-16: The FTIR (a) TRIR (b-e) spectra in the FP IR region for Re(dppp2) (left), Re(dppp3) (middle) and Re(dpp2Br) (right) in d-DMSO following 400 nm photoexcitation. The FTIR shown was acquired in the solid state for Re(dppp2Br) and Re(dppp3).

Table 3-2: A summary of the FTIR and TRIR spectral features and kinetics observed for Re(dppp2), Re(dppp3) and Re(dppp2Br) in d-DMSO following 400 nm photoexcitation.

Solvent	ν (cm^{-1})	τ decay (ps)	τ growth (ps)	Assignment
Re(dppp2)	2060	70 ± 10	-	MLCT(phen)
	2086, 2002, 1961, 1266, 1299, 1337	65 ± 4	3.1 ± 0.7	MLCT(phz)
	2019, 1915, 1897 1358, 1804	22 ± 2	7 ± 1	parent
	2025, 1925, 1901	-	-	GS FTIR[a]
Re(dppp3)	2070	2 ± 1	-	MLCT(phen)
	2087, 2002, 1965	75 ± 9	3.9 ± 0.3	MLCT(phz)
	1873	70 ± 40	40 ± 30	IL ππ*
	2020, 1918, 1895	-	130 ± 10	Parent
	2025, 1925, 1901	-	-	GS FTIR[a]
Re(dppp2Br)	2063	5 ± 0.3		MLCT(phen)
	2086, 1966, 1256, 1299	37 ± 4	3 ± 0.6	MLCT(phz)
	1877, 2004	30 ± 10	30 ± 10	IL ππ*
	2019, 1917, 1897	-	46 ± 6	Parent
	2020, 1916, 1894	-	-	GS FTIR[a]

[a]Acquired in CH_2Cl_2.

The TRIR spectra of Re(dppp2) obtained following photoexcitation at 400 nm in d-DMSO (ε_r = 46.7)[149, 150] clearly shows that at 1 ps following photoexcitation the three parent bands at 2017, 1915 and 1897 cm^{-1} are bleached. Simultaneously, the formation of transient bands at 2079, 2060, 2002, 1960 cm^{-1} are observed.

More detailed analysis shows the presence of characteristic bands for an MLCT(phen) state at 2060 cm^{-1} which appears to decay to an MLCT(phz) state with a band at 2079 cm^{-1} over the first 5 ps, although this timescale is also consistent with vibrational cooling.[40, 53] This MLCT(phz) state subsequently decays to the ground state with τ = 65 ± 4 ps matching parent recovery 70 ± 3 ps. Both the MLCT(phen) and MLCT(phz) states are populated at 1 ps.

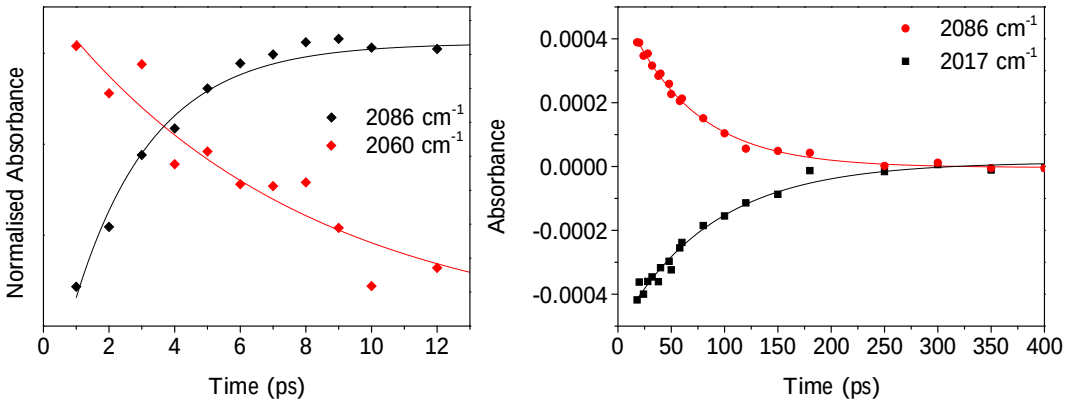

Figure 3-17: The kinetics of Re(dppp2) in d-DMSO following 400 nm photoexcitation. The decay of the band at 2060 cm^{-1} assigned to an MLCT(phen) state, is in good agreement with the growth of the transient band at 2086 cm^{-1} assigned to an MLCT(phz) state (left). The decay of the band at 2086 cm^{-1} assigned to an MLCT(phz) state, is in good agreement with growth of the band at 2017 cm^{-1} assigned to the parent (right).

The TRIR spectra of Re(dppp3) obtained following photoexcitation at 400 nm in d-DMSO also shows that the parent bands (2020, 1918 and 1895 cm^{-1}) are bleached and simultaneously new transient bands are observed (2087, 2070, 2002 1965 cm^{-1}). This transient species is assigned as for Re(dppp2), as an MLCT(phen) state (2070 cm^{-1}) decaying to an MLCT(phz) state (2087 cm^{-1}). Furthermore, the growth (τ = 40 ± 30 ps) of a lower energy band to the parent at 1873 cm^{-1} is observed which was not previously seen for Re(dppp2). This is tentatively assigned as a ligand centred, IL$\pi\pi^*$ state, and is observed to decay at the same rate as the MLCT(phz) state. Therefore the lowest energy excited state for Re(dppp3) is assigned as MLCT(phz)/IL$\pi\pi^*$ in nature. The increased electron density on the ligand results in turn in increased electron density on the Re metal which in turn leads to increased back bonding from Re(dπ) orbitals to the CO(π^*) orbitals. This increased back bonding results in a strengthened Re-C bond and a weaker CO bond. Thus the CO reporter group demonstrates a red shift in the TRIR spectra.

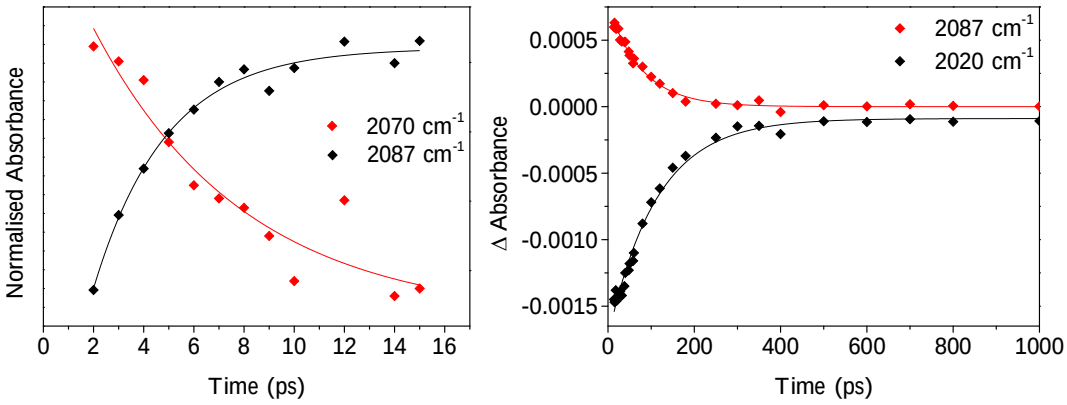

Figure 3-18: The kinetics of Re(dppp3) in d-DMSO following 400 nm photoexcitation. The decay of the band at 2070 cm^{-1} assigned to an MLCT(phen) state, is in good agreement with the growth of the transient band at 2087 cm^{-1} assigned to an MLCT(phz) state. The decay of the band at 2087 cm^{-1} assigned to the MLCT(phz) state and the growth of the band at 2020 cm^{-1} assigned to the parent.

Finally the TRIR spectra of Re(dppp2Br) in d-DMSO exhibit a similar spectral profile to Re(dppp3) whereby immediately following 400 nm photoexcitation, the parent bands (2020, 1918, 1895 cm^{-1}) are observed to bleach and new transients are formed (2087, 2070, 2002, 1965 cm^{-1}). At 1ps bands representative of an MLCT(phen) at 2070 cm^{-1} and an MLCT(phz) state at 2087 cm^{-1} are observed. The MLCT(phen) state is observed to decay to the MLCT(phz) state which subsequently decays to an equilibrium with an IL$\pi\pi^*$ state. Where for this complex the lowest excited states observed are MLCT(phz)/IL$\pi\pi^*$.

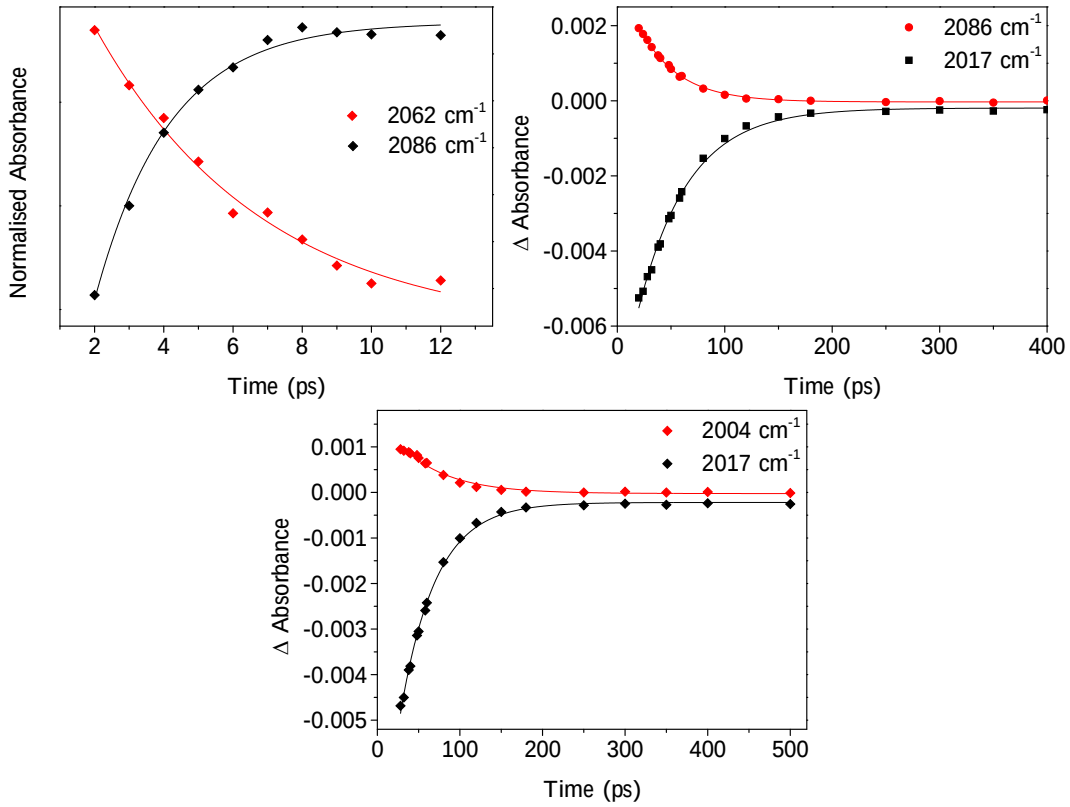

Figure 3-19: The kinetics of Re(dppp2Br) in d-DMSO following 400 nm photoexcitation. The growth of a transient band at 2086 cm^{-1} assigned to an MLCT(phz) state, is in good agreement with the decay of the band at 2062 cm^{-1} assigned to an MLCT(phen) state (top, left). The decay of the band 2086 cm^{-1} assigned to the MLCT(phz) state, is in good agreement with growth of the band at 2017 cm^{-1} assigned to the parent (top, right). The early ps growth followed by long ps decay of the band at 2004 cm^{-1} assigned to an IL$\pi\pi^*$ state, where the decay is in good agreement with the growth of band at 2017 cm^{-1} assigned to the parent (bottom).

The assignment of the MLCT(phen) and MLCT(phz) states is based on distinctive characteristic bands for MLCT(phen) and MLCT(phz) at *ca.* $\Delta\nu$ of +40 and +60 cm^{-1} respectively, with respect to the parent bleach.[32] The larger blue shift observed for MLCT(phz) than for MLCT(phen) reflects the distance from the Re($d\pi$) orbital to the Phen/Phz(π^*) orbital respectively. Furthermore, due to the broad nature of these bands overlap between the two bands is observed, as a result Gaussian band fitting has been completed to identify the presence of both bands and is shown in Appendix A.

The MLCT(phen)/MLCT(phz) interconversion occurs on a similar timescale to vibrational cooling and the ps-TRIR ν(CO) IR region data do not allow for accurate distinction between these two processes. Therefore further study has been conducted on the IR fingerprint (FP) region (*ca.* 1200-1800 cm^{-1}), which shows clearer spectral

differences.[40] However, as discussed in Chapter 2, assignments in the FP region are often more difficult than the CO region.

At 1 ps following 400 nm photoexcitation, a range of transient bands are observed in the FP region TRIR spectra (Figure 3-16). For Re(dppp2) transient bands at 1337, 1299 and 1266 cm^{-1} are observed which exhibit similar kinetics to the MLCT(phz) state observed in the CO region. The bands at 1804 and 1358 cm^{-1} assigned to the parent display similar lifetimes to the parent bands observed in the CO region, and their recovery matches decay of the band assigned to the MLCT(phz) state in the FP region, shown in Figure 3-20. No bands are observed in the FP region with kinetics that match the decay of the band at 2060 cm^{-1} assigned to the MLCT(phen) state.

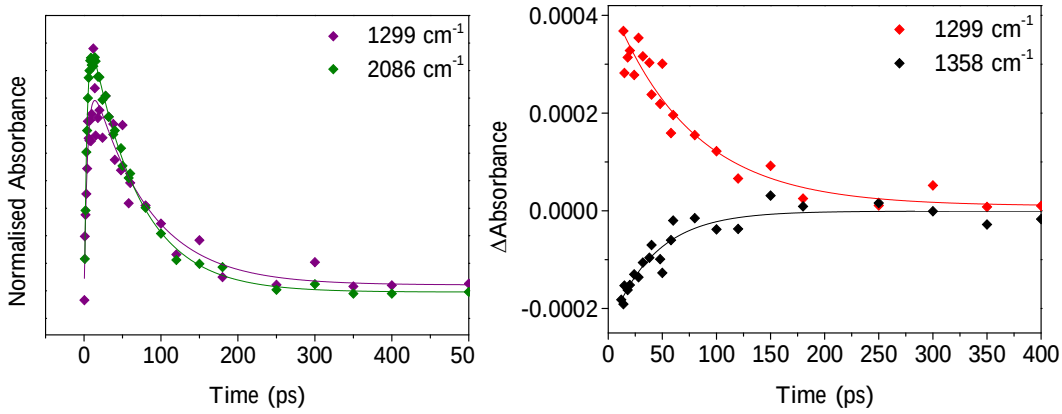

Figure 3-20: The kinetics of the complex Re(dppp2) in d-DMSO where the band at 2086cm^{-1}, assigned to an MLCT(phz) state, is in good agreement with the decay of the band at 1299 cm^{-1} also assigned to an MLCT(phz) state (left). The decay of the band at 1299 cm^{-1} assigned to an MLCT(phz) state, is in good agreement with the growth of the band at 1358 cm^{-1} assigned to the parent (right).

The TRIR spectra in the fingerprint region for Re(dppp3) also exhibits transient bands (1249 and 1305 cm^{-1}) that are at similar positions to the bands observed in the FP TRIR spectra of Re(dppp2) (Figure 3-21). These bands are observed to decay with similar kinetics to the CO region bands assigned to the MLCT(phz), supporting their assignment as MLCT(phz) in nature. As observed for Re(dppp2) and Re(dppp3), transient bands are observed in the 1250-1340 cm^{-1} region for Re(dppp2Br) at 1256 and 1305 cm^{-1} and these are tentatively assigned to an MLCT(phz) state (Figure 3-22).

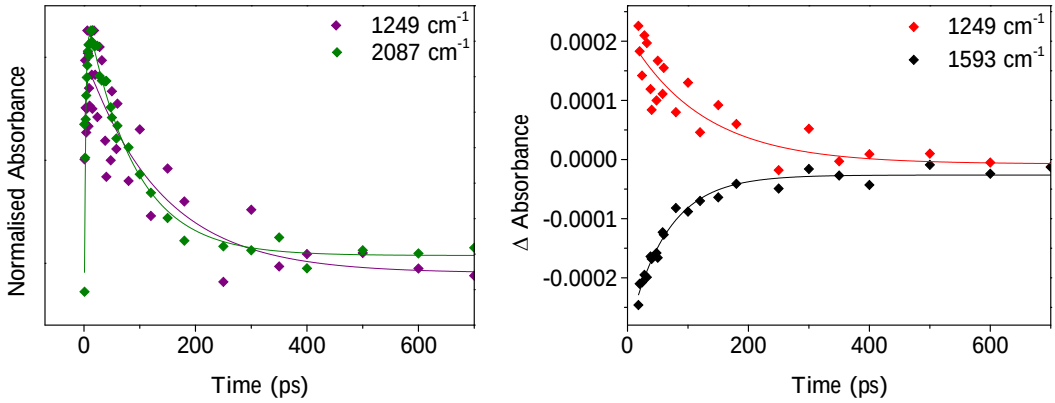

Figure 3-21: The kinetics of the complex Re(dppp3) in d-DMSO where the band at 2087 cm^{-1}, assigned to an MLCT(phz) state, exhibits kinetics which are in good agreement with the band at 1249 cm^{-1} also assigned to an MLCT(phz) state (left). The decay of the band at 1249 cm^{-1} assigned to an MLCT(phz) state, is in good agreement with the growth of the band at 1593 cm^{-1} assigned to the parent (right).

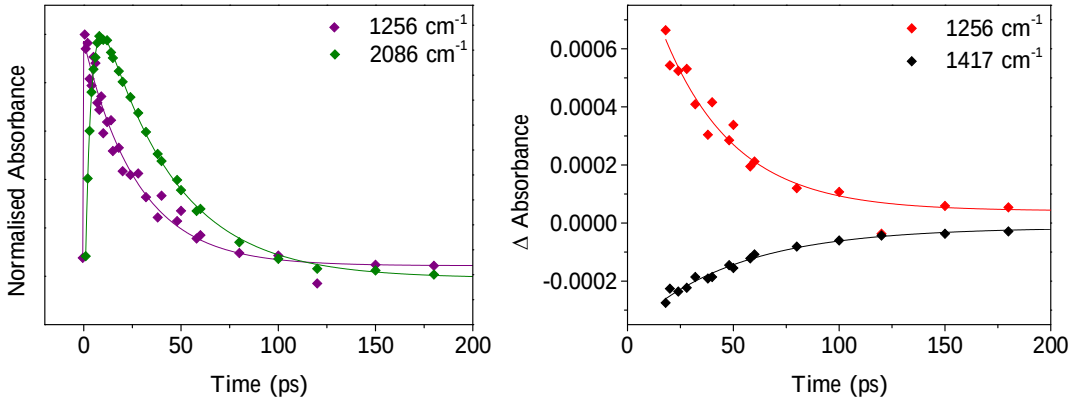

Figure 3-22: The kinetics of the complex Re(dppp2Br) in d-DMSO where the band at 2086cm^{-1} assigned to an MLCT(phz) state, is in good agreement with the band at 1256 cm^{-1} also assigned to an MLCT(phz) state (left). The decay of the band at 1256 cm^{-1} assigned to an MLCT(phz) state, is in good agreement with the growth of the band at 1417 cm^{-1} assigned to the parent (right).

The presence of excited states MLCT(phz) and IL$\pi\pi^*$ in equilibrium for Re(dppp2Br) is further confirmed by global analysis (Figure 3-23). A short ps excited state is observed with a band at 2063 cm^{-1} which is consistent with the assignment of an MLCT(phen) state. A longer ps excited state is observed to have bands at 2086, 1966, 1299 and 1256 cm^{-1}, which are consistent with an MLCT(phz) state and bands at 2004 and 1877 cm^{-1} which are consistent with an IL$\pi\pi^*$ state.

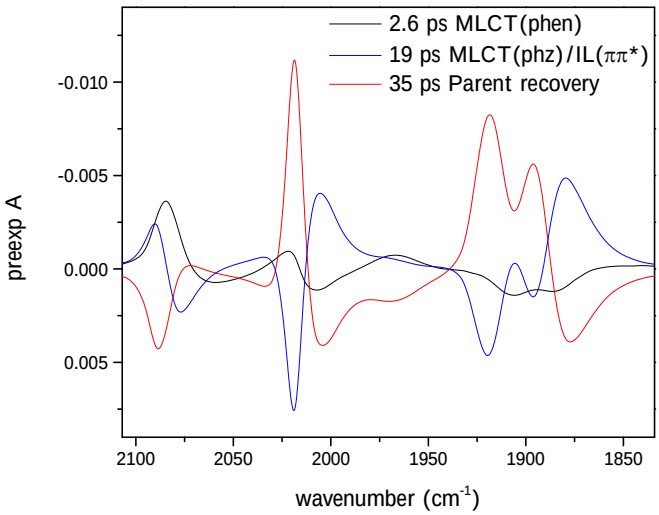

Figure 3-23: The global analysis of Re(dppp2Br) in the CO IR region, calculated from TRIR spectra obtained in d-DMSO following 400 nm photoexcitation. Three states are elucidated.

Jabłoński diagrams summing up the excited states observed for the complexes in d-DMSO identified from the TRIR spectra, are shown in Figure 3-24. A ILππ* state, is expected to exhibit a longer lifetime than that observed for Re(dppp3) and Re(dppp2Br), and this would indicate that the excited state population is limited by the decay of a shorter lived excited state, where this shorter lived excited state is likely to be the MLCT(phz) state.

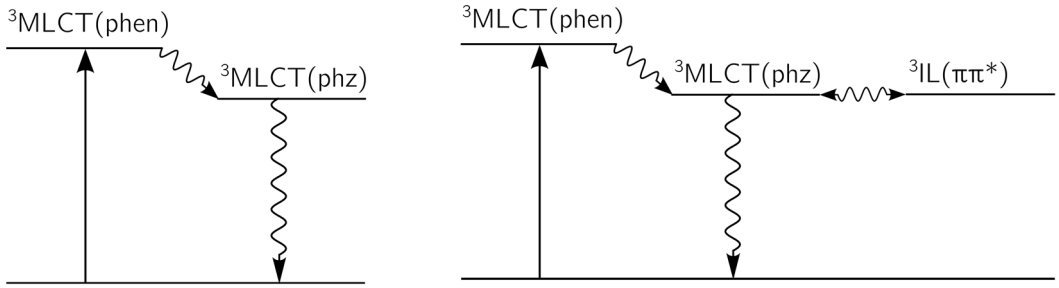

Figure 3-24: A Jabłoński diagram summing up the excited states observed in d-DMSO following 400 nm photoexcitation for Re(dppp2) and Re(dppp3) (left), and for Re(dppp2Br) (right).

TRIR Spectroscopy in CH_3CN, CH_2Cl_2 and THF

The TRIR spectra of the three complexes Re(dppp2), Re(dppp3) and Re(dppp2Br) in CH_3CN, CH_2Cl_2 and THF following 400 nm photoexcitation at several time delays are summarised in Table 3-3, 3-4 and 3-5 respectively. The complexes in these solvents exhibit a similar spectral profile to that observed in d-DMSO and each other, thus they are only briefly summarised here with the spectra and kinetic traces for the processes observed shown in Appendix A.

At 1 ps following photoexcitation, the complexes all exhibit parent bleaching and the formation of several transient bands. An MLCT(phen) state is observed to decay to an MLCT(phz) state, where both states are present at 1ps. The identification of bands assigned to an MLCT(phen) and an MLCT(phz) states have been confirmed with band fitting for each complex (Appendix A). This MLCT(phz) state is observed to decay to the ground state in good agreement with parent recovery, except for Re(dppp2Br) in CH_3CN where the MLCT(phz) state is observed to decay to an equilibrium with an $IL\pi\pi^*$ state. This equilibrium is then observed to decay to the ground state, which is in good agreement with the recovery of the parent.

Table 3-3: A summary of the TRIR spectral features and kinetics observed for Re(dppp2), Re(dppp3) and Re(dppp2Br) in CH_3CN following 400 nm photoexcitation.

Solvent	ν (cm^{-1})	τ decay (ps)	τ growth (ps)	Assignment
Re(dppp2)	2071	1.4 ± 0.3		MLCT(phen)
	2089, 2003, 1972	70 ± 20	4.7 ± 0.8	MLCT(phz)
	2022, 1921, 1903	-	119 ± 3	parent
	2025, 1924, 1902	-	-	GS FTIR[a]
Re(dppp3)	2071	4 ± 1	-	MLCT(phen)
	2089, 2004, 1973	70 ± 20	7 ± 2	MLCT(phz)
	2022, 1922, 1903	-	80 ± 10	parent
	2025, 1924, 1901	-	-	GS FTIR[a]
Re(dppp2Br)	2070	6 ± 0.9		MLCT(phen)
	2088, 2008, 1971	50 ± 10	7 ± 0.1	MLCT(phz)
	1884	70 ± 10	6.2 ± 0.9	$IL\pi\pi^*$
	2022, 1922, 1901	-	50 ± 10	parent
	2025, 1924, 1902	-	-	GS FTIR[a]

[a]GS FTIR taken from solution FTIR in CH_2Cl_2 due to solubility.

Table 3-4: A summary of the TRIR spectral feature and kinetics observed for Re(dppp2), Re(dppp3) and Re(dppp2Br) in CH_2Cl_2 following 400 nm photoexcitation.

Solvent	ν (cm^{-1})	τ decay (ps)	τ growth (ps)	Assignment
Re(dppp2)	2060	11 ± 3	-	MLCT(phen)
	2081, 2008, 1968, 1295	650 ± 30	8.5 ± 0.6	MLCT(phz)
	2021, 1925, 1903	-	710 ± 10	parent
	2025, 1925, 1902	-	-	GS FTIR
Re(dppp3)	2061	10 ± 2	-	MLCT(phen)
	2081, 2006, 1970, 1301	400 ± 100	6.9 ± 0.5	MLCT(phz)
	2023, 1925, 1903	-	460 ± 8	parent
	2026, 1926, 1901	-	-	GS FTIR
Re(dppp2Br)	2072	7 ± 0.4		MLCT(phen)
	2081, 2008, 1971, 1299	300 ± 40	3.1 ± 0.2	MLCT(phz)
	2022, 1926, 1901	-	330 ± 10	parent
	2026, 1925, 1901	-	-	GS FTIR

Table 3-5: A summary of the TRIR band positions and kinetics of Re(dppp2), Re(dppp3) and Re(dppp2Br) in THF following 400 nm photoexcitation.

Solvent	ν (cm^{-1})	τ decay (ps)	τ growth (ps)	Assignment
Re(dppp2)	2060	5.2 ± 0.7	-	MLCT(phen)
	2081, 2000, 1964	600 ± 20	6.4 ± 0.2	MLCT(phz)
	2020, 1921, 1897	-	590 ± 10	parent
	2025, 1925, 1902			GS FTIR[a]
Re(dppp3)	2064	5.2 ± 0.7	-	MLCT(phen)
	2081, 2001, 1966	330 ± 40	7.2 ± 0.4	MLCT(phz)
	2020, 1922, 1897	-	425 ± 4	parent
	2026, 1926, 1901			GS FTIR[a]
Re(dppp2Br)	2064	7.4 ± 0.4		MLCT(phen)
	2083, 2002, 1966	143 ± 8	3.1 ± 0.1	MLCT(phz)
	2020, 1922, 1897	-	117 ± 6	parent
	2026, 1925, 1901			GS FTIR[a]

[a]GS FTIR taken from solution FTIR in CH_2Cl_2 due to solubility.

TRIR Spectroscopy in Toluene

The TRIR spectra of Re(dppp2), Re(dppp3) and Re(dppp2Br) have been collected in toluene following 400 nm photoexcitation and are shown in Figures 3-25 and 3-26, with band positions and kinetics summarised in Table 3-6. Due to poor solubility the FTIR is given in d-DMSO, with ATR-FTIR for the complexes shown in Appendix A. At 1 ps following photoexcitation for Re(dppp2) and Re(dppp3) transient bands assigned to an MLCT(phen) state are observed to form while simultaneously, the parent bands are observed to bleach. Subsequently, bands assigned to the MLCT(phen) state are observed to decay in good agreement with the recovery of the parent bands.

For Re(dppp2Br) at 1ps following photoexcitation, transient bands at 2071, 2052, 1999, 1962, 1295 and 1247 cm^{-1} are observed and bands assigned to the parent are observed to bleach. At 1-10 ps the higher energy transient band at 2071 cm^{-1} is assigned to an MLCT(phz) state and intensifies while the band at 2052 cm^{-1} assigned to an MLCT(phen) state decays, while simultaneously in the FP region the MLCT(phz) marker bands at 1295 and 1247 cm^{-1} intensify, consistent with MLCT(phen)/MLCT(phz) interconversion of states. The MLCT(phz) state is then observed to decay to the ground state.

Table 3-6: A summary of the TRIR spectral features and kinetics of Re(dppp2), Re(dppp3) and Re(dppp2Br) in toluene following 400 nm photoexcitation.

Solvent	ν (cm^{-1})	τ decay (ns)	τ growth (ns)	Assignment
Re(dppp2)	2059, 1993, 1955	18 ± 2		MLCT(phen)
	2020, 1927, 1897		15.1 ± 0.3	parent
	2025, 1925, 1902			GS FTIR
Re(dppp3)	2064, 1991, 1957	9 ± 1	0.007 ± 0.001	MLCT(phen)
	2020, 1926, 1895	-	0.02 ± 0.01	parent
			9.4 ± 0.2	
	2026, 1925, 1901			GS FTIR
Re(dppp2Br)	2052	0.0068 ± 0.0006		MLCT(phen)
	2071, 1999, 1962, 1247, 1295	5.3 ± 0.3	0.0046 ± 0.0002	MLCT(phz)
	2020, 1926, 1897	-	5.1 ± 0.3	parent
	2026, 1925, 1901			GS FTIR

[a]GS FTIR taken from solution FTIR in CH_2Cl_2 due to solubility.

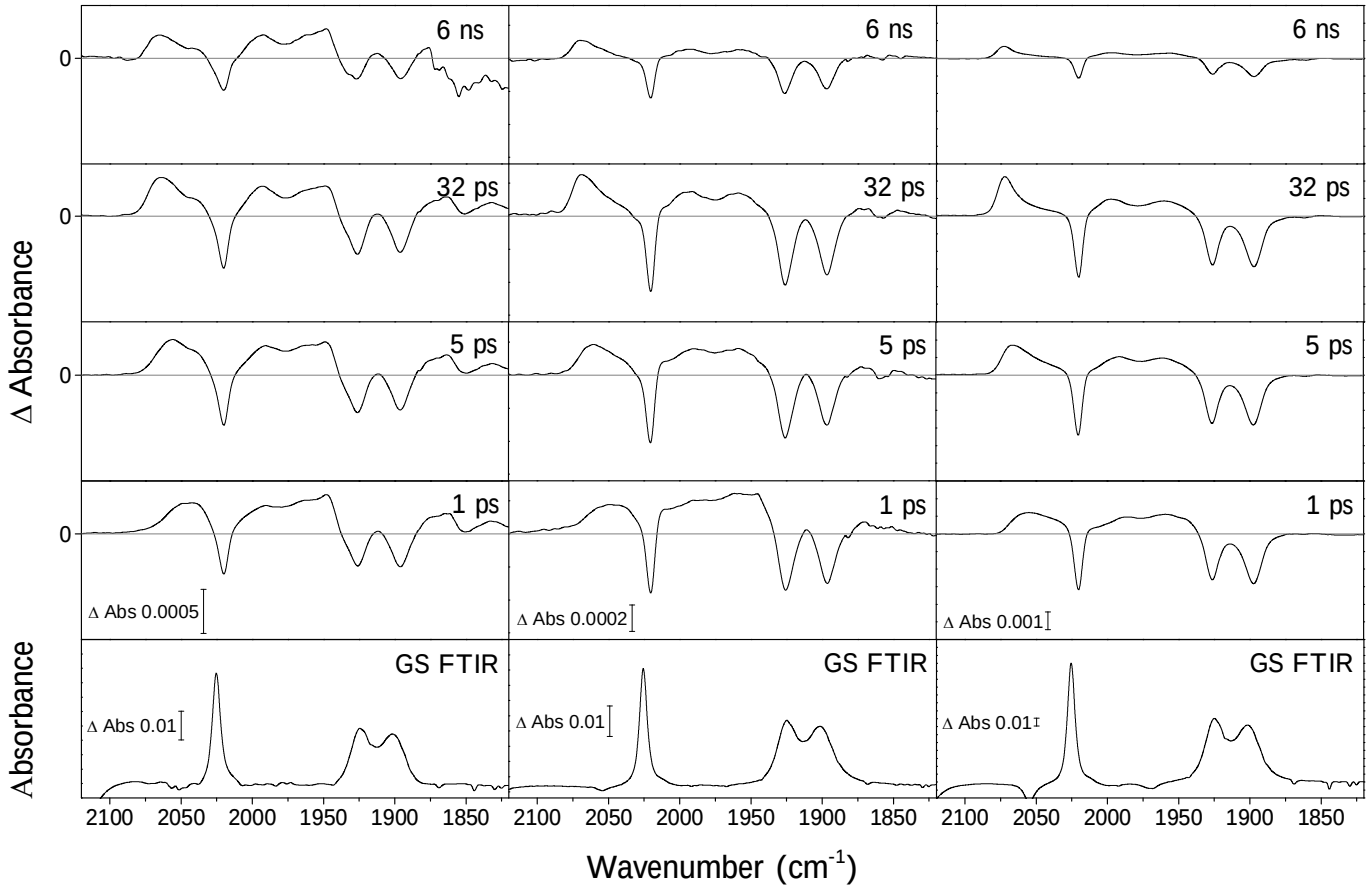

Figure 3-25: The FTIR (a) and TRIR (b-e) spectra in the CO IR region in toluene following 400 nm photoexcitation for Re(dppp2) (left), Re(dppp3) (middle) and Re(dpp2Br) (right). The FTIR shown was acquired in CH_2Cl_2 due to poor solubility.

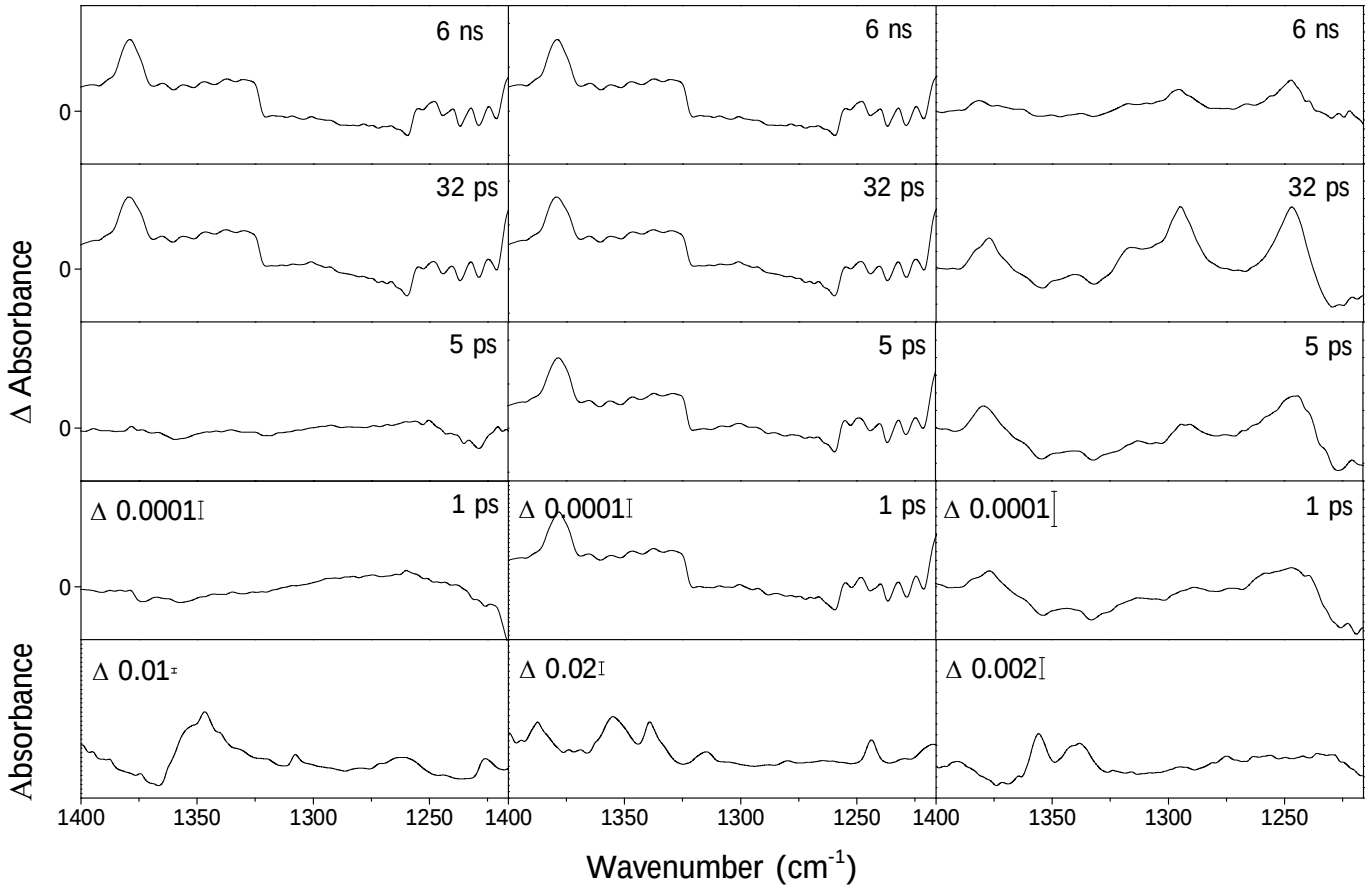

Figure 3-26: The FTIR (a) and TRIR (b-e) spectra in the FP IR region in toluene following 400 nm photoexcitation for Re(dppp2) (left), Re(dppp3) (middle) and Re(dpp2Br) (right). The FTIR shown was acquired in the solid state for Re(dppp2) and Re(dppp3) and in d-DMSO for Re(dppp2Br) due to poor solubility.

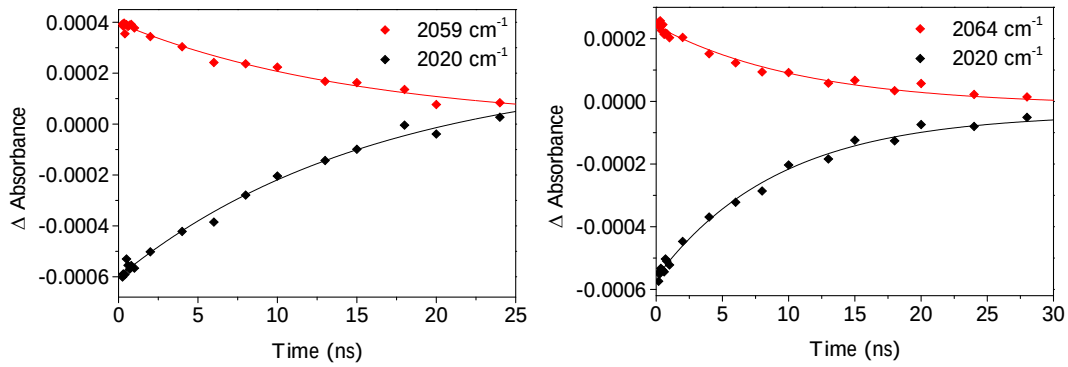

Figure 3-27: The kinetics of Re(dppp2) (left) and Re(dppp3) (right) in toluene following photoexcitation at 400 nm. The decay of the band at *ca.* 2060 cm^{-1} assigned to an MLCT(phen) state, is in good agreement with the growth of the band at 2020 cm^{-1} assigned to the parent.

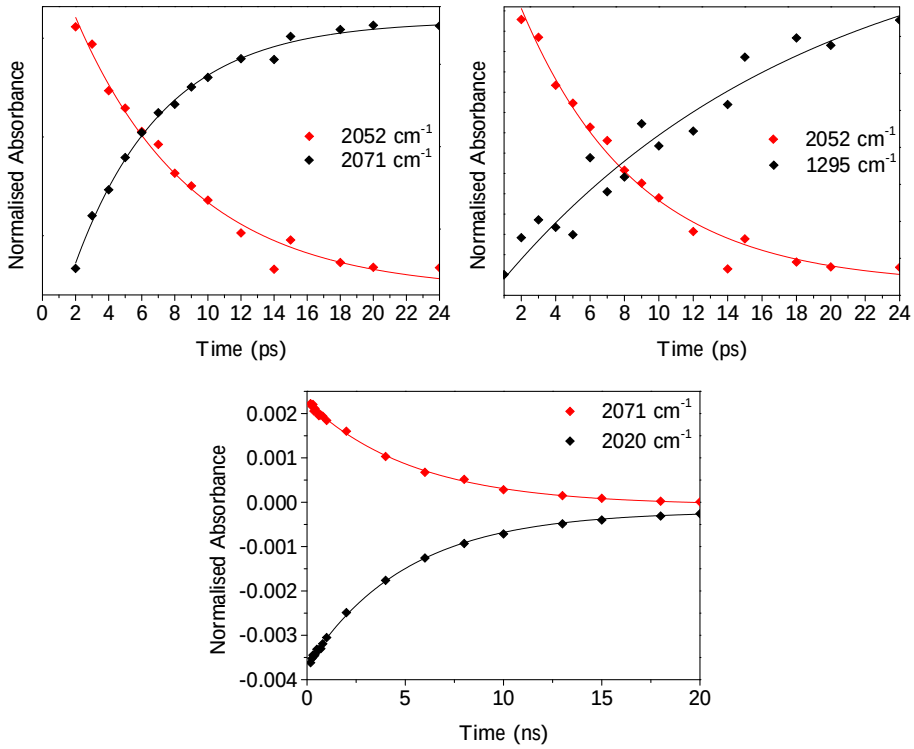

Figure 3-28: The kinetics of Re(dppp2Br) in toluene following photoexcitation at 400 nm. The decay of the band at 2052 cm^{-1} assigned to an MLCT(phen) state, is in good agreement with the growth of the band at 2071 cm^{-1} assigned to an MLCT(phz) state (top, left). The decay of band assigned to the MLCT(phen) state at 2052 cm^{-1} is in good agreement with the growth of the FP marker band for the MLCT(phz) state at 1295 cm^{-1} (top, right). The decay of the band at 2071 cm^{-1} assigned to the MLCT(phz) state is in good agreement with the growth of the band at 2020 cm^{-1} assigned to the parent (bottom).

3.2 Absorption Spectra

The absorption spectra of Re(dppp2), Re(dppp3) and Re(dppp2Br) have been collected in a range of solvents and are shown in Figure 3-29. The absorption spectra of all three complexes are dominated by bands in the 300-350 nm region, indicative of IL transitions centred on the dppz ligand.

There are two structured bands observed at *ca.* 357 and 375 nm, which is most clearly seen for Re(dppp2Br), where the higher energy band is indicative of an IL$\pi\pi^*$ transition located on the dppz, seen previously for Re(dppz) based complexes.[28] The lower energy of the two bands has been observed previously for similar M(diimine) complexes including [Re(dppz)$(CO)_3$Cl] and [Re(phen)$(CO)_3$Cl] and is representative of the MLCT(phen) transition.[53, 86]

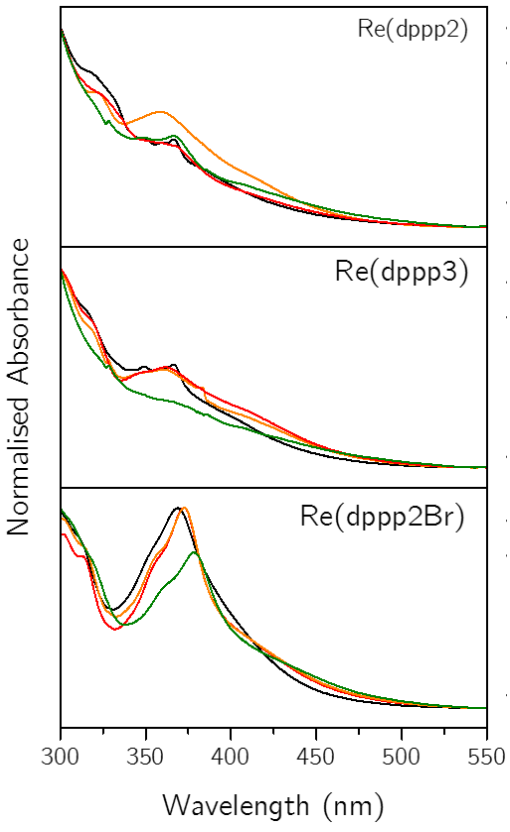

	λ_{abs} (nm)
Re(dppp2)	
CH_3CN	318, 349, 367
CH_2Cl_2	324, 358
THF	322, 360
Toluene	317, 349, 368
Re(dppp3)	
CH_3CN	315[a], 349, 360, 366
CH_2Cl_2	317[a], 348, 361
THF	317[a], 347, 361
Toluene	346, 364
Re(dppp2Br)	
CH_3CN	310[a], 353[a], 369
CH_2Cl_2	313[a], 358[a], 373
THF	313[a], 357[a], 373
Toluene	316[a], 363[a], 378

[a]shown spectrally as a shoulder

Figure 3-29: The absorption spectra (left) in CH_3CN (black), CH_2Cl_2 (red), THF (orange) and toluene (green). The band positions detailed (right) for Re(dppp2) (top) and Re(dppp3) (middle) Re(dppp2Br) (bottom).

3.3 Molecular Orbital Calculations

DFT calculations have been used to obtain the frontier molecular orbitals of Re(dppp2), Re(dppp3) and Re(dppp2Br). The partial energy diagram for each complex is shown in Figure 3-30 alongside representative calculated MOs, all MO orbitals for the energies shown are in Appendix B.

All three complexes exhibit similar molecular orbitals, where the HOMO to HOMO-2 are predominantly Re(dπ) in nature. Two closely lying ligand based, dppz(π) occupied orbitals are calculated, *ca.* 1.2 eV lower than the HOMO. The calculated energies of the occupied MOs are reasonably similar to those calculated for [Re(dppz)$(CO)_3$Cl].

The three complexes also exhibit similar unoccupied orbitals, where the LUMOs are predominantly phz(π*) based, with higher energy unoccupied orbitals that are best described as phen(π*) and dppz(π*), similar to [Re(dppz)$(CO)_3$Cl]. The phz moiety is at considerably lower energies compared to the other unoccupied orbitals, especially when compared to [Re(dppz)$(CO)_3$Cl], whereby the phen/phz energy gap is *ca.* 1.5 eV larger for the Re(dppp) complexes compared to [Re(dppz)$(CO)_3$Cl], consistent with previous literature for Ru(dppp) and Ru(dppz).[31] For Re(dppp) complexes the phen(π*) orbital and the dppz(π*) orbital are at similar and slightly lower energies compared to [Re(dppz)$(CO)_3$Cl]. This reflects the addition of nitrogen atom in the phz moiety for the Re(dppp) complexes. Furthermore, this results in a smaller HOMO/LUMO gap compared to [Re(dppz)$(CO)_3$Cl] by *ca.* 0.2 eV.

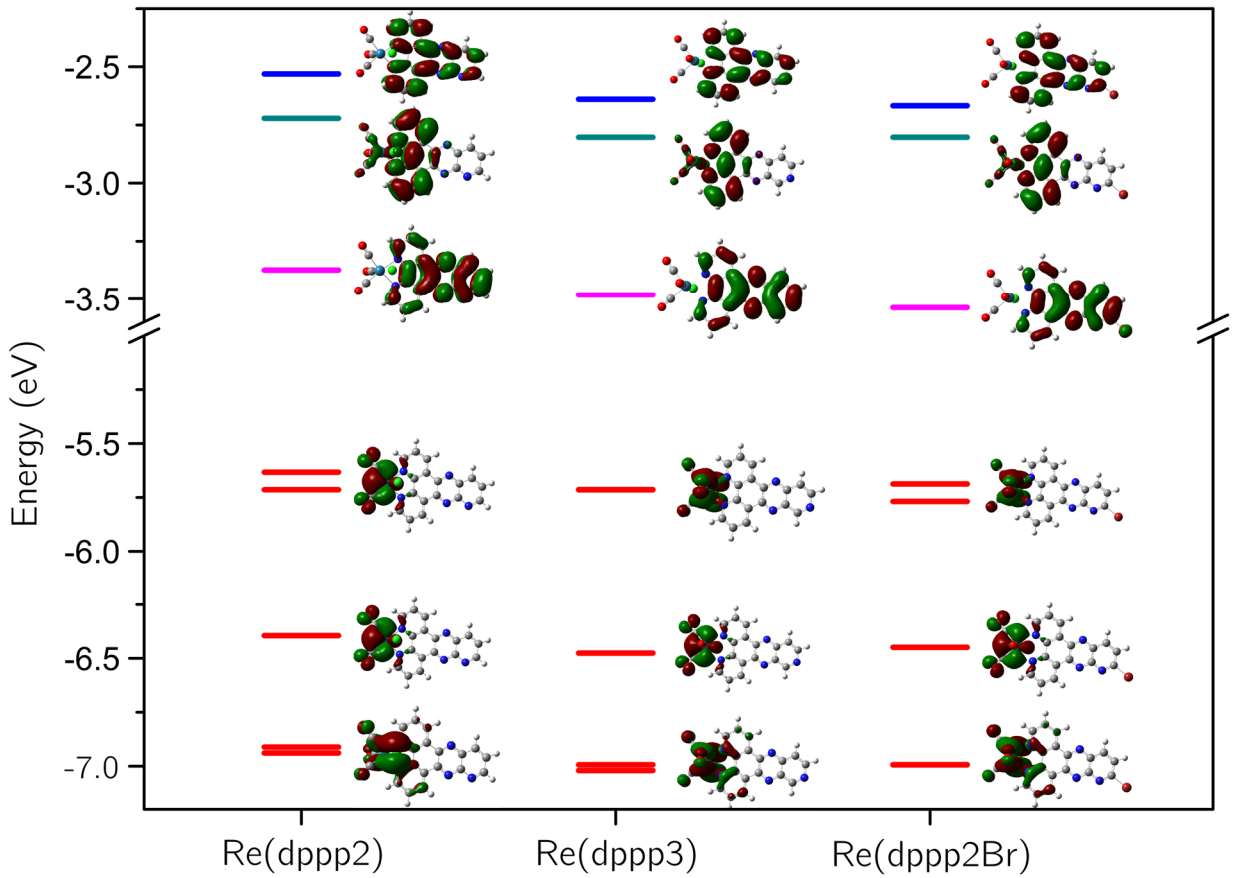

Figure 3-30: The partial energy diagram and representative frontier molecular orbitals for Re(dppp2), Re(dppp3) and Re(dppp2Br) from DFT calculations. Metal based occupied MOs are shown in red. The unoccupied phen, phz and dppz MOs are shown in pink, turquoise and blue respectively.

3.4 The Nature of the Excited States Observed

The complexes Re(dppp2), Re(dppp3) and Re(dppp2Br) contain an extra nitrogen heteroatom in the phenazine moiety compared to [Re(dppz)$(CO)_3$Cl]. The lone pair of electrons on the additional nitrogen is not delocalised across the aromatic dppp ligand π-system and as a result has an electron withdrawing effect. Therefore, the heteroatom increases the electron density on the phz moiety. This electron withdrawing behaviour of the pyridine nitrogen is expected to increase the MLCT(phen)/MLCT(phz) states energy gap.

As shown by previous work, the MLCT(phz) state is lower in energy than the MLCT(phen) state for M(dppz) complexes,[30] although the MLCT(phz) state is not populated directly following UV/Vis photoexcitation due to the poor overlap between the phz(π*) and the Re(dπ) orbitals.[25] Therefore it is assumed that the MLCT(phen) state is instead initially populated, as observed experimentally and shown in literature for [Re(dppz)$(CO)_3$Cl].[24] Subsequently this MLCT(phen) state is observed to undergo interconversion to the MLCT(phz) state. The rate of the interconversion of the MLCT(phen) to MLCT(phz) states is dependent on the driving force of this process, ΔG, shown in Equation 3-1. It has been widely shown that solvents with higher dielectric solvents stabilise charge transfer states more relative to solvents with lower dielectric constants. The MLCT(phz) state exhibits a larger charge separation distance than the MLCT(phen) state, due to the larger distance between the Re(dπ) and phz(π*) than the distance between the Re(dπ) and the phen(π*) orbitals. As a result it is expected the MLCT(phz) state will be stabilised more than the MLCT(phen) state by higher dielectric solvents, assuming the difference in entropy contribution (ΔS) is negligible between the solvents. Therefore, a larger difference in energy between the MLCT(phen) and MLCT(phz) states is likely to occur as solvent polarity increases. This larger distance in energy between the two states results in a larger enthalpy difference and as such more effective population of the MLCT(phz) state would be likely to occur. A larger enthalpy difference results in a faster rate of interconversion of states from MCLT(phen) to MLCT(phz).

$$\Delta G = \Delta H - T\Delta S \qquad \text{Equation 3-1}$$

Previous work has shown that [Re(dppz)(CO)$_3$Cl] demonstrates a clear trend in the rate of interconversion of MLCT(phen)/MLCT(phz) states, where the rate is observed to increase with increasing dielectric constant, from 10 ps in CH_3CN (ε_r = 37.5) to no interconversion observed in CH_2Cl_2 (ε_r = 8.9).[32] This dependence of the rate of MLCT(phz)/MLCT(phen) interconversion of states on solvent polarity is also observed for other Re(dppz) derivatives such as [Re(dppz-F_2)(CO)$_3$Cl] and [Re(dppz-Cl_2)(CO)$_3$Cl].[32] Furthermore, studies of the complex, [Ru(bpy)$_2$(dppp2)]$^{2+}$ have shown the MLCT(phen)/MLCT(phz) state interconversion to decrease from 67 to 6.7 ps in CH_2Cl_2 and CH_3CH_2OH respectively.[139]

However, for the three complexes studied within this Chapter, Re(dppp2), Re(dppp3) and Re(dppp2Br), the dependence of the rate of MLCT(phen)/MLCT(phz) states interconversion on solvent polarity is not as a distinct and as such a discernible trend is not apparent, except at the more extreme ends of solvent polarities studied, with rates detailed in Table 3-7. For Re(dppp2) and Re(dppp3) MLCT(phen)/MLCT(phz) interconversion is not observed for toluene (ε_r = 2.3)[151] as expected with decreasing solvent polarity. However, for Re(dppp2Br) with an extra electron withdrawing group substituted onto the phz moiety, the population of an MLCT(phz) state is observed indicating conversion between the phen and phz states. This suggest that the bromine electron withdrawing group lowers the phz(π^*) LUMO more than for Re(dppp2) and Re(dppp3), and that when the phz moiety is substituted with a nitrogen atom and a Br substituent it is more electron withdrawing than when substituted with only a nitrogen atom.

Table 3-7: The rate of interconversion of states from MLCT(phen) to MLCT(phz), measured in a range of solvents following 400 nm photoexcitation. The kinetic values are taken from TRIR measurements. The values for the dielectric constants are taken from references [149, 151, 152]. Rate of interconversion is taken from decay of phen state.

Solvent	ε_r	τ MLCT(phen)→MLCT(phz) (ps)		
		dppp2	dppp3	dppp2Br
d-DMSO	46.7	7 ± 1	2 ± 1	6 ± 1
CH_3CN	37.5	1.4 ± 0.3	4 ± 1	6.0 ± 0.9
CH_2Cl_2	8.9	11 ± 3	10 ± 2	7 ± 4
THF	7.5	5.2 ± 0.7	5 ± 0.7	7.4 ± 0.4
Toluene	2.3	N/A	N/A	6.8 ± 0.6

As expected the presence of the electron withdrawing group lowers the energy of the phz(π^*) orbital, which is most evident on comparison with [Re(dppz)$(CO)_3$Cl]. Firstly, an MLCT(phz) state is observed more commonly for the dppp complexes than for [Re(dppz)$(CO)_3$Cl], where Re(dppp2), Re(dppp3) and Re(dppp2Br) all possess an MLCT(phz) state as the lowest energy state in CH_2Cl_2, while [Re(dppz)$(CO)_3$Cl] exhibits an equilibrium of IL$\pi\pi^*$/MLCT(phen) states.[32] In CH_3CN the lowest energy excited state observed is MLCT(phz) for Re(dppp2) and Re(dppp3), and IL$\pi\pi^*$/MLCT(phz) states for Re(dppp2Br), in comparison to the IL$\pi\pi^*$/MLCT(phen) states observed for [Re(dppz)$(CO)_3$Cl].[32] This indicates that the phen/phz energy gap is larger for Re(dppp) complexes than for [Re(dppz)$(CO)_3$Cl], which is supported by DFT calculations of the MO orbitals where the phen/phz energy gap is shown to be 0.52 eV for [Re(dppz)$(CO)_3$Cl] increasing to 0.65, 0.68 and 0.73 eV for Re(dppp2), Re(dppp3) and Re(dppp2Br) respectively. This is consistent with previous results whereby the phen/phz energy gap was observed to be larger for $[Ru(bpy)_2(dppp2)]^{2+}$ than for $[Ru(bpy)_2(dppz)]^{2+}$ complex.[31]

Further differences in the complexes may be observed from the TRIR spectra, where the greatest MLCT(phen) contribution is observed for Re(dppp2) and the least for Re(dppp2Br), supporting the above conclusion that the Br has the largest electron withdrawing effect, favouring an MLCT(phz) state. Furthermore, Re(dppp2) appears to show more MLCT(phen) character than observed for Re(dppp3). This would indicate that the meta position nitrogen, Re(dppp3), has more of an electron withdrawing effect than the ortho position nitrogen, Re(dppp2). This is further supported by the MO calculations where the phen/phz energy gap is observed to follow the order Re(dppp2Br) > Re(dppp3) > Re(dppp2).

All three complexes exhibit a decrease in the MLCT(phz) lifetime with increasing dielectric constant of the solvent, owing to the further stabilisation of MLCT(phz) state, with lifetimes detailed in Table 3-8. The shortest excited state lifetime is consistently observed for Re(dppp2Br) and the longest for Re(dppp2) reconfirming the conclusion that Re(dppp2Br) has the lowest energy phz(π^*) orbital compared to Re(dppp2) and Re(dppp3). From the calculated MOs, the LUMOs for all complexes are phz(π^*) in

nature and the HOMOs are Re(dπ) based. The above lifetimes are reflected in the HOMO/LUMO energy gap which is observed to decrease from 2.26 to 2.23 to 2.15 eV for Re(dppp2), Re(dppp3) and Re(dppp2Br) respectively, compared to the larger HOMO/LUMO gap of 2.42 eV for [Re(dppz)$(CO)_3$Cl], shown in Chapter 2. This is consistent with the presence of the substituted nitrogen atom, which lowers the phz energy. Furthermore, the lifetimes for Re(dppp2), Re(dppp3) and Re(dppp2Br) are nearly two orders of magnitude smaller compared to [Re(dppz)$(CO)_3$Cl] in CH_2Cl_2 and CH_3CN,[92] further consistent with the less phen character and significantly more phz character observed upon substitution of a nitrogen into the phz moiety.

However, for all three complexes the lifetime of the MLCT(phz) state is longer in CH_2Cl_2 than in THF despite CH_2Cl_2 possessing a higher ε_r. Further inspection of the TRIR spectrum reveals that the $\Delta\nu$(CO) from the parent band to the MLCT(phz) band is larger in THF than in CH_2Cl_2. This larger shift is indicative of the distance from Re(dπ) to phz(π*) and thus indicating the degree of separation in the resultant MLCT(phz) state. Therefore THF appears to be a better solvent at stabilising the MLCT(phz) state, which may be due to the interaction of the oxygen present in the cyclic ether structure of THF with the phz moiety.

In addition, the more frequent observation of the population of the ILππ* state in the TRIR for Re(dppp2Br) compared to the other complexes, indicates more electron density is on the dppz ligand than for the other two complexes. Re(dppp3) exhibits a decrease in lifetime compared to Re(dppp2) although to a lesser extent, confirming that the meta position of the additional nitrogen is more electron withdrawing than the ortho position.

Table 3-8: The nature and lifetimes of the most stable excited states of Re(dppp2), Re(dppp3) and Re(dppp2Br), in solvents with a range of dielectric constants following 400 nm photoexcitation. The kinetics are taken from TRIR measurements. MLCT(phz) and MLCT(phen) states are abbreviated to phz and phen respectively and IL$\pi\pi^*$ state is abbreviated to $\pi\pi^*$. The values for dielectric constant are taken from references [149, 151, 152].

ε_r	Re(dppp2)		Re(dppp3)		Re(dppp2Br)	
	Ex. State	τ (ps)	Ex. State	τ (ps)	Ex. State	τ (ps)
46.7	phz	65 ± 4	phz/IL$\pi\pi^*$	75 ± 9	phz/$\pi\pi^*$	37 ± 4
37.5	phz	70 ± 20	phz	70 ± 20	phz/$\pi\pi^*$	70 ± 10
8.9	phz	650 ± 30	phz	400 ± 100	phz	300 ± 40
7.5	phz	600 ± 20	phz	330 ± 40	phz	143 ± 8
2.3	phen	18000 ± 200	phen	9000 ± 100	phz	5300 ± 300

3.5 An Investigation into Photophysical Properties of [Re(dppz-I)(CO)$_3$Cl]

The results shown above have indicated that the electron withdrawing effect of the bromine substitutent is significant on the photophysical properties observed. The effect of halogen substitution onto the phz portion of the dppz ligand on the photophysical properties observed for the complex [Re(dppz)(CO)$_3$Cl] has been previously investigated in literature and a summary is shown below in Table 3-9. The lifetime of the excited state is observed to decrease with decreasing electronegativity of the substituent, indicating a decreased electron withdrawing effect. Furthermore, the more electron withdrawing the substituent the larger the MLCT(phen)/MLCT(phz) energy gap where, for [Re(dppz-X$_2$)(CO)$_3$Cl] an MLCT(phz) state is observed for X = F and an equilibrium of MLCT(phen)/MLCT(phz) states for X = Br.[32, 34] Furthermore, the difference in lifetime between the mono and disubstituted dppz complexes appears to be negligible.[32, 34]

Table 3-9: The nature of the excited state and lifetime for [Re(dppz-X)(CO)$_3$Cl] and [Re(dppz-X$_2$)(CO)$_3$Cl] complexes, in CH_2Cl_2. Two states listed next to each other denotes an equilibrium of states.

Complex	State	τ (ns)	Ref
[Re(dppz)(CO)$_3$Cl]	IL ππ*/MLCT(phen)	40 ± 10	32
[Re(dppz-F$_2$)(CO)$_3$Cl]	MLCT(phen)	0.006[a]	32
	MLCT(phz)	3.05 ± 0.04	
[Re(dppz-Cl$_2$)(CO)$_3$Cl]	MLCT(phz)	1.5 ± 0.2	32
[Re(dppz-Br$_2$)(CO)$_3$Cl]	MLCT(phen)/MLCT(phz)	1.3	34
[Re(dppz-Br)(CO)$_3$Cl]	MLCT(phen)/MLCT(phz)	1.2	34
[Re(dppz-I)(CO)$_3$Cl]	MLCT(phen)/MLCT(phz)	4.1 ± 0.5	This work

As the effect of an iodine substituent appended onto the phz has not previously been investigated, the previously unreported complex [Re(dppz-I)(CO)$_3$Cl] has been synthesised and the photophysical properties examined. The structure of [Re(dppz-I)(CO)$_3$Cl] is shown in Figure 3-31.

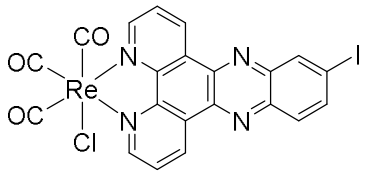

Figure 3-31: The structure of [Re(dppz-I)(CO)$_3$Cl].

3.5.1 Molecular Orbital Calculations

DFT calculations have been used to obtain the frontier molecular orbitals of [Re(dppz-I)$(CO)_3$Cl]. The partial energy diagram is shown in Figure 3-32 alongside representative calculated MOs, all MO orbitals for the energies shown are in Appendix B.

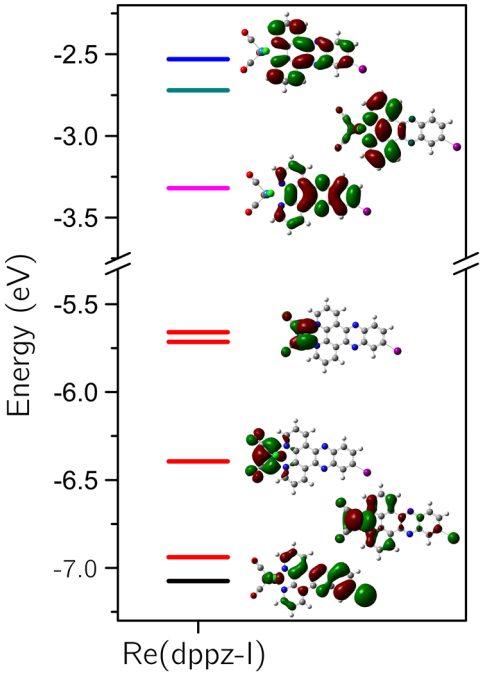

Figure 3-32: DFT calculated frontier molecular orbitals and partial energy diagram for [Re(dppz-I)$(CO)_3$Cl]. Metal based occupied MOs are shown in red and ligand centred occupied MOs in black. The unoccupied phen, phz and dppz MOs are shown in pink, turquoise and blue respectively.

From the DFT molecular orbital calculations the iodine moiety is shown to slightly decrease the phz(π^*) energy in comparison to [Re(dppz)$(CO)_3$Cl], resulting in a larger phen/phz energy gap of 0.60 and 0.52 eV for Re(dppz-I) and [Re(dppz)$(CO)_3$Cl] respectively. Furthermore, this lowering of the phz energy has resulted in a decrease in the HOMO/LUMO energy observed from 2.42 to 2.34 eV for [Re(dppz)$(CO)_3$Cl] and Re(dppz-I) respectively. Therefore, it would be expected that the nature of the excited state observed for Re(dppz-I) would have more phz character than observed for [Re(dppz)$(CO)_3$Cl] and also exhibit a decrease in the excited state lifetime.

3.5.2 TRIR spectroscopy

The TRIR spectra of Re(dppz-I) have been collected in CH_2Cl_2 following 400 nm photoexcitation and are shown in Figure 3-33, with bands and kinetics summarised in Table 3-10. Immediately following photoexcitation at 1ps, the parent bands (2022, 1921 and 1899 cm^{-1}) are observed to bleach and several transient bands (2053, 2001 and 1961 cm^{-1}) are observed assigned to an MLCT(phen) state based on previously reported shifts.[32] Over the first 30 ps, the band at 2053 cm^{-1} is observed to blue shift and sharpen to a final position 2061 cm^{-1}, while simultaneously a band at 2075 cm^{-1} is observed to grow in, and is assigned to an MLCT(phz) state. The confirmation of the presence of two bands at 2061 and 2075 cm^{-1} assigned to an MLCT(phen) and an MLCT(phz) state respectively is confirmed *via* band fitting, shown in Appendix A. The equilibrium of MLCT(phen)/MLCT(phz) states is then observed to decay to the ground state (τ = 4.1 ± 0.5 ns) in good agreement with parent recovery (τ = 4.50 ± 0.08 ns). The kinetics for this process are also shown in Figure 3-33.

Table 3-10: The FTIR and TRIR spectral features and kinetics of Re(dppz-I) in CH_2Cl_2 following 400 nm photoexcitation.

ν (cm^{-1})	τ decay (ns)	τ growth (ns)	Assignment
2061, 2075, 1998, 1962	4.1 ± 0.5	-	MLCT(phen)
	4.1 ± 0.5		MLCT(phz)
2022, 1921, 1899	-	4.50 ± 0.08	parent
2025, 1923, 1900	-	-	GS FTIR

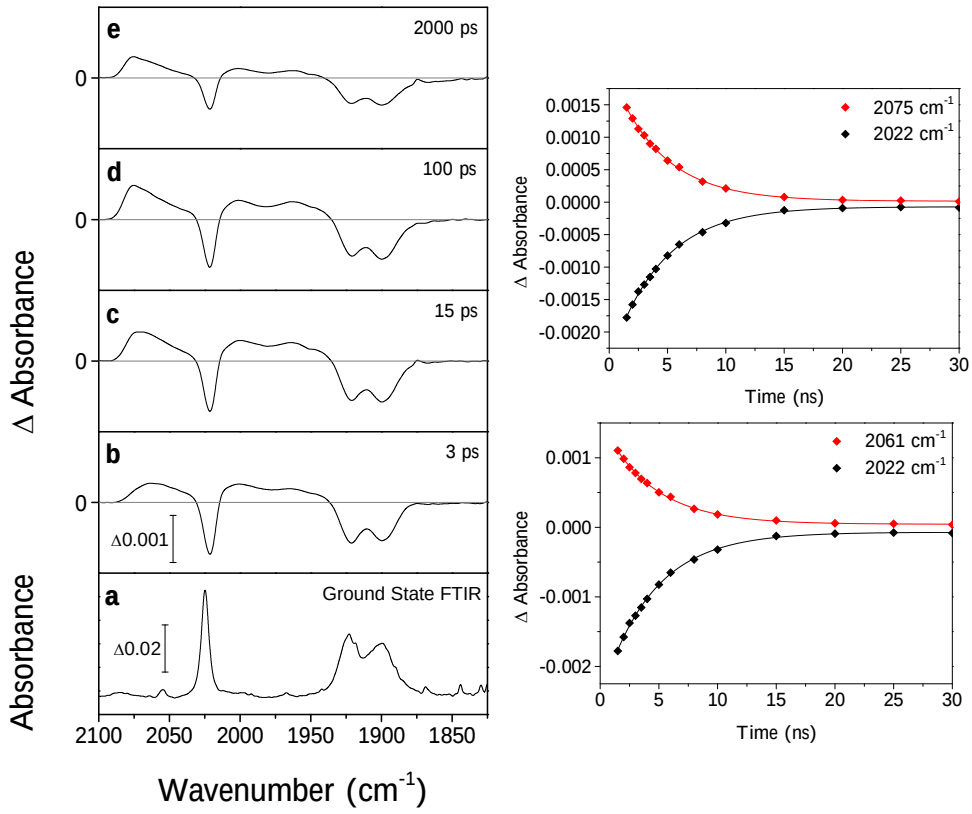

Figure 3-33: The FTIR (a) and TRIR (b-e) spectra (left) for [Re(dppz-I)(CO)$_3$Cl] in CH_2Cl_2 following photoexcitation at 400 nm. The decay of the band at 2075 cm^{-1} assigned to an MLCT(phz) state, is in good agreement with the growth of the band at 2022 cm^{-1} assigned to the parent (top, right). The decay of the band at 2061 cm^{-1} assigned to the MLCT(phen) state is in good agreement with the growth of the band at 2022 cm^{-1} assigned to the parent (bottom, right).

3.5.3 Absorption Spectroscopy

The absorption spectra of [Re(dppz-I)(CO)$_3$Cl] are dominated by ππ* transitions 200-380 nm, shown in Figure 3-34. The band at *ca.* 380 nm appears to be composed of two bands, the higher energy of these is representative of the ILππ* transition of the dppz ligand and the lower energy band assigned to the MLCT(phen) transition.[28, 53, 85, 86] Emission corresponding to an MLCT(phen) band at 678 nm was observed in CH_2Cl_2.

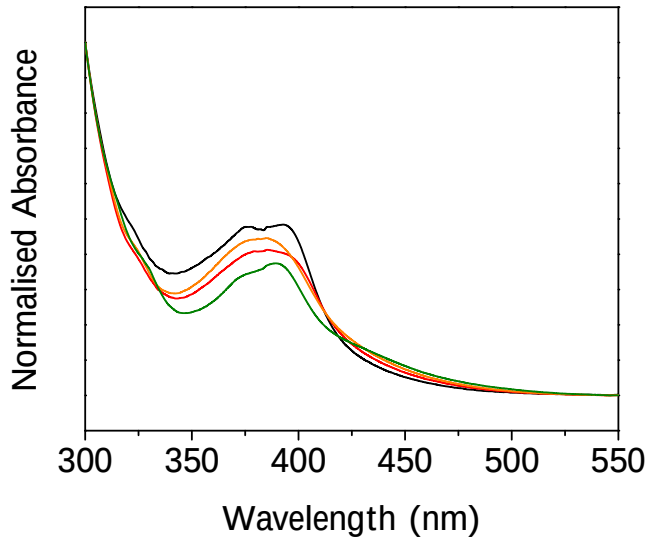

Solvent	ε_r	λ_{abs} (nm)
CH_3CN	37.5	376, 393
CH_2Cl_2	8.9	379, 392
THF	7.8	376, 387
Toluene	2.38	375, 389

Values for dielectric constant taken from references [151, 152].

Figure 3-34: The absorption spectra of Re(dppz-I) in CH_3CN (black), CH_2Cl_2 (red), THF (orange) and toluene (green) (left) with band positions and solvents detailed (right).

3.5.4 Effect of Iodine Substitution

As predicted from the MO calculations, there is more phz character observed for Re(dppz-I), where more phz contribution is observed for the transient bands in the TRIR spectra, compared to [Re(dppz)$(CO)_3$Cl]. The observed excited state for Re(dppz-I) is an equilibrium of MLCT(phen)/MLCT(phz) states and for [Re(dppz)$(CO)_3$Cl] is an equilibrium of $IL\pi\pi^*$/MLCT(phen) states.[32] Furthermore, the excited state lifetime is an order of magnitude smaller, from 40 ns to 4 ns for [Re(dppz)$(CO)_3$Cl] and Re(dppz-I) respectively in CH_2Cl_2,[32] consistent with more phz character observed for Re(dppz-I). Furthermore, the decreased electron withdrawing nature of iodine causes an increased phen contribution to the excited state than is observed for [Re(dppz-Br)$(CO)_3$Cl]. As the electronegativity of the halogen substituent increases, the phen contribution and excited state lifetime are observed to increase. However, expectantly, the lifetime of the Re(dppz-I) complex is longer than observed for [Re(dppz-Br)$(CO)_3$Cl] at 4.1 and 1.2 ns respectively. This has been tentatively attributed to the observation of more MLCT(phen) character for Re(dppz-I) than for [Re(dppz-Br)$(CO)_3$Cl], where larger charge distribution if observed for Re(dppz-I) compared to [Re(dppz-Br)$(CO)_3$Cl].

3.6 An Investigation into the Photophysical Properties of [Re(dpppn-$(NH_2)_2$)$(CO)_3Cl$]

The effects of an additional nitrogen atom substituted in the phz moiety of dppz has been investigated and discussed for the Re(dppp) complexes. Furthermore, in Chapter 2 the effect of electron donating amine groups substituted onto the phz moiety have been detailed. Following on from this work, the effect of an additional electron withdrawing nitrogen substituted in the phz moiety in conjunction with amine substituents appended onto the phz moiety on the photophysical properties of a Re(dppz) complex has been investigated.

The previously unreported complex [Re(dpppn-$(NH_2)_2$)$(CO)_3Cl$], Re(dpppn-$(NH_2)_2$), has been synthesised as detailed in Chapter 8, and the structure, alongside the optimised geometry, is shown in Figure 3-39. The optimised geometry shows the NH_2 groups are pseudo coplanar with the dppz ring, with the dihedral angle as 1.73 and 6.73° for the 13 and 11 position substituted NH_2 respectively.

3.6.1 Time Resolved Infrared Studies

The photophysical properties of Re(dpppn-$(NH_2)_2$) have been probed in three solvents with a range of dielectric constants (ε_r 46.7 - 2.3)[149, 151], d-DMSO, CH_2Cl_2 and toluene using time resolved infrared spectroscopy.

TRIR Spectroscopy in d-DMSO

The TRIR spectra of Re(dpppn-$(NH_2)_2$) were collected in d-DMSO in both the CO and FP IR regions following photoexcitation at 400 nm and are shown in Figure 3-35 and summarised in Table 3-11. In the CO region at 1 ps after photoexcitation, the parent bands are observed to have bleached and new transient bands formed at 2013, 1882 and 2001 cm^{-1}, labelled as States I and II. State I is characterised by the prominent shoulder at 2001 cm^{-1} and this shoulder is observed to decay as State II, characterised by bands at 2013 and 1882 cm^{-1}, is observed to grow in. State II is then observed to decay to the

ground state in good agreement with parent recovery. The transient bands are observed at lower energies to the parent and the magnitude of the shift is consistent with the formation of a ligand centred ππ* state. Therefore States I and II are assigned as IL ππ*.

Further information may be gleaned from the fingerprint region where several transient bands (1541, 1455 and 1296 cm^{-1}) are observed to decay with similar kinetics to State I observed in the CO region. Additionally a new band at 1404 cm^{-1} is observed to grow in and decay with kinetics matching State II. This further indicates that an initially formed State I decays to State II.

A ps-timescale shoulder decaying as a second state intensifies draws strong parallels to the TRIR spectra described in Chapter 2. This shoulder may be due to vibrational cooling as observed for other Re(dppz) complexes,[40, 53] or may be due to slow ISC discussed in Chapter 2. Therefore State I has tentatively been assigned as a ^{1}IL ππ*, and this decays to State II a ^{3}IL ππ* state, which is observed to decay to the ground state on the microsecond timescale.

Table 3-11: The FTIR and TRIR spectral features and kinetics of Re(dpppn-$(NH_2)_2$) in d-DMSO following 400 nm photoexcitation.

ν (cm^{-1})	τ decay (ns)	τ growth (ns)	Assignment
2001, 1541, 1455, 1296	0.020 ± 0.005	-	State I
2013, 1882, 1404	4650 ± 50	0.01 ± 0.006	State II
2017, 1918, 1896	-	0.015 ± 0.004 7000 ± 1000	parent
2020, 1914, 1893			GS FTIR

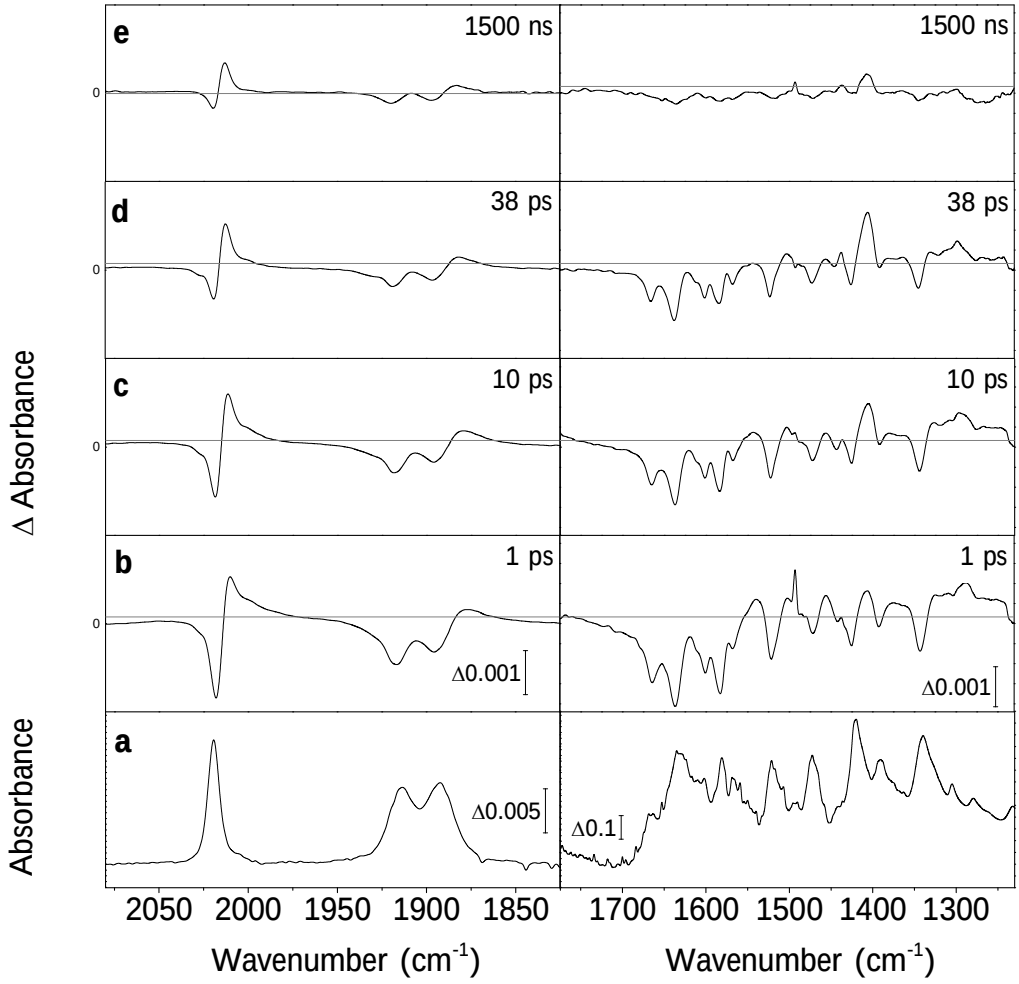

Figure 3-35: The FTIR (a) and TRIR (b-e) spectra of Re(dpppn-$(NH_2)_2$) in the CO (left) and FP (right) IR regions in d-DMSO following 400 nm photoexcitation. FTIR shown was acquired in the solid state for the FP region due to poor solubility.

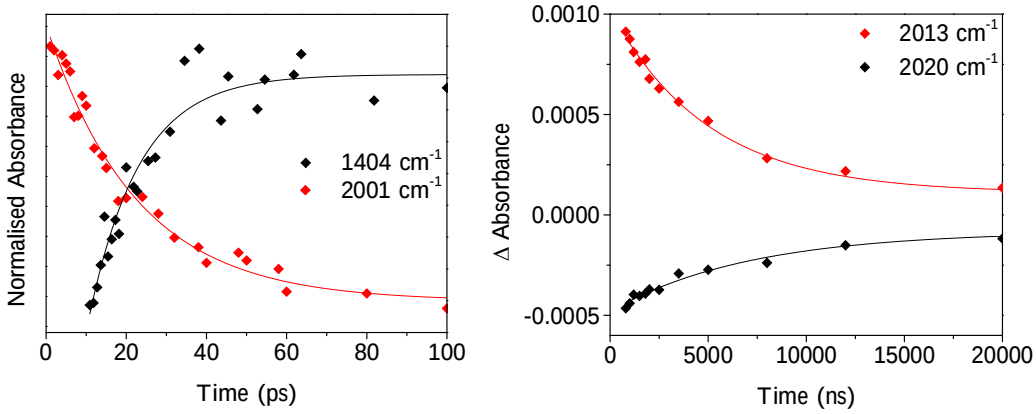

Figure 3-36: The kinetics of Re(dpppn-$(NH_2)_2$) in d-DMSO following 400 nm photoexcitation. The decay of the band at 2001 cm^{-1} assigned to State I, is in good agreement with the growth of a transient band at 1404 cm^{-1} assigned to State II (left). The decay of the band at 2013 cm^{-1} assigned to State II, is in good agreement with the growth of the band at 2020 cm^{-1} assigned to the parent (right).

TRIR Spectroscopy in CH_2Cl_2

The TRIR spectra of Re(dpppn-$(NH_2)_2$) in CH_2Cl_2 following 400 nm photoexcitation have been collected and are shown in Figure 3-37, with features summarised in Table 3-12. At 1 ps after photoexcitation the parent bands are observed to bleach and several transient bands are observed at 2081, 2015 and 1884 cm^{-1}. The former band at 2081 cm^{-1} is assigned to an MLCT(phz) state and the latter bands at 2015 and 1884 cm^{-1} are assigned to an IL$\pi\pi^*$. The bands attributed to an MLCT(phz) and IL$\pi\pi^*$ are observed to decay simultaneously to the ground state as the parent is observed to recover. The observation of an equilibrium of MLCT(phz)/IL$\pi\pi^*$ states has been observed for $[Re(dppz\text{-}F_2)(CO)_3(py)]^+$ in CH_2Cl_2,[36] a complex which exhibits an electron poor group (py) and an electron withdrawing group (F).

Table 3-12: The TRIR spectral features and kinetics of Re(dpppn-$(NH_2)_2$) in CH_2Cl_2 following photoexcitation at 400 nm.

ν (cm^{-1})	τ decay (ps)	τ growth (ps)	Assignment
2081	100 ± 30	-	MLCT(phz)
2015, 1884	72 ± 9	-	IL$\pi\pi^*$
2024, 1930, 1905	-	53 ± 2	parent
2020, 1914, 1893			GS FTIR[a]

[a]GS FTIR taken from solution FTIR in d-DMSO due to solubility.

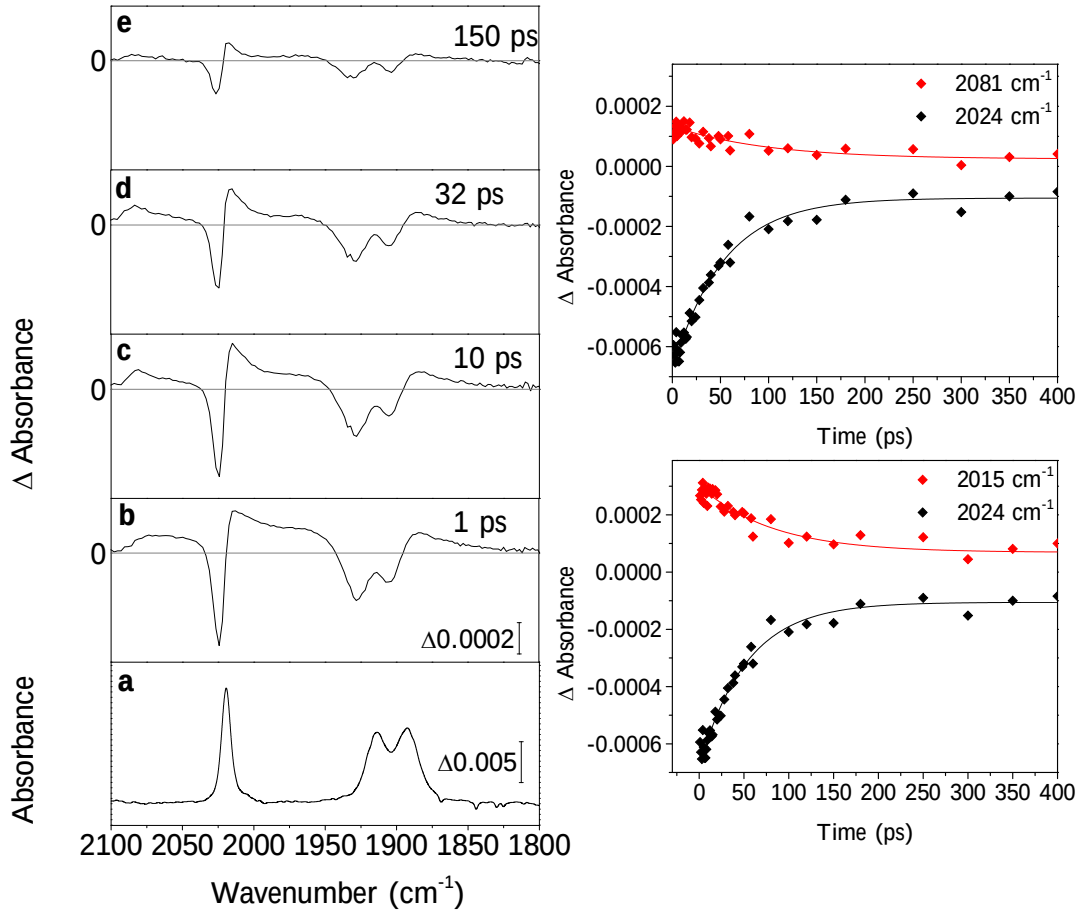

Figure 3-37: The FTIR (a) and TRIR (b-e) spectra of Re(dpppn-$(NH_2)_2$) in CH_2Cl_2 following 400 nm photoexcitation (left). The decay of band at 2081 cm^{-1} assigned to an MLCT(phz) state, is in good agreement with the band at 2024 cm^{-1} assigned to the parent (top, right). The decay of band at 2015 cm^{-1} assigned to an IL$\pi\pi^*$ state, is in good agreement with the parent band at 2024 cm^{-1} (bottom, right).

TRIR Spectroscopy in Toluene

The TRIR spectra of Re(dpppn-$(NH_2)_2$) have been acquired at several time delays following 400 nm photoexcitation in toluene and are shown in Figure 3-38, with spectral features summarised in Table 3-13. At 1 ps following photoexcitation, the parent bands are observed to bleach (2022, 1929, 1905 cm^{-1}) and the formation of a new transient band at 2015 cm^{-1} is observed. The transient band is assigned to an IL$\pi\pi^*$ state which decays in good agreement with the recovery of the parent bands, shown in Figure 3-38. The observation of a ligand centred excited state is unusual in toluene, where the low dielectric solvent would be expected to favour an MLCT(phen) state as observed for

Re(dppp2) and Re(dppp3). This would indicate that the NH_2 appended groups have a significant effect on the photophysics observed.

Table 3-13: The TRIR spectral features and kinetics of Re(dpppn-$(NH_2)_2$) in toluene following photoexcitation at 400 nm.

ν (cm^{-1})	τ decay (ps)	τ growth (ps)	Assignment
2015	30 ± 10	*ca.* 5	ILππ*
2022, 1929, 1905		22 ± 1	parent
2020, 1914, 1893			GS FTIR[a]

[a]GS FTIR taken from solution FTIR in d-DMSO

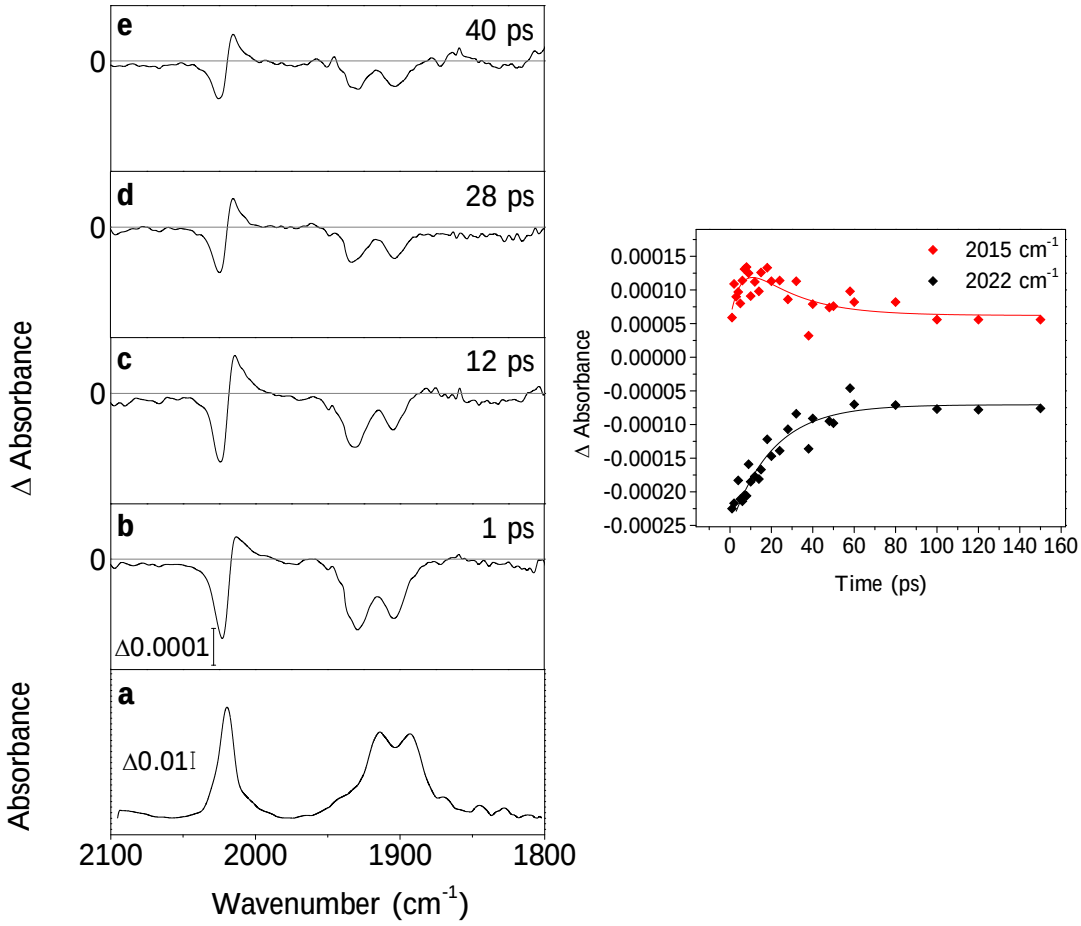

Figure 3-38: The FTIR (a) and TRIR (b-e) spectra of Re(dpppn-$(NH_2)_2$) in toluene following 400 nm photoexcitation (left). Initial growth and then decay of the band at 2015 cm^{-1} assigned to an ILππ* state where the decay, is in agreement with the growth of the band at 2022 cm^{-1} assigned to the parent (right).

3.6.2 Molecular Orbitals

The frontier molecular orbitals of Re(dpppn-$(NH_2)_2$) have been calculated using DFT. The partial energy diagram and representative MOs are shown in Figure 3-39, with all MOs listed in Appendix B.

The HOMO to HOMO-2 for the complex are Re(dπ) in nature similar to [Re(dppz)$(CO)_3$Cl] and Re(dppp2), Re(dppp3) and Re(dppp2Br) complexes unlike the ligand centred NPh_2 HOMO for the complexes in Chapter 2. Furthermore the energies of the occupied MOs at *ca.* -5.5 to -7 eV are consistent with occupied MOs for [Re(dppz)$(CO)_3$Cl] and Re(dppp2), Re(dppp3) and Re(dppp2Br). However, several ligand based unoccupied MOs are slightly higher in energy than observed for [Re(dppz)$(CO)_3$Cl] and Re(dppp2), Re(dppp3) and Re(dppp2Br) complexes. This is consistent with the complexes containing electron donating groups (NH_2).

The LUMO of Re(dpppn-$(NH_2)_2$) is predominantly phz in nature, followed by phen and dppz based MOs at higher energy. This is consistent with the complexes within this Chapter and Chapter 2. The HOMO/LUMO energy gap is 2.53 eV and is similar to that observed for [Re(dppz)$(CO)_3$Cl] (2.421 eV) and Re(dppp) complexes (*ca.* 2.2 eV), although it is significantly smaller than for [Re(dppz-NPh_2)$(CO)_3$Cl] (*ca.* 5.0 eV). This is because the unoccupied MOs for Re(dpppn-$(NH_2)_2$) are slightly higher in energy than observed for [Re(dppz)$(CO)_3$Cl] at *ca.* -3.0 to -2.2 and -3.2 to -2.3 eV respectively, owing to the electron donating NH_2 group. However the effect is not as stark as for the complexes in Chapter 2 where the unoccupied MOs energies are -1.8 to -0.8 eV.

The phen(π*)/phz(π*) energy gap of 0.44 eV is similar to the observed phen(π*)/phz(π*) energy gap for Re(dppz-NPh_2) complexes (*ca.* 0.4 eV), which is far smaller than observed for Re(dppp) complexes (*ca.* 1.5 eV) and for [Re(dppz)$(CO)_3$Cl] (2.421 eV). This difference reflects the presence of the electron donating NH_2 groups which raise the unoccupied phz MO energy.

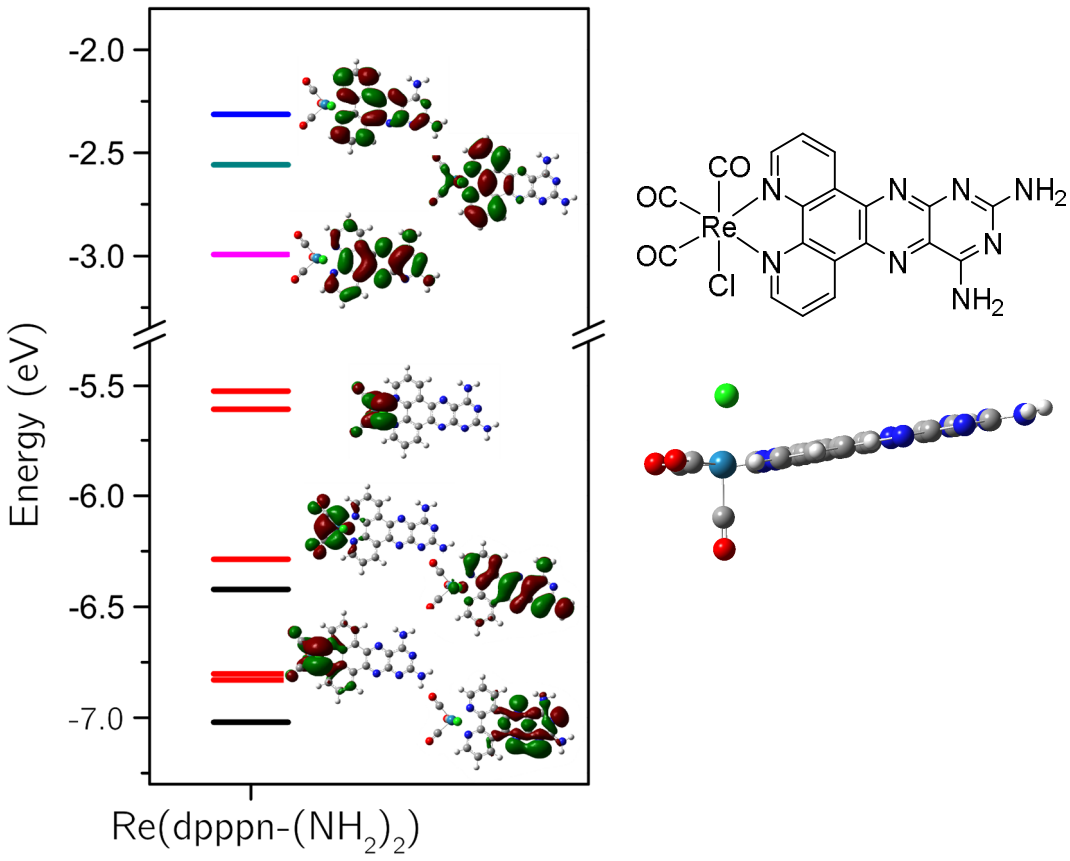

Figure 3-39: The DFT calculated frontier molecular orbitals and partial energy diagram for Re(dpppn-(NH_2)$_2$). Metal based occupied MOs are shown in red and ligand centred occupied MOs in black. The unoccupied phen, phz and dppz MOs are shown in pink, turquoise and blue respectively (left). The structure (top, right) and optimised geometry (bottom, right) for Re(dpppn-(NH_2)$_2$).

3.6.3 Discussion

The addition of electron donating NH_2 groups and the substitution of the electron withdrawing nitrogen atom groups do not appear to 'cancel' the electron pushing effects of each other to produce similar photophysical properties to [Re(dppz)$(CO)_3$Cl]. As discussed previously, the substituted nitrogen atom in Re(dppp) complexes encourages an MLCT(phz) excited state, as the phz unoccupied MO is lowered in energy. For Re(dppp3) and Re(dppp2Br) complexes in d-DMSO an equilibrium between MLCT(phz)/^{1}LLππ* states is observed. Conversely for the Re(dppz-NPh_2) complexes discussed in Chapter 2, the presence of the electron donating group results in a ligand centre ^{1}LLππ* state. However, that has only been investigated in CH_2Cl_2.

Interestingly the excited state lifetime of Re(dpppn-$(NH_2)_2$) doesn't appear to show a distinct trend with the dielectric constant of the solvent unlike for the Re(dppp) complexes discussed earlier and for most [Re(dppz)$(CO)_3$Cl] derivatives.[92] In d-DMSO ISC of states (^{1}ILππ*→^{3}ILππ*) is observed, which is similar to observations in Chapter 2. This indicates that potentially the NH_2 electron donating groups are dominant and there is a significant amount of electron density on the dppz ligand. Conversely, an equilibrium of ILππ*/MLCT(phz) states is observed for Re(dppp3) and Re(dppp2Br), which are more electron withdrawing than Re(dppp2). Therefore for Re(dpppn-$(NH_2)_2$) the additional nitrogen atom in the phz moiety may potentially result in more ligand centred electron density resulting in only an ILππ* state. In CH_2Cl_2 an equilibrium of MLCT(phz)/ILππ* excited states is observed, reflecting the behaviour of Re(dppp) complexes in the higher polarity d-DMSO solvent.

However, in toluene only an ILππ* excited state is observed. Further spectroscopic studies in a wider range of solvents are required to ascertain the nature of the trend observed and the effect of both the electron donating and withdrawing groups present.

Table 3-14: The nature and lifetime of the excited state observed for Re(dpppn-$(NH_2)_2$) in a range of solvents taken from the TRIR data. Where two states are written an equilibrium exists. Dielectric constant values taken from references [149, 151, 152].

Solvent	Nature ES	τ (ns)
d-DMSO	^{1}ILππ*	0.02 ± 0.005
	^{3}ILππ*	4650 ± 50
CH_2Cl_2	MLCT(phz)/ILππ*	0.9 ± 0.1
Toluene	ILππ*	0.03 ± 0.01

4 Conclusions

The effect of an additional electron withdrawing nitrogen substituted within the phz moiety of [Re(dppz)$(CO)_3$Cl] complex has been explored by investigating the photophysical properties of [Re(dppp2)$(CO)_3$Cl], [Re(dppp3)$(CO)_3$Cl] and [Re(dppp2Br)$(CO)_3$Cl] through time resolved infrared studies. The energy of the phz state is observed to decrease as a result of the additional nitrogen atom, where population of an MLCT(phz) state is more commonly observed for dppp derivative complexes than for the analogous dppz complex.

The effect of the position of the electron withdrawing additional nitrogen on the photophysical properties has been investigated by comparing [Re(dppp2)$(CO)_3$Cl] and [Re(dppp3)$(CO)_3$Cl]. The latter was shown to have a stronger electron withdrawing effect resulting in more observed MLCT(phz) character in the excited state. This is consistent with the lower energy of the phz(π^*) orbital from MO calculations for Re(dppp3) compared to Re(dppp2).

Subsequently, the effect of an additional withdrawing group appended onto the phz moiety has been assessed by comparing Re(dppp2Br) to Re(dppp2) and Re(dppp3). The electron withdrawing group has been shown to have a larger effect at lowering the phz state energy and increasing the phen/phz energy gap. The electron withdrawing nature of the complexes is assigned to follow the pattern: Re(dppp2Br) > Re(dppp3) > Re(dppp2). This is reflected in the larger phen contribution and the longer lifetime exhibited compared to the analogous Br complex. The effect of altering the halogen substitution has been further investigated by examining [Re(dppz-I)$(CO)_3$Cl], a previously unreported complex.

The effect of the solvent media on the photophysical properties has also been investigated by acquiring time resolved infrared spectra of Re(dppp2), Re(dppp3) and Re(dppp2Br) in a range of solvents, with varying dielectric constants. Solvent media has been shown to have a strong effect on the photophysics observed where the rate of MLCT(phen)/MLCT(phz) interconversion is shown to increase with increasing solvent polarity, although to a lesser extent than for the unsubstituted [Re(dppz)$(CO)_3$Cl]

complex. Furthermore, the excited state lifetime for each complex is shown to increase with decreasing dielectric constant, where the lifetime in toluene is more than two orders of magnitude longer than the excited state lifetime observed in d-DMSO. These observations are consistent with the further stabilisation of an MLCT(phz) compared to an MLCT(phen) excited state with increasing dielectric constant of the solvent.

Parallels have been drawn to the complexes in Chapter 2 through preliminary investigations of the photophysical properties of [Re(dpppn-$(NH_2)_2$)$(CO)_3$Cl] in a range of solvents. Preliminary work has shown, from the TRIR spectra in d-DMSO, an ISC from ^{1}ILππ* to ^{3}ILππ* states is observed. This slow ISC is similar to observations of the nature of the excited states for Re(dppz-NPh_2) complexes in Chapter 2. However, further work is required to ascertain the dependence of the excited states on the solvent media for Re(dpppn-$(NH_2)_2$).

Chapter 4

The Photophysical Properties of Nitro-Appended Rhenium Dipyrido[3,2-*a*:2',3'-*c*]phenazine Complexes

1 Introduction

Altering the substituents on the phz moiety of the dppz ligand can have a profound effect on the observed photophysical properties, as discussed in Chapters 2 and 3. The addition of the electron donating NPh_2 groups and substitution of a carbon atom for an electron withdrawing nitrogen atom on the photophysical properties of $[Re(dppz)(CO)_3Cl]$ complexes has been discussed in Chapters 2 and 3 respectively. Furthermore, the position of the nitrogen atom within the phz moiety has been investigated in Chapter 3, and shown to have a clear effect on the photophysical properties.

Following on from these investigations, this Chapter will focus on the effect of a strong electron withdrawing nitro-group (NO_2) substituted onto the phz moiety on the photophysical properties observed. Additionally, the effect of the position of the electron withdrawing group will be investigated by exploring the NO_2 at the 12 and 13 substituted phz positions of the dppz ligand.

Nitro-substituent groups are strongly electron withdrawing and when attached to a π-system the NO_2 group decreases the electron density on the aromatic ring and thus may be thought of as deactivating it.[153-155] The electron withdrawing effect is often attributed

to the small localised positive charge on the nitrogen atom and secondly, to resonance effects.[153-155] Previous work on $[Ru(bpy\text{-}NO_2)_3]^{2+}$ has indicated that the NO_2 group is resonant with the bpy π-system causing an electron withdrawing effect, this is also manifested by a greater decrease in reduction potential compared to the non-substituted $[Ru(bpy)_3]^{2+}$.[154] As discussed in the introduction of Chapters 2 and 3, electron withdrawing groups can cause a lowering of the MLCT(phen/phz) energy in relation to the ILππ* state. Furthermore, the MLCT(phen)/MLCT(phz) energy gap is increased leading to more population of the MLCT(phz) state compared to the MLCT(phen) state.

The NO_2 group has previously been observed to significantly affect the photophysical properties observed for M(diimine) complexes. Previous work has shown that $[Ru(bpy\text{-}4\text{-}NO_2)_3]^{2+}$, $[Ru(bpy\text{-}4,4'\text{-}(NO_2)_2)_3]^{2+}$, $[Re(bpy\text{-}4,4'\text{-}(NO_2)_2)(CO)_3Cl]$ and $[Re(phen\text{-}5\text{-}NO_2)(CO)_3Cl]$ are all non-emissive at room temperature unlike their non-substituted analogues.[154-158] This has been attributed to a very short lived MLCT excited state, which decreases from *ca.* 200 ns to 7.6 ± 1.8 ps in CH_3CN for $[Re(phen)(CO)_3Cl]$ and $[Re(phen\text{-}5\text{-}NO_2)(CO)_3Cl]$ respectively.[155, 159, 160] This decrease in lifetime has been assigned to the localisation of electron density in the MLCT state on the NO_2 group and is consistent with resonance Raman studies of $[Ru(bpy\text{-}NO_2)_3]^{2+}$, $[Ru(bpy\text{-}(NO_2)_2)_3]^{2+}$, and $[Re(phen\text{-}5\text{-}NO_2(CO)_3(imH)]$.[153-155]

Work by Vlček and co-workers has previously investigated the nature and kinetics of the excited states observed for $[Re(phen\text{-}NO_2)(CO)_3L]^+$, structure shown in Figure 4-1.[155, 158]

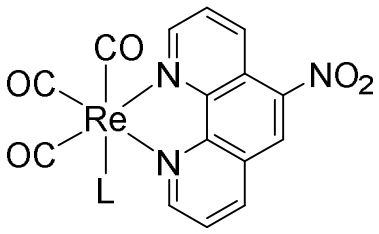

Figure 4-1: The structure of $[Re(phen\text{-}5\text{-}NO_2)(CO)_3L]^+$.

The TRIR spectra of $[Re(phen\text{-}5\text{-}NO_2)(CO)_3Cl]$ in CH_3CN after 400 nm photoexcitation are shown in Figure 4-2.[158] Transient bands which are blue shifted in relation to the

parent are observed and assigned to an MLCT/LLCT excited state, comprising of mainly Re(dπ)→phen(π*) but also of some Cl(π)→phen(π*) character. This initially formed MLCT/LLCT state is then observed to decay (τ = 10.4 ± 0.4 ps) to a new transient species assigned to an nπ* state from the oxygen lone pair of NO_2 to the π*(phen). This nπ* state subsequently decays to the ground state with lifetime 30.5 ± 2 ps, where the excited state assignment is consistent with DFT calculations.

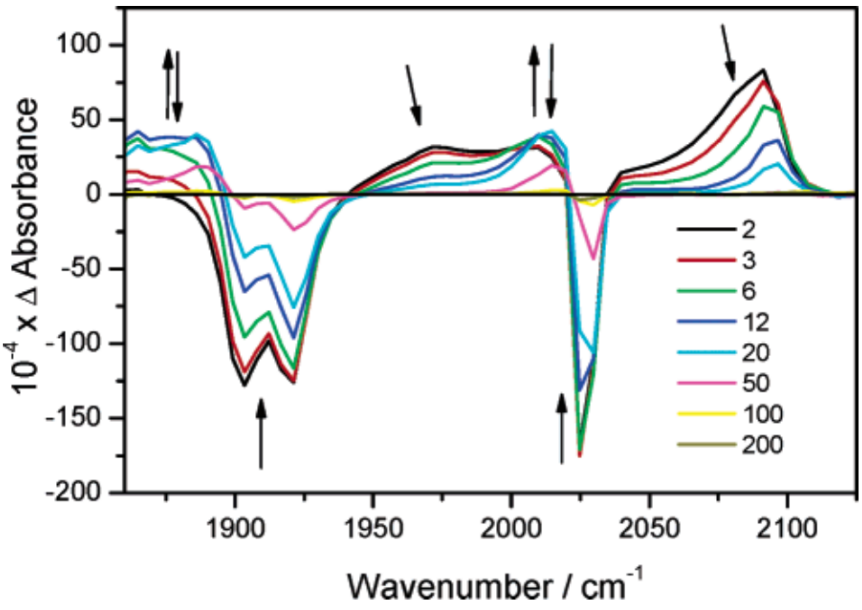

Figure 4-2: The TRIR spectra of [Re(phen-5-NO_2)$(CO)_3$Cl] in CH_3CN after 400 nm photoexcitation at a variety of ps-time delays. Reproduced from reference 158.

DFT calculations of [Re(phen-5-NO_2)$(CO)_3$Cl] have shown that the NO_2 group is not coplanar with the phenanthroline, where a 22.3° torsion angle is observed.[161] This is attributed to the attractive N-O···H interaction among the 5-NO_2-phen ligands of neighbouring molecules.[161] Furthermore, the calculations support the assignment of an MLCT/LLCT state for phen-5-NO_2 complexes by Vlček where for [Re(phen-5-NO_2)$(CO)_3$Cl] the HOMO-1 mainly consists of Re(dπ) and Cl(π), while the LUMO+1 is composed of phen(π*) character. Therefore the lowest lying absorption band of the complex has been assigned as a Re(dπ)Cl(π)→phen(π*) transition with MLCT/LLCT character.[161] This is reflected in the spin density distribution for the lowest triplet state T_1 of [Re(phen-5-NO_2)$(CO)_3$Cl] as shown in Figure 4-3.

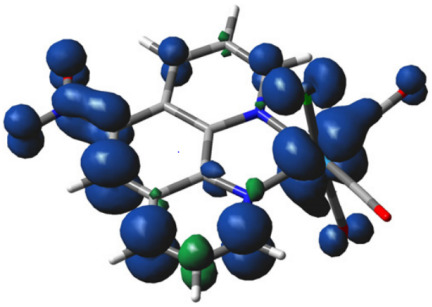

Figure 4-3: The spin density distribution for the lowest triplet state T1 of [Re(phen-5-NO_2)$(CO)_3$Cl] which is observed to be MLCT/LLCT in character. Reproduced from reference 161.

The TRIR spectra of [Re(phen-5-NO_2)$(CO)_3$(imH)]$^+$, where imH is imidazole, following 400 nm photoexcitation in CH_3CN are shown in Figure 4-4. Transient bands blue shifted with respect to the parent are assigned to an MLCT state. These MLCT bands are observed to decay in agreement with the growth of transient bands at lower energy to the parent assigned to an LLCT state, imH(π)phen(π*). The LLCT state subsequently decays to the ground state.

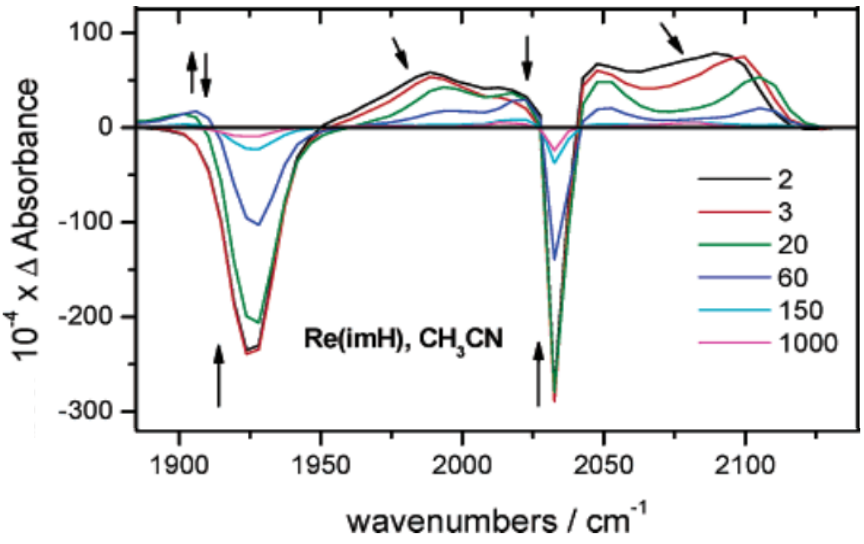

Figure 4-4: The TRIR spectra of [Re(phen-5-NO_2)$(CO)_3$(imH)] measured at selected ps-time delays following 400 nm excitation in CH_3CN, where the MLCT state is observed to decay to an LLCT state. Reproduced from reference 155.

The effect of NO_2 substitution has been investigated for M(dppz) complexes, albeit to lesser extent then M(bpy) and M(phen) complexes. Previously the TRIR spectra of [Re(dppz-12-NO_2)$(CO)_3$(DMAP)]$^+$ in CH_3CN have been collected following 400 nm photoexcitation and are shown in Figure 4-5.[53] Transient bands higher in energy than

the parent are observed and assigned to an MLCT(phen) excited state, which decays to the ground state with lifetime 120 ± 20 ps, over two orders of magnitude faster than the MLCT(phz) excited state observed for $[Re(dppz)(CO)_3Cl]$.[32] This is possibly due to the localisation of the electron density in the MLCT state on the NO_2, observed for $[Re(phen\text{-}NO_2)(CO)_3Cl]$.[158]

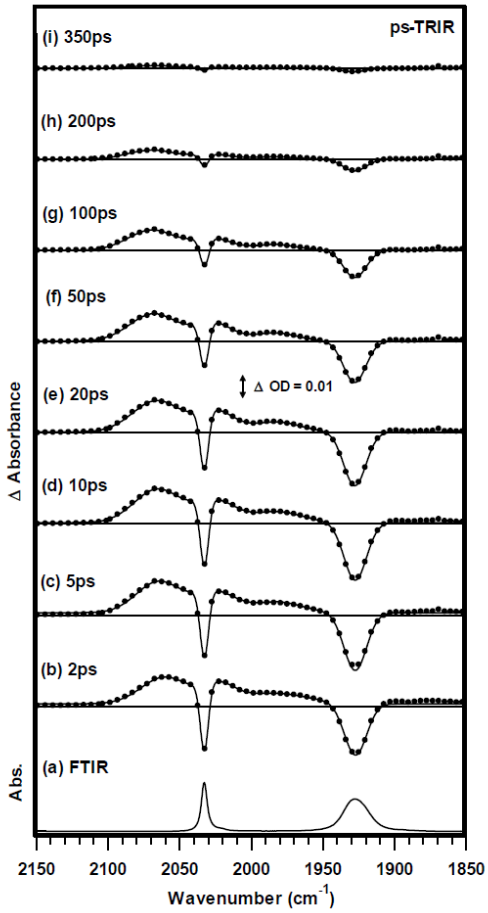

Figure 4-5: The FTIR spectrum of $[Re(dppz\text{-}12\text{-}NO_2)(CO)_3(DMAP)]^+$ (a) and TRIR spectra of $[Re(dppz\text{-}13\text{-}NO_2)(CO)_3(DMAP)]^+$ in CH_3CN at various time delays. Reproduced from reference 53.

Subsequent MO calculations of $[Re(dppz\text{-}12\text{-}NO_2)(CO)_3(DMAP)]^+$ have shown that the LUMO and LUMO+1 are centred on the dppz ligand but with different electronic distribution compared to $[Re(dppz)(CO)_3(DMAP)]$.[162] The LUMO is distributed along the dppz ligand although centralised on the phz while in contrast the LUMO+1 is phen centred, Figure 4-6. The LUMO is located on the phz, while the HOMO-1 is Re based, with some contribution from the CO(π*) indicating some Re-CO back-bonding nature. This would support the observations from the TRIR spectra, where an MLCT state is

observed. In addition, the calculations indicate the presence of an ILCT state, which is LC and more characteristic of an n→π* state, as seen for [Re(phen-NO_2)$(CO)_3$Cl] and [Re(bpy-NO_2)$(CO)_3$Cl].[155, 158]

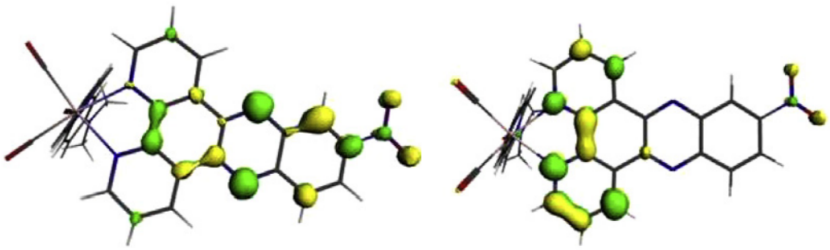

Figure 4-6: The LUMO (left) and LUMO+1 (right) of [Re(dppz-12-NO_2)$(CO)_3$(DMAP)], where the LUMO is dppz based with contribution from the NO_2. Reproduced from reference 162.

2 Aims

The aim of this Chapter is to investigate the effect of the addition and position of a nitro group onto the phz moiety for a [Re(dppz)$(CO)_3$Cl] derivative complex. This aim has been split into three objectives:

1. To synthesise nitro-group appended [Re(dppz)$(CO)_3$Cl] derivative complexes: [Re(dppz-12-NO_2)$(CO)_3$Cl] and the previously unreported [Re(dppz-13-NO_2)$(CO)_3$Cl].

2. To investigate the effect of the nitro group substitution on the observed photophysical properties and draw comparison to the unsubstituted [Re(dppz)$(CO)_3$Cl], through time-resolved infrared, absorption and emission spectroscopic techniques, alongside electrochemical studies and DFT calculations.

3. To elucidate the effect of the nitro-group phz substitution position on the photophysical properties observed by comparing [Re(dppz-13-NO_2)$(CO)_3$Cl] and [Re(dppz-12-NO_2)$(CO)_3$Cl].

3 Results and Discussion

The photophysical properties of the complexes [Re(dppz-12-NO_2)$(CO)_3$Cl], (Re(dppz-12-NO_2)) and [Re(dppz-13-NO_2)$(CO)_3$Cl], (Re(dppz-13-NO_2)), structures shown in Figure 4-7, have been investigated through TRIR, absorption, emission, electrochemical and DFT studies.

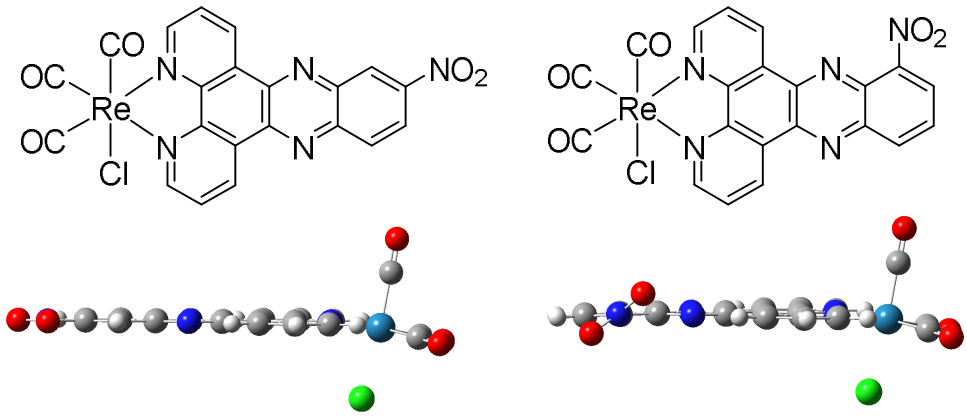

Figure 4-7: The structure of Re(dppz-12-NO_2) (top, left) and Re(dppz-13-NO_2) (top, right) with the optimised geometry of Re(dppz-12-NO_2) (bottom, left) and Re(dppz-13-NO_2) (bottom, right) showing the dihedral angle of the NO_2 group in relation to the phz ring.

The optimised geometries of both complexes, shown in Figure 4-7, indicate that for Re(dppz-12-NO_2) the NO_2 group is planar with respect to the dppz ring as observed for [Re(bpy-NO_2)$(CO)_3$Cl].[163, 164] However, this is not the case for Re(dppz-13-NO_2) where the NO_2 group exhibits a dihedral angle of 36° to the dppz ring, as seen for [Re(phen-5-NO_2)$(CO)_3$Cl].[155]

3.1 Absorption Spectroscopy

The absorption spectra of both Re(dppz-12-NO_2) and Re(dppz-13-NO_2) have been acquired in a range of solvents and are shown in Figure 4-8 with band positions detailed in Table 4-1. Re(dppz-12-NO_2) has been previously investigated in CH_2Cl_2 and this work is consistent with the results presented here.[28] The absorption spectra of both Re(dppz-12-NO_2) and Re(dppz-13-NO_2) in all solvents are dominated by bands in the 250-380 nm region indicative of transitions that are ππ* in nature.[28, 53, 85, 86] There are two clear

structured bands at *ca.* 352 and 362 nm for both complexes, the higher energy of which is representative of the ^{1}LCππ* transition of the dppz,[28] and the lower energy band representative of the ^{1}MLCT(phen) transition.[53, 85, 86] These assignments have been further confirmed by TD-DFT calculations.

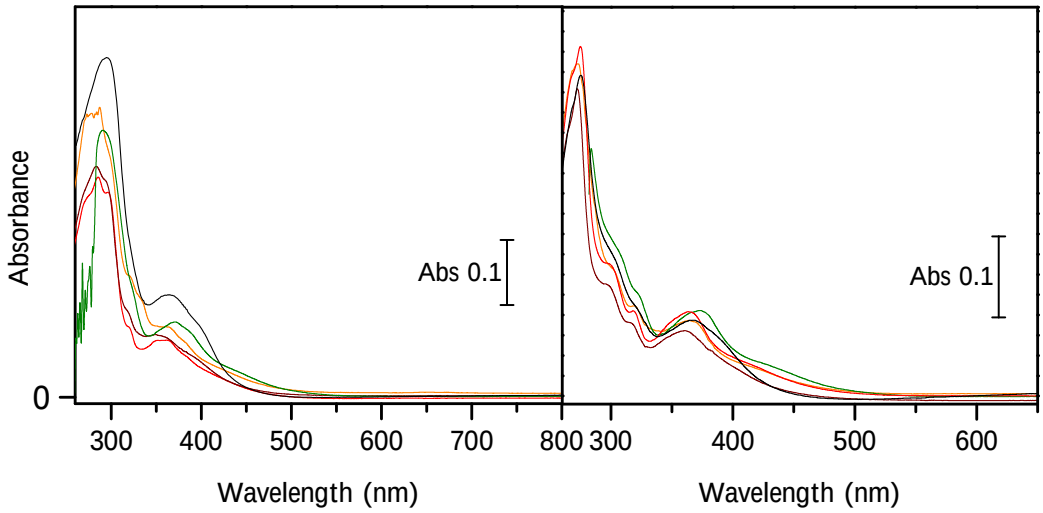

Figure 4-8: The absorption spectra of Re(dppz-12-NO2) (left) and Re(dppz-13-NO2) (right) in DMSO (black), CH_3CN (brown), CH_2Cl_2 (red), THF (orange) and toluene (green).

Table 4-1: The band positions from the absorption spectra of Re(dppz-12-NO_2) and Re(dppz-13-NO_2) in a range of solvents with varying dielectric constant (ε_r). The values for the dielectric constants are taken from references 149, 151, 152.

Solvent	ε_r	λ_{abs} (nm)	
		Re(dppz-12-NO_2)	Re(dppz-13-NO_2)
DMSO	46.7	296, 365, 397	275, 297, 319, 367, 383(sh)
CH_3CN	37.5	271(sh), 282, 295(sh), 318, 352, 390	272, 296(sh) 317(sh), 360
CH_2Cl_2	8.9	270(sh), 285, 296, 318(sh), 352, 361	273, 298(sh), 317(sh), 364, 410(sh)
THF	7.8	320(sh), 333(sh), 363, 382	273, 302(sh), 320(sh), 363, 417(sh)
Toluene	2.3	292(sh), 371, 389, 435(sh)	304(sh), 320(sh), 374, 426(sh)

Emission studies were also carried out in the same solvents as for absorption. The complexes were observed to be non-emissive in all solvents, consistent with previous literature for Re(diimine-NO_2) complexes.[154-158]

3.2 Cyclic Voltammetry

The electrochemical properties of Re(dppz-12-NO_2) and Re(dppz-13-NO_2) were investigated in CH_2Cl_2 containing [nBu_4N][BF_4] (0.4 M), using cyclic voltammetry, with the results summarised in Table 4-2. For both complexes two cathodic processes and one anodic process were observed within the solvent window, shown in Figure 4-9.

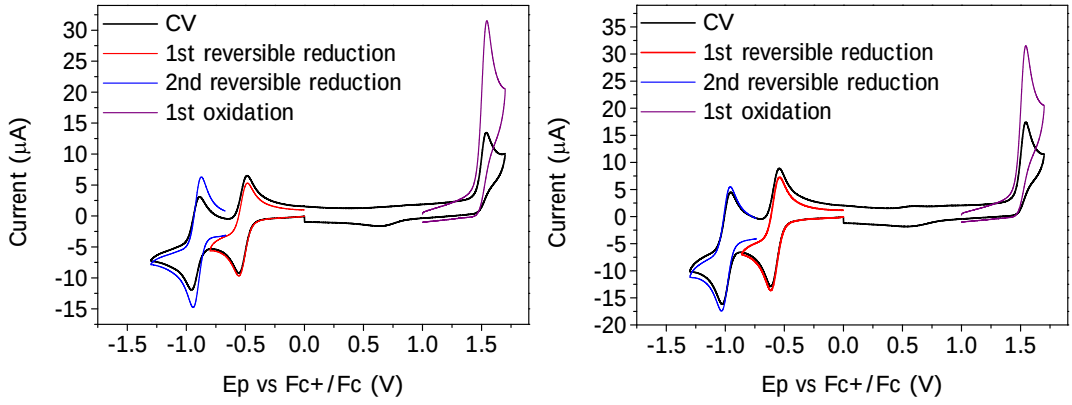

Figure 4-9: The CVs of Re(dppz-12-NO_2) (left) and Re(dppz-13-NO_2) (right) (0.4 M) in CH_2Cl_2 containing [nBu_4N][BF_4] (0.4 M) at 100 mVs^{-1} for full CV (black), first reversible reduction process (red) and second reversible reduction process (blue).

The two cathodic processes (E_{red1} and E_{red2}), shown in Figures 4-10 and 4-11, are shown to be thermodynamically reversible Nernstian processes, demonstrated through the linearity of the plot of I_p^a and I_p^c *vs.* (scan rate)$^{1/2}$, shown in Appendix A. Conversely, the oxidation process observed (E_{ox}) was shown to be chemically irreversible.

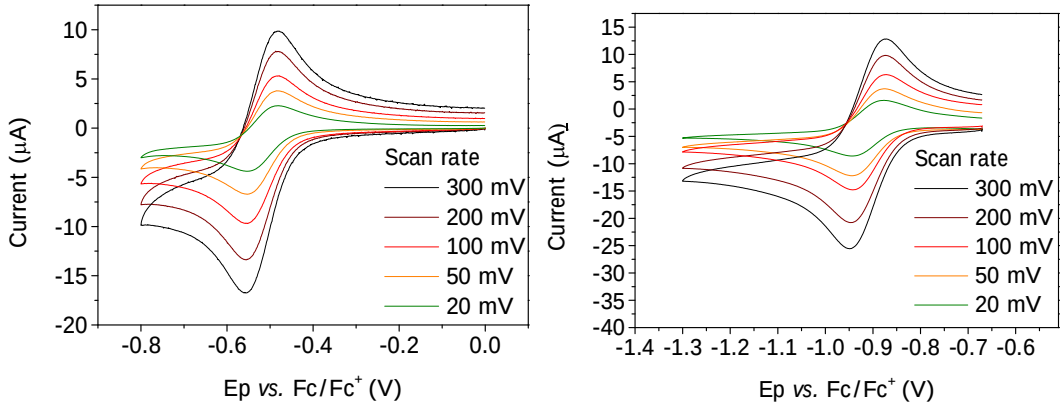

Figure 4-10: The 1st (left) and 2nd (right) electrochemically reversible reduction processes for Re(dppz-12-NO_2) in CH_2Cl_2 containing [nBu_4N][BF_4] (0.4 M) at a series of scan rates.

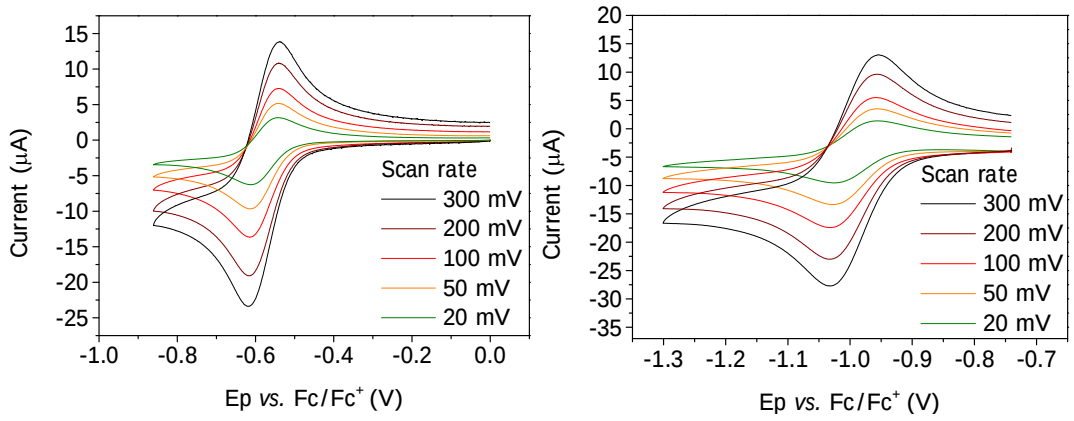

Figure 4-11: The 1st (left) and 2nd (right) electrochemically reversible reduction processes for Re(dppz-13-NO_2) in CH_2Cl_2 containing [nBu_4N][BF_4] (0.4 M) at a series of scan rates.

Table 4-2: The electrochemical data for Re(dppz-12-NO_2) and Re(dppz-13-NO_2) in CH_2Cl_2 containing 0.4 M [Bu_4N][BF_4].

Complex	*vs.* Fc/Fc$^+$ (V)		
	E_{red1}	E_{red2}	E_{ox}
[Re(dppz)(CO)$_3$Cl][a]	-1.42	-2.05	0.96
Re(dppz-12-NO_2)	-0.56	-0.95	1.54
Re(dppz-13-NO_2)	-0.62	-1.03	1.55

[a]Data taken from reference 32.

The complexes exhibit first reduction potentials (E_{red1}) at -0.56 and -0.62 V for Re(dppz-12-NO_2) and Re(dppz-13-NO_2) respectively, which are at considerably more positive values than normally observed for [Re(dppz)(CO)$_3$Cl] at -1.42 V.[32] Similarly, a more positive value is observed for both complexes for the second reversible reduction process (E_{red2}) at -0.95 and -1.03 V, for Re(dppz-12-NO_2) and Re(dppz-13-NO_2) respectively, in comparison to [Re(dppz)(CO)$_3$Cl] at -2.05 V.[32] This large shift has been observed for M(bpy-NO_2) complexes,[165, 166] where the addition of a NO_2 group moves the E_{red} by *ca.* 0.4 V from -0.74 to -0.34 V *vs.* Ag/AgCl in 0.1 M [TBA][BF_4]/DMF at 293 K for [Pt(bpy)Cl_2] and [Pt(4-NO_2-bpy)Cl_2] respectively.[166] The more positive E_{red1} and E_{red2} observed for Re(dppz-NO_2) compared to [Re(dppz)(CO)$_3$Cl] is caused by the electron withdrawing NO_2 group lowering the LUMO energy, resulting in more positive E_{red} values.[165-167] Furthermore, E_{red1} is likely associated with a reduction of the nitro group forming NO_2^- and the E_{red2} localised on the phz portion of the dppz ligand.

The more positive E_{red1} and E_{red2} values observed for Re(dppz-12-NO_2) compared to Re(dppz-13-NO_2) indicate that the HOMO/LUMO gap is smaller for Re(dppz-12-NO_2) than for Re(dppz-13-NO_2), as Re(dppz-12-NO_2) is more easily reduced.

3.3 Infrared Spectroelectrochemistry

The FTIR spectra of the one and two electron reduced species ($1e^-$ RS and $2e^-$ RS respectively) of complexes Re(dppz-12-NO_2) and Re(dppz-13-NO_2) have been acquired in CH_2Cl_2 containing [nBu_4N][BF_4] (0.4 M) and are shown in Figure 4-12, with band positions summarised in Table 4-3. The non-reduced species FTIR spectrum exhibits three bands indicative of the C_s symmetry of the complexes and are independent of the substitution position of the NO_2 group. For both complexes the $1e^-$ reduced state has three bands which are red shifted in energy compared to the non-reduced complex by *ca.* 5 cm^{-1}. This is consistent with an electron residing on the dppz ligand, causing a slight increase in the electron density seen by the Re metal centre and thus, a slight increase in Re-CO back bonding. The observed 5 cm^{-1} shift is less than the shift observed when the electron is localised on the phz orbital of *ca.* 10 cm^{-1}, observed in Chapter 2. It is also inconsistent with the larger shift of *ca.* 30 cm^{-1} which would be expected if the electron were localised on the phen orbital, in line with observations for [Re(bpy)$(CO)_3$Cl] and [Re(phen)$(CO)_3$Cl].[91]

The second electron reduction results in a collection of bands observed in the FTIR. This has been attributed to the instability associated with the $2e^-$ reduced state and therefore a large amount of the $1e^-$ reduced state is also present. Therefore the bands assigned to the $2e^-$ reduced state are observed as small shoulders at *ca.* 2004, 1987 and 1869 cm^{-1}. This $2e^-$ reduced state is red shifted with respect to the non-reduced complex by *ca.* 20 cm^{-1} for both complexes. This would indicate that the electron in the $2e^-$ reduced species is located on the dppz ligand and is nearer to the Re metal than in the $1e^-$ reduced species. The FTIR spectra of the $1e^-$ and $2e^-$ reduced state could indicate the electron in the $1e^-$ reduced state is localised on the NO_2 substituent and the second electron ($2e^-$ RS) is localised on the dppz ligand. The small shift *ca.* 5cm^{-1} exhibited by

the $1e^-$ reduced state indicates that less electron density is on the Re metal than when the electron is localised on a phz moiety, this is consistent with the assignment of the electron localised on the NO_2 group for the $1e^-$ reduced state.

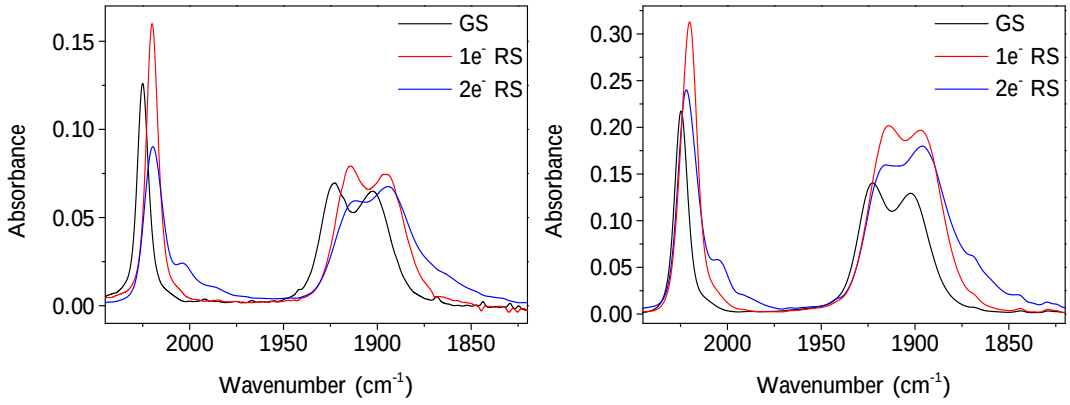

Figure 4-12: The FTIR of the non-reduced species (black), $1e^-$ reduced state (red) and $2e^-$ reduced state (blue) for Re(dppz-12-NO_2) (left) and Re(dppz-13-NO_2) (right).

Table 4-3: The FTIR bands observed for the non-reduced, $1e^-$ and $2e^-$ reduced species in CH_2Cl_2 containing $[nBu_4N][BF_4]$ (0.4 M).

Complex	ν(CO) (cm^{-1})		
	Neutral	**$1e^-$ RS**	**$2e^-$ RS**
Re(dppz-12-NO_2)	2025, 1923, 1902	2020, 1914, 1896	2020, 2003(sh), 1987(sh), 1912, 1894, 1862(sh)
Re(dppz-13-NO_2)	2025, 1923, 1902	2020, 1914, 1897	2022, 2004(sh), 1991(sh), 1916, 1896, 1869(sh)

3.4 Absorption Spectroelectrochemistry

Absorption spectroelectrochemistry experiments were conducted in CH_2Cl_2 for Re(dppz-12-NO_2) and Re(dppz-13-NO_2), where the non-reduced, $1e^-$ reduced species and $2e^-$ reduced species and are shown in Figure 4-13, with band positions detailed in Table 4-4.

The non-reduced complexes absorption spectra of Re(dppz-12-NO_2) and Re(dppz-13-NO_2) have been discussed previously and two bands centred at *ca*. 357 nm are observed, representative of an $IL\pi\pi^*$ transition of the dppz ligand and of a ^{1}MLCT(phen) transition.[28, 53, 85, 86] For the $1e^-$ reduced species, the ^{1}MLCT(phen) band is observed to

decrease in intensity while the IL$\pi\pi^*$ transition of the dppz band increases, consistent with previous observations for Re(dppz) complexes.[92] Furthermore, the presence of two new bands at *ca.* 500 nm are observed for both complexes and are consistent with the one electron reduced complexes of M(dppz) complexes where M = Re, Ru or Os and based on previous literature this band has been attributed to an IL$\pi\pi^*$ transition based on the phz moiety of the dppz ligand.[24, 25, 28] The IL$\pi\pi^*$ phz transition bands observed for Re(dppz-12-NO_2) and Re(dppz-13-NO_2) are observed at higher energies compared to analogous Re(dppz) complexes such as [Re(dppz-X_2)$(CO)_3$Cl] where X = H, CF_3, CH_3, F and Cl,[92] this shift to higher energies indicates that the Re is more electron poor and is attributed to the strong electron withdrawing effect of the NO_2 group.

Furthermore, the $1e^-$ reduced species exhibits a lower energy band at 836 and 879 nm for Re(dppz-12-NO_2) and Re(dppz-13-NO_2) respectively, consistent with the observed blue colour of the $1e^-$ reduced species. The NO_2 group is often considered an electron sink and this low energy band is representative of an n$\rightarrow\pi^*$ transition assigned as from the n-orbital of oxygen of the NO_2 group to the phz moiety of the dppz ligand. This is consistent with previous literature where the NO_2^- exhibits a band in the absorption spectra at 900 nm.[168] Furthermore, an analogous broad band has been observed in the transient absorption spectra of $[Re(phen\text{-}5\text{-}NO_2)(CO)_3(4\text{-}Etpy)]^+$ and $[Re(phen\text{-}5\text{-}NO_2)(CO)_3(imH)]^+$ and has been assigned to an MLCT(phen-5-NO_2) state with significant NO_2 character. Further analogous absorption bands are observed for nitroaromatic compounds including nitrotoluene and nitrobenzene.[155] This NO_2^- band is lower in energy for Re(dppz-13-NO_2) than for Re(dppz-12-NO_2).

The $2e^-$ reduced species shows an absence of this low energy nπ^* transition. This indicates that the first electron likely resides on the NO_2 group and the subsequent electron resides on the phz orbital of dppz. This is consistent with observations made from the CV data and the $1e^-$ and $2e^-$ reduced species FTIR.

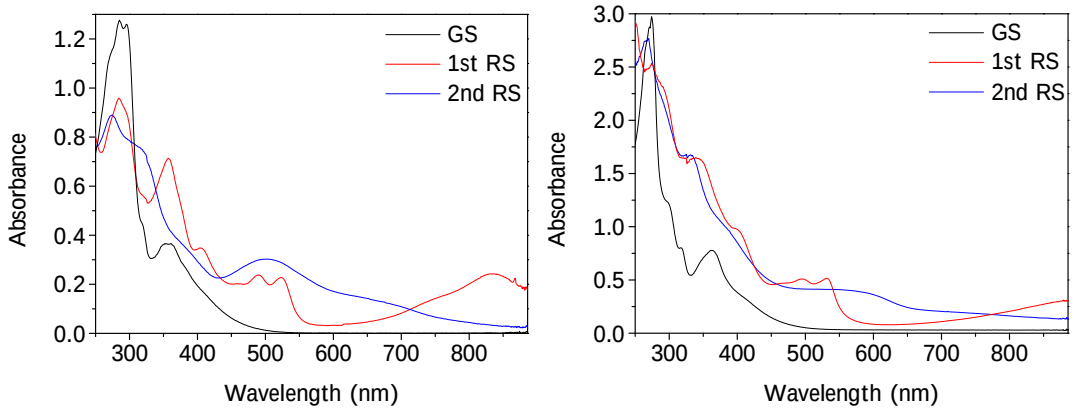

Figure 4-13: The absorption spectra of Re(dppz-12-NO_2) (left) and Re(dppz-13-NO_2) in CH_2Cl_2 containing [nBu_4N][BF_4] (0.4 M) (right), with the non-reduced species (black), $1e^-$ reduced species (red) and $2e^-$ reduced species (blue).

Table 4-4: The absorption bands for Re(dppz-12-NO_2) and Re(dppz-13-NO_2) for the non-reduced species, $1e^-$ reduced species (RS) and $2e^-$ reduced species (RS) in CH_2Cl_2 containing [nBu_4N][BF_4] (0.4 M).

	Non-reduced species	$1e^-$ RS	$2e^-$ RS
Re(dppz-12-NO_2)	270(sh), 285, 296, 318(sh), 352, 361	285, 296(sh), 357, 407, 490, 524, 743(sh), 836	274, 384(sh), 505, 669(sh)
Re(dppz-13-NO_2)	273, 298(sh), 317(sh), 364, 410(sh)	276, 291(sh), 343(sh), 400, 495, 533, 879	269, 329(sh), 382(sh), 579

3.5 Time Resolved Infrared Studies

The TRIR spectra of Re(dppz-12-NO_2) and Re(dppz-13-NO_2) have been collected in a range of solvents (d-DMSO, CH_3CN, CH_2Cl_2, THF and Toluene) following photoexcitation at 355 nm and are detailed below.

3.5.1 TRIR Spectroscopy in CH_3CN

The TRIR spectra of complexes Re(dppz-12-NO_2) and Re(dppz-13-NO_2) in CH_3CN are shown in Figure 4-14, with features summarised in Table 4-5. For Re(dppz-12-NO_2), at 1 ps after photoexcitation the parent bands are observed to bleach and the formation of several transient bands (2005 and 1880 cm^{-1}) at lower energies to the parent are observed. The transient species is assigned to an $IL\pi\pi^*$ state and is observed to decay

to the ground state with a lifetime which is in good agreement with parent recovery, shown in Figure 4-15.

The spectral profile of Re(dppz-13-NO_2) is significantly different to Re(dppz-12-NO_2). At 1 ps following photoexcitation the parent bands are observed to bleach and the formation of several transient bands are observed at higher energies to the parent, which are assigned to an MLCT(phz) state. This MLCT(phz) state is observed to decay to the ground state and is in good agreement with parent recovery, shown in Figure 4-15.

Table 4-5: A summary of the FTIR and TRIR spectral features observed for Re(dppz-12-NO_2) and Re(dppz-13-NO_2) in CH_3CN following 355 nm photoexcitation.

Re(dppz-12-NO_2)

ν (cm^{-1})	**τ decay (ps)**	**τ growth (ps)**	**Assignment**
2005, 1880	50 ± 10	-	IL$\pi\pi^*$
2019, 1919, 1900	-	37 ± 7	parent
2024, 1921, 1903			GS FTIR

Re(dppz-13-NO_2)

ν (cm^{-1})	**τ decay (ps)**	**τ growth (ps)**	**Assignment**
2088, 2006, 1970	25 ± 2	5 ± 1	MLCT(phz)
2021, 1919, 1901	-	30 ± 5	parent
2024, 1921, 1903			GS FTIR

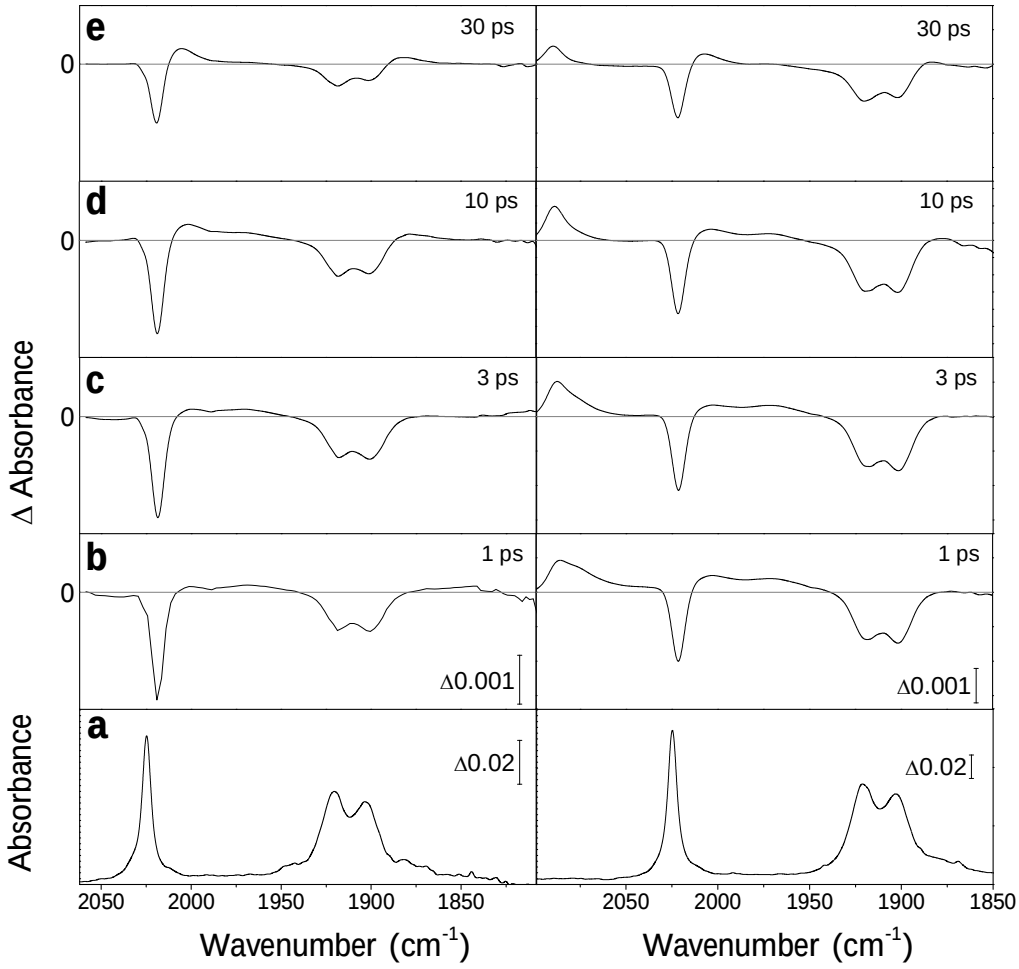

Figure 4-14: The FTIR (a) and TRIR (b-e) spectra of Re(dppz-12-NO_2) (left) and Re(dppz-13-NO_2) (right) in CH_3CN following 355 nm photoexcitation.

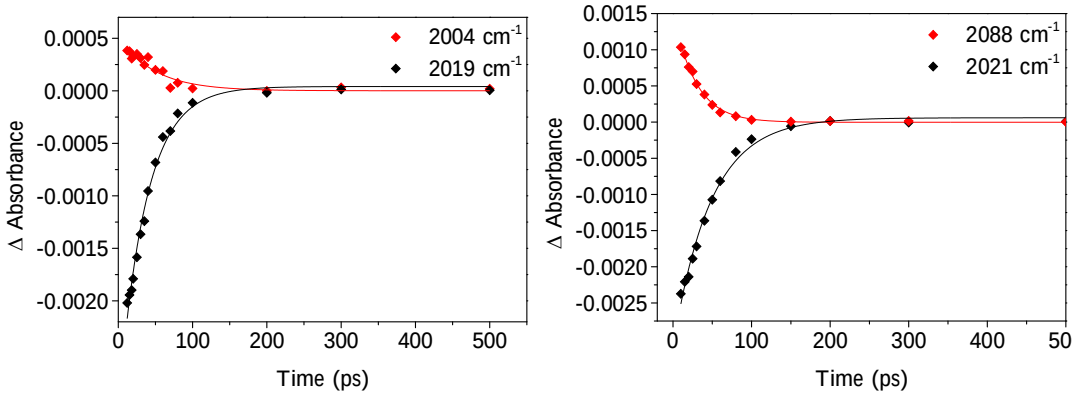

Figure 4-15: The kinetics of Re(dppz-12-NO_2) in toluene following 355 nm photoexcitation. The decay of the band at 2004 cm^{-1} assigned to an IL$\pi\pi^*$ state, is in good agreement with the growth of the band at 2019 cm^{-1} assigned to the parent (left). For Re(dppz-13-NO_2) the decay of the band at 2088 cm^{-1} assigned to an MLCT(phz) state, is in good agreement with the recovery of the band at 2021 cm^{-1} assigned to the parent (right).

3.5.2 TRIR Spectroscopy in CH_2Cl_2

The TRIR spectra of Re(dppz-12-NO_2) and Re(dppz-13-NO_2) in CH_2Cl_2 following photoexcitation are shown in Figure 4-16 with feature summarised in Table 4-6. For Re(dppz-12-NO_2) at 1 ps following photoexcitation, the parent bands are observed to bleach and several new transient bands are observed. These transient bands are assigned to an MLCT(phz) state, which is observed to decay to the ground state in good agreement with the parent recovery.

A different spectral profile is observed for Re(dppz-13-NO_2) where at 1 ps following photoexcitation the parent bands are observed to bleach and new transient bands observed. The band at 2066 cm^{-1} is assigned to an MLCT(phen) state and the band at 2080 cm^{-1} is assigned to an MLCT(phz) state. The MLCT(phen) state decays as the MLCT(phz) state is observed to grow in. Therefore the MLCT(phen) state is observed to decay to the MLCT(phz) state and subsequently the MLCT(phz) state is observed to decay to the ground state in good agreement with the recovery of the parent. The kinetics for the processes detailed are shown in Figure 4-17.

Table 4-6: A summary of the FTIR and TRIR spectral features observed for Re(dppz-12-NO_2) and Re(dppz-13-NO_2) in CH_2Cl_2 following 355 nm photoexcitation.

Re(dppz-12-NO_2)

ν (cm^{-1})	τ decay (ps)	τ growth (ps)	Assignment
2080, 2010, 1971	73 ± 8	-	MLCT(phz)
2024, 1925, 1901	-	83 ± 3	parent
2026, 1926, 1901	-	-	GS FTIR

Re(dppz-13-NO_2)

ν (cm^{-1})	τ decay (ps)	τ growth (ps)	Assignment
2066	11 ± 8	-	MLCT(phen)
2080, 2006, 1966	219 ± 8	3.1 ± 0.2	MLCT(phz)
2022, 1923, 1898	-	207 ± 2	parent
2025, 1925, 1901	-	-	GS FTIR

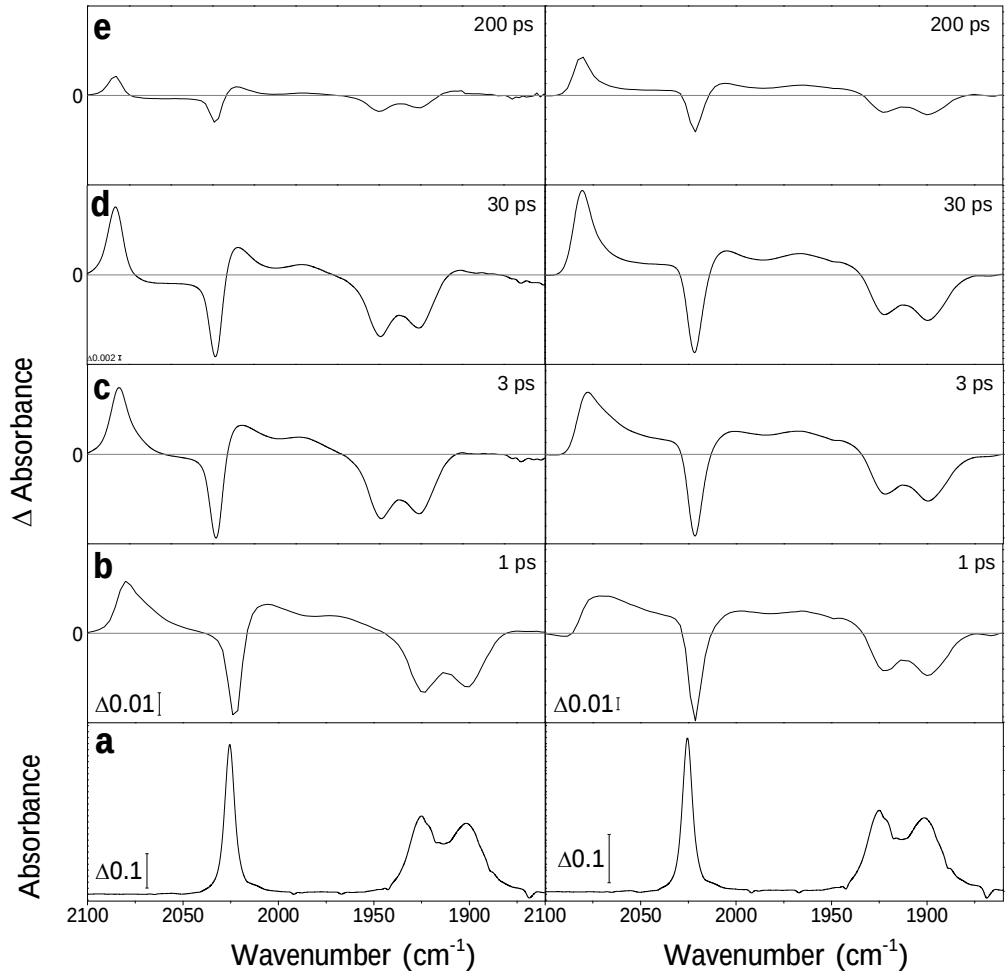

Figure 4-16: The FTIR (a) and TRIR (b-e) spectra of Re(dppz-12-NO_2) (left) and Re(dppz-13-NO_2) (right) in CH_2Cl_2 following 355 nm photoexcitation.

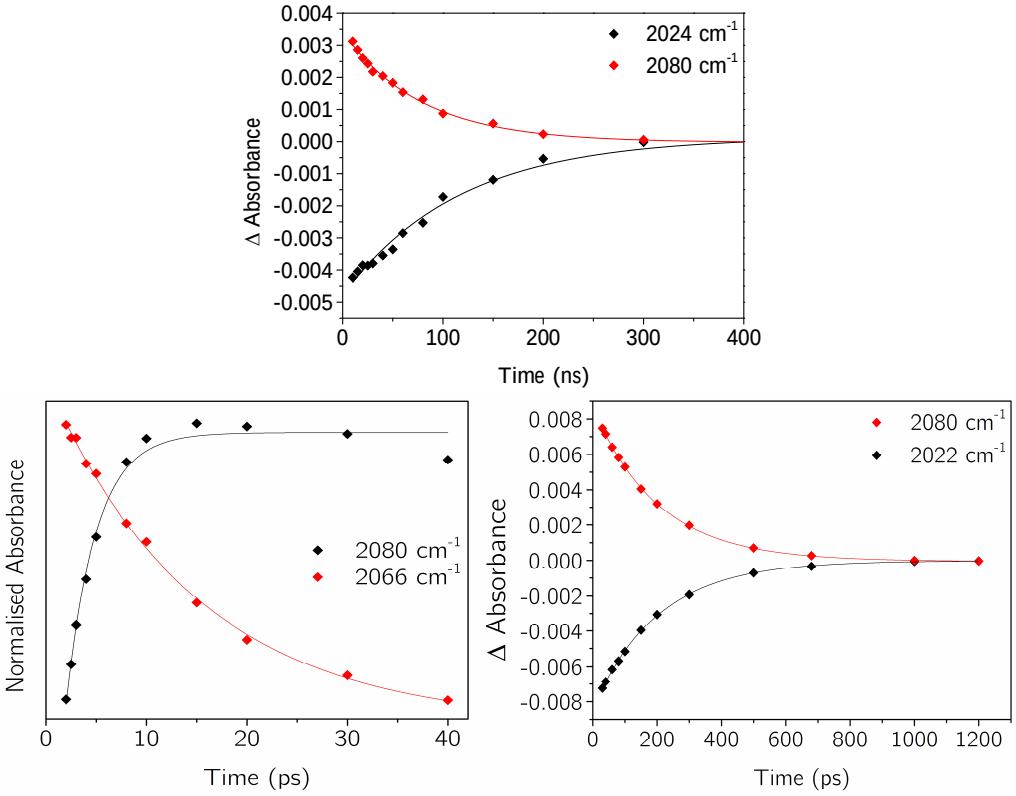

Figure 4-17: The kinetics of Re(dppz-12-NO_2) and for Re(dppz-13-NO_2) in CH_2Cl_2 following 355 nm photoexcitation. The decay of the band at 2080 cm^{-1} assigned to an MLCT(phz) state, is in good agreement with the recovery of the band at 2019 cm^{-1} assigned to the parent (top and bottom right for Re(dppz-12-NO_2) and Re(dppz-13-NO_2) respectively). The decay of the band at 2066 cm^{-1} assigned to an MLCT(phen) state, is in good agreement with the growth of the band at 2080 cm^{-1} assigned to an MLCT(phz) state (bottom, left).

3.5.3 TRIR Spectroscopy in THF

The TRIR spectra of Re(dppz-12-NO_2) and Re(dppz-13-NO_2) collected in THF following photoexcitation are shown in Figure 4-18 and the features observed are summarised in Table 4-7. At 1 ps following photoexcitation, parent bleaches and several transient bands are observed for both complexes. The transient band at 2072 cm^{-1} assigned to an MLCT(phen) state is observed to decay as the band at 2082 cm^{-1} assigned to an MLCT(phz) state intensifies, indicating the decay of an MLCT(phen) state to an MLCT(phz) state. The MLCT(phz) state is subsequently observed to decay to the ground state, which is in good agreement with parent recovery. The kinetics for the processes detailed are shown in Figure 4-19.

Table 4-7: A summary of FTIR and TRIR spectral features observed for Re(dppz-12-NO_2) and Re(dppz-13-NO_2) in THF following 355 nm photoexcitation.

Re(dppz-12-NO_2)

ν (cm^{-1})	τ decay (ps)	τ growth (ps)	Assignment
2066	9 ± 2	-	MLCT(phen)
2082, 1998, 1965	100 ± 30	3.7 ± 0.3	MLCT(phz)
2019, 1921, 1893	-	120 ± 30	parent
2021, 1922, 1896	-	-	GS FTIR

Re(dppz-13-NO_2)

ν (cm^{-1})	τ decay (ps)	τ growth (ps)	Assignment
2066	8 ± 1	-	MLCT(phen)
2080, 2000, 1961	190 ± 20	3.3 ± 0.1	MLCT(phz)
2019, 1921, 1893	0.9 ± 0.2	185 ± 6	parent
2021, 1921, 1897	-	-	GS FTIR

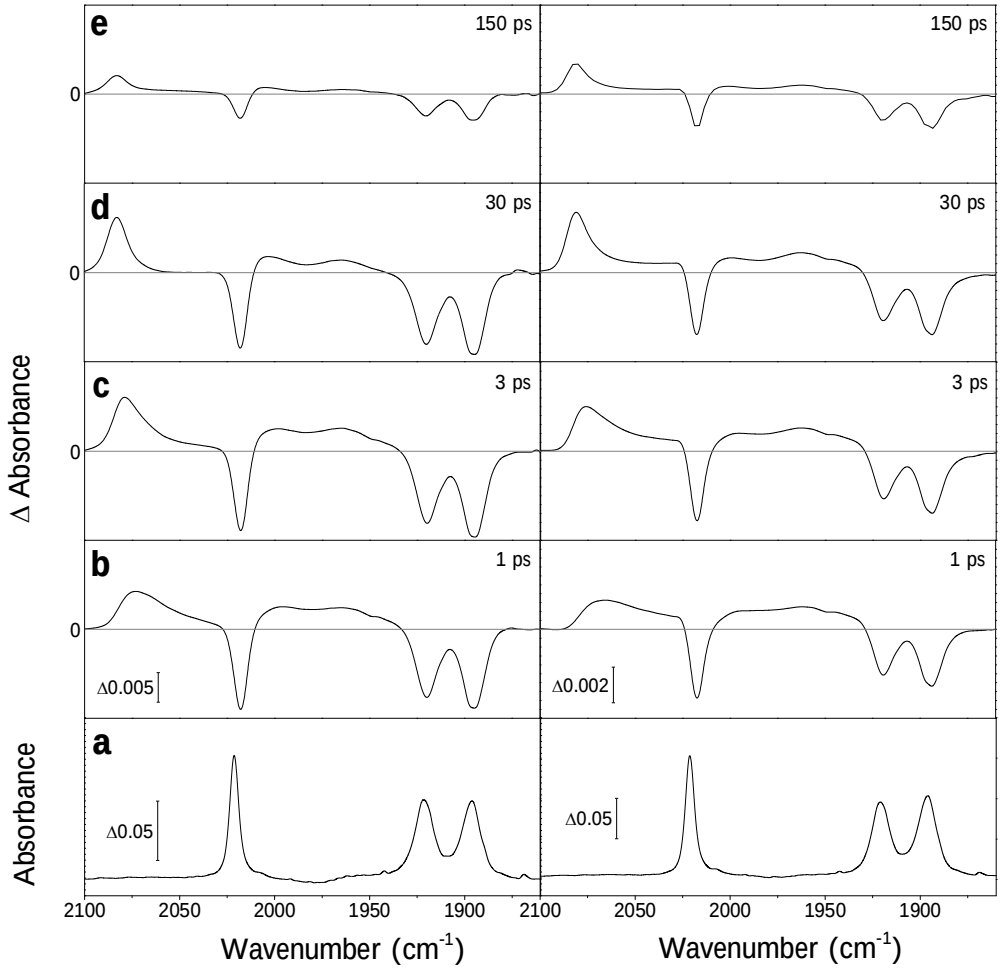

Figure 4-18: FTIR (a) and TRIR (b-e) spectra of Re(dppz-12-NO_2) (left) and Re(dppz-13-NO_2) (right) in THF following 355 nm photoexcitation.

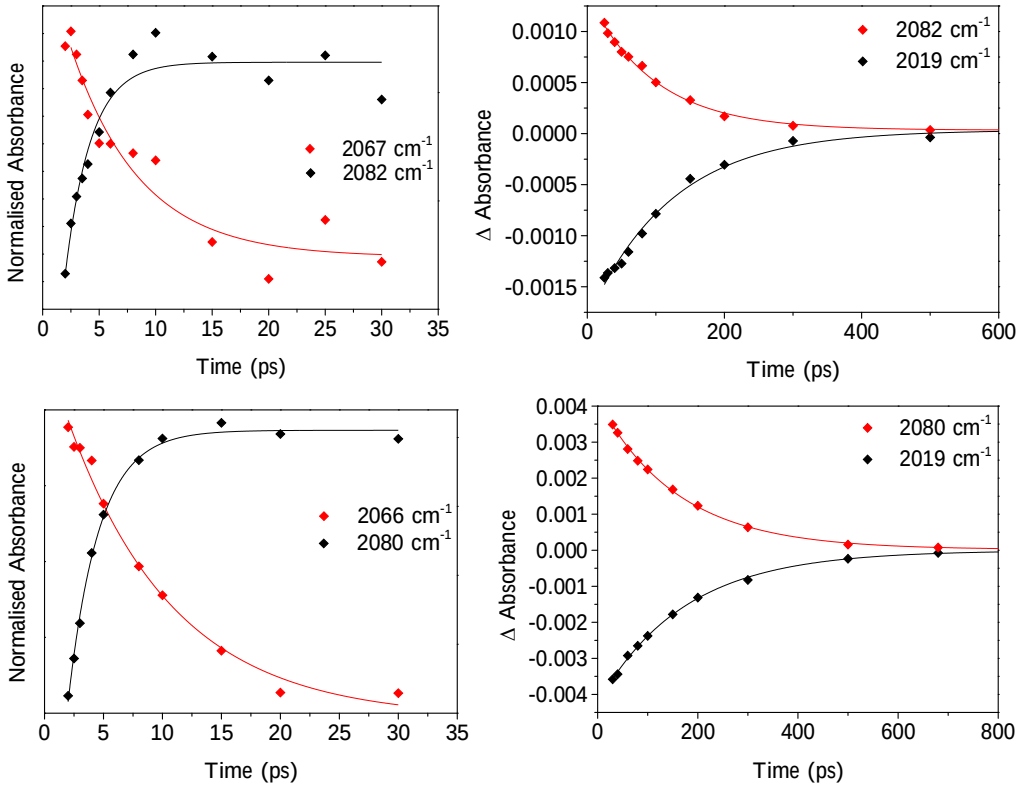

Figure 4-19: The kinetics of Re(dppz-12-NO_2) (top) and Re(dppz-13-NO_2) (bottom) in THF following 355 nm photoexcitation. The decay of the band at *ca.* 2066 cm^{-1} assigned to an MLCT(phen) state, is in good agreement with the growth of the band at *ca.* 2081 cm^{-1} assigned to an MLCT(phz) state (left). The decay of the band at *ca.* 2081 cm^{-1} assigned to an MLCT(phz) state, is in good agreement with the recovery of the band at 2019 cm^{-1} assigned to the parent (right).

3.5.4 TRIR Spectroscopy in Toluene

The TRIR spectra of complexes Re(dppz-12-NO_2) and Re(dppz-13-NO_2) in toluene following photoexcitation are shown in Figure 4-20 and features summarised in Table 4-7. For both complexes at 1 ps following photoexcitation parent bands were observed to bleach and several transient bands are observed to form. Over the first 10 ps, the transient band at *ca.* 2059 cm^{-1} is observed to decay, while the transient band at 2072 cm^{-1} is observed to intensify, this has been assigned as the interconversion of states from MLCT(phen) to MLCT(phz). The MLCT(phz) state subsequently decays to the ground state, which is in good agreement with parent recovery. In comparison to the other solvents the $\Delta\nu$ observed is not as large for both the MLCT(phen) and MLCT(phz) states, where the MLCT(phz) band at 2072 cm^{-1} is only shifted by +53 cm^{-1} compared

to the parent. However the band has been assigned as representative of an MLCT(phz) state owing to the lack of emission observed for both complexes in toluene.

Table 4-7: A summary of FTIR and TRIR spectral features observed for Re(dppz-12-NO_2) and Re(dppz-13-NO_2) in toluene following 355 nm photoexcitation.

Re(dppz-12-NO_2)

ν (cm^{-1})	τ decay (ps)	τ growth (ps)	Assignment
2058	7 ± 3	-	MLCT(phen)
2072, 1996, 1956	3430 ± 50	4.3 ± 0.4	MLCT(phz)
2019, 1925, 1893	-	3500 ± 300	parent
2021, 1922, 1896	-	-	GS FTIR[a]

Re(dppz-13-NO_2)

ν (cm^{-1})	τ decay (ps)	τ growth (ps)	Assignment
2060	15 ± 2	-	MLCT(phen)
2072	4200 ± 500	5.8 ± 0.2	MLCT(phz)
2020, 1926, 1894	-	4200 ± 200	parent
2023, 1925, 1896	-	-	GS FTIR

[a]GS FTIR data from measurements in THF due to solubility

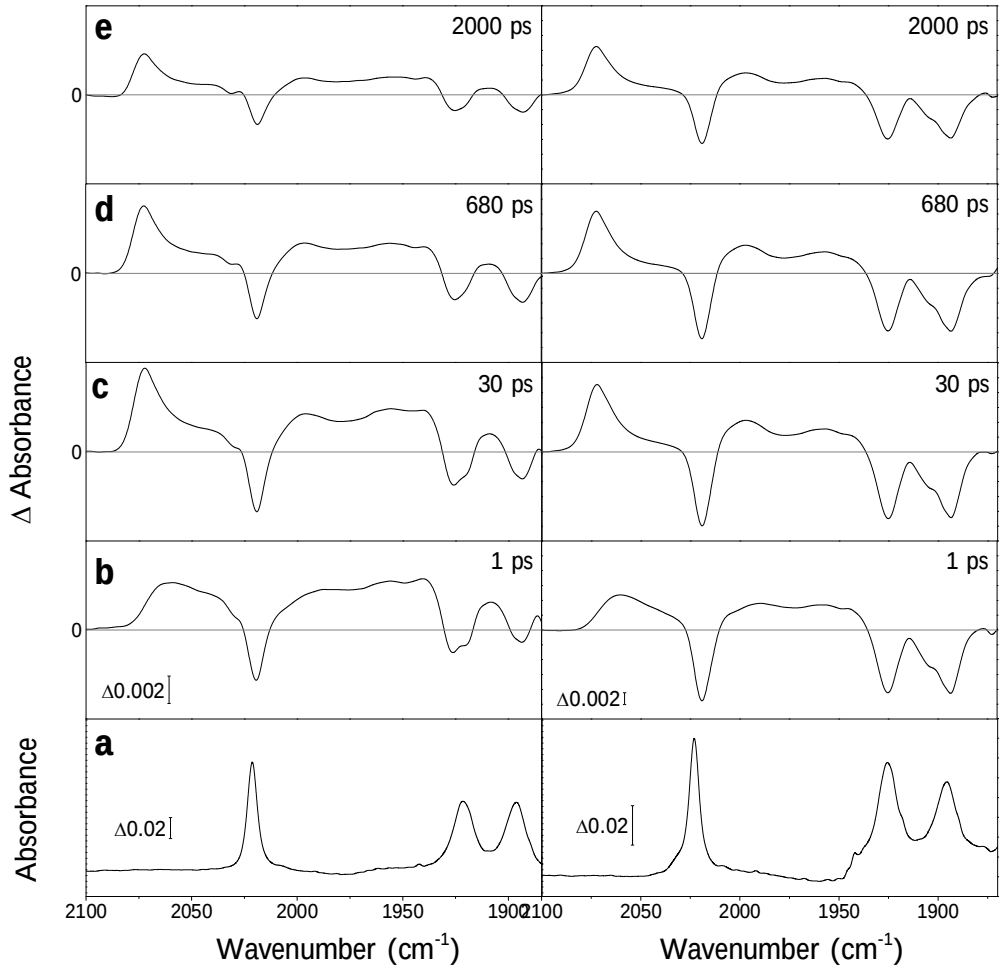

Figure 4-20: The FTIR (a) and TRIR (b-e) spectra of Re(dppz-12-NO_2) (left) and Re(dppz-13-NO_2) (right) in toluene following 355 nm photoexcitation. For Re(dppz-12-NO_2) the FTIR is shown in THF due to solubility.

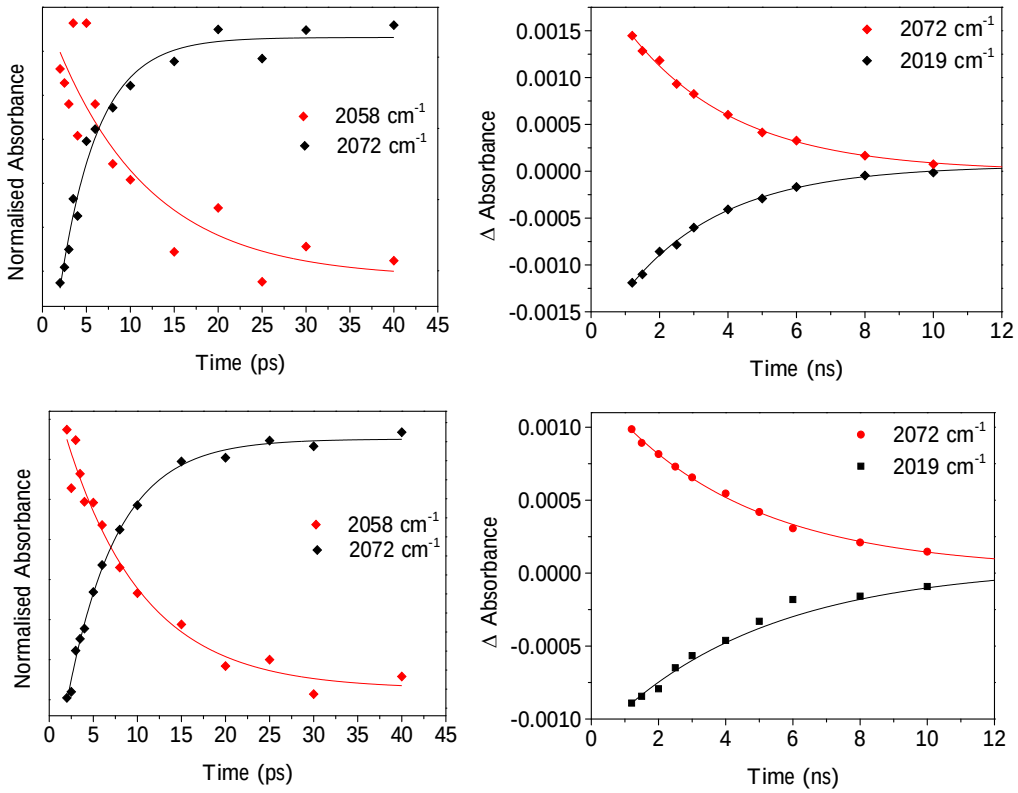

Figure 21: The kinetics of Re(dppz-12-NO_2) (top) and Re(dppz-13-NO_2) (bottom) in toluene following 355 nm photoexcitation. The decay of the band at 2058 cm^{-1} assigned to an MLCT(phen) state, is in good agreement with the growth of the band at 2072 cm^{-1} assigned to an MLCT(phz) state (left). The decay of the band at 2072 cm^{-1} assigned to an MLCT(phz) state, is in good agreement with the recovery of the band at 2019 cm^{-1} assigned to the parent (right).

3.6 Molecular Orbital Calculations

DFT calculations have been used to derive the geometry-optimised structure of the ground state for the complexes Re(dppz-12-NO_2) and Re(dppz-13-NO_2) in the gas phase and are shown in Figure 4-7. The calculations have provided a clear insight into the molecular orbital framework for each complex. The partial energy diagram for both complexes and representative MOs are shown in Figure 4-22. Further MOs are shown in Appendix B. Comparisons have been drawn to [Re(dppz)$(CO)_3$Cl], the partial energy diagram of which is discussed and shown in Chapter 2.

For both complexes the HOMO is predominantly Re(dπ) in nature, similar to [Re(dppz)$(CO)_3$Cl] and the HOMO-1 to HOMO-4 are also Re(dπ) while the HOMO-5

is dppz(π) in nature and are calculated at lower energies. The HOMO for Re(dppz-12-NO_2) is slightly lower in energy than the corresponding HOMO orbital for Re(dppz-13-NO_2) at -5.77 and -5.71 eV respectively. The HOMO/LUMO energy gap is slightly larger for Re(dppz-13-NO_2) than for Re(dppz-12-NO_2) at 1.98 and 2.07 eV respectively.

For both complexes the LUMO is phz/NO_2(π*) in agreement with the spectroelectrochemistry and cyclic voltammetry where, the first electron reduced species has been tentatively assigned as NO_2 in nature. This differs from the phz(π*) in nature LUMO observed for [Re(dppz)$(CO)_3$Cl]. The LUMO is lower in energy for Re(dppz-12-NO_2) than for Re(dppz-13-NO_2) at -3.782 and -3.646 eV respectively, indicating the increased electron withdrawing behaviour of 12-NO_2 compared to 13-NO_2. Furthermore, for Re(dppz-13-NO_2) the LUMO+1 is observed to be phen(π*) in nature while the LUMO+2 is observed to be dppz(π*) in nature, similar to [Re(dppz)$(CO)_3$Cl]. However, for Re(dppz-12-NO_2) the phen(π*) MO is observed to be at similar energy as for Re(dppz-13-NO_2) but the dppz(π*) is at lower energy, resulting in the LUMO+1 for this complex as dppz(π*) in nature and the LUMO+2 as phen(π*) in nature. The dppz(π*) and phen(π*) energy reversal between the complexes is consistent with the much more electron withdrawing effect of 12-NO_2 compared to 13-NO_2. As the electron density is favourably localised on the dppz ligand for Re(dppz-12-NO_2) compared to only on the phen moiety.

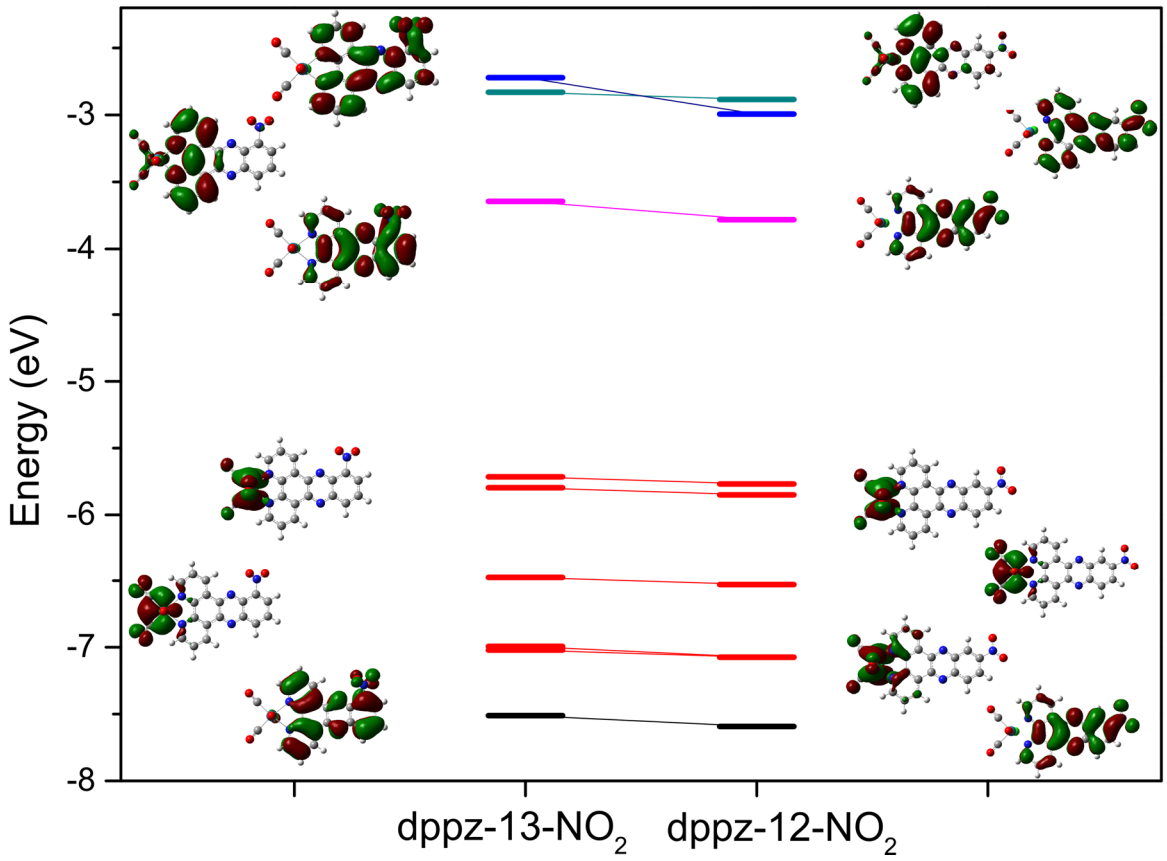

Figure 4-22: The partial energy diagram and representative molecular orbitals for Re(dppz-13-NO_2) (left) and Re(dppz-12-NO_2) (right). Metal based occupied MOs are shown in red and ligand centred occupied MOs in black. The unoccupied phen, phz and dppz MOs are shown in pink, turquoise and blue respectively.

3.7 Effect of NO_2 substitution

The NO_2 group is considered as an electron-withdrawing group, owing to the partial positive charge on the nitrogen atom and to resonance effects, thus the group is considered able to deactivate the aromaticity of the dppz ligand π* system. This results in a lowering of the phz energy and encourages the population of an MLCT(phz) state. The spectroelectrochemistry and CV of both complexes indicate that the LUMO is not solely phz in nature but also contains significant NO_2 character. The two electron reduced species is localised on the phz moiety as expected for the $1e^-$ reduced species for other $[Re(dppz)(CO)_3Cl]$ complexes.[25, 32] The MO calculations are consistent with the assignment of the LUMO and LUMO+1 as phz-NO_2 and dppz in nature respectively.

The effect of the NO_2 group lowering the phz energy is further supported in the TRIR spectra. For Re(dppz-12-NO_2) and Re(dppz-13-NO_2) in CH_2Cl_2 the most stable excited state is MLCT(phz), whereas for $[Re(dppz)(CO)_3Cl]$ in CH_2Cl_2 the lowest excited states are MLCT(phen)/^{1}LTππ*.[32]

Following the investigation into the effect of NO_2 substitution on the phz portion of the dppz ligand on the photophysical properties observed, the effect of the substituent position has been examined. The results indicate that the NO_2 substituted onto the 12-position of the phz moiety has more of an electron withdrawing effect than when substituted on the 13-position. Therefore the MLCT(phz) is lower in energy for Re(dppz-12-NO_2) than for Re(dppz-13-NO_2). This results in a more distance charge separated MLCT(phz) state for Re(dppz-12-NO_2) than for Re(dppz-13-NO_2) and therefore the MLCT(phen)/MLCT(phz) energy gap is larger for the former compared to the latter. As detailed in Chapter 3, the rate of MLCT(phen)/MLCT(phz) interconversion of states is dictated by the size of this energy gap, where the larger the energy gap the more populated the MLCT(phz) state. The gas phase MO calculations are consistent with a larger MLCT(phen)/MLCT(phz) energy gap for Re(dppz-12-NO_2) (0.90 eV) than for Re(dppz-13-NO_2) (0.82 eV). Furthermore, from the absorption spectra, more MLCT(phen) character is observed for Re(dppz-13-NO_2) than for Re(dppz-12-NO_2).

From the TRIR spectra the interconversion of MLCT(phen) to MLCT(phz) states is faster for Re(dppz-12-NO_2) than for Re(dppz-13-NO_2). The excited state is longer lived for Re(dppz-13-NO_2) than Re(dppz-12-NO_2) in all solvents where an MLCT(phz) is observed as the most stable excited state *i.e.* CH_2Cl_2, THF and toluene. This would indicate that the energy gap for MLCT(phen)/MLCT(phz) is smaller for Re(dppz-13-NO_2) than for Re(dppz-12-NO_2) and therefore more MLCT(phen) state is populated for Re(dppz-13-NO_2) than Re(dppz-12-NO_2), resulting in a longer excited state lifetime.

As discussed in Chapter 2, the dihedral angle between the donor and the acceptor moieties has a significant effect on the photophysical properties observed.[63, 66, 84] Re(dppz-12-NO_2) and Re(dppz-13-NO_2) exhibit a change in the dihedral angle, defined as between the NO_2 group and the phz portion of the dppz ligand. The 12-NO_2 group is pseudo-coplanar (dihedral angle 0.036°) with respect to the dppz ligand while the 13-NO_2 group exhibits a dihedral angle of 36°. This dihedral angle has been assigned as affecting the amount of resonance observed, where the NO_2 group on the 12-position is tentatively assigned as being more electron withdrawing compared to the 13-position. Increased resonance behaviour with the NO_2 group causes a deactivating of the aromatic ring and thus a more electron withdrawing effect. Previous DFT calculations of para-nitro-aniline and nitrobenzene have shown that as the dihedral C-N angle increases the electron withdrawing effect of the NO_2 decreases, due to decreased resonance efficiency.[169, 170]

The observation that the NO_2 group in the 12 substituted position on the dppz ligand (meta substituted) is more electron withdrawing than the NO_2 group in the 13 (ortho substituted) substituted position, agrees with previous conclusions from Chapter 3. The Re(dppp3) complex (meta position N) is more electron withdrawing than Re(dppp2) (ortho positioned N) and more MLCT(phz) character is observed, which may be attributed to conjugation effects previously observed for NO_2 substituted complexes.[62] Therefore following on from the conclusion that substituent position has a profound effect on the photophysical properties observed, the effect of surrounding solvent media was investigated.

The MLCT(phen)/MLCT(phz) energy gap may be altered by the solvent environment and it is expected that more polar solvents would stabilise charge transfer states further in comparison to less polar solvents, resulting in a larger difference in energy between the MLCT(phen) and MLCT(phz) states. The results obtained from the TRIR data, summarised in table 4-8, do not appear to show a consistent trend.

Table 4-8: The lifetime of the interconversion of states from MLCT(phen) to MLCT(phz) from TRIR measurements for Re(dppz-12-NO_2) and Re(dppz-13-NO_2). The values for the dielectric constant are taken from references [151, 152].

Solvent	ε_r	τ MLCT(phen)/MLCT(phz) interconversion (ps)	
		Re(dppz-12-NO_2)	Re(dppz-13-NO_2)
CH_3CN	37.5	-	-
CH_2Cl_2	8.9	-	7 ± 4
THF	7.5	6 ± 3	6 ± 2
Toluene	2.3	6 ± 1	10 ± 5

The excited state lifetimes are summarised in Table 4-9 and are observed to decrease with increasing solvent polarity, owing to further stabilisation of charge transfer states with increasing solvent polarity. The lifetime of the excited state observed in toluene is more than x10 of the lifetime observed in the other solvents and this is attributed to the contribution from an MLCT(phen) state being present. The excited state lifetimes observed for Re(dppz-12-NO_2) and Re(dppz-13-NO_2) are nearly three orders of magnitude shorter than for [Re(dppz)$(CO)_3$Cl].[32] This is attributed to the localisation of the electron density in the MLCT state on the NO_2 group, consistent with previous observations for NO_2 substituted Re(diimine) complexes.[153-155] The localisation of electron density on the NO_2 group is also consistent with the previous experimental results within this work which demonstrate significant NO_2 contribution to the phz based LUMO.

Table 4-9: The nature and lifetime of the most stable excited state observed for Re(dppz-12-NO_2) and Re(dppz-13-NO_2) in a range of solvents listed. The values are taken from the TRIR data.

Solvent	Re(dppz-12-NO_2)		Re(dppz-13-NO_2)	
	Nature ES	**τ (ps)**	**Nature ES**	**τ (ps)**
CH_3CN	IL$\pi\pi^*$	50 ± 10	MLCT(phz)	25 ± 2
CH_2Cl_2	MLCT(phz)	73 ± 8	MLCT(phz)	219 ± 8
THF	MLCT(phz)	100 ± 30	MLCT(phz)	190 ± 20
Toluene	MLCT(phz)	4200 ± 500	MLCT(phz)	3430 ± 50

In CH_3CN, the most polar solvent investigated within this work, an IL$\pi\pi^*$ state is observed as the most stable excited state for Re(dppz-12-NO_2) and an MLCT(phz) state for Re(dppz-13-NO_2). The increased polarity has caused this IL$\pi\pi^*$ state to be accessed which has been observed before for [Re(dppz)$(CO)_3$Cl] complexes with electron withdrawing substituents including in Chapter 3 and for [Re(dppz-Br(CF_3))$(CO)_3$Cl].[34] The access of an IL$\pi\pi^*$ state for Re(dppz-12-NO_2) and not for Re(dppz-13-NO_2) is in agreement with the assignment of the 12-position being more electron withdrawing.

4.4 Conclusions

The complexes [Re(dppz-12-NO_2)$(CO)_3$Cl] and [Re(dppz-13-NO_2)$(CO)_3$Cl] have been synthesised and their photophysical properties investigated comprehensively through emission, absorption, infrared and time resolved infrared studies. The spectroscopic results have been supported through DFT calculations.

Initially the effect of substituting the phz moiety of dppz with the electron withdrawing group, NO_2 has been investigated. The NO_2 group has been shown to lower the phz energy. This has been demonstrated through the presence of an MLCT(phz) state in the TRIR for both complexes which is not observed for the analogous unsubstituted dppz complex, which is further supported by the non-emissive behaviour of the complexes in a range of solvents.

Furthermore, the one electron and two electron reduced species of both complexes has been probed by CV and spectroelectrochemistry. The results have indicated that the substitution of the NO_2 group results in the presence of two reversible reduction processes, the first of which is localised on the NO_2 group and the second on the phz moiety. The localisation of electron density on the NO_2 group is consistent with the considerably shorter excited state lifetimes observed from the TRIR data compared to [Re(dppz)$(CO)_3$Cl].

Subsequently, the effect of substituent position on the phz moiety on the electron withdrawing group behaviour has been assessed. The NO_2 group substituted at the 12-position has been shown to exhibit more of an electron withdrawing effect than when substitution at the 13-position attributed to resonance effects. This has been indicated by more MLCT(phen) state character observed in the TRIR spectra of 13-NO_2 complex than the 12-NO_2 complex, supported by similar observation from the absorption spectra and by the calculated MO energies, which show a larger phen(π^*)/phz(π^*) energy gap for 12-NO_2 than for 13-NO_2.

Chapter 5

The Photophysical Properties of Rhenium Diimine Complexes in Apolar Media

1 Introduction

As shown in Chapters 3 and 4, the solvent environment can have a profound effect on the photophysical properties of [Re(dppz)(CO)$_3$Cl] derivative complexes. However, owing to the solubility of these complexes, previous studies have been limited by solvent media. In addition previous work has shown that Re(diimine) complexes are interesting potential photocatalysts for CO_2 reduction,[102-104, 171, 172] although current implementation requires the use of a co-solvent for solubility.[173-179] Therefore this Chapter will focus on the synthesis of previously unreported Re(diimine) complexes which are soluble in apolar media and to examine their photophysical properties. Dielectric constant will be considered as a metric for polarity.

Various methods have been reported in literature to increase the solubility of organometallic complexes in low dielectric media including the addition of co-solvents,[173-179] and using hydrophobic counterions.[173, 180, 181] Furthermore, advances in analytical techniques have also allowed for the probing of very low solubility solutions for example the implementation of an ultramicroelectrode for cyclic voltammetry in CO_2.[173]

Organic co-solvents have been shown to improve the solubility of ions in low dielectric solvents such as CO_2, including methanol,[173, 174] dimethylformamide,[175] acetonitrile[173, 176] and water.[177-179] Wightman *et al.* exhibited the water aided solvation of electrolyte $[^nHex_4N]^+$ $[PF_6]^-$ allowing for a defined ferrocene (Fc/Fc^+) redox wave to be observed.[177-

[179] Further work with the use of water as a co-solvent has included the electrochemical deposition of zinc oxide meso-crystals[182] and electroplating of nickel and copper.[183, 184] However, the use of organic co-solvents often results in a reduction of the electrochemical window of the solvent.[185]

The exploration of counter ions has been studied for a range of SCFs where Abbott *et al.*[180, 181] demonstrated that very hydrophobic electrolytes could dissolve into CO_2 to a limited extent without the use of counterions. The results demonstrated that electrolytes of the class tetra-alkylammonium and tetra-arylborate salts had the highest solubility.[77, 78] The focus of hydrophobic counterions has shifted to halogenation of ions, as more recent work has demonstrated that increased fluorination and the size of the counterion may aid in solubility.[173] Furthermore, tetra-alkylammonium and tetra-arylborate salts (BAr^f), have been shown to be most effective at improving solubility of complexes in low polarity media and therefore will be the focus of this work.[180, 186, 187]

For the complex $[NBu^n_4][BAr^f]$ a range of BAr^f anions have been investigated: $[B(C_6H_4F)_4]^-$, $[B(C_6H_4CF_3)_4]^-$, $[B(C_6F_5)_4]^-$ and $[B(3,5\text{-}C_6H_3(CF_3)_2)_4)]^+$ alongside a range of fluorinated tetra-alkylammonium cations $[NR_fMe_3]^+$ and $[NR_fBu^n_3]^+$ (R_f = $CF_3(CF_2)_7(CH_2)_3$).[173] The results demonstrate that increased fluorination increases solubility in CO_2 and that the fluorination of cations demonstrated little effect on the solubility of a complex while the fluorination of the anion yielded a far better result. For this reason, fluorination of the anion will be the focus of this work.

Further work has investigated an even more fluorinated BAr^f derivative anion,[188] $[B(3,5\text{-}C_6H_3(R_{f6})_2)_4)]^-$ (BAr^{f6}), structure shown in Figure 5-1, which has been shown to increase the solubility of the cation $[Co(en)_3]Cl_3]$ in perfluoromethylcyclohexane (PFMCH). The anion resulted in the complete transfer of the cation from the organic phase to the PFMCH phase.

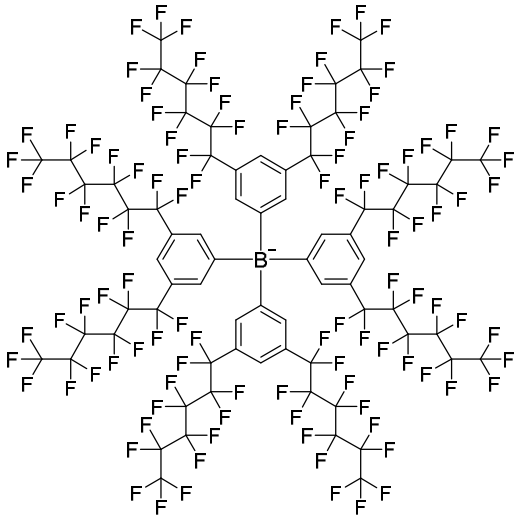

Figure 5-1: The structural formula of the [B(3,5-$C_6H_3(R_{f6})_2)_4$)] (BAr^{f6}) anion.

Perfluorinated solvents have very low polarities ($\varepsilon < 2$),[152] and as a result, generally have low miscibility in organic solvents. This allows for the formation of biphasic layers which is key for anion exhange. For this Chapter perfluoromethyl cyclohexane (PFMCH) will be the low dielectric solvent of focus.

This chapter will focus on the commonly reported Re(diimine) complexes $[Re(bpy)(CO)_3L]^+$ and $[Re(dppz)(CO)_3L]^+$. In order to use large tetra-arylborate anions, the ionic complexes $[Re(bpy)(CO)_3L]^+$ and $[Re(dppz)(CO)_3L]^+$ need to be investigated, and therefore to achieve this the spectator axial ligand (L) must be neutral e.g. pyridine. Previous work has investigated the effect of altering the axial ligand in $[Re(bpy)(CO)_3L]^+$ on the photophysics observed.[86, 189, 190] Modifying the axial ligand affects the state energetics by influencing the electron density on the central metal ion (Re) which is directly involved in the excited state.[86] Therefore altering the axial ligand is often exploited for changing the energy level of the lowest excited state, for example extending the π-conjugation of L lowers the ππ* levels and may even result in phosphorescence from the axial ligand.[86, 190]

Work by Yue *et al.*[191] focussed on a series of $[Re(bpy)(CO)_3L]^+$ complexes where L = benzonitrile (BN), 4-dimethylaminobenzonitrile (4-DMABN) and 3-dimethylaminobenzonitrile (3-DMABN), Figure 5-3. These complexes were shown to be sensitive to the substitution of L and the solvent media due to the presence of several

close lying states. Inspection of TRIR spectra results in the assigned excited states shown in Figure 5-3. For BN, 4-DMABN and 3-DMABN in CH_2Cl_2 the excited states are MLCT in nature, where an initially populated ^{1}MLCT relaxes on the picosecond timescale to a ^{3}MLCT state. However, for 3-DMABN this ^{3}MLCT state decays on the picosecond timescale to a ^{3}IL state. This lowest energy populated state (^{3}IL) for 3-DMABN exhibits a lifetime an order of magnitude longer than for the lowest energy populated state (^{3}MLCT) for BN and 4-DMABN. Furthermore, when the complexes are studied in a CH_3OH/CH_2Cl_2 mixture, the addition of CH_3OH is observed to decrease the energies of charge transfer states, as a result for 3-DMABN the lowest energy populated excited state is a Re(dπ)3DMABN(π)→bpy(π*) CT state labelled as ^{3}MLLCT. For 4-DMABN a similar ^{3}MLLCT state is observed but the state is in equilibrium with an LLCT state, arising from the para-nature of the amine donating group resulting in a quinoidal resonance structure. As a result charge transfer coupled across the entire 4-DMABN ligand is possible.

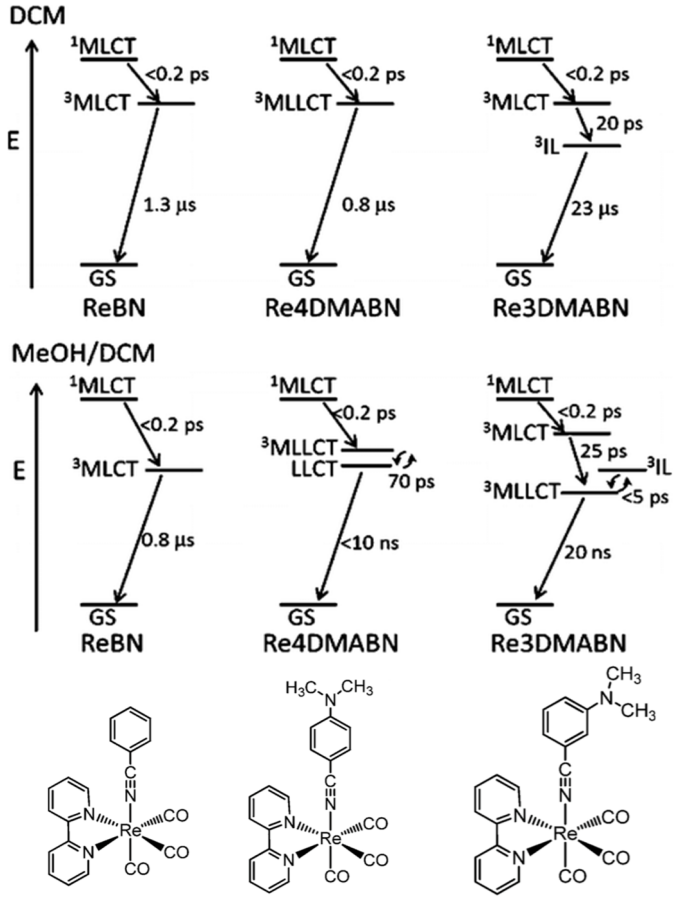

Figure 5-3: Jabłoński diagrams and structures for ReBN, Re4DMABN and Re3DMABN. Reproduced from reference 191.

Various axial ligands have previously been investigated including halides and pyridine (py) derivatives. As the work requires a cationic complex, L = py-R derivatives will be the main focus, with a comparison drawn to the neutral complex, where L = Cl^-. Re(diimine) complexes [Re(diimine)$(CO)_3$L] where L=py-R have been shown to be good sensors for metal ions,[192] anions,[193] indole binding proteins,[194] and pH changes.[195] Firstly the effect of changing the axial ligand on the photophysics of $[Re(bpy)(CO)_3L]^+$ will be discussed where the photophysics observed for L = Cl^- and a range of pyridine derivatives are detailed in Table 5-1.

Table 5-1: A summary of the MLCT excited state and lifetime observed for $[Re(bpy)(CO)_3Cl]$ and $[Re(bpy)(CO)_3(py\text{-}R)]^+$.

Complex	Solvent	MLCT		Ref
		λ_{em} (nm)	τ (ns)	
$[Re(bpy)(CO)_3Cl]$	CH_2Cl_2	622	51	190, 196
$[Re(bpy)(CO)_3Cl]$	CH_3CN	622	25	106, 108 197, 198
$[Re(bpy)(CO)_3Cl]$	THF		65	198
$[Re(bpy)(CO)_3Br]$	THF	610	55	171, 199
$[Re(bpy)(CO)_3(py)]^+$	H_2O	567	200	189
$[Re(bpy)(CO)_3(py)]^+$	CH_3CN	558	658	86
$[Re(bpy)(CO)_3(py)]^+$	CH_2Cl_2	558	669	190
$[Re(bpy)(CO)_3(4\text{-}CH_3py)]^+$	CH_3CN	564	535	86
$[Re(bpy)(CO)_3(3\text{-}CH_3py)]^+$	CH_3CN	566	619	86
$[Re(bpy)(CO)_3(3,5\text{-}(CH_3)_2py)]^+$	CH_3CN	564	589	86
$[Re(bpy)(CO)_3(3\text{-}NCpy)]^+$	CH_3CN	546	964	86
$[Re(bpy)(CO)_3(4\text{-}NCpy)]^+$	CH_3CN	556	789	86
$[Re(bpy)(CO)_3(2\text{-}CH_3py)]^+$	CH_3CN	560	721	86
$[Re(bpy)(CO)_3(2,4,6\text{-}(CH_3)_3py)]^+$	CH_3CN	566	585	86
$[Re(bpy)(CO)_3(AP)]^+$	CH_2Cl_2	597	129	190
$[Re(bpy)(CO)_3(DMAP)]^+$	H_2O	602	13	189
$[Re(bpy)(CO)_3(DMAP)]^+$	CH_3CN	616	110	86
$[Re(bpy)(CO)_3(DMAP)]^+$	CH_2Cl_2	610	95	190
$[Re(bpy)(CO)_3(C_2H_5py)]^+$	CH_2Cl_2	567	604	190
$[Re(bpy)(CO)_3(4\text{-}Phpy)]^+$	CH_3CN	568	561	86
$[Re(bpy)(CO)_3(3\text{-}CH_3COpy)]^+$	CH_3CN	556	789	86
$[Re(bpy)(CO)_3(4\text{-}CH_3COpy)]^+$	CH_3CN	552	837	86
$Re(bpy)(CO)_3(bnNCS)]^+$	H_2O	527	1200	189
$[Re(bpy)(CO)_3(MI)]^+$	CH_2Cl_2	589	161	190

*bnNCS benzyl isocyanide, AP Aminopyridine, MI methylimidazole

[Re(bpy)(CO)$_3$Cl] exhibits an MLCT state (τ = 25 ns in CH_3CN) which is Re(dπ)bpy(π^*) in nature. In the TRIR spectra following photoexcitation at 400 nm, the parent bands are observed to bleach and three new transient bands are observed to form and are attributed to this MLCT state, shown in Figure 5-2.[200]

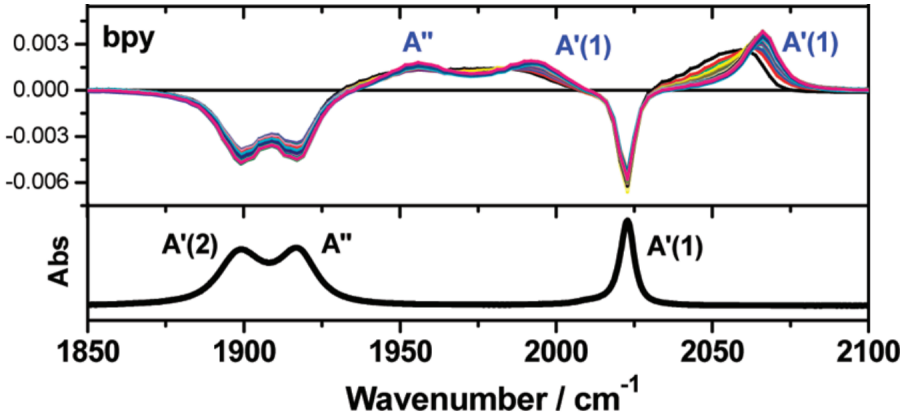

Figure 5-2: The FTIR (bottom) and TRIR (top) spectra or [Re(bpy)(CO)$_3$Cl] in CH_3CN following 400 nm photoexcitation over a time interval of 1-250 ps (top). Reproduced from reference 200.

[Re(bpy)(CO)$_3$Cl] has C_s symmetry with three clear bands observed in the CO region of the FTIR spectrum. However the presence of a nitrogen donor ligand such as NCS, py and DMAP changes of symmetry to pseudo C_{3v} which results in an overlap of the two lower energy bands, as shown in Figure 5-2.[189, 201]

Pyridine analogues have been investigated previously, with work focussing on methylated pyridines and dimethylaminopyridine where DMAP is considered more basic than py.[202] Further work on the excited states of [Re(bpy)(CO)$_3$(py)]$^+$ includes TRIR spectra following photoexcitation at 400 nm of [Re(bpy)(CO)$_3$(py)] in D_2O,[189] the instantaneous formation of a ^{3}MLCT state is observed, (Figure 5-4, top yellow) and decays with τ = 200 ns. In the presence of reductive quencher the ^{3}MLCT state is reduced to form [Re(bpy)(CO)$_3$(py)]$^-$ characterised by a red shift in energy of the transient species at 2012 cm^{-1} and 1895 cm^{-1} in relation to the parent, (Figure 5-4, blue, green and pink).

Changing the axial ligand from Cl to py does not appear to affect the nature of the excited state observed, where for L = Cl and py in CH_3CN, the most stable excited state

is MLCT in character. However, the lifetime of this excited state is observed to change dramatically from 25 to 669 ns for L = Cl and py respectively.[106, 108, 190, 197, 198]

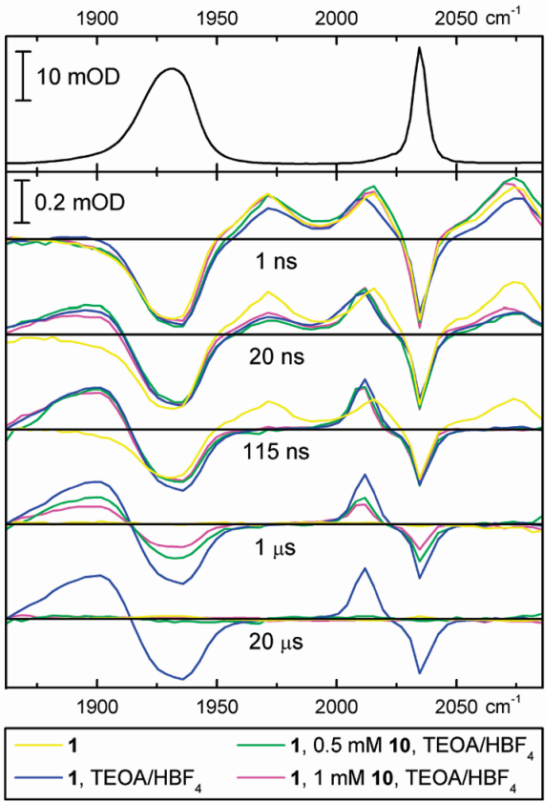

Figure 5-4: FTIR spectrum (top, black) and difference spectra after 400 nm excitation pulse of $[Re(bpy)(CO)_3(py)]^+$. For time-resolved IR conditions are 0.25 mM of $[Re(bpy)(CO)_3(py)]^+$ in D_2O (top yellow) and in 1 M TEOA and 0.1 M HBF_4 with varying concentrations of Co quencher (green, blue and pink). Reproduced from reference 189.

As well as the photophysical properties of $[Re(bpy)(CO)_3L]^+$ the complex $[Re(dppz)(CO)_3L]^+$ will also be investigated in this Chapter. Tuning the excited state observed in $[Re(dppz)(CO)_3L]^+$ complexes is also possible through modifying the axial ligand, as shown in Figure 5-5. Electron donating groups, such as nitrogen based ligands, have been shown to increase the energy of the MLCT state. This effect has been attributed to the increase of electron density on the Re metal centre,[53] which in theory stabilises the formation of a positive charge at the Re and thus lowers the energy involved in an MLCT transition. Conversely, the presence of electron withdrawing group decreases the energy of the MLCT state.

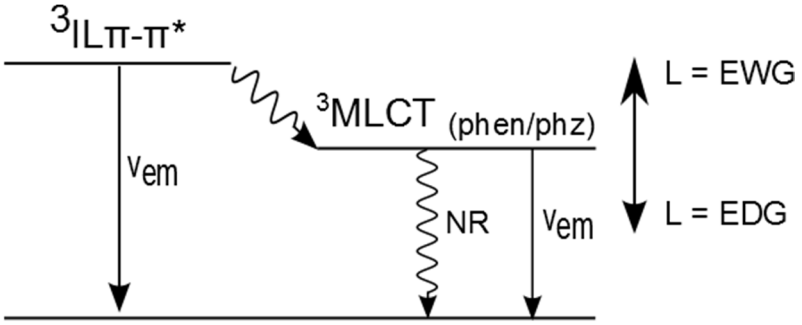

Figure 5-5: The effect on the excited states observed for Re(dppz) derivatives through modifying the axial ligand (L).

Table 5-2: Nature and kinetics of excited states observed for $[Re(dppz)(CO)_3(py)]^+$ derivative complexes

Complex	Solvent	λ_{MLCT} (nm)	τ (ns)	Ref
$[Re(dppz)(CO)_3(py)]^+$	CH_2Cl_2	556, 598(sh)		57
$[Re(dppz)(CO)_3(py)]^+$	CH_3CN	558, 594(sh)		57
$[Re(dppz)(CO)_3(py)]^+$	CH_3OH			
$[Re(dppz)(CO)_3(py)]^+$	CH_3CN			
$[Re(dppz)(CO)_3(DMAP)]^+$	CH_3CN	573		53
$[Re(dppz\text{-}Cl_2)(CO)_3(DMAP)]^+$	CH_3CN	570	1.5 ± 1	35
$[Re(dppz)(CO)_3(4\text{-}CH_3py)]^+$	CH_2Cl_2	559	2800	85
$[Re(dppz)(CO)_3(4\text{-}CH_3py)]^+$	CH_3CN	557	18500	85
$[Re(dppz)(CO)_3(4\text{-}CH_3py)]^+$	CH_2CH_5OH	557	1500	85
$[Re(dppz)(CO)_3(4\text{-}CH_3py)]^+$	CH_3OH	556	4300	85

4-CH_3py 4-methylpyridine

$[Re(dppz)(CO)_3L]^+$ complexes commonly exhibit three types of excited states, ILππ*, MLCT(phen) or MLCT(phz) as discussed in detail in Chapter 2. Owing to the pseudo C_{3v} symmetry of $[Re(dppz)(CO)_3(py)]^+$ two bands in the FTIR ν(CO) are expected, as seen for $[Re(bpy)(CO)_3(py)]^+$. Following 400 nm photoexcitation of $[Re(dppz)(CO)_3(py)]^+$ in CH_3CN, the parent bands (2036 and 1933 cm^{-1}) are observed to bleach, with the simultaneous formation of transient bands (2016 and 1907 cm^{-1}) at lower energies shown in Figure 5-6.[38] These bands are assigned to an ILππ* state which is the lowest energy excited state and consistent with observations for $[Re(dppz)(CO)_3Cl]$,[32] $[Re(dppz\text{-}F_2)(CO)_3(py)]^+$,[36] (Figure 5-6) and $[Re(dppz\text{-}Cl_2)(CO)_3(py)]^+$.[35] However, for $[Re(dppz\text{-}F_2)(CO)_3(py)]^+$ following 400 nm photoexcitation measurements on the ns timescale an initially formed ILππ* state which

decays to an equilibrium with an MLCT(phz) state *ca.* 400 ns is observed. The ILππ*/MLCT(phz) states decay to the ground state *ca.* 2500 ns

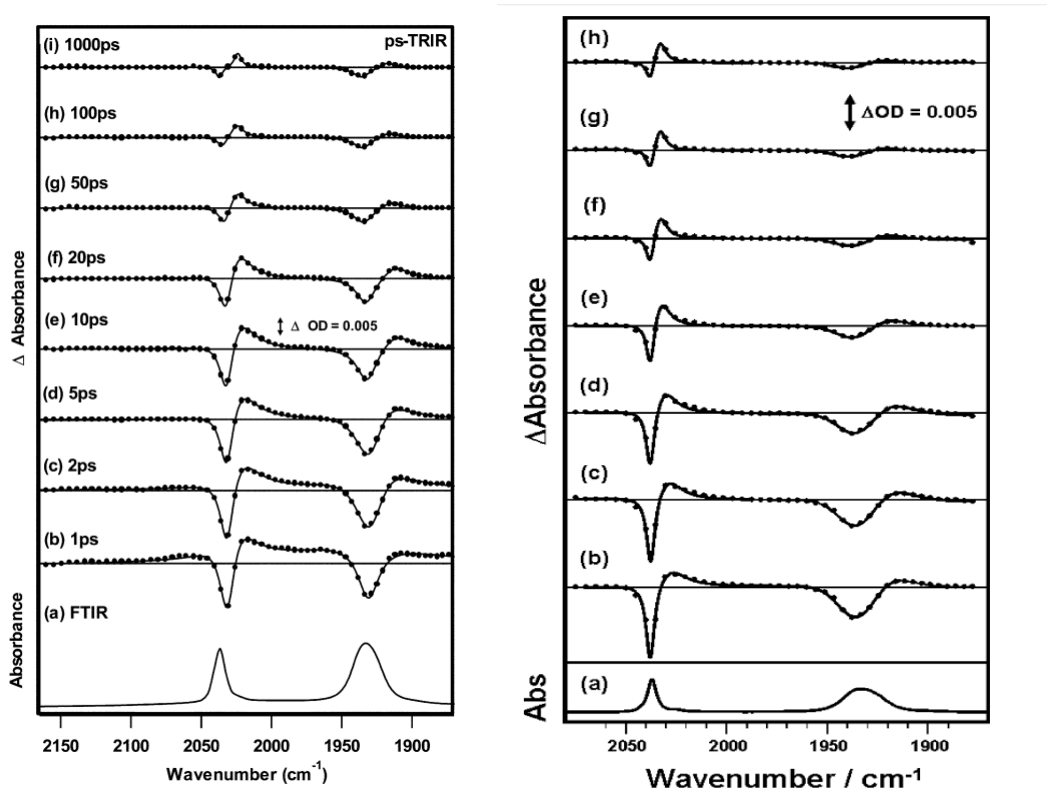

Figure 5-6: The FTIR spectrum of $[Re(dppz)(CO)_3(py)]^+$ (left) and $[Re(dppz\text{-}F_2)(CO)_3(py)]^+$ (left) in CH_3CN (a) and TRIR spectra obtained Δt 1 – 1000 ps following 400 nm excitation (b-j). For $[Re(dppz\text{-}F_2)(CO)_3(py)]^+$ at 2 ps (b), 5 ps (c), 10 ps (d), 25 ps (e), 50 ps (f), 100 ps (g) and 500 ps (h) (left). Reproduced from references 38 and 36.

The axial ligand 4-dimethylaminopyridine (DMAP) has previously been investigated, and the TRIR spectra of $[Re(dppz\text{-}Cl_2)(CO)_3(DMAP)]^+$ in CH_3CN following 400 nm photoexcitation are shown in Figure 5-7.[35] At 1 ps parent band bleaching and the formation of several transient bands assigned to a ^{3}MLCT state are observed. As for $[Re(dppz)(CO)_3(py)]^+$ the two lower energy bands in the FTIR spectrum are convoluted. The TRIR of the comparative neutral complex $[Re(dppz\text{-}Cl_2)(CO)_3Cl]$ has been shown in Figure 5-7 with clear spectral differences observed between the two complexes. The excited states for $[Re(dppz\text{-}Cl_2)(CO)_3(DMAP)]$ are MLCT(phen)/ILππ* and for $[Re(dppz\text{-}Cl_2)(CO)_3Cl]$ are MLCT(phz)/ILππ* in nature Other complexes with L = DMAP including $[Re(dppz\text{-}CO_2Et)(CO)_3(DMAP)]$,[52] and $[Re(dppz\text{-}12\text{-}NO_2)(CO)_3(DMAP)]^+$,[53] also exhibit an equilibrium of MLCT(phen)/IL(ππ*) states.

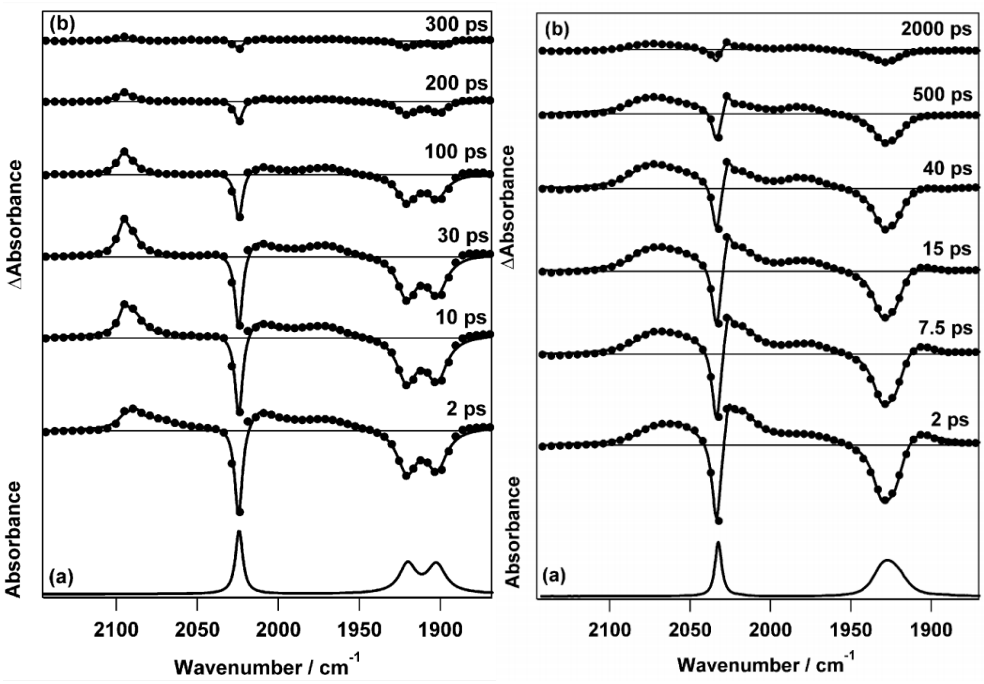

Figure 5-7: FTIR spectrum (a) and TRIR spectrum (b) of [Re(dppz-Cl_2)$(CO)_3$Cl] (left) and [Re(dppz-Cl_2)$(CO)_3$(DMAP)]$^+$ (right) in CH_3CN after excitation at 400 nm. Reproduced from reference 35.

2 Aims

The aim of this Chapter is to further investigate the effect of solvent on the photophysical properties of $[Re(bpy)(CO)_3L]^+$ and $[Re(dppz)(CO)_3L]^+$, by exploring the previously unreported photophysics of these complexes in an apolar media. This aim is split into two objectives.

1. To synthesise $[Re(bpy)(CO)_3(DMAP)]^+$ and $[Re(dppz)(CO)_3(DMAP)]^+$ derivative complexes which exhibit previously unreported solubility in an apolar solvent media.

2. To investigate the effect of an apolar solvent media on the photophysical properties through absorption, emission and time resolved infrared studies of the complexes $[Re(bpy)(CO)_3(DMAP)]^+$ and $[Re(dppz)(CO)_3(DMAP)]^+$.

3 Results and Discussion

This work will focus on the complexes $[Re(bpy)(CO)_3(DMAP)]^+$ and $[Re(dppz)(CO)_3(DMAP)]^+$, the structures of which are shown in Figure 5-8. $[Re(dppz)(CO)_3(DMAP)]^+$ has been well studied and was chosen in order to draw conclusions to previously reported work in conventional polar solvents. Furthermore, $[Re(bpy)(CO)_3(DMAP)]^+$ has also been investigated in order to help assign the excited states exhibited by $[Re(dppz)(CO)_3(DMAP)]^+$, as the bpy complex is a more straight forward system and will offer an important comparison.

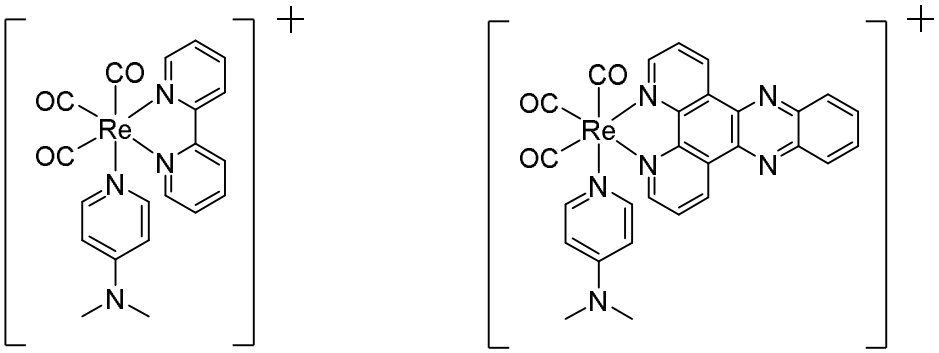

Figure 5-8: The structural formulae of $[Re(bpy)(CO)_3(DMAP)]^+$ and $[Re(dppz)(CO)_3(DMAP)]^+$ complexes which are studied within this work.

Previous literature has shown that Re(diimine) complexes have poor solubility in low polarity solvents. To this end the solubility of both $[Re(bpy)(CO)_3(DMAP)][BF_4]$ and $[Re(dppz)(CO)_3(DMAP)][BF_4]$ have been assessed in commonly used solvents, listed in Table 5-3. From FTIR measurements, Figure 5-11, it was observed that the complexes exhibited reasonable solubility in solvents with $\varepsilon_r < 7.5$, as expected. Furthermore, the decrease in observed absorbance with decreasing dielectric constant of the solvent reflects the decrease in solubility of the Re(diimine) complexes. $[Re(bpy)(CO)_3(DMAP)]^+$ and $[Re(dppz)(CO)_3(DMAP)]^+$ complexes exhibit two bands in the FTIR spectra for solvents with a $\varepsilon_r < 7.8$, which is consistent with previous literature.[35, 39, 53] This has been attributed to the DMAP group, where the optimised geometry for $[Re(bpy)(CO)_3(DMAP)]^+$ is shown in Figure 5-9, and is consistent with the previously reported crystal structure for the complex.[202]

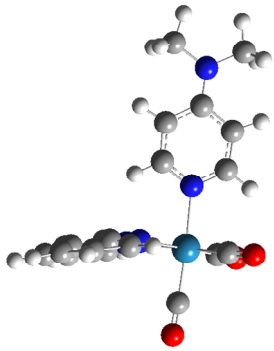

Figure 5-9: The optimised geometry of $[Re(bpy)(CO)_3(DMAP)]^+$ obtained from DFT calculations.

In order to understand the photophysics of $[Re(bpy)(CO)_3(DMAP)]^+$ and $[Re(bpy)(CO)_3(DMAP)]^+$ in low dielectric solvents (PFMCH, $\varepsilon_r < 2$), a method for increasing solubility of these complexes was required. From previous literature it has been shown that the solubility of molecules may be increased in PFMCH through the use of fluorination, specifically through fluorination of the anion.[173, 180, 186] Therefore, to increase solubility of both $[Re(bpy)(CO)_3(DMAP)]^+$ and $[Re(dppz)(CO)_3(DMAP)]^+$ in PFMCH, the use of non-coordinating tetra-arylborate fluorous anions has been investigated.

Firstly the commonly used fluorinated anion tetrakis[3,5-bis(trifluorohexyl)pheny]borate was investigated to increase solubility of both rhenium complexes in non-polar solvents, however, little increase in solubility of either complex in PFMCH was observed. This was attributed to the length of fluorination of the alkyl chains being insufficient. Therefore a more fluorinated version of the anion, tetrakis[3,5-bis(perfluorohexyl)phenyl]borate (BAr^{f6}) (Figure 5-1), was investigated as this possess longer fluorinated alkyl chains yielding the complexes $[Re(bpy)(CO)_3(DMAP)][BAr^{f6}]$ and $[Re(dppz)(CO)_3(DMAP)][BAr^{f6}]$.

The solubility of both complexes containing the BAr^{f6} anion in PFMCH was assessed and it was observed that both complexes demonstrated good solubility in PFMCH, where the FTIR spectra collected are shown in Figure 5-10. For both complexes a blue shift in the energy of the carbonyl stretches is observed from CH_3CN to PFMCH. The FTIR

spectra of both $[Re(bpy)(CO)_3(DMAP)]^+$ and $[Re(dppz)(CO)_3(DMAP)]^+$ in PFMCH exhibit a splitting of the lower energy band into its two constituent bands.

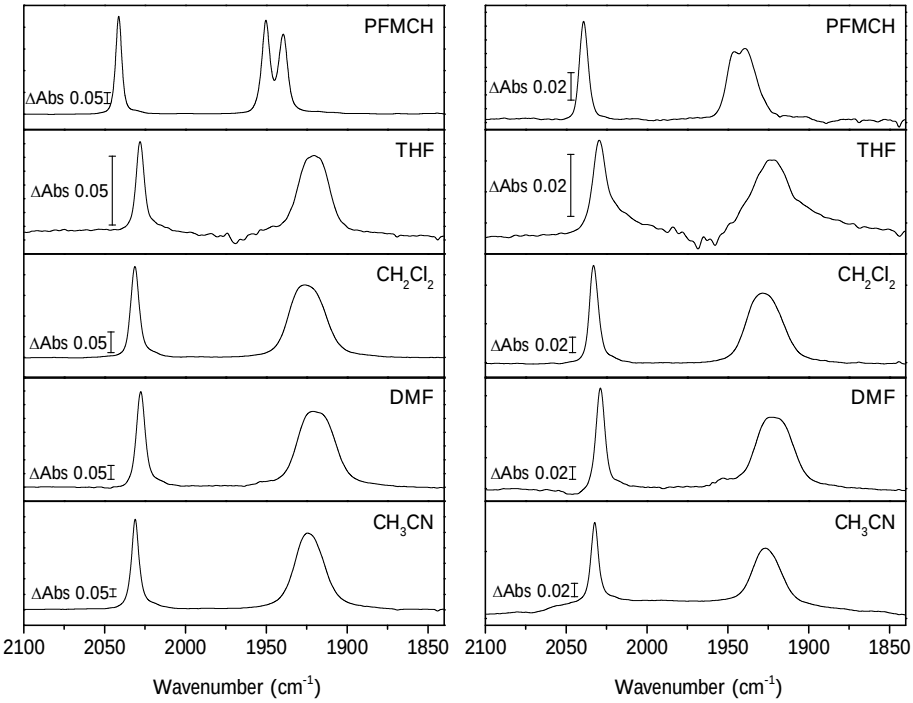

Figure 5-10: The FTIR spectra of $[Re(bpy)(CO)_3(DMAP)]^+$ (left) and $[Re(dppz)(CO)_3(DMAP)]^+$ (right) in a range of listed solvents.

Table 5-3: The FTIR band positions for $[Re(bpy)(CO)_3(DMAP)]^+$ and $[Re(dppz)(CO)_3(DMAP)]^+$ in a range of listed solvents with varying dielectric constants (ε_r). The values for the dielectric constants are taken from reference 152.

Solvent	ε_r	ν (cm^{-1})	
		$[Re(bpy)(CO)_3(DMAP)]^+$	$[Re(dppz)(CO)_3(DMAP)]^+$
PFMCH	1.8	2041, 1950, 1940	2039, 1946, 1939
THF	7.8	2028, 1921	2030, 1923
CH_2Cl_2	8.9	2032, 1927	2033, 1928
DMF	36.7	2028, 1920	2029, 1922
CH_3CN	37.5	2031, 1925	2034, 1927

This splitting of the lower energy in the FTIR spectra observed for both complexes in PFMCH is unexpected and has been attributed to interactions with the solvent. A splitting of the lower energy band in C_{3v} complexes has not been widely observed, although is reminiscent of other pseudo C_3 complexes which show a coalescence of the lower energy bands with temperature as a result of changes in the position of the CO

moieties.[203] A splitting of the lower energy band for pseudo C_{3v} complex $[Re(bpy)(CO)_3(OH_2)]^+$,[189] has been reported under basic conditions (pH 11) and this is attributed to deprotonation, shown in Figure 5-12, causing a small change in geometry to give less pseudo C_{3v} character.

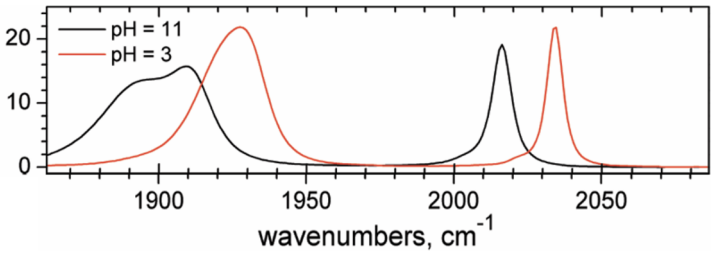

Figure 5-12: The change in the FTIR of $[Re(bpy)(CO)_3(OH_2)]^+$ depending on the solvent pH. Pseudo C_{3v} symmetry is observed under acidic conditions (pH 3, red line). The lower energy band is observed to split under more basic conditions (pH 11, black line). Reproduced from reference 189.

3.1 Photophysical Properties of $[Re(bpy)(CO)_3(DMAP)]^+$

As the bpy ligand may be considered to be a component of the dppz ligand, the photophysical properties of $[Re(bpy)(CO)_3(DMAP)]^+$ were considered first, in order to aid the interpretation of the more complex $[Re(dppz)(CO)_3(DMAP)]^+$.

The photophysical properties of $[Re(bpy)(CO)_3(DMAP)]^+$ have been limitedly studied in the literature before. Therefore, an initial room temperature emission study was carried out in solvents with $\varepsilon < 7.6$ and the results are shown in Figure 5-13. A large shift in emission energy was observed with increasing solvent polarity from 16234 to 15432 cm^{-1} for THF to CH_3CN respectively. The emission is attributed to the $Re(d\pi)bpy(\pi^*)$ transition, MLCT state, consistent with previous literature.[86, 189, 190] This observed positive solvatochromism indicates that the MLCT excited state observed is further stabilised with solvent polarity. However, this is the converse to the negative solvatochromism observed for the parent complex $[Re(bpy)(CO)_3X]$ where X = Cl, Br and I and for $[Re(bpy)(CO)_3(py)]^+$.[86, 190, 204, 205]

This change in the nature of solvatochromism is attributed to the DMAP ligand, possibly due to changes in the coordination sphere of the complex. Previous results have shown

that [Re(bpy)(CO)$_3$(□)], shown in Figure 5-13, does not follow a clear negative solvatochromic dependence.[206] This has been attributed to changes in the coordination sphere.

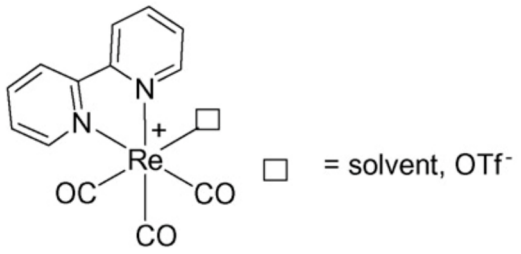

Figure 5-13: The structural formula of [Re(bpy)(CO)$_3$(□)]. Reproduced from reference 206.

Subsequently, the emission energy of [Re(bpy)(CO)$_3$(DMAP)][BAr^{f6}] in PFMCH was measured and was observed to follow this positive solvatochromic trend, exhibiting a blue shift in emission energy from 16234 to 16529 cm^{-1} for THF and PFMCH respectively (Figure 5-14). Assuming the λ_{abs} and λ_{em} are representative of the (0,0) transition, then a decrease in the energy gap is observed for [Re(bpy)(CO)$_3$(DMAP)]$^+$ from 12346 cm^{-1} in CH_3CN to 8534 cm^{-1} in PFMCH.

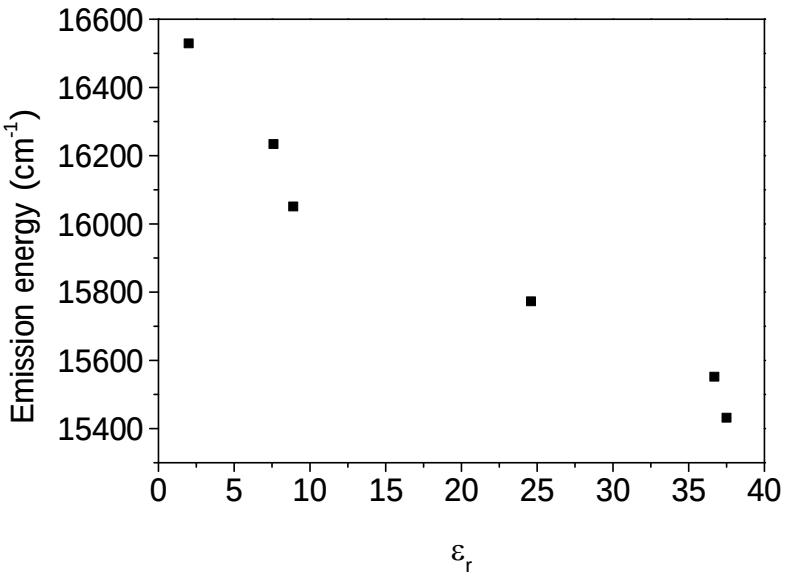

Figure 5-14: The MLCT emission energy of [Re(bpy)(CO)$_3$(DMAP)]$^+$ as a function of the dielectric constant of the solvent.

Table 5-4: The observed emission (λ_{em}) and absorption (λ_{abs}) energies of $[Re(bpy)(CO)_3(DMAP)]^+$ in a range of listed solvents with varying dielectric constants (ε_r). The values of dielectric constants are taken from reference 152.

Solvent	ε_r	λ_{Abs} (cm^{-1})	λ_{em} (cm^{-1})
CH_3CN	37.5	27778	15432
DMF	36.7	26525	15552
CH_3OH	24.6	26042	15773
CH_2Cl_2	8.9	26110	16051
THF	7.5	27397	16234
PFMCH	1.8	25063	16529

The photophysical properties of $[Re(bpy)(CO)_3(DMAP)][BAr^{f6}]$ in PFMCH have been further investigated by TRIR spectroscopy at several time delays following 400 nm photoexcitation. The spectra are shown in Figure 5-15 and the features are summarised in Table 5-5. At 1 ps the parent bands (2040, 1949 and 1939 cm^{-1}) are observed to bleach and simultaneously the formation of several transient bands (2069, 2011 and 1966 cm^{-1}) are observed. Over the first 30 ps the transient bands shift to higher energies, which is attributed to vibrational cooling. The transient bands are assigned to an MLCT state which is $Re(d\pi)bpy(\pi^*)$ in nature, Figure 5-15.

Table 5-5: A summary of the FTIR and TRIR spectral features and kinetics of $[Re(bpy)(CO)_3(DMAP)][BAr^{f6}]$ observed following photoexcitation at 355 nm in PFMCH.

ν(CO) (cm^{-1})	τ decay (ns)	τ growth (ns)	Assignment
2069, 2011, 1966	66 ± 4	-	
2040, 1949, 1939	-	60 ± 10	Parent
2040, 1946, 1940	-	-	GS FTIR

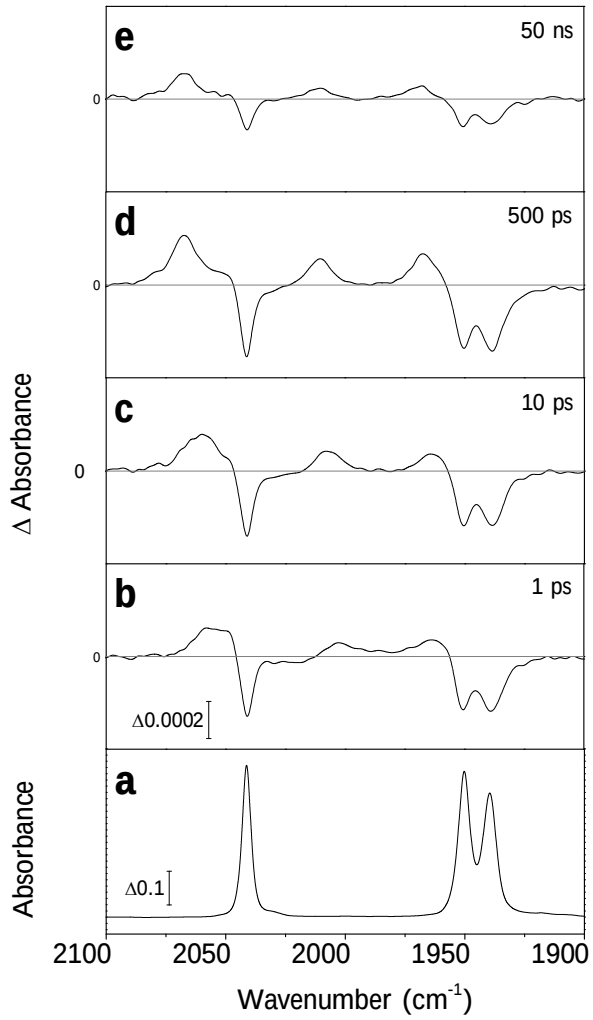

Figure 5-15: The FTIR (a) and TRIR (b-e) spectra of $[Re(bpy)(CO)_3(DMAP)][BAr^{f6}]$ in PFMCH where a transient band at 2069 cm^{-1} is observed and assigned to an MLCT excited state.

There is good agreement observed between the decay of the MLCT excited state bands (66 ± 4 ns) and the recovery of the parent bands as shown in Figure 5-16. The MLCT lifetime observed in PFMCH is of a similar magnitude to the same complex in CH_3CN and CH_2Cl_2.[86, 190] The presence of an MLCT state as the lowest energy excited state is as expected for a $[Re(bpy)(CO)_3(DMAP)]^+$ complex.[86, 189, 190]

For $[Re(bpy)(CO)_3(DMAP)]^+$ the lifetime of the MLCT state is observed to decrease, as the energy of the MLCT increases, where the emission energy decreases for $[Re(bpy)(CO)_3(DMAP)]^+$ from 16611 to 16234 cm^{-1} and the lifetime increases from 13 to 110 ns in D_2O and CH_3CN respectively.[86, 189] The MLCT excited state lifetime observed in PFMCH is 66 ns which is consistent with the emission energy of

$[Re(bpy)(CO)_3(DMAP)]^+$ observed in PFMCH at 16529 cm^{-1}, which is higher in energy than in CH_3CN and lower than in D_2O.

A higher MLCT emission energy for $[Re(bpy)(CO)_3(DMAP)]^+$ complexes results in a shorter lifetime.[86, 189, 190] The further decrease in the excited state lifetime observed for PFMCH compared to CH_3CN and CH_2Cl_2, is consistent with the higher energy MLCT state observed from emission measurements.

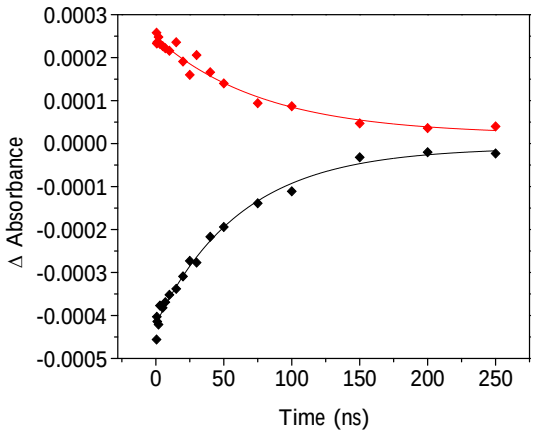

Figure 5-16: The decay of the band at 2069 cm^{-1} assigned to an MLCT state, is in good agreement with the growth of the band at 2040 cm^{-1} assigned to the parent.

3.2 Photophysical Properties of $[Re(dppz)(CO)_3(DMAP)]^+$

The emission of $[Re(dppz)(CO)_3(DMAP)][BAr^{f6}]$ have been acquired in a range of solvents. A positive solvatochromic shift in the emission energy is observed shown in Figure 5-17 and the emission has been attributed to the MLCT(phen) state. Furthermore, the emission observed in PFMCH clearly follows this solvatochromic trend.

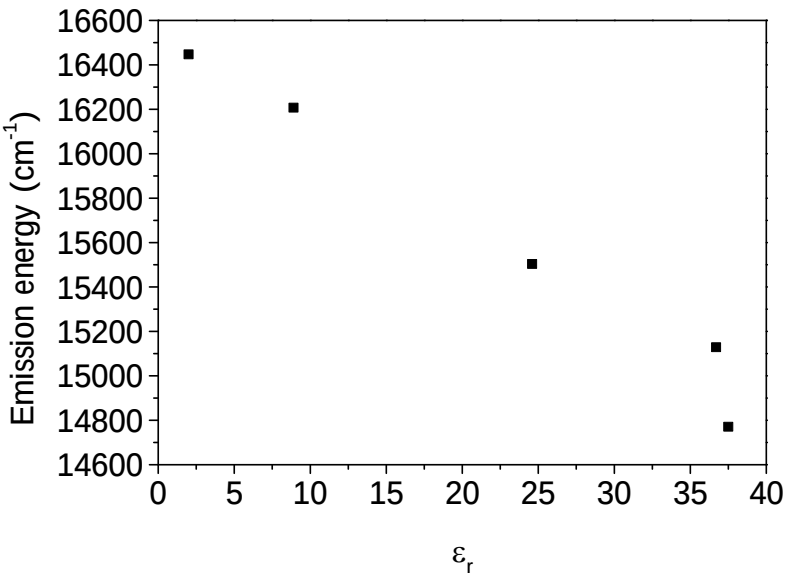

Figure 5-17: The MLCT emission energy of $[Re(dppz)(CO)_3(DMAP)]^+$ as a function of the dielectric constant (ε_r) of the solvent.

Table 5-5: The absorption and emission energy of $[Re(dppz)(CO)_3(DMAP)]^+$ in a range of listed solvents with varying dielectric constants (ε_r). The values for the dielectric constants have been taken from reference 152.

Solvent	ε_r	λ_{abs} (cm^{-1})	λ_{em} (cm^{-1})
CH_3CN	37.5	27397	14771
DMF	36.7	27397	15129
CH_3OH	24.6	27778	15504
CH_2Cl_2	8.9	27778	16207
PFMCH	1.8	27701	16447

The time dependent photophysics of $[Re(dppz)(CO)_3(DMAP)][BAr^{f6}]$ has been probed on the nanosecond timescales using TRIR spectroscopy in CH_3CN. The TRIR spectra obtained after photoexcitation at 355 nm are shown in Figure 5-18, with the features observed summarised in Table 5-6. This allows for comparison to the photophysical properties in PFMCH but also to assess the effect of the $[BAr^{f6}]$ anion by comparison to $[Re(dppz)(CO)_3(DMAP)][BF_4]$ photophysical properties in conventional higher polarity solvents.

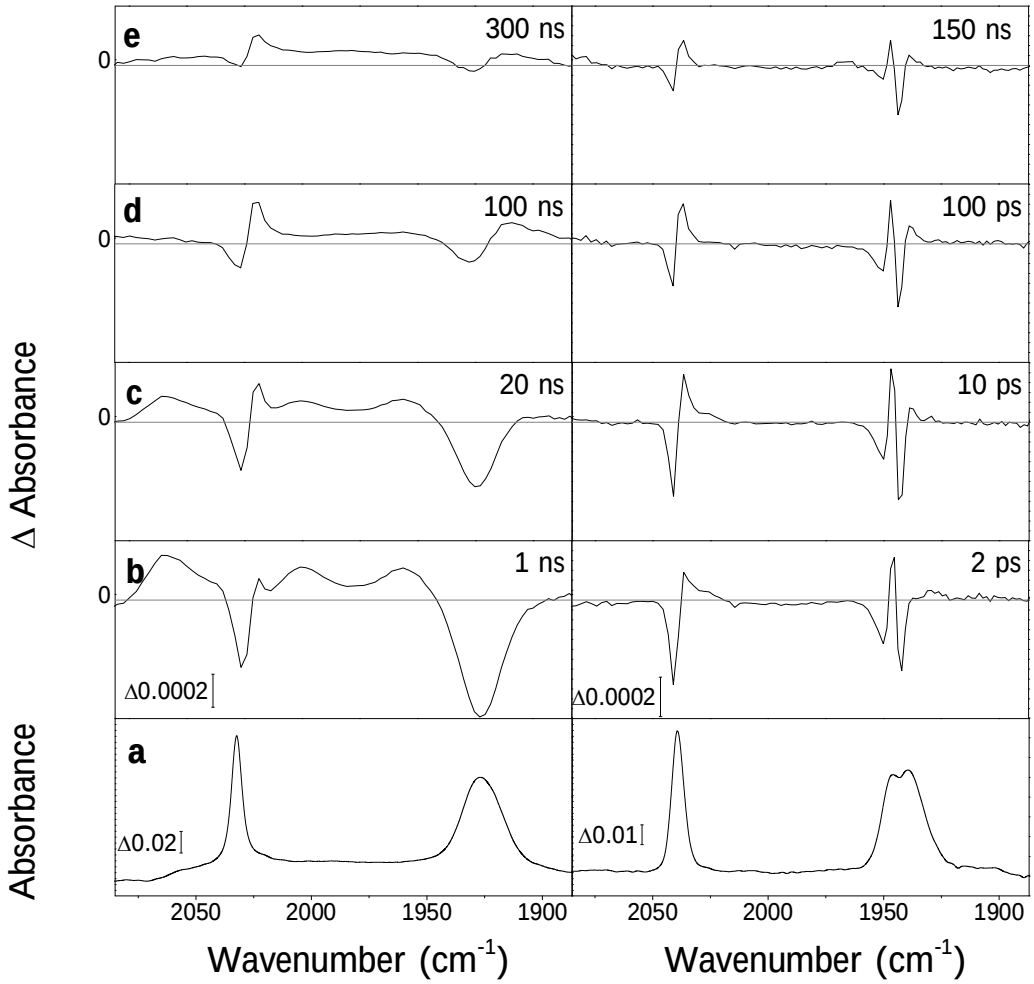

Figure 5-18: The FTIR (a) and TRIR (b-e) spectra of [Re(dppz)(CO)$_3$(DMAP)][BAr^{f6}] in CH$_3$CN (left) and PFMCH (right) following 355 and 400 nm photoexcitation.

Table 5-6: A summary of the FTIR and TRIR spectral features observed for [Re(dppz)(CO)$_3$(DMAP)][BAr^{f6}] in CH$_3$CN following 355 nm photoexcitation.

ν(CO) (cm^{-1})	τ decay (ns)	τ growth (ns)	Assignment
2058, 2001, 1959	27 (± 2)		MLCT(phen)
2018, 1909	370 (± 60)	15 (± 3)	IL$\pi\pi^*$
2030, 1927		31 (± 4)	Parent
		210 (± 30)	
2033, 1927	-	-	GS FTIR

In CH$_3$CN the parent bands (2030 and 1927 cm^{-1}) are observed to bleach and simultaneously the formation of several transient bands are observed (2061, 2018, 2001, 1956 and 1909 cm^{-1}). The broad band at 2061 cm^{-1} is blue shifted compared to the parent bleach at 2019 by *ca.* 30 cm^{-1}, indicative of an MLCT(phen) band.[33] The decay

of the band assigned to the MLCT(phen) state (τ = 27 ± 2 ns), is in good agreement with the growth of the bands at 2018 and 1909 cm^{-1} (τ = 15 ± 2 ns) assigned to an IL$\pi\pi^*$ state. Additionally, the decay of the MLCT(phen) state band, is in agreement with the recovery of the bands assigned to the parent (τ = 31 ± 4 ns). This indicates that the MLCT(phen) state decays to both the ground state and to an IL$\pi\pi^*$ state. The IL$\pi\pi^*$ band at 2018 cm^{-1} decays with the lifetime 360 ± 60 ns and the parent peak at 2026 cm^{-1} recovers with the lifetime 200 ± 30 ns. This indicates that the IL$\pi\pi^*$ state decays to the ground state.

The observed population of an IL$\pi\pi^*$ state and an MLCT state agrees with previous literature where L = DMAP, including $[Re(dppz\text{-}CO_2Et)(CO)_3(DMAP)]^+$ and $[Re(dppz\text{-}Cl_2)(CO)_3(DMAP)]^+$ and $[Re(dppz\text{-}NO_2)(CO)_3(DMAP)]^+$ in CH_3CN.[35, 39, 53] For these complexes an equilibrium of IL$\pi\pi^*$/MLCT(phen) states is observed.

Furthermore, the population of an MLCT(phz) state is not observed for $[Re(dppz)(CO)_3(DMAP)]^+$, which differs from the IL$\pi\pi^*$/MLCT(phz) lowest energy states observed for $[Re(dppz)(CO)_3Cl]$ in CH_3CN. This has been attributed to the lower electron donating ability of the DMAP compared to Cl, which stabilizes the MLCT(phen) state.[4, 39, 53]

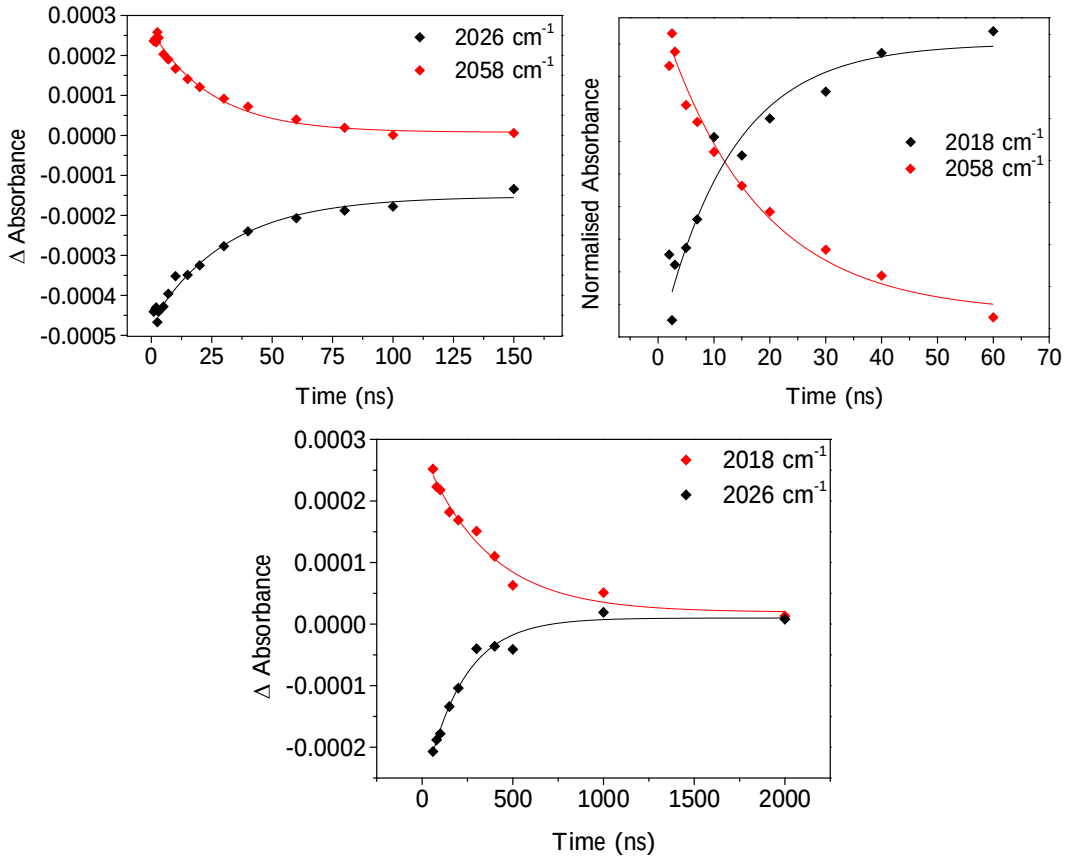

Figure 5-19: The kinetics of $[Re(dppz)(CO)_3(DMAP)]^+$ in CH_3CN following 355 nm photoexcitation. The decay of the 2058 cm^{-1} band assigned to an MLCT(phen) state, is in good agreement with the growth of the band at 2026 cm^{-1} assigned to the parent (top, left). The decay of the band at 2058 cm^{-1} assigned to an MLCT(phen) state and the growth of a new transient band at 2018 cm^{-1} assigned to an ILππ* state (top, right). The decay of the band at 2018 cm^{-1} assigned to an ILππ* state, is in good agreement with recovery of the band at 2026 cm^{-1} assigned to the parent (bottom).

Subsequently the TRIR spectra of $[Re(dppz)(CO)_3(DMAP)][BAr^{f6}]$ in PFMCH were collected and these are shown in Figure 5-18, with feature summarised in Table 5-7. At 2 ps after photoexcitation parent bands at 2041, 1950 and 1942 cm^{-1} are observed to bleach, while simultaneously, transient bands are observed to form at 2037, 2025, 1947 and 1939 cm^{-1}. The parent peaks at 1950 and 1942 cm^{-1} are observed as two clearly resolved bands, unlike in the ground state FTIR where some overlapping of the bands is observed. This is attributed to the growth of a transient band at 1947 cm^{-1}.

Table 5-7: A summary of the FTIR and TRIR spectral features observed for [Re(dppz)(CO)$_3$(DMAP)][BAr^{f6}] in PFMCH following 400 nm photoexcitation.

ν(CO) (cm^{-1})	τ decay (ns)	τ growth (ns)	Assignment
2025	0.03 (± 0.01)	-	State I
2036, 1947, 1939	300 (± 30)	0.013 (± 0.004)	ILππ*
2041, 1950, 1944	-	270 (± 70)	parent
2040, 1946, 1940	-	-	GS FTIR

The presence of transient bands which are red shifted to the parent are indicative of an ILππ* state, due to an increase in the electron density on the ligand. The shoulder at 2025 cm^{-1} is observed to decay over the course of 30 ps, which is consistent with vibrational cooling.[40, 53] However, the presence of a shoulder on this timescale has been observed previously for Re(dppz) complexes as discussed in Chapter 2. This band may be indicative of a singlet state, where the low polarity of PFMCH may cause slow ISC. If the band at 2025 cm^{-1} is representative of a singlet state, then this slow ISC has not been observed previously for an unsubstituted [Re(dppz)(CO)$_3$L]$^+$ complex.

Good agreement is observed between the decay of the band at 2036 cm^{-1} assigned to an ILππ* excited state (τ = 300 ± 30 ns), and the recovery of the band at 2041 cm^{-1} assigned to the parent (τ = 270 ± 70 ns). The kinetics for this process are shown in Figure 5-20.

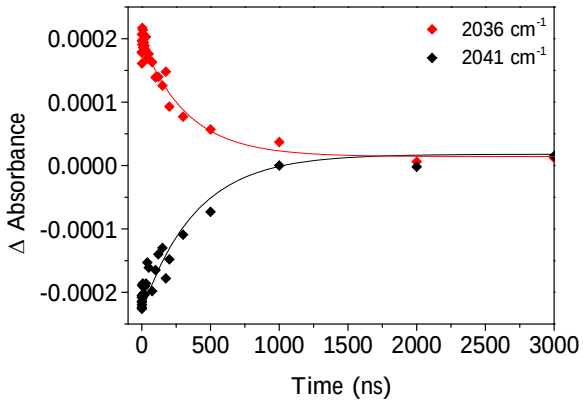

Figure 5-20: The decay of the band at 2036 cm^{-1} assigned to an ILππ* excited state, is in good agreement with the recovery of the band at 2041 cm^{-1} assigned to the parent.

Cationic complexes of Re(dppz) have been shown to be ILππ* emissive at room temperature with microsecond lifetimes.[42] Unusually for Re(dppz) complexes where L =

DMAP, no MLCT excited state is observed in the TRIR. This may be attributed to the very high energy of the MLCT(phen) state in PFMCH observed in emission studies, Figure 5-17.

In addition, the observation of only an IL$\pi\pi^*$ excited state may be due to the lack of interaction between the PFMCH solvent and the Re(dppz) complex. The torsional disorder between the nitrogen of the DMAP ligand and the Re would be expected to be higher than observed in CH_3CN. As a result less charge transfer occurs from the DMAP to the Re,[63, 66, 84] causing less stabilisation of an MLCT state, resulting in a favoured IL$\pi\pi^*$ excited state.

The unusual observation of only an excited IL$\pi\pi^*$ state, has not previously been seen for a Re(dppz) complex unless accompanied by intraligand charge transfer such as for the complexes discussed in Chapter 2 and for L = py-10-(4-picolyl)phenothiazine complexes.[41]

3.3 Molecular Orbital calculations

The molecular orbitals for the complexes $[Re(bpy)(CO)_3(DMAP)]^+$ and $[Re(dppz)(CO)_3DMAP]$ have been calculated with the partial energy diagram and representative MOs for each complex shown in Figure 2-21, with all MOs detailed in Appendix B. The calculations have been used to provide an insight in to the molecular orbital framework and are used to provide support for the states assigned from the spectroscopic data.

$[Re(bpy)(CO)_3(DMAP)]^+$ has been shown to have Re($d\pi$) based occupied orbitals with significant DMAP character observed for the HOMO and HOMO-2. Two unoccupied orbitals are also shown in Figure 5-21, a LUMO and LUMO+1, which are both bpy(π^*) in character. The orbitals nature observed is analogous to $[Re(bpy)(CO)_3Cl]$, shown in Appendix B, which also exhibits Re($d\pi$) in nature occupied MOs and bpy(π^*) in nature unoccupied MOs.

The unoccupied orbitals appear reasonable unperturbed by the axial ligand and are bpy(π*) in nature for L = Cl and DMAP, with a similar energy gap between the LUMO and LUMO+1 orbitals at 0.217 and 0.272 eV respectively.

In contrast the two complexes where L = Cl and DMAP for Re(bpy) exhibit very different occupied molecular orbitals. The HOMO for $[Re(bpy)(CO)_3Cl]$ is Re(dπ) in nature while for $[Re(bpy)(CO)_3(DMAP)]^+$ the HOMO is also Re(dπ) but with significant DMAP(π) character, reflecting the large aromatic π-system of DMAP. Furthermore, for $[Re(bpy)(CO)_3Cl]$ the subsequent Re(dπ) and bpy(π) occupied MOs are calculated at lower energies to the HOMO, at 0.245 and 0.435 eV lower for each respectively. This separation of occupied MOs is significantly reduced for L=DMAP. A Re(dπ) HOMO-1 orbital is calculated at only 0.028 eV lower in energy than the HOMO. A Re(dπ) HOMO-2 obrital is calculated to have significant bpy(π) contribution, unlike the bpy(π) HOMO-2 for L = Cl. Furthermore, for L = DMAP, the HOMO-2 is only 0.109 eV lower in energy than the HOMO, which is a significantly smaller energy gap than observed for $[Re(dppz)(CO)_3Cl]$.

For $[Re(dppz)(CO)_3(DMAP)]^+$ the Re(dπ) based HOMO has significant contribution from the DMAP ligand, as observed for $[Re(bpy)(CO)_3(DMAP)]^+$, unlike the Re(dπ) based HOMO observed for $[Re(dppz)(CO)_3Cl]$. Furthermore, the subsequent calculated HOMO-1 Re(dπ) orbital is at significantly lower energy to the HOMO at 0.517 eV compared to the nearly degenerate Re(dπ) HOMO and HOMO-1 orbitals observed for L = Cl.

The unoccupied MOs differ greatly for $[Re(dppz)(CO)_3Cl]$ and $[Re(dppz)(CO)_3(DMAP)]^+$, where for the former three clear MOs, phz(π*) LUMO, phen(π*) LUMO+1 and dppz(π*) LUMO+2 are calculated. In contrast the addition of the DMAP group as the axial ligand causes a significant change in the unoccupied orbitals where the LUMO is observed for be dppz(π*) in nature with a phen(π*) LUMO+1 with significant phz character and a dppz(π*) LUMO+2.

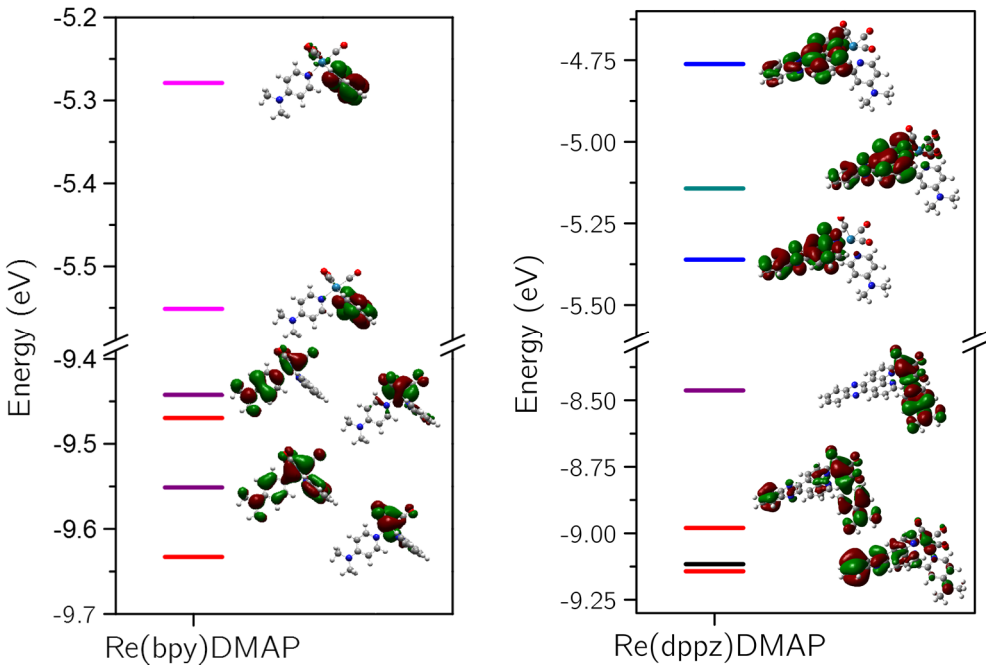

Figure 5-21: The partial energy diagram and representative MOs of $[Re(bpy)(CO)_3(DMAP)]^+$ (left) and $[Re(dppz)(CO)_3(DMAP)]^+$ (right). Metal based occupied MOs are shown in red and ligand centred occupied MOs in black. Axially ligand occupied MOs are also shown in purple. The unoccupied bpy MOs are shown in pink. The unoccupied phz and dppz MOs are shown in turquoise and blue respectively.

4 Conclusions

The complexes [Re(bpy)(CO)$_3$(DMAP)][BAr^{f6}] and [Re(dppz)(CO)$_3$(DMAP)][BAr^{f6}] have been synthesised and their photophysical properties have been investigated through TRIR, absorption, emission and DFT studies. Their photophysical properties in higher polarity solvents, commonly used for Re(diimine) investigations, have been compared to their previously unreported behavior in an apolar media.

Their photophysical properties have been probed in an apolar media (PFMCH), the results have shown that the [Re(bpy)(CO)$_3$(DMAP)][BAr^{f6}] complex exhibited positive solvatochromism in emission studies, unlike the analogous pyridine or chloride complex. From TRIR spectra, the complex exhibited an MLCT excited state in PFMCH which exhibited a lifetime similar to the complex in other solvents. The emission energy was observed to be higher for this MLCT state in PFMCH than CH_3CN and the lifetime shorter, where a trend between emission energy and lifetime has been indicated.

In contrast, [Re(dppz)(CO)$_3$(DMAP)][BAr^{f6}] also exhibited positive solvatochromism in the emission energy which is consistent with the analogous chloride complex. However, unlike [Re(bpy)(CO)$_3$(DMAP)][Bar^{f6}], the nature of the excited state was shown to vary considerable with the solvent. From the TRIR spectra in CH_3CN an IL$\pi\pi^*$/MLCT(phen) excited states were observed, consisted with other [Re(dppz)(CO)$_3$(DMAP)]$^+$ complexes. The photophysical properties in PFMCH were considerably different with a long nanosecond lived IL$\pi\pi^*$ state, which appears to decay solely to the ground state. This unexpected excited state nature has only previous been observed for [Re(dppz)(CO)$_3$L]$^+$ complexes when accompanied by a charge transfer state.

Chapter 6

Probing the Phase Properties of Confined Fluids Through the Use of Luminescence Spectroscopy

1 Introduction

The vast majority of modern technology utilises nanoscale devices, exemplified by transistors, a small device which turns electrical signal on and off and is ubiquitous through a plethora of electronic applications.[207] The need for smaller technology is paramount for the fabrication of devices that possess greater processing power. The drive to produce smaller and smaller electronic features has been commonly described by Moore's Law, which states that the size of transistors will decrease at a rate such that the power of a computer chip could double every year.[207] For the past four decades Moore's law has remarkably held, with transistors decreasing exponentially in size and thus the number of transistors that can be present in a single chip increasing exponentially as shown in Figure 6-1.[208] However, Moore's law is slowly faltering and the decrease in transistor size with current fabrication technology cannot continue to decrease at such an exponential rate, due to the economic cost and limitations in the methods currently used.[207, 208]

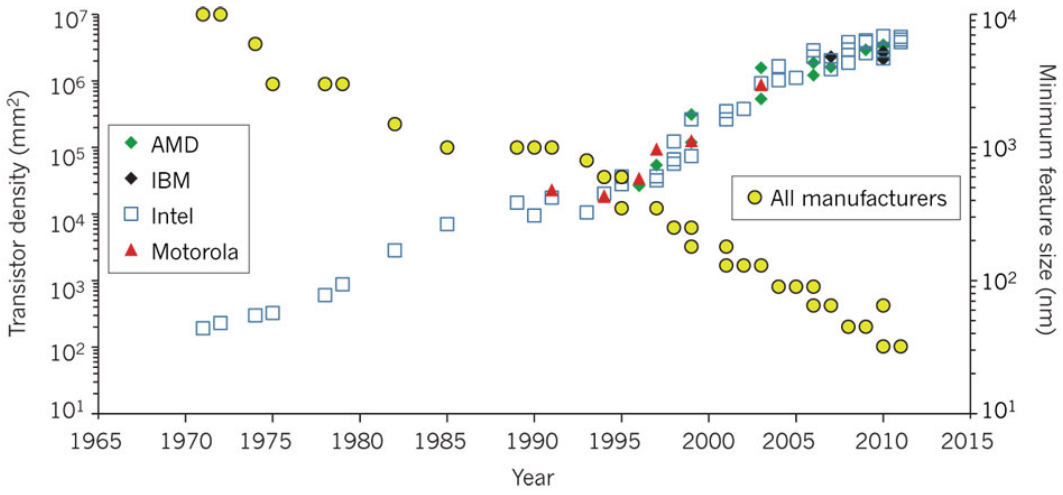

Figure 6-1: The transistor gate length (minimum feature size) and the density of transistors in a microprocessor. The transistor size has been shown to decrease exponentially as a function of year, allowing for an exponential increase in transistor density and therefore power processing. Reproduced from reference 208.

1.1 Limitations in the Current Fabrication Methods of Nanoscale Electronics

Current nanoscale-device fabrication methods limit the possible size of components that can be produced. For example, one of the most commonly employed methods of fabrication is chemical vapour deposition (CVD), which involves chemical reactions of gaseous reactants on or near the vicinity of the heated surface of the substrate.[209] However limitations are found when using nano-scale templates, as deposition may occur at the pore entrance leading to a blockage and loss of uniform deposition through the template.

Alternative methods are employed to overcome the problems exhibited in CVD such as laser annealing, thermal evaporation and sputtering; however, these methods exhibit their own unique set of limitations. Firstly, the feature size produced by laser annealing is physically limited to the wavelength of the light used to etch the material, however, this may be overcome by expensive double patterning methods.[210] Secondly, an underside coating or film results due to lack of control over deposition thickness when using thermal evaporation. Thus, when retention of the template topography is required,

sputtering is often used for deposition. However sputtering can result in plasma damage such as implanted argon which introduces impurities.[211]

Another alternative to thermal evaporation and sputtering for the fabrication of high quality thin films is molecular beam epitaxy (MBE).[212] During the MBE process, beams of atoms or molecules in an ultra-high vacuum environment are incident upon a heated crystal. This crystal has previously been processed to produce a nearly atomically clean surface. The arriving constituent atoms form an epitaxial film.[213] Through the use of ultra-high vacuum and crystal growth the limitations expressed by thermal evaporation and sputtering discussed earlier are overcome. However MBE is a slow method of fabrication with crystal growth occurring at a rate of around a few microns an hour.

Due to the limitations of current fabrication methods there is an immediate and pressing demand for new methods to produce nanoscale electronics, which can offer control over spatial growth, conformality and aspect ratio at the desired rate of production.

1.2 Supercritical Fluid Electrodeposition

Another attractive technique for nanoscale fabrication is electrodeposition owing to its ability to provide spatially defined growth, direct control over the driving force for deposition *via* the application of potential, and highly efficient use of reagents.[212, 214] Furthermore, unlike MBE, the process is not limited by a slow rate of production and thus is viable for the manufacturing of large quantities of electronic devices. However, in the case of nano-scale fabrication, the entrance of the porous template may become easily blocked due to the surface tension of the conventional liquid solvents employed, thus limiting the size of template that may be used and therefore the size of device.

If an alternative solvent, one that is not hindered by surface tension, were to be used for the process then electrodeposition would offer a fabrication method with many of the desirable properties. This leads to the work presented within this Chapter, with an overall aim of working towards microelectronic fabrication by depositing materials into nanosized porous templates, using supercritical fluids (SCFs). This process is shown in

Figure 6-2.[173, 185, 212, 214-216] SCFs are proposed as this alternative solvent as they exhibit negligible surface tension. In addition to this one key advantage SCFs offer, they also display a wide electrochemical window allowing for the deposition of a wide range of materials *via* an electric potential,[215] and may be thought of as '*tuneable*' solvents.[173, 6, 217, 218] SCFs are considered '*tuneable*' as small changes in temperature and pressure near the critical point of an SCF result in significant changes in its properties, such as density, viscosity and dielectric constant.

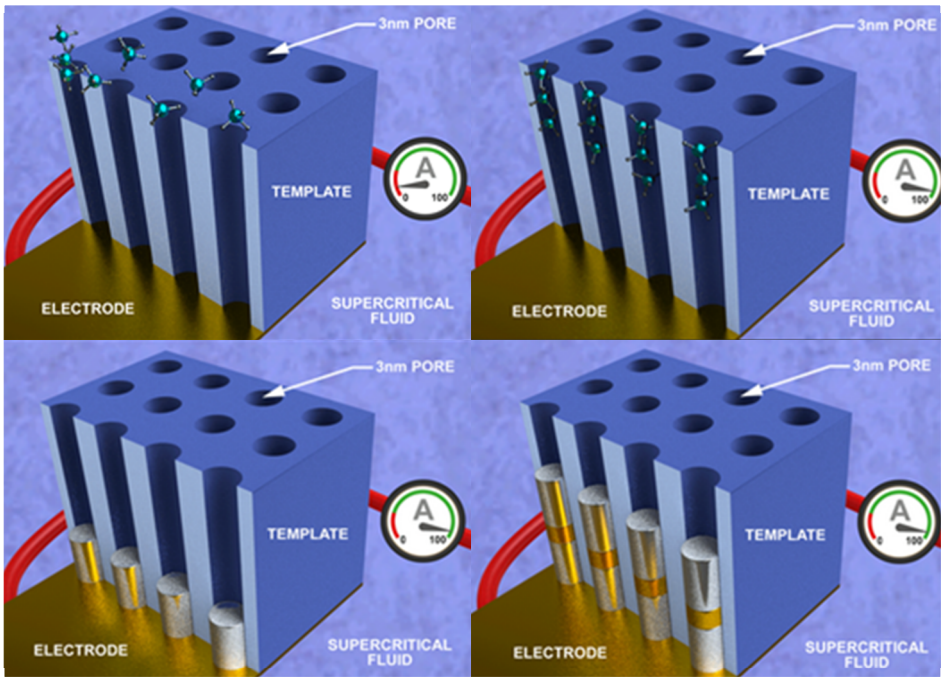

Figure 6-2: The process of supercritical fluid electrodeposition, whereby materials are deposited into nanosized pores to yield nanowires for use in microelectronics. Reproduced from reference 215.

Previous work using supercritical fluid electrodeposition (SCFED) has already shown the successful deposition of various conductive materials using SCFs for example silver and germanium from supercritical carbon dioxide ($scCO_2$) with an acetonitrile (CH_3CN) co-solvent,[214, 216] as well as germanium from liquid and supercritical difluoromethane (R32) to form nanowires.[214] The SCFED method could potentially allow for production of bespoke transistors, for example the schematic shown in Figure 6-3, where altering the template and electrolyte would result in the desired deposition and structure.

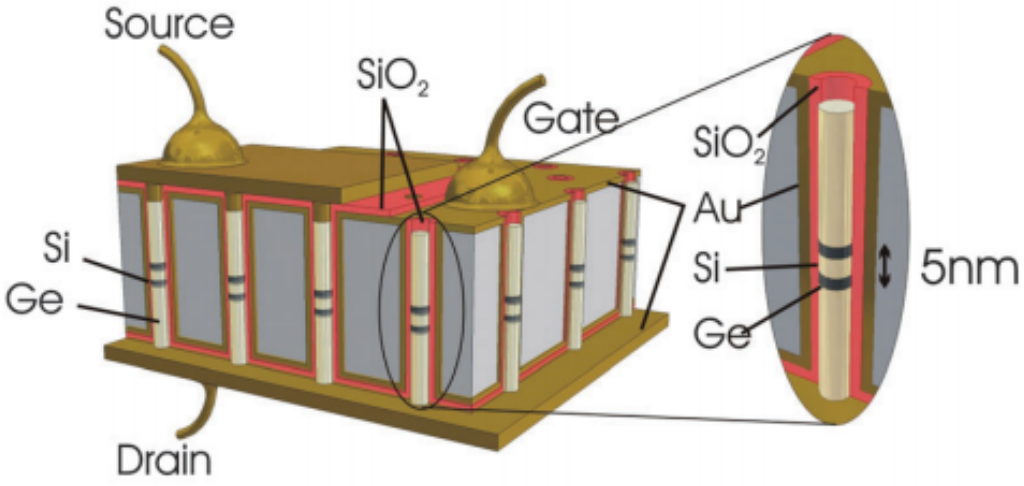

Figure 6-3: A schematic of an example bespoke transistor that could be produced with the SCFED method. Reproduced from reference 215.

The work within this Chapter examines the phase behaviour of SCFs confined within the porous templates, which exhibits considerably different properties when compared to the bulk fluid. Understanding these unique phase phenomena is imperative to refine and guide the SCFED process. This phase behaviour will affect fluid properties such as density and dielectric constant, which will dictate the conditions of the system required to successfully deposit and the nature of electrolytes that can be used.

1.3 Supercritical Fluids

A fluid is defined as supercritical when it is above its critical pressure (P_c) and critical temperature (T_c);[219, 220] the point at which both parameters is achieved is known as the critical point, Figure 6-4.

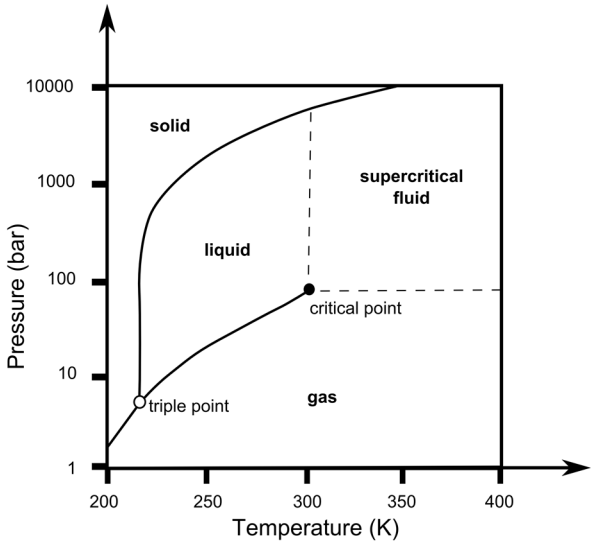

Figure 6-4: The phase diagram of CO_2 where the fluid can be defined as supercritical when it is above its critical temperature (T_c) and critical pressure (P_c) defined as the critical point.[219, 220] Adapted from reference 221.

The SCFs used thus far in SCFED include $scCO_2$, which is widely considered to be non-toxic and thus an excellent replacement to many organic solvents especially chlorinated liquid solvent, the use of which have been limited or banned under environmental legislation.[218, 222]

CO_2 is presently considered the most widely used SCF,[218, 223, 224] and it exhibits relatively mild critical parameters (T_c 31.1 ^oC, P_c 1070.38 psi, ε_r = 1.1-1.4 at 80 ^oC, 1450-3626 psi).[224-227] Thus it is able to dissolve many low molecular weight organic compounds.[186, 228, 229] CO_2 is considered to be non-toxic in nature with easy removal after use by expansion, it also offers the possibility to use it without declaration.[230] For example, $scCO_2$ is used in the extraction of caffeine to yield decaffeinated tea and coffee, polymer synthesis, extraction of hops, spices and flavourings. It is also used for the extraction of pharmaceuticals from seeds and barks, and cleaning.[218, 231-233]

1.4 Probing Phase Behaviour within Porous Materials

As mentioned previously, the phase behaviour of a fluid is key to guiding the electrodeposition process. Previous work has demonstrated that confinement of a fluid affects its phase behaviour,[173, 234-239] this includes shifts in the freezing point,[240] changes

in the critical temperature,[241-243] and pore condensation effects.[244, 245] However, these changes have yet to be fully understood.

An example of this is the observed shift of the gas-liquid critical point of SF_6, CO_2, xenon and argon in porous materials.[246] [242, 247] [248] This shift has been determined by analysing sorption isotherms near and below the bulk critical temperature of these fluids. This shift in the gas-liquid critical point has been further supported by heat capacity studies of ^4He and light scattering experiments of N_2 confined within aerogels.[249, 250] These affects have also been modelled with an adapted Peng-Robinson equation of state which produced adsorption isotherms of CO_2 confined in three different porosities each showing a deviation in saturation pressure and density from the bulk parameters, Figure 6-5.[251]. Where porosity is defined as the fraction of the volume of voids over the total volume,

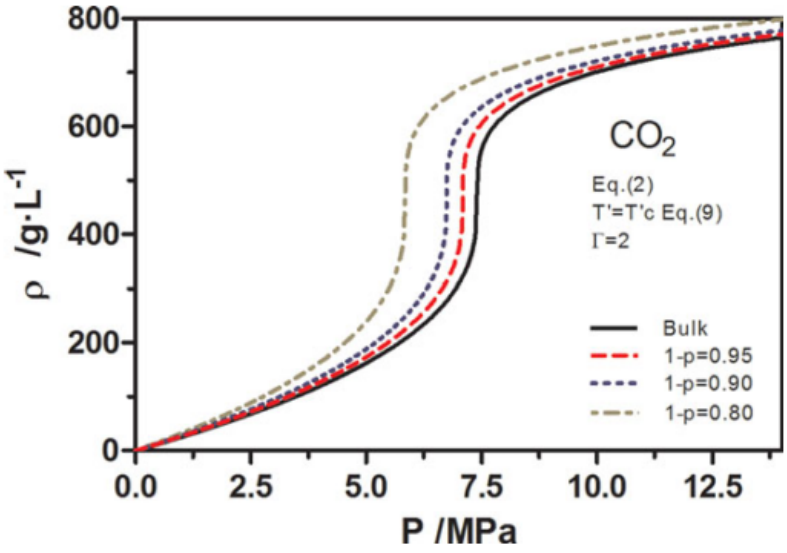

Figure 6-5: Calculated adsorption isotherms of CO_2 at its critical temperature confined in materials with three different porosities. These isotherms are compared to the bulk isotherm. A larger shift is observed in the isotherm with smaller porosity (1-p=0.80), where porosity is the fraction of voids over the total volume. This shows the effect of pore size on the critical temperature depression. Reproduced from reference 251.

The dielectric constant of the deposition bath dictates the materials that can be deposited using SCFED, where the dielectric constant affects the conductivity. The dielectric constant has been shown to be positively correlated to the fluid density.[252, 253] Previous work has shown that density of a fluid changes upon confinement,[173] where a

lower density of the fluid leads to lower viscosity and greater mobility of the ions, therefore an increase in the molar conductivity will be observed.[254] However, as has been shown for CH_2F_2 and CH_3CN/CO_2 mixtures, as the density decreases the dielectric constant is observed to also decrease.[173, 255] This decrease in dielectric constant may result in greater ion pairing and therefore fewer overall charge carriers, resulting in a decrease in the conductivity of the system. Therefore, investigating and further understanding how the density of the fluid changes within the porous templates is key to refining the SCFED process.

A myriad of problems arise when calculating and measuring the density of a fluid within a porous material as the density is affected by a variety of phenomena which arise from the interaction of the fluid with the surface of the pore, including pore condensation and wetting. As a result the density profile of a fluid inside a confined space is not constant in the proximity of the pore walls.[256] This phenomena which arises from this interaction has been predicted by gas sorption measurements.[242] For microporous materials (<2 nm), gas sorption is dominated by interactions between the fluid and the wall. However this effect diminishes with increasing pore size. In the case of mesoporous materials (2-50 nm) gas sorption can also be affected by interactions between the fluid molecules, as well as interactions between the fluid and the wall.

Furthermore, fluid confined inside the porous material may be adsorbed onto the wall during wetting.[238, 257-260] As a result it is possible to consider the confined fluid as a two phase system. One phase can be thought of as a layer of constant density and thickness next to the wall of the pore and a subsequent phase, which is a remaining region with a different density.[261-263] The size of the pore affects the proportion of the wetted phase as the surface area to volume ratio of the pores changes with pore size. This two phase system and its density has been further investigated using small angle neutron scattering (SANS), which is a powerful *in situ* method for monitoring the density of confined fluids.[236, 237, 261]

Melnichenko *et al.* noted that in pores <40 Å in diameter a dense adsorbed phase was observed at low pressures for both sub- and supercritical CO_2 as a result of wetting.

Furthermore, the density of this adsorbed phase may exceed the non-adsorbed confined CO_2 density by as much as 6.5 and 3.5 times at 22 and 60 ^oC respectively.[261] This increase in density has been attributed to the stronger attraction between adsorbed and non-adsorbed CO_2 molecules compared to the attraction between non-adsorbed CO_2 molecules. Furthermore, the density of the adsorbed phase is almost constant over a large pressure range, while the density of the non-adsorbed phase increases with pressure. Eventually, at high enough pressures the two phase system becomes a homogenous phase (Figure 6-6, left blue and purple).[40] Measurements with SANS have confirmed that the density of confined CO_2, both non-adsorbed and adsorbed, is consistently higher than the bulk CO_2 at the equivalent temperatures and pressures.[238, 260]

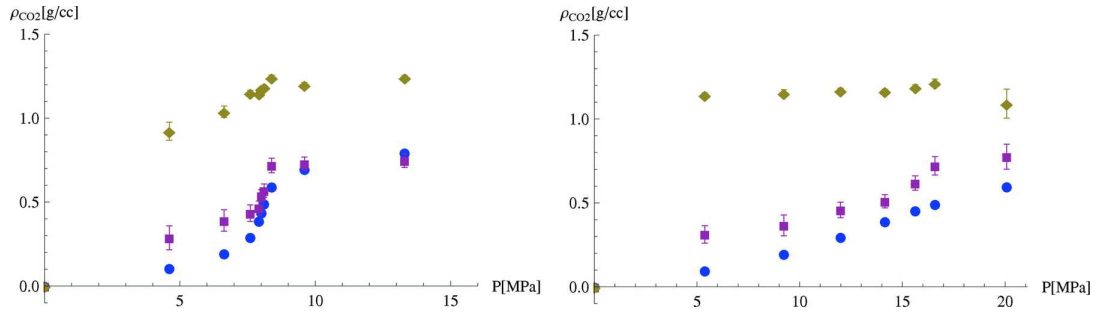

Figure 6-6: Plots of the CO_2 density as a function of pressure. Filled circles indicate bulk CO_2 phase, filled squares represent non-adsorbed confined CO_2 and the diamonds represent density of CO_2 film adsorbed on the silica wall, for samples at T= 308K (34.85 ^oC) (left) and for samples at T=353K (79.85 ^oC) (right). Reproduced from reference 260.

However, SANS exhibits some drawbacks, it is limited by the angle of diffraction that can be achieved, due to the nature of the equipment required for high pressure and temperature measurements, the detection angle can be drastically reduced. An alternative more readily available technique is vibrating tube densimetry (VTD) which allows for direct measurement of the average confined fluid density, such as for CO_2 confined within silica aerogel.[238] The results are consistent with previous conclusions that at high enough pressures a homogeneous phase is observed between the wetted and bulk densities. However, limitations with VTD include readily occurring obstructions to the flow of the liquid which can lead to a loss in pressure and inaccurate density measurements and it is not possible to obtain chemical information (Figure 6-7).[264]

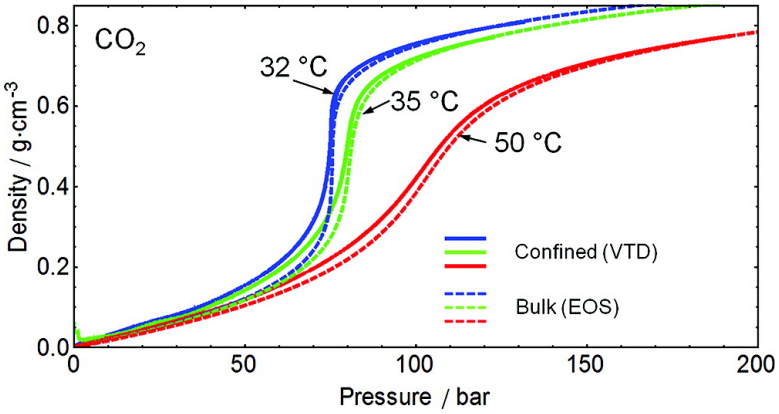

Figure 6-7: The supercritical (32, 35 and 50 °C) isotherms of confined and bulk fluid CO_2 density in silica aerogel. Reproduced from reference 238.

1.5 Fluorescent Based Sensors in Supercritical Fluids

Current techniques for measuring density have been discussed previously and exhibit limitations such as high cost and lack of chemical information. To overcome these limitations an alternative technique that is sensitive to density changes and more accessible is required. To this end, work within this Chapter exploits the use of luminescence spectroscopy as an analytical tool to probe density owing to its sensitivity to viscosity and local solvent environment.[6, 7, 265]

The work within this Chapter focuses on the phase behaviour of both bulk and confined fluids, however, limited research has previously been carried out on the photophysical behaviour of molecules in supercritical media, with many studies focussing only on the solute-solute and solute-solvent clustering observed in SCFs.[6, 217, 266-270] The vast majority of literature has focussed on CO_2 with both experimental and theoretical studies being carried out for molecules in this fluid.[220, 268-271] Most of the previous work has focussed on the study of fluorescence quenching in fluids, mainly CO_2, where quenching has been used to confirm the presence of solute-solvent clustering. This clustering commonly results in local density augmentation where the density of solvent molecules in close proximity to a solute molecule is greater than in the bulk, as shown in Figure 6-8.[6, 217, 220, 266-269, 272, 273]

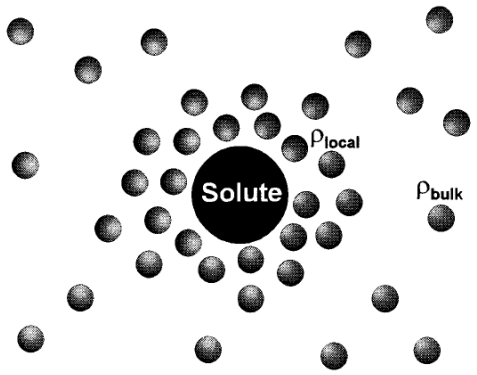

Figure 6-8: Depiction of solute-fluid density augmentation, where a higher local density of solvent surrounds the solute compared to the bulk. Reproduced from reference 274.

Solute-solute and solute-solvent clustering have previously been investigated with the use of pyrene as a probe molecule, making use of its well-studied photophysics.[273, 275, 276] Brennecke and Zagrobelny observed excimer like emission for pyrene at a mole fraction of 5.5 x 10^{-6} in supercritical ethylene at much lower concentration than is required for excimer formation.[275, 276] The excimer emission observed at *ca.* 450 nm, shown in Figure 6-9, is attributed to clustering effects which result in local density augmentation.

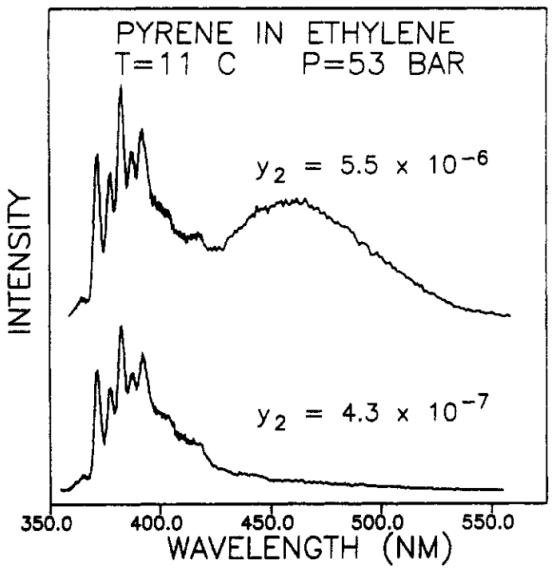

Figure 6-9: The emission spectra of pyrene where pyrene-pyrene excimer like emission is observed at mole fraction 5.5 x 10^{-6} (top) compared to only monomer emission observed at 4.3 x 10^{-7} (bottom). At such low concentrations the presence of excimer emission is assigned to the presence of local density enhancement. Reproduced from reference 276.

Additional work by Brennecke and co-workers, involved determining the strength of these local interactions within fluids on a molecular scale.[7] Several solutes in $scCO_2$ and supercritical ethyne at pressures of 50-250 bar were used to investigate the presence of local density augmentation. The results indicated the presence of more solute-solvent interactions, even when the bulk density is relative low. The solvatochromic shift observed for pyrene as a result of local density augmentation has additionally been experimentally observed by Rice *et al.*[273, 277] here a pyrene probe was utilised to demonstrate a red shift as the density is increased from 300 to 900 $kg.m^{-3}$ [56, 76]

Further work exploring the formation of solvent clusters around the probe molecules 3-hydroxyglavone and 4'-dimethylamino-3-hydroxyflavone, in $scCO_2$ demonstrated that at lower bulk pressures of CO_2, clusters of varying sizes may be formed and co-exist in rapid equilibrium.[6, 267] As the pressure was increased the clusters were observed to merge and result in a more homogeneous microscopic structure indicating the formation of a '*solvent shell*'. This behaviour is shown in Figure 6-10, where the steady state fluorescence of the 4'-dimethylamino-3-hydroxyflavone dye shows a decrease in tautomer peak intensity (at *ca.* 550 nm) with decreasing density. This decrease in peak intensity with density indicates that the 4'-dimethylamino-3-hydroxyflavone loses part of its solvation shell.

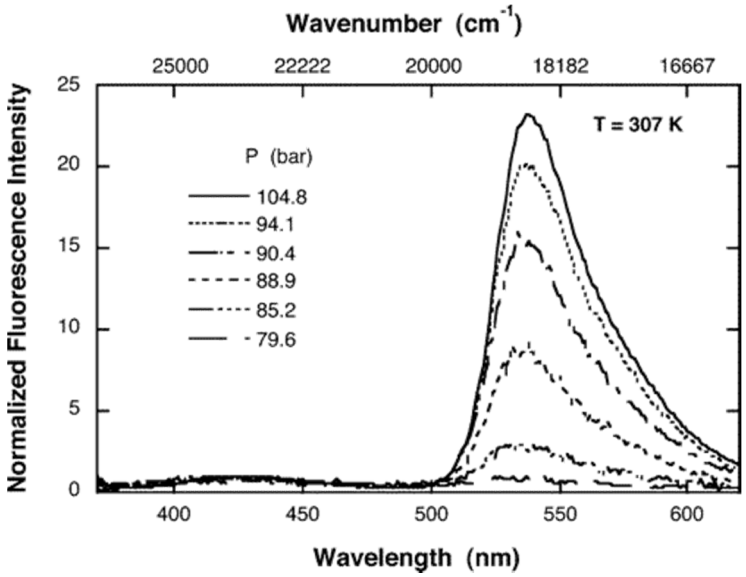

Figure 6-10: The emission spectra of 4'-dimethylamino-3-hydroxyflavone in $scCO_2$ as a function of pressure under isothermal conditions. A decrease in the tautomer band intensity with a decrease in CO_2 pressure can be observed. Reproduced from reference 267.

The presence of local density augmentation has been further confirmed by high pressure absorption studies with a range of solutes for CO_2/co-solvent mixtures where co-solvents studied include acetone, methanol, ethanol, n-octane and propanol. The results demonstrated that due to local density augmentation, the density around the probe molecule could be up to *ca.* x10 that of the bulk density.[278, 279]

As well as the assignment of local density augmentation at low bulk densities, the effect of density at higher bulk densities on the emission of dyes has been investigated. Additional work by Zhang *et al.* has indicated the stabilisation of the excited state with increasing density.[269] Both the excitation and emission wavelength of anthracene in CO_2 is observed to red shift with increasing pressure, as shown in Figure 6-11. The red shift observed with increasing pressure in both the excitation and emission spectra was then plotted as a function of density (Figure 6-11). For both excitation and emission wavelength with increasing density there is a deviation from linearity observed, indicative of solvent clustering. Furthermore, this solvent clustering was not observed at higher pressures.

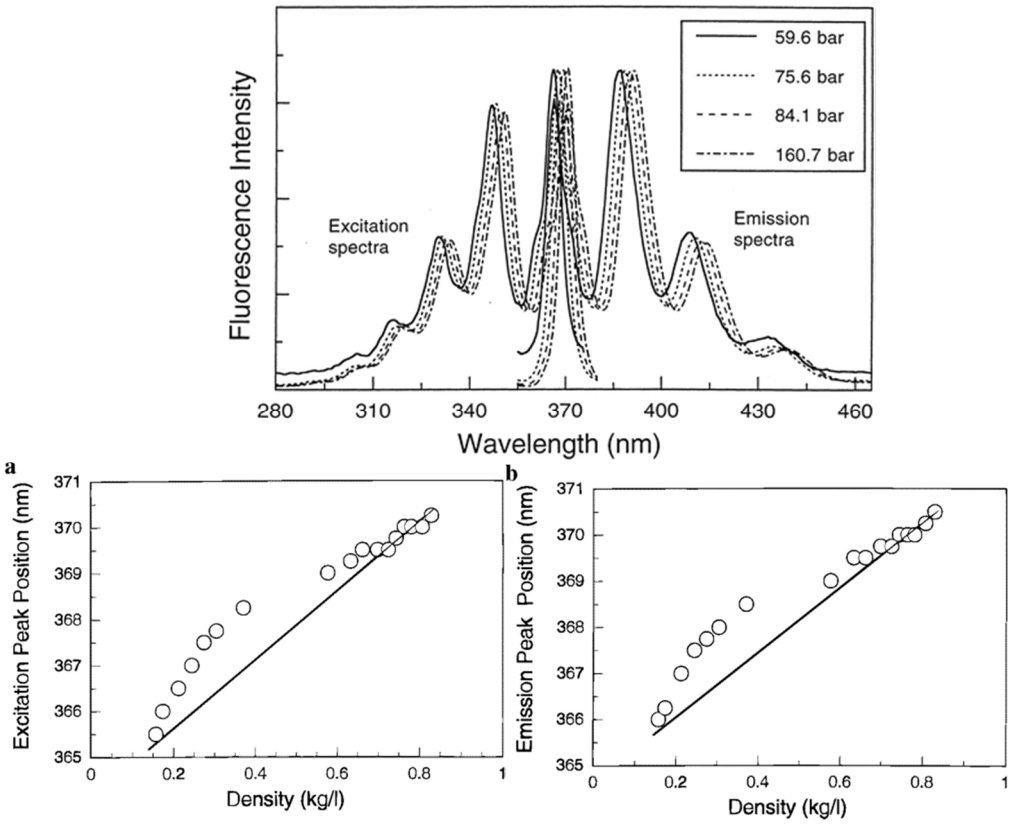

Figure 6-11: The excitation and emission spectra of anthracene fluorescence in pure CO_2 at 35 ^oC with increasing pressure (top). The change of the (0,0) peak positions with density for excitation (bottom; left) and emission spectra (bottom; right) of the anthracene fluorescence in CO_2 at 35 ^oC. The solid line is the linear least squares fit to the high pressure data. Reproduced from reference 269.

Further studies of anthracene based dyes have included 9-cyanoanthracene (9-CNA) and 9,10-bis(phenylethynyl)anthracene (PEA).[268, 270] A red shift was observed in the emission and absorption wavelength with increasing density, shown in Figure 6-12 for 9-CNA and PEA respectively. The observed red shift with increasing density indicates that at higher densities of CO_2 the excited state is stabilised, resulting in a smaller energy difference between the ground and excited state. As observed for anthracene, a deviation from linearity is observed at lower densities, which again is indicative of solvent clustering around the probe molecule.

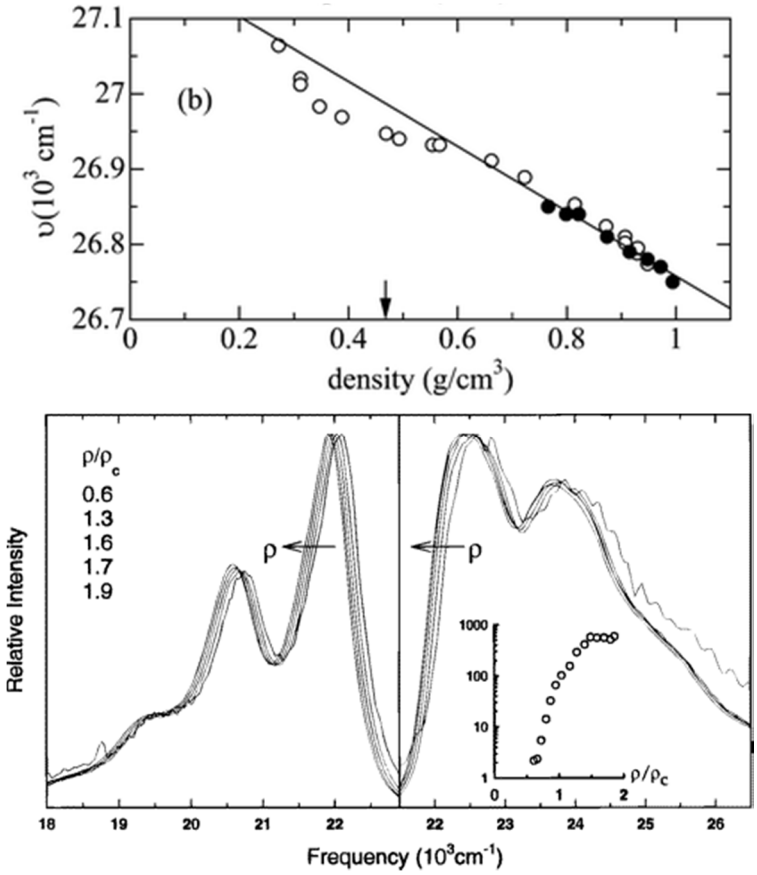

Figure 6-12: The density dependence of the maximum wavelength of the 0-1 band of 9-cyanoanthracene for absorption spectra in $scCO_2$ at 35 °C (o) and liquid CO_2 at 25 °C (●), where the critical density is indicated by the arrow (top). Steady-state emission (bottom, left) and excitation spectra (bottom, right) of PEA in CO_2 shown as a function of density (ρ) The direction of increasing density is indicated by the arrow. The increase in relative emission intensity as a function of reduced density resulting from the density dependent solubility of PEA in $scCO_2$ is also shown (inset). Reproduced from references [268, 270].

Experimental observations of clustering have been further supported by molecular dynamic simulations. Nugent *et al.* studied the spectral line shift for molecules that become more polar upon excitation.[271] At $1.05T_c$, the results indicated that the extent of local density enhancement is strongly correlated with solvent-solute electrostatic attraction with the emission shifting to reflect this density dependence. However, at $2T_c$ no density enhancement is observed. Bromine was used as a probe and was considered as a quadrupole partial charge. The dipolar charges coinciding with atom positions were arbitrarily assigned d5 and d8, wherein d8 exhibited a higher dipole moment than d5. Local density augmentation effects were observed at *ca.* 1.05Tc in contrast to *ca.* $2T_c$.

This was demonstrated by the non-linear increase in emission seen at $1.05T_c$, which was not observed at $2T_c$. This behaviour is displayed in Figure 6-13.

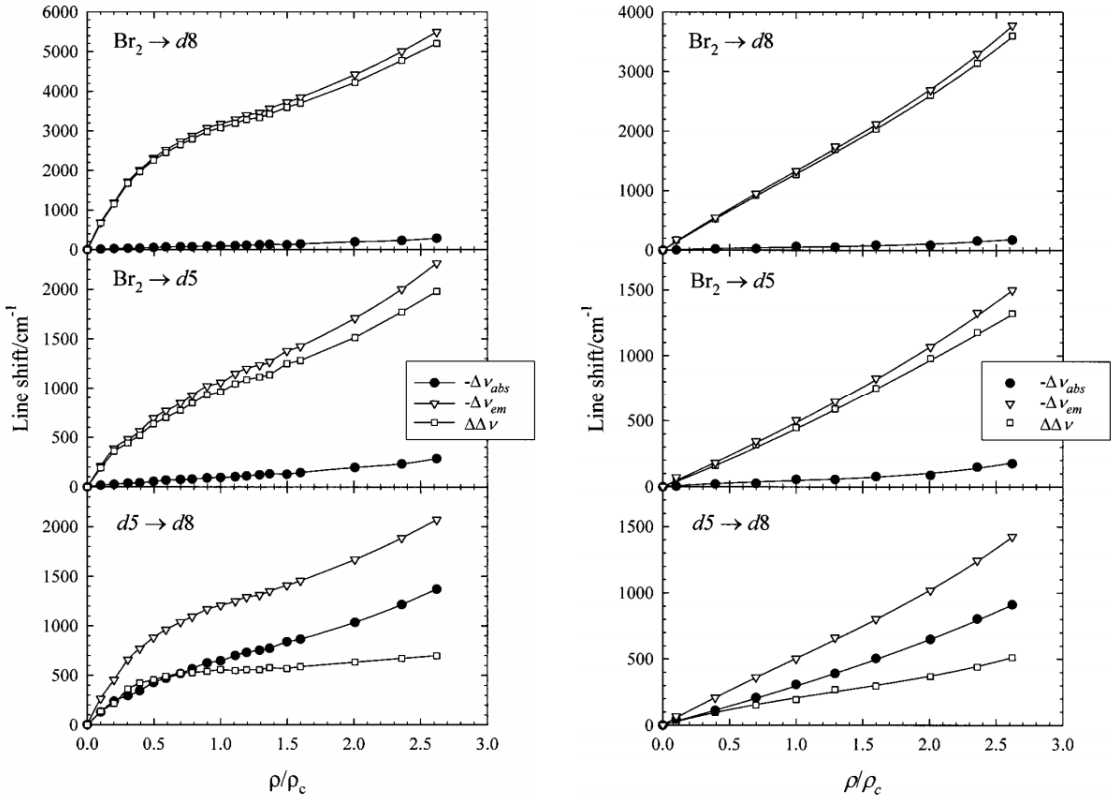

Figure 6-13: The shifts in emission for the partial charges of the bromine probe considered, quadrupole moment for bromine, dipole moments, d5 and d8, wherein the dipole moment d8 is larger than d5. The effect of local density augmentation is observed at $1.05T_c$ (left) and not observed at $2T_c$ (right). Reproduced from reference 271.

Mathematical models have shown that the density augmentation around solutes results in the characteristic deviation from linearity for solvation energy, Figure 6-14.[220] The behaviour of the solvation energy in a SCF includes a very rapid change in solvation energy at densities below the critical density, followed by little variance at density beyond the critical density. The rapid change at densities below the critical density, are the direct result of rapid increase in the local solvent density, *i.e.* solvent shell formation.[220]

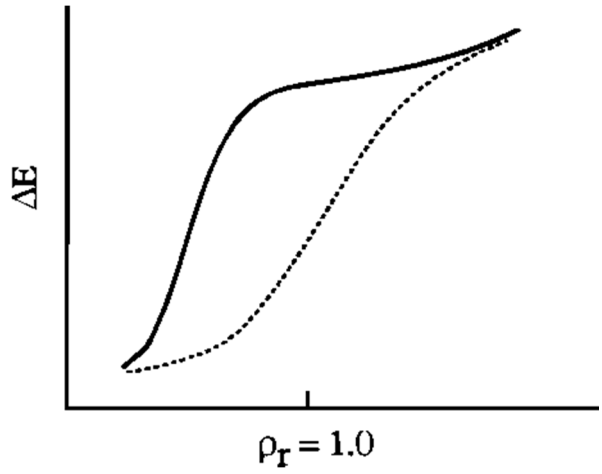

Figure 6-14: Schematic diagram of the typical bulk density dependence observed for solvation energy differences in highly compressible SCFs (solid line) and the behaviour expected on the basis of the bulk density (dashed line) for polar solvents, plotted as a function of reduced density (ρ_r). $\rho_r = \rho/\rho_c$. Reproduced from reference 220.

From the previous literature it is observed that the emission energy is not linear with density at higher densities where this effect which is attributed to appreciable local density enhancement effects even at densities above the critical density and has been confirmed through theoretical simulations,[271] and experimental emission studies for a 1,3,6,8-tetraphenylpyrene probe.[270]

Examination of 2-nitroanisole in CO_2 revealed a red spectral shift with density. At higher reduced densities a non-linear dependence of spectral shift with density is observed, as shown in Figure 6-15.[280, 281] The plot (Figure 6-15) also exhibits data obtained by maintaining a constant pressure and varying the temperature to change density. This indicates that it is density and not temperature, which dictates the magnitude of the observed spectral shift.

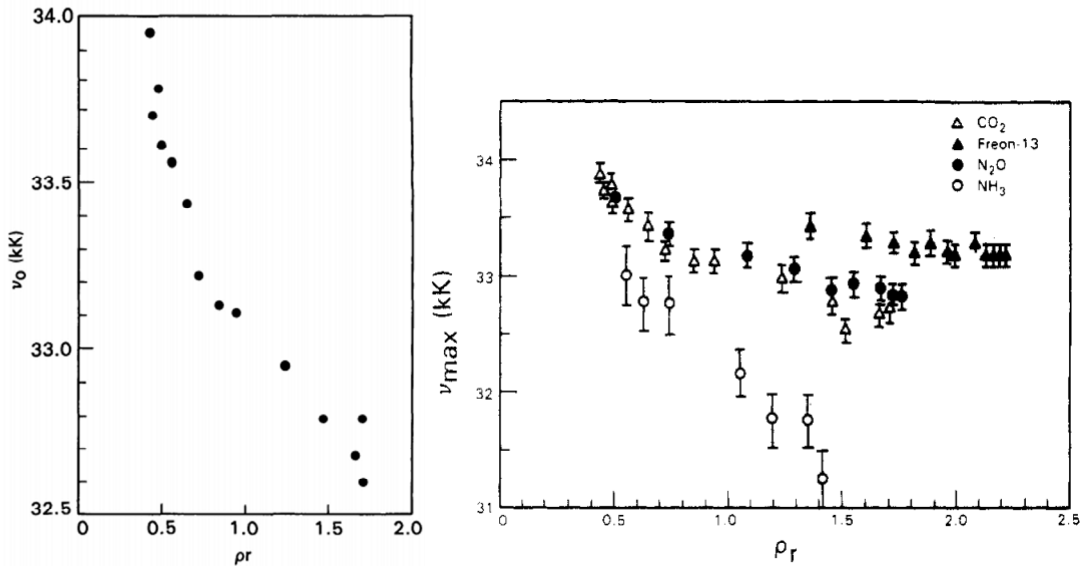

Figure 6-15: The shift in the λ_{max} of 2-nitroanisole at reduced densities (ρ_r) of CO_2. Where $\rho_r = \rho/\rho_c$. Reproduced from references 280 and 281.

Limited previous work on the photophysical behaviour of other SCFs has been conducted previously, with the work primarily focussing on the solvatochromic shifts of dyes and local density augmentation effects. A sequential quantum mechanics/molecular mechanics method has been used to calculate the solvatochromic shift for aqueous benzene, where at relatively high reduced densities (*ca.* >0.75),[282] a similar non-linear increase in solvatochromic shift with increasing density was determined as seen for measurements in CO_2. This is shown in Figure 6-16.

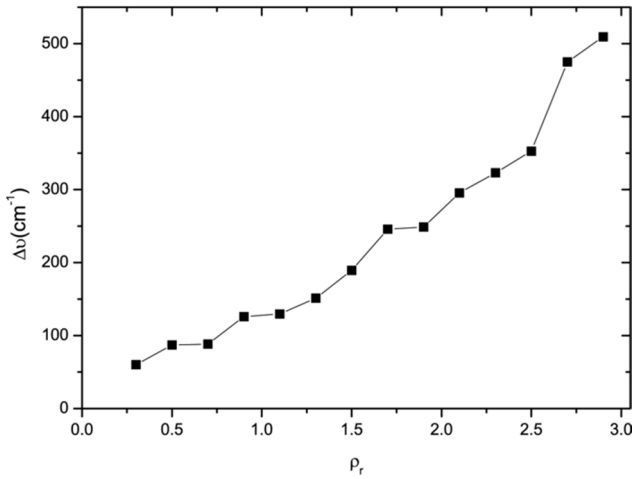

Figure 6-16: The sequential quantum mechanics/molecular mechanics method calculated solvatochromic shift of aqueous benzene at varying reduced densities. Non-linear increase in solvatochromic shift is observed with density. Reproduced from reference 282.

Further work by Sun and co-workers also used (N,N-dimethylamino)benzonitrile as a probe as well as ethyl(N,N-dimethylamino)benzoate in R23.[283] Again a decrease in absorption energy was observed as the density of R23 increased, Figure 6-17. The observed deviation from linearity was again attributed to local density augmentation.

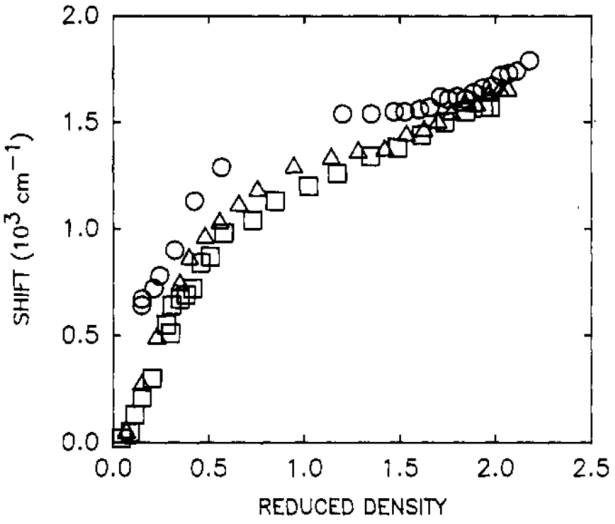

Figure 6-17: The absorption of (N,N-dimethylamino)benzonitrile in scR23 wherein a positive solvatochromic shift was observed with increasing density. (o) 30 °C, (Δ) 44.7 °C, (▫) 59.6 °C where the critical density is at ρ_r = 1. Reproduced from reference 283.

1.6 Fluorescent Sensors for Polarisability

As well as employing solvatochromic fluorescent dyes to study the density of fluids, they have also been used to assess the polarisability of fluids. This is an important property which needs to be understood in order to tune the SCFED process. This is because the polarisability of the fluid dictates the nature of the electrolyte that may be used and therefore the materials that can be deposited. The change in dipole of the excited state (ES) compared to the ground state (GS) results in stabilisation of the ES and GS to varying extents depending on the polarity or polarisability of the solvent. For a molecule with an increased dipole moment in the ES a spectral red shift will be observed as the dielectric constant and/or polarisability of the fluid is increased, as was observed when fluid density is increased. Thus, solvatochromism may be used to determine the polarisability and polarity of a fluid surrounding a probe molecular, indicating its ability to dissolve more polar solutes. This occurs because of the stabilising interaction of a

solute and the solvent.[284] The commonly implemented Lippert-Mataga equation relies on changes to the solvents dielectric constant and ignores solvent polarisability effects. For this reason, the equation will not be utilise to establish the polarisability of CO_2. This ionising power of the solvent may be denoted by the Dimroth-Reichardt $E_T(30)$ index,[285] which uses the maximum wavelength of the lowest energy electronic absorption of the dye in a given solvent as metric, an example of which is shown in Figure 6-18.

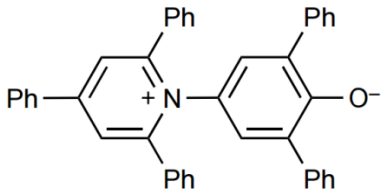

Figure 6-18: The dye employed by Dimroth and Reichardt for determining the $E_T(30)$ index. Where the index is a measure of the ionising power of a solvent based on the maximum wavelength of the lowest energy electronic absorption band of the dye in a given solvent.

The first study that utilised solvatochromic effects in SCFs was the assignment of polarity values completed by Hyatt *et al.*[224] which attempted to establish a comparison between the polarity of $scCO_2$ and common organic solvents. Examination of the $E_T(30)$ scale indicates that CO_2 exhibits similar polarity to toluene, hexane, methylcyclohexane, decahydronapthalene and tetrachloroethylene.

Kamlet, Taft, Abboud and co-workers, developed four distinct solvatochromic scales of solvent polarity including the Kamlet-Taft π* scale (KTπ*) of solvent dipolarity/polarisability, with solvent parameters for over 500 different liquids having been established.[186, 286-288] The index of solvent dipolarity/polarisability is defined as the measure of ability of the solvent to stabilise a charge or a dipole by its polarisation. The solvents investigated were all non-chlorinated, non-protonic and aliphatic with a single dominant bond dipole.

The KTπ* scale of solvent dipolarity/polarisability was calculated through the observation of various nitroaromatic dyes, which demonstrate a large solvatochromatic shift, responding minimally to changes in the hydrogen bond basicity and acidity of the solvent. The KTπ* scale can be determined with the use of Equation 6-1 where ν_i,

$\nu_{cyclohexane}$, $\nu_{dimethylsulfoxide}$ are the frequencies of absorption for the molecules, cyclohexane and dimethyl sulfoxide respectively, in the solvent.

$$\pi^* = \frac{\nu_i - \nu_{cyclohexane}}{\nu_{dimethylsulfoxide} - \nu_{cyclohexane}} \qquad \textbf{(Equation 6-1)}$$

In contrast, limited work has been carried out on solvatochromism in SCFs, with studies including CO_2,[224, 281, 289-291] water and fluorocarbons.[289, 291] The assignment of KTπ* values for a limited range of SCFs using nitroaromatic dyes has been conducted in literature, with the results summarised in Table 6-1. These probes have been used because they exhibit very large solvatochromic shifts.

Table 6-1: Literature KTπ* values for a range of fluids using nitroaromatic KTπ* dyes.

Fluid	Probe	ρ (kg.m^{-3})	KTπ*	Ref
CO_2	2-nitroanisole	950	0.04 ± 0.03	281, 290
CO_2	4-nitroanisole	860	-0.11	292
CO_2	N,N-diethyl-3-nitroaniline	860	-0.07	292
CO_2	4-methoxy-β-nitrostyrene	850	-0.29	292
CO_2	1-ethyl-4-nitro-benzene	860	-0.17	292
CO_2	N-methyl-2-nitro-p-toluidine	860	-0.01	292
CO_2	N,N-diethyl-4-nitro-aniline	860	-0.01	292
CO_2	4-(dimethylamino)benzophenone	860	-0.21	292
CO_2	4-nitroaniline	860	-0.09	292
CO_2	4-nitrophenol	860	-0.17	292
$CClF_3$	2-nitroanisole	870	-0.29 ± 0.03	281
$CClF_3$	2-nitroanisole	1150	-0.21 ±0.04	281
N_2O	2-nitroanisole	950	-0.03 ± 0.02	281
NH_3	2-nitroanisole	360	0.34 ± 0.07	281
NH_3	2-nitroanisole	620	0.80 ± 0.02	281

Additionally, the observed solvatochromic shift of (N,N-dimethylamino)benzonitrile has been correlated to the solvent polarisability (KTπ*) of supercritical trifluoromethane (scR23),[293] where this solvatochromic shift has been calculated as a function of solvent polarity (Figure 6-19), for both the liquid phase (represented by bromobenzene, *n*-butyl chloride, tetrahydrofuran, butyronitrile, cyclohexanol, ethanol and methanol) and for

scR23. The liquid phase data show a linear increase in shift with increasing polarisability. However, this linearity is not conserved for the R23 data, which exhibits deviation from linearity. This deviation can be attributed to the local density augmentation effects that arise from solute-solvent clustering affects.

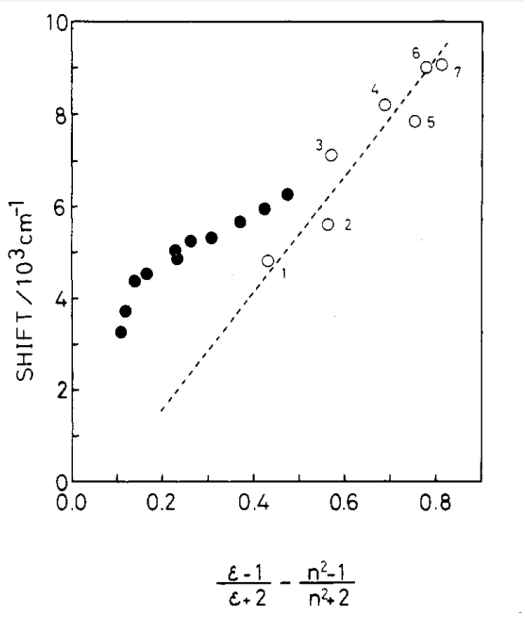

Figure 6-19: Solvatochromic shift of (N,N-dimethylamino)benzonitrile as a function of the solvent polarity. Data shown for both the liquid phase (bromobenzene (1), n-butyl chloride (2), tetrahydrofuran (3), butyronitrile (4), cyclohexanol (5), ethanol (6) and methanol (8)) denoted by the symbol (o) and for scR23 denoted by the symbol (●). Reproduced from reference 293.

Further work by Maiwald, Schneider *et al.*[289, 291] probed the solvatochromic shifts of five different nitrobenzene derivative dyes in five SCFs (CO_2, N_2O, $CClF_3$, SF_6 and NH_3). Where the KTπ* values are calculated with 2-nitrosnisole as a dye and are shown in Figure 6-20. The isotherms have a similar shape for all of the fluids listed where subcritical isotherms follow a continuous curve. The KTπ* values for $scCO_2$ are shown to decrease from -0.12 to -0.46 as density decreases from 860 to 460 kg.m^{-3}. These results have been further corroborated by Yonker *et al.*[281] and O'Neill *et al.*[290] where the KTπ* value for $scCO_2$ has been shown to increase with respect to density with a 2-nitroanisole probe.

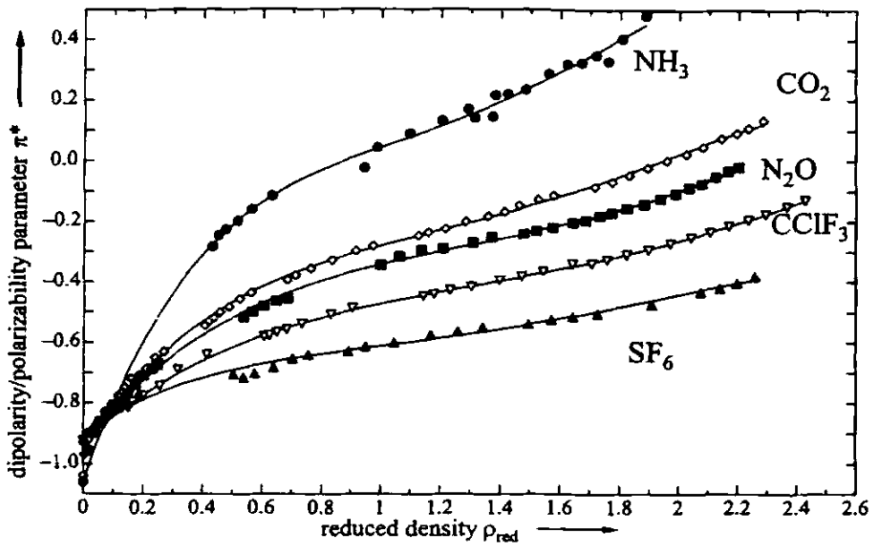

Figure 6-20: KTπ* values of five different supercritical fluids, ammonia (NH_3), CO_2, nitrous oxide (N_2O), chlorotrifluoromethane ($CClF_3$) and sulphur hexafluoride (SF_6) at reduced temperature of 1.1 T_c as a function of reduced density (ρ_{red}). The measurements were conducted with 2-nitroanisole as the probe. Reproduced from reference 289.

The study demonstrated that SCF solvents such as $scCO_2$, resemble non-polar solvents such as alkanes and fluoroalkanes, whereas $scNH_3$ resembles a polar solvent such as pyridine, with positive values of KTπ* being obtained at reduced densities above 1.9 (*i.e.* at all densities above 890 $kg.m^{-3}$) for CO_2.

1.7 Spectroscopic Cell Designs for High Pressure Measurements

Bespoke apparatus is required for spectroscopic measurements at high pressures and temperatures in order to study the supercritical phase. Important considerations include maximum operating pressure and temperature and path length, which will dictate the concentrations that may be used. The spectroscopic region of interest will also dictate the material which can be used for the cell windows. A range of cells used previously for supercritical fluid spectroscopic measurements have been described in literature,[294-296] all of which have common features, including windows which are transparent in the spectroscopic region of interest and the ability to contain high pressure fluids. They also exhibit designs which allow for the filling and venting of the fluid.

The window can often be the weakest part of a cell in terms of high-pressure containment, with sealing the window(s) to the cell body thought of as the most difficult part of designing a high pressure cell. There are two methods employed in order to seal a window. These are the '*opposed force*' and '*Poulter*' approaches. The former, relies on sealing the cell body to the face of the window in contact with the fluid using a seal such as a Teflon® o-ring or gasket and are often supported with the use of glue. However, there are two main limitations. Pressure must be applied to the window to make the seal and some o-rings can absorb supercritical fluids causing swelling, both of which may be sufficient to cause the window to break or the o-ring to fail. The latter Poulter method relies on sealing the window to the cell body on the face in contact with the cell, using the internal pressure of the fluid to force the window to seal. Two main limitations of this method are the fact that this design often results in dead volumes which may be penetrated by the supercritical fluid, resulting in non-quantitative measurements. Secondly, when evacuating the cell precautions must be taken to prevent atmospheric pressure pushing the window away from its seal.[294]

Studies concerning a cell and methodology for supercritical fluorescence measurements are extremely limited in the literature. Although a typical cell set-up involves a stainless steel body with four windows combined with temperature controls and pressure monitors.[7, 276, 283, 297-299]

Rhodes and Fox studied the photophysics of phenanthrene in $scCO_2$ using a cell shown in Figure 6-21.[297] The cell consists of four sapphire windows, which are sealed *via* Teflon® o-rings in a stainless steel body. The cell consists of two fluid compartments: the inner compartment is the sample chamber with volume of 15 mL and a path length of 4 cm, while the outer compartment is a separate internal flow loop used for temperature control *via* recirculation from a water bath.

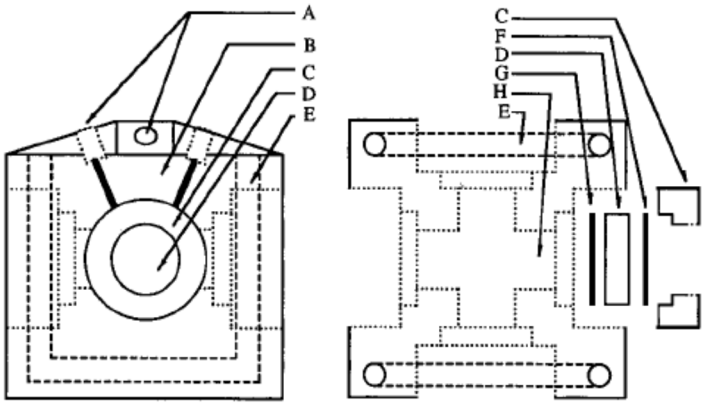

Figure 6-21: High pressure absorbance/fluorescence cell design schematic used by Rhodes and Fox: side view (left) and the top view (right). Shown is the high pressure inlet (A), stainless steel body (B), threaded cap for holding a sapphire window (D), the flow loop for water bath temperature control (E), O-rings (F, G), and the sample compartment (H). Reproduced from reference 297.

This cell has a much larger internal volume and path length when compared to the commonly used traditional quartz cells, which have a path length of 1 cm and a volume of *ca.* 3 mL. The large internal volume was reported to be for practical reasons, allowing for sufficient water cooling, as it increases the water contact with the sample holder, leading to a larger path length. Furthermore, a larger path length allows for lower concentrations of solution to be used, increasing the detection limit as stated by the Beer-Lambert law. Additionally, Rhodes and Fox demonstrated the benefit of using commercially available sealing compartments in the form of Teflon® seals, nuts and ferrules. This allowed for the inexpensive replacement of parts in case of a leak. A thermocouple is also located inside the high pressure chamber allowing for accurate temperature monitoring. The pressure is monitored *via* an external pressure transducer. However, a water flow loop for cooling may result in inconsistent temperature application due to external factors. An example of this may occur if the flow loop transferring water to the cell cooling system is of considerable length, resulting in an unavoidable change in water temperature. The cell differs from previous designs by Brennecke and Eckert who also utilise a non-commercially designed cell. Their cell consists of 6mm thick fused quartz discs and four Peltier coolers fastened to the bottom of the cell for heating and cooling.[299] Rhodes and Fox suggest an improved homogeneous temperature control

through the use of recirculating water. Furthermore, Brennecke and Eckert's cell design had a far smaller internal volume of 3.4 mL.

Sun *et al.* reported the design of a three inch cubic stainless steel cell for $scCO_2$ measurements. This cell consists of four sapphire windows and Teflon® seals,[283] similar to previous designs.[297, 299, 300] However, the system relies on two cartridge heaters to reach desired temperatures, as opposed to a water cooling or heating system. Again a temperature controller was used to monitor and maintain temperature. It is suggested that this results in a much more consistent temperature within the high pressure chamber (± 0.2 ^{o}C). An inlet tap was used to introduce the fluid into the system and an outlet tap to vent the system after an experiment. A schematic of the cell is shown in Figure 6-22. Again, commercially available parts were used where possible and the cell can withstand pressures up to *ca.* 5000 psi, as the commercially available window and cell body are rated to this value.

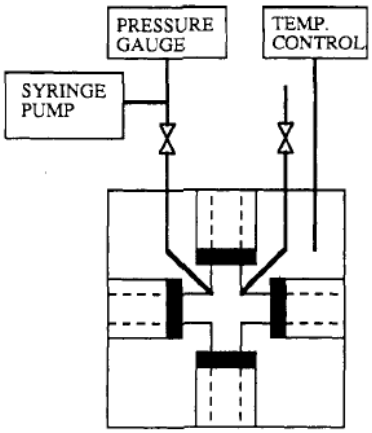

Figure 6-22: A schematic of the high pressure cell used by Sun *et al.* which consists of a stainless steel body, four sapphire windows and an inlet tap for introduction of the fluid. The cell is kept at temperature by two heating cartridges. Reproduced from reference 283.

In contrast to Rhodes and Fox, Brennecke *et al.* used a custom made cell which had path length of only 1.3 cm and quartz windows were used over sapphire.[7, 276, 298] However, similarly to Sun *et al.* heating cartridges over a water bath were employed to obtain a constant stable temperature.[283]

A high-pressure rig system is required to introduce and remove fluid from the cell. Brennecke and Eckert detailed their high pressure assembly with a schematic shown in Figure 6-23. The gas is compressed from the cylinder into the mixing vessel, which is connected to a vacuum pump which evacuates the vessel prior to use, minimising atmospheric contamination. A solute (such as a probe dye) is either added directly to the mixing vessel or into a special solute chamber located in the inlet line to the vessel. The latter results in the solute being dissolved as the mixing vessel is pressurised. The solvent vessel is used to fill the optical cell with pure solvent before the mixture is introduced. This prevents the solute falling out of solution when introduced into the cell. The cell is then flushed with the mixture until all the solvent is displaced.

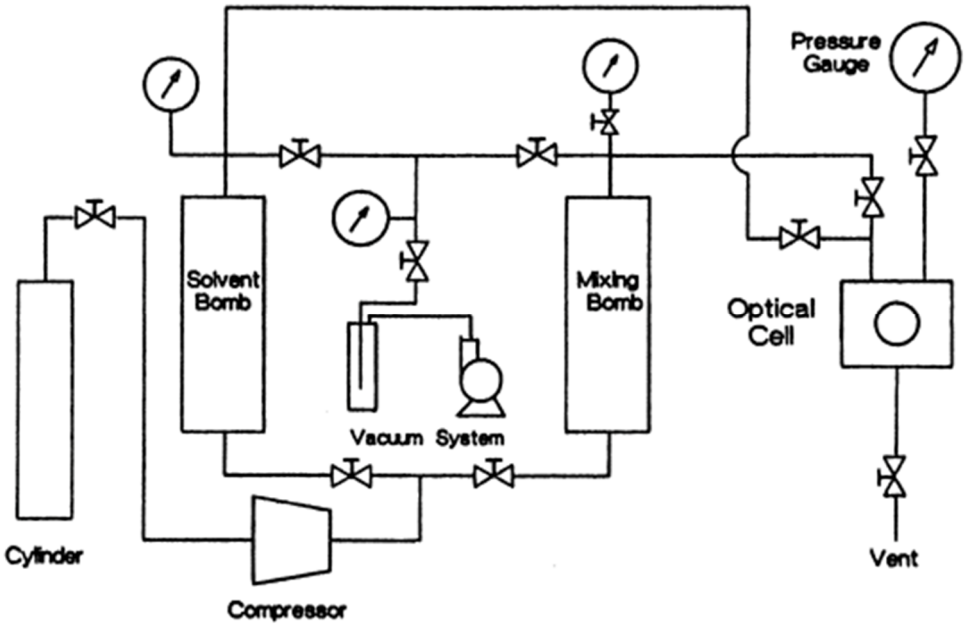

Figure 6-23: Schematic of the high pressure assembly used by Brennecke and Eckert to introduce and remove fluid from a high pressure optical cell. Reproduced from reference 299.

2 Aims

The aim of this work is to further the understanding of both the bulk and confined phase behaviour of the fluids used in the SCFED process, through the use of luminescence spectroscopy. Furthermore, this work aims to establish a relationship between the phase behaviour and spatial confinement of a fluid, in particular the fluid density. This is because the density of a fluid is of paramount importance when guiding and refining the SCFED process. The aim breaks down into three objectives.

1. To develop a cell and rig system suitable for conducting luminescence measurements in SCFs and subsequently to establish a methodology for conducting luminescence measurements on bulk and confined fluid systems.

2. To identify a suitable probe dye for density, which is soluble in CO_2 possessing a spectral signature which is indicative of fluid density and possible to follow spectroscopically.

3. To determine the density of the fluid inside the confined environments and investigate any changes to the fluids polarisability and dielectric constant.

3 Results and Discussion

3.1 Cell Design and Development

The first crucial step within this work was to design a cell for use in high pressure luminescence measurements, where there is limited precedent in the literature.[46, 59, 63, 78, 79] The design of this cell is shown in Figure 6-24 and is referred to as the Nottingham Cubic Cell in the rest of the Chapter. Additionally, a system and methodology for conducting supercritical fluorescence measurements has also been produced. The cell was designed to conform to the nature of luminescence spectroscopy utilising the fluorimeter detailed in Chapter 8, which requires emission to be detected at 90^{o} to excitation. Additionally, the energy source for lifetime measurements is at 180^{o} to the energy source for steady state measurements with both energy sources at 90^{o} to the photomultiplier detector. As a result, the cell requires a four window layout. Furthermore, the window material needs to be transparent to light with wavelengths between *ca.* 200 - 800 nm, the range required for this work. Therefore, quartz was chosen as the window material. All four windows are sealed using Teflon® o-rings, a method proven effective in previous literature.[295]

The internal volume of the cell was calculated experimentally to be 3.64×10^{-6} m^3 measured gravimetrically using methanol as a standard, and has an optical path length of 1 cm. The cell has been designed to be suitable to withstand pressures up to 5000 psi, allowing for the high pressures required to perform the phase probing luminescence spectroscopy in this work.

This resulted in a rig system containing two taps, where Tap 1 allows for introduction and pressurisation of fluids using a syringe pump, and Tap 2 allows for the venting of the fluid post experiment. In order to obtain the temperatures required, heating cartridges can be used. These can be configured in all four corners or as two cartridges in an opposite corner of the cell configuration. Experimental investigation demonstrated a negligible difference between the four and two-series heating cartridge configuration for reaching and maintaining the desired temperature, as a result the two series heating cartridge arrangement was chosen for ease of use and to minimise the cost.

The rig system, a schematic of which is shown in Figure 6-24, contains a pressure transducer to monitor the pressure inside the cell and system. Two thermocouples are also employed one for the regulation of the heating cartridges and one for monitoring the internal temperature of the windowed chamber.

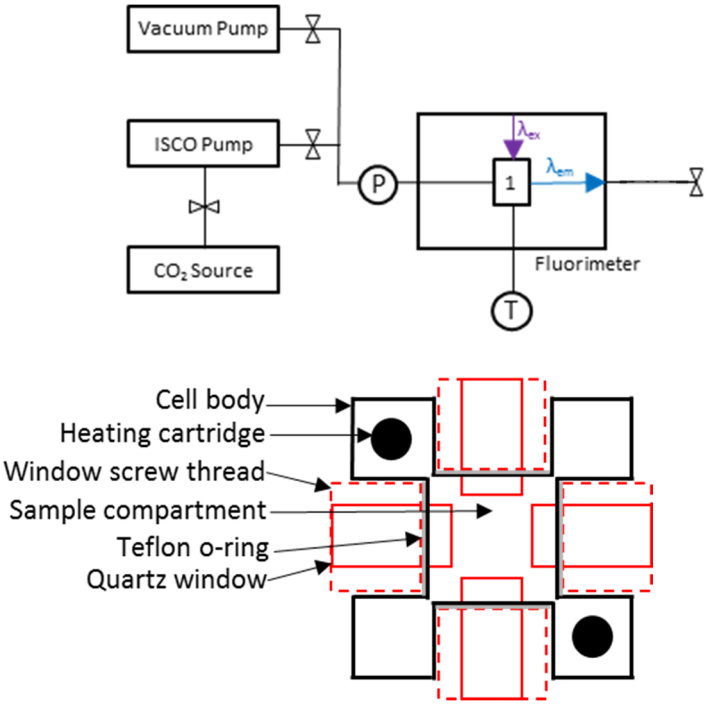

Figure 6-24: The cell and rig system developed at the University of Nottingham for luminescence spectroscopic measurements in SCFs (top). The cell (1) consists of a stainless steel body, four quartz windows, a possible four heating cartridges – one in each corner of the cell body, an inlet tap for introduction of the solvent, pressure transducer (P) for monitoring the pressure and a thermocouple (T) to monitor the temperature in the cell. A top down view of the Nottingham cubic cell showing the cell body, window holder which screws into the cell body sealed with a Teflon o-ring, the quartz windows and heating cartridges. Not shown is the thermocouples which are inserted into the steel cell body and into the sample compartment.

Firstly the cell was tested using conventional liquid solvents to ensure that the apparatus provided reliable measurements in comparison to traditional quartz cells. Excitation and emission measurements of 9-cyanoanthracene (9CNA) in hexane was carried out in both a conventional quartz cell and in the Nottingham Cubic Cell for luminescence measurements and the results showed a good correlation with each other.

Subsequently, the cell was tested by performing measurements in SCFs to ensure the reliability of the cell at high pressures and the viability of the chosen methodology.

Therefore, the emission spectra of 9CNA (Figure 6-25) was measured in $scCO_2$ and a maximum emission wavelength of 422 nm was observed, which corresponds well with the literature value.[268, 301]

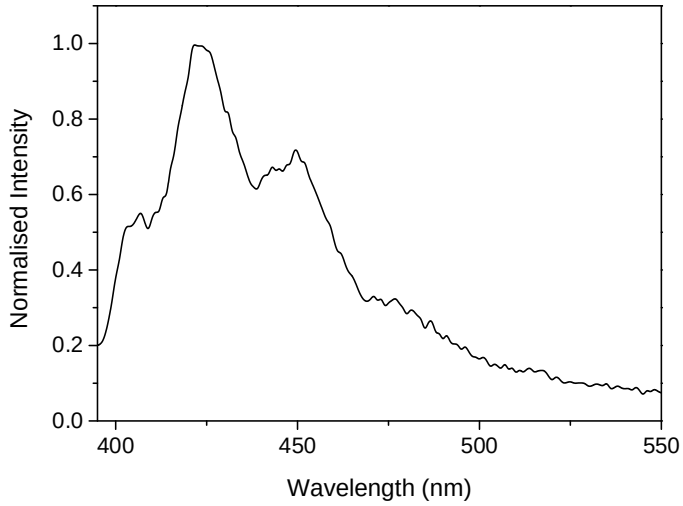

Figure 6-25: The emission spectrum of 9-cyanoanthracene in $scCO_2$ obtained from Nottingham Cubic Cell and by following the methodology implemented within this work. An emission maximum of 422 nm is observed.

3.2 Porous Measurements Development of a Methodology in Order to Measure Emission Spectra from within the Pores

The aim of this work is to investigate the phase behaviour of confined fluids within porous materials *via* luminescence measurements. Following the design of a cell, rig system and methodology for supercritical fluid measurements, it was important that a methodology for in pore measurements was also developed. This method development will be discussed in the following section.

It is expected that an emission of anthracene in bulk and confined CO_2 differs and thus it is imperative to ascertain if the difference is due to the confinement of the CO_2 or due to an interaction between anthracene and silica. In order to establish this influence a control experiment was conducted to assess the effect of the interaction between silica and the anthracene dye in the absence of a solvent on the emission spectra. The effect on anthracene emission when adsorbed onto the silica has been investigated by probing the emission of solid state anthracene, anthracene absorbed within the porous material

and adsorbed anthracene onto the silica porous material using literature methods and detailed in Chapter 8.[302]

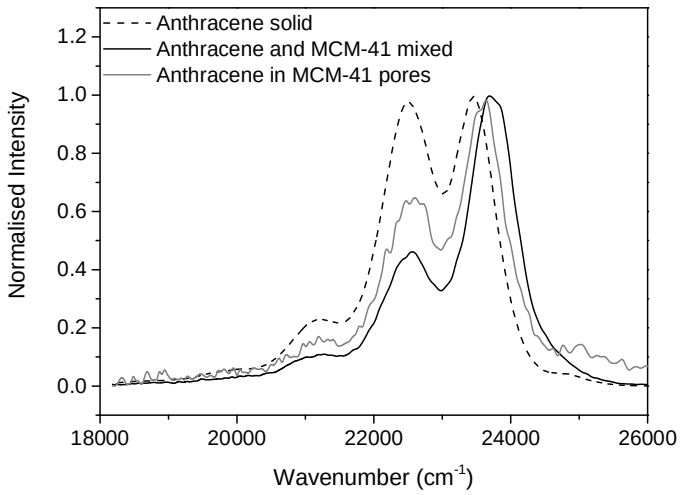

Figure 6-26: The emission spectrum of pure anthracene (dashed), anthracene and porous silica material ground up together (black) and anthracene adsorbed inside the 3.2 nm porous silica material (grey).

As illustrated in Figure 6-26, a small blue shift in emission is observed from anthracene (dashed) to anthracene adsorbed onto silica material (black) and to anthracene absorbed in the silica (grey). This observed blue shift in the anthracene control measurements is almost negligible for the emission, indicating that there is very limited interaction between the silica and the anthracene probe without solvent present.

Further work was carried out to draw a conclusion on the extent any possible interaction of anthracene with silica in the presence of CO_2 and the effect on the observed anthracene emission energy. Measurements of anthracene in silica (Zeolite Y, *ca.* 0.24 nm) possessing pore width which are too small for anthracene, where anthracene has a molecular size of *ca.* 1 nm were carried out. This material may be considered as 'non-porous' for the sake of this investigation. As shown in Figure 6-27, a blue shift is observed with increasing pressure, as exhibited by anthracene and porous material measurements in the absence of solvent (Figure 6-27). Over *ca.* 850 psi and 150 $kg.m^{-3}$ of CO_2, an emission resembling only anthracene in CO_2 was observed indicating that no absorption into the pores occurs in $scCO_2$. Therefore, due to the small change in emission energy, which shows no correlation to pressure, the effect of silica on the measurements is not considered when drawing conclusions within this work.

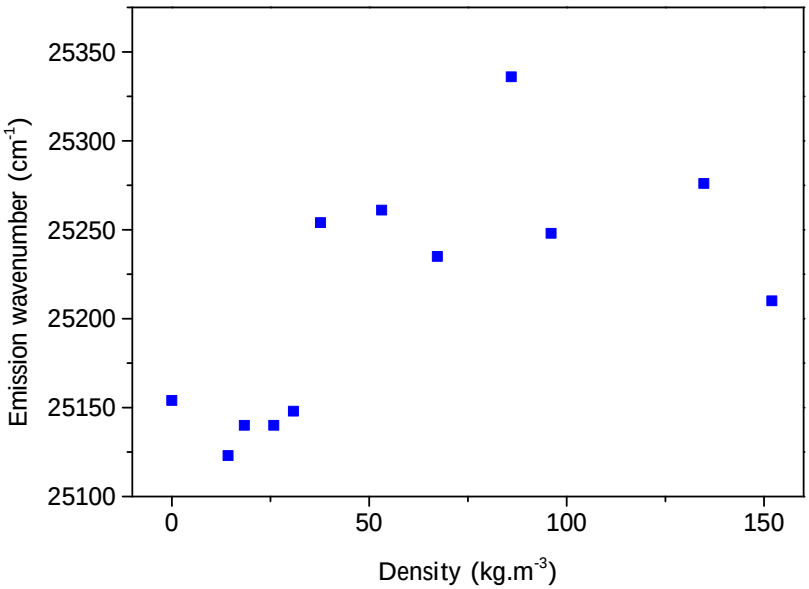

Figure 6-27: Emission of anthracene as a function of CO_2 density in the presence of zeolite Y ('non-porous silica'). The size of the pores is smaller than that of anthracene so any interaction can be attributed to the surface effect of silica with anthracene.

After determining the negligible effect of the silica on the emission energy of anthracene, the development of a methodology for luminescence measurements in SCFs within porous materials was investigated. Owing to the lack of literature precedent, the development of this methodology may have far reaching implications as a metric for phase behaviour within confined systems, which will provide chemical information at a lower cost owing to the lack of specialised equipment in contrast to current methods such as SANS.

Silica does not absorb light in the spectral region of interest, therefore, it was reasoned that the simplest method to conduct luminescence measurements within porous materials was to add a small known amount of anthracene dye to the cell and to subsequently fill the cell body with silica, removing any volatile impurities *in vaccuo*. However, an emission spectrum could not be obtained using this method, due to the scattering of light by the silica.

Subsequently, to limit the light scattering observed, the volume of silica was reduced by fabricating thin discs of silica, both pure and impregnated with the dye and tested. A variety of disc sizes (0.1 – 0.25 mm thickness, 13 mm diameter) were tested and all were unchanged after initial testing up to pressures of 2500 psi and subsequently venting

the CO_2. The disc was placed into the cell *via* the removal of one of the four windows. However, the aperture of the window is significantly smaller than that of the cell body, therefore for a diameter of disc which can fit into the cell through the aperture of the window results in a disc diameter that is significantly smaller than the cell body.

Having established that using a silica disc resting upon the window gave reasonable spectra, the subsequent method was tested. Both impregnated and pure silica was left immobilised on the cell window as shown in Figure 6-28. For the former, a known quantity of anthracene was also added to the cell, then for both methods the cell and rig system were sealed and CO_2 introduced. However as the impregnation methods utilised requiring conventional solvents it is not possible to conclude that there is complete remove of the solvent during the drying process.

Figure 6-28: A suspension of silica in methanol was added drop wise onto the cell window and subsequently evaporated resulting in an immobilised layer of silica.

However, although spectra were obtained for methods utilising both pure and impregnated discs and pure and impregnated silica immobilised on the window, it was not possible to prove conclusively that there is no interaction between the methanol and porous material which may prevent the complete removal of the methanol solvent during the drying process, despite following well establish drying methods.[302, 303] Furthermore, due to pressure changes the silica layer was often removed from the window when fluid was added to the cell making measurements challenging to reproduce.

Finally, a glass holder specially designed to fit within the cell was produced containing a mixture of the porous material and anthracene, Figure 6-29. Preliminary testing ensured

that the glass did not emit in the spectral window of interest and did not absorb at the excitation wavelengths used.

Subsequently a method for filling the glass holder was required and three different procedures were tested. Firstly, the glass holder was filled with only silica and anthracene was added separately to the cell body. However, it was noted that only bulk emission was observed. Secondly the silica was impregnated *via* organic solvents as per literature.[302, 303] However, as discussed before it is not possible to prove the complete removal of the organic solvent.

Therefore, an alternative method for impregnating the silica which did not rely on conventional liquid solvents was explored. Thus, $scCO_2$ was used to impregnate the silica with anthracene, detailed in Chapter 7.

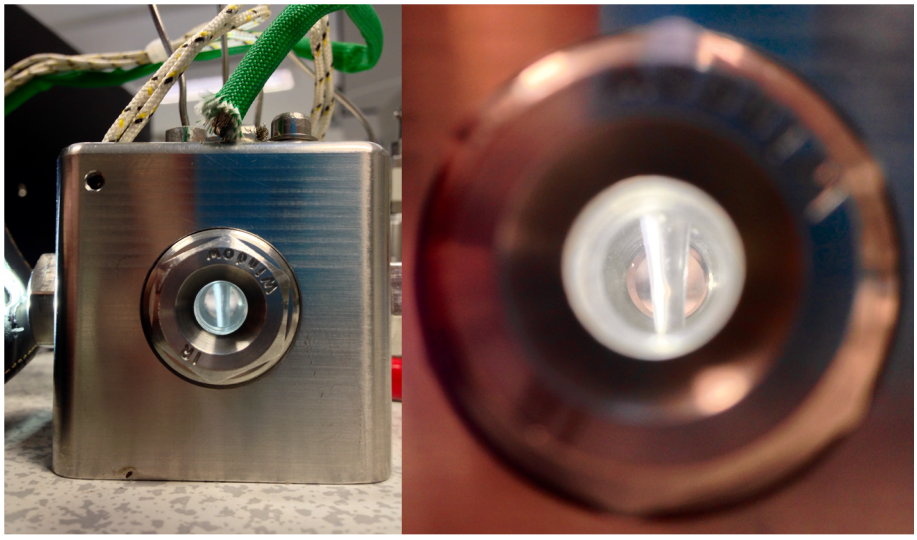

Figure 6-29: The glass holder containing silica impregnated, using CO_2, with anthracene dye position within the Nottingham Cubic Cell.

The sample was placed in the cell outside of the aperture of the window. CO_2 was slowly added at increasing pressures and absorption spectra taken. The presence of any leached anthracene in the absorption spectra is easily distinguishable from the absorption from the confined CO_2. Furthermore, leaching results in only anthracene emission in CO_2 due to the size of the cell holder, where leached anthracene in CO_2 would be the majority of the path length. Emission of anthracene in CO_2 is easily distinguishable from any

measurements obtained from the confined CO_2 environment due to significant shift in emission energy as shown in Figure 6-30.

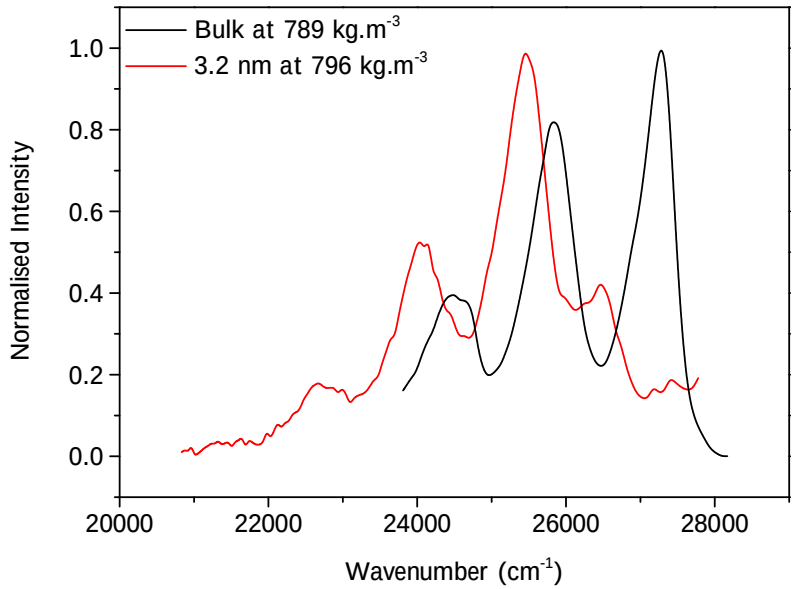

Figure 6-30: The anthracene emission energy in CO_2, in bulk conditions at a density of 789 kg.m^{-3} (red) and confined in porous material with 3.2 nm pore width, at a bulk CO_2 density of 796 kg.m^{-3} (black). All measurements conducted at 35 ^{o}C.

3.3 Towards Density Sensing of CO_2 Using Luminescence

Following the development of a methodology for high pressure luminescent measurements of both bulk and confined fluids, a suitable dye is required to act as a density probe in CO_2. The dye must exhibit sensitivity to changes in solvent density with clearly defined peaks which can be followed spectroscopically. Small polyaromatic hydrocarbons have been shown to have good solubility in CO_2 and therefore have been the main focus for potential probe dyes within this work. Some of the dyes tested experimentally are shown in Table 6-2, where anthracene, 9-cyanoanthracene and triphenylene yielded good spectra and clearly resolved peaks that show a clear solvatochromic shift with changing density of CO_2. These dyes are shown in Figure 6-31.

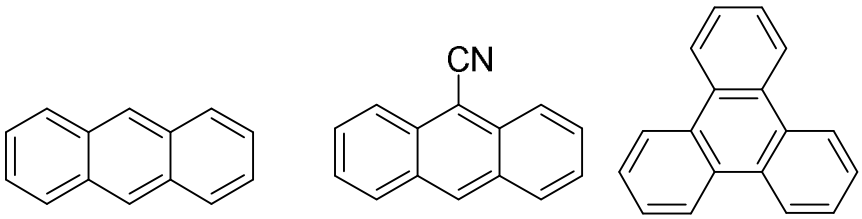

Figure 6-31: The structural formulae of anthracene (left), 9-cyanoanthracene (middle) and triphenylene (right).

Table 6-2: The dyes investigated experimentally within this work and an assessment of their viability as potential probes for density using luminescence.

Dye	Viability as a density sensor
Anthracene	Good solubility in CO_2, observed experimentally.
Rubrene	Poor solubility in CO_2, observed experimentally.
Pyrene	Good solubility in CO_2, observed experimentally, however peaks are poorly resolved and thus difficult to track.
Benzophenone	Shown to have good solubility in Hexane,[304] but poor solubility in CO_2, observed experimentally.
Biphenyl	Shown to have good solubility in cyclohexane,[305] but poor solubility in CO_2, observed experimentally.
Naphthalene	Shown to have good solubility in cyclohexane and hexane,[306] but poor solubility in CO_2, observed experimentally.
Chrysene	Good solubility in CO_2, peaks do not exhibit clear solvatochromic behaviour.
Triphenylene	Good solubility in CO_2, observed experimentally.
9-Cyanoanthracene	Good solubility in CO_2, observed experimentally.[301] Discussed below.
[Re([4,4]CF_3bpy)$(CO)_3$Cl]	Good solubility in CO_2, clear solvatochromic shifts observed, molecule is too large for pores.
[Re($R_{F8}(CH_2)$bpy)$(CO)_3$Cl]	Good solubility in CO_2, clear solvatochromic shifts observed, molecule is too large for pores.

Anthracene, 9-cyanoanthracene and triphenylene demonstrate good solubility in CO_2 and the effect of increasing CO_2 density on the observed emission energy has been tracked at a range of CO_2 pressures at 35 ^oC as shown in Figure 6-32. Triphenylene demonstrates emission in CO_2 and is in good agreement with literature.[307] However, a large and clear solvatochromic shift with density is not observed, making it unsuitable as a density sensor.

For anthracene, emission in CO_2 is observed and is in good agreement with the literature.[269] Additionally this emission is clearly observed to red shift with increasing density, where this red shift is because the dipole moment of the excited state (μ_E) of anthracene is larger than the dipole moment of the ground state (μ_G), thus as solvent density is increased the solvent polarisability is increased, and so the excited state can be stabilised causing a red shift.

Following on from this, 9-cyanoanthracene was investigated to ascertain the effect of substitution on the magnitude of the solvatochromic shift observed. The emission of 9CNA in CO_2 is in good agreement with literature.[268] and demonstrates a red shift with increasing density as seen for anthracene. However, the observed solvatochromic shift was smaller than that observed for anthracene. Therefore anthracene was identified as the most suitable probe molecule for the density investigations within this chapter.

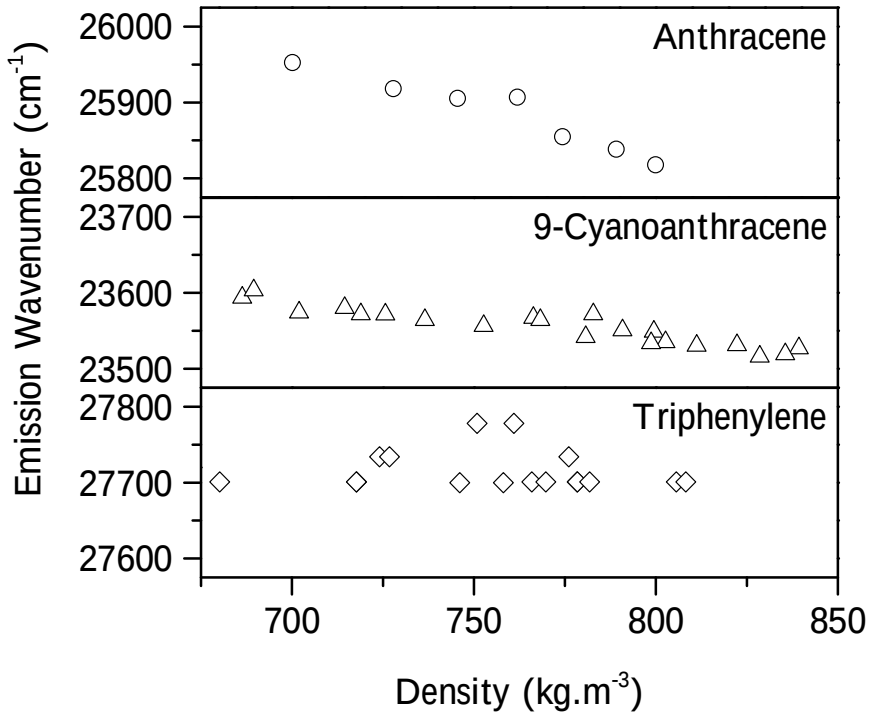

Figure 6-32: The emission energy of anthracene, 9-cyanoanthracene and triphenylene in CO_2 at 35 °C, as a function of density.

3.4 Anthracene as a Density Sensor

Following the investigation into polyaromatic probe molecules, anthracene was shown to have clearly resolved peaks and a clear red solvatochromic shift with density. The emission observed in CO_2 at 35 ^oC and 1915 psi, shown in Figure 6-33, is consistent with literature.[269] Measurements were conducted at 35 ^oC, which is $1.13T_c$ (T_c of CO_2 = 31.1 ^oC) to minimise local density augmentation effects which have been shown to be decrease above $1.05T_c$ and are negligible at densities above 600 $kg.m^{-3}$.[269, 271]

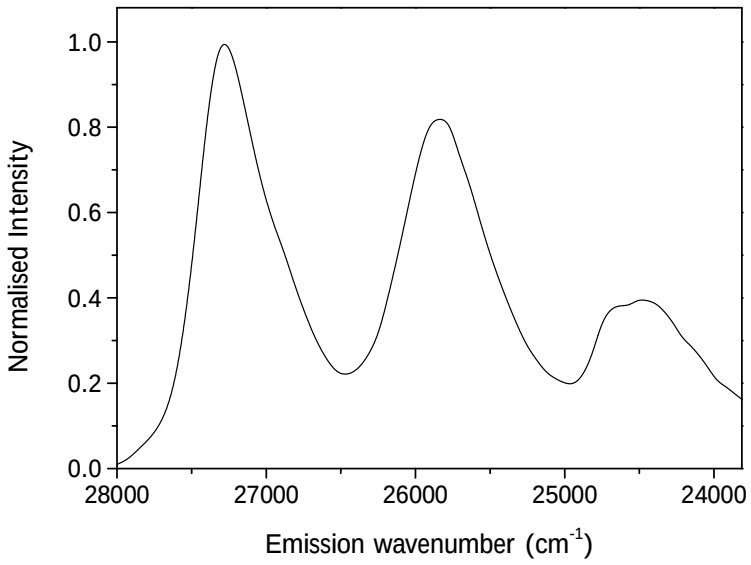

Figure 6-33: The emission of anthracene in CO_2 (35 ^oC, 1915 psi)

Three clear bands are observed for anthracene emission in CO_2. Therefore, the work within this Chapter focuses on the peak at *ca.* 25900 cm^{-1}. Previous research on polycyclic aromatic compounds has shown that the peak at *ca.* 27400 cm^{-1} shows far more dependence on solute and solvent clustering. Therefore, this peak has not been used for the solvatochromic measurements within this work.[299] The peak at *ca.* 25900 cm^{-1} was observed to have a solvatochromic red shift in emission energy of *ca.* 150 cm^{-1} at a CO_2 pressure of 1300-1900 psi. Where the shift in this band can be clearly seen, as shown in Figure 6-34.

Subsequently, when the emission energy of this peak is plotted against pressure a near linear relationship is observed, as displayed in Figure 6-34, bottom. The emission energy is chosen as a metric due to its linear relationship with energy where, $E = h\nu$.

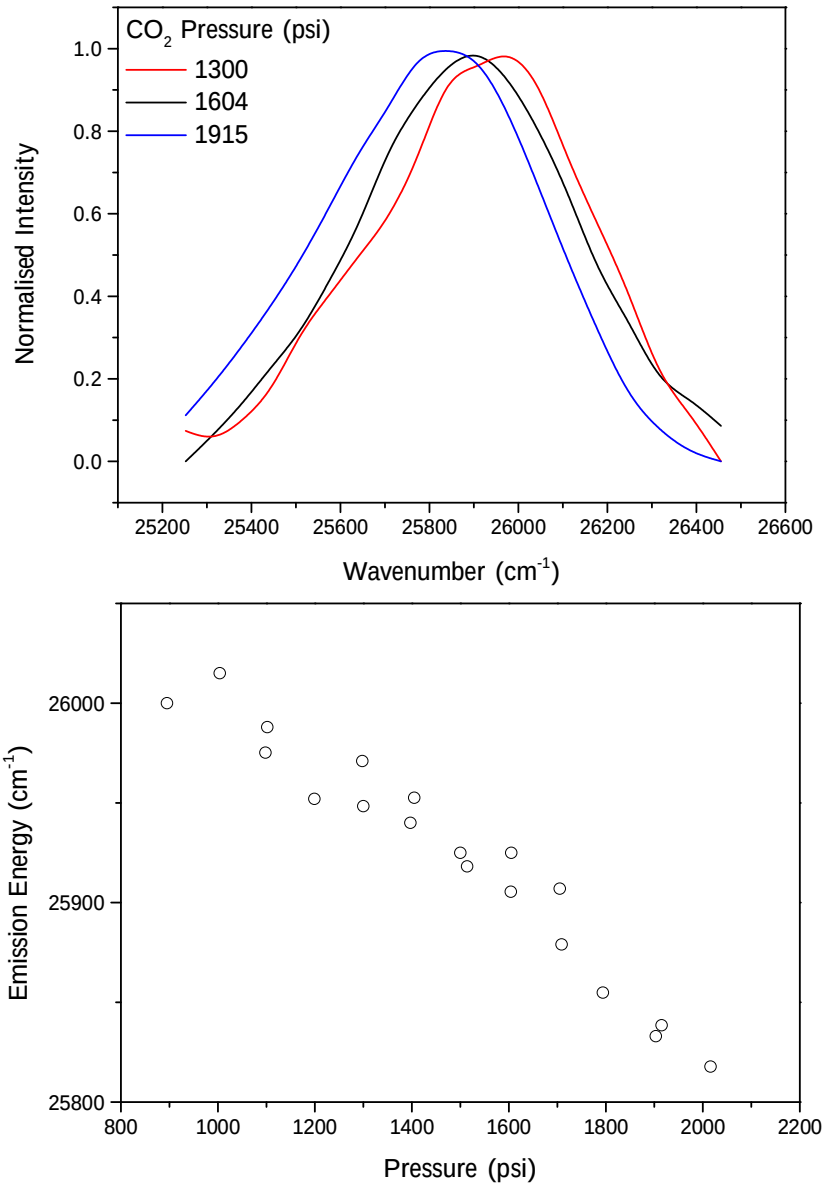

Figure 6-34: The emission spectrum of anthracene in varying pressures of CO_2 (1300, 1604 and 1915 psi) (top) Plot of the emission energy of anthracene as a function of CO_2 pressure (bottom). All measurements were conducted at 35 ^{O}C.

Subsequent repeats of this pressure range were completed and the data obtained were converted to density using the NIST equation of state.[308] Emission energy is calibrated as a function of density and not as a function of pressure, this is due to the non-linear relationship between pressure and density. This relationship is non-linear due to the change in density resulting from phase transitions.

As the density changes (between *ca.* 600-800 kg.m^{-3}), a decrease in emission is observed, as shown in Figure 6-35. Although obvious local density augmentation effects are not observed, the relationship between emission energy and density shows deviation from

linearity, which is as expected from previous literature, particularly for anthracene based dyes and is attributed to appreciable local density enhancement affects still being present.[270, 271, 280, 281] To this end, the calibration plot has been fitted to an exponential decay function to account for this non-linear decrease of emission energy with density. A calibration of the emission energy of anthracene observed and CO_2 density is required in order to exploit this relationship to calculate density of the confined CO_2 from the observed emission of anthracene.

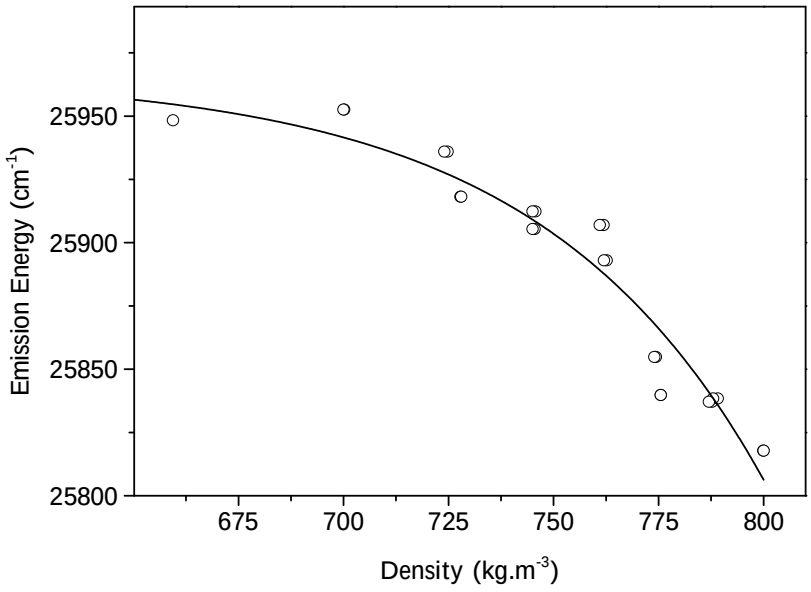

Figure 6-35: The emission energy of anthracene in CO_2 plotted as a function of CO_2 density.

The validity of the emission energy of anthracene as a function of CO_2 density calibration (Figure 6-35), needed to be assessed before it could be employed to calculate the density of confined CO_2 within this chapter. Therefore, a calibration plot has been used to obtain the density *vs.* pressure relationship, shown in Figure 6-36. This pressure-density curve has subsequently been compared to the equation of state values for density of CO_2 as a function of pressure, also shown in Figure 6-36. Good agreement is observed between the calculated density *via* the calibration plot and the pressure-density curve obtained from equation of state, indicating that the calibration from experimental data is reliable and thus anthracene is a viable luminescence probe for sensing the density of fluids confined in pores.

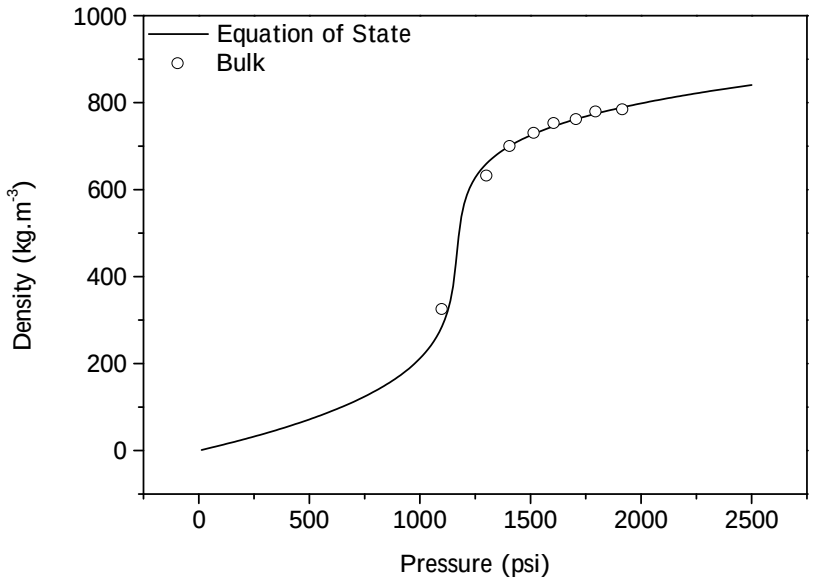

Figure 6-36: The calculated density of CO_2 from the emission energy of anthracene compared to the equation of state. Good agreement is observed between both data sets indicating that the calibration plot shown in Figure 6-35 is viable.

6.3.5 Measuring the Density of CO_2 Confined in Porous Materials

Having established a methodology and reliable probe for measurements within porous materials, the density of CO_2 confined in a range of mesoporous materials with mean pore widths of 3.2, 4.5 and 8.3 nm, was explored. The mean pore width was established by gas sorption measurements and are shown in Chapter 8. The optimised geometry of anthracene has been calculated using DFT to ensure the size is sufficiently small enough to fit inside the porous materials of interest with the width of anthracene calculated to be *ca.* 1 nm, Figure 6-37.

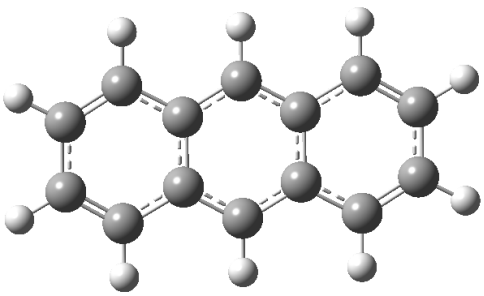

Figure 6-37: The optimised geometry of anthracene obtained from DFT calculations, exhibiting a width of *ca.* 1 nm.

The emission energy of anthracene was measured in bulk and confined CO_2 at varying pressures. All measurements were conducted at 35 °C and are shown in Figure 6-38. It was observed that the emission energy of anthracene was consistently lower for confined CO_2 measurements compared to the bulk. Furthermore, the emission energy of anthracene was observed to decrease with increasing pore size. An example of this behaviour can be seen for the emission energy of anthracene in CO_2 within 8.3 nm pore, showing an emission energy of 25474 cm^{-1} at 1551 psi. This is in contrast to the emission energy of anthracene in CO_2 confined in the 3.2 nm pores of 24154 cm^{-1}, at 1553 psi.

This decrease in emission energy with decreasing pore size, indicates that the excited state is stabilised more in smaller porous materials. Where a higher stabilisation of the excited state leads to a decrease in the excited state energy, reflected in a decrease in the emission energy. The relationship between CO_2 pressure and emission energy exhibits deviations from linearity, which are particularly apparent for emission energy observed for CO_2 confined in the 4.5 nm porous material at relatively low bulk CO_2 pressures. Furthermore, the emission energy of anthracene in bulk CO_2 is observed to decrease with increasing CO_2 pressure therefore indicating further that the lower emission energy due to the higher pressure of the fluid environment.

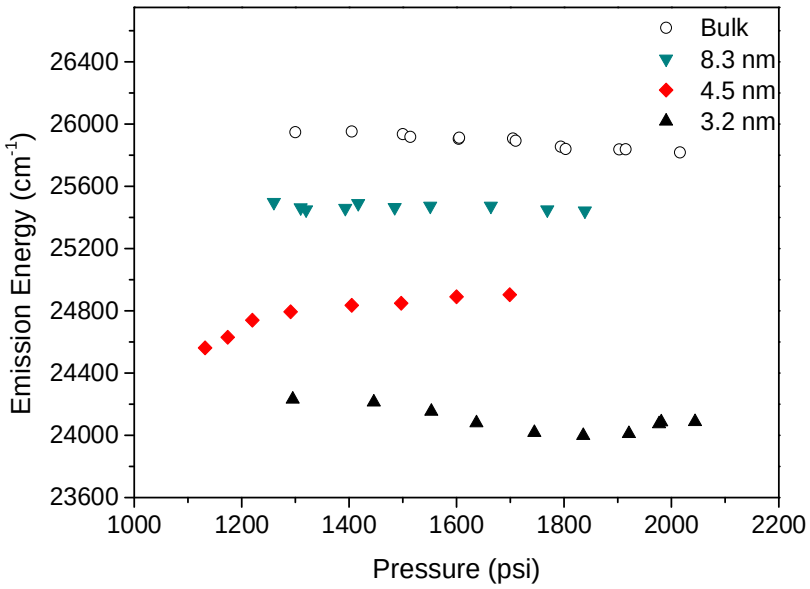

Figure 6-38: The emission energy of anthracene in materials with various pore sizes wherein the emission energy is seen to decrease with decreasing pore size.

The deviation from linearity observed for CO_2 confined in 4.5 nm porous material is observed at pressures below 1200 psi, corresponding to density of 567 $kg.m^{-3}$. This is due to the non-linear relationship between pressure and density, the latter of which emission energy is dependent on. The non-linear relationship is most extreme at reduced densities closer to 1, hence the large deviation from linearity observed for 4.5 nm porous material at pressures below 1200 psi. Therefore as with the calibration, emission energy of anthracene has been plotted as a function of CO_2 density (Figure 6-39). The deviation from linearity for the emission energy of anthracene and CO_2 confined within the 4.5 nm porous materials is now observed to be linear, as expected.

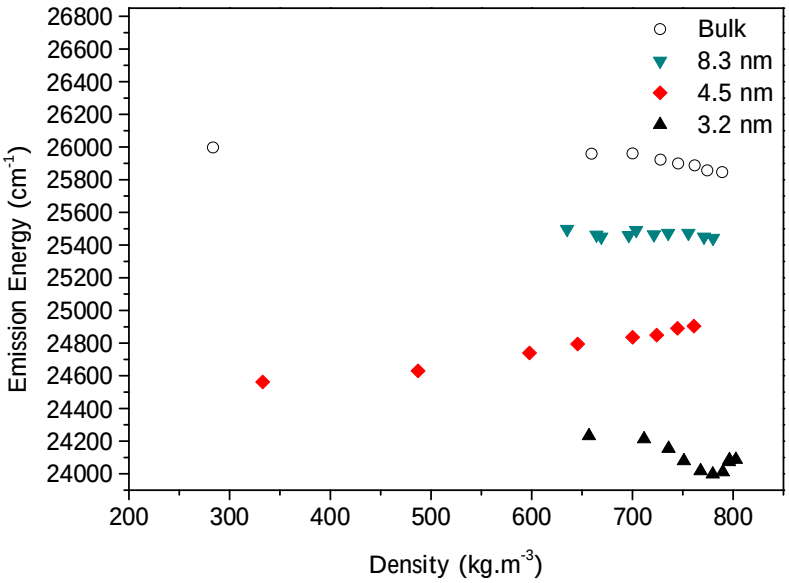

Figure 6-39: The emission energy of anthracene in CO_2 as a function of density under bulk and confined conditions

The decrease in emission energy of anthracene in confined CO_2 observed would indicate that the excited state of anthracene is stabilised further in confined CO_2 than its bulk counterpart, as observed when emission energy is plotted as a function of bulk CO_2 pressure.

As the emission energy of anthracene in bulk CO_2 is observed to decrease with increasing density, the decreased emission energy observed for anthracene in a confined CO_2 environment indicates that the density of CO_2 within the porous material is higher than the bulk.

This increase in CO_2 density when confined within the pores, raises the question of whether it is possible that an emission may be observed from anthracene in the confined CO_2 environment at bulk CO_2 densities which are insufficient to dissolve anthracene. Therefore, the emission of anthracene in CO_2 within porous materials was investigated at lower CO_2 pressures. However, only emission indicating anthracene adsorbed on a silica surface was observed. As a result, only the CO_2 measurements at higher pressures are considered for calculating the density within the porous materials. The calibration of the anthracene emission energy as a function of CO_2 pressure, detailed previously was applied to the emission energies of anthracene in CO_2 confined within the 3.2 nm, 4.5 nm and 8.3 nm porous materials, as shown in Figure 6-38. This calibration gives a value for the calculated density of confined CO_2 which was then plotted as a function of bulk CO_2 pressure and is shown in Figure 6-40 and Table 6-3.

The density of confined CO_2 was determined to be consistently higher than the density of bulk CO_2 over the range of pressures stated, which agrees with previous conclusions from other density sensing techniques.[238, 257-263] Furthermore, the density of CO_2 was shown to increase with decreasing pore width where the density of CO_2 increases from 860 $kg.m^{-3}$ to 930 $kg.m^{-3}$ at *ca.* 1552 psi as the pore size decreased from 8.3 to 3.2 nm.

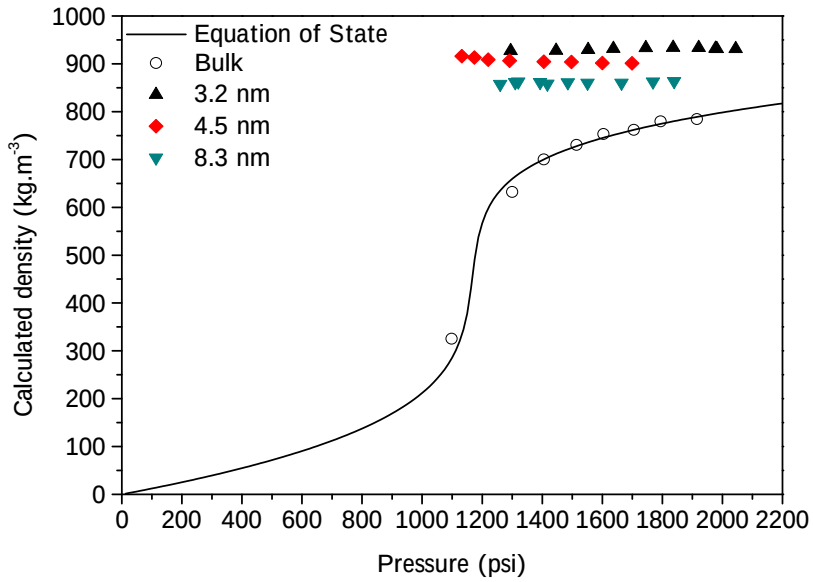

Figure 6-40: The calculated density of CO_2 as a function of pressure for both the both the bulk and confined fluid, determined from luminescence spectroscopic measurements. It is observed that as mean pore size decreases, the density of the CO_2 increases.

Table 6-3: The calculated confined CO_2 density in a range of porous materials compared to bulk CO_2 pressure.

Pore Size (nm)	Temperature (^oC)	Bulk CO_2 Pressure (psi)	Calculated Density ($kg.m^{-3}$)
Bulk	35	1250 – 2000	628 – 798
3.2	35	1295 – 2044	927 – 931
4.5	35	1220 – 1699	901 – 916
8.3	35	1260 – 1839	863 – 857

3.5 Using 5,10,15,20–Tetrakis(pentafluorophenyl)porphyrin as a Potential Density Sensor

As the density of fluids confined within porous materials has not previously been investigated in literature using luminescence spectroscopy, the results obtained using anthracene were verified with an alternative luminescent probe and the measurements were repeated. 5,10,15,20-tetrakis(pentafluorophenyl)porphyrin (tfpp), structure shown in Figure 6-41, has been used as an alternate density sensor as it demonstrated good solubility in CO_2 with a clear change in the peak emission ratio with density. Change in emission peak ratio offered an alternate metric in order to probe the fluids density, corroborating the previous technique. Furthermore, DFT has been used to calculate the optimised geometry and tfpp is shown to have a width of *ca.* 1.8 nm, therefore it is suitable for use in the porous materials studied in this work.

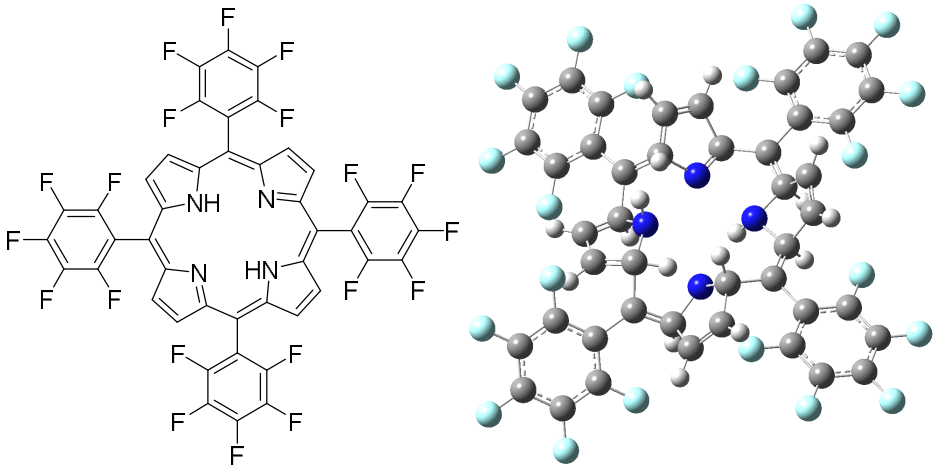

Figure 6-41: The structural formula (left) and optimised geometry obtained from DFT calculations (right) of tfpp.

The absorption spectrum of tfpp in CO_2 is shown in Figure 6-42 with two bands observed in the absorption spectra at *ca.* 24876 and 19960 cm^{-1}. To probe the emission of tfpp in CO_2, an excitation wavelength of 395 nm corresponding to the λ_{max} band was chosen.

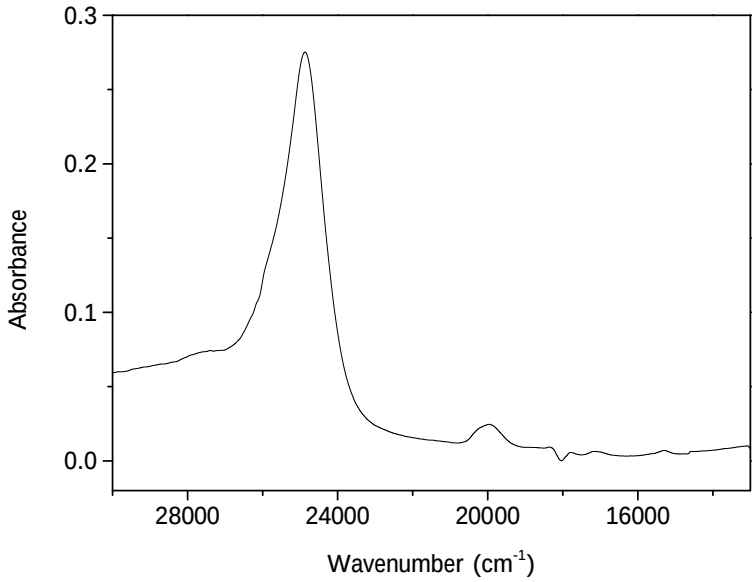

Figure 6-42: The absorption spectrum of tfpp in CO_2 at 2007 psi, 35 ^{o}C.

An emission study of tfpp in bulk CO_2 at varying pressures at 35 ^{o}C was conducted, the results of which are shown in Figure 6-43. Two clear peaks are observed at *ca.* 15070 and 13960 cm^{-1}, where the former peak possesses an additional shoulder (shown in Figure 6-43, inset). The ratio of the two peaks is observed to change with pressure (shown in Figure 6-43). The equation used to determine peak ratio (Equation 6-2) is shown below. As pressure increases there is an observed increase in the emission of the band at *ca.* 15070 cm^{-1} and decrease in the band observed at 13960 cm^{-1}.

$$\text{Peak ratio} = \frac{\text{Peak nominally at 15070 cm}^{-1}}{\text{Peak nominally at 13960 cm}^{-1}} \qquad \textbf{Equation 6-2}$$

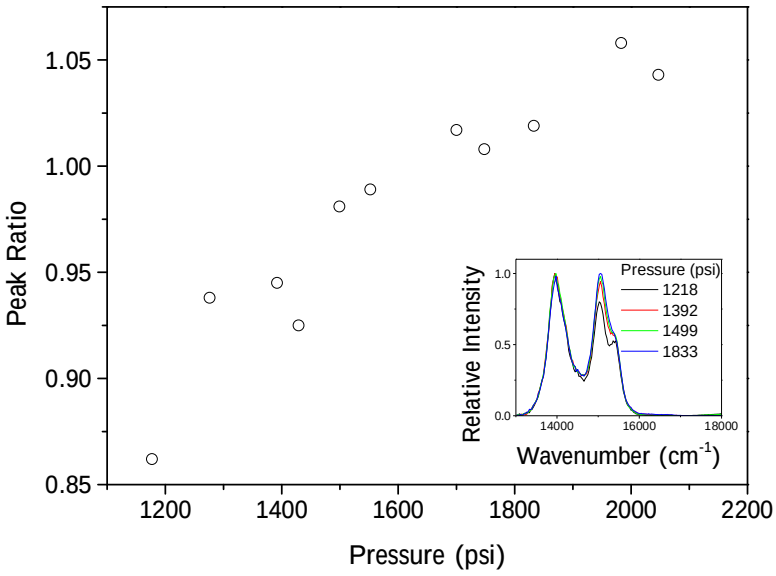

Figure 6-43: The peak ratio of tfpp observed in emission as a function of CO_2 pressure. Inset: Emission spectra of tfpp in CO_2 demonstrating the change in peak ratio with CO_2 pressure.

The change in peak ratio has been plotted as a function CO_2 density and a linear relationship is observed, as shown in Figure 6-44, unlike the non-linear relationship observed for emission energy of anthracene in CO_2 as a function of density. This is in agreement with previous work which has shown that the peak ratio of polycyclic aromatic dyes can be used for investigating fluid behaviour in CO_2, as mentioned previously, and exhibits a linear relationship with CO_2 density. This is in contradiction to emission wavenumber which exhibits a non-linear dependence.[299] This linear relationship between CO_2 density and peak ratio has been used to produce a calibration plot (Figure 6-44), and has been validated in the same way as for anthracene.

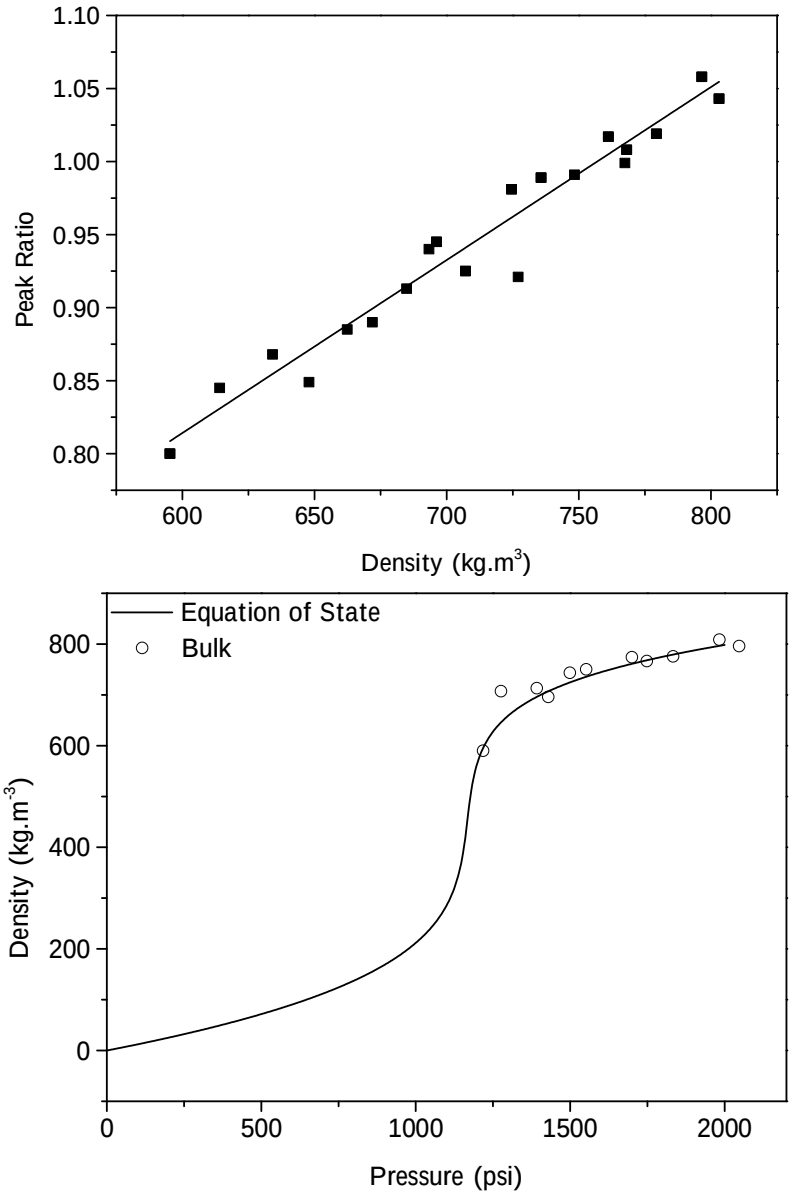

Figure 6-44: The peak ratio (Equation 6-2) from the emission of tfpp in CO_2 plotted as a function of density (top). The pressure *vs.* density curve for bulk measurements of tfpp in CO_2 using the calibration plot, demonstrating good agreement with the NIST equation of state (bottom).

Reasonable agreement is observed between the calibration plot obtained of emission peak ratio of tfpp as a function of density, Figure 6-44, and the equation of state values. The agreement is not as close to the anthracene probe and this is likely due to the inherent nature of peak ratio compared to emission energy as a metric. Previous research has shown that peak ratio is more sensitive to changes in the dye concentration and therefore, increases in the dye solubility at higher densities of CO_2 may affect the spectrum.[7, 299] However, the agreement indicated that the calibration may be employed

for calculating the density of confined CO_2 within the porous materials. As with the measurements of the confined CO_2 density with an anthracene probe, materials with mean pore widths of 3.2, 4.5 and 8.3 nm have been investigated.

Prior to any measurements of the confined fluid, the effect of tfpp adsorption on silica was first investigated using the same method as for anthracene. Where a silica material, which can be considered '*non-porous*' for the sake of this work (Zeolite Y, mean pore size 0.24 nm) was investigated. No discernible trend was observed between emission peak ratio of tfpp and pressure of CO_2. Therefore, the density of CO_2 confined within porous materials was calculated using tfpp as a probe dye. The change in emission peak ratio of tfpp as a function of bulk CO_2 pressure at 35 ^{o}C for CO_2 in 3.2, 4.5 and 8.3 nm porous materials are shown in Figure 6-45.

For bulk measurements the emission peak ratio for tfpp is observed to increase with increasing pressure, indicating the density of CO_2 is increasing. The emission peak ratio is higher for CO_2 confined in the porous materials compared to bulk measurements, furthermore, the emission peak ratio is observed to increase with decreasing pore size. This increase in emission peak ratio with decreasing peak size indicates that the density of CO_2 is higher when confined in smaller pores, in agreement with calculated density from the anthracene probe. The emission peak ratio of tfpp was then plotted as a function of CO_2 density, shown in Figure 6-45. As observed with pressure, the emission peak ratio is observed to increase with decreasing pore width, indicating a higher density of CO_2.

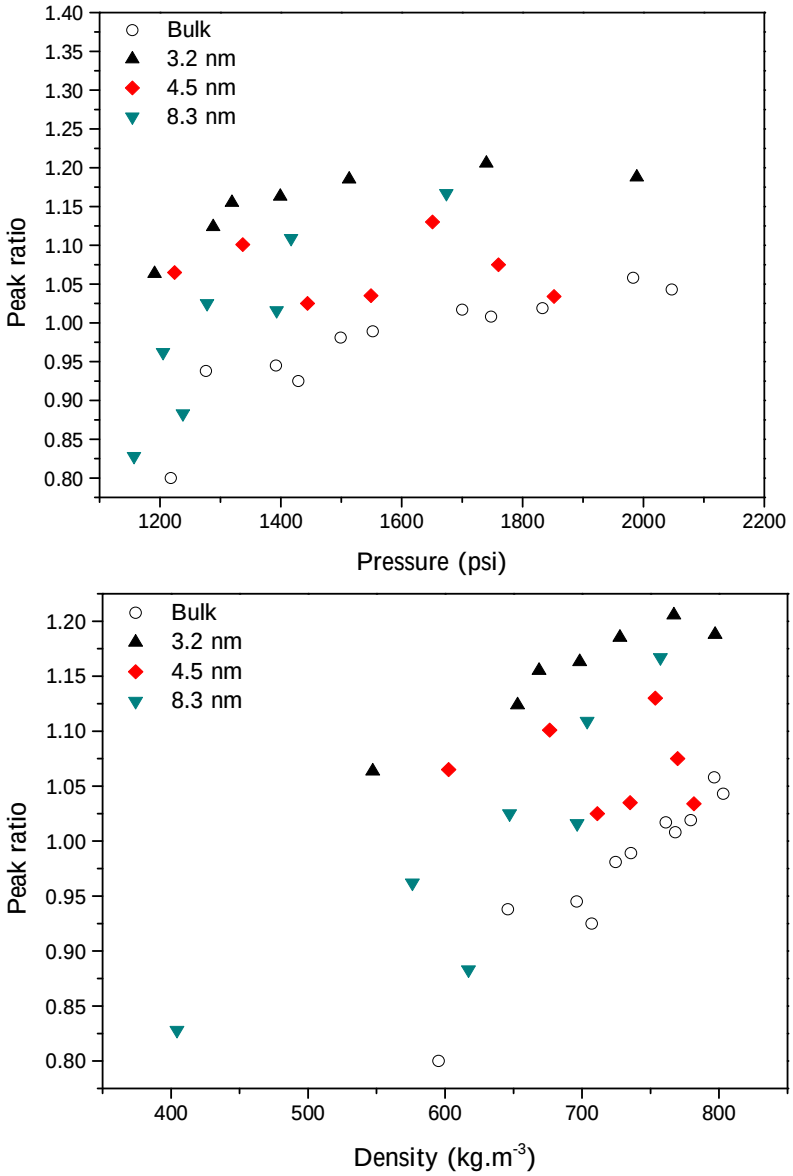

Figure 6-45: The emission peak ratio of tfpp in CO_2 confined within 3.2, 4.5 and 8.3 nm porous materials as a function of CO_2 pressure (top) and as a function of CO_2 density (bottom).

The calibration of the emission peak ratio as a function of CO_2 density, shown in Figure 6-46, was then applied to calculate the density of CO_2 confined within the porous materials. This calculated density has been shown as a function of bulk CO_2 pressure in Figure 6-46 with the values listed in Table 6-4. The resulting CO_2 calculated pressure density curves have been compared to the CO_2 pressure density curve obtained for the bulk and from the equation of state values. The results show that the density of CO_2 is

consistently higher when confined within the porous materials compared to bulk measurements. Furthermore, the density increases with decreasing pore width.

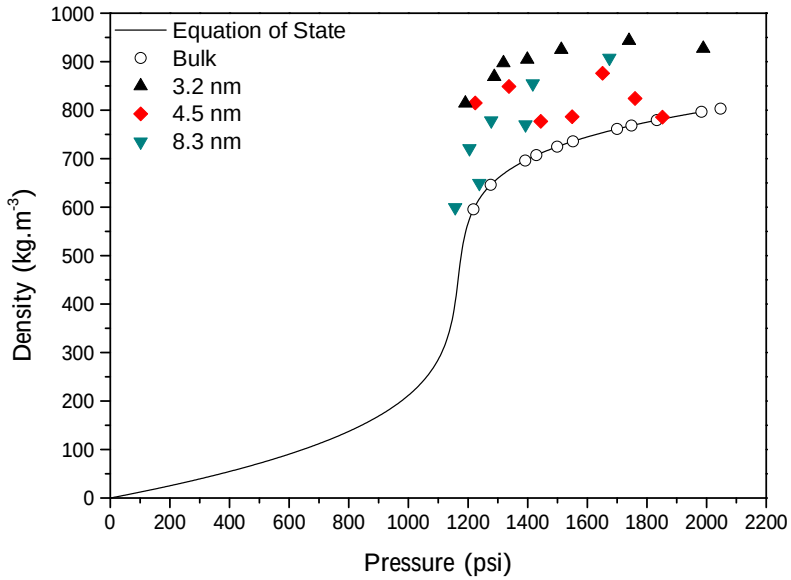

Figure 6-46: The bulk CO_2 pressure *vs.* the calculated density of CO_2 within the porous materials. As pore size decreases the density of CO_2 within the pore increases.

Table 6-4: The calculated density of CO_2 inside the nanoporous templates with sizes (PS) 3.2, 4.5 and 8.3 nm, probed with two separate dyes.

		tfpp		anthracene	
PS (nm)	T (^oC)	Bulk CO_2 Pressure (psi)	Calculated Density ($kg.m^{-3}$)	Bulk CO_2 Pressure (psi)	Calculated Density ($kg.m^{-3}$)
3.2	35	1191 - 1989	814 - 943	1295 - 2044	927 - 931
4.5	35	1224-1852	777 - 876	1220 – 1699	901 - 916
8.3	35	1157 - 1674	599 - 907	1260 - 1839	863 - 857

The calculated density results for CO_2 inside 8.3, 4.5 and 3.2 nm material can be compared to those obtained from anthracene as a probe molecule, Table 6-4. The results for calculated density of confined CO_2 between the two dyes and therefore the two metrics, emission energy and emission peak ratio, show reasonable agreement. Results obtained from the tfpp dye show a larger range in calculated densities for each porous material compared to anthracene results, this is possibly due to the larger error present when using peak ratio as a metric.

The increase of CO_2 density within smaller pores has been shown theoretically, experimentally and through simulations to be due to macroscopic ordering of the CO_2 molecules as a result of the spatial confinement. The ordering is observed to be more severe with increasing spatial confinement, and occurs due to the packing constraints resulting from both the confining surfaces and the other CO_2 molecules present.[309-312]

The calculated density of CO_2 confined within the porous materials is a key property that can guide the SCFED process, dictating the electrolytes, temperature and pressures that can be used in the SCFED process. The calculated density dictates that the bulk CO_2 density need not be as a high as previously thought, owing to the density enhancement observed upon confinement. This allows for lower bulk pressures of CO_2 to be utilised resulting in a safer and more cost efficient process. Furthermore, the solubility and therefore choice of electrolyte may now be further understood and guided quantitatively.

3.6 Towards a Density Sensor Using Luminescence in Difluoromethane

Due to the variety of electrolytes used within the SCFED process, a range of fluids are employed. Alongside CO_2, as discussed previously, difluoromethane (R32) is also used. R32 exhibits a larger dielectric constant (ε_r = 12.51 at 30 ^oC, 711 psi)[313] compared to CO_2 (ε_r = 1.1-1.4 at 80 ^oC 1450-3626 psi).[225] This potentially increases the range of electrolytes that may be employed owing to their solubility. However, R32 exhibits a higher critical temperature (78.4 ^oC)[314] than CO_2, therefore, a potentially higher cost would be required for R32 than for CO_2 in order to obtain supercritical conditions. The potential for using luminescence as a density sensing technique for R32 will be explored.

As discussed previously, anthracene was determined to be a more accurate probe compared to tfpp for sensing density. Therefore density measurements with R32 were conducted using anthracene as a probe molecule are compared to the previously obtained CO_2 data. Due to limitations with the Nottingham Cubic Cell, a temperature of 1.1 T_c would be unachievable. Therefore, 40 ^oC and 30 ^oC (0.51 and 0.38 T_c respectively) were chosen for measurements. As a result of the temperatures possible, the work is limited

to the liquid phase of R32 and therefore a far smaller change in density over the possible pressure range was achievable using the cell. Hence, two temperatures are studied in order to obtain a larger density range within the temperature limits of the cell. The emission energy of anthracene as a function of R32 pressure is shown in Figure 6-47. A general trend of a decrease in emission energy with increasing pressure is observed, similar to CO_2.

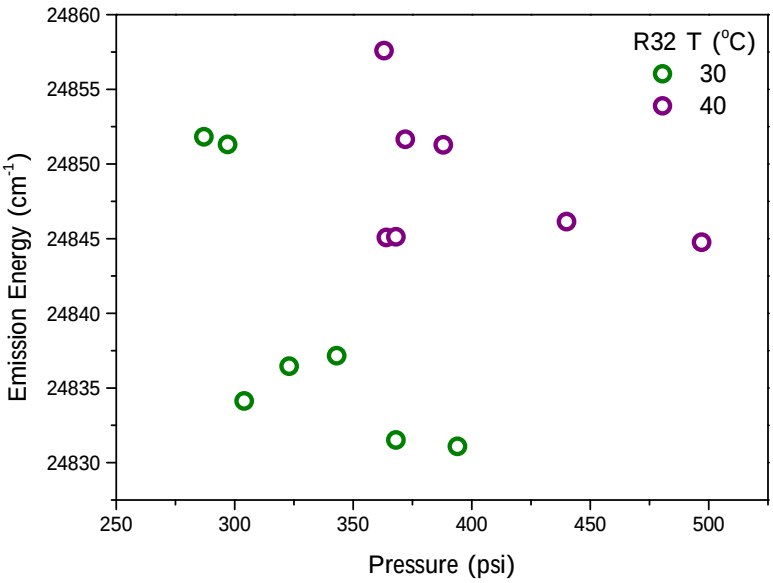

Figure 6-47: The emission energy of anthracene in R32 at a range of pressures at 30 °C and 40 °C.

The emission energy of anthracene has subsequently been plotted as a function R32 density (Figure 6-48) where, the observed shift in emission energy of anthracene with R32 density is *ca.* an order of magnitude smaller than that observed in CO_2. Furthermore a discernible trend is not observed and thus it was not possible to calibrate the emission energy of anthracene to the density of R32. This may be due to the small change in emission energy of anthracene as a function of pressure which is close to the resolution limit of the spectrometer.

The small observed change in emission energy is possibly due to the larger dielectric constant of R32 (ε_r = 12.51 at 30 °C, 711 psi)[313] compared to CO_2 (ε_r = 1.1-1.4 at 80 °C 1450-3626 psi).[225] This distinct difference in dielectric constant of the solvent reflects the more polarisable nature of R32 compared to CO_2. Therefore the emission energy of

anthracene is stabilised further by R32 and thus is not readily perturbed by changes in density.

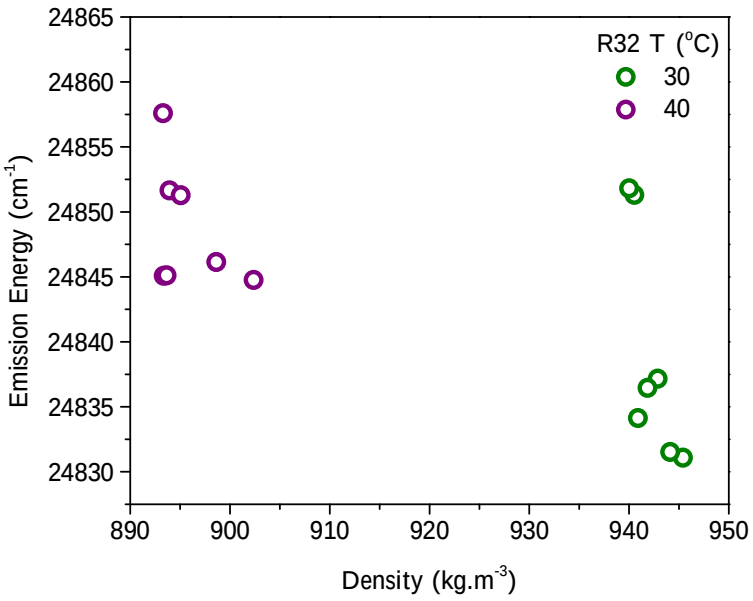

Figure 6-48: The emission energy of anthracene in R32 as a function of density.

3.7 Probing Fluid Polarisability and Dielectric constant

In addition to density, the dielectric constant and polarisability of a fluid is important when guiding the SCFED process. For example, the dielectric constant (ε_r) and the polarisability of a fluid can be responsible for dictating the solubility of electrolytes, effecting the choice of those employed. Therefore, determining the effect of density on both of these properties is important to further understand the SCFED process.

Firstly, the relationship between ε_r and density of CO_2 has been investigated. Precedent for exploiting the relationship between the emission behaviour of a probe as a function of fluid ε_r in conventional liquid solvents have been used to determine the ε_r of SCFs.[293] The emission of anthracene was observed to change with the ε_r of the solvent, Figure 6-49, where the ε_r of the solvents used are shown in Table 6-5.[315] As the dielectric constant of the solvent increases from 1.8 to 5.7,[152] the emission spectrum of anthracene demonstrates a positive solvatochromic shift from 25126 to 24690 cm^{-1}, in hexane and chlorobenzene respectively. Focusing on the observed peak at ca. 25000 cm^{-1} a plot of

ε_r as a function of wavenumber was produced, Figure 6-49. The relationship between ε_r and emission wavenumber of anthracene has subsequently been fitted to give a calibration of emission energy of anthracene as a function of the ε_r of the fluid.

Table 6-5: The ε_r and KTπ* values for solvents used within this work, taken from reference [315].

Solvent	ε_r	KTπ* value
Chlorobenzene	5.6	0.71
Chloroform	4.8	0.58
Diethylether	4.3	0.27
Dibutylether	3.1	0.27
Toluene	2.3	0.54
Hexane	1.8	-0.04

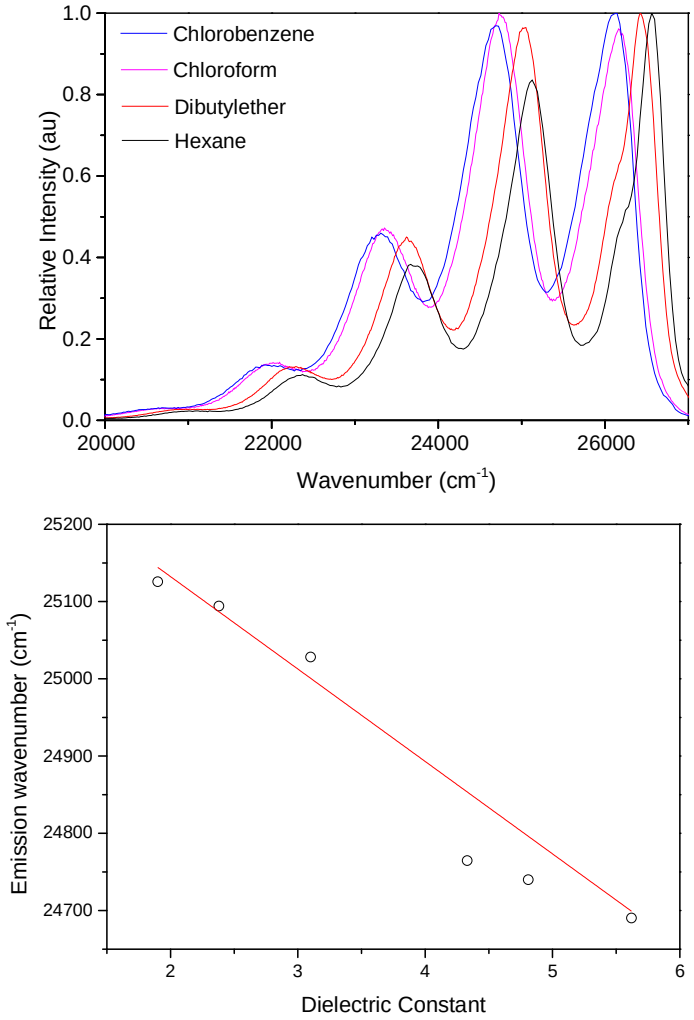

Figure 6-49: The emission spectra of anthracene in solvents with varying dielectric constants: hexane (ε_r = 1.9), dibutylether (ε_r = 3.1), chloroform (ε_r = 4.81) and chlorobenzene (ε_r = 5.62) (top). The emission energy of anthracene as a function of ε_r, fitted to give a calibration of anthracene emission energy and fluid ε_r (bottom).

This calibration can then be used to calculate ε_r for the dense CO_2 confined within the porous materials. The calculated ε_r of both bulk and confined CO_2 is shown in Figure 6-50. The plot exhibits an increase in the calculated ε_r of the fluid with increasing CO_2 density. Previous literature has shown the dielectric constant of CO_2 is *ca.*1.0-1.7.[225, 316] However, from luminescence experimental measurements, the ε_r of $scCO_2$ is far lower (*ca.* ε_r 1.1-1.4 at 650-800 $kg.m^{-3}$). This inconsistency between literature and measurements obtained experimentally may be attributed to the fact that CO_2 does not exhibit a dipole. Therefore calculated values of the fluids ε_r may not accurately reflect the fluid behaviour, resulting in far lower values of ε_r obtained for bulk CO_2 under the conditions used in literature.

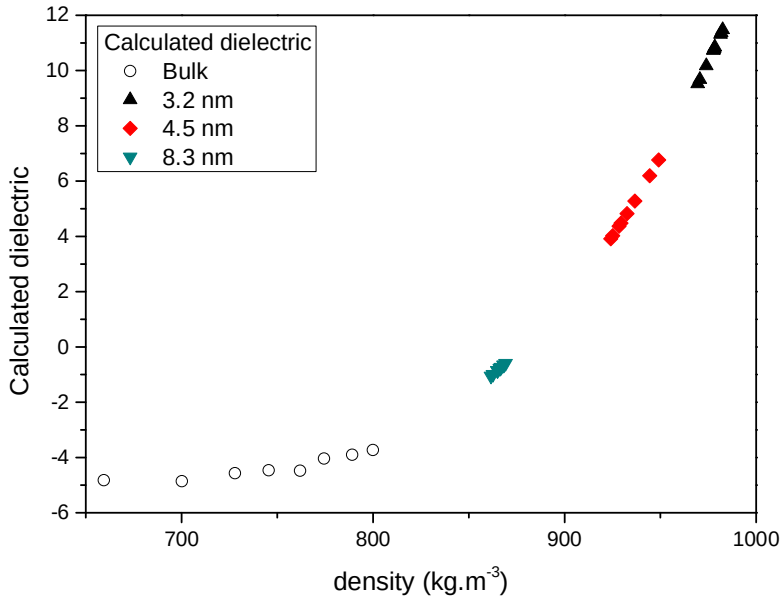

Figure 6-50: The calculated dielectric constant based on the emission energy calibration obtained from variable solvent anthracene measurements, along with the calculated densities within the pores.

Owing to the inaccuracies in calculating ε_r for CO_2, the $KT\pi^*$ values which measures polarisability have also been investigated. These values are calculated from the emission energy of the probe in cyclohexane and dimethyl sulfoxide using the equation shown below, Equation 6-3.

$$KT\pi^* = \frac{\nu_i - \nu_{cyclohexane}}{\nu_{dimethyl\ sulfoxide} - \nu_{cyclohexane}} \qquad \textbf{Equation 6-3}$$

KTπ* values are usually calculated with nitroaromatic dyes as discussed previously,[279, 281, 290, 292] as this class of dyes demonstrate a solvatochromic shift but respond minimally to changes in the hydrogen bond basicity and acidity of the solvent, allowing changes in the spectroscopic measurements to polarisability and not hydrogen bonding. The effect of density on the polarisability of supercritical CO_2 has been previously explored with this class of dye, and the polarisability has been shown to increase with increasing density.[281 186, 286, 288, 317] As discussed previously, the two solvatochromic dyes, anthracene and tfpp, have been used within this work at luminescent probes for density owing to their good solubility in CO_2 with emission profiles that are sensitive to density and are possible to follow spectroscopically. In addition to these properties, KTπ* probes also need to exhibit large solvatochromic shifts and be reasonably independent of hydrogen bond basicity and acidity.[318] Anthracene is observed to be reasonably independent of hydrogen bond basicity and acidity and furthermore, the basicity and acidity constants have been shown to be very similar in the ground and excited state.[319, 320] Therefore anthracene has been used within this work as a probe for calculating KTπ* values.

Conventionally, when calculating KTπ* values of a fluid, the λ_{max} values obtained from absorption spectroscopic measurements are used. However, as the emission of the anthracene probe confined in CO_2 has been studied in this work, both λ_{max} and λ_{em} have been explored as potential KTπ* metrics. The emission of anthracene in cyclohexane and dimethyl sulfoxide are detailed in Table 6-6.

Table 6-6: The absorption and emission max values of anthracene in DMSO and cyclohexane, obtained experimentally.

Solvent	DMSO	Cyclohexane
Absorption (cm^{-1})	27701	28011
Emission (cm^{-1})	24783	25221

As λ_{abs} is conventionally used for calculating KTπ* values, the λ_{abs} values of anthracene in CO_2 obtained experimentally have been used to calculate the KTπ* values and are shown in Figure 6-51. These values have been compared to literature KTπ* values for CO_2 at the same density range also shown in Figure 6-51. The fit of both data sets

show good agreement in terms of their gradient, but the values differ by *ca.* 2 orders of magnitude. Large discrepancies in their values are common when changing the KTπ* probe and have previously been observed in literature.[290, 292]

Following the indications that the λ_{abs} of anthracene may be implemented as a KTπ* probe, the emission of anthracene (λ_{em}) has been explored as a potential KTπ* metric. The emission of anthracene in CO_2 at a range of densities has been collected and used to calculate KTπ* values using an adapted Equation 6-3 implementing λ_{em} instead of λ_{abs}, where the emission maximum has been used. The resulting KTπ* values as a function of CO_2 density are also shown in Figure 6-52 (bottom). The results show a clear change in KTπ* and density. The calibration of λ_{em} with KTπ* values has been applied to the λ_{em} values of anthracene from the confined measurements, within the range of porous templates, Figure 6-51. The results indicate the KTπ* value of CO_2 increases with increasing density, pointing to an increase of the CO_2 polarisability at higher CO_2 densities.

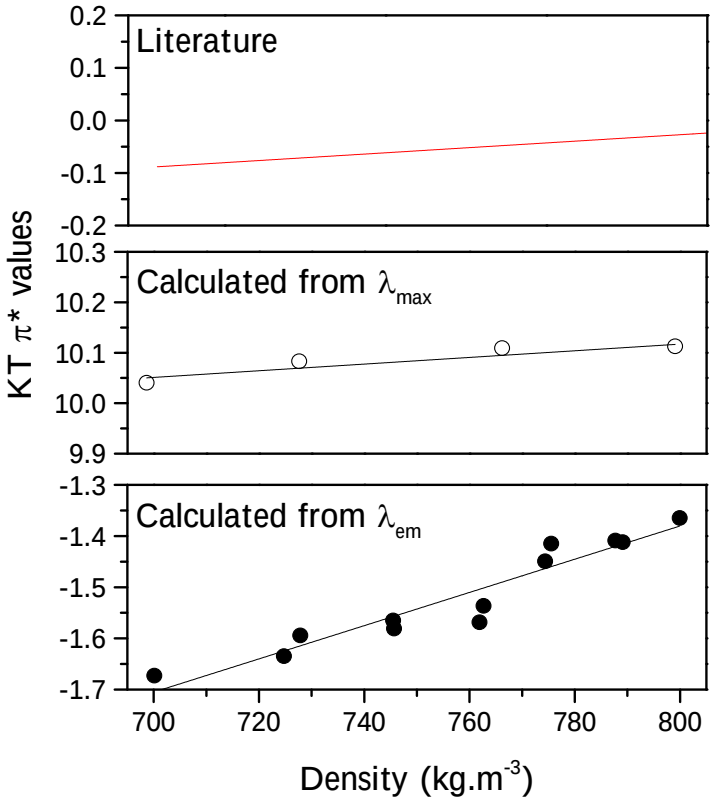

Figure 6-51: The literature measurement of KTπ* values for CO_2 using nitroaromatic based dyes,[281, 290] compared to calculated KTπ* values for CO_2 with anthracene as a probe from experimental λ_{max} (top) and λ_{em} (bottom) values.

These calculated KTπ* values from the λ_{em} of anthracene, Figure 6-52, have then been calibrated to literature values,[281, 290, 321-323] where the calibration can be seen in more detail in Appendix A. The resulting calibration of λ_{em} of anthracene to KTπ* of CO_2 has been used to elucidate the calculated KTπ* of CO_2 values from within the porous templates. The KTπ* values of CO_2 are displayed as a function of CO_2 density in Figure 6-52.

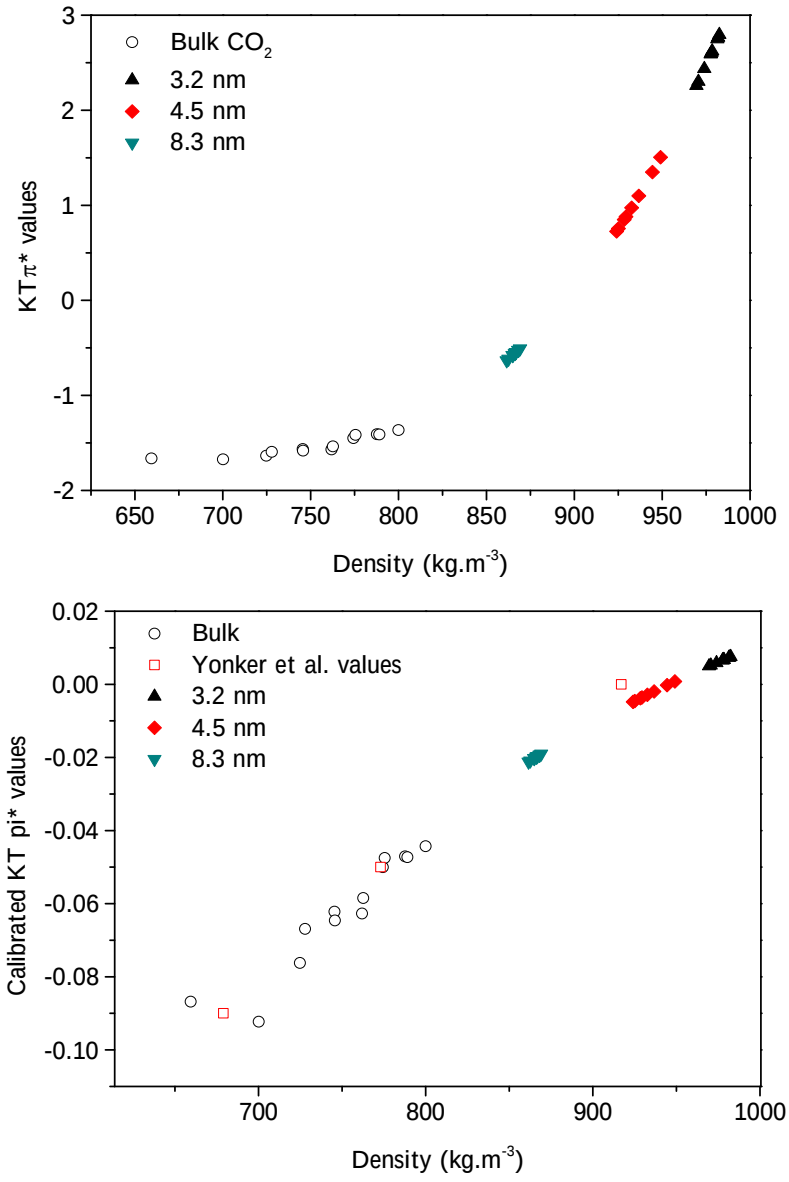

Figure 6-52: The KTπ* values (top) and calibrated KTπ* values (bottom) as a function of CO_2 density from measurements with an anthracene probe.

Table 6-7: The polarisability of CO_2 expressed as KTπ* values, as a function of CO_2 density.

PS (nm)	CO_2 density ($kg.m^{-3}$)	KTπ*
Bulk	659 - 800	-0.0870 - -0.0443
8.3	861 - 869	-0.0212 - -0.019
4.5	924 - 949	-0.0048 - 0.0007
3.2	970 – 982	0.0050 - 0.0075

The calculated values indicate that as the density of CO_2 increases the polarisability of CO_2 (KTπ*) also increases. Furthermore, this increase in polarisability is observed to be highest for CO_2 confined within the smallest pores (3.2 nm). The KTπ* value is *ca.* 0.01 at a CO_2 density of 975 $kg.m^{-3}$, decreasing to *ca.* -0.06 at a CO_2 density of 750 $kg.m^{-3}$ in the bulk. In comparison to conventional organic liquid solvents, the results indicate that CO_2 exhibits similar polarisability to octane when confined in the 3.2 nm porous material at density of 975 $kg.m^{-3}$.[287]

This further understanding of the polarisability of a confined fluid is key for guiding the SCFED process, where the quantitative values of CO_2 polarisability (KTπ*) confined within the porous templates dictates the nature of the electrolyte that may be used.

4 Conclusions

In conclusion this work has developed a cell and methodology allowing for luminescence measurements in SCFs. Spectroscopic measurements have been conducted to verify the reliability of the results obtained from the Nottingham Cubic Cell and these have shown that the developed method is an effective one. The measurements have also shown to be in good agreement with previous literature. The cell has been shown to work in the temperature range of interest for this Thesis (30 ^{o}C to 40 ^{o}C). Investigation into the windows used and path length obtained has also been conducted and as a result the cell comprises of four quartz windows with a path length of 1 cm. The cell has been shown to be effective for 90^{o} measurements which are required due to the design of the fluorimeter used.

A methodology for conducting luminescence spectroscopy within porous materials has also been developed. A range of methods have been tested including creating both silica and impregnated silica discs, and immobilising both silica and impregnated silica onto the windows. It has been shown within this work that using a 2.17 mm diameter glass holder is the most efficient method.

Investigation towards the identification of a dye suitable for use as a density sensor has also been carried out. Solubility in CO_2 and sensitivity to changes in the density of the surrounding solvent have been identified as the most important factors. Anthracene and tfpp have been determined as viable density sensors.

Investigation into the effect of silica presence on the emission of anthracene in the absence of solvent has been investigated. Subsequently, a study into anthracene as a density sensor has been conducted. A red shift in the emission energy of anthracene is observed with increasing pressure and subsequently CO_2 density. The emission of anthracene has been plotted against CO_2 density, producing a calibration plot. A deviation from linearity is observed which is in agreement with literature.[269] The calibration plot was then used to calculate the density from the bulk emission and compared to the equation of state values. A good agreement between both sets of values was observed and the calibration was subsequently deemed viable.

Measurements of anthracene within 8.3, 4.5 and 3.2 nm porous materials were then conducted. A small red shift was observed for each porous silica with increasing bulk CO_2 density. A large red shift is observed between the porous materials and bulk, where the smaller pore diameter material exhibits a larger red shift. Investigation into the effect of silica on the emission of anthracene in the presence of CO_2 has been conducted using a silica with pore width considerably smaller than the molecular size of anthracene and no discernible effect was seen with changing CO_2 density. Overall, a bulk CO_2 pressure *vs.* calculated CO_2 density within the pores was obtained, along with the calculated density increase with decreasing pore diameter.

Investigation into tfpp as a density sensor was then completed, where peak ratio was shown to increase with increasing CO_2 density. A calibration plot of peak ratio of tfpp *vs.* density of CO_2 was subsequently obtained. The calibration plot was used to obtain the calculated densities for bulk CO_2 based on emission and compared to the values obtained from equation of state, good agreement between both sets of values was observed. Thus, the calibration was deemed to be accurate.

Investigation into the effect of silica on the emission measurements was studied with the use of the 'non-porous silica,' similarly to anthracene, no discernible trend was observed. Measurements of tfpp were subsequently conducted in 8.3, 4.5 and 3.2 nm porous materials and bulk CO_2 pressure *vs.* calculated CO_2 density plots were obtained. The density is seen to increase as pore size decreases, which are in good agreement with results obtained from anthracene. The calculated densities of CO_2 within porous materials using anthracene and tfpp as probe molecules are shown to be in reasonable agreement.

A brief investigation into fluid polarisability and dielectric constant has been conducted with anthracene as a probe. The initial results indicate Kamlet-Taft polarisability to be a better metric of fluid behaviour than dielectric constant. The polarisability of CO_2 is observed to increase with increasing density and decreasing pore size.

Chapter 7

Conclusions and Future Outlook

This Chapter will summarise the findings that have arisen from this Thesis and outline the implications that these results may have. Subsequently, the future outlook of this work and suggested avenues of study will be detailed.

1 Summary

The photophysical properties of metal polypyridyl complexes have been implemented in a wide range of applications and as such, a comprehensive understanding of the nature of their excited states is paramount for guiding and directing their use. In Chapters 2-5 of this thesis the photophysical properties of rhenium diimine complexes are investigated through the use of time resolved infrared studies, spectro-electrochemical measurements, absorption and emission spectroscopy. The conclusions drawn from these spectroscopic investigations have also been supported by molecular orbital calculations obtained *via* DFT.

The photophysics of NPh_2 donor appended rhenium dipyrido[3,2-*a*:2',3'-*c*]phenazine complexes, Re(dppz), has been assessed in Chapter 2. The electron donating NPh_2 group results in three observed excited states, with initially formed ^{1}IL$\pi\pi^*$ and charge transfer $NPh_2(\pi)phz(\pi^*)$ states. The former state decays on the picosecond timescale to an ^{3}IL$\pi\pi^*$ state which exhibits a microsecond lifetime. Charge transfer from the NPh_2 donor to the phz acceptor has been explored through the lifetime of the $NPh_2(\pi)phz(\pi^*)$ state, which has been shown to decrease with increasing donor-acceptor distance, Figure 7-1.

The lifetime of the $NPh_2(\pi)phz(\pi^*)$ state decreases from 2.5 ns to 38 ps for [Re(dppz-NPh_2)$(CO)_3Cl$] and [Re(dppz-Ph_3NPh_2)$(CO)_3Cl$] respectively. The charge transfer state lifetime is also observed to decrease with increasing insulator character of the bridge moiety between the donor and acceptor. This was attributed to planarity and aromaticity effects which is also illustrated in Figure 7-1. The insulator character of the bridge was observed to increase in the following order, (C_4H_3S) > Ph > (N_3C_2H), with the (N_3C_2H) bridge the greatest insulator.

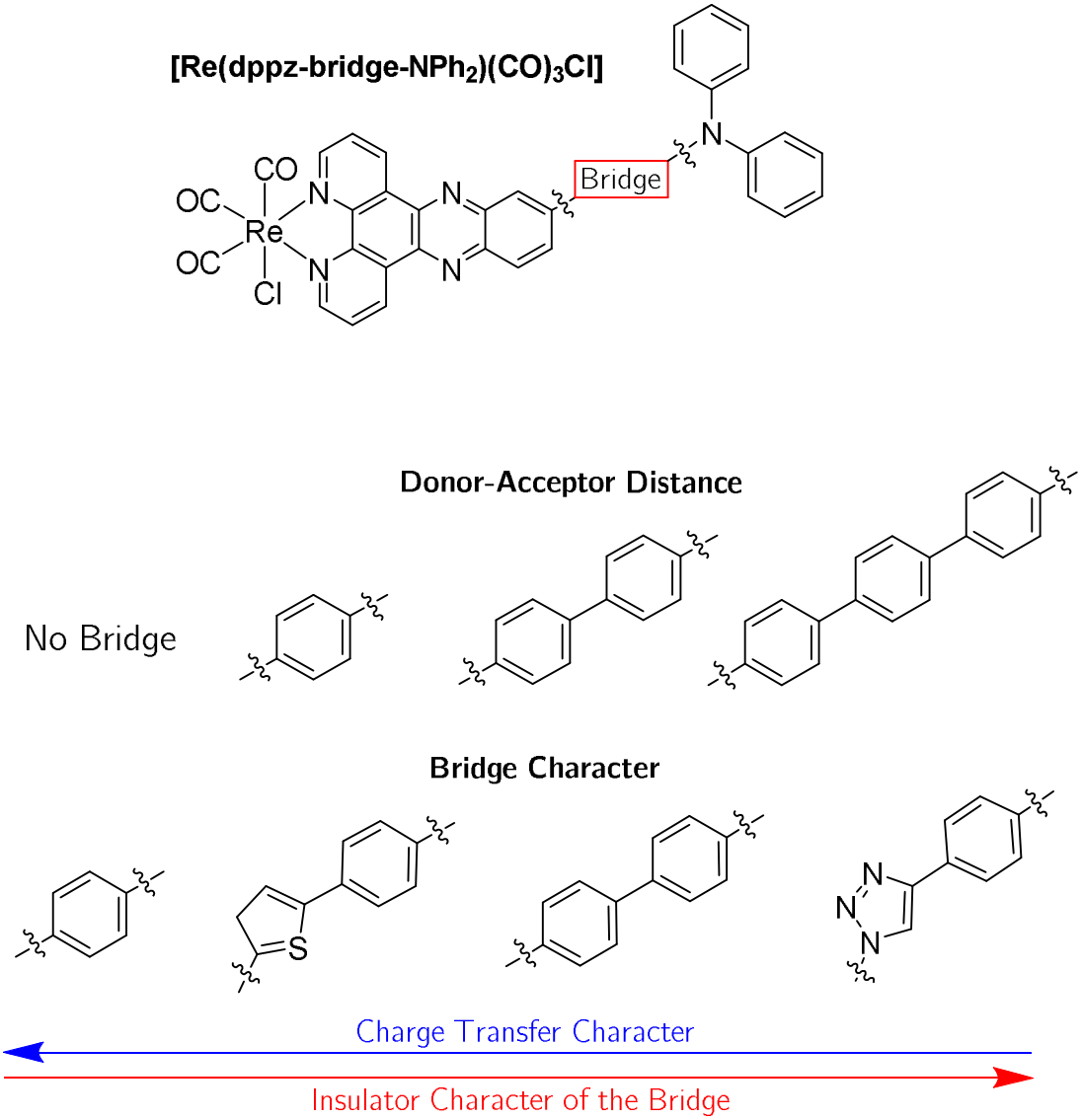

Figure 7-1: The [Re(dppz-NPh_2)$(CO)_3Cl$] (top) complexes investigated in Chapter 2 through TRIR, emission, absorption, spectroelectrochemical spectroscopies and molecular orbital calculations. Two of the important trends identified are shown, the effect of the distance between the donor-acceptor moieties (middle) and the effect of bridge character (bottom) on the charge transfer observed.

The effect on the photophysical properties of [Re(dppz)(CO)$_3$Cl] of an electron withdrawing group appended and substituted on the phz portion of the dppz ligand has been studied in Chapters 3 and 4. A nitrogen atom has been substituted into the phz moiety (Chapter 3) and an NO_2 group was appended onto the phz moiety (Chapter 4), are both shown to lower the phz(π^*) energy. Firstly, for the nitrogen substituted complexes Re(dppp2), Re(dppp3) and Re(dppp2Br), the position of the nitrogen is shown to have a significant effect on the photophysical properties observed, where the meta position was observed to have more of an electron withdrawing effect than the corresponding ortho position. This observation was consistent with the NO_2 electron withdrawing appended Re(dppz) complexes, shown in Figure 7-2. Furthermore the additional electron withdrawing halogen group for Re(dppp2Br) was shown to have a significant effect, which was further probed by investigating the complex [Re(dppz-I)(CO)$_3$Cl].

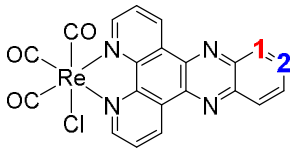

less electron withdrawing

more electron withdrawing

1	2	Φ_{da}		
C	N		More electron withdrawing	**Chapter 3**
N	C		Less electron withdrawing	
C	NO_2	0°	More electron withdrawing	**Chapter 4**
NO_2	C	36°	Less electron withdrawing	

Figure 7-2: The effect of substituent position on the electron withdrawing ability investigated in Chapters 3 & 4.

The effect of an electron withdrawing group incorporated and an electron donating group appended onto a Re(dppz) derivative complex was investigated to draw a comparison between the NPh_2 donor appended and pyridine N incorporated Re(dppz) complexes studied. The complex, [Re(dpppn-(NH_2)$_2$)(CO)$_3$Cl], in d-DMSO was observed to exhibit a similar TRIR spectral profile to the Re(dppz-NPh_2) derivative complexes for the ^{1}IL$\pi\pi^*$ and ^{3}IL$\pi\pi^*$ states. A similar photoproduct marker band is observed in the fingerprint region of the IR spectra, therefore, an excited state which is ^{1}IL$\pi\pi^* \rightarrow {}^3IL\pi\pi^*$ in nature was tentatively assigned. The observed photophysics were attributed to the NH_2 electron donor group. However, as the solvent's dielectric constant is varied, significantly different photophysics is observed, where the excited state lifetime is observed to decrease with decreasing solvent dielectric constant. This is in contradiction

to observations made for Re(dppz) based complexes, where the photophysical properties observed for [Re(dpppn-$(NH_2)_2$)$(CO)_3Cl$] in CH_2Cl_2 were consistent with observations for the Re(dppp) complexes. Further work is required to ascertain the trend between solvating media and the observed photophysical properties.

The nature and kinetics of the excited states observed for the complexes studied in Chapters 3 & 4 exhibit a significant solvent dependence. However, owing to solubility of Re(diimine) complexes, studies have previously been limited to polar media. In Chapter 5, the photophysics of common Re(diimine) dyes, [Re(dppz)$(CO)_3Cl$] and [Re(bpy)$(CO)_3Cl$] have been investigated in an apolar medium, PFMCH. Interestingly, the results show a long lived excited state which is IL$\pi\pi^*$ in nature as shown in Figure 7-3. This is in contradiction to the previously reported excited states of [Re(dppz)$(CO)_3Cl$] in polar solvents.

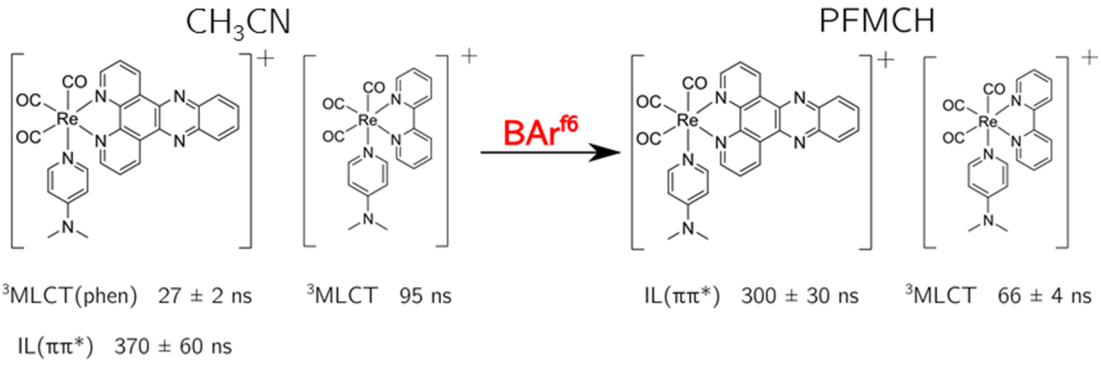

Figure 7-3: The nature and lifetimes of [Re(bpy)$(CO)_3$(DMAP]$^+$ and [Re(dppz)$(CO)_3$(DMAP]$^+$ excited states in conventional solvent CH_3CN, and in a previously unstudied apolar medium, PFMCH.

The observation of solvent dependent photophysics from Chapters 3-5 was further exploited in Chapter 6 to probe phase behaviour of fluids in mesoporous materials which are relevant to supercritical fluid electrodeposition (SCFED). Firstly, a methodology for conducting luminescence spectroscopic measurements of confined high pressure fluids was designed. Subsequently, an investigation into suitable probe molecules conducted where anthracene and tfpp emission was observed to change with CO_2 fluid density. Finally the density of CO_2 confined within the porous templates was investigated. The results show that the fluid behaviour of CO_2 varies significantly when confined in a

mesoporous template compared to the bulk. The density of CO_2 was observed to increase with decreasing mean pore width, as shown in Figure 7-4, where the density of CO_2 confined within a 3.2 nm wide pore is *ca.* 1.25 times higher than its bulk counterpart.

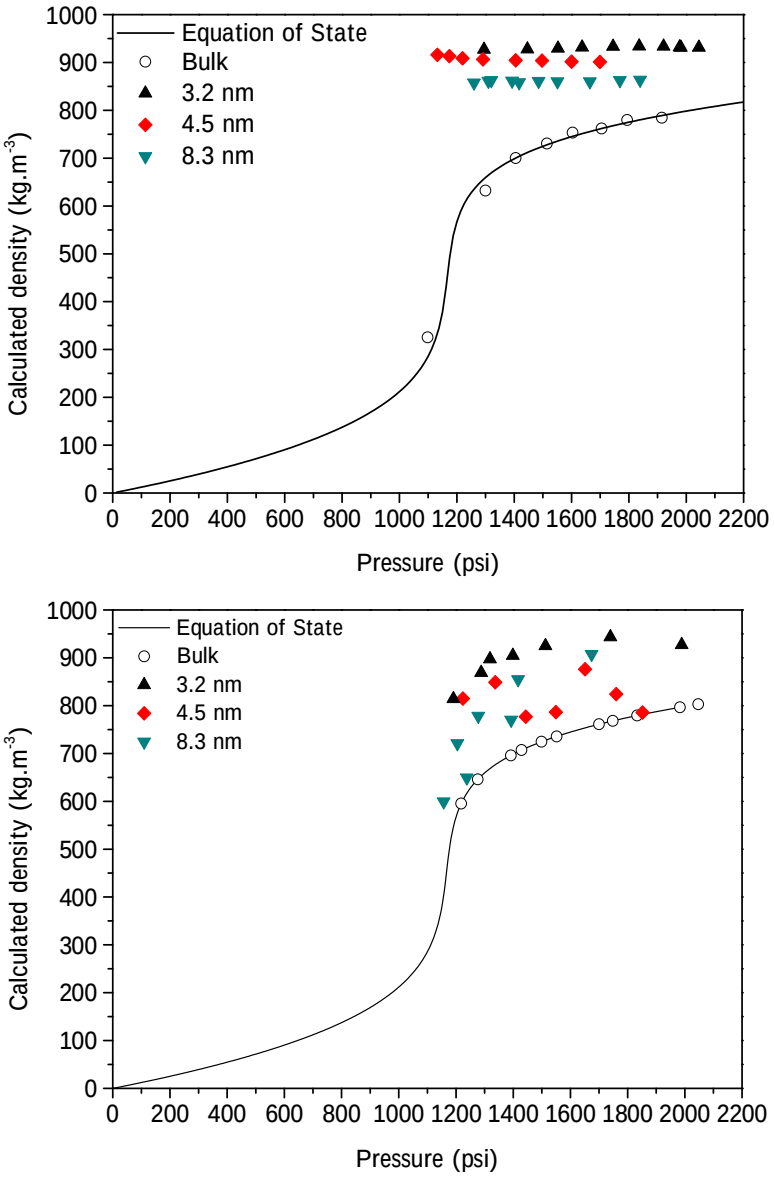

Figure 7-4: The calculated density of CO_2 confined within porous templates. The mean pore width of the templates are 3.2, 4.5 and 8.3 nm. The density of CO_2 was shown to be *ca.* 1.25 times higher confined in the 3.2 nm pores compared to the bulk. Anthracene (top) and tfpp (bottom) were utilised as the probe dyes in Chapter 6.

2 Implications and Future Work

Understanding donor-acceptor complexes is crucial for directing and altering the charge transfer character observed. There has been limited studies of these complexes previously in the literature, with the majority of work focussing on electron withdrawing group appended dipyridophenazine complexes. Guiding charge transfer character is vital for many future applications, for example dye sensitised solar cells.[60, 61]

Further work can involve a more in depth investigation into the bridge nature and length in [Re(dppz-NPh_2)$(CO)_3Cl$] complexes on the photophysical properties observed. Firstly, longer phenyl-unit bridge systems may further elucidate the effect of planarity on charge transfer character. Secondly, a study of large conjugated systems which have been previously used as bridges due to their rigidity resulting in the donor and acceptor being held in specific positions.[71-73] A large conjugated system may result in the '*bridge*' exhibiting behaviour more common of a wire, where charge may be localised on the spacer and therefore allowing for the additional control of charge transfer.[61] This could potentially allow for the further understanding of charge transfer behaviour. Additionally, the effect of donor-acceptor dihedral angle on the charge transfer observed was unclear and further work would be required in this area. This may include synthesising and investigating the photophysical properties of [Re(dppz-$(NPh_2)_2$)$(CO)_3Cl$] and [Re(dppz-$(Ph(OCH_3)$-$PhNPh_2)_2$)$(CO)_3Cl$] and comparing the behaviour to the complexes studied within this work.

This Thesis has focussed on the modification of the phz portion of the dppz ligand and the effect of this on the photophysical properties of [Re(dppz)$(CO)_3Cl$]. This is because these modifications leave the phen orbitals relatively unperturbed. Therefore, it would be of interest to change the nature of the phen orbital in a similar manner, as this is expected to affect properties such as luminescence. This would allow for the interplay between the phen and the phz orbitals to be further characterised.

Modified Re(diimine) complexes offer many potential applications, such as DNA sensors, solar cells, sensors and in catalysis. For example, charge transfer complexes have been shown to be important photoredox catalysts. However, due to the large scale use of

these complexes, a relatively cheap cost is required. It would be interesting to assess the nature of charge transfer, if any, observed for the complexes in Chapter 2, [Re(dppz-NPh_2)$(CO)_3$Cl] derivatives, with the use of a relatively inexpensive metal such as iron.

For CO_2 reduction pyridine based complexes have been shown to yield the more useful $6e^-$ reduced product methanol over the $2e^-$ reduced products CO and formate, which usually result from metal-diimine catalysts. Studies on the potential for the [Re(dppp)$(CO)_3$Cl] complexes in Chapter 3 to be used as catalysts for CO_2 reduction would be of interest, as the substituted nitrogen within the phz portion of the ligand may encourage the formation of more useful products compared to commonly employed $[Re(dppz)(CO)_3L]^+$ catalysts.

The ability to synthesise metal organic complexes, which exhibit good solubility in apolar solvent media, opens up a range of applications previously inaccessible or limited to the use of a co-solvent. Understanding and increasing the solubility of conventional metal based dyes in CO_2 and other low polarity SCFs, will allow for advances in these SCF based processes. For example, CO_2 reduction without the need of a conventional liquid co-solvent. This may result in a more facile separation of the products, such as increasing the solubility of $[Re(dppp)(CO)_3(DMAP)]^+$ into CO_2 allowing the production the favoured methanol product. Additionally, a long lived photosensitiser excited state is important for CO_2 reduction, $[Re(dppz)(CO)_3(DMAP)][BAr^{f6}]$ has been shown to exhibit a μs excited state in PFMCH.

Additionally, supercritical fluids are a growing area of research which allow alternative approaches to conventional techniques such as electrodeposition, as discussed in Chapter 6. This would allow for use of Re(diimines) as solvatochromic probes for further investigations of phase behaviour in low polarity supercritical fluids, such as CO_2.

The exploitation of solvatochromic dyes in CO_2 has been implemented in Chapter 6 to probe the phase behaviour within the porous templates. The results of this work will allow for the further refinement of the SCFED process, such as understanding the bulk conditions required to achieve the favoured confined density. The development of high

pressure luminescence within porous materials may have applications outside of SCFED, such as for phase behaviour of confined catalytic systems.

The SCFED process is working towards the use of SCFs such as difluoromethane and trifluoromethane, owing to their high dielectric constant compared to CO_2. Therefore, future work can focus on the phase behaviour of these fluids upon confinement. In addition to the investigation of phase behaviour in a wider range of porous materials, including the phase behaviour inside functionalised porous templates. This will allow for refinement of the SCFED process, when work within these solvents is prominent.

Chapter 8

Experimental

This Chapter outlines the materials, apparatus, sample preparation, synthetic procedures and methods of analysis used in this Thesis.

Firstly, a description of the materials for each Chapter is provided, followed by synthetic procedures and characterisation of complexes produced during this work.

Secondly, a description of experimental techniques and apparatus required is given followed by sample preparation.

Finally, a key part of the work in this Thesis relies on luminescence spectroscopic measurements in supercritical fluids both in bulk and confined within porous materials. The development of a cell for these measurements and a rig system are detailed below including a method for conducting in porous measurements.

1 Materials

1.1 Commercially Available Compounds and Solvents

All chemicals and reagents were used as supplied from the manufacturer unless otherwise stated. The commercially available complexes and solvents used within this Thesis are listed here by supplier.

2,4,5,6-tetraaminopyrimidine sulphate and tetrakis(pentafluorophenyl)-porphyrin were obtained from Acros Organics.

Hexane and toluene were obtained from Fischer Scientific.

Anthracene was obtained from J. T. Baker® Chemicals.

Chloroform, dichloromethane, diethyl ether, 4-(dimethylamino)-pyridine, dimethylformide, dimethyl sulfoxide, deuterated dimethyl sulfoxide, 4-iodo-1,2-diaminobenzene, 1,10-phenanthroline-5,6-dione, rhenium (I) pentacarbonyl bromide, rhenium (I) pentacarbonyl chloride, tetrabutylammonium hexafluorophosphate were obtained from Sigma Aldrich.

Acetone, acetonitrile, tetrahydrofuran, ethanol, methanol, 2-propanol, sodium hydroxide pellets, tetrahydrofuran were obtained from VWR International.

1.2 Non-Commercially Provided Samples

The complexes [Re(dppz-NPh_2)$(CO)_3Cl$], [Re(dppz-$(PhNPh_2)_2$)$(CO)_3Cl$], [Re(dppz-Ph_2NPh_2)$(CO)_3Cl$], [Re(dppz-Ph_3NPh_2)$(CO)_3Cl$], [Re(dppz-$(C_4H_3S)PhNPh_2$)$(CO)_3Cl$], [Re(dppz-$(Ph\text{-}(OCH_3)_2)NPh_2$)$(CO)_3Cl$] and [Re(dppz-$(N_3C_2H)PhNPh_2$)$(CO)_3Cl$] used in Chapter 2 were synthesised and provided by Dr Chris Larsen, Keith Gordon Group at the University of Otago

The complexes [Re(dppp2)$(CO)_3Cl$], [Re(dppp3)$(CO)_3Cl$] and [Re(dppp2Br)$(CO)_3Cl$] used in Chapter 3 were previously synthesised within the George Group at the University of Nottingham.

The complex Tetrakis[3,5-bis(perfluorohexyl)phenyl]borate in Chapter 5 was synthesised and provided by Dr Zacharias Amara, whilst a member of the George Group at the University of Nottingham.

1.2.1 Porous Templates Used in Chapter 6

The 3.2 nm MCM-41 (Mobil Crystalline materials-41) and 8.3 nm MSU-h (Silica, mesostructured large pore 2D hexagonal) (Sigma-Aldrich) were used as received from

the manufacturer. The 4.5 nm MCM-41-180 silica was synthesised at the University of Nottingham by the Mokaya Group. Adsorption isotherm analysis was conducted by the Mokaya Group to verify the pore size and pore size distribution of each material; the isotherms are shown in Figure 8-2, wherein MCM-41 (black), MCM-41-180 (red) and MSU-H (blue) are observed. The porous structure of the silica is shown in Figure 8-1, where regular hexagonal pores are observed.

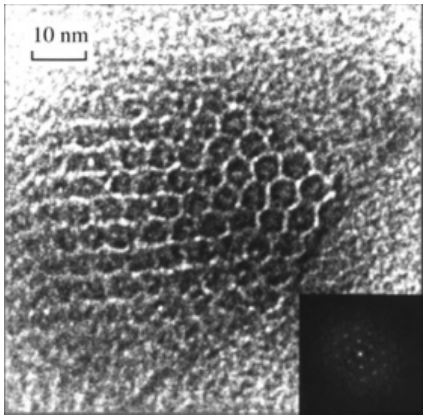

Figure 8-1: Transition electron micrograph (TEM) of MCM-41, showing uniform pores of hexagonal cross section. Reproduced from reference 258.

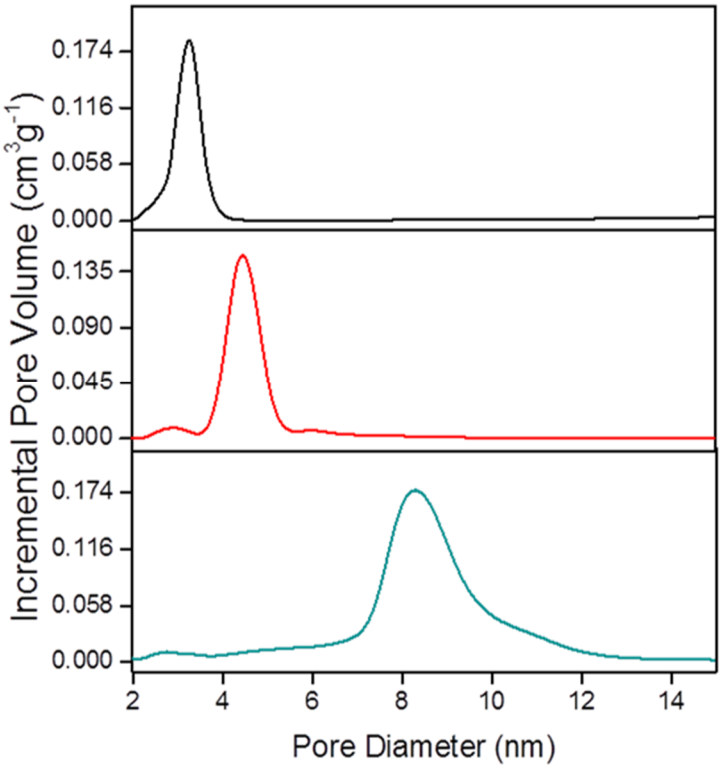

Figure 8-2: Adsorption isotherms conducted to verify the pore size and pore size distribution of materials used within this report wherein MCM-41 (black), MCM-41-180 (red) and MSU-h (blue).

2 Synthetic Procedures

2.1 Synthesis Chapter 3

2.1.1 [Re(dppz-I)(CO)$_3$Cl]

The complex rhenium dipyrido[3,2-*a*:2',3'-*c*]phenazine iodine tricarbonyl chloride, [Re(dppz-I)(CO)$_3$Cl], was synthesised in two steps detailed below.

Synthesis of dipyrido[3,2-a:2',3'-c] phenazine iodine: (dppz-I)

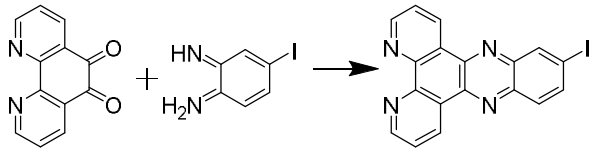

1,10-phenanthroline-5,6-dione (500 mg, 5.45 mmol) and 4-iodo-1,2-diaminobenzene (500 mg, 2.14 mmol) was refluxed in ethanol (10 mL, 80 ^{o}C) under an inert atmosphere and in the absence of light (24 hrs). The solution was cooled (25 ^{o}C) and the solvent removed under vacuum. The crude green paper like product was washed with ethanol and then recrystallised from $CHCl_3$ to yield the final dark purple solid product dppz-I (670 mg, 80 %).

^{1}H NMR (400 MHz, $CDCl_3$); δ 9.07 (m, 4H), 8.35 (s, 1H), 7.90 (d, 1H, J = 8.77 Hz), 7.54 (m, 3H); (CH_3CN sol), m/z – 430.98 $[C_{18}H_9N_4I]^+$ Na. Calculated; C (52.96 %), H (2.22%), N (13.73 %); Found; C (53.38%), H (2.21%), N (13.19%).

Synthesis of rhenium dipyrido[3,2-a:2',3'-c] phenazine iodine tricarbonyl chloride: [Re(dppz-I)(CO)$_3$Cl]

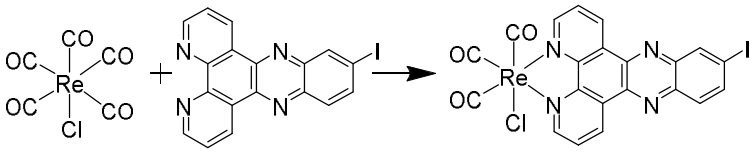

[Re(CO_5)Cl] (20 mg, 0.055 mmol) and dppz-I (15 mg, 0.037 mmol) were refluxed in ethanol (25 mL, 80 ^{o}C) under an inert atmosphere (24 hrs). The solution was cooled (25 ^{o}C) and the resulting yellow/brown crude product solid collected by suction filtration. The crude product was purified by repeat recrystallization with ethanol. The final product [Re(dppz-I)(CO)$_3$Cl] (10 mg, 38%) was obtained as a yellow microcrystalline solid.

^{1}H NMR (400 MHz, CD_3CN); δ 9.78 (t, 3H, J = 8 0 Hz), 9.47 (m, 2H), 8.92 (s, 1H), 8.36 (d, 1H, J = 4 Hz), 8.16 (m, 2H); (CH_2Cl_2 sol), ν(CO): 2025, 1923, 1899 cm^{-1} ; m/z – 734.89 $[C_{21}H_9N_4O_3ClReI]^+Na$; Calculated C (35.33 %), H (1.27%), N (7.85 %); Found; C (34.44%), H (1.49%), N (6.81%).

2.1.2 [Re(dpppn-$(NH_2)_2$)$(CO)_3Cl$]

The complex rhenium pterdino[6,7-f][1,10]phenanthroline-11,13-diamine tricarbonyl chloride, [Re(dpppn-$(NH_2)_2$)$(CO)_3$Cl], was synthesised in two steps detailed below, in collaborations with Elizabeth Hampson, a 4th year Masters Student within the George Group.

Synthesis of pterdino[6,7-f][1,10]phenanthroline-11,13-diamine: (dpppn-$(NH_2)_2$)

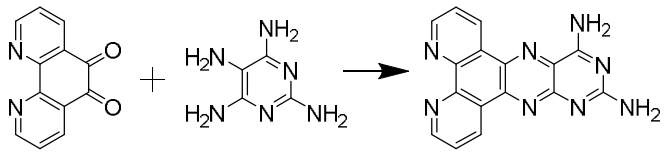

NaOH (2 M) was added dropwise to a solution of 2,4,5,6-tetraaminopyrimidine sulphate (103 mg, 0.432 mmol) in water (8 mL) until the solution pH was 11. A suspension of 1,10-phenantroline-5,6-dione (295 mg, 1.40 mmol) in methanol (8 mL) was added to the solution and the resultant mixture was stirred in the absence of light (25 °C, 20 hrs). The resultant precipitate was collected by gravity filtration, washed with water, methanol and excess diethylether, and dried under vacuum to yield the final product dpppn-$(NH_2)_2$ (53 mg, 39 %)

^{1}H NMR (300 MHz, d-DMSO); δ 9.73 (dd, 1H, J = 8.19, 1.79 Hz), 9.39 (dd, 1H, J = 8.15, 1.54 Hz), 9.20 (dd, 1H, J = 4.38, 1.84 Hz), 9.10 (dd, 1H, J = 4.38, 1.74 Hz), 8.52 (s, 1H), 8.05 (s, 1H), 7.89 (m, 2H), 7.00 (s, 2H) ppm; m/z – 315.11 $[C_{16}H_{10}N_8]^+H$

Synthesis of rhenium pterdino[6,7-f][1,10]phenanthroline-11,13-diamine tricarbonyl chloride: [Re(dpppn-$(NH_2)_2$)$(CO)_3$Cl

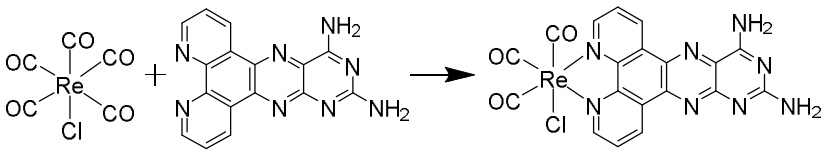

A suspension of $[Re(CO)_5Cl]$ (45.9 mg, 0.127 mmol) and dpppn-$(NH_2)_2$ (39.7 mg, 0.126 mmol) in ethanol (20 mL) was stirred under inert atmosphere and in the absence of light (80 °C, 2 hrs). The solution was then allowed to cool (25 °C) and then evaporated to dryness. The resultant crude product was washed with hexane, recrystallized multiple times with acetonitrile-ether and dried under vacuum to yield the final dark yellow product $[Re(dpppn\text{-}(NH_2)_2)(CO)_3Cl]$ (6.60 mg, 8 %).

^{1}H NMR (300 MHz, d-DMSO); δ 10.17 (dd, 1H, J = 8.36, 1.42 Hz), 9.64 (dd, 1H, J = 8.30, 1.46 Hz), 9.50 (dd, 1H, J = 5.20, 1.46 Hz), 9.38 (dd, 1H, J = 5.11, 1.41 Hz), 8.70 (s, 1H), 8.25 (s, 1H), 8.18 (m, 2H), 7.30 (s, 2H) ppm; (d-DMSO, sol), ν(CO): 2020, 1913, 1895 cm^{-1}; m/z – 643.00 $[C_{19}H_{10}N_8O_3ClRe]^+Na$. Calculated C (36.81 %), H (1.63 %), N (18.07 %); Found C (35.62 %), H (1.98 %), N (16.61 %)

2.2 Synthesis Chapter 4

The complexes $[Re(dppz\text{-}12\text{-}NO_2)(CO)_3Cl]$ and $[Re(dppz\text{-}13\text{-}NO_2)(CO)_3Cl$ were synthesised in collaboration with Elizabeth Hampson, an undergraduate masters student within the George Group, University of Nottingham.

2.2.1 [Re(dppz-12-NO_2)$(CO)_3$Cl]

The complex rhenium 12-nitrodipyrido[3,2-a:2',3'-c]phenazine tricarbonyl chloride, $[Re(dppz\text{-}12\text{-}NO_2)(CO)_3Cl]$, was synthesised in two steps.

Synthesis of 12-nitrodipyrido[3,2-a:2',3'-c]phenazine: (dppz-12-NO_2)

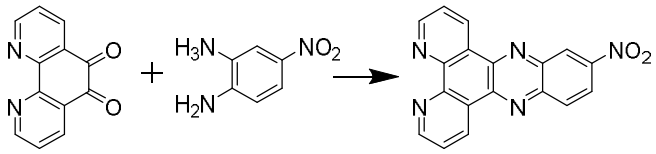

1,10-phenanthroline-5,6-dione (295 mg, 1.40 mmol) and 2-nitro-1,2-phenylenediamine (262 mg, 1.71 mmol) was refluxed in ethanol (15 mL, 80 ^{o}C) under an inert atmosphere and in the absence of light (4.5 hrs). The solution was cooled (25 ^{o}C) and the crude yellow precipitate collected by gravity filtration and washed with methanol. The crude product was dried under vacuum and recrystallized with chloroform/methanol (50:50) to yield the pure dppz-12-NO_2 ligand yellow solid (407 mg, 80 %).

^{1}H NMR (300 MHz, $CDCl_3$); δ 9.67 (m, 2H), 9.35 (dt, 2H, J = 4.43, 1.7, 1.7 Hz), 9.31 (d, 1H, J = 2.17 Hz), 8.70 (dd, 1H, J = 9.28, 2.5 Hz), 8.54 (d, 1H, J = 9.23 Hz), 7.87 (ddd, 2H, J = 8.01, 4.62, 3.11 Hz) ppm; m/z – 328.08 $[C_{18}H_9N_5O_2]^+$ H

Synthesis of rhenium dipyrido[3,2-a:2',3'-c] phenazine iodine tricarbonyl chloride: [Re(dppz-12-NO_2)$(CO)_3$Cl]

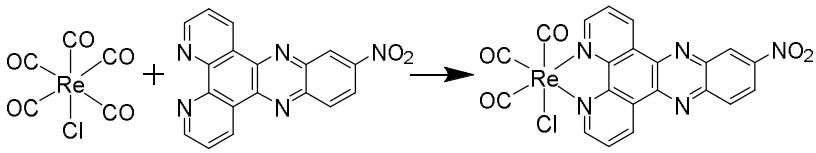

To a suspension of $[Re(CO)_5Cl]$ (88 mg, 0.243 mmol) in toluene (15 mL) and a suspension of dppz-12-NO_2 (79.3 mg, 0.242 mmol) in toluene (15 mL) was added. The resultant solution was heated to reflux (110 ^{o}C) under an inert atmosphere until completion (3 hrs). The solution was cooled (25 ^{o}C) and the resultant crude orange precipitate collected by gravity filtration. The crude product was washed with diethyl ether/hexane (50:50) and dried under vacuum to yield the pure orange product [Re(dppz-12-NO_2)$(CO)_3$Cl] (101 mg, 66 %).

^{1}H NMR (300 MHz, $CDCl_3$); δ 9.89 (dt, 2H, J = 8.2, 1.4, 1.3 Hz), 9.54 (ddd, 2H, J = 5.19, 0.94, 0.71, 0.69 Hz), 9.40 (dd, 2H, J = 2.45, 0.38 Hz), 8.83 (dd, 1H, J = 9.32, 2.54 Hz), 8.65 (d, 1H, J = 9.7 Hz), 8.10 (ddd, 1H, J = 8.24, 5.23, 4.33 Hz) ppm; (CH_3CN sol), ν(CO): 2024, 1921, 1903 cm^{-1} ; m/z – 655.91 $[C_{21}H_9N_5O_5ClRe]^+$ Na.

Calculated; C (39.85 %), H (1.43 %), N (11.06 %); Found; C (39.85 %), H (1.43 %), N (11.06 %).

2.2.2 [Re(dppz-13-NO_2)$(CO)_3Cl$]

The complex rhenium 13-nitrodipyrido[3,2-a:2',3'-c] phenazine tricarbonyl chloride, [Re(dppz-13-NO_2)$(CO)_3Cl$], was synthesised in two steps.

Synthesis of 13-nitrodipyrido[3,2-a:2',3'-c]phenazine: (dppz-13-NO_2)

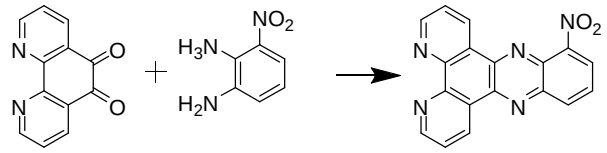

1,10-phenanthroline-5,6-dione (298 mg, 1.43 mmol) and 3-nitro-1,2-phenylenediamine (262 mg, 1.71 mmol) was refluxed in ethanol (15 mL, 80 ^oC) under an inert atmosphere and in the absence of light (4.5 hrs). The solution was cooled (25 ^oC) and the crude yellow precipitate collected by gravity filtration and washed with methanol. The crude product was dried under vacuum and recrystallized with chloroform/methanol (50:50) to yield the pure dppz-12-NO_2 pale orange solid (376 mg, 80 %).

^1H NMR (300 MHz, $CDCl_3$); δ 9.64 (ddd, 2H, J = 11.4, 8.1, 1.79 Hz), 9.34 (ddd, 2H, J = 4.52, 3.58, 1.79 Hz), 8.63 (dd, 1H, J = 8.62, 1.37 Hz), 8.37 (dd, 1H, J = 7.54, 1.32 Hz), 8.01 (dd, 1H, J = 16.1, 7.5 Hz), 7.85 (ddd, 2H, J = 8.12, 4.5, 2.45 Hz) ppm; m/z – 328.08 $[C_{18}H_9N_5O_2]^+$ H

Synthesis of rhenium dipyrido[3,2-a:2',3'-c] phenazine iodine tricarbonyl chloride: [Re(dppz-13-NO_2)$(CO)_3Cl$]

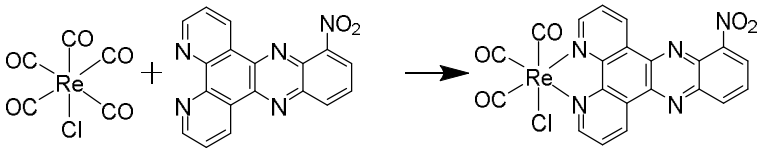

To a suspension of $[Re(CO)_5Cl]$ (111 mg, 0.307 mmol) in toluene (15 mL) and a suspension of dppz-12-NO_2 (100 mg, 0.306 mmol) in toluene (15 mL) was added. The resultant solution was heated to reflux (110 ^oC) under an inert atmosphere until completion (3 hrs). The solution was cooled (25 ^oC) and the resultant crude orange precipitate collected by gravity filtration. The crude product was washed with diethyl ether/hexane (50:50) and dried under vacuum to yield the pure orange product $[Re(dppz\text{-}12\text{-}NO_2)(CO)_3Cl]$ (407 mg, 81 %).

^1H NMR (300 MHz, $CDCl_3$); δ 9.83 (ddd, 2H, J = 12.95, 8.24, 1.51 Hz), 9.52 (ddd, 2H, J = 5.13, 3.39, 1.46 Hz), 8.72 (dd, 1H, J = 8.67, 1.32 Hz), 8.51 (dd, 1H, J = 7.44, 1.32 Hz), 8.16 (dd, 1H, J = 8.67, 7.54 Hz), 8.08 (ddd, 2H, J = 8.29, 5.27, 0.57 Hz) ppm; ($CHCl_3$, sol), ν(CO): 2024, 1921, 1903 cm^{-1}; m/z – 655.97 $[C_{21}H_9N_5O_5ClRe]^+$ Na. Calculated; C (39.85 %), H (1.43 %), N (11.06 %); Found; C (39.82 %), H (1.19 %), N (10.82 %).

2.3 Synthesis Chapter 5

The complexes $[Re(CO)_3(bpy)(DMAP)][BF_4]$, $[Re(CO)_3(dppz)(DMAP)][BF_4]$, $[Re(CO)_3(bpy)(DMAP)][BARf^6]$) and $[Re(CO)_3(dppz)(DMAP)][BARf^6]$ were synthesised in collaboration with Katherine Reynolds, an undergraduate masters student within the George Group, University of Nottingham.

2.3.1 $[Re(CO)_3(dppz)(DMAP)][BARf^6]$

The complex rhenium dipyrido [3,2-a:2',3'-c] phenazine tricarbonyl 4-dimethylaminopyridine tetrakis(3,5-bis-(perfluorohexyl)phenyl)borate, $[Re(dppz)(CO)_3(DMAP)][BARf^6]$ was synthesised in four steps described below

Synthesis of rhenium 1,10-phenanthroline-5,6-dione bromide tricarbonyl: [Re(phen)(CO)$_3$Cl]

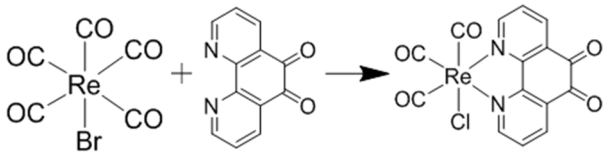

$Re(CO_5)Br$ (268 mg, 0.66 mmol) and 1,10 phenanthroline-5,6-dione (139 mg, 0.66 mmol) was refluxed in toluene (7 mL, 110 ^oC) under an inert atmosphere (6 hrs). The solution was cooled (25 ^oC) and the resulting orange/brown crude product solid collected by suction filtration. The crude product was purified by column chromatography on silica gel with THF as an eluent. The final product $[Re(phen)(CO)_3Br]$ (230 mg, 69%) was obtained as an orange/brown microcrystalline solid.

^1H NMR (270 MHz, $CDCl_3$); δ 9.33 (d, 2H), 8.72 (d, 2H), 7.82 (dd, 2H); (CH_3CN sol), ν(CO): 2026, 1925, 1908 cm^{-1} ; m/z – 582.89 $[C_{15}H_6N_2O_5ReBr]^+$ Na

Synthesis of rhenium bromide dipyrido[3,2-a:2',3'-c] phenazine tricarbonyl: [Re(dppz)(CO)$_3$Cl]

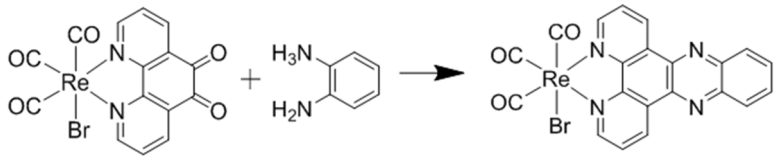

$[Re(CO)_3Br(phen\text{-}5,6\text{-}dione)]$ (250 mg, 0.48 mmol) in ethanol (30 mL) was heated to reflux (78 ^oC). A solution of 1,2-diaminobenzene (67 mg, 0.62 mmol) in ethanol (5 mL) was then added drop-wise. The resultant reaction mixture was refluxed under inert atmosphere (2 hrs). After cooling (0 ^oC), the precipitate was collected by suction filtration, washed with diethyl ether (20 mL) and subsequently dried under vacuum to afford product rhenium bromide dipyrido [3,2-a:2',3'-c] phenazine tricarbonyl ($[Re(CO)_3(dppz)Br]$) as a dark yellow solid (270 mg, 86%).

^1H NMR (270 MHz, $CDCl_3$); δ 9.85 (dd, 2H), 9.46 (dd, 2H), 8.44 (dd, 2H), 8.05 (dd, 2H), 8.01 (t, 2H); (CH_3CN sol), ν(CO): 2024, 1924, 1901 cm^{-1} ; m/z – 654.93 $[C_{21}H_{10}N_4O_3ReBr]^+$ Na

Synthesis of rhenium dipyrido [3,2-a:2',3'-c] phenazine tricarbonyl dimethylamino pyridine tetrafluoroborate: [Re(dppz)(CO)$_3$(DMAP)][BF$_4$]

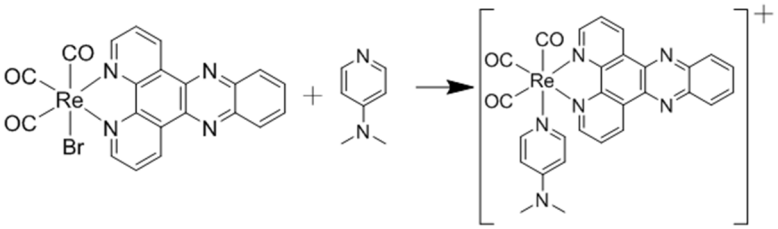

$[Re(CO)_3Br(dppz)]$ (90 mg, 0.14mmol) in dimethylformamide (20 mL) was purged under argon (15 mins) then heated (50 ^oC). $AgBF_4$ (82 mg, 0.42 mmol) was added to the reaction mixture. After 10 mins, a solution of 4-(dimethylamino)-pyridine (324 mg, 2.80 mmol) in DMF (3 mL). The reaction mixture was heated (80 ^oC) under an inert atmosphere in the absence of light (6 hrs). The resulting solution was cooled (0 ^oC) over 30 mins and then the very fine silver bromide precipitate was removed by filtration. The filtrate was dried under vacuum to yield a yellow-brown crude product solid. The crude product was purified by column chromatography on silica with CH_3CN/CH_2Cl_2 (1:5 v/v) to yield the final product rhenium dipyrido [3,2-a:2',3'-c] phenazine 4-dimethylamino pyridine tricarbonyl tetrafluoroborate ($[Re(CO)_3(dppz)(DMAP)]BF_4$) as a fine bright yellow solid (83 mg, 67%).

^{1}H NMR (270 MHz, $CDCl_3$); δ 9.97 (d, 2H, J = 5.4 Hz), 9.56 (m, 2H), 8.46 (dd, 2H, J = 5.4, 2.7 Hz), 8.30 (t, 2H, J = 8.1 Hz), 8.07 (dd, 2H, J = 5.4, 2.7 Hz), 7.75 (d, 2H, J = 2.7 Hz), 6.36 (d, 2H, J = 2.7 Hz), 2.86 (s, 6H). (CH_3CN sol), ν(CO): 2032, 1926 cm^{-1} ; m/z – 675.11 $[C_{28}H_{20}N_6O_3Re]^+$; Calculated; C (44%), H (2.6%), N (11%); Found; C (42.7%), H (2.6%), N (9.4%).

Synthesis of rhenium dipyrido [3,2-a:2',3'-c] phenazine tricarbonyl 4-dimethylamino pyridine tetrakis(3,5bis-(perfluorohexyl)phenyl)borate: [Re(dppz)(CO)$_3$(DMAP)][BAr^{f6}]

Anion manipulation was carried out as per literature.[188]

$[Re(CO)_3(dppz)(DMAP)][BF_4]$ (1 mg, 0.0015 mmol) in CH_3CN (1 ml) and a solution BAr^{f6} (4.2 mg, 0.0015 mmol) in PFMCH (1 ml) were mixed to form a biphasic layer. Upon mixing of the two layers, a colour change was observed indicating an ion exchange. The product obtained from the PFMCH layer and dried under vacuum to give yellow oil

rhenium dipyrido[3,2-a:2',3'-c] phenazine 4-dimethylamino pyridine tricarbonyl tetrakis (3,5 bis(perfluorohexyl)phenyl) borate, [Re(dppz)(CO)$_3$(DMAP)][BAr^{f6}]. The crude product was then dissolved again in PFMCH to ensure no residual CH_3CN present. [Re(CO)3(dppz)(DMAP)][BAr^{f6}]; (PFMCH sol), ν(CO): 2039, 1945, 1939 cm^{-1} .

2.3.2 [Re(CO)$_3$(bpy)(DMAP)][BARf^6]

The synthesis of rhenium 2,2'-bipyridine tricarbonyl 4-dimethylamino pyridine tetrakis (3,5 bis(perfluorohexyl)phenyl) borate, [Re(bpy)(CO)$_3$(DMAP][BARf^6], is detailed in the four steps below.

Synthesis of rhenium 2,2'-bipyridine bromide tricarbonyl

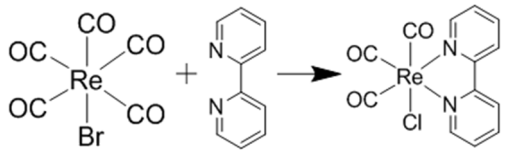

2,2'-bipyridine (75 mg, 0.48 mmol) and rhenium pentacarbonyl bromide (209 mg, 0.51 mmol) were added to toluene (4 mL) and the solution refluxed under an inert atmosphere in the absence of light (2hrs). The yellow solid product [Re(bpy)(CO)$_3$Cl] (255 mg, 99 %) was obtained by suction filtration.

^{1}H NMR (270 MHz, $CDCl_3$); δ 9.10 (d, 2H), 8.22 (d, 2H), 8.11 (t, 2H), 7.45 (t, 2H). (CH_3CN sol), ν(CO): 2022, 1918, 1901 cm^{-1}; m/z – 528.91 $[C_{13}H_8N_2O_3ReBr]^+$ Na

Synthesis of rhenium 2,2'-bipyridine tricarbonyl acetonitrile tetrafluoroborate

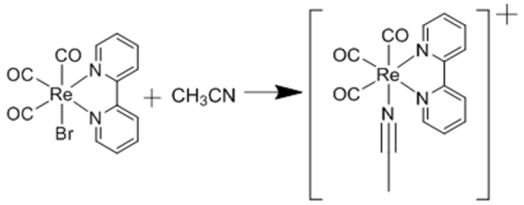

[Re(bpy)(CO)$_3$Br] (207 mg, 0.41 mmol) and silver tetrafluoroborate ($AgBF_4$) (77 mg, 0.40 mmol) were added together in CH_3CN (45 mL). The mixture was sealed under an argon atmosphere and heated to sub-reflux (75 ^{o}C) in the absence of light (8 hrs). The solution was cooled (0 ^{o}C), filtered through celite and evaporated to dryness. The crude

product was redissolved in CH_3CN and diethyl ether added to precipitate out the product $[Re(bpy)(CO)_3(CH_3CN)][BF_4]$ as a yellow solid (144.5 mg, 65 %).

^1H NMR (270 MHz, $CDCl_3$); δ 8.94 (d, 2H), 8.56 (d, 2H), 8.25 (t, 2H), 7.65 (t, 2H). (CH_3CN sol), ν(CO): 2040, 1937; m/z – 468.03 $[C_{15}H_{11}N_3O_3Re]^+$ Na

Synthesis of rhenium 2,2'-bipyridine tricarbonyl 4-dimethylamino pyridine tetrafluoroborate

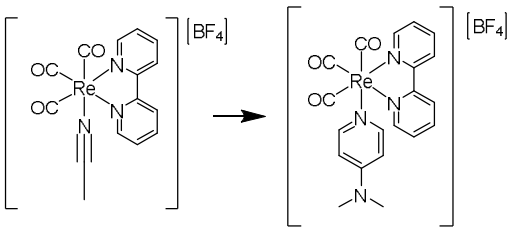

4-dimethylamino pyridine (928 mg, 7.6 mmol) was added to a solution of $[Re(bpy)(CO)_3(CH_3CN)][BF_4]$ (120 mg, 0.22 mmol) in tetrahydrofuran (THF) (7 mL). The mixture was heated to sub-reflux (60 ^oC) under an inert atmosphere in the absence of light (16 hrs). The solution was allowed to cool (0 °C) and dried under vacuum to yield the crude product. The crude product was dissolved in CH_3CN and the pure product $[Re(bpy)(CO)_3(DMAP)][BF_4]$ (82 mg, 68 %) precipitated out through the addition of diethyl ether.

^1H NMR (270 MHz, $CDCl_3$); δ 9.05 (d, 2H, J = 5.52 Hz), 8.82 (d, 2H, J = 8.18 Hz), 8.35 (t, 2H, J = 10.8, 5.4), 7.69 (t, 2H, J = 8.1, 2.7), 7.49 (d, 2H, J = 7.14 Hz), 2.01 (s, 6H). (CH_3CN sol), ν(CO): 2030, 1924; m/z – 549.09 $[C_{15}H_{11}N_3O_3Re]^+$ Na. Calculated C (37.7 %), H (2.8 %), N (8.8 %); Found; C (36.7 %), H (2.7 %), N (8.1 %).

Synthesis of rhenium 2,2'-bipyridine tricarbonyl 4-dimethylamino pyridine Tetrakis (3,5 bis(perfluorohexyl)phenyl) borate

Anion exchange was carried out as per literature methods.[188]

A yellow solution of $[Re(bpy)(CO)_3(DMAP)][BF_4]$ (1 mg, 0.0015 mmol) in CH_3CN (1 mL) was added to a colourless solution of $BARf^6$ (4.2 mg, 0.0015 mmol) in perfluromethylcyclohexane (PFMCH) and a biphasic layer formed. The two layers were

mixed and a colour change observed indicating ion exchange had occurred. The yellow crude product obtained from the PFMCH layer was dried under vacuum. The crude product was then redissolved in PFMCH to ensure no residual CH_3CN present. The final product $[Re(bpy)(CO)_3(DMAP)][BARf^6]$ was obtained as a yellow solid (*ca.* 3 mg, 59 %) (PFMCH, sol), ν(CO) 2039, 1945, 1939 cm^{-1}.

3 Experimental Techniques

3.1 Time Resolved Infra-Red Spectroscopy

All ultra-fast TRIR experiments were performed on the apparatus at Nottingham in collaboration with Dr. Xue-Zhong Sun using a 1 KHz laser excited at 400 nm and at the STFC Rutherford Appleton Laboratory with a 10Khz laser excited at 400 nm.

For both TRIR apparatus the sample is continually flowed through the cell throughout the experiment to prevent degradation effects. Furthermore, for both picosecond and nanosecond TRIR experiments, the change in absorbance (ΔAbs) is measured by determining the ratio between the pump-on and pump-off IR intensity using a chopper (500 Hz) to block consecutive pump pulses.

3.1.1 TRIR Spectroscopy at University of Nottingham

The experimental set-up at Nottingham is discussed in detailed in literature and only a brief outline is given below.[324]

For ultrafast TRIR experiments, a Ti:sapphire oscillator (MaiTai, Spectra Physics®) and a regenerative amplifier system (Spitfire Pro, Spectra Physics®) are used to produce laser pulses at 800 nm (2.3 mJ, 1 kHz, 140 fs). This laser pulse is split into two beams, a pump and a probe beam. The pump pulse of 400 nm is produced by harmonic generation (TimePlate Tripler, Minioptic Technology Inc.). The probe beam is produced by a TOPAS-C optical parametric amplifier (Light Conversion Ltd.) and a difference frequency generator to produce tuneable mid-IR pulses (180 cm^{-1} fwhm, *ca.* 2 μJ at

2000 cm^{-1}). A germanium beam splitter is used to separate this probe beam with 50 % of the beam used as a reference and going to a MCT detector (Kolmar Technology Inc.), the other 50 % of the beam is directed towards the sample. The pump beam is optically delayed on a translational stage (LMA, Actuator), which allows for delays of up to *ca.* 2 ns.

Following transmittance through the sample the probe beam is dispersed, by an IR monochoromator (250 mm, DK240, Spectra Products Inc) with 150 L/mm gratings resulting in a resolution of *ca.* 4 cm^{-1}, onto an MLCT detector array (Infrared Associates) with 128 elements (1 mm high, 0.25 mm wide). The electronic signal is amplified with a 144-channel amplifier (Infrared Associates Inc.) and digitised by a 16-bit analogue-digital converter (IR0144, Infrared Systems Development Corp).

For nanosecond experiments a Q-switched Nd:YVO laser (1064 nm, 600 ps, Advanced Optical Technology Ltd.) is frequency trebled to produce a 355 nm pump beam. Delay of this pump pulse is controlled by a pulse generator (DG535, Stanford Research Systems Inc.) allowing delays of 0.5 to 100000 ns. This pump pulse is synchronised to the probe pulse from the regenerative amplifier. The diameter of the pump beam (*ca.* 500 μm) is greater than the IR probe beam (*ca.* 200 μm) to ensure uniform spatial excitation of the sample.

3.1.2 TRIR Spectroscopy at the Rutherford Appleton Laboratory

The experimental set-up at the Rutherford Appleton Laboratory is discussed in detailed in literature and only a brief outline is given below.[325, 326]

A Ti:sapphire laser amplifier (Thales Laser Ltd.) produced 800 nm laser pulses (0.8 mJ, 10 kHz, 50 fs pulse width). The 800 nm pulses are split into a pump and probe beam. The pump beam (diameter *ca.* 150 μm) is generated at 400 nm by harmonic generation and the probe beam (diameter *ca.* 80 μm) is sent through an optical parametric amplifier (Light Conversion Ltd.) and the tuneable mid-IR beam achieved from a difference frequency generator.

A small amount of the probe beam is dispersed onto a 64 element MCT detector array (Infrared Associates Inc.) to prove a reference beam with the rest of the probe beam is sent to the sample. The probe beam transmitted through the sample is dispersed onto two linear 128 element MCT detector arrays (Infrared Associates Inc.).

Time resolved multiple probe spectroscopy (TR^MPS) was performed for all experiments conducted at the Rutherford Appleton Laboratory. The probe laser has a higher repetition rate than the pump laser and as such two laser amplifiers were employed operating at 1 kHz at the pump and 10 kHz at the probe. The two pulses were synchronised using a common 65 MHz oscillator and this allows for a pump and multiple probe data recording scheme.

3.1.3 TRIR Sample Prep

All of the samples for TRIR experiments conducted within this Thesis were prepared with solvents dried over CaH_2 and stored under an argon atmosphere. Concentrations of the compounds were typically in the range 10^{-3}-10^{-4} M, with both UV/Vis and IR absorbance less than 1 at the pump and probe wavelengths. An infrared solution cell (Harrick Scientific Products Inc.) with CaF_2 windows (25 x 2 mm, Crystran Ltd.) were used with a typical path length of 390 μm. A peristaltic pump and Teflon tubing was used to circulate the sample during the experiment to minimise local heating and sample degradation.

Measurements for Re(dppp2), Re(dppp3) and Re(dppp2Br) in the fingerprint IR region were conducted using a Harrick cell without circulation, owing to the concentration of sample required.

3.1.4 TRIR Experiments

Chapter 2

TRIR for complexes [Re(dppz-NPh_2)] were collected at the University of Nottingham in collaboration with Dr. Xue-Zhong Sun, with photoexcitation λ of 355 nm for both ps and ns.

Chapter 3

TRIR for complexes [Re(dppp2)$(CO)_3$Cl], [Re(dppp3)$(CO)_3$Cl], [Re(dppp2Br)$(CO)_3$Cl] and [Re(dpppN$_2$-$(NH_2)_2$)$(CO)_3$Cl] were collected at Rutherford Appleton Laboratory in collaboration with Dr Raphael Horvath and David Tiemenssen, and supervised by members of staff at the facility.

TRIR spectra of [Re(dppz-I)$(CO)_3$Cl] were collected at the University of Nottingham in collaboration with Dr Xue-Zhong Sun.

Chapter 4

TRIR for complexes [Re(dppz-12-NO_2)$(CO)_3$Cl] and [Re(dppz-13-NO_2)$(CO)_3$Cl] were collected at the University of Nottingham in collaboration with Dr Xue-Zhong Sun and Elizabeth Hampson.

Chapter 5

The TRIR data for the complexes [Re(dppz)$(CO)_3$DMAP][BAr^{f6}] and [Re(bpy)$(CO)_3$DMAP][BAr^{f6}] were collected at Rutherford Appleton Laboratory by Dr Raphael Horvath and supervised by members of staff at the facility.

3.1.5 TRIR Analysis

Data processing for all experiments was performed with the use of custom software designed by M. R. Pollard and G. M. Greetham. The difference spectra obtained from TRIR measurements is acquired as a change in absorbance (ΔAbs) as a function of pixel number of the detector arrays. Therefore calibration of the spectra is required and performed using a standard compounds and confirmed with parent bleaches.

3.2 Luminescence Spectroscopy

All excitation and emission spectra were recorded on an Edinburgh Instruments FLS920 combined fluorescence lifetime and steady state spectrometer. A xenon arc lamp was used as the excitation source for all steady state excitation and emission spectra. All conventional liquid measurements were conducted in a 1 x 1 x 1 cm quartz fluorescence cuvette, where degassed samples were obtained using three freeze pump thaw cycles on a Schlenk line. Solutions never exceeded an Abs = 0.3 at the excitation wavelength to minimise inner filter effects. All high-pressure measurements were taken with the use of a specifically designed high pressure Nottingham Cubic Cell discussed previously.

The sample is irradiated by a tuneable source of radiation *via.* a xenon arc lamp and monochromator and the excitation light is absorbed. The emitted light is then collected at a perpendicular angle to the excitation source to minimise the amount of detected scattered light, where the wavelengths of interest are obtained *via* the stepwise use of a monochromator (emission monochromator). A monochromator is used to disperse polychromatic light *i.e.* the white light from the xenon arc lamp source, into various wavelength utilising a diffraction grating.[8] The spectra are corrected for the wavelength response of the emission monochromator and photomultiplier using internal Edinburgh Instrument FLS900 correction files, additionally the excitation intensity is normalised by correcting the spectral output of the lamp and the wavelength dependent throughput of the excitation monochromator.

3.3 UV/Visible Absorption Spectroscopy

All UV/Vis absorption spectra were taken with a Perkin Elmer Lambda 5 spectrophotometer with 1 nm data spacing. Liquid samples were measured in a 1cm path length and high pressure samples were measured in the Nottingham Cubic Cell, with path length of 1 cm. All solutions exhibited an absorbance of between 0.10 and 0.30 at the excitation wavelength

3.4 Fourier Transform Infra-Red Spectroscopy

All Fourier Transform Infra-Red (FTIR) measurements were made using a Thermo Nicolet 6700 nexus FTIR spectrometer at 2 cm^{-1} resolution with a MTC/A detector and 32 or 64 scan rate. All measurements were conducted in an IR solution cells (Harrick Corp.) with calcium fluoride (CaF_2) windows (25 x 2 mm, Crystran) with a path length of *ca.* 0.39 mm unless otherwise stated.

3.5 Mass Spectrometry

All mass spectra were recorded by the Mass Spectrometry Service at the University of Nottingham. Positive ion electrospray mass spectra were recorded using an automated Micromass LCT spectrometer based on a Bruker MicroTOF (time of flight) mass spectrometer using ElectroSpray Ionisation (ESI), in either ethanol or acetonitrile (chromatography grade >99%) at 293 K.

3.6 Electrochemistry

All electrochemistry measurements were performed in collaboration with Dr E. S. Davies at the University of Nottingham.

Cyclic voltammetry measurements were conducted on 1mM degassed solutions in CH_2Cl_2 with 0.4 M supporting electrolytes [$^nBu_4N$][BF_4]. Measurements were made using an Autolab PGSTAT20 potentiostat and recorded using a glassy carbon working electrode, Pt wire secondary electrode and a saturated calomel reference electrode at 293 K. The potentials for all measurements were reported against the Fc^+/Fc couple used as an internal standard

A controlled potential electrode cell was used for spectroelectrochemistry measurements consisting of a Pt gauze basket working electrode which is separated by a glass frit, from a Pt gauze secondary electrode. The working electrode containing compartment was filled with test solution and stirred rapidly during electrolysis. The secondary

electrode compartment contained a solution of solvent and electrolyte. A reference electrode, saturated calomel, was bridged to the test solution through a vycor frit orientated at the centre of the working electrode.

For Chapter 2 the electrochemical potentials for complexes Re(dppz-NPh_2), Re(dppz-$(PhNPh_2)_2$), Re(dppz-Ph_2NPh_2), Re(dppz-Ph_3NPh_2), Re(dppz-$(C_4H_3S)NPh_2$), Re(dppz-$(Ph\text{-}(OCH_3)_2)NPh_2$) and Re(dppz-$(N_3C_3H)PhNPh_2$) were provided by Christopher Larsen, Keith Gordon Group, Department of Chemistry, University of Otago.

3.7 Band fitting

Where the assignment of MLCT(phen) and MLCT(phz) has been made with the help of band fitting, Gaussian band fitting has been performed using OriginPro 9.0 software. Several time delays were fitted to ensure correct assignment.

3.8 DFT Calculations

Optimisation and frequency calculations were conducted in the Gaussian 03 Revision-D.01 suite of programs,[327] with the B3LYP functional.[328, 329] For all atoms apart from Re, a 6-31G* basis set was used, where LANL2DZ was implemented for Re.

Optimised geometries and MO energies calculated in the gas phase for complexes [Re(dppz)$(CO)_3Cl$], [Re(dppp2)$(CO)_3Cl$], [Re(dppp3)$(CO)_3Cl$], [Re(dppp2Br)$(CO)_3Cl$], [Re(dppz-I)$(CO)_3Cl$], [Re(dpppN$_2(NH_2)_2$)$(CO)_3Cl$], [Re(dppz-12-NO_2)$(CO)_3Cl$], [Re(dppz-13-NO_2)$(CO)_3Cl$], [Re(dppz)$(CO)_3$(DMAP)] and [Re(bpy)$(CO)_3$(DMAP)].

TD-DFT for complexes [Re(dppz-12-NO_2)$(CO)_3Cl$] and [Re(dppz-13-NO_2)$(CO)_3Cl$] calculated in gas phase and in an SCRF toluene.

DFT calculations for complexes [Re(dppz-NPh_2)$(CO)_3Cl$], [Re(dppz-$PhNPh_2$)$(CO)_3Cl$], [Re(dppz-Ph-$(OCH_3)_2NPh_2$)$(CO)_3Cl$] and [Re(dppz-$(PhNPh_2)_2(CO)_3Cl$] were performed by Georgina Shillito, Keith Gordon Group, Department of Chemistry,

University of Otago. Calculations for these complexes were completed using Gaussian 09, B3LYP 6-31G(D) and LANL2DZ for Re in an SCRF.

4 Method Development of High Pressure Luminescence Spectroscopic Measurements of Fluids confined in Porous Templates

4.1 Anthracene and MCM-41 control experiment

Four samples of anthracene in MCM-41 were made. For the first sample, appropriate amounts of anthracene were grounded into a fine powder and mixed with MCM-41. The resultant mixture was subsequently grounded together again. The second sample was made in a similar way to the first sample, with the presence of minimal dichloromethane (*ca.* 0.1 mL). The third sample was made by the addition of MCM-41 to anthracene in the presence of dichloromethane with constant agitation (24 hrs). The solvent was then allowed to evaporate and the fluorescence studies conducted on the dry sample. The fourth and final sample was made in a similar way to the third sample only MCM-41 was dried in the oven (*ca.* 24 hrs) to remove any moisture present first.

The design of the Nottingham Cubic Cell is discussed in Chapter 6, primarily it comprises of a stainless steel body with four quartz windows sealed with Teflon seals. Two of four series heating cartridges are also present. The rig consists of a 5k-pressure transducer for monitoring the pressure inside the system and two thermocouples: one for the regulation of the heating cartridges and one for monitoring the temperature inside the cell. The cell is suitable for pressures up to 5000 psi although work within this report only requires pressures up to 2500 psi. The cell has a measured internal volume of 3.64 x 10^{-6} m^3.

4.2 High Pressure Bulk Luminescence Spectroscopic Measurements

Standard Operating Procedure for the Nottingham Cubic Cell for in Porous Measurements

1. The pressure transducers and thermocouple are connected to the appropriate output device to show the pressure and temperature. The pressure should read 0 psi at both transducers, and the temperature as room temperature. Throughout use both pressure transducers should read the same pressure, a difference indicates a blockage and measurments should be stopped and the system checked. The two heating cartridges are inserted into opposite corners of the cell and secured using appropriate fixings. The thermostat is set to the desired temperature.

2. Once the cell is at temperature, the system is vacuumed and CO_2 is introduced *via* the ISCO pump (35 ^{o}C, 1500 psi). An emission spectrum recorded to ensure the cell is clean and suitable for use.

3. The tap to the ISCO pump is subsequently closed and the system vented through the second tap attached directly to the pressure transducer and cell, on the alternate side to the pumps. Following complete removal of the CO_2, the windows of the cell are removed using the appropriate tool.

4. The glass holder is filled with the porous material *e.g.* MCM-41, and secured inside the cell. The chosen probe dye *e.g.* anthracene is added to the cell body. The windows are subsequently resealed to the cell and the cell is evacuated. CO_2 is added (35 ^{o}C, 1500 psi) again *via* the ISCO pump. The cell is left at the set pressure and temperature for *ca.* 30 mins. The tap to the ISCO pump is sealed and the CO_2 evacuated. The windows are subsequently removed and the glass holder containing the porous material is carefully removed. The cell is then cleaned as per the process detail in Chapter 8.

6. Step 2 is repeated without the glass holder present to ensure there is no residual dye in the cell body. Repetition of the cell cleaning process and step 2 is carried out until the cell is clean and suitable for use.

7. CO_2 is again introduced via the ISCO pump. An absorption spectrum is taken to ensure an absorption of 0.1-0.3 to minimise inner filter effects.

8. The ISCO pump is used to increase the pressure incrementally and emission spectrum recorded at each pressure.

9. Following the final pressure measurement, the tap to the ISCO pump is closed and the cell evacuated. The thermostat is turned off and the temperature of the cell is monitored until room temperature is reached. The cell is then cleaned following the cleaning procedure detailed in Chapter 8.

4.2.1 Bulk supercritical fluid Measurements

Steps 1-3 of the Standard Operating Procedure are followed. Subsequently, a solution of a known concentration of dye in a volatile solvent, most commonly hexane, is introduced into the cell and the solvent evaporated off resulting in a small known quantity of dye in the cell. The windows are then installed the cell is evacuated (35 ^{o}C, 1hr) to remove any impurities such as oxygen or moisture, which may quench the excited state. Subsequently steps 7-9 of the Standard Operating Procedure are followed.

4.2.2 Measurements within Porous Material

Below is detailed the method development steps for conducting high pressure luminescent spectroscopic measurements on fluids confined within porous materials.

Silica filled cell

Steps 1-3 are followed of the Standard Operating Procedure. Subsequently, all four quartz windows are screwed into place and a known concentration of dye in hexane is added to give an absorbance of 0.1 – 0.3. The solvent is then evaporated off leaving a known amount of dye in the cell. The cell is then evacuated (1hr, 35 ^{o}C). Subsequently upon removal of one window, the cell body is filled with silica and the window is screwed back in place. Steps 7-9 of the Standard Operating Procedure are then followed.

Silica disc

Steps 1-3 are followed of the Standard Operating Procedure. Subsequently, 250 mg of silica is placed in a high pressure disc press (9 tonnes) (hydraulic polymer press, Specac), producing a disc of thickness 0.1 – 0.25 mm and diameter 13 mm.

For impregnation of a silica disc, 250 mg of silica was added to anthracene (2 mg, 1.1 x 10^{-5} mol) and stirred in 10 ml of dichloromethane (24 hr). The solid was then obtained by filtration and dried (60 ^{o}C, 48 hr). The silica disc was then obtained *via* the method stated above. The impregnation process above was repeated with the use of 10 ml of tetrahydrofuran instead of dichloromethane and a disc made as stated previously. The disc was subsequently placed inside the sample compartments and the windows sealed. Steps 7-9 of the standard operating procedure where then followed.

Silica on window

Steps 1-3 of the Standard Operating Procedure were followed. Subsequently, Silica (5.1 mg) was added to methanol and stirred (24 hrs). The suspension of silica in methanol was then added drop-wise onto the window. The solvent was then evaporated from the suspension to result in an immobilised silica layer on the window. The above process was also repeated for the dye impregnated silica. Anthracene (2 mg, 1.1 x 10^{-5} mol) was added to 5 ml of methanol and stirred (24 hr) and then added drop-wise to the window. The sample was dried under argon and in an oven, following literature methods. [300, 301]

The windows with the immobilised silica layer were screwed into the cell body and steps 7-9 of the standard operating procedure were followed.

Silica in a glass holder

Glass holders with a cut off at *ca*. 300 nm or lower were a range of diameter and sizes were made from 1.80 mm to 4.79mm. The glass holder is secured into place in the middle of the cell. Three methods of filling the tube were tested. Firstly the cell was filled with silica and the dye of interested added to the cell body. The cell was then heated and pressurised to result in scCO_2. The second method impregnated the dye first using organic solvents. In the final method CO_2 was used to impregnate the silica.

The whole process using the final method is detailed in the Standard Operating Procedure.

Cell Cleaning

The cell is separated into its component parts and the cell body and windows are separately cleaned with a suitable solvent, most commonly acetone and isopropyl alcohol. The cell is then washed multiple times with water and left to dry (50 ^{o}C, 24 hrs). The cell and system is then fitted together and purged with CO_2

References

1. J. W. Verhoeven, *Pure Appl. Chem.*, 2009, **68**, 2223-2286.
2. R. G. W. Norrish and G. Porter, *Discuss. Faraday Soc.*, 1954, 40-46.
3. R. G. W. Norrish and G. Porter, *Nature*, 1949, **164**, 658-658.
4. J. R. Schoonover, G. F. Grills, R. B. Dyer, W. D. Bates, P. Chen and T. J. Meyer, *Inorg. Chem.*, 1996, **35**, 273-274.
5. P. O. Stoutland, R. B. Dyer and W. H. Woodruff, *Science*, 1992, **257**, 1913-1917.
6. N. Chattopadhyay, M. Barroso, C. Serpa, S. M. Isilda, L. G. Arnaut and S. J. Formosinho, *Chem. Phys. Lett.*, 2004, **387**, 263-266.
7. J. F. Brennecke, D. L. Tomasko, J. Peshkin and C. A. Eckert, *Ind. Eng. Chem. Res.*, 1990, **29**, 1682-1690.
8. J. R. Lakowicz, *Principles of Fluorescence Spectroscopy*, 2 edn., Kluwer Academic/Plenum Publishers, New York, 1999.
9. M. Maroncelli and G. R. Fleming, *J. Chem. Phys.*, 1987, **86**, 6221-6239.
10. M. Maroncelli, J. Macinnis and G. R. Fleming, *Science*, 1989, **243**, 1674-1681.
11. E. Akesson, G. C. Walker and P. F. Barbara, *J. Chem. Phys.*, 1991, **95**, 4188-4194.
12. A. E. Friedman, J. C. Chambron, J. P. Sauvage, N. J. Turro and J. K. Barton, *J. Am. Chem. Soc.*, 1990, **112**, 4960-4962.
13. E. J. C. Olson, D. Hu, A. Hormann, A. M. Jonkman, M. R. Arkin, E. D. A. Stemp, J. K. Barton and P. F. Barbara, *J. Am. Chem. Soc.*, 1997, **119**, 11458-11467.
14. C. Turro, S. H. Bossmann, Y. Jenkins, J. K. Barton and N. J. Turro, *J. Am. Chem. Soc.*, 1995, **117**, 9026-9032.
15. R. B. Nair, B. M. Cullum and C. J. Murphy, *Inorg. Chem.*, 1997, **36**, 962-965.
16. S. Ardo and G. J. Meyer, *Chem. Soc. Rev.*, 2009, **38**, 115-164.
17. J. F. Yin, M. Velayudham, D. Bhattacharya, H. C. Lin and K. L. Lu, *Coord. Chem. Rev.*, 2012, **256**, 3008-3035.
18. N. J. Lundin, A. G. Blackman, K. C. Gordon and D. L. Officer, *Angew. Chem. Int. Ed.*, 2006, **45**, 2582-2584.
19. K. K. W. Lo, K. Y. Zhang and S. P. Y. Li, *Eur. J. Inorg. Chem.*, 2011, 3551-3568.
20. K. K. W. Lo, W. K. Hui, C. K. Chung, K. H. K. Tsang, T. K. M. Lee, C. K. Li, J. S. Y. Lau and D. C. M. Ng, *Coord. Chem. Rev.*, 2006, **250**, 1724-1736.
21. Q. A. Zhao, F. Y. Li and C. H. Huang, *Chem. Soc. Rev.*, 2010, **39**, 3007-3030.
22. E. Amouyal, A. Homsi, J. C. Chambron and J. P. Sauvage, *J. Chem. Soc., Dalton Trans.*, 1990, 1841-1845.
23. W. Kaim, *J. Am. Chem. Soc.*, 1982, **104**, 3833-3837.
24. J. Fees, W. Kaim, M. Moscherosch, W. Matheis, J. Klima, M. Krejcik and S. Zalis, *Inorg. Chem.*, 1993, **32**, 166-174.
25. J. Fees, M. Ketterle, A. Klein, J. Fiedler and W. Kaim, *J. Chem. Soc., Dalton Trans.*, 1999, 2595-2599.
26. C. G. Coates, J. Olofsson, M. Coletti, J. J. McGarvey, B. Onfelt, P. Lincoln, B. Norden, E. Tuite, P. Matousek and A. W. Parker, *J. Phys. Chem. B*, 2001, **105**, 12653-12664.

27. B. Onfelt, P. Lincoln, B. Norden, J. S. Baskin and A. H. Zewail, *Proc. Natl. Acad. Sci. U. S. A.*, 2000, **97**, 5708-5713.
28. M. R. Waterland, K. C. Gordon, J. J. McGarvey and P. M. Jayaweera, *J. Chem. Soc., Dalton Trans.*, 1998, 609-616.
29. M. K. Brennaman, J. H. Alstrum-Acevedo, C. N. Fleming, P. Jang, T. J. Meyer and J. M. Papanikolas, *J. Am. Chem. Soc.*, 2002, **124**, 15094-15098.
30. M. K. Brennaman, T. J. Meyer and J. M. Papanikolas, *J. Phys. Chem. A*, 2004, **108**, 9938-9944.
31. Y. Sun, D. A. Lutterman and C. Turro, *Inorg. Chem.*, 2008, **47**, 6427-6434.
32. M. K. Kuimova, W. Z. Alsindi, A. J. Blake, E. S. Davies, D. J. Lampus, P. Matousek, J. McMaster, A. W. Parker, M. Towrie, X. Jhong Sun, C. Wilson and M. W. George, *Inorg. Chem.*, 2008, **47**, 9857-9869.
33. M. K. Kuimova, D. C. Grills, P. Matousek, A. W. Parker, X. Z. Sun, M. Towrie and M. W. George, *Vib. Spectrosc.*, 2004, **35**, 219-223.
34. H. van der Salm, M. G. Fraser, R. Horvath, S. A. Cameron, J. E. Barnsley, X. Z. Sun, M. W. George and K. C. Gordon, *Inorg. Chem.*, 2014, **53**, 3126-3140.
35. M. K. Kuimova, W. Z. Alsindi, J. Dyer, D. C. Grills, O. S. Jina, P. Matousek, A. W. Parker, P. Portius, X. Z. Sun, M. Towrie, C. Wilson, J. X. Yang and M. W. George, *Dalton Trans.*, 2003, 3996-4006.
36. J. Dyer, C. M. Creely, J. C. Penedo, D. C. Grills, S. Hudson, P. Matousek, A. W. Parker, M. Towrie, J. M. Kelly and M. W. George, *Photochem. Photobiol. Sci.*, 2007, **6**, 741-748.
37. Q. Cao, C. M. Creely, E. S. Davies, J. Dyer, T. L. Easun, D. C. Grills, D. A. McGovern, J. McMaster, J. Pitchford, J. A. Smith, X.-Z. Sun, J. M. Kelly and M. W. George, *Photochem. Photobiol. Sci.*, 2011, **10**, 1355-1364.
38. J. Dyer, W. J. Blau, C. G. Coates, C. M. Creely, J. D. Gavey, M. W. George, D. C. Grills, S. Hudson, J. M. Kelly, P. Matousek, J. J. McGarvey, J. McMaster, A. W. Parker, M. Towrie and J. A. Weinstein, *Photochem. Photobiol. Sci.*, 2003, **2**, 542-554.
39. M. K. Kuimova, X. Zhong Sun, M. Towrie, C. Wilson, J. Yang and M. W. George, *Dalton Trans.*, 2007, **6**, 1158-1163.
40. C. B. Larsen, H. van der Salm, C. A. Clark, A. B. S. Elliott, M. G. Fraser, R. Horvath, N. T. Lucas, X.-Z. Sun, M. W. George and K. C. Gordon, *Inorg. Chem.*, 2014, **53**, 1339-1354.
41. D. M. Dattelbaum, K. M. Omberg, P. J. Hay, N. L. Gebhart, R. L. Martin, J. R. Schoonover and T. J. Meyer, *J. Phys. Chem. A*, 2004, **108**, 3527-3536.
42. R. Lopez, B. Loeb, D. Striplin, M. Devenney, K. Omberg and T. J. Meyer, *J. Chil. Chem. Soc.*, 2004, **49**, 149-155.
43. A. Cannizzo, A. M. Blanco-Rodriguez, A. El Nahhas, J. Sebera, S. Zalis, A. Vlcek and M. Chergui, *J. Am. Chem. Soc.*, 2008, **130**, 8967-8974.
44. J. R. Schoonover, W. D. Bates and T. J. Meyer, *Inorg. Chem.*, 1995, **34**, 6421-&.
45. J. J. Turner, M. W. George, F. P. A. Johnson and J. R. Westwell, *Coord. Chem. Rev.*, 1993, **125**, 101-114.
46. E. D. Olmon, P. A. Sontz, A. M. Blanco-Rodriguez, M. Towrie, I. P. Clark, A. Vlcek, Jr. and J. K. Barton, *J. Am. Chem. Soc.*, 2011, **133**, 13718-13730.
47. J. A. Smith, M. W. George and J. M. Kelly, *Coord. Chem. Rev.*, 2011, **255**, 2666-2675.

48. J. M. Butler, M. W. George, J. R. Schoonover, D. M. Dattelbaum and T. J. Meyer, *Coord. Chem. Rev.*, 2007, **251**, 492-514.
49. R. Horvath, G. S. Huff, K. C. Gordon and M. W. George, *Coord. Chem. Rev.*, 2016, **325**, 41-58.
50. K. M. Omberg, J. R. Schoonover, S. Bernhard, J. A. Moss, J. A. Treadway, E. M. Kober, R. B. Dyer and T. J. Meyer, *Inorg. Chem.*, 1998, **37**, 3505-3508.
51. K. M. Omberg, J. R. Schoonover, J. A. Treadway, R. M. Leasure, R. B. Dyer and T. J. Meyer, *J. Am. Chem. Soc.*, 1997, **119**, 7013-7018.
52. M. K. Kuimova, X. Z. Sun, P. Matousek, D. C. Grills, A. W. Parker, M. Towrie and M. W. George, *Photochem. Photobiol. Sci.*, 2007, **6**, 1158-1163.
53. J. Dyer, D. C. Grills, P. Matousek, A. W. Parker, M. Towrie, J. A. Weinstein and M. W. George, *Chem. Commun.*, 2002, 872-873.
54. J. Olofsson, L. M. Wilhelmsson and P. Lincoln, *J. Am. Chem. Soc.*, 2004, **126**, 15458-15465.
55. R. M. Hartshorn and J. K. Barton, *J. Am. Chem. Soc.*, 1992, **114**, 5919-5925.
56. N. Komatsuzaki, R. Katoh, Y. Himeda, H. Sugihara, H. Arakawa and K. Kasuga, *J. Chem. Soc., Dalton Trans.*, 2000, 3053-3054.
57. V. W. W. Yam, K. K. W. Lo, K. K. Cheung and R. Y. C. Kong, *J. Chem. Soc., Chem. Commun.*, 1995, 1191-1193.
58. G. P. Moss, P. A. S. Smith and D. Tavernier, *P.A.C.*, 1995, **67**, 1307.
59. P. Muller, *P.A.C.*, 1994, **66**, 1077-1184.
60. A. D. Joran, B. A. Leland, G. G. Geller, J. J. Hopfield and P. B. Dervan, *J. Am. Chem. Soc.*, 1984, **106**, 6090-6092.
61. B. Albinsson, M. P. Eng, K. Pettersson and M. U. Winters, *Phys. Chem. Chem. Phys.*, 2007, **9**, 5847-5864.
62. S. B. Nielsen, M. B. Nielsen and A. Rubio, *Acc. Chem. Res.*, 2014, **47**, 1417-1425.
63. Y. A. Berlin, F. C. Grozema, L. D. A. Siebbeles and M. A. Ratner, *J. Phys. Chem. C*, 2008, **112**, 10988-11000.
64. R. A. Keller and L. J. Dolby, *J. Am. Chem. Soc.*, 1969, **91**, 1293-1299.
65. L. T. Calcaterra, G. L. Closs and J. R. Miller, *J. Am. Chem. Soc.*, 1983, **105**, 670-671.
66. G. L. Closs, L. T. Calcaterra, N. J. Green, K. W. Penfield and J. R. Miller, *J. Phys. Chem.*, 1986, **90**, 3673-3683.
67. J. Kroon, A. M. Oliver, M. N. Paddonrow and J. W. Verhoeven, *J. Am. Chem. Soc.*, 1990, **112**, 4868-4873.
68. J. R. Miller, L. T. Calcaterra and G. L. Closs, *J. Am. Chem. Soc.*, 1984, **106**, 3047-3049.
69. T. A. Moore, D. Gust, P. Mathis, J. C. Mialocq, C. Chachaty, R. V. Bensasson, E. J. Land, D. Doizi, P. A. Liddell, W. R. Lehman, G. A. Nemeth and A. L. Moore, *Nature*, 1984, **307**, 630-632.
70. B. S. Brunschwig, S. Ehrenson and N. Sutin, *J. Am. Chem. Soc.*, 1984, **106**, 6858-6859.
71. H. McConnell, *J. Chem. Phys.*, 1961, **35**, 508.
72. J. Halpern and L. E. Orgel, *Discuss. Faraday Soc.*, 1960, 32-41.
73. P. W. Anderson, *Phys. Rev.*, 1959, **115**, 2-13.
74. S. Namuangruk, R. Fukuda, M. Ehara, J. Meeprasert, T. Khanasa, S. Morada, T. Kaewin, S. Jungsuttiwong, T. Sudyoadsuk and V. Promarak, *J. Phys. Chem. C*, 2012, **116**, 25653-25663.

75. I. Fujita, J. Fajer, C. K. Chang, C. B. Wang, M. A. Bergkamp and T. L. Netzel, *J. Phys. Chem.*, 1982, **86**, 3754-3759.
76. M. Velusamy, K. R. J. Thomas, J. T. Lin, Y. C. Hsu and K. C. Ho, *Org. Lett.*, 2005, **7**, 1899-1902.
77. S. Jungsuttiwong, T. Yakhanthip, Y. Surakhot, J. Khunchalee, T. Sudyoadsuk, V. Promarak, N. Kungwan and S. Namuangruk, *J. Comput. Chem.*, 2012, **33**, 1517-1523.
78. C. G. Wu, M. F. Chung, H. H. G. Tsai, C. J. Tan, S. C. Chen, C. H. Chang and T. W. Shih, *ChemPhysChem*, 2012, **77**, 832-843.
79. H. Choi, M. Shin, K. Song, M. S. Kang, Y. Kang and J. Ko, *J. Mater. Chem. A*, 2014, **2**, 12931-12939.
80. A. Baheti, P. Tyagi, K. R. J. Thomas, Y. C. Hsu and J. T. Lin, *J. Phys. Chem. C*, 2009, **113**, 8541-8547.
81. C. G. Wu, W. T. Shieh, C. S. Yang, C. J. Tan, C. H. Chang, S. C. Chen, C. Y. Wu and H. H. G. Tsai, *Dyes Pigm.*, 2013, **99**, 1091-1100.
82. R. K. Chen, X. C. Yang, H. N. Tian, X. N. Wang, A. Hagfeldt and L. C. Sun, *Chem. Mater.*, 2007, **19**, 4007-4015.
83. S. Chaurasia, Y. C. Chen, H. H. Chou, Y. S. Wen and J. T. Lin, *Tetrahedron*, 2012, **68**, 7755-7762.
84. C. J. Tan, C. S. Yang, Y. C. Sheng, H. W. Amini and H. H. G. Tsai, *J. Phys. Chem. C*, 2016, **120**, 21272-21284.
85. H. D. Stoeffler, N. B. Thornton, S. L. Temkin and K. S. Schanze, *J. Am. Chem. Soc.*, 1995, **117**, 7119-7128.
86. L. Sacksteder, A. P. Zipp, E. A. Brown, J. Streich, J. N. Demas and B. A. Degraff, *Inorg. Chem.*, 1990, **29**, 4335-4340.
87. S. Manoharan and A. Sambandam, *Dyes Pigm.*, 2014, **105**, 223-231.
88. X. Zhang, X. P. Gan, S. Yao, W. J. Zhu, J. H. Yu, Z. C. Wu, H. P. Zhou, Y. P. Tian and J. Y. Wu, *RSC Adv.*, 2016, **6**, 60022-60028.
89. T. Yasuda, Y. Shinohara, Y. Kusagaki, T. Matsuda, L. Han and T. Ishi-I, *Polymer*, 2015, **58**, 139-145.
90. A. L. Tang, L. J. Li, Z. H. Lu, J. H. Huang, H. Jia, C. L. Zhan, Z. A. Tan, Y. F. Li and J. N. Yao, *J. Mater. Chem. A*, 2013, **1**, 5747-5757.
91. F. P. A. Johnson, M. W. George, F. Hartl and J. J. Turner, *Organometallics*, 1996, **15**, 3374-3387.
92. M. K. Kuimova, W. Z. Alsindi, A. J. Blake, E. S. Davies, D. J. Lampus, P. Matousek, J. McMaster, A. W. Parker, M. Towrie, X. Z. Sun, C. Wilson and M. W. George, *Inorg. Chem.*, 2008, **47**, 9857-9869.
93. D. E. Morris, K. W. Hanck and M. K. Dearmond, *J. Am. Chem. Soc.*, 1983, **105**, 3032-3038.
94. D. Collison, F. E. Mabbs, E. J. L. McInnes, K. J. Taylor, A. J. Welch and L. J. Yellowlees, *J. Chem. Soc., Dalton Trans.*, 1996, 329-334.
95. A. M. Blanco-Rodriguez, H. Kvapilova, J. Sykora, M. Towrie, C. Nervi, G. Volpi, S. Zalis and A. Vlcek, *J. Am. Chem. Soc.*, 2014, **136**, 5963-5973.
96. J. M. Kelly, C. M. Creely, M. M. Feeney, S. Hudson, W. J. Blau, B. Elias, A. Kirsch-De Mesmaeker, P. Matousek, M. Towrie and A. W. Parker, in *Rutherford Appleton*

Laboratory Central Laser Facility Annual Report 2011/2012, Rutherford Appleton Laboratory Central Laser Facility, 2002, pp. 111-114.
97. M. W. George and J. J. Turner, *Coord. Chem. Rev.*, 1998, **177**, 201-217.
98. A. C. Bhasikuttan, M. Suzuki, S. Nakashima and T. Okada, *J. Am. Chem. Soc.*, 2002, **124**, 8398-8405.
99. C. Kvarnstrom, A. Petr, P. Damlin, T. Lindfors, A. Ivaska and L. Dunsch, *J. Solid State Electrochem.*, 2002, **6**, 505-512.
100. J. Bae, B. Chae, H. Seo, Y. M. Jung and S. W. Lee, *J. Mol. Struct.*, 2014, **1069**, 200-204.
101. F. A. Black, C. A. Clark, G. H. Summers, I. P. Clark, M. Towrie, T. Penfold, M. W. George and E. A. Gibson, *Phys. Chem. Chem. Phys.*, 2017, **19**, 7877-7885.
102. J. Hawecker, J. M. Lehn and R. Ziessel, *Helv. Chim. Acta*, 1986, **69**, 1990-2012.
103. J. Hawecker, J. M. Lehn and R. Ziessel, *J. Chem. Soc., Chem. Commun.*, 1983, 536-538.
104. H. Hori, Y. Takano, K. Koike and Y. Sasaki, *Inorg. Chem. Commun.*, 2003, **6**, 300-303.
105. P. Christensen, A. Hamnett, A. V. G. Muir and J. A. Timney, *J. Chem. Soc., Dalton Trans.*, 1992, 1455-1463.
106. K. Kalyanasundaram, *J. Chem. Soc., Faraday Trans.*, 1986, **82**, 2401-2415.
107. A. I. Breikss and H. D. Abruna, *J. Electroanal. Chem.*, 1986, **201**, 347-358.
108. M. D. Doherty, D. C. Grills and E. Fujita, *Inorg. Chem.*, 2009, **48**, 1796-1798.
109. K. Koike, H. Hori, M. Ishizuka, J. R. Westwell, K. Takeuchi, T. Ibusuki, K. Enjouji, H. Konno, K. Sakamoto and O. Ishitani, *Organometallics*, 1997, **16**, 5724-5729.
110. A. H. A. Tinnemans, T. P. M. Koster, D. Thewissen and A. Mackor, *Recl.: J. R. Neth. Chem. Soc.*, 1984, **103**, 288-295.
111. R. Maidan and I. Willner, *J. Am. Chem. Soc.*, 1986, **108**, 8100-8101.
112. E. Kimura, S. Wada, M. Shionoya and Y. Okazaki, *Inorg. Chem.*, 1994, **33**, 770-778.
113. H. Takeda, K. Koike, H. Inoue and O. Ishitani, *J. Am. Chem. Soc.*, 2008, **130**, 2023-2031.
114. H. Hori, F. P. A. Johnson, K. Koike, K. Takeuchi, T. Ibusuki and O. Ishitani, *J. Chem. Soc., Dalton Trans.*, 1997, 1019-1023.
115. H. Hori, K. Koike, K. Takeuchi and Y. Sasaki, *Chem. Lett.*, 2000, 522-523.
116. N. Kitamura and S. Tazuke, *Chem. Lett.*, 1983, 1109-1112.
117. J. M. Lehn and R. Ziessel, *Proc. Natl. Acad. Sci. U. S. A.*, 1982, **79**, 701-704.
118. R. Ziessel, J. Hawecker and J. M. Lehn, *Helv. Chim. Acta*, 1986, **69**, 1065-1084.
119. H. Ishida, K. Tanaka and T. Tanaka, *Chem. Lett.*, 1988, 339-342.
120. H. Ishida, T. Terada, K. Tanaka and T. Tanaka, *Inorg. Chem.*, 1990, **29**, 905-911.
121. H. Ishida, K. Tanaka and T. Tanaka, *Organometallics*, 1987, **6**, 181-186.
122. C. A. Craig, L. O. Spreer, J. W. Otvos and M. Calvin, *J. Phys. Chem.*, 1990, **94**, 7957-7960.
123. J. L. Grant, K. Goswami, L. O. Spreer, J. W. Otvos and M. Calvin, *J. Chem. Soc., Dalton Trans.*, 1987, 2105-2109.
124. I. Willner, R. Maidan, D. Mandler, H. Durr, G. Dorr and K. Zengerle, *J. Am. Chem. Soc.*, 1987, **109**, 6080-6086.
125. E. Kimura, X. H. Bu, M. Shionoya, S. J. Wada and S. Maruyama, *Inorg. Chem.*, 1992, **31**, 4542-4546.
126. B. Gholamkhass, H. Mametsuka, K. Koike, T. Tanabe, M. Furue and O. Ishitani, *Inorg. Chem.*, 2005, **44**, 2326-2336.

127. W. Leitner, *Angew. Chem. Int. Ed. (English)*, 1995, **34**, 2207-2221.
128. M. D. Doherty, D. C. Grills, J. T. Muckerman, D. E. Polyansky and E. Fujita, *Coord. Chem. Rev.*, 2010, **254**, 2472-2482.
129. H. A. Schwarz and R. W. Dodson, *J. Phys. Chem.*, 1989, **93**, 409-414.
130. B. Kumar, M. Llorente, J. Froehlich, T. Dang, A. Sathrum and C. P. Kubiak, *Annu. Rev. Phys. Chem.*, 2012, **63**.
131. E. E. Barton, D. M. Rampulla and A. B. Bocarsly, *J. Am. Chem. Soc.*, 2008, **130**, 6342-6344.
132. E. B. Cole, P. S. Lakkaraju, D. M. Rampulla, A. J. Morris, E. Abelev and A. B. Bocarsly, *J. Am. Chem. Soc.*, 2010, **132**, 11539-11551.
133. A. J. Morris, R. T. McGibbon and A. B. Bocarsly, *ChemSusChem*, 2011, **4**, 191-196.
134. G. Seshadri, C. Lin and A. B. Bocarsly, *J. Electroanal. Chem.*, 1994, **372**, 145-150.
135. D. J. Boston, C. D. Xu, D. W. Armstrong and F. M. MacDonnell, *J. Am. Chem. Soc.*, 2013, **135**, 16252-16255.
136. D. J. Boston, Y. M. F. Pachon, R. O. Lezna, N. R. de Tacconi and F. M. MacDonnell, *Inorg. Chem.*, 2014, **53**, 6544-6553.
137. K. Saravanan and J. A. Keith, *Dalton Trans.*, 2016, **45**, 15336-15341.
138. K. Y. Wong, W. H. Chung and C. P. Lau, *J. Electroanal. Chem.*, 1998, **453**, 161-169.
139. Y. J. Sun, Y. Liu and C. Turro, *J. Am. Chem. Soc.*, 2010, **132**, 5594-5595.
140. Y. J. Sun and C. Turro, *Inorg. Chem.*, 2010, **49**, 5025-5032.
141. V. W. W. Yam, V. W. M. Lee, F. Ke and K. W. M. Siu, *Inorg. Chem.*, 1997, **36**, 2124-2129.
142. B. Y. Wu, L. H. Gao, Z. M. Duan and K. Z. Wang, *J. Inorg. Biochem.*, 2005, **99**, 1685-1691.
143. X. Chen, F. Gao, W. Y. Yang, J. Sun, Z. X. Zhou and L. N. Ji, *Inorg. Chim. Acta*, 2011, **378**, 140-147.
144. S. Shi, H. L. Huang, X. Gao, J. L. Yao, C. Y. Lv, J. Zhao, W. L. Sun, T. M. Yao and L. N. Ji, *J. Inorg. Biochem.*, 2013, **121**, 19-27.
145. X. W. Liu, J. C. Chen, X. Hu, H. Li, K. C. Zheng and L. N. Ji, *Helv. Chim. Acta*, 2008, **91**, 1374-1388.
146. J. Li, Y. M. Sun, Z. Y. Zhu, H. Zhao and L. F. Tan, *J. Inorg. Biochem.*, 2016, **161**, 128-133.
147. S. R. Dalton, S. Glazier, B. Leung, S. Win, C. Megatulski and S. J. N. Burgmayer, *J. Biol. Inorg. Chem.*, 2008, **13**, 1133-1148.
148. B. L. Li, L. F. Tan and X. Q. Zou, *J. Iran. Chem. Soc.*, 2012, **9**, 357-366.
149. R. A. Hovermale and P. G. Sears, *J. Phys. Chem.*, 1956, **60**, 1579-1580.
150. R. W. Weast, *CRC Handbook of Chemistry and Physics*, The Chemical Rubber Co., Boca Raton, FL, 1972-1973.
151. U. V. Mardolcar, C. A. N. Decastro and F. J. V. Santos, *Fluid Phase Equilib.*, 1992, **79**, 255-264.
152. R. C. Weast, *Handbook of Chemistry and Physics* 53 edn., The Chemical Rubber Co, Cleveland, Ohio, 1972.
153. R. F. Dallinger and W. H. Woodruff, *J. Am. Chem. Soc.*, 1979, **101**, 4391-4393.
154. A. Basu, M. A. Weiner, T. C. Strekas and H. D. Gafney, *Inorg. Chem.*, 1982, **21**, 1085-1092.

155. M. Busby, A. Gabrielsson, P. Matousek, M. Towrie, A. J. Di Bilio, H. B. Gray and A. Vlcek, *Inorg. Chem.*, 2004, **43**, 4994-5002.
156. J. K. Hino, L. Dellaciana, W. J. Dressick and B. P. Sullivan, *Inorg. Chem.*, 1992, **31**, 1072-1080.
157. M. Wrighton and D. L. Morse, *J. Am. Chem. Soc.*, 1974, **96**, 998-1003.
158. A. Gabrielsson, P. Matousek, M. Towrie, F. Hartl, S. Zalis and A. Vlcek, *J. Phys. Chem. A*, 2005, **109**, 6147-6153.
159. J. E. Yarnell, J. C. Deaton, C. E. McCusker and F. N. Castellano, *Inorg. Chem.*, 2011, **50**, 7820-7830.
160. I. E. Pomestchenko, D. E. Polyansky and F. N. Castellano, *Inorg. Chem.*, 2005, **44**, 3412-3421.
161. F. Zhao, W. Q. Liu, H. Y. Xia and Y. B. Wang, *Comp. Theor. Chem.*, 2012, **997**, 49-54.
162. L. Sanhueza, M. Barrera and I. Crivelli, *Polyhedron*, 2013, **57**, 94-104.
163. R. Boese, D. Blaser, M. Nussbaumer and T. M. Krygowski, *Struct. Chem.*, 1992, **3**, 363-368.
164. J. Trotter, *Acta Crystallogr.*, 1959, **12**, 884-888.
165. E. J. L. McInnes, R. D. Farley, C. C. Rowlands, A. J. Welch, L. Rovatti and L. J. Yellowlees, *J. Chem. Soc., Dalton Trans.*, 1999, 4203-4208.
166. P. Murray, L. Jack, E. J. L. McInnes and L. J. Yellowlees, *Dalton Trans.*, 2010, **39**, 4179-4185.
167. S. Er, C. Suh, M. P. Marshak and A. Aspuru-Guzik, *Chem. Sci.*, 2015, **6**, 885-893.
168. A. Bueno, D. Lahem, C. Caucheteur and M. Debliquy, *Sensors*, 2015, **15**, 9870-9881.
169. M. A. Dobrowolski, T. M. Krygowski and M. K. Cyranski, *Croat. Chem. Acta*, 2009, **82**, 139-147.
170. H. Szatylowicz, O. A. Stasyuk, C. F. Guerra and T. M. Krygowski, *Crystals*, 2016, **6**.
171. C. Kutal, M. A. Weber, G. Ferraudi and D. Geiger, *Organometallics*, 1985, **4**, 2161-2166.
172. C. Kutal, A. J. Corbin and G. Ferraudi, *Organometallics*, 1987, **6**, 553-557.
173. P. N. Bartlett, D. C. Cook, M. W. George, J. Ke, W. Levason, G. Reid, W. T. Su and W. J. Zhang, *Phys. Chem. Chem. Phys.*, 2010, **12**, 492-501.
174. J. Jun and P. S. Fedkiw, *J. Electroanal. Chem.*, 2001, **515**, 113-122.
175. S. Chanfreau, P. Cognet, S. Camy and J. S. Condoret, *J. Electroanal. Chem.*, 2007, **604**, 33-40.
176. K. E. Toghill, P. Voyame, D. Momotenko, A. J. Olaya and H. H. Girault, *Phys. Chem. Chem. Phys.*, 2013, **15**, 972-978.
177. M. E. Philips, M. R. Deakin, M. V. Novotny and R. M. Wightman, *J. Phys. Chem.*, 1987, **91**, 3934-3936.
178. D. Niehaus, M. Philips, A. Michael and R. M. Wightman, *J. Phys. Chem.*, 1989, **93**, 6232-6236.
179. A. C. Michael and R. M. Wightman, *Anal. Chem.*, 1989, **61**, 270-272.
180. A. P. Abbott, T. A. Claxton, J. Fawcett and J. C. Harper, *J. Chem. Soc., Faraday Trans.*, 1996, **92**, 1747-1749.
181. A. P. Abbott and J. C. Harper, *Phys. Chem. Chem. Phys.*, 1999, **1**, 839-841.
182. W.-H. Lin, T.-F. M. Chang, Y.-H. Lu, T. Sato, M. Sone, K.-H. Wei and Y.-J. Hsu, *J. Phys. Chem. C*, 2013, **117**, 25596-25603.

183. T.-F. M. Chang, T. Shimizu, C. Ishiyama and M. Sone, *Thin Solid Films*, 2013, **529**, 25-28.
184. T.-F. M. Chang and M. Sone, *Surf. Coat. Technol.*, 2011, **205**, 3890-3899.
185. D. Cook, P. N. Bartlett, W. Zhang, W. Levason, G. Reid, J. Ke, W. Su, M. W. George, J. Wilson, D. Smith, K. Mallik, E. Barrett and P. Sazio, *Phys. Chem. Chem. Phys.*, 2010, **12**, 11744-11752.
186. A. P. Abbott, C. A. Eardley and J. E. Scheirer, *J. of Phys. Chem. B*, 1999, **103**, 8790-8793.
187. A. Abbott, *Chem. Soc. Rev.*, 1993, **22**, 435-440.
188. S. K. Ghosh, A. S. Ojeda, J. Guerrero-Leal, N. Bhuvanesh and J. A. Gladysz, *Inorg. Chem.*, 2013, **52**, 9369-9378.
189. B. Probst, M. Guttentag, A. Rodenberg, P. Hamm and R. Alberto, *Inorg. Chem.*, 2011, **50**, 3404-3412.
190. J. V. Caspar and T. J. Meyer, *J. Phys. Chem.*, 1983, **87**, 952-957.
191. Y. K. Yue, T. Grusenmeyer, Z. Ma, P. Zhang, T. T. Pham, J. T. Mague, J. P. Donahue, R. H. Schmehl, D. N. Beratan and I. V. Rubtsov, *J. Phys. Chem. B*, 2013, **117**, 15903-15916.
192. M. J. Li, C. C. Ko, G. P. Duan, N. Y. Zhu and V. W. W. Yam, *Organometallics*, 2007, **26**, 6091-6098.
193. T. P. Lin, C. Y. Chen, Y. S. Wen and S. S. Sun, *Inorganic Chemistry*, 2007, **46**, 9201-9212.
194. K. K. W. Lo, K. S. Sze, K. H. K. Tsang and N. Y. Zhu, *Organometallics*, 2007, **26**, 3440-3447.
195. M. Cattaneo, F. Fagalde, N. E. Katz, C. D. Borsarelli and T. Parella, *European Journal of Inorganic Chemistry*, 2007, 5323-5332.
196. M. W. George, F. P. A. Johnson, J. R. Westwell, P. M. Hodges and J. J. Turner, *J. Chem. Soc., Dalton Trans.*, 1993, 2977-2979.
197. P. Y. Chen and R. A. Palmer, *Appl. Spectrosc.*, 1997, **51**, 580-583.
198. S. Sato, Y. Matubara, K. Koike, M. Falkenstrom, T. Katayama, Y. Ishibashi, H. Miyasaka, S. Taniguchi, H. Chosrowjan, N. Mataga, N. Fukazawa, S. Koshihara, K. Onda and O. Ishitani, *Chem. Eur. J.*, 2012, **18**, 15722-15734.
199. G. J. Stor, F. Hartl, J. W. M. Vanoutersterp and D. J. Stufkens, *Organometallics*, 1995, **14**, 1115-1131.
200. A. El Nahhas, C. Consani, A. M. Blanco-Rodriguez, K. M. Lancaster, O. Braem, A. Cannizzo, M. Towrie, I. P. Clark, S. Zalis, M. Chergui and A. Vlcek, *Inorg. Chem.*, 2011, **50**, 2932-2943.
201. A. M. Blanco-Rodriguez, A. Vlcek, P. Matousek and M. Towrie, *Photophysics of [Re(NCS)(CO)$_3$(a-diimine) complexes: character of the lowest excited state*, Central Laser Facility, 2005.
202. T. R. Hayes, S. C. Bottorff, W. S. Slocumb, C. L. Barnes, A. E. Clark and P. D. Benny, *Dalton Trans.*, 2017, **46**, 1134.
203. J. J. Turner, C. M. Gordon and S. M. Howdle, *Journal of Physical Chemistry*, 1995, **99**, 17532-17538.
204. B. D. Rossenaar, D. J. Stufkens and A. Vlcek, *Inorg. Chem.*, 1996, **35**, 2902-2909.
205. K. A. Walters, Y. J. Kim and J. T. Hupp, *Inorg. Chem.*, 2002, **41**, 2909-2919.

206. L. Rodriguez, M. Ferrer, O. Rossell, F. J. S. Duarte, A. G. Santos and J. C. Lima, *J. Photochem. Photobiol., A*, 2009, **204**, 174-182.
207. L. Lerner, ed. A. N. Laboratory, Argonne National Laboratory, Argonne, IL, 2013, vol. 2015.
208. I. Ferain, C. A. Colinge and J. P. Colinge, *Nature*, 2011, **479**, 310-316.
209. K. L. Choy, *Prog. Mater. Sci.*, 2003, **48**, 57-170.
210. M. Cho, Y. Ban and D. Pan, Z., in *The International Conference on Computer Aided Design*, IEEE, University of L'Aquila Conference center San Basilio, 2008.
211. M. C. Moore, N. Kalyanasundaram, J. B. Freund and H. T. Johnson, *Nucl. Instru. Methods Phys. Res., Sect. B*, 2004, **225**, 241-255.
212. P. N. Bartlett, D. Cook, M. W. George, A. L. Hector, J. Ke, W. Levason, G. Reid, D. C. Smith and W. Zhang, *Phys. Chem. Chem. Phys.*, 2014.
213. J. R. Arthur, *Surf. Sci.*, 2002, **500**, 189-217.
214. J. Ke, P. N. Bartlett, D. Cook, T. L. Easun, M. W. George, W. Levason, G. Reid, D. Smith, W. Su and W. Zhang, *Phys. Chem. Chem. Phys.*, 2012, **14**, 1517-1528.
215. in *The Science of SCFED*, SCFED, vol. 2016.
216. P. N. Bartlett, M. Perdjon-Abel, D. Cook, G. Reid, W. Levason, F. Cheng, W. Zhang, M. W. George, J. Kie, R. Beanland and R. Sloan, *ChemElectroChem*, 2014, **1**, 187-195.
217. M. Okamoto, O. Wada, F. Tanaka and S. Hirayama, *J. Phys. Chem. A*, 2001, **105**, 566-572.
218. M. A. Kane, S. N. Daniel, E. D. Niemeyer and F. V. Bright, *New Trends in Fluorescence Spectroscopy*, 2001, **1**, 81-97.
219. K. M. Schlosky, *J. Chem. Educ.*, 1989, **66**, 989.
220. S. C. Tucker and W. Maddox, *J. Phys. Chem, B.*, 1998, **102**, 2437-2453.
221. A. Mazzoldi, D. Picard, P. G. Sriram and C. M. Oldenburg, *Greenhouse Gases: Sci. Technol.*, 2013, **3**, 309-310.
222. D. L. Goldfarb and H. R. Corti, *Electrochem. Commun.*, 2000, **2**, 663-670.
223. **W. Leitner**, *Acc. Chem. Res*, 2002, **35**, 746-756.
224. J. A. Hyatt, *J. Org. Chem*, 1984, **49**, 5097-5101.
225. G. Leeke, R. Santos, B. Al-Duri, J. Seville, C. Smith and A. B. Holmes, *J. Chem. Eng. Data*, 2005, **50**, 1370-1374.
226. A. P. Abbott and C. A. Eardley, *J. Phys. Chem. B*, 1998, **102**, 8574-8578.
227. Y. Arai, T. Sako and Y. Takebayashi, *Supercritical Fluids: Molecular Interactions, Physical Properties, and New Applications*, 1 edn., Springer, Verlag Berline Heidelber New York, 2002.
228. J. C. Giddings, M. N. Myers, L. McLauren and R. A. Keller, *Science*, 1968, **162**, 67-73.
229. F. G. Keyes and J. G. Kirkwood, *Phys. Rev.*, 1930, **36**, 754-761.
230. G. Brunner, *J. Food. Eng*, 2005, **67**, 21-33.
231. S. G. Kazarian, N. H. Brantley and C. A. C. A. Eckert, *Chemtech*, 1999, **29**, 36-41.
232. A. I. Cooper, *J. Mater. Chem*, 2000, **10**, 207-234.
233. S. D. Yeo and E. Kiran, *J. Supercrit. Fluids*, 2005, **34**, 287-308.
234. E. W. Hansen, C. Simon, R. Haugsrud, H. Raeder and R. Bredesen, *J. Phys. Chem. B*, 2002, **106**, 12396-12406.
235. F. Chen, C. L. Chen, S. W. Ding, Y. Yue, C. H. Ye and F. Deng, *Chem. Phys. Lett.*, 2004, **383**, 309-313.

236. G. Rother, Y. B. Melnichenko, D. R. Cole, H. Frielinghaus and G. D. Wignall, *J. Phys. Chem. C*, 2007, **111**, 15736-15742.
237. D. Liu, Y. Zhang, Y. Liu, J. Wu, C.-C. Chen, C.-Y. Mou and S.-H. Chen, *J. Phys. Chem. B*, 2008, **112**, 4309-4312.
238. M. S. Gruszkiewicz, G. Rother, D. J. Wesolowski, D. R. Cole and D. Wallacher, *Langmuir*, 2012, **28**, 5070-5078.
239. M. K. Kidder, P. F. Britt, Z. T. Zhang, S. Dai, E. W. Hagaman, A. L. Chaffee and A. C. Buchanan, *J. Am. Chem. Soc.*, 2005, **127**, 6353-6360.
240. A. Schreiber, I. Ketelsen and G. H. Findenegg, *Phys. Chem. Chem. Phys.*, 2001, **3**, 1185-1195.
241. P. Lopez-Aranguren, L. F. Vega, C. Domingo and E. H. Chimowitz, *AIChE J.*, 2012, **58**, 3597-3600.
242. M. Thommes and G. H. Findenegg, *Langmuir*, 1994, **10**, 4270-4277.
243. A. Love, 2014.
244. B. Coasne, S. K. Jain and K. E. Gubbins, *Mol. Phys.*, 2006, **104**, 3491-3499.
245. A. Striolo, K. E. Gubbins, M. S. Gruszkiewicz, D. R. Cole, J. M. Simonson and A. A. Chialvo, *Langmuir*, 2005, **21**, 9457-9467.
246. C. G. V. Burgess, D. H. Everett and S. Nuttall, *Pure Appl. Chem.*, 1989, **61**, 1845-1852.
247. A. Dekeizer, T. Michalski and G. H. Findenegg, *Pure Appl. Chem.*, 1991, **63**, 1495-1502.
248. W. D. Machin, *Langmuir*, 1994, **10**, 1235-1240.
249. A. P. Y. Wong and M. H. W. Chan, *Phys. Rev. Lett.*, 1990, **65**, 2567-2570.
250. A. P. Y. Wong, S. B. Kim, W. I. Goldburg and M. H. W. Chan, *Phys. Rev. Lett.*, 1993, **70**, 954-957.
251. P. López-Aranguren, L. F. Vega, C. Domingo and E. H. Chimowitz, *AIChE J.*, 2012, **58**, 3597-3600.
252. W. Eltringham and O. J. Catchpole, *J. Chem. Eng. Data*, 2007, **52**, 363-367.
253. W. Eltringham, S. J. Tallon, O. J. Catchpole and K. Fenton, *J. Chem. Eng. Data*, 2008, **53**, 826-829.
254. A. P. Abbott, E. G. Hope and D. J. Palmer, *Anal. Chem.*, 2005, **77**, 6702-6708.
255. A. P. Abbott, E. G. Hope and D. J. Palmer, *J. Phys. Chem. B*, 2007, **111**, 8114-8118.
256. F. F. Abraham and Y. Singh, *J. Chem. Phys.*, 1977, **67**, 2384-2393.
257. P. G. Gennes, *Rev. Mod. Phys.*, 1985, **57**, 827-863.
258. L. Gelb, R. Gubbins, R. Radhakrishnan and M. Sliwinska-Bartowiak, *Rep. Prog. Phys.*, 1999, **62**, 1573-1659.
259. P. D. Sanctis Lucentini and G. Pellicane, *Phys. Rev. Lett.*, 2008, **101**, 1-4.
260. S. Ciccariello, Y. B. Melnichenko and L. He, *J. Appl. Crystallogr.*, 2011, **44**, 43-51.
261. Y. B. Melnichenko, H. Mayam, H. Cheng and T. Blach, *Langmuir*, 2010, **26**, 6374-6379.
262. B. M. Smarsly, C. Goltner, M. Antonietto, W. Rulan and E. Hoinkis, *J. Phys. Chem, B.*, 2001, **105**, 831-840.
263. S. Jahnert, D. Muter, J. Prass, G. A. Zickler, O. Paris and G. H. Findenegg, *J. Phys. Chem. C*, 2009, **113**, 15201-15210.
264. S. A. Dyer, in *Wiley Survey of Instrumentation and Measurement*, John Wiley & Sons, 2004, p. 549.

265. D. Basabe-Desmonts, M. Reinhoudt and M. Crego-Calama, *Chem. Soc. Rev.*, 2007, **36**, 993-1017.
266. C. E. Bunker and Y. P. Sun, *J. Am. Chem. Soc.*, 1995, **117**, 10865-10870.
267. M. Barroso, N. Chattopadhyay, A. S. Klymchenko, A. P. Demchenko, L. G. Arnaut and S. J. Formosinho, *J. Phys. Chem. A*, 2006, **110**, 13419-13424.
268. M. Okamoto, H. Nagashima and F. Tanaka, *Phys. Chem. Chem. Phys.*, 2002, **4**, 5627-5633.
269. J. W. Zhang, D. P. Roek, J. E. Chateauneuf and J. F. Brennecke, *J. Am. Chem. Soc*, 1997, **119**, 9980-9991.
270. M. P. Heitz and M. Maroncelli, *J. Phys. Chem. A*, 1997, **101**, 5852-5868.
271. S. Nugent and B. M. Ladanyi, *J. Chem. Phys.*, 2004, **120**, 874-884.
272. Y. Ikushima, N. Saito and M. Arai, *J. Phys. Chem.*, 1992, **96**, 2293.
273. J. K. Rice, E. D. Niemeyer, R. A. Dunbar and F. V. Bright, *J. Am. Chem. Soc*, 1995, **117**, 5830-5839.
274. M. A. Kane, S. N. Daniel, E. D. Niemeyer and F. V. Bright, in *New Trends in Fluorescence Spectroscopy Springer Series on Fluorescence*, Springer Berlin HeidelBerg, 2001, vol. 1, pp. 81-97.
275. J. Zagrobelny, T. A. Betts and F. V. Bright, *J. Am. Chem. Soc*, 1992, **114**, 5249-5257.
276. J. F. Brennecke, D. L. Tomasko and C. A. Eckert, *J. Phys. Chem.*, 1990, **94**, 7692-7700.
277. J. K. Rice, E. D. Niemeyer and F. V. Bright, *Anal. Chem.*, 1995, **67**, 4354-4357.
278. S. W. Kim and K. P. Johnston, *AIChE J.*, 1987, **33**, 1603-1611.
279. C. R. Yonker and R. D. Smith, *J. Phys. Chem.*, 1988, **92**, 2374-2378.
280. S. L. Frye, C. R. Yonker, D. R. Kalkwarf and R. D. Smith, *Abstr. Pap. Am. Chem. Soc.*, 1985, **190**, 26.
281. C. R. Yonker, S. L. Frye, D. R. Kalkwarf and R. D. Smith, *J. Phys. Chem.*, 1986, **90**, 3022-3026.
282. H. B. Ma and Y. J. Ma, *J. Chem. Phys.*, 2012, **137**.
283. Y. P. Sun, M. A. Fox and K. P. Johnston, *J. Am. Chem. Soc*, 1992, **114**, 1187-1194.
284. R. Vangrieken and M. Debruin, *Pure Appl. Chem.*, 1994, **66**, 2513-2526.
285. Y. Marcus, *J. Phys. Org. Chem.*, 2005, **18**, 373-384.
286. P. W. Carr, *Microchem. J.*, 1993, **48**, 4-28.
287. M. J. Kamlet, J. L. M. Abboud, M. H. Abraham and R. W. Taft, *J. Org. Chem*, 1983, **48**, 2877-2887.
288. M. J. Kamlet, J. L. Abboud and R. W. Taft, *J. Am. Chem. Soc.*, 1977, **99**, 6027-6038.
289. M. Maiwald and G. M. Schneider, *Phys. Chem. Chem. Phys.*, 1998, **102**, 960-964.
290. M. L. Oneill, P. Kruus and R. C. Burk, *Can. J. Chem*, 1993, **71**, 1834-1840.
291. G. M. Schneider, *J. Supercrit. Fluids*, 1998, **13**, 5-14.
292. M. E. Sigman, S. M. Lindley and J. E. Leffler, *J. Am. Chem. Soc*, 1985, **107**, 1471-1472.
293. O. Kajimoto, M. Futakami, T. Kobayashi and K. Yamasaki, *J. Phys. Chem.*, 1988, **92**, 1347-1352.
294. M. Poliakoff, S. M. Howdle and S. G. Kazarian, *Angew. Chem. Int. Ed.*, 1995, **34**, 1275-1295.
295. X. Z. Sun, S. M. Nikiforov, J. X. Yang, C. S. Colley and M. W. George, *Appl. Spectrosc.*, 2002, **56**, 31-39.
296. M. Buback, *J. Mol. Struct.*, 1995, **347**, 113-129.

297. T. A. Rhodes and M. A. Fox, *J. Phys. Chem.*, 1996, **100**, 17931-17939.
298. C. B. Roberts, J. F. Brennecke and J. E. Chateauneuf, *AIChE J.*, 1995, **41**, 1306-1318.
299. J. F. Brennecke and C. A. Eckert, *ACS Sym. Ser.*, 1989, **406**, 14-26.
300. R. B. Fox, *Pure Appl. Chem.*, 1972, **30**, 87-104.
301. E. Z. M. Ebeid, S. E. Morsi, M. A. Elbayoumi and J. O. Williams, *J. Chem. Soc., Faraday Trans.*, 1978, **74**, 1457-1466.
302. S. Setzu, S. Letant, P. Solsona, R. Romestain and J. C. Vial, *J. Lumin.*, 1998, **80**, 129-132.
303. Q. G. Meng, P. Boutinaud, A.-C. Franville, H. J. Zhang and R. Mahiou, *Micropor. Mesopor. Mat.*, 2003, **65**, 127-136.
304. Y. I. Kiryukhin, Z. A. Sinitsyna and K. S. Bagdasaryan, *High Energy Chem.*, 1979, **13**, 432-437.
305. I. B. Berlman, H. O. Wirth and O. J. Steingraber, *J. Am. Chem. Soc.*, 1968, **90**, 4.
306. D. P. Roek, J. E. Chateauneuf and J. F. Brennecke, *Ind. Eng. Chem. Res*, 2000, **39**, 3090-3096.
307. Y. Yamini and N. Bahramifar, *J. Chem. Eng. Data*, 2000, **45**, 53-56.
308. E. W. Lemmon, M. O. McLinden and D. G. Friend, eds., *Thermophysical Properties of Fluid Systems*, National Institute of Standards and Technology, Gaithersburg MD, 20899, 2017.
309. K. Nygard, S. Sarman, K. Hyltegren, S. Chodankar, E. Perret, J. Buitenhuis, J. F. van der Veen and R. Kjellander, *Phys. Rev. X*, 2016, **6**.
310. M. J. Zwanenburg, J. H. H. Bongaerts, J. F. Peters, D. O. Riese and J. F. van der Veen, *Phys. Rev. Lett.*, 2000, **85**, 5154-5157.
311. E. Perret, K. Nygard, D. K. Satapathy, T. E. Balmer, O. Bunk, M. Heuberger and J. F. van der Veen, *Epl*, 2009, **88**.
312. G. Karlstrom, *Chem. Scr.*, 1985, **25**, 89-91.
313. A. P. Abbott, C. A. Eardley and R. Tooth, *J. Chem. Eng. Data*, 1999, **44**, 112-115.
314. Y. Higashi, *Int. J. Refrig.*, 1995, **17**, 524-531.
315. R. Stenutz, in *Tables for Chemistry*, Stockholm University, Stockholm.
316. H. H. Uhlig, J. G. Kirkwood and F. G. Keyes, *J. Chem. Phys.*, 1933, **1**, 155-159.
317. M. J. Kamlet, J. L. M. Abboud, M. H. Abraham and R. W. Taft, *J. Org. Chem.*, 1983, **48**, 2877-2887.
318. H. Oka and O. Kajimoto, *Phys. Chem. Chem. Phys.*, 2003, **5**, 2535-2540.
319. E. Vanderdonckt and G. Porter, *Trans. Faraday Soc.*, 1968, **64**, 3218-+.
320. H. H. Perkampus, in *The Basicity of Unsaturated Compounds*, ed. V. Gold, Academic Press, London and New York, London, 1966, vol. 4, p. 279.
321. M. J. Kamlet, P. W. Carr, R. W. Taft and M. H. Abraham, *J. Am. Chem. Soc.*, 1981, **103**, 6062-6066.
322. R. W. Taft, J. L. M. Abboud and M. J. Kamlet, *J. Am. Chem. Soc.*, 1981, **103**, 1080-1086.
323. M. J. Kamlet and R. W. Taft, *J. Am. Chem. Soc.*, 1976, **98**, 377-383.
324. M. A. H. Alamiry, N. M. Boyle, C. M. Brookes, M. W. George, C. Long, P. Portius, M. T. Pryce, K. L. Ronayne, X. Z. Sun, M. Towrie and K. Q. Vuong, *Organometallics*, 2009, **28**, 1461-1468.

325. G. M. Greetham, P. Burgos, Q. A. Cao, I. P. Clark, P. S. Codd, R. C. Farrow, M. W. George, M. Kogimtzis, P. Matousek, A. W. Parker, M. R. Pollard, D. A. Robinson, Z. J. Xin and M. Towrie, *Appl. Spectrosc.*, 2010, **64**, 1311-1319.
326. M. Towrie, D. C. Grills, J. Dyer, J. A. Weinstein, P. Matousek, R. Barton, P. D. Bailey, N. Subramaniam, W. M. Kwok, C. S. Ma, D. Phillips, A. W. Parker and M. W. George, *Appl. Spectrosc.*, 2003, **57**, 367-380.
327. M. J. Frisch, G. W. Trucks, H. B. Schlegel, G. E. Scuseria, M. A. Robb, J. R. Cheeseman, J. Montgomery, T. Vreven, K. N. Kudin, J. C. Burant, J. M. Millam, S. S. Iyengar, J. Tomasi, V. Barone, B. Mennucci, M. Cossi, G. Scalmani, N. Rega, G. A. Patersson, H. Nakatsuji, M. Hada, M. Ehara, K. Toyota, R. Fukuda, J. Hasegawa, M. Ishida, T. Nakajima, Y. Honda, O. Kitao, H. Nakai, M. Klene, X. Y. Li, J. E. Knox, H. P. Hratchian, J. B. Cross, V. Bakken, C. Adamo, J. Jaramillo, R. Gomperts, R. E. Stratmann, O. Yazyev, A. J. Austin, R. Cammi, C. Pomelli, J. W. Ochterski, P. Y. Ayala, K. Morokuma, G. A. Voth, P. Salvador, J. J. Dannenberg, V. G. Zakzewski, S. Dapprich, A. D. Daniel, M. C. Strain, O. Farkas, D. K. Malick, A. D. Rabuck, K. Raghavachari, J. B. Foresman, J. V. Ortiz, Q. Cui, A. G. Baboul, S. Clifford, J. Cioslowski, B. B. Stefanov, G. T. Liu, A. Liashenko, P. Piskorz, I. Komaromi, R. L. Martin, D. J. Fox, T. Keith, A. Al-Laham, C. Y. Peng, A. Nanayakkara, M. Challacombe, P. M. W. Gill, B. Johnson, W. Chen, W. Wong, C. Gonzalez and J. A. Pople, *Gaussian 03, Revision D.01*, (2004) Gaussian Inc., Wallingford, CT.
328. A. D. Becke, *J. Chem. Phys.*, 1993, **98**, 5648-5652.
329. J. A. Stephens and C. H. Greene, *J. Chem. Phys.*, 1994, **100**, 7135-7143.

Appendix A

A.1 Chapter 2

A.1.1 Spectroelectrochemistry FTIR

Below are the ground state and 1e$^-$ reduced state FTIR spectra

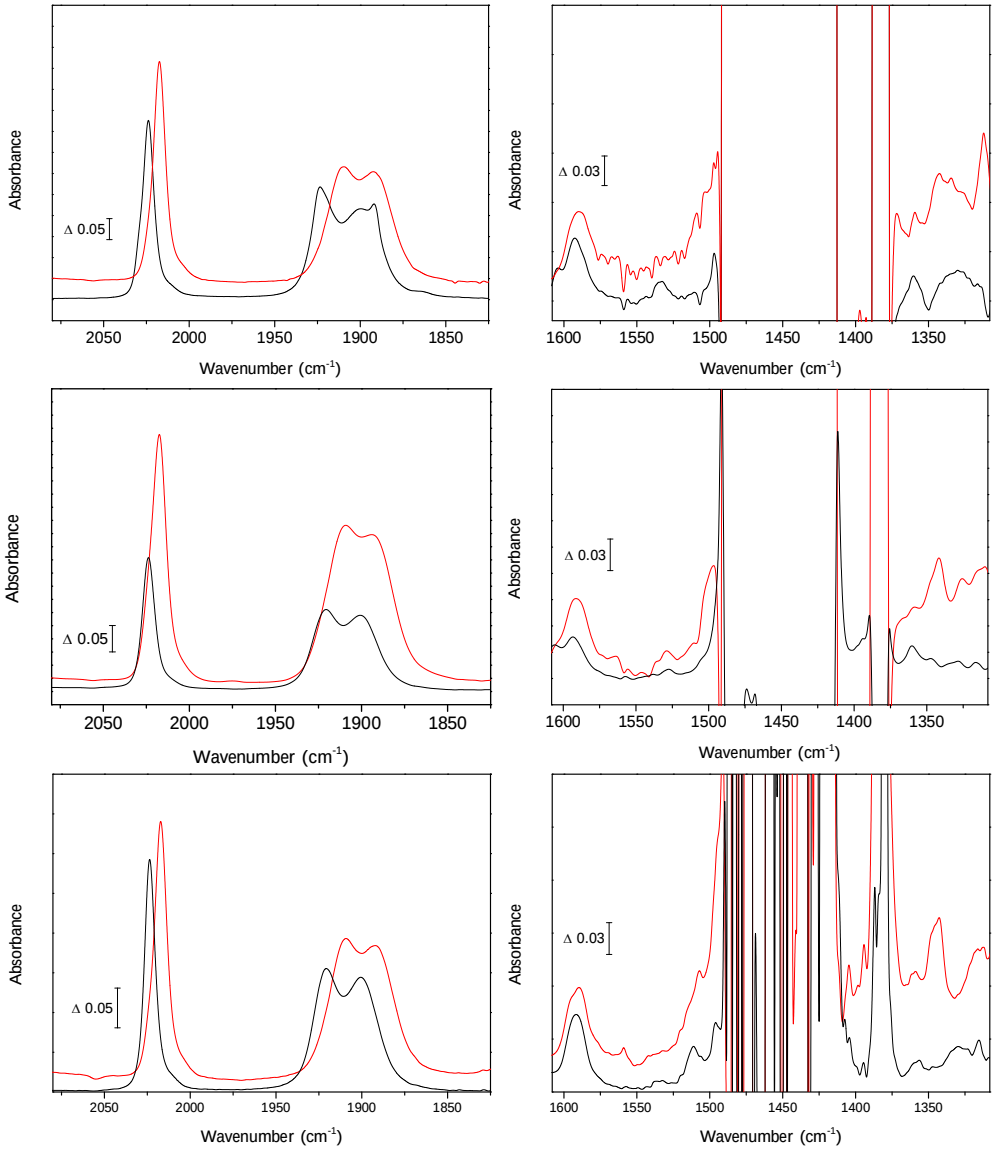

Figure A-1: Ground state (black) and 1e$^-$ reduced state (red) FTIR in CH_2Cl_2 in the ν(CO) (left) and ν(FP) (right) IR regions. For Re(dppz-(C_4H_3S)PhNPh_2) (top), Re(dppz-Ph_2NPh_2) (middle) and Re(dppz-(PhNPh_2)$_2$) (bottom).

A.2 Chapter 3

A.2.1 TRIR spectra collected for Re(dppp), Re(dppp3) and Re(dppp2Br)

The TRIR spectra of Re(dppp2), Re(dppp3) and Re(dppp2Br) are shown below in CH_3CN, CH_2Cl_2 and THF in the ν(CO) IR region, and ν(FP) IR region for CH_2Cl_2, following 400 nm photoexcitation. The kinetic traces for the processes observed are also detailed below, where the nature and kinetics of the excited states observed are discussed in detail in Chapter 3. The small shoulder at *ca.*1925 cm^{-1}, observed in the TRIR spectrum for Re(dppp2Br) in CH_3CN is an artefact of connecting the two spectral windows used to collect the TRIR data and is detailed in Chapter 8.

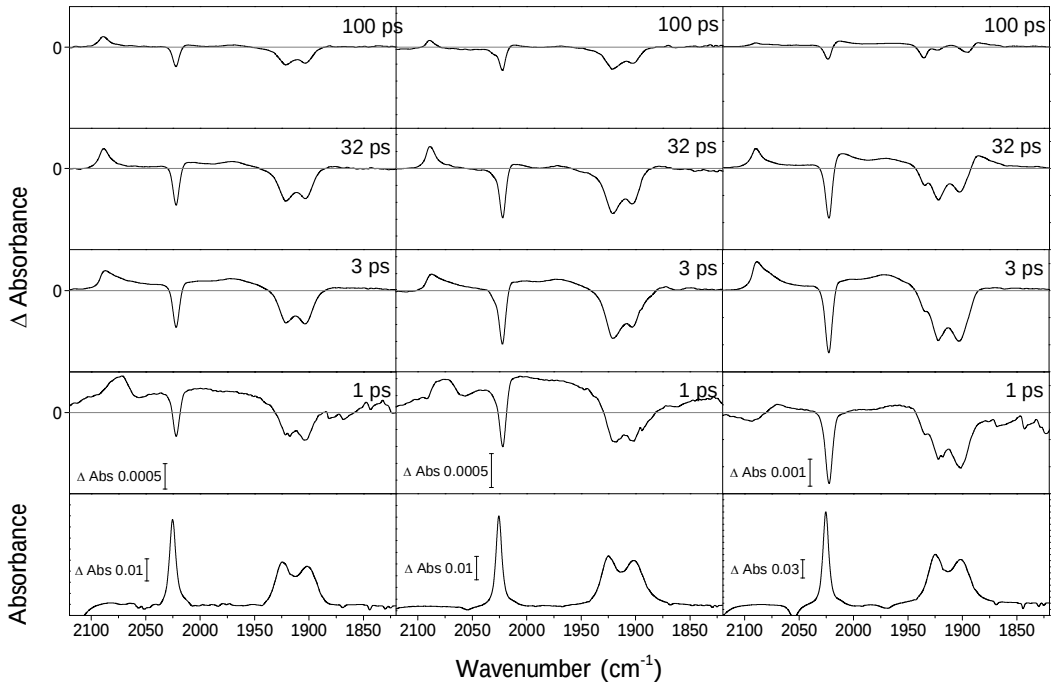

Figure A-2: The FTIR (a) and TRIR (b-e) spectra in the CO IR region in CH_3CN following 400 nm photoexcitation for Re(dppp2) (left), Re(dppp3) (middle) and Re(dpp2Br) (right). The FTIR shown was acquired in d-DMSO due to poor solubility.

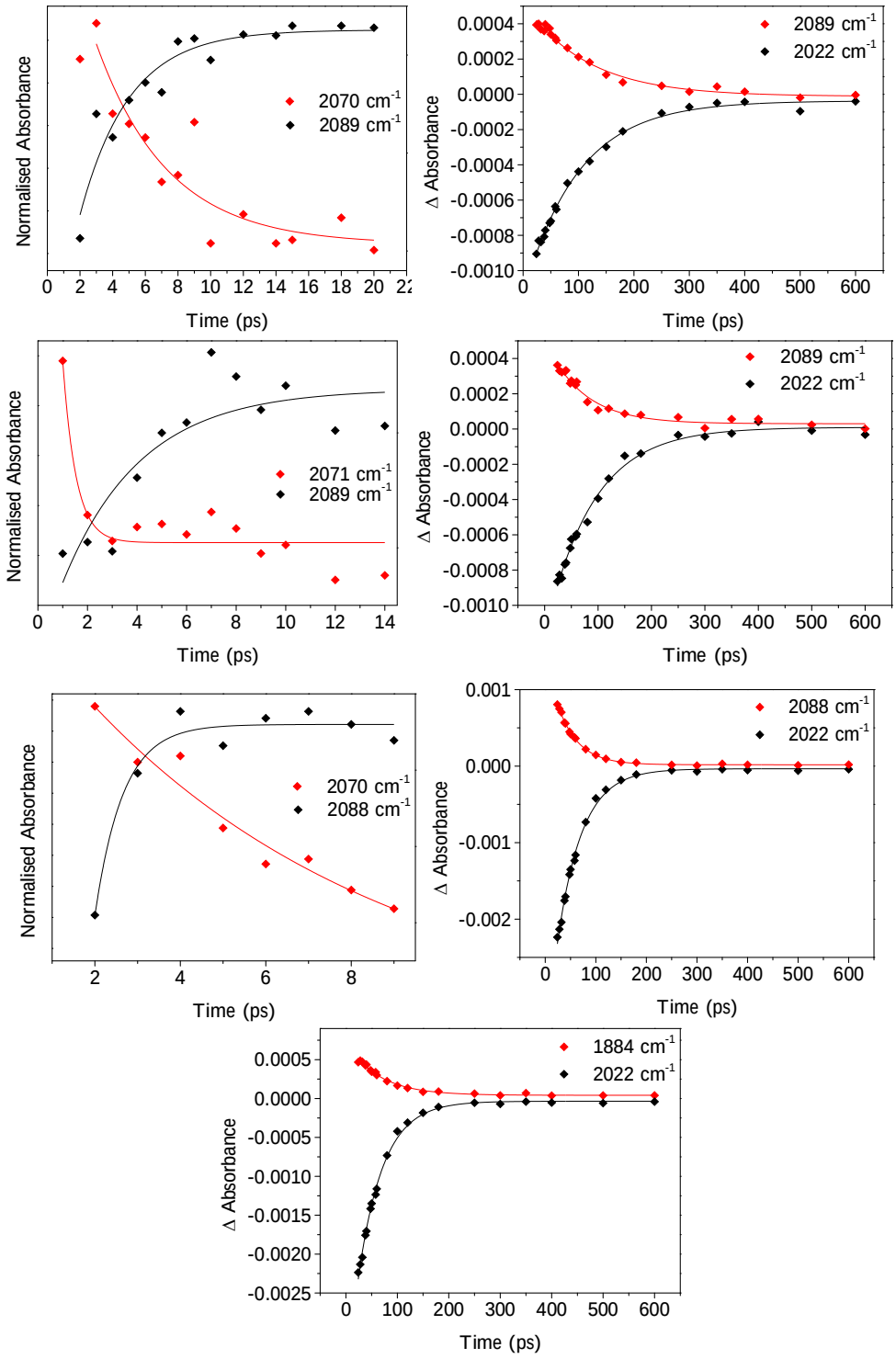

Figure A-3: The Kinetics of Re(dppp2) (first row), Re(dppp3) (second row) and Re(dppp2Br) (third and fourth row) in CH_3CN following photoexcitation at 400 nm. The decay of the band at *ca.* 2070 cm^{-1} assigned to a MLCT(phen) state, in good agreement with the growth of the band at 2089 cm^{-1} assigned to a ^{3}MLCT(phz) state. Subsequent decay of the band at 2089 cm^{-1} assigned to the ^{3}MLCT(phz) state in good agreement with the growth of the band at 2022 cm^{-1} assigned to the parent. Additionally for Re(dppp2Br), the initial growth followed by decay of the band at 1884 cm^{-1}, assigned to a ^{3}IL$\pi\pi^*$ state, where decay is in good agreement with the growth of the band at 2022 cm^{-1} assigned to the parent.

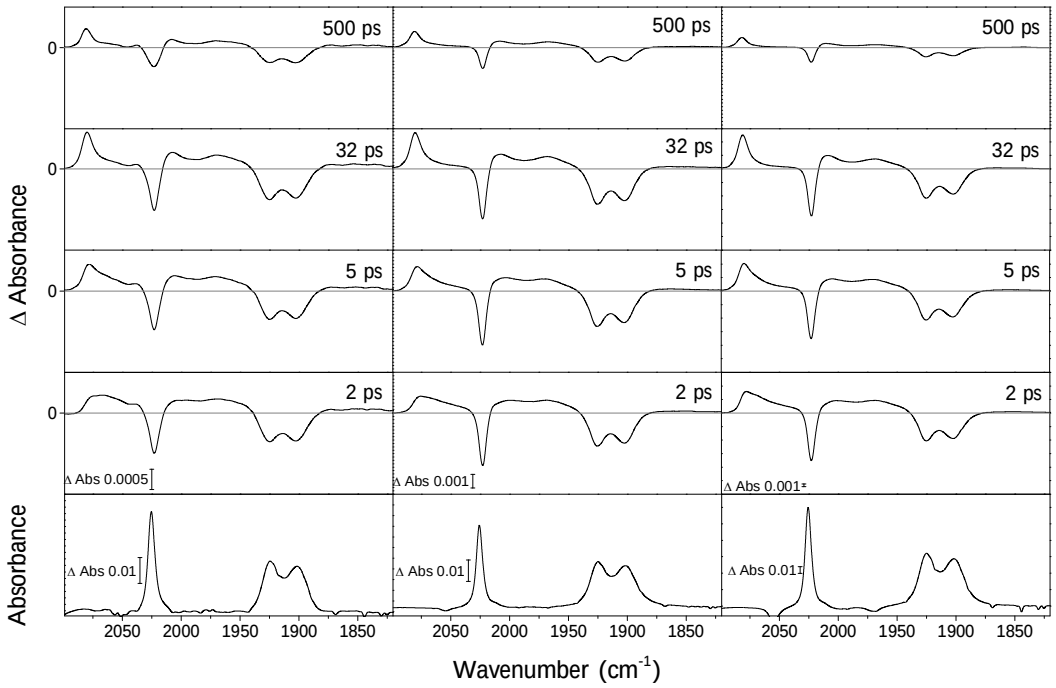

Figure A-4: FTIR (a) and TRIR (b-e) spectra in the CO IR region in CH_2Cl_2 following 400 nm photoexcitation for Re(dppp2) (left), Re(dppp3) (middle) and Re(dpp2Br) (right). The FTIR shown was acquired in d-DMSO due to poor solubility.

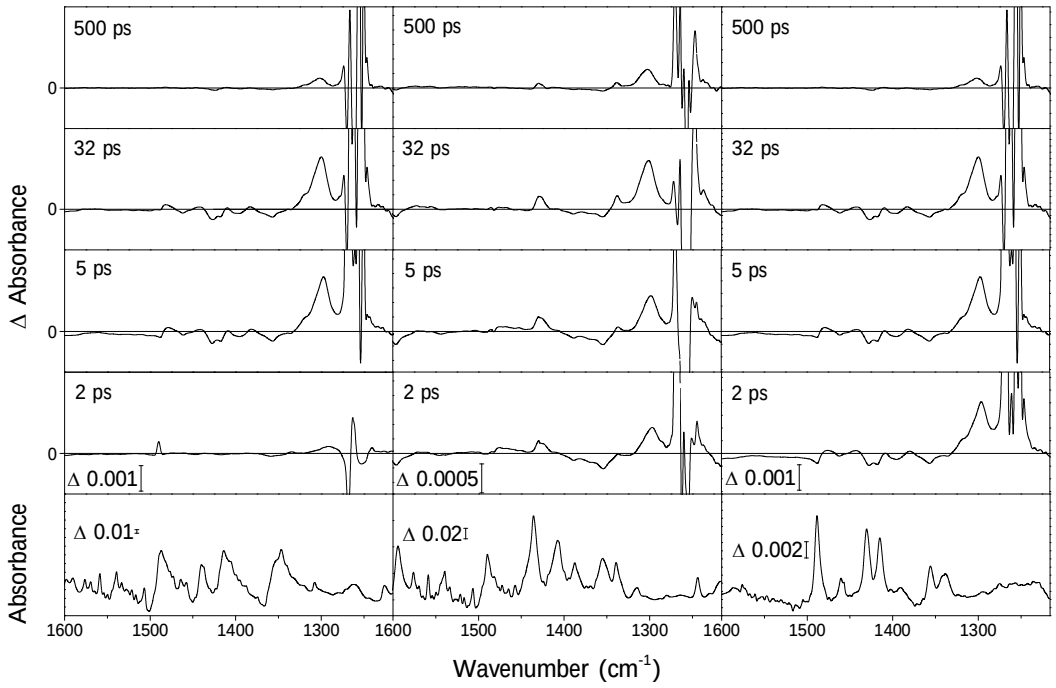

Figure A-5: FTIR (a) and TRIR (b-e) spectra in the FP IR region in CH_2Cl_2 following 400 nm photoexcitation for Re(dppp2) (left), Re(dppp3) (middle) and Re(dpp2Br) (right). The FTIR shown was acquired in the solid state for Re(dppp2) and Re(dppp3) and in d-DMSO for Re(dppp2Br) due to poor solubility.

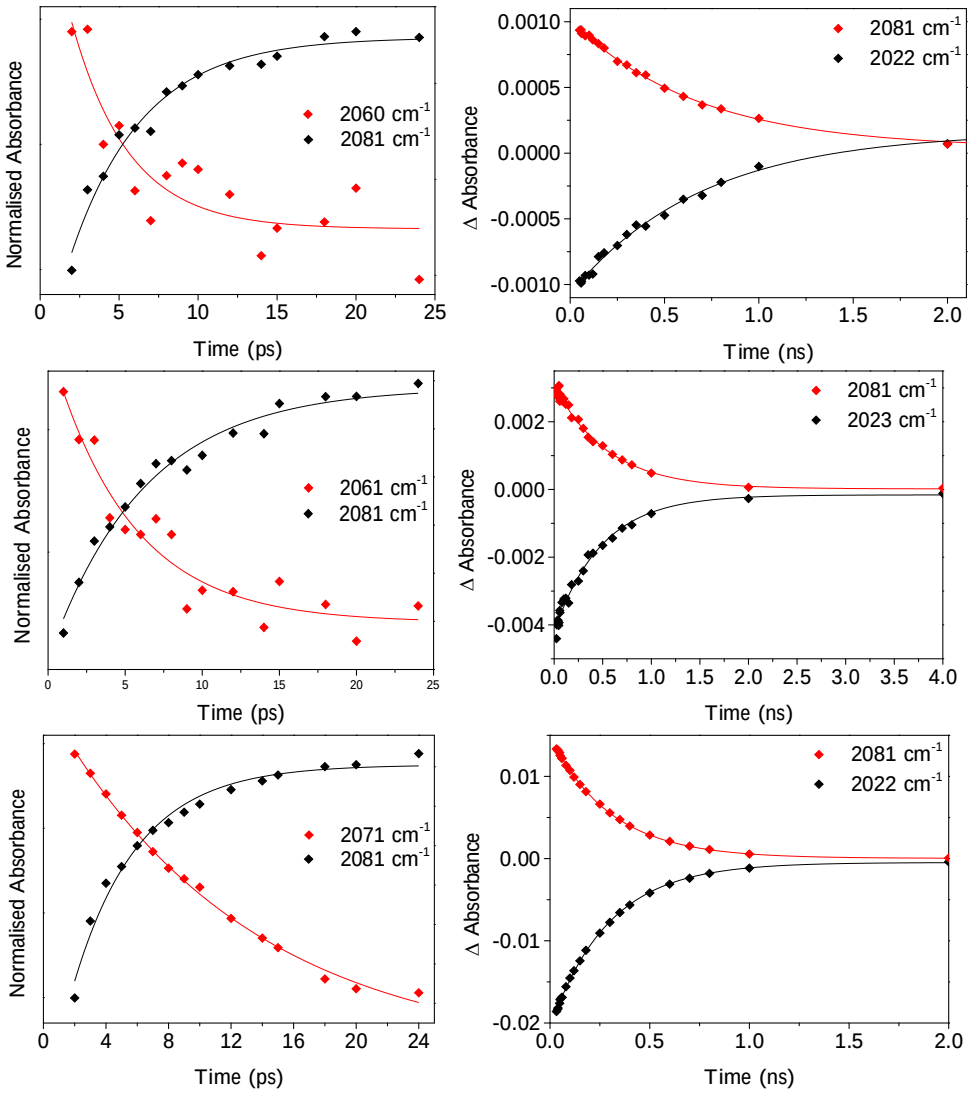

Figure A-6: The kinetics of Re(dppp2) (top), Re(dppp3) (middle) and Re(dppp2Br) (bottom) in CH_2Cl_2 following photoexcitation at 400 nm. The decay of the transient band at *ca.* 2060-2070 cm^{-1} assigned to a ^{3}MLCT(phen) state, in good agreement with the growth of the band at *ca.* 2081 cm^{-1} assigned to a ^{3}MLCT(phz) state (left). The decay of the band at 2081 cm^{-1} assigned to the ^{3}MLCT(phz) state in good agreement with the growth of the band at *ca.* 2022 cm^{-1} assigned to the parent (right).

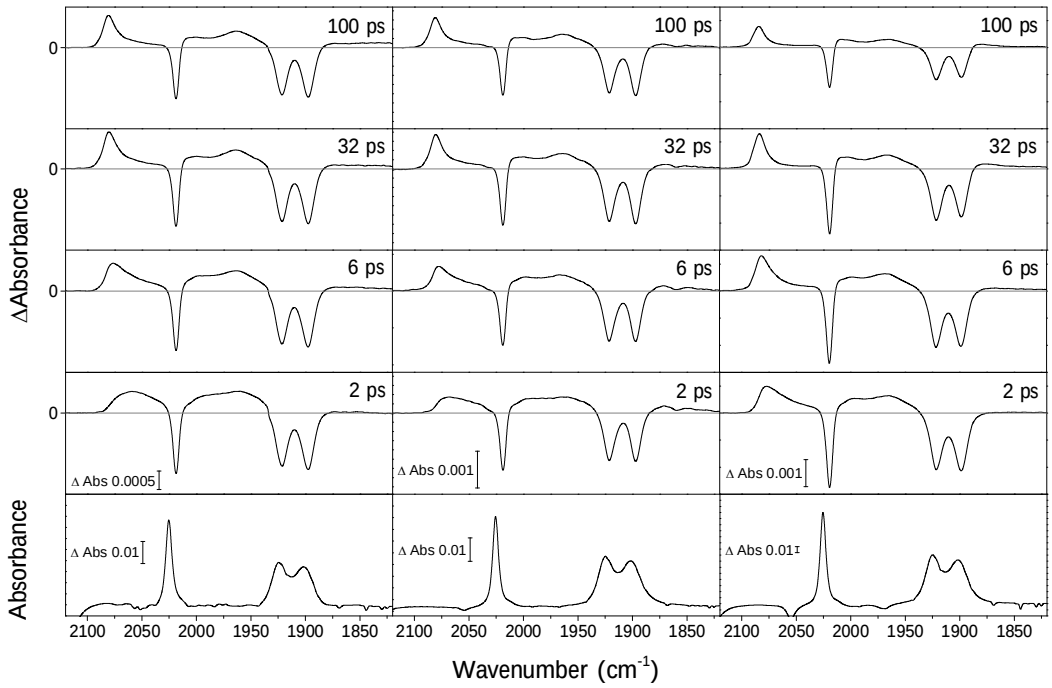

Figure A-7: FTIR (a) and TRIR (b-e) spectra in the CO IR region in THF following 400 nm photoexcitation for Re(dppp2) (left), Re(dppp3) (middle) and Re(dpp2Br) (right). The FTIR shown was acquired in d-DMSO due to poor solubility.

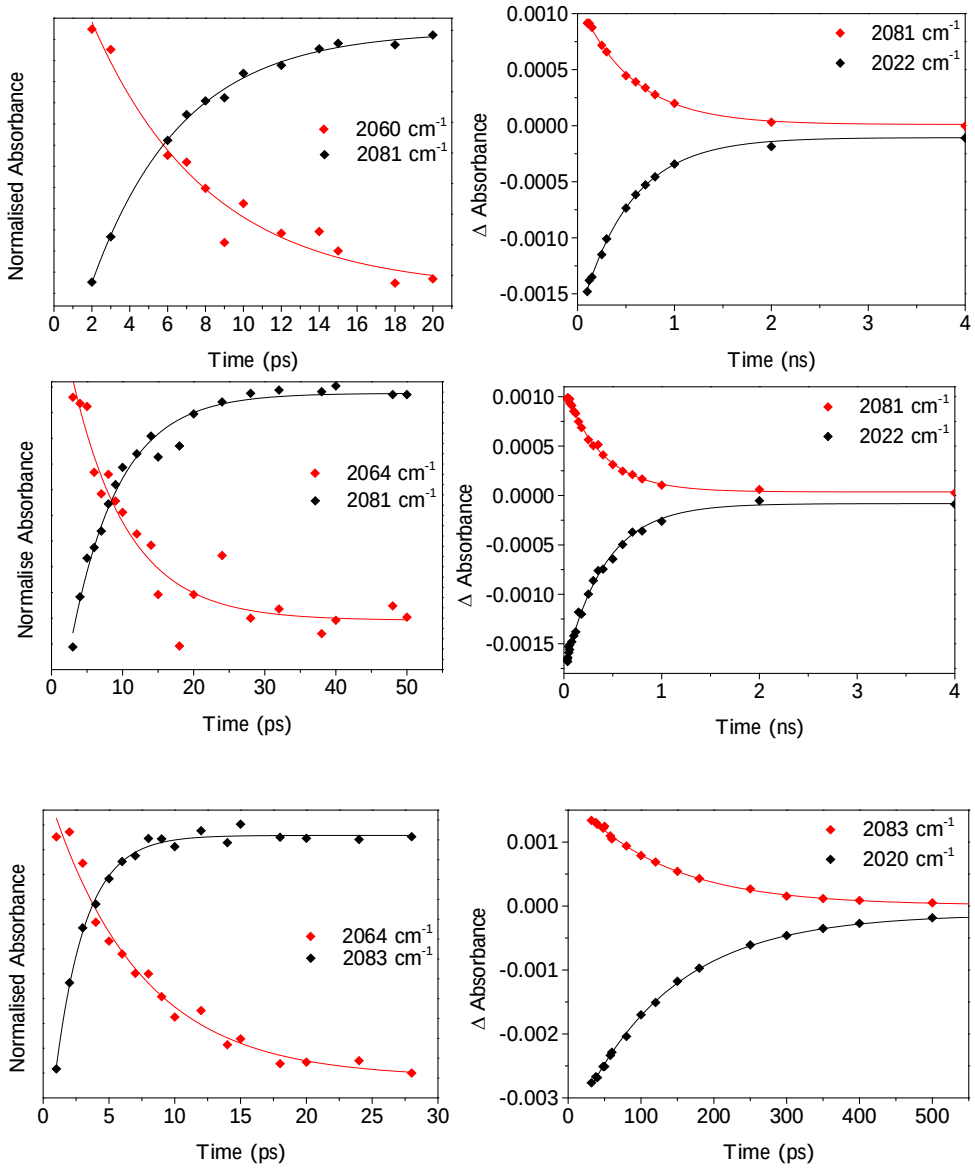

Figure A-8: The kinetics of Re(dppp2) (top), Re(dppp3) (middle), and Re(dppp2Br) (bottom) in THF following photoexcitation at 400 nm. The decay of the band at *ca.* 2060 cm^{-1} assigned to a ^{3}MLCT(phen) state, in good agreement with the growth of the band at *ca.* 2081 cm^{-1} assigned to a ^{3}MLCT(phz) state (left). Decay of the band at *ca.* 2081 cm^{-1} assigned to the ^{3}MLCT(phz) state in good agreement with the growth of the band at *ca.* 2022 cm^{-1} assigned to the parent (right).

A.2.3 Band Fitting

Below are the band fitting for Re(dppp2), Re(dppp3) and Re(dppp2Br) in CH_3CN, CH_2Cl_2, THF and toluene, showing the presence of transient band assigned to an MLCT(phz) state and a transient band assigned to MCLT(phen) state.

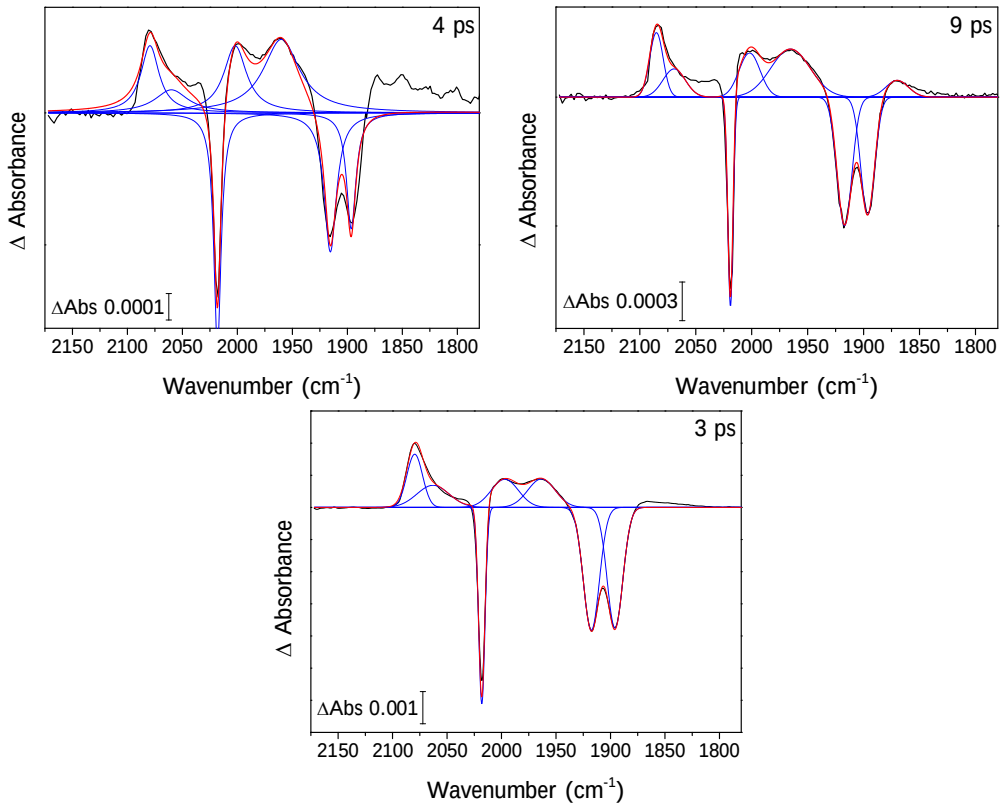

Figure A-9: Band fitted spectra in d-DMSO following 400 nm photoexcitation where bands assigned to the MLCT(phen) and MLCT(phz) states are observed for Re(dppp2) (top, left), Re(dppp3) (top, right) and Re(dppp2Br) (bottom).

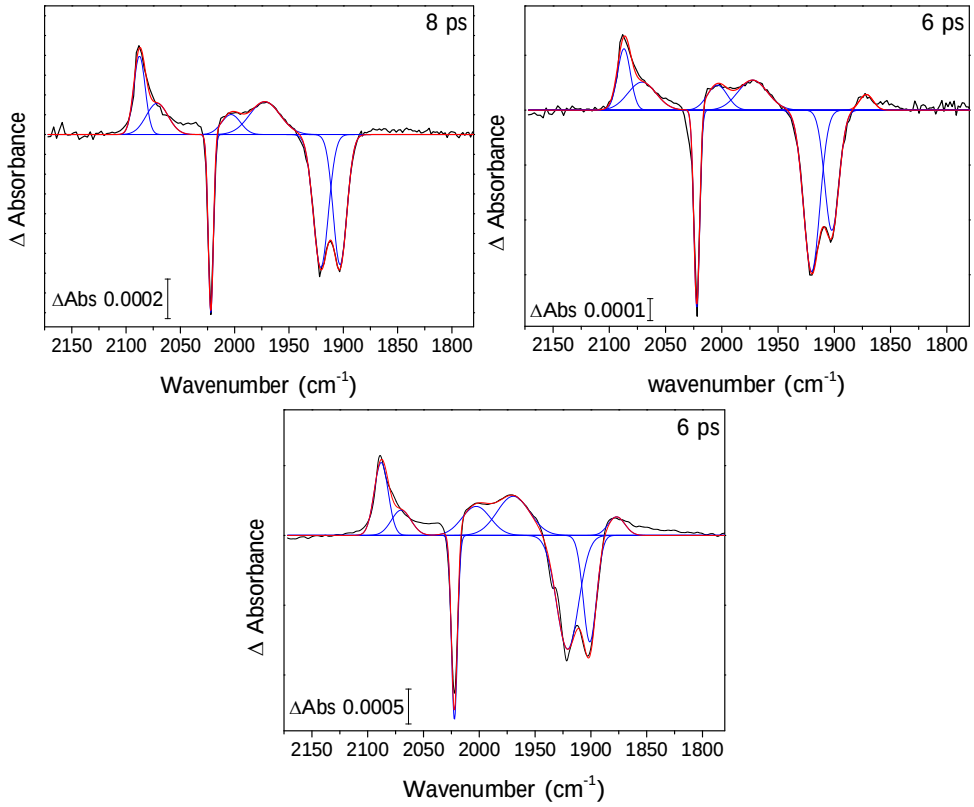

Figure A-10: Band fitted spectra confirming the presence of MLCT(phen) and MLCT(phz) states in CH_3CN for Re(dppp2) (top, left), Re(dppp3) (top, right) and Re(dppp2Br) (bottom).

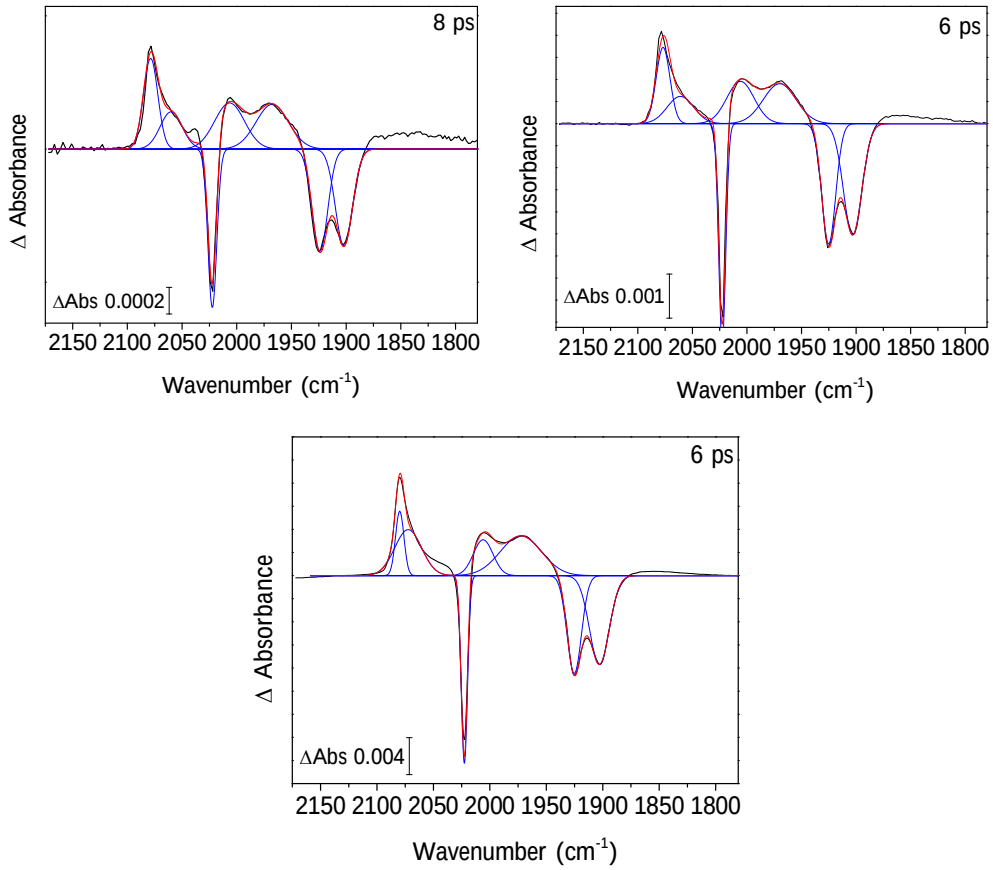

Figure A-11: Band fitted spectra confirming the presence of MLCT(phen) and MLCT(phz) states in CH_2Cl_2 for Re(dppp2) (top, left), Re(dppp3) (top, right) and Re(dppp2Br) (bottom).

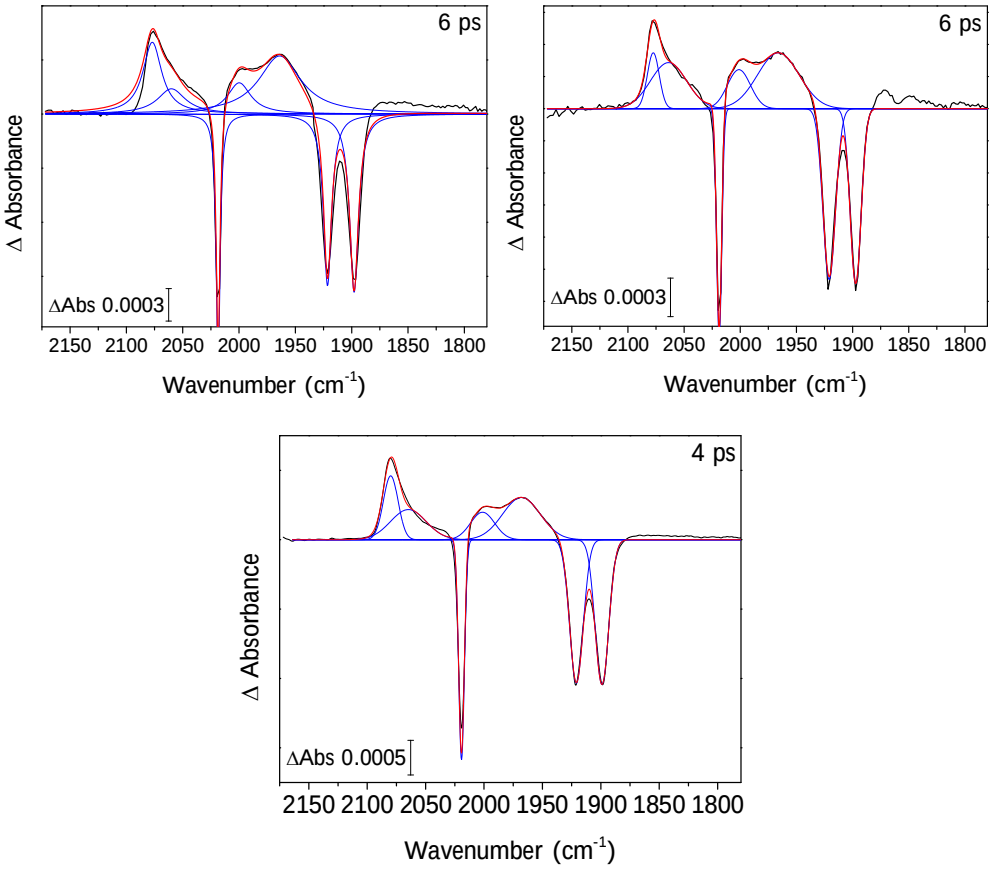

Figure A-12: Band fitted spectra confirming the presence of MLCT(phen) and MLCT(phz) states in THF for Re(dppp2) (top, left), Re(dppp3) (top, right) and Re(dppp2Br) (bottom).

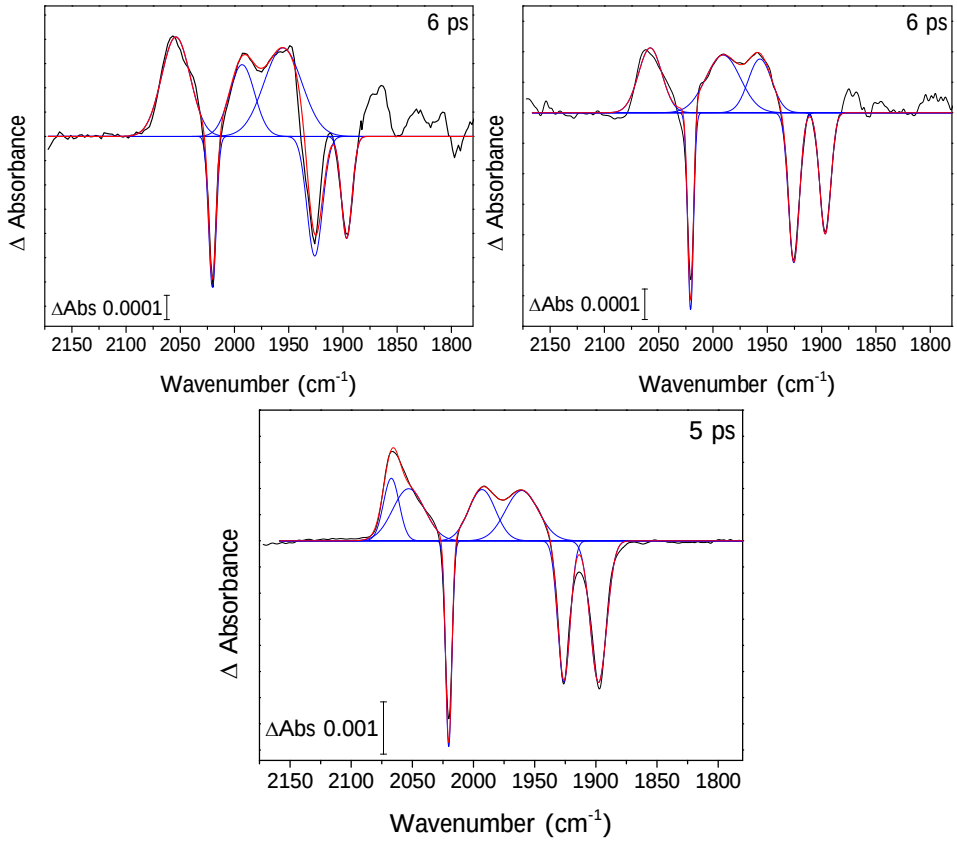

Figure A-13: Band fitted spectra confirming the presence of MLCT(phen) state in Toluene for Re(dppp2) (top, left), Re(dppp3) (top, right) and MLCT(phen) and MLCT(phz) states for Re(dppp2Br) (bottom).

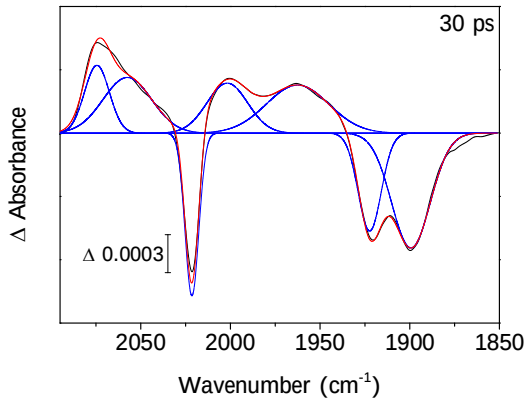

Figure A-14: Band fitting confirming the presence of 2075 and 2061 cm^{-1} bands assigned to MLCT(phz) and MLCT(phen) in CH_2Cl_2 for Re(dppz-I) following 400 nm photoexcitation.

A.3 Chapter 4

A.3.1 Anodic and cathodic peak current as a function of scan rate

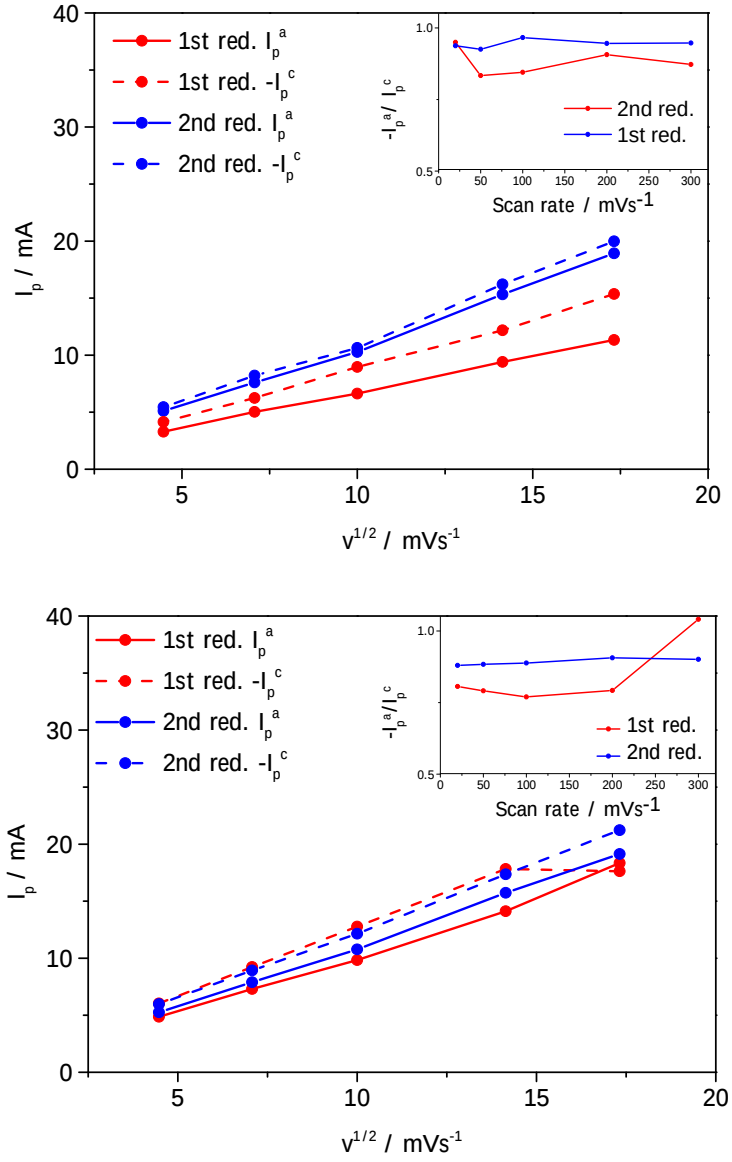

Figure A-15: The reversible behaviour of both [Re(dppz-12-NO_2)$(CO)_3$Cl] (top) and [Re(dppz-13-NO_2)$(CO)_3$Cl] (bottom) from CV experiments. The near-linear relationship between the square root of the scan rate and anodic (i_p^a) and cathodic (i_p^c) peak currents. Additionally the ratio of peak current of each reduction process as a function of scan rate (inset).

A.4 Chapter 6

A.4.1 Calibration of KTπ* values

Below details the process used to calibrate the experimentally obtained KT(π*) values to previously determined literature values.

Fit of density vs. Emission (ν) $\nu=(-4.93E\text{-}5\times e^{(\frac{\rho}{53.4})})+26000$

Rearrange to give ρ: $\rho=53.36284\times\ln(\frac{\nu-25600}{-4.93E\text{-}5})$

Fit of density vs. KTπ* is $KT\pi^{*}=0.00325\rho-3.98$

Fit for density vs KTπ* by Yonker et al is $KT\pi^{*} = 0.000375\rho - 0.343$

Therefore by calibrating the density vs KTπ* values to those obtained by yonker et al gives the equation for density vs KTπ* as

$$KT\pi^{*}=\left(\frac{3.76E\text{-}4}{0.00325}\right)(0.00325\rho)-0.343$$

Which rearranged gives:

$$KT\pi^{*}=0.116\times0.00325\left(53.4\times\ln\left(\frac{\nu-25600}{-4.93E\text{-}5}\right)\right)-0.343$$

Further rearrangement gives:

$$KT\pi^{*}=3.76E\text{-}4(53.4\times\ln\left(\frac{\nu-26000}{-4.93E\text{-}5}\right)-0.343$$

A.5 NMR spectra for complexes synthesised within this work

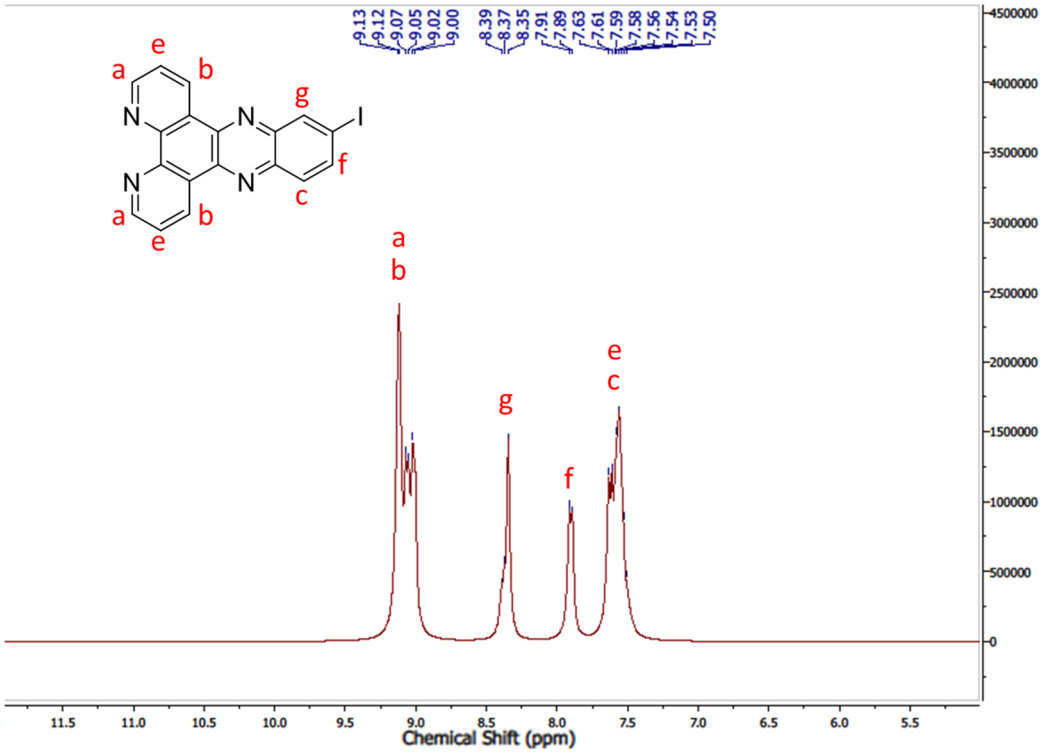

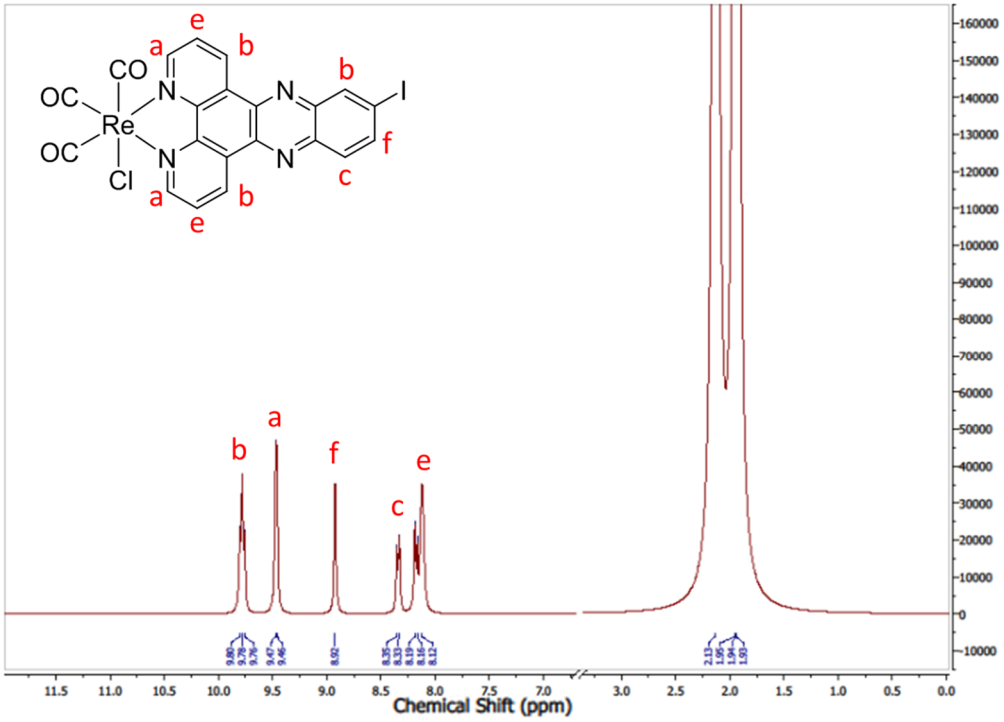

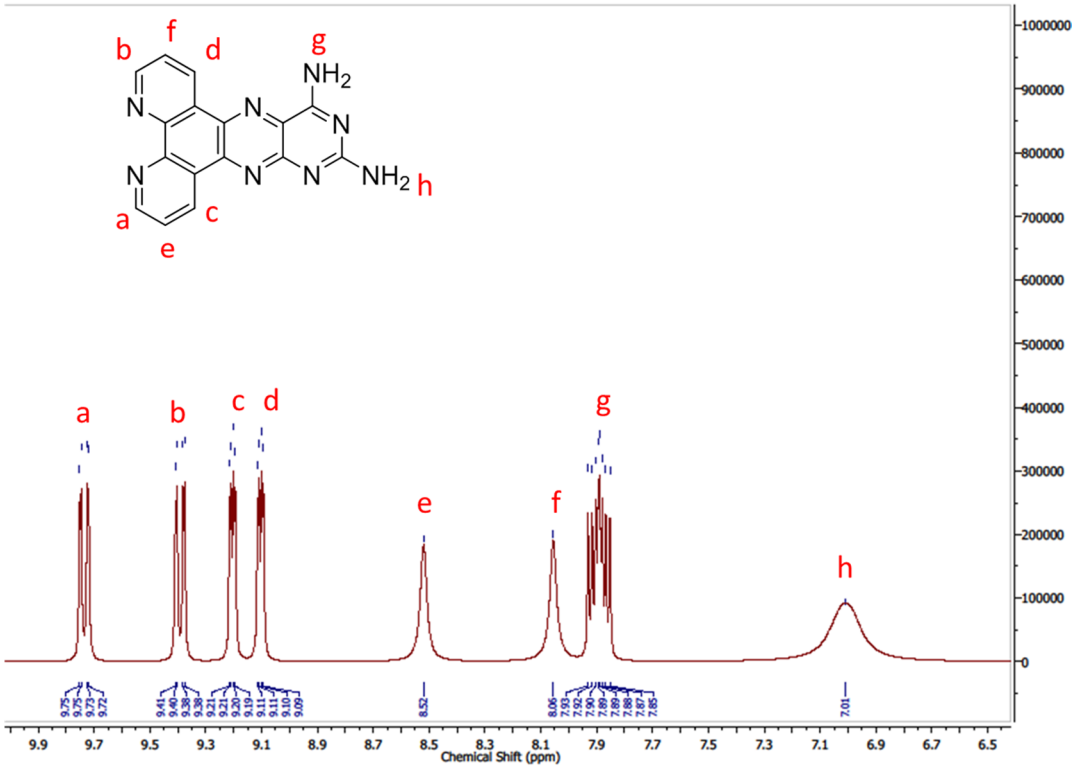
b
f
d
g
NH2
N
N
N
N
N
N
NH2
h
a
c
e
a
b
c
d
e
f
g
h
Chemical Shift (ppm)

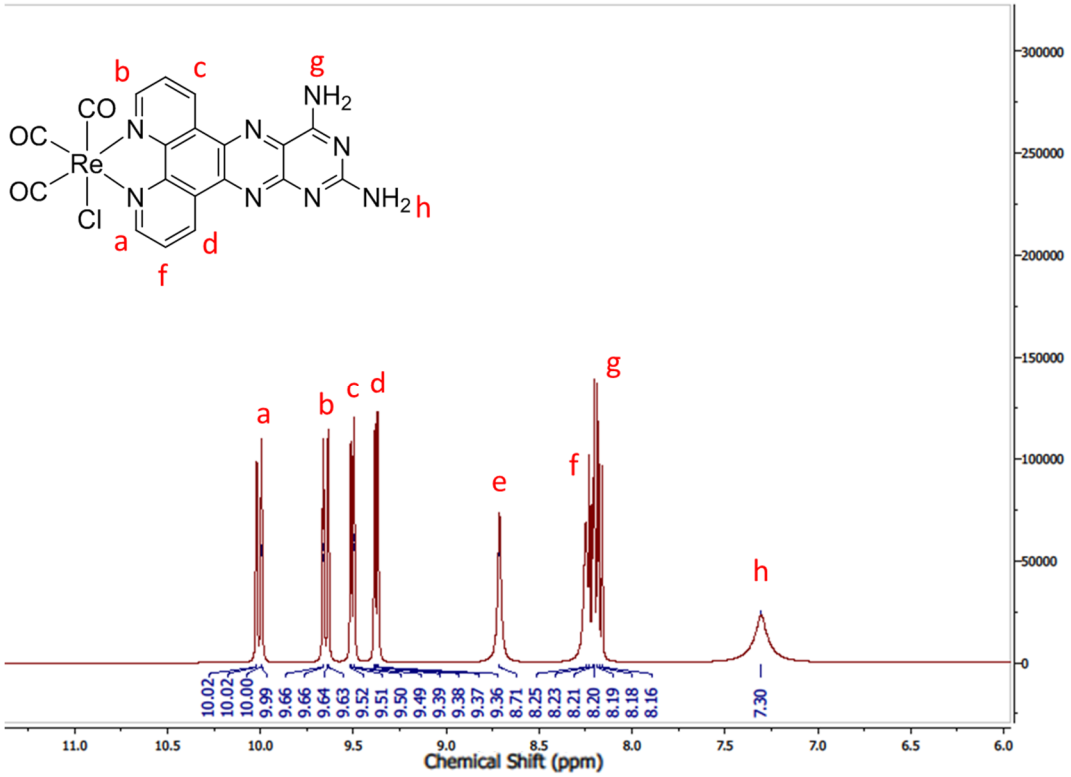
b
c
g
CO
NH2
OC
Re
N
N
N
N
OC
N
N
N
NH2
h
Cl
a
d
f
a
b
c
d
e
f
g
h
Chemical Shift (ppm)

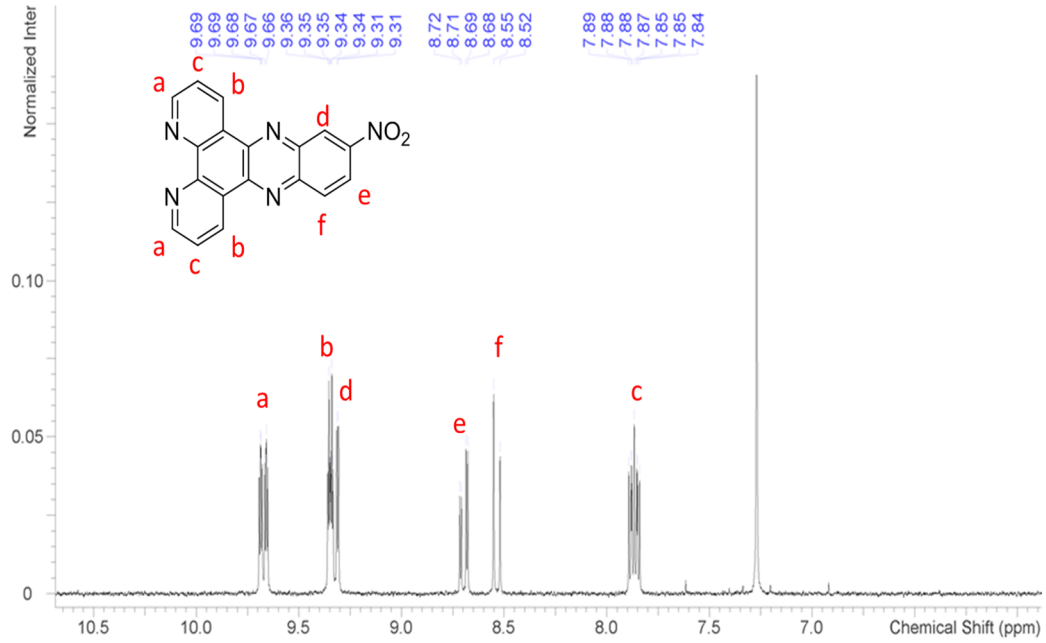
9.69
9.69
9.68
9.67
9.66
9.36
9.35
9.35
9.34
9.34
9.31
9.31
8.72
8.71
8.69
8.68
8.55
8.52
7.89
7.88
7.88
7.87
7.85
7.85
7.84
Normalized Inter
0.10
0.05
0
10.5
10.0
9.5
9.0
8.5
8.0
7.5
7.0
Chemical Shift (ppm)
NO2

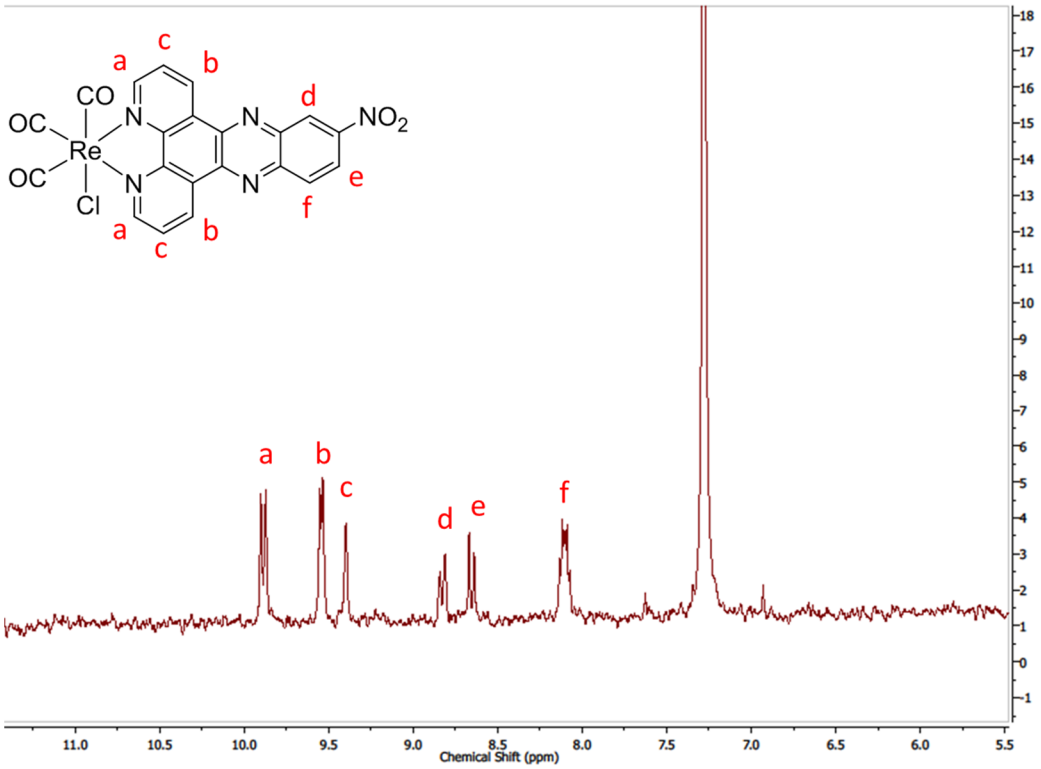
CO
OC
OC
Re
Cl
NO2
11.0
10.5
10.0
9.5
9.0
8.5
8.0
7.5
7.0
6.5
6.0
5.5
Chemical Shift (ppm)

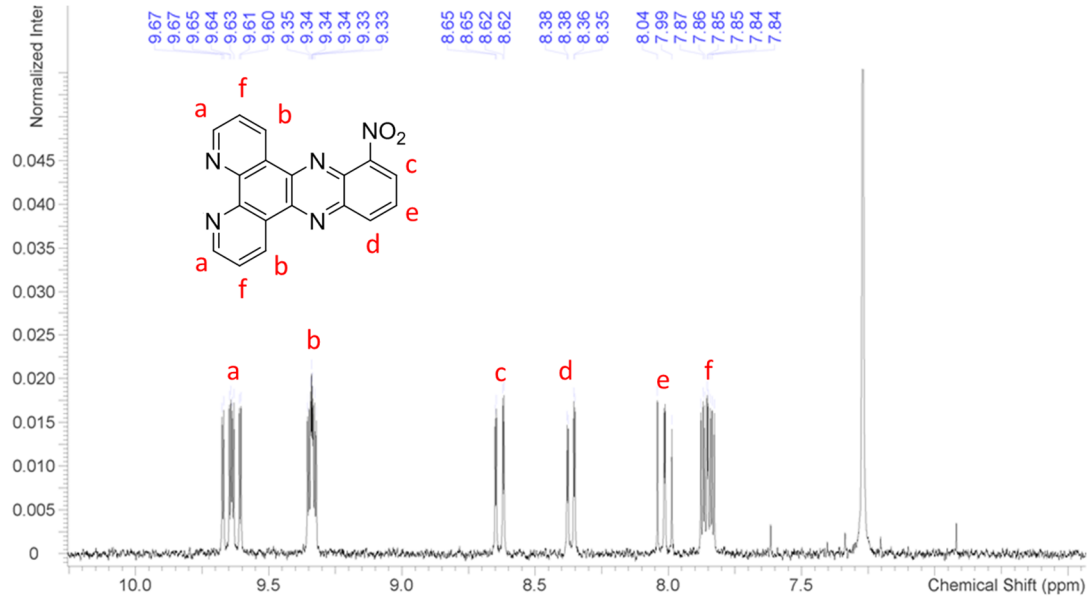
Normalized Inter
9.67 9.67 9.65 9.64 9.63 9.61 9.60 9.35 9.34 9.34 9.34 9.33 9.33
8.65 8.65 8.62 8.62
8.38 8.38 8.36 8.35
8.04 7.99 7.87 7.86 7.85 7.85 7.84 7.84
NO2
a b c d e f
0.045 0.040 0.035 0.030 0.025 0.020 0.015 0.010 0.005 0
10.0 9.5 9.0 8.5 8.0 7.5
Chemical Shift (ppm)

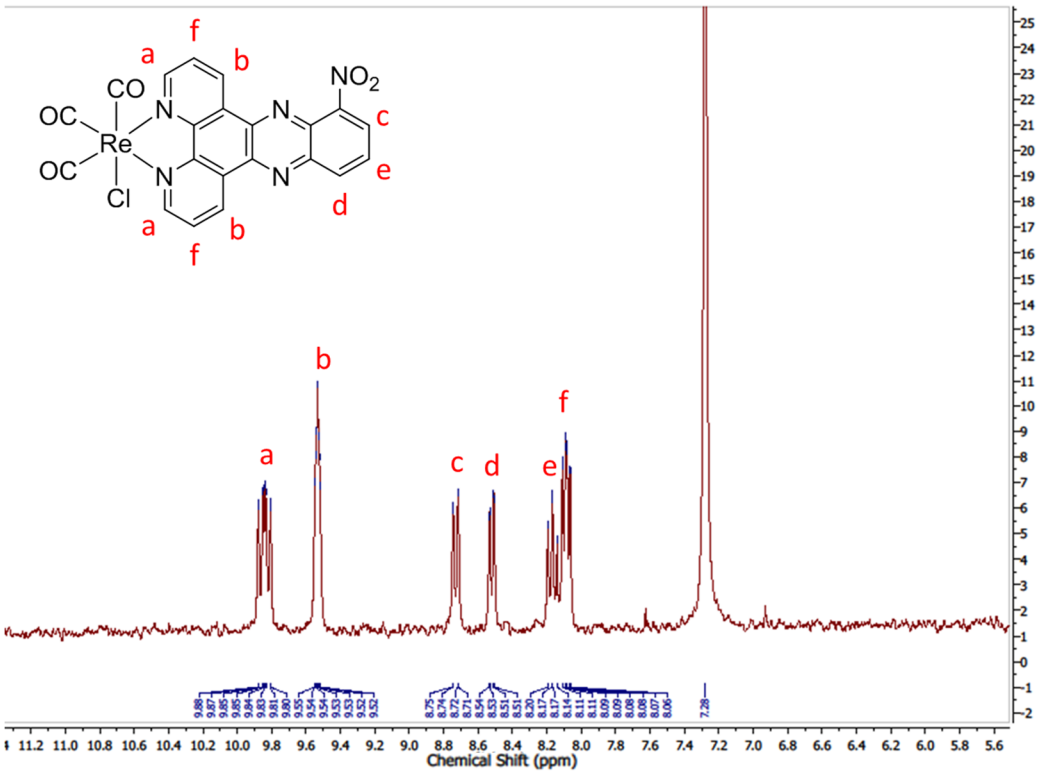
CO
OC
OC
Re
Cl
N
NO2
a b c d e f
Chemical Shift (ppm)

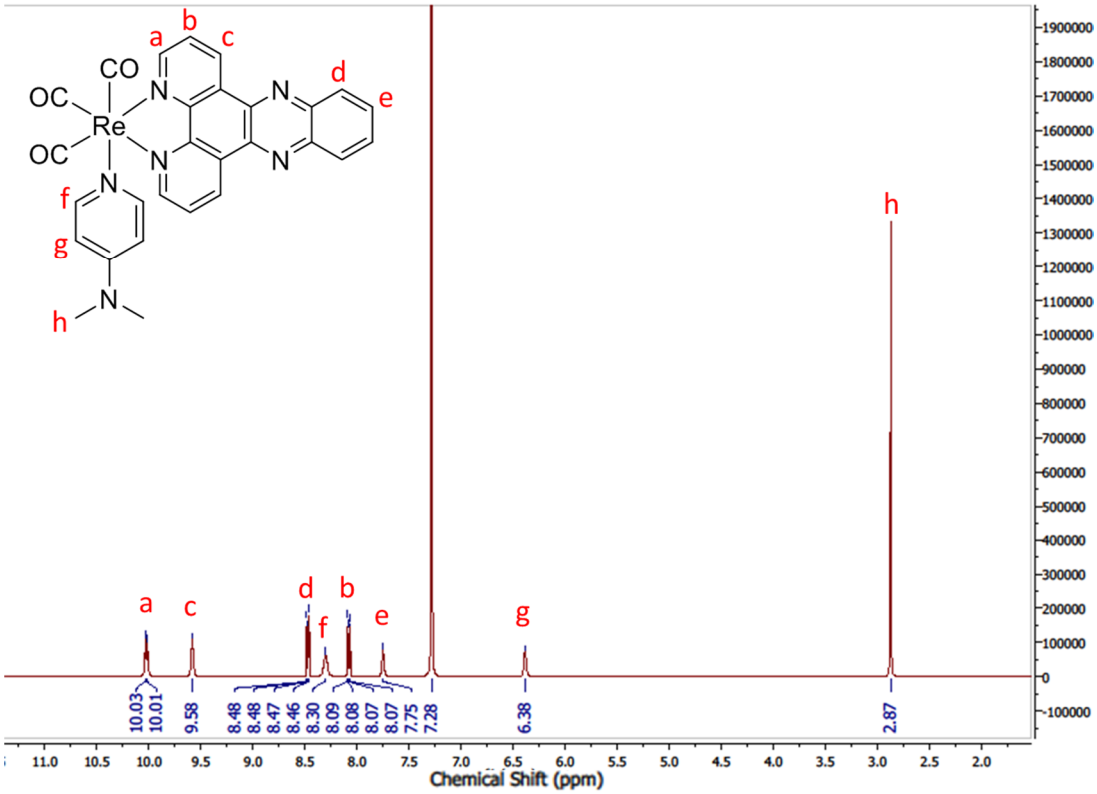
a
b
c
d
e
f
g
h
CO
OC
OC
Re
N
10.03
10.01
9.58
8.48
8.48
8.47
8.46
8.30
8.09
8.08
8.07
8.07
7.75
7.28
6.38
2.87
Chemical Shift (ppm)

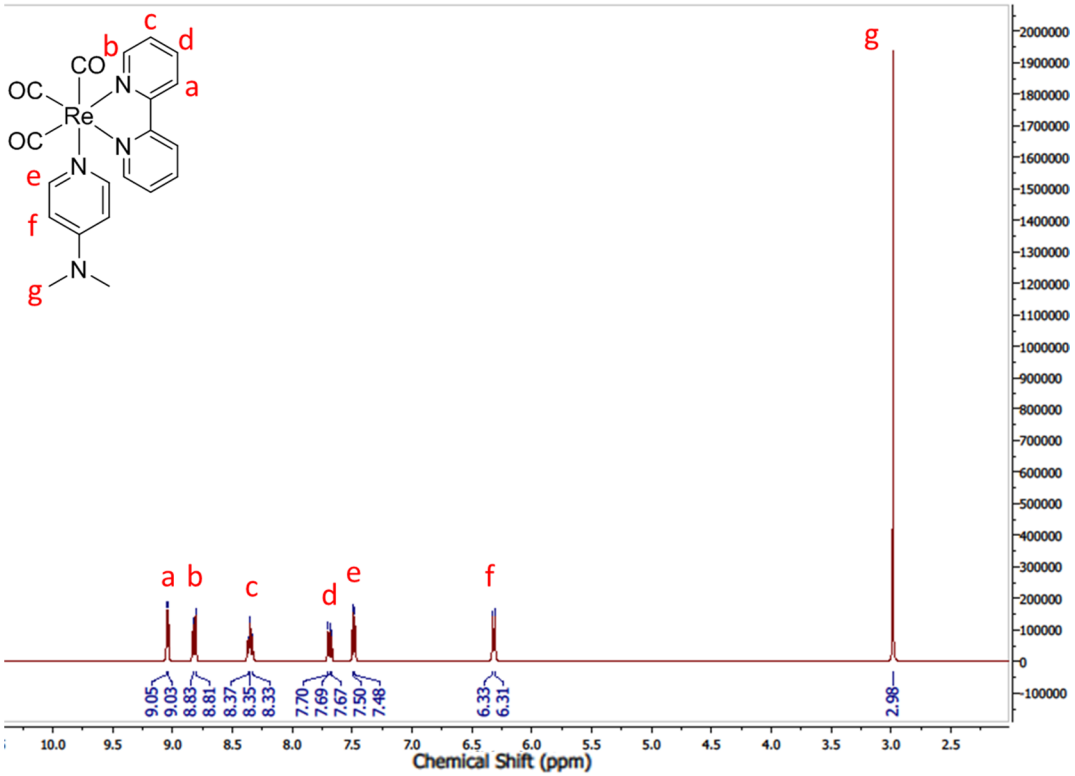
a
b
c
d
e
f
g
CO
OC
OC
Re
N
9.05
9.03
8.83
8.81
8.37
8.35
8.33
7.70
7.69
7.67
7.50
7.48
6.33
6.31
2.98
Chemical Shift (ppm)

Appendix B

Below are the DFT calculated frontier molecular orbitals including the energies, discussed within this Thesis.

[Re(dppz)(CO)$_3$Cl]			**[Re(dppz-I)(CO)$_3$Cl]**		
MO	Energy (eV)		MO	Energy (ev)	
L+2	-2.39	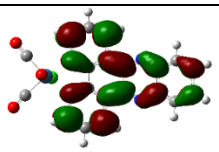	L+2	-2.53	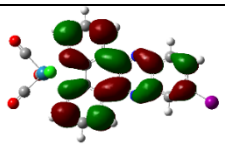
L+1	-2.64	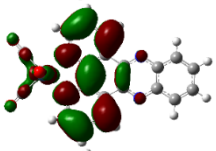	L+1	-2.72	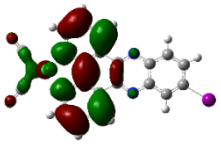
LUMO	-3.16	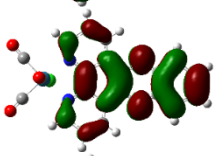	LUMO	-3.32	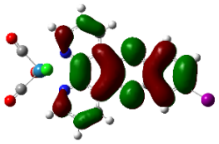
HOMO	-5.58	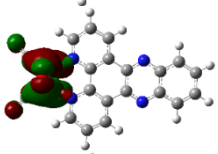	HOMO	-5.66	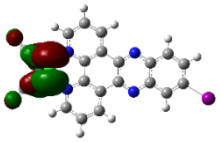
H-1	-5.66	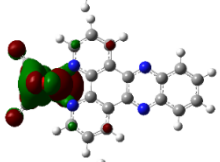	H-1	-5.71	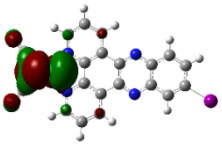
H-2	-6.34	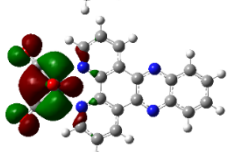	H-2	-6.39	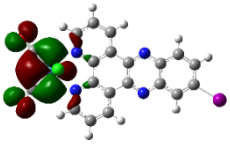
H-3	-6.86	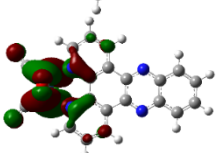	H-3	-6.94	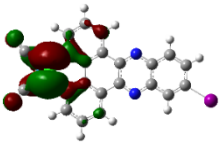
H-4	-6.88	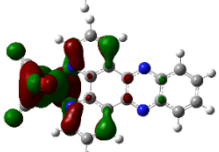	H-4	-6.94	
H-5	-7.10	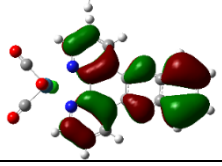	H-5	-7.07	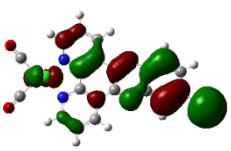

MO	**Re(dppz-NPh_2)**	**Re(dppz-(Ph-$(OCH_3)_2NPh_2$)**	**Re(dppz-$PhNPh_2$)**	**Re(dppz-$(PhNPh_2)_2$)**
L+2	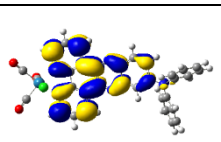	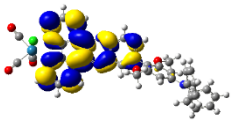	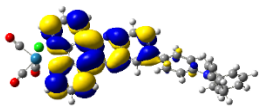	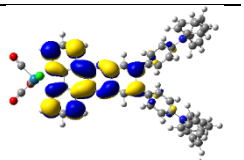
L+1	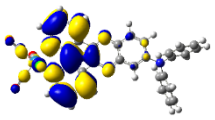	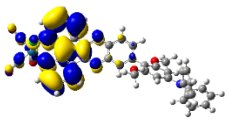	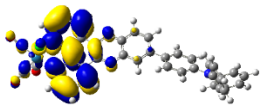	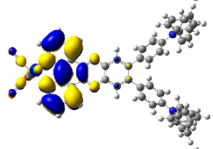
L	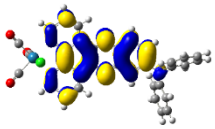	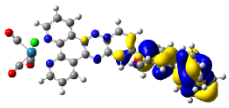	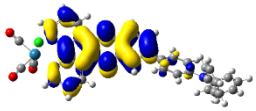	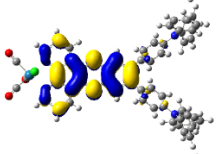
H	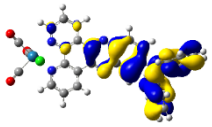	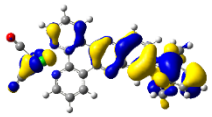	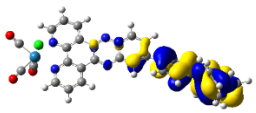	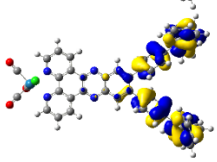
H-1	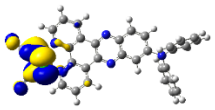	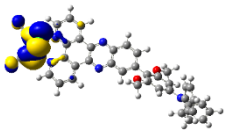	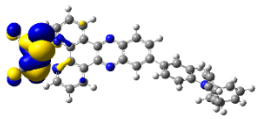	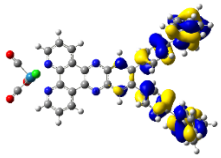
H-2	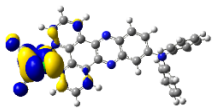	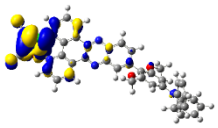	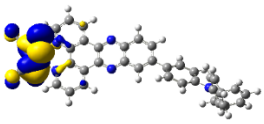	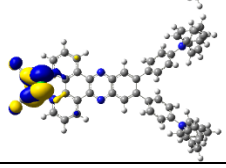

MO	Energy e(V)			
	dppz-NPh_2	**dppz-(Ph-$(OCH_3)_2NPh_2$**	**dppz-$PhNPh_2$**	**dppz-$(PhNPh_2)_2$**
L+2	-0.88	-0.89	-0.95	-1.02
L+1	-1.21	-1.23	-1.26	-1.29
L	-1.61	-1.63	-1.73	-1.80
H	-6.69	-6.40	-6.40	-6.35
H-1	-7.43	-7.43	-7.45	-6.45
H-2	-7.50	-7.48	-7.50	-7.44

MO	[Re(dppp2)(CO)$_3$Cl]	[Re(dppp3)(CO)$_3$Cl]	[Re(dppp2Br)(CO)$_3$Cl]
L+2	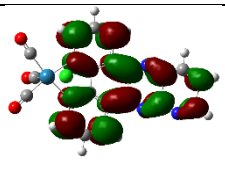	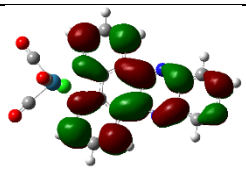	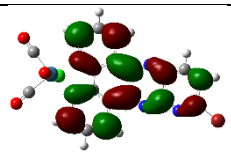
L+1	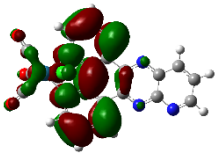	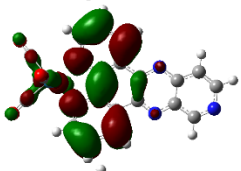	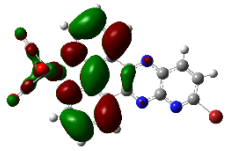
L	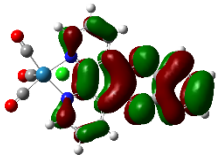	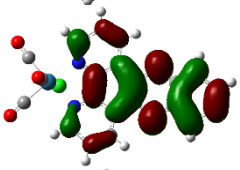	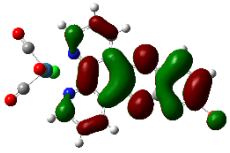
H	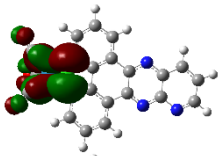	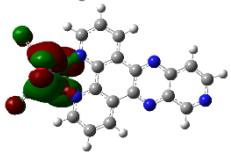	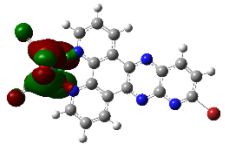
H-1	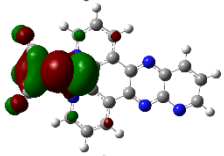	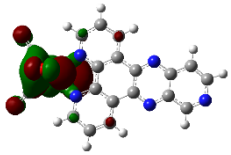	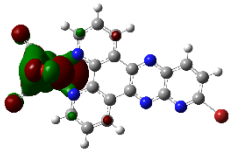
H-2	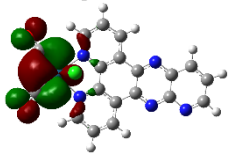	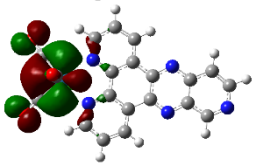	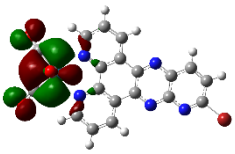
H-3	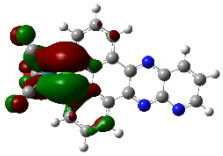	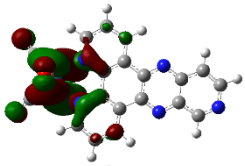	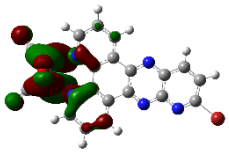
H-4	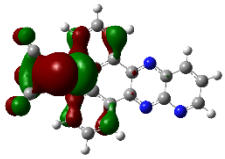	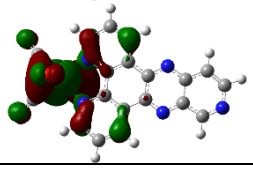	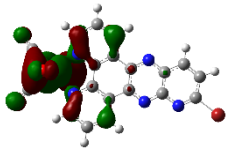

MO	Energy (eV)		
	[Re(dppp2)(CO)$_3$Cl]	**[Re(dppp3)(CO)$_3$Cl]**	**[Re(dppp2Br)(CO)$_3$Cl]**
L+2	-2.53	-2.64	-2.67
L+1	-2.72	-2.80	-2.80
LUMO	-3.37	-3.48	-3.54
HOMO	-5.63	-5.71	-5.69
H-1	-5.71	-5.71	-5.77
H-2	-6.39	-6.48	-6.45
H-3	-6.91	-6.99	-6.99
H-4	-6.94	-7.02	-6.99

	[Re(dppz-12-NO_2)$(CO)_3$Cl]		**[Re(dppz-12-NO_2)$(CO)_3$Cl]**	
MO	Energy (eV)		Energy (eV)	
L+2	-3.10	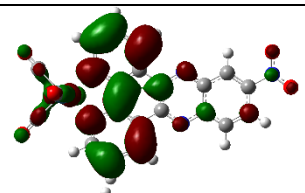	-2.88	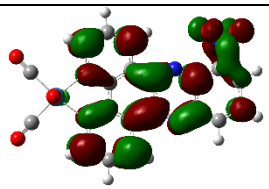
L+1	-3.32	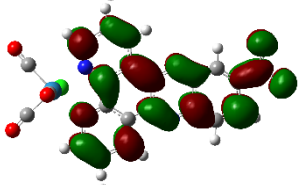	-2.99	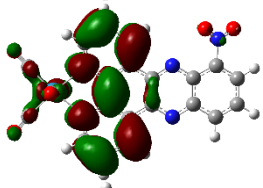
LUMO	-3.97	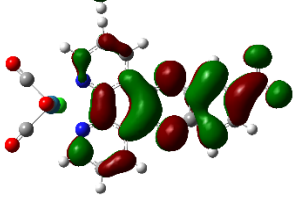	-3.78	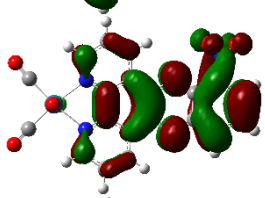
HOMO	-5.96	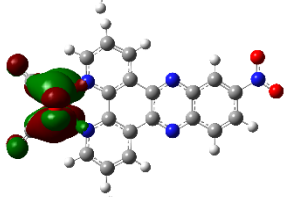	-5.77	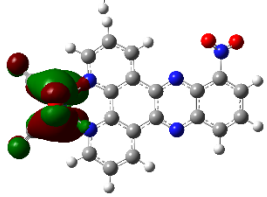
H-1	-6.01	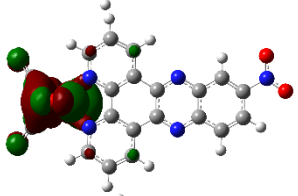	-5.85	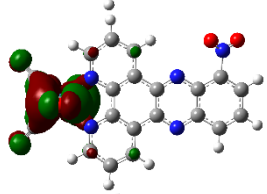
H-2	-6.72	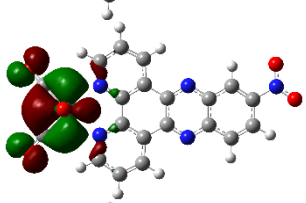	-6.53	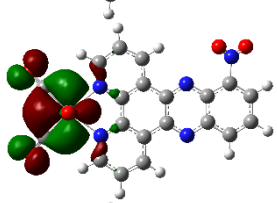
H-3	-6.78	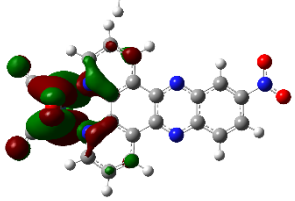	-7.07	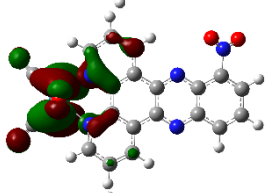
H-4	-6.80		-7.07	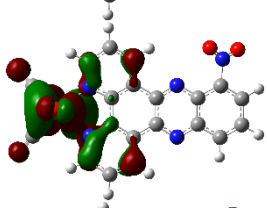
H-5	-7.35		-7.59	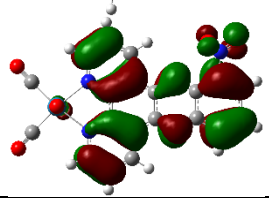

$[Re(bpy)(CO)_3(DMAP)]^+$			$[Re(bpy)(CO)_3Cl]$		
MO	Energy (eV)		MO	Energy (eV)	
L+1	-5.279	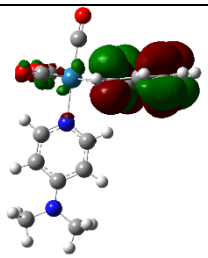	L+1	-2.395	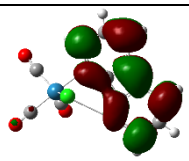
LUMO	-5.551	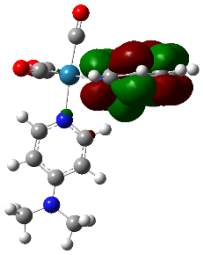	LUMO	-2.612	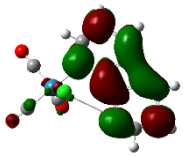
HOMO	-9.442	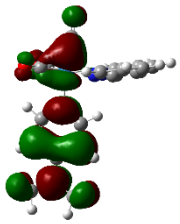	HOMO	-6.286	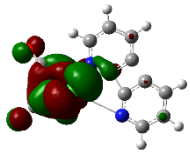
H-1	-9.470	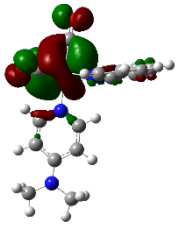	H-1	-6.531	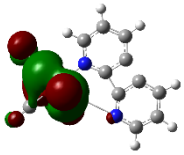
H-2	-9.551	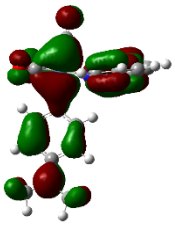	H-2	-6.721	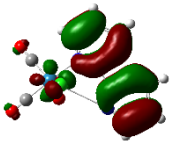
H-3	-9.662	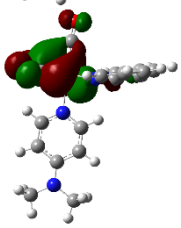	H-3	-6.776	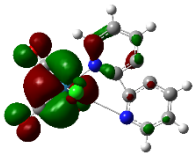

[Re(dppz)(CO)$_3$(DMAP)]$^+$

MO	Energy (eV)	
L+2	-4.762	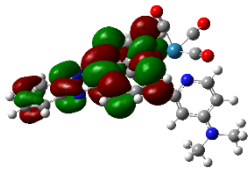
L+1	-5.143	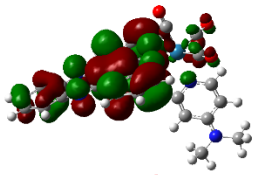
LUMO	-5.361	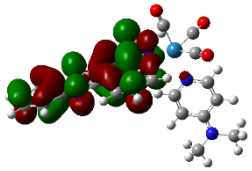
HOMO	-8.463	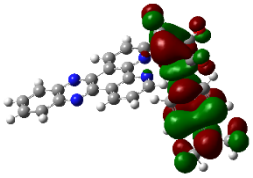
H-1	-8.980	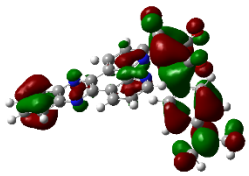
H-2	-9.116	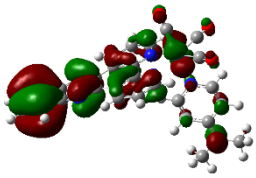
H-3	-9.143	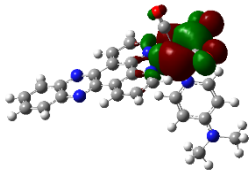
H-4	-9.143	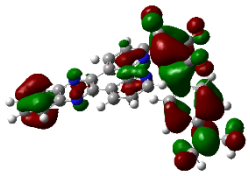
H-5	-9.606